AJNR

AMERICAN JOURNAL OF NEURORADIOLOGY

APRIL 2015
VOLUME 36
NUMBER 4
WWW.AJNR.ORG

THE JOURNAL OF DIAGNOSTIC AND INTERVENTIONAL NEURORADIOLOGY

Cerebral microbleeds and dementia
Intracranial atherosclerosis at 7T
SWI in pediatric stroke

Official Journal ASNR • ASFNR • ASHNR • ASPNR • ASSR

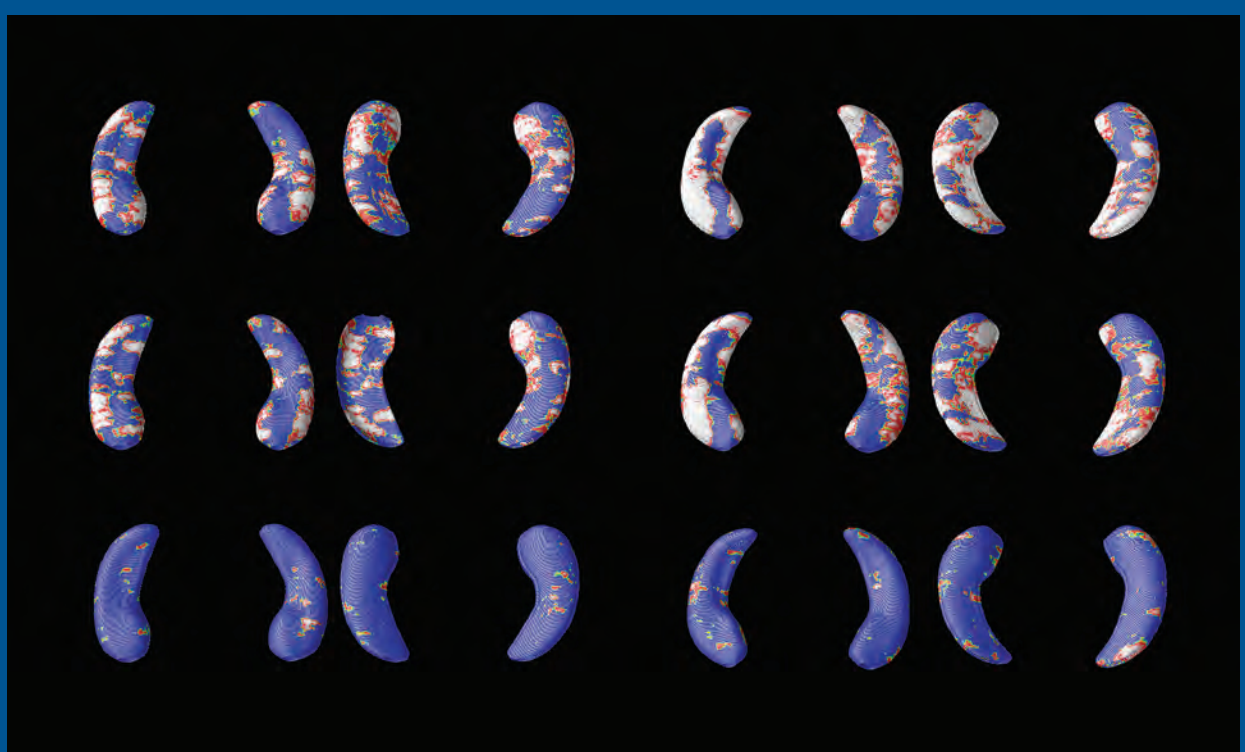

Advanced

by MicroVention

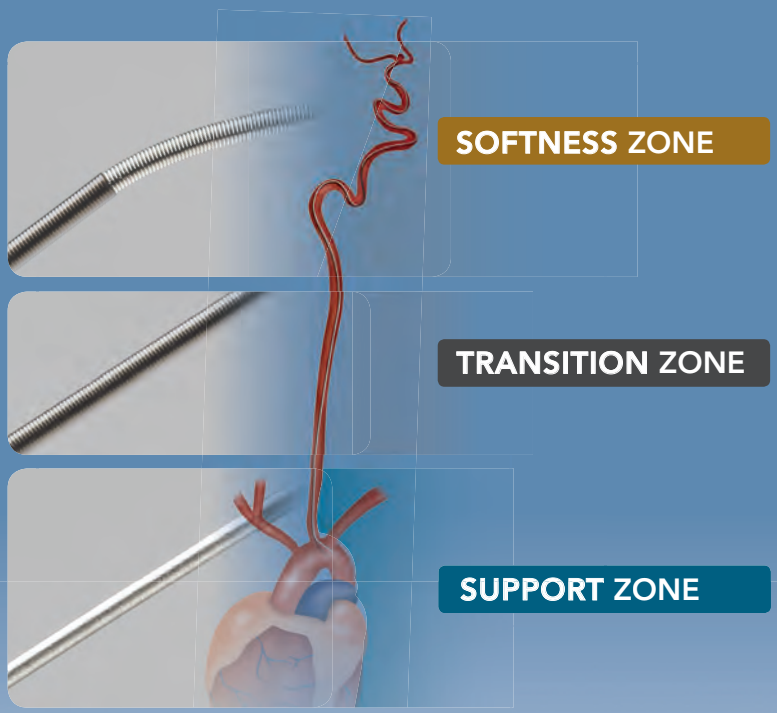

V-Trak® Advanced Coil System

ENHANCED CONTROL TO MAXIMIZE COIL PERFORMANCE

The **V-Trak® Advanced Coil System**, the next generation to power the performance of our most technically advanced line of coils. Offering the optimal combination of support and flexibility.

microvention.com

CE 0297

Support

by MicroVention

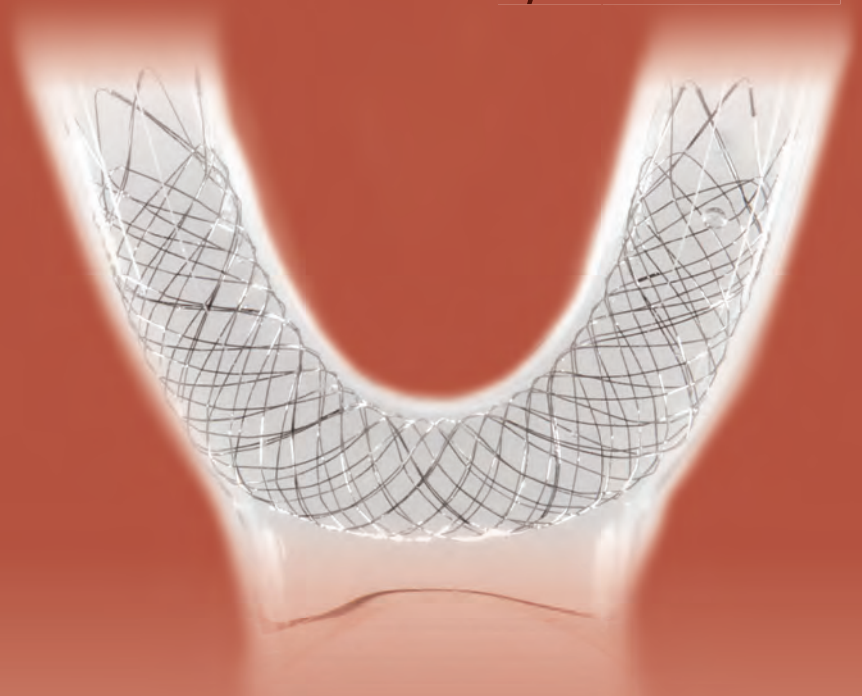

LVIS® Intraluminal Support Device

LVIS® Jr. Intraluminal Support Device

LOW-PROFILE VISUALIZED INTRALUMINAL SUPPORT

The **LVIS® and LVIS® Jr. devices** are the next generation technology for optimal intraluminal support and coverage for stent-assist coil procedures.

Used with Headway® Microcatheter

RX only.

Humanitarian Device:
Authorized by Federal Law for use with bare platinum embolic coils for the treatment of unruptured, wide neck (neck ≥ 4 mm or dome to neck ratio < 2), intracranial, saccular aneurysms arising from a parent vessel with a diameter ≥ 2.5 mm and ≤ 4.5 mm. The effectiveness of this device for this use has not been demonstrated.

For more information or a product demonstration, contact your local MicroVention representative:

MicroVention® TERUMO

MicroVention, Inc.
Worldwide Headquarters PH +1.714.247.8000
1311 Valencia Avenue
Tustin, CA 92780 USA
MicroVention UK Limited PH +44 (0) 191 258 6777
MicroVention Europe, S.A.R.L. PH +33 (1) 39 21 77 46
MicroVention Deutschland GmbH PH +49 211 210 798-0

AJNR

ANNOUNCEMENT: THE NEW EDITOR-IN-CHIEF OF AJNR

On behalf of the Search Committee for Editor-in-Chief of the *AJNR*, I am pleased to announce that the new Editor-in-Chief starting July 1, 2015 will be Jeffrey S. Ross, MD.

First, I would like to thank all the other members of the Search Committee, including James Barkovich, Barton Branstetter, Harry Cloft, Nancy Fischbein, Tabassum Kennedy, Laurie Loevner, Robert Quencer, Alireza Radmanesh, Howard Rowley, Charles Strother, Jody Tanabe, Tina Young Poussaint, and Robert D. Zimmerman, as well as Karen Halm, James Gantenberg, and Angelo Artemakis, from ASNR Headquarters, for their work and dedication in this task. There were several qualified applicants for the position and the committee members devoted cumulatively hundreds of hours to a decision.

Second, I would like to thank Maurico Castillo who has built on the work of prior illustrious editors, Juan Taveras, Michael Huckman, Robert Quencer, and Robert Grossman. From its look to its organization to the quality of its articles, Mauricio has brought the journal into the forefront of all radiology journals. *AJNR* now ranks #2 in Impact Factor among all radiology journals. It is the premier clinical neuroimaging journal and we should all be proud that we are turning it over in stellar shape to a new editor.

Finally, I would like to take this opportunity to highlight Jeff's career. Jeff was graduated from the Medical College of Ohio, where he was ranked 1st in his class. He showed an early aptitude for his future field and was awarded the Clinical Neurosciences Award, as well as the Glidden L. Brooks Award for Superiority in All Phases of the Curriculum, the Award of Excellence in Pharmacology, and the Marion C. Anderson Award in Surgery. He then went on to do his residency in diagnostic radiology at the Cleveland Clinic where he served as Chief Resident. Residency was followed by neuroradiology fellowship at Case Western Reserve University and the University Hospitals of Cleveland.

After finishing his training, Jeff returned to the Cleveland Clinic, where he spent the next 19 years, becoming Professor of Radiology at the Cleveland Clinic Lerner College of Medicine of Case Western Reserve University and Head of Radiology Research at the Cleveland Clinic. In 2006, he left the Cleveland Clinic to relocate to Barrow Neurological Institute, where he serves as Professor of Radiology.

Jeff's involvement with *AJNR* began soon after finishing his training when he became a manuscript reviewer. Even that early, he had the judgment and capabilities to earn "Honors" for his reviews for several successive years. His abilities did not go unnoticed and he became an Editorial Board Member in 2000, followed by appointment to Senior Editor under Robert Grossman in 2006. In addition to his duties at the *AJNR*, Jeff serves or has served on the Editorial Board of many other journals, including *AJR, JCAT,* and *Investigative Radiology*.

At the ASNR, Jeff has served on numerous committees, including the Executive Committee and as Chair of the Nominating Committee. He is a founding member and President of the ASSR and has been involved in numerous committees of that organization. Other activities include the Program Committee of the RSNA, past President of the Eastern Neuroradiology Society, and numerous committees of the ACR. He was a board examiner for many years and continues to serve on the ABR Neuro Core examination committee. Most recently, he won the Neuroradiology Fellow Teacher of the Year award at Barrow Neurological Institute and the Gold Medal of the American Society of Spine Radiology.

Jeff's work in imaging of the spine is well known and he has over 100 peer-reviewed papers. Of these, a most important one was the carefully done seminal work utilizing contrast-enhanced MR imaging to differentiate recurrent disk from scar in the postoperative spine, involving precise correlation of imaging findings with exact surgical pathology. This concept is now, of course, basic to our interpretations of spine MR imaging and is used in our daily work. Although Jeff's legacy to imaging research will be his articles on the spine, his publications show a diversity of interests and include articles on sickle cell disease, aneurysms and other vascular lesions, new methods of imaging the internal auditory canals, in addition to many articles on MRA and advanced techniques. Jeff is an author or co-author on 23 papers that have been cited more than 100 times, and 2 that have been cited more than 1000 times. Given that 80% of published papers receive less than 10 citations, this is a significant achievement. Jeff has experience with both electronic and traditional publishing, serving as the lead author for spine within the StatDx and RadPrimer Web-based tools, and the lead author for the books *Diagnostic Imaging Spine, Craniovertebral Junction,* and *Postoperative Spine.*

Please join me in welcoming Jeffrey S. Ross, MD, to the position of Editor-in-Chief of the *AJNR*, starting in July 2015. We are fortunate to have such a talented individual in the position to build on the work of past editors and to take us to new heights in these times of rapid change in the publishing world.

Gordon Sze, MD
Chair, Search Committee for the EIC of the *AJNR*
President, ASNR
Past-President, ASSR

AJNR

AMERICAN JOURNAL OF NEURORADIOLOGY

APRIL 2015
VOLUME 36
NUMBER 4
WWW.AJNR.ORG

Publication Preview at www.ajnr.org features articles released in advance of print. Visit www.ajnrblog.org to comment on AJNR content and chat with colleagues and AJNR's News Digest at http://ajnrdigest.org to read the stories behind the latest research in neuroimaging.

Indicates Editor's Choices selection

Indicates Fellows' Journal Club selection

Indicates open access to non-subscribers at www.ajnr.org

Indicates article with supplemental on-line table

Indicates article with supplemental on-line photo

Indicates article with supplemental on-line video

Indicates Evidence-Based Medicine Level 1

Indicates Evidence-Based Medicine Level 2

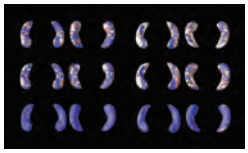

Hippocampal atrophy in Alzheimer disease is better detected at 3T when compared with 1.5T.

COILING OPTIMIZED

NOW AVAILABLE

BARRICADE COMPLEX FINISHING COIL

- Extremely soft profile of The Barricade Finishing coil now in a complex shape
- Excellent microcatheter stability for confident coil placement
- Available in a size range of 1mm-5mm

BARRICADE™ COIL SYSTEM

MADE IN AMERICA

The Barricade Coil System is intended for the endovascular embolization of intracranial aneurysms and other neurovascular abnormalities such as arteriovenous malformations and arteriovenous fistulae. The System is also intended for vascular occlusion of blood vessels within the neurovascular system to permanently obstruct blood flow to an aneurysm or other vascular malformation and for arterial and venous embolizations in the peripheral vasculature. Refer to the instructions for use for complete product information.

18 TECHNOLOGY DRIVE #169, IRVINE CA 92618
p: 949.788.1443 | f: 949.788.1444

WWW.BLOCKADEMEDICAL.COM

MKTG-031 Rev. A

BLOCKADE MEDICAL

Stent Retrievers:
The evidence is clear

stryker® Neurovascular

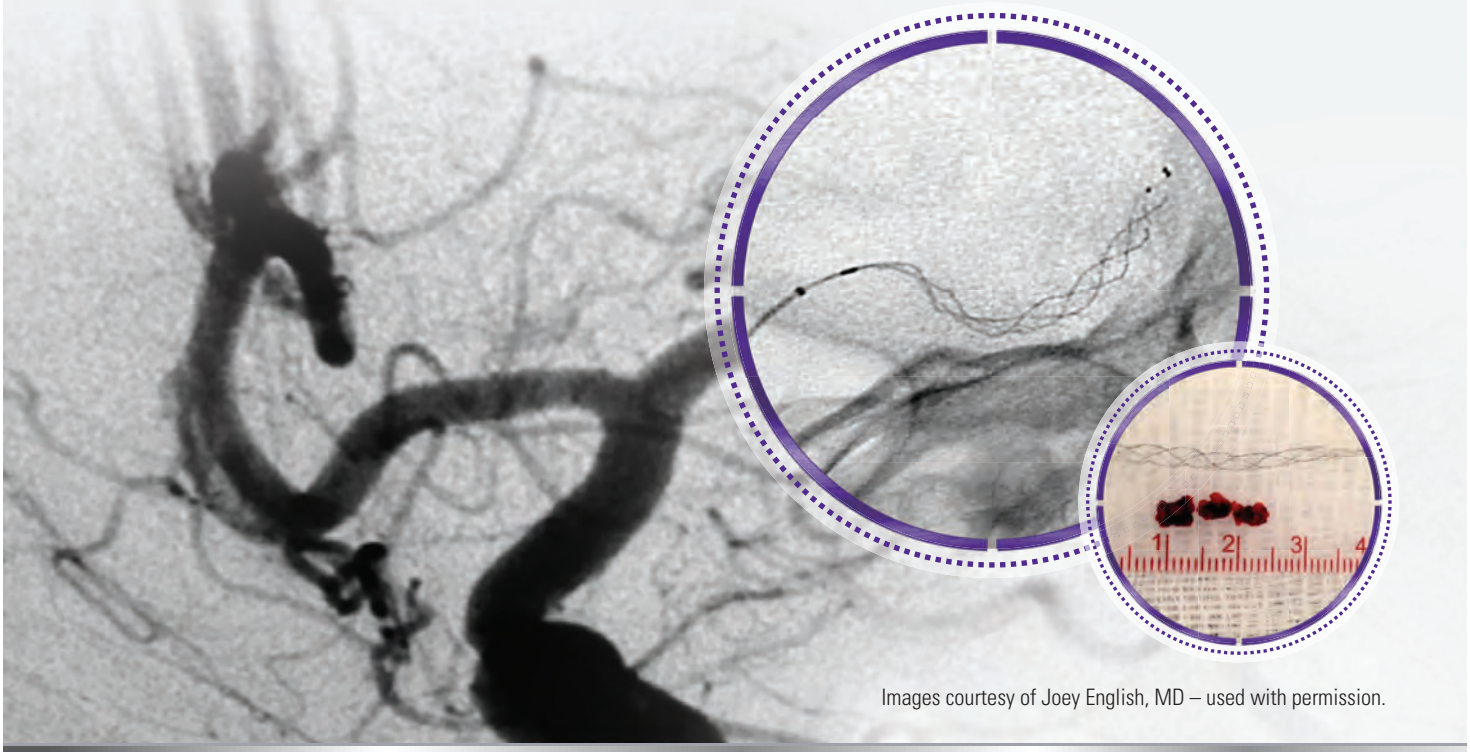

Images courtesy of Joey English, MD – used with permission.

Trial	Number of Patients	Statistically Superior Result for Endovascular Therapy
MR CLEAN[1]	500	✓
ESCAPE[2]	316	
EXTEND-IA[3]	70	
SWIFT PRIME[4]	196	

Stent retrievers ± IV-tPA gave patients up to 3x higher likelihood of an mRS 0-2 at 90 days than IV-tPA alone[1,2,3,4]

1. O.A. Berkhemer et al. A Randomized Trial for Intraarterial Treatment for Acute Ischemic Stroke. *N Eng J Med* December 2014.
2. M. Goyal et al. Randomized Assessment of Rapid Endovascular Treatment of Ischemic Stroke. *N Eng J Med* published on February 11, 2015.
3. B.C.V. Campbell et al. Endovascular Therapy for Ischemic Stroke with Perfusion-Imaging Selection. *N Eng J Med* published on February 11, 2015.
4. Results of the SWIFT PRIME Trial were presented by Dr. Jeffrey Saver at the International Stroke Conference in Nashville, TN on Wednesday, February 11, 2015.

Stroke: *Our Only Focus. Our Ongoing Promise.*

Trevo® XP

PROVUE RETRIEVER

Take Control. Capture More.

The newly designed Trevo® XP ProVue Retriever takes proven Trevo Retriever performance to new levels for **easy delivery, easy placement,** and **easy visualization.**

When you're in control, it's amazing what you can capture.

stryker® Neurovascular

Stroke: *Our Only Focus. Our Ongoing Promise.*

AJNR

AMERICAN JOURNAL OF NEURORADIOLOGY

Publication Preview at www.ajnr.org features articles released in advance of print. Visit www.ajnrblog.org to comment on AJNR content and chat with colleagues and AJNR's News Digest at http://ajnrdigest.org to read the stories behind the latest research in neuroimaging.

APRIL 2015 • VOLUME 36 • NUMBER 4 • WWW.AJNR.ORG

Official Journal:
American Society of Neuroradiology
American Society of Functional Neuroradiology
American Society of Head and Neck Radiology
American Society of Pediatric Neuroradiology
American Society of Spine Radiology

AJNR (Am J Neuroradiol ISSN 0195–6108) is a journal published monthly, owned and published by the American Society of Neuroradiology (ASNR), 800 Enterprise Drive, Suite 205, Oak Brook, IL 60523. Annual dues for the ASNR include $170.00 for journal subscription. The journal is printed by Cadmus Journal Services, 5457 Twin Knolls Road, Suite 200, Columbia, MD 21045; Periodicals postage paid at Oak Brook, IL and additional mailing offices. Printed in the U.S.A. POSTMASTER: Please send address changes to American Journal of Neuroradiology, P.O. Box 3000, Denville, NJ 07834, U.S.A. Subscription rates: nonmember $380 ($450 foreign) print and online, $305 online only; institutions $440 ($510 foreign) print and basic online, $875 ($940 foreign) print and extended online, $365 online only (basic), extended online $790; single copies are $35 each ($40 foreign). Indexed by PubMed/Medline, BIOSIS Previews, Current Contents (Clinical Medicine and Life Sciences), EMBASE, Google Scholar, HighWire Press, Q-Sensei, RefSeek, Science Citation Index, and SCI Expanded.

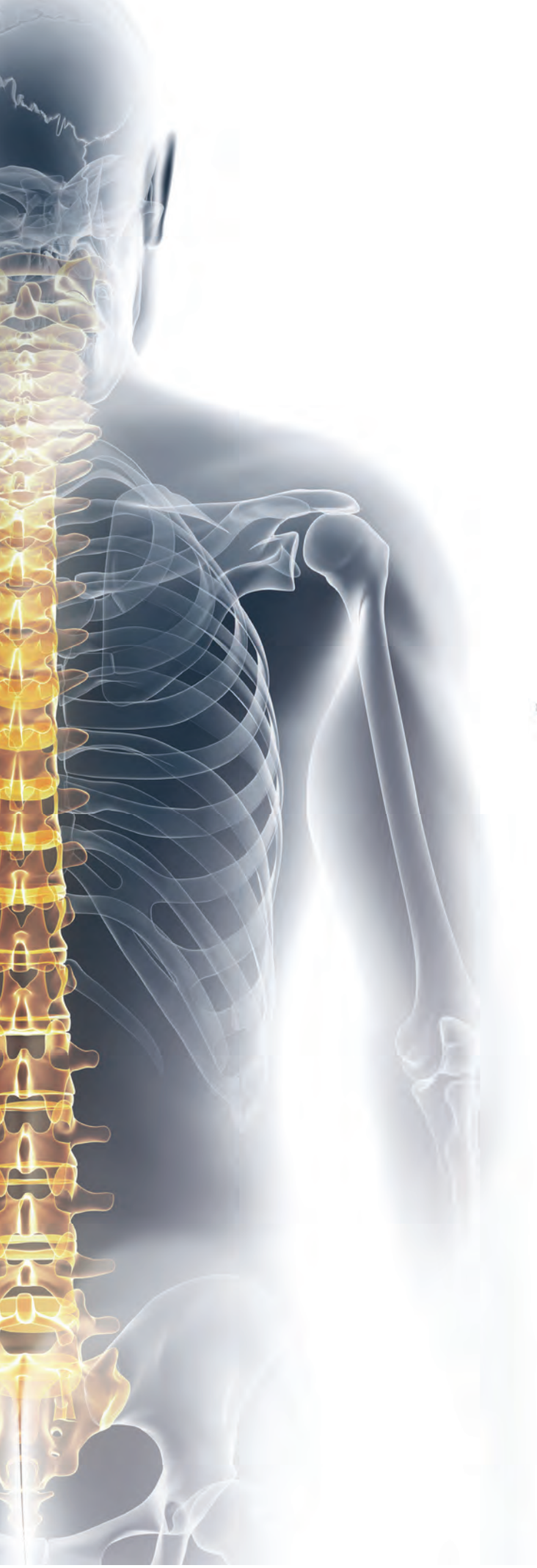

stryker®

Your **single source** for the latest in innovative **solutions.**

Introducing **the most complete and least invasive vertebral augmentation portfolios** on the market today.

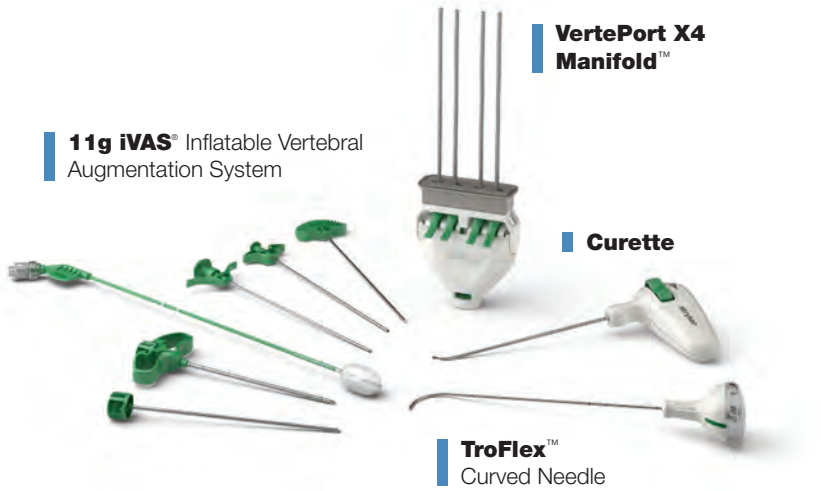

The latest **paradigm in radiofrequency ablation**, the Venom™ Cannula and Electrode combination.

strykerIVS.com

1000-025-308 Rev D

AJNR

AMERICAN JOURNAL OF NEURORADIOLOGY

APRIL 2015
VOLUME 36
NUMBER 4
WWW.AJNR.ORG

Publication Preview at www.ajnr.org features articles released in advance of print. Visit www.ajnrblog.org to comment on AJNR content and chat with colleagues and AJNR's News Digest at http://ajnrdigest.org to read the stories behind the latest research in neuroimaging.

Indicates Editor's Choices selection

Indicates Fellows' Journal Club selection

Indicates open access to non-subscribers at www.ajnr.org

Indicates article with supplemental on-line table

Indicates article with supplemental on-line photo

Indicates article with supplemental on-line video

Indicates Evidence-Based Medicine Level 1

Indicates Evidence-Based Medicine Level 2

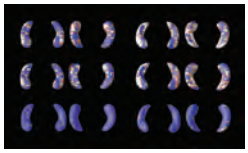

Hippocampal atrophy in Alzheimer disease is better detected at 3T when compared with 1.5T.

Of Girths and Brains

M. Castillo, *Editor-in-Chief*

It is now official: We Americans are no longer the heaviest in the Western World. This ignominious claim belongs south of the border, to Mexico. The obesity rate of Mexicans (32.8%) has now surpassed that of Americans (31.8%). However, that is just obesity; if you take all of those who are overweight, the rate goes up to 70%. Mexican child obesity has tripled in the last 10 years, and though a difficult concept to grasp, many obese individuals are also malnourished. Eating junk food makes one fatter but does not provide the necessary nutrients to be healthy. This weight gain trend is reflected throughout Latin America and other parts of the developing world. Lack of education and a desire to imitate the United States have led to this global problem, and now, being overweight far outstrips being underweight throughout the entire world (a landmark change in humanity that occurred in 2000).[1] In Nauru and the Cook and Marshall Islands, obesity rates have reached 71%, 64%, and 46%, respectively, the highest rates worldwide.[2] High ingestion of fried foods is probably the main culinary culprit, but Mexicans are also the highest consumers of sugary soft drinks in our hemisphere: 43 gallons (163 L) per person per year. Very soon, the world will have more than 900 million obese individuals. Obesity predominantly affects our 2 largest "minorities": Hispanics and African Americans; and despite what some reports say, their obesity rates have not changed significantly in the last few years.[3] Because Hispanics and African Americans will soon together account for most of our population, it is very disturbing that by 2048, the entire US population will be obese if we do not stop this trend!

Apart from probably being unable to fit these patients into our MR imaging and CT units, neuroradiologists will become very involved in their care. Two of the most common obesity-related disorders are stroke and diabetes, with all of their neurologic complications.[4] The current rate of stroke in the general population is about 0.5% per year, while in diabetics, it reaches 1.2% per year. In patients with diabetes, the risk of stroke increases with age, heart disease, previous stroke, smoking, and—not surprisingly—waist circumference. Of course, even without diabetes, stroke is more common in Hispanics and African Americans. Because the older population in the United States will increase from 13% to 19% and Hispanics, from 14% to 19% by 2025, stroke will become even more prevalent (the African American population will experience no significant growth and is expected to remain at the current 13% until about 2050).[5]

The cost of caring for patients with obesity is staggering. Currently, more than US $190 billion is spent on it every year (21% of all annual medical spending in the United States), and even if obesity rates remained stable, that cost will increase to $550 billion by 2030. About $14 billion is spent every year caring for obese children. Disease due to obesity costs businesses about $5 billion in absenteeism every year. While Mexico is also a big country, its gross national product is only 13% of ours, so it faces a considerable challenge dealing with its obesity problem.

Although the main impetus for eating is a negative energy balance, many other nonhomeostatic factors, such as attractiveness of food, time and season (we tend to eat more during winter), and emotion (we eat more when sad or depressed), all affect our intake. An interesting observation is that these nonhomeostatic factors are so strong that they generally override the homeostatic ones.[6] Different brain regions are involved for each of these mechanisms. The hypothalamus, parabrachial nucleus,* and the nucleus of the tractus solitarius are all in charge of the homeostatic mechanisms. Various cortical locations, the amygdalae, ventral striata, hippocampi, and the substantia nigra, are in charge of the nonhomeostatic mechanisms and have complex connections with those in charge of homeostatic control. fMRI can identify activity in all of these regions. In one experiment, levels of peptide YY (PYY) in the bowel were manipulated and its effect was observed by fMRI. PYY activates vagal nerve afferents that activate homeostatic mechanisms and result in a reduction of food intake. fMRI is capable of showing that the homeostatic circuit is activated when the levels of PYY are manipulated. Another substance, leptin, a food-intake-reducing hormone, also results in brain changes measurable with fMRI. In a leptin-deficient state, individuals show activation of parts of the nonhomeostatic circuit and their desire for food increases, but when given leptin, the desire for food goes away, meaning the homeostatic mechanisms return.

There are 2 types of thin individuals: those who do not gain weight (obesity-resistant) and those who do (obesity-prone).[6] Overfeeding significantly attenuates fMRI activation in the visual cortex of obesity-resistant individuals compared with obesity-prone ones, meaning that signals that operate to reduce food rewards and thus reduce intake in lean individuals are not present in those prone to gain weight. The practical applications of these observations are not certain, but manipulation of their function by medications or even brain stimulation/ablation could be possible in the future as a means of curing obesity.

Can obesity be inherited? Those who argue against this notion claim that altering our genes takes many generations and that the obesity epidemic is a fairly recent phenomenon; therefore, not enough time has gone by to change our genes. Those in favor state that the development of "energy-thrifty genes" occurred when

http://dx.doi.org/10.3174/ajnr.A4156

* The parabrachial nucleus complex (unknown to many neuroradiologists) is located at the junction of the midbrain and pons at the level of the superior cerebellar peduncle and is involved in the transmission of gustatory impulses.

humans had less food, and now that we have an abundance of it, these genes favor the storage of fat and make us gain weight. Studies show that genetic factors may be responsible for 50%–80% of weight variations.[7] About 5% of cases of obesity are monogenic—that is, caused by single gene defects (11 different genes identified so far). In polygenic obesity, more than 100 candidate genes have been identified. Genome-wide association studies have consistently pointed to the *FTO* gene as being a main culprit in obesity, and because it is a highly conserved gene, it is passed to subsequent generations. This gene leads to production of a protein that is predominantly expressed in the hypothalamus, so its absence may lead to the nonhomeostatic circuit overriding the homeostatic one. *FTO* gene polymorphism results in increased food intake in children and loss of control over eating, and *FTO* polymorphism carriers do not respond well to diets. What is more, *FTO* is also associated with diabetes independent of weight.

The second most common gene to be associated with obesity is called *transmembrane protein 18*. The polymorphism of this gene leads to weight gain and increased waist circumference and, even when adjusted for weight, also carries a higher risk of diabetes. Deletion of the *SH2B adaptor protein* (located in 16p11.2) leads to resistance to leptin and obesity and, once more, insulin resistance. Again, this gene is expressed in the hypothalamus and is capable of overriding homeostatic mechanisms. *Neuronal growth regulator 1* (1p31.1) is also highly expressed in the brain, and when absent, weight gain, larger circumference, and diabetes ensue. Both of these latter genes also modulate the growth of adipose cells. The hypothalamus produces something called an agouti-related peptide, which is an antagonist of the *melanocortin-4 receptor,* which, if activated, decreases food intake. Homeostatic mechanisms in the hypothalamus block these receptors, increasing food intake, and if the gene that encodes for them is deficient and the receptors absent, satiety does not occur, leading to extreme eating, decline in energy use, and obesity.

Obese children may also have a genetic defect that makes them eat more carbohydrates. Animal studies show that mothers fed a long-standing high-fat diet produce offspring who demonstrate increased adiposity, glucose intolerance, and altered brain appetite regulators.[8] Even in the face of only mild maternal overnutrition, these traits persist. It is hoped that knowledge of these gene defects will lead to personalized weight management and prediction of obesity and even perhaps gene manipulation in individuals at risk and that the effects of drugs may be monitored with fMRI. However, as always, things are not that easy, and epigenetic factors may further alter the functions of these genes. Ingestion of monounsaturated fats changes the way many of these genes act. So, do these genes change us or do we change these genes? Maybe both.

Once obesity is established, even in absence of diabetes, it increases arterial disease such as atherosclerosis. In one study, children with risk factors that included obesity had increased atherosclerosis progression in adulthood.[9] Because 4%–6% of all US children are obese, the neurologic implications of these findings are important. Unfortunately, there is no easy fix because lifestyle modifications, behavior treatments, and even medications are only minimally effective and most participants remain obese after completion of these treatments.[10] In obese children, the carotid arteries become thicker and stiff, and plasma markers of endothelial activation and injury are high. As the arteries stiffen, they cannot dilate to accommodate increased flow and the brain may not get enough blood when higher demand is in order.

Low back pain, the most common indication for lumbar spine MR imaging studies, is also correlated with weight. In one study in which participants were followed for 11 years, low back pain was either present at the beginning or developed during the study independent of other factors such as education, physical activity, and smoking.[11] Neurosurgeons know that physical therapy and surgery commonly fail when the lumbar spine of obese patients is operated on. Infections and re-operation rates are also higher in the obese.

A newly recognized and significant risk factor for back pain in the obese is metabolic syndrome. Metabolic syndrome is associated with a special type of weight: a large waistline (individuals with excess fat in their abdomen but relatively little elsewhere). Other conditions associated with it are diabetes, high blood pressure, and high lipids. Overall, this syndrome is present in up to 20% of the adult US population and is highest in Hispanics. The prevalence of the syndrome is about 5% in those with a normal weight, nearly 60% in the obese, and nearly 39% in those with low back pain.[12,13] Tumor necrosis factor-α (*TNF-*α) is produced by individuals with the metabolic syndrome and is known to cause low back pain; when it is blocked, the pain disappears. Furthermore, aortic atherosclerosis associated with metabolic syndrome has been linked to degenerative disk disease and low back pain. The syndrome is also known to cause silent cerebral infarctions.

It is interesting that some investigators postulate that metabolic syndrome originates in the brain due to alterations in our circadian clocks. Normally, during sleep, our brain prepares our body for the next day's physical activity, but in modern life in which physical activity is minimal, this mechanism has been disrupted. The hypothalamus releases hormones and alters the function of the autonomic nervous system, resulting in changes in blood pressure, insulin, abdominal fat breakdown, and glucose uptake, but all of these activities are no longer needed as we sit at our desks all day long. The more abdominal fat we have, the greater the amount of adipokines we produce. Adipokines are cell-signaling proteins secreted by fatty tissues that have immunomodulating capacities, TNF-α being one of the most important ones. Additionally, adipose tissues produce hormones (called adipose-derived hormones), and their production becomes abnormal in patients with metabolic syndrome. One of these hormones is leptin, which as we saw above, can affect food intake. Obese individuals produce too much leptin, but instead of decreasing hunger, their brains become resistant to leptin and they just eat more.

There is a popular belief that up until the 1900s, fat was seen as attractive, that in women it signified health and the ability to have babies, while in men, it meant prosperity. Newer research shows that most pre-Victorians and others before were thin, and their diets, nutritious.[14] They ate many fruits and vegetables (mostly

organic) and fiber, a diet akin to what we now call Mediterranean eating. No, they were not malnourished characters from a Dickens novel. They were actually healthy, and their physical activity is said to have been 3–4 times as much as ours.[15] Recent evidence suggests that back then, life expectancy was not much different from now, the incidence of degenerative disease was 10% of ours, and cancer was basically nonexistent (of course, infections were rampant and childbirth fatalities and accidents were common). By the mid-Victorian times, diet and health had deteriorated significantly (cheap sugar, salted meats, and vegetable oils are just 3 popular products from the Agricultural Revolution responsible for obesity). The year 1900 was probably the last time we were a lean human race. Coming back to where I started, obesity was basically unknown in pre-Columbian Mesoamerica where the diet was gluten-free, low-carb, nutrient attenuated, and high in protein and fiber. Unfortunately, it is now in Mesoamerica where obesity is more prominent.

NB: For those who are interested in this topic, this is a very nice article: Caballero B. **The global epidemic of obesity: an overview.** *Epidemiol Rev* 2007;29:1–5

REFERENCES

1. Food and Agriculture Organization of the United Nations. The nutrition transition and obesity. http://www.fao.org/focus/e/obesity/obes2.htm. Accessed January 22, 2014
2. LATINOVOICES. Mexico obesity rate surpasses the United States', making it fattest country in the Americas. http://www.huffingtonpost.com/2013/07/09/mexico-obesity_n_3567772.html. Accessed January 22, 2014
3. Flegal KM, Carroll MD, Kit BK, et al. **Prevalence of obesity and trends in the distribution of body mass index among US adults, 1999–2010.** *JAMA* 2012;307:491–97
4. Centers for Disease Control and Prevention. Adult obesity facts. http://www.cdc.gov/obesity/data/adult.html. Accessed January 22, 2014
5. Passel JS, Cohn D. **US population projections: 2005–50.** *Pew Research Hispanic Trends Project*. February 11, 2008. http://www.pewhispanic.org/2008/02/11/us-population-projections-2005-2050. Accessed January 28, 2014
6. Grill HJ, Skibicka KP, Hayes MR. **Imaging obesity: fMRI, food reward, and feeding.** *Cell Metabolism* 2007;6:423–25
7. Moleres A, Martinez JA, Marti A. **Genetics of obesity.** *Curr Obes Rep* 2013;2:23–31
8. Rajia S, Chen H, Morris MJ. **Maternal overnutrition impacts offspring adiposity and brain appetite markers: modulation by postweaning diet.** *J Neuroendocrinol* 2010;22:905–14
9. Juonala M, Viikari JSA, Kanonen M, et al. **Life-time risk factors and progression of carotid atherosclerosis in young adults: the cardiovascular risk in young Finns study.** *Eur Heart J* 2010;31:1745–51
10. Kelly A, Barlow SE, Rao G, et al. **Severe obesity in children and adolescents: identification of health risks, and treatment approaches—a scientific statement from the American Heart Association.** *Circulation* 2013;128:1698–712
11. Heuch I, Heuch I, Hagen K, et al. **Body mass index as a risk factor for developing chronic low back pain: a follow-up in the Nord-Trondelag health study.** *Spine* 2013;38:133–39
12. Park YW, Palaniappan L Heshka S, et al. **The metabolic syndrome: prevalence and associated risk factor findings in the US population from the third national health and nutrition examination survey, 1988–1994.** *Arch Intern Med* 2003;163:427–36
13. Ha JY. **Evaluation of metabolic syndrome in patients with chronic low back pain: using the fourth Korea national health and nutrition examination survey data.** *Chonnam Med J* 2011;47:160–64
14. Westcott P. Healthy eating Victorian style. Saga. http://www.saga.co.uk/health/healthy-Eating/healthy-eating-victorian-style.aspx. Accessed January 30, 2014
15. Clayton P, Rowbotham J. **How the mid-Victorians worked, ate and died.** *Int J Environ Res Public Health* 2009;6:1235–53

EDITORIAL

Viewpoints on the ARUBA Trial

J.P. Mohr, A. Hartmann, H. Kim, J. Pile-Spellman, and C. Stapf

A Randomized Trial of Unruptured Brain Arteriovenous Malformations (ARUBA), the first randomized clinical trial for brain arteriovenous malformations (bAVMs), was planned as a straightforward simple attempt to learn whether deferring intervention for a bAVM that had not bled would prove superior to incurring the risks of intervention needed to eradicate the lesion. The trial was justified by longitudinal data on true natural history (ie, for those receiving no intervention to eradicate the bAVM), reports of mild syndromes from many who had bled, and literature with treatment outcomes that were a mix of those who had bled before treatment versus those who had not. Having no wish to disturb current established interventional practice, the investigators offered randomization only to those whose bAVMs were considered suitable for eradication; none whose bAVMs were deemed too daunting for intervention would be eligible. Medical management for headaches and seizures is well-established, but no standards have yet appeared dictating interventional management. Widely misquoted literature citing annual hemorrhage rates approximating 4% and estimates of low risks for intervention allowed the assumption that the trial might well end within 5 years with a win for intervention.[1] Moreover, more insight would be gained for the true natural history.

The National Institute of Neurological Disorders and Stroke (NINDS) application followed well-established guidelines: an aim, a primary null hypothesis, clear and simple primary outcomes, and a host of secondary aims should enough data be available for useful analysis, with all information posted on the Web.[2] Participating centers sought, were offered, and were assumed to use their experience-based choices of interventions to achieve the goals of lesion eradication. The 39 active centers randomized fully 61% of those eligible. They also showed their qualifications by publishing fully 630 PubMed references for bAVMs during 2000–2010. Outcomes were reported at fixed intervals and after each intervention (many interventions not yielding single-stage eradication) and were adjudicated by a distinguished 4-member panel. An NINDS-appointed equally distinguished Data and Safety Monitoring Board (DSMB) provided independent oversight of study conduct and participant safety. National Institutes of Health (NIH) trials are typically funded in cycles of 5 years or less. Continuation depends on successful review and priority scores

Indicates open access to non-subscribers at www.ajnr.org
http://dx.doi.org/10.3174/ajnr.A4204

for the reapplication when the research questions remain unsettled.

In April 2013, with 226 subjects randomized (3 within the previous month) and outcome data available for 223 subjects with a mean follow-up for the cohort of 3.3 years, the DSMB recommended halting the randomization phase after a planned interim analysis found superiority for the medical arm. They also recommended continued follow-up to determine whether the disparity would persist. The results were presented at the 22nd European Stroke Conference in May, and published in *The Lancet* as an Epub in November 2013 and in print in February 2014.[3]

Although pleased that ARUBA has generated so much interest, we remain bemused at the nature of the commentaries. During the trial, some critical publications suggested that those offering the criticisms were either unaware of the design or were also unaware the investigators were blinded to outcomes.[4] After the first public presentation of the data but before our formal publication, the first of the outcome-based critical reviews appeared.[5] Despite our responses in the publication and to letters to the editor and published debates at national and international meetings along with favorable reviews, similar criticisms continue to accumulate.

ARUBA is indeed a biased sample. Compared with population-based studies and many case series, there is overrepresentation of the smaller bAVMs with lower Spetzler-Martin grades. It is no surprise that the centers chose for randomization those expected to show more favorable results from intervention. ARUBA did not have numerous contentious cases considered at higher risk for intervention, despite published speculations.[6] For transparency, we reported those screened, eligible, having refused participation, and treated outside the trial, a plan lacking in most of the major stroke trials. We offered to organize a registry option to meet the objections directed at earlier trials. No centers replied.

Objections against randomized clinical trials as a process led to our publishing not only the classic "as-randomized" but also "as-treated" analyses. (The latter assigned to the medical arm those outcomes that occurred for those randomized to intervention before intervention could begin; it also assigned to the interventional arm those randomized to the medical arm who elected intervention and then had an interventional outcome event.) The disparity favoring medical management for the "as randomized" analysis was even greater for the "as-treated" analysis: The latter showed a more than 5-fold increased risk of the primary outcomes for those undergoing invasive therapy (hazard ratio, 5.26; 95% CI, 2.63–11.11) and a significantly increased risk of major neurologic deficits (relative risk, 2.77; 95% CI, 1.20–6.25). The distribution of modified Rankin score by Spetzler-Martin Grade refutes speculations that the clinical severity of outcome events in the interventional arm was overestimated, a concern raised by Gary Steinberg, MD, from the audience after presentation of the results at the Treatment of Unruptured Brain Arteriovenous Malformations debate on February 11 at the 2014 International Stroke Conference in San Diego, California.[7]

The outcomes for the medical arm were the new data. As expected, the randomization process yielded essentially the same clinical characteristics in the 2 arms. All patients in the medical arm continued their normal activities of daily living, though their personal quality of life reports showed a higher degree of anxiety for their future.

It has been inferred by comments in the literature that hemorrhage rates are expected to be stable, steadily accumulating with time, making the risk for hemorrhage likely in the lifetime of the individual. However, recent publications suggest a decline in hemorrhage events with time.[8] Yet even if one assumes stable event rates, the disparity between the medical and interventional arms in ARUBA is great enough that 12–30 years may be needed before outcomes in the medical arm will cross those of the interventional arm.[9] (These calculations are based on the assumption that no further outcomes will occur in the interventional arm, in which a number of participants were still in the incomplete treatment phase when randomization was halted.)

Considerable literature exists on the anatomic features of those who presented with hemorrhage, many sharing the well-known Spetzler-Martin grading system predicting risks for surgical intervention. Except for deep venous drainage, these factors did not predict the frequency or severity of the first hemorrhage in our earlier reports or in ARUBA. Perhaps the anatomic features for those considered suitable for attempted eradication are less likely to predict hemorrhage.

Most reports—including meta-analyses—typically describe a demographic table that includes those who bled or did not bleed before intervention, after which the outcomes are described as if all the patients share the same risk for adverse events and their severity.[10] Only a few publications provide direct comparison with ARUBA and show that results are in the same range. The lack of registry data prevents comments on the outcomes for those eligible but not randomized to ARUBA.

Concerns that primary surgical intervention was not well-represented cannot be answered from ARUBA, in which intervention choice was made by the local centers. However, the latest meta-analyses do not emphasize the superiority of outcomes for surgery.[10] Single-technique surgery was not a recommended option in the 1 published management algorithm we found for bAVMs that did not bleed,[11] despite objections about too few surgical cases in ARUBA lodged by the senior author in letters to *The Lancet*.[12]

The Future

To our disappointment and despite insistence from us, the ARUBA participants, the DSMB, and many critics, the NINDS Study Section and Council recommended against NIH funding for continuation of the follow-up. The review cited the assumption of no likely changes in the outcomes disparity. Our goals of assessing long-term hemorrhage risk and the degree of clinical improvement after adverse events during intervention remain unsatisfied. Although we could cite the decisions of reviewers as acceptance of the trial as definitive, we hope ARUBA will prove a starting point for further studies.

Preventive eradication of bAVMs remains costly: $75,000–

$100,000 per patient when last estimated 15 years ago, plus additional costs for potential treatment complications.[13]

Although intervention after hemorrhage often shows little worsening and sometimes improvement, ARUBA documents the difficulties in achieving lesion eradication without some disturbance in perilesional brain function for those previously asymptomatic. While we await new studies, the need for interventional management for those who have bled should justify studying elements of bAVMs that predict hemorrhage. The ARUBA data can be read as a challenge to the justification of interventions in those who have not bled.

ACKNOWLEDGMENTS

This work was supported in part from a gift from Vital Projects Fund Inc, New York, New York.

Disclosures: J.P. Mohr—*RELATED*: *Grant*: NINDS (U01 NS051483).* Christian Stapf—*RELATED*: *Grant*: NIH/NINDS.* Andreas Hartmann—*RELATED*: *Grant*: NIH (U01 NS051483).* John Pile-Spellman—*UNRELATED*: *Expert Testimony*: against a doctor who published and treated a patient who subsequently died, with an unruptured Spetzler-Martin grade 4 AVM; the doctor documented in the chart that he told the family the patient had a grade 2. Helen Kim—*RELATED*: *Grant*: NIH,* *Comments*: for patient enrollment into the ARUBA trial (money received directly and by institution). *Money paid to the institution.

REFERENCES

1. Ondra SL, Troupp H, George ED, et al. **The natural history of symptomatic arteriovenous malformations of the brain: a 24-year follow-up assessment.** *J Neurosurg* 1990;73:387–91
2. A Randomized Trial of Unruptured Brain AVMs (ARUBA). http://clinicaltrials.gov/ct/show/NCT00389181. Accessed March 23, 2006
3. Mohr JP, Parides MK, Stapf C, et al. **Medical management with or without interventional therapy for unruptured brain arteriovenous malformations (ARUBA): a multicentre, non-blinded, randomised trial.** *Lancet* 2014;383:614–21
4. Cockroft KM, Jayaraman MV, Amin-Hanjani S, et al. **A perfect storm: how a randomized trial of unruptured brain arteriovenous malformations' (ARUBA's) trial design challenges notions of external validity.** *Stroke* 2012;43:1979–81
5. Bambakidis NC, Cockroft K, Connolly ES, et al. **Preliminary results of the ARUBA study.** *Neurosurgery* 2013;73:E379–81
6. Mocco J, O'Kelly C, Arthur A, et al. **Randomized clinical trials: the double edged sword.** *J Neurointerv Surg* 2013;5:387–90
7. Mohr JP, Parides M, Moquete E, et al. **Spetzler-Martin Grade and outcomes by randomization assignment in the ARUBA trial (abstract).** *Stroke* 2014;45:A160
8. Kim H, Al-Shahi Salman R, McCulloch CE, et al. **Untreated brain arteriovenous malformation: patient-level meta-analysis of hemorrhage predictors.** *Neurology* 2014;83:590–97
9. Parides MK, Overbey JR, Stapf C, et al. **Projecting longer term results in the ARUBA trial.** In: *Proceedings of the 23rd European Stroke Meeting*, Nice, France. May 6–9, 2014:97
10. van Beijnum J, van der Worp HB, Buis DR, et al. **Treatment of brain arteriovenous malformations: a systematic review and meta-analysis.** *JAMA* 2011;306:2011–19
11. Stieg PE, Janardhan V, Riina HA. **Multimodality therapy: treatment algorithms.** In: Stieg PE, Batjer HH, Samson D, eds. *Intracranial Arteriovenous Malformations*. New York: Informa Healthcare; 2006: 135–43
12. Knopman J, Stieg PE. **Management of unruptured brain arteriovenous malformations.** *Lancet* 2014;383:581–83
13. Berman MF, Hartmann A, Mast H, et al. **Determinants of resource utilization in the treatment of brain arteriovenous malformations.** *AJNR Am J Neuroradiol* 1999;20:2004–08

EDITORIAL

The Role of AVM Microsurgery in the Aftermath of A Randomized Trial of Unruptured Brain Arteriovenous Malformations

M.T. Lawton

Microsurgical resection is the first-line therapy or criterion standard for many brain arteriovenous malformations because of its high cure rate, low complication rate, and immediacy. Surgical results have improved with time with the following: 1) the creation of grading systems to select patients likely to experience optimal outcomes; 2) the development of instruments like bipolar forceps and AVM microclips that coagulate or occlude feeding arteries effectively; 3) the recognition of AVM subtypes that help decipher AVM anatomy; and 4) the refinement of surgical approaches, strategies, and dissection techniques that facilitate safe AVM resection.[1-3] This impressive evolution of AVM surgery is at odds with the finding of A Randomized Trial of Unruptured Brain Arteriovenous Malformations (ARUBA) that medical management alone was superior to interventional therapy for the prevention of death or stroke in patients with unruptured AVMs followed for 33 months.[4]

An important explanation for the ARUBA finding is the surprisingly nonsurgical management of patients in the interventional group in the trial. Overall, 81% of patients were treated with embolization alone (32%), radiosurgery alone (33%), or combined embolization and radiosurgery (16%), and only 17 patients (18%) were treated surgically, with or without embolization. Therefore, the 3-fold increase in death or stroke in the interventional arm reflects current nonsurgical therapies and should not be interpreted as an indictment of AVM surgery. In the aftermath of ARUBA, it is important to clarify the safety, efficacy, and outcomes associated with AVM resection.

Our experience in managing 232 Spetzler-Martin grade I and II AVMs, the most favorable AVMs for surgery and the ones most likely to have been selected for treatment outside the randomization process of ARUBA, exemplifies a surgical posture toward low-grade AVMs that regards curative resection as the first-line or criterion standard therapy for most lesions.[5] We used embolization as a preoperative adjunct and reserved radiosurgery for risky AVMs in deep, inaccessible locations; in eloquent areas that might be associated with postoperative neurologic deficits; and/or with diffuse nidus morphology that might complicate microdissection. Patients were carefully selected to optimize outcomes, with a mean age of 38 years, Lawton-Young grades of ≤III in 69% of

http://dx.doi.org/10.3174/ajnr.A4193

patients, and few (<4%) AVMs in deep locations or the brain stem. Conservative embolization minimized additional treatment risk, with only 43% of patients undergoing embolization and no patients experiencing endovascular complications. Surgical cures were confirmed in all patients who underwent postoperative angiography. Overall, 6 patients (3%) were worse neurologically after surgery, with 161 patients (78%) in total and 91 patients (91%) with unruptured AVMs experiencing good outcomes (modified Rankin Scale scores, 0–1). These surgical results are consistent with other reports in the literature. In a review of 1235 patients with low-grade AVMs, the average surgical morbidity and mortality rates were 2.2% and 0.3%, respectively, with an average cure rate of 98.5% and a postoperative or delayed hemorrhage rate of 0.3%.[5]

The management of AVMs in other parts of the world is diverging from the surgical approach described above. In Europe, for example, treatment is often limited to only ruptured AVMs, beginning with aggressive embolization, frequently adding radiosurgery for incompletely embolized AVMs, and rarely resorting to surgical resection. Onyx (Covidien, Irvine, California) is an important endovascular advancement over N-butyl 2-cyanoacrylate glue and has improved the efficacy of endovascular therapy, but cure rates are still low and curative attempts are associated with increased complications, occlusion of critical draining veins, and adverse imaging findings in as many as 40% of patients. In a review of 1297 patients with mostly low-grade AVMs, the average endovascular morbidity and mortality rates were 6.2% and 1.6%, respectively, with an average cure rate of 29% and a postoperative or delayed hemorrhage rate of 8.0%.[5] Therefore, aggressive endovascular therapy has higher procedural risks, substantially lower cure rates, and increased hemorrhage risks compared with surgery.

A similar comparison can be made with radiosurgery for low-grade AVMs. Although these lesions are ideal for radiosurgery because of their lower target volumes and higher obliteration rates, the 2- to 3-year latency period between treatment and obliteration opens a time window for AVM hemorrhage and associated complications. Radiation-induced complications are low, but in a review of 1051 patients with low-grade AVMs, 7.2% of patients hemorrhaged after treatment, resulting in morbidity and mortality rates of 6.5% and 1.2%, respectively.[5] The 75.2% radiosurgical cure rate was substantially better than the endovascular cure rate, but still less than that of surgery. Therefore, despite the technologic advances in endovascular and radiosurgical therapy, surgery still offers the best cure rate, lowest risk profile, and greatest protection against hemorrhage for low-grade AVMs. Surgery cannot compete with the minimally invasive appeal of these other modalities, but this issue remains secondary to functional outcome.

How do we interpret the ARUBA findings in this context? First, on the basis of the surgical experience described above, a substantial number of neurosurgical investigators in ARUBA did not consider AVMs with low Spetzler-Martin grades (low treatment risk) to be in equipoise with medical management (high hemorrhage risk) and "selected treatment outside of the randomization process"[4] (177 patients, or close to the number of included patients). Conversely, intermediate (31.8%) and high-grade AVMs (10.3%) that are generally considered to have a more benign natural history and high risk for any treatment were included in the trial, diminishing the interventional results.

Second, with its unusual bias toward nonsurgical therapy and no data published on cure rates, the number of incompletely obliterated AVMs was likely high and resulted in ongoing ruptures. Therefore, the event rates observed in Kaplan-Meier estimates of "as-treated" patients reflected the procedural morbidity of interventional therapies plus the delayed morbidity of latency hemorrhages associated with radiosurgery and incomplete embolization. The outcome of such a group could never exceed that of an observational group whose only morbidity was the natural history risk.

Third, the shortage of surgical expertise in the ARUBA trial is apparent. Two-thirds of patients in the interventional group had low-grade, surgical AVMs; yet, only 18% underwent surgery, which is well below the expectation for the criterion standard therapy. The rates of stroke and death in this trial do not match the reported surgical outcomes. Therefore, the management of AVMs in ARUBA reflects a nonsurgical posture consistent with the fact that 38 of the 65 ARUBA sites were in Europe, Australia, and Brazil. Centers were required to manage 10 patients with AVMs per year, but there were no minimum requirements for neurosurgeons. AVM resection is among the most challenging neurosurgical cases, and the best AVM surgeons typically perform more than 25 resections annually. Had the ARUBA trial been embraced by the neurosurgical community, the application of surgical therapy would have been higher, the interventional outcomes would have been better, and the benefits of intervention would have been apparent. Had ARUBA been more surgical with complete resections and no delayed hemorrhages in incompletely treated patients, the event rates observed in Kaplan-Meier estimates of "as-treated" patients would have plateaued and the benefits of intervention would have been realized in much fewer than 10 years.

These critiques were validated in an analysis of our ARUBA-eligible patients managed outside the trial. As a participating ARUBA site, the University of California, San Francisco, screened 473 patients for eligibility, enrolled 4 patients, and had complete data on 74 eligible patients managed outside the trial, of whom half had low-grade AVMs. Forty-three patients (71% of treated patients) were treated surgically with or without preoperative embolization, 15 patients (25% of treated patients) were treated radiosurgically, and 13 patients (18% of the overall cohort) were observed. The risk of stroke and death and the degree of clinical impairment among treated patients were lower than those in ARUBA, with primary outcome rates of 11%, 27%, and 8% for surgery, radiosurgery, and observation, respectively. The 3-fold difference in primary outcome reported in ARUBA disappeared with a different management strategy and a different surgical expertise, leaving no significant difference in the rate of stroke or death between treated and observed patients (hazard ratio, 1.34; 95% CI, 0.12–14.53; $P = .807$).[6] Therefore, our results in ARUBA-eligible patients managed outside that trial led to an entirely different conclusion about AVM intervention, due to the primary role of surgery, judicious surgical selection with estab-

lished outcome predictors, and technical expertise developed at a high-volume AVM center.

These critiques beg for another trial to re-establish the role of surgery in AVM management, this time conducted and embraced by the neurosurgical community: *Be*yond *A*RUBA: *R*andomized Low-Grade *B*rain *A*VM stu*D*y, *O*bservation versus *S*urgery (BARBADOS). Effort is ongoing to organize, fund, and initiate it. There is now urgency among neurosurgeons to respond to ARUBA, which we expect to increase acceptance of such a trial. In the meantime, the management of ruptured AVMs should remain unaffected by ARUBA and surgery should be regarded as the first-line or criterion standard therapy for most low-grade AVMs, with conservative embolization as a preoperative adjunct. High surgical cure rates and excellent functional outcomes in patients with both ruptured and unruptured AVMs support a dominant surgical posture, with radiosurgery reserved for risky AVMs in deep, inaccessible, and highly eloquent locations.

REFERENCES

1. Spetzler RF, Martin NA. **A proposed grading system for arteriovenous malformations.** *J Neurosurg* 1986;65:476–83
2. Lawton MT, Kim H, McCulloch CE, et al. **A supplementary grading scale for selecting patients with brain arteriovenous malformations for surgery.** *Neurosurgery* 2010;66:702–13; discussion 713
3. Lawton MT. *Seven AVMs: Tenets and Techniques for Resection*. New York: Thieme Medical Publishers; 2014
4. Mohr JP, Parides MK, Stapf C, et al. **Medical management with or without interventional therapy for unruptured brain arteriovenous malformations (ARUBA): a multicentre, non-blinded, randomised trial.** *Lancet* 2014;383:614–21
5. Potts MB, Lau D, Abla AA, et al; UCSF Brain AVM Study Project. **Current surgical results with low-grade brain arteriovenous malformations.** *J Neurosurg* 2015 Feb 6. [Epub ahead of print]
6. Rutledge WC, Abla AA, Nelson J, et al **Treatment and outcomes of ARUBA-eligible patients with unruptured brain arteriovenous malformations at a single institution.** *Neurosurg Focus* 2014;37:E8

EDITORIAL

A Randomized Trial of Unruptured Brain Arteriovenous Malformations Study: What Impact on Clinical Care and Therapeutic Decision?

C. Cognard

One hundred nine patients presenting with an unruptured AVM have been recruited in A Randomized Trial of Unruptured Brain Arteriovenous Malformations (ARUBA) in the no-treatment arm and have been followed up for 33.7 months (306.1 patient years).[1] Eight hemorrhages (2.6% annual bleed rate) and 4 ischemic strokes (1.3%) occurred, bringing the annual stroke risk to 3.9%. ARUBA confirmed what we already knew—that is, leaving an AVM untreated brings a high lifetime stroke risk.

http://dx.doi.org/10.3174/ajnr.A4294

According to the New York Islands AVM Study,[2,3] there are 3 identified factors associated with an increased risk of rupture of an AVM (previous rupture, deep venous drainage, deep location), leading to a reported annual risk from 0.9% to 32%. Some other factors such as arterial/nidal aneurysms and venous stenosis or dilations are considered to increase the annual risk of bleeding, even if there are no good estimates of their respective impacts.

Interventional treatments have been developed in the past decades to select patients presenting with an unruptured AVM; but in the absence of exhaustive data on the comparative risks of treatment/no treatment, the decision to offer treatment or observation lies entirely on the individual center and physician running the risk of intervention or rather the risk of rupture without treatment. Even more contingency-dependent, a patient with an unruptured AVM is offered the option of surgery, endovascular embolization, radiosurgery, or a combination of these 3 options, depending on the level of skill, experience, or mere availability of a trained operator.

Despite a plethora of single-center or multicenter reports in the literature, the methodology is rather weak and nothing could support the drafting of guidelines for this very difficult therapeutic decision.

The only piece of evidence useful to this purpose is a randomized controlled trial comparing the different options, ideally featuring a large number of patients, a long follow-up, a precise clinical end point, and an analysis of the influence of the risk factors of natural history and different treatments.

The objective of such a trial would be to define the option with the longest deficit-free survival stratified for AVM characteristics.

Randomized controlled trials (RCTs) are particularly adapted to homogeneous diseases. As an example, coronary stenosis is ideal for randomization: The disease appears homogeneous for the sake of screening, the study sample is very large, and the time of observation is short, with an expected outcome at short term. The interventional procedure is well-established and standardized across centers.

Brain AVMs are not ideal subjects for RCTs. The disease is rare and extremely heterogeneous (age, AVM size, location, eloquence, depth, architecture, and flow dynamics, just to mention a few variables), and therapeutic options can vary among centers and among physicians in the same centers on the basis of their experience and their level of technology expertise.

Designing an RCT that could compare multiple treatment options in such a heterogeneous disease is definitely a challenge, one that ARUBA could not handle but that we still need to take.

To give a patient the highest chance of deficit-free survival, the operator should be able to do the following:

1) Identify factors of increased bleeding risk
2) Identify factors of the increased interventional treatment risk
3) Compare the risk of death and handicap in the long term of an untreated AVM with the risk of performing an intervention (also evaluating the option of complete or incomplete occlusion of the AVM).

To answers these questions, we have 2 options: either running an RCT that looks at a limited study population (eg, no treatment versus surgery in superficial small AVMs in a noneloquent area or no treatment versus radiosurgery in deeply located deep venous

drainage AVMs), or alternatively, we need to design an RCT with a large volume of patients with long-term follow-up that would allow a strong subgroup analysis to try to determine which patients should or should not be treated and how.

Why ARUBA Is Not the RCT We Need

ARUBA starts from the hypothesis that no treatment is better than any interventional treatment for unruptured brain AVMs. The success of ARUBA was meant to show that interventions should not be performed.[4]

The original design approved by the National Institutes of Health/National Institute of Neurological Disorders and Stroke planned randomization of 800 patients during a 30-month period, with a statistical power analysis based on an expected 5-year event rate of 12% in the no-treatment group and 22% in the interventional therapy group. There was an intention-to-treat analysis, and 2 interim analyses were planned.

Due to slow randomization, the recruitment period was extended to 60 months and the targeted study population was reduced to 400 participants. Enrollment was halted after the second preplanned interim analysis, when data for 223 patients were available and the predetermined threshold for safety/efficacy was met, as reviewed by the independent Data and Safety Monitoring Board of the trial.

Primary End Point

The primary end point of the trial was time to a composite event of death or stroke, defined as "any new focal neurologic deficit, seizure, or new-onset headache associated with imaging findings."[1]

It is difficult to understand why time to this composite end point was selected. It is very unusual to consider a new-onset headache associated with minimal bleed on MR imaging that does not carry any permanent morbidity as a stroke. That complications of interventions occur early in the observed period while complications of the natural evolution of the untreated disease occur in the long term is also fairly normal. With this design, not surprisingly, the primary end point was reached by 11 (10.1%) patients in the no-treatment arm versus 35 (30.7%) in the interventional arm.

The primary end point should have been the mRS score at last follow-up, a criterion that is used in all stroke trials and that actually reflects, in a simple way, the clinical status of the patient.

The secondary end point was risk of death and neurologic disability, with an mRS score of ≥2. At 36 months, this secondary end point was 6/43 patients (14%) in the no-treatment versus 17/44 (38.6%) in the treatment arm. Most interesting, the difference in the number of deaths between the 2 groups was not statistically significant, with 3 in the interventional arm and 2 in the medical management arm. A 38.6% severe (death and neurologic disability with mRS score of ≥2) complication rate is very high compared with that published in the literature for surgery of small unruptured AVMs in a noneloquent territory or for radiosurgery in small AVMs. No analysis is available on the factors associated with these complications (a technique in particular or a specific AVM profile?).

Duration of Follow-Up

In fact, for a patient presenting with a lifetime risk of stroke, the main question is which strategy will give him or her the better life in the long term?

In ARUBA, the design of the study was to obtain the last follow-up clinical data at 5 years. The mean follow-up was 33.3 months at the intermediate preplanned analysis when the study was stopped. Such a protocol is aimed at comparing a preventive interventional treatment that is supposed to cure the AVM and eliminate the risk of bleed but induces a treatment risk with a nontreatment strategy not producing any therapeutic risk but leaving a lifetime risk of bleed. In the treatment group, death and neurologic disability happens immediately at the time of treatment. In the nontreatment group, it happens progressively due to AVM bleed in the follow-up. The real question is when will the 2 curves of death and neurologic disability cross? It was obvious before ARUBA that a long follow-up was needed to show the potential benefits of the treatment. The shorter the follow-up, the higher is the risk of the procedure and the lower is the risk of the disease and the benefit of the intervention. A 10-year follow-up was mandatory in ARUBA as it was used in the Trial on Endovascular Aneurysm Management study[5] and a shorter one would bias the results toward the benefit of no treatment. It is even more amazing to analyze the results of radiosurgery after 36 months, the time required for radiosurgery to cure the AVM. Then only complications of radiosurgery are evaluated, not the benefit of it.

Methodology

From April 4, 2007, to April 15, 2013, 1740 patients were screened for eligibility, and finally, 223 were randomized. Indeed, 1514 patients were not randomized because 1014 of them were ineligible for enrollment due to evidence of previous hemorrhage or a history of previous treatment. In the other 500 patients deemed eligible, 323 refused to participate in the trial, and 177 patients were treated outside the randomization process. Finally, 226 patients were randomized, but 3 were excluded because randomization occurred after database lock, 109 were randomized to no treatment, 114 were randomized to intervention, and only 91 finally received an interventional therapy (neurosurgery alone, 5; embolization alone, 30; radiosurgery alone, 31; embolization and surgery, 12; embolization and radiosurgery, 15; embolization, surgery, and radiosurgery, 1). The number of patients in all the different types of interventions is then extremely small, and indeed ARUBA could not explain the potential benefit of one type of intervention in 1 selected patient. For sure, the risk is that the results of ARUBA will lead to the conclusion that abstinence is better than any interventions. This conclusion cannot be derived from ARUBA due to the every limited number of patients in every treatment type. How could it be possible to conclude that surgery should not be performed in unruptured AVMs after the inclusion of 5 patients or that radiosurgery should not be performed after inclusion of 31?

Centers and Operators

Of the proposed 104 centers, only one-third participated (39 centers). Of these 39 centers, 10 centers included only 1 patient each,

questioning their qualification as high-volume centers, one of the initial criteria to participate to the study ("center experience with management of at least 10 brain AVMs per year").[1] Nevertheless, during a time when each center managed at least 60 patients, 10 centers (25% of total) included only 1 patient each or 1.7% of all their patients with AVMs. Furthermore, 22 centers (56% of total) included only ≤5% of all their patients with AVMs seen during the study period. Recruitment looks biased; we do know the reason for excluding many patients from randomization, with 323 refusing to participate and 177 patients being treated outside the study, leaving only 114 subjects in the intervention arm and 91 finally treated.

The idea of equipoise on which the decision to randomize relies is a difficult one: We do not randomize patients whose disease seems (to us) to have a low risk of intervention and a high natural risk. We randomize patients in whom treatment is difficult (risky) as well as those having a long-term natural risk, but then we only observe the short-term results. Those are biases that undermine the validity of the conclusions.

When one conducts an RCT on AVMs, every patient presenting with a brain AVM should be randomized consecutively and none treated outside. As in the most recent MR CLEAN trial (Multicenter Randomized Clinical Trial of Endovascular Treatment for Acute Ischemic Stroke in the Netherlands), comparing intravenous with intravenous and intra-arterial mechanical thrombectomy for acute stroke, institutions performing thrombectomies were not reimbursed for patients treated outside the trial.[6] Some raw data show that in 44 months, 502 patients underwent randomization in 16 Dutch centers and almost all treated patients were randomized.

Impact of ARUBA on Patient Clinical Care and Therapeutic Decisions

If we follow the conclusions of ARUBA (no treatment is better than any interventional treatment for unruptured brain AVMs), at long-term follow-up, we will be faced with consequences of no treatment, consequences that are unknown and about which ARUBA does not provide an answer.

We are eliminating the option of surgery, relying on 5 patients included in the study, or of radiosurgery, which is clearly a long-term suitable treatment strategy for a life-long risky condition, moreover whose results cannot be measured in a short 36-month follow-up period.

The authors replied that the National Institutes of Health/National Institute of Neurological Disorders and Stroke does not fund trials with longer than 5 years of follow-up.

Well, we have an answer, valid for 3 years, to a problem that lasts an entire life. Like the built-in obsolescence in industrial design, we can offer our patients a solution with an expiration date, a solution that will not serve their long-term safety.

In my own center serving nearly 3 million inhabitants, people are relatively settled and we follow patients for decades. My main concern with a patient presenting an unruptured AVM is his or her condition in the next 10, 15, or 20 years, not in the next 36 months.

The results of the New York Islands AVM Study (which were at the origin of the design of ARUBA) were very useful by giving a better knowledge of the annual risk of bleeds, depending on the presence of risk factors. On the contrary, the results of ARUBA will not give any new information that could be used in the decision process.

Why ARUBA Is Helpful

ARUBA showed the risk of unruptured AVM interventions. There are multiple reasons that encourage an operator to intervene. Many do not concern the patient and his or her disease, but the operator or his or her institution, for example, the operator and hospital financial turnover, the need for increasing center caseload for the operator and hospital reputation, partnership with industry, and even operator self-persuasion that the technique is safe and efficient. There are then definitely many patients who are treated for murky reasons and who probably have complications of a treatment that should not have been performed. The results of ARUBA should then convince the operators that they should only treat a limited number of selected patients because of these arguments.

What Is Next?

There are not many options. We still need a well-designed randomized trial, which is the best reliable level of evidence.

Minimal Requirements

A very large number of patients are needed to overcome the extreme heterogeneity of the disease (patient and AVM characteristics) and the huge variety of proposed interventions.

A very long follow-up (at least 10 years) is needed to depict the long-term morbidity/mortality of the disease and not only the treatment complication rate.

A consecutive enrollment is needed to avoid patient-selection biases.

A method to try to somehow counterbalance cultural resistances to necessary trials is to use the modified Zelen trial method, with preconsent randomized allocation to treatment groups, a method that had previously saved difficult breast cancer trials.[7,8]

A suboptimal alternative to randomization would be a cluster study, comparing centers oriented toward no treatment or toward 1 treatment type. Such a study has the advantage of being easier to organize and might enroll a huge number of patients much more rapidly. The minimal requirement would be the independent evaluation of the primary end point (mRS score) at long term (see Safe Implementation of Treatments in Stroke-OPEN as an example, https://sitsinternational.org/studies/open).

REFERENCES

1. Mohr JP, Parides MK, Stapf C, et al; international ARUBA investigators. **Medical management with or without interventional therapy for unruptured brain arteriovenous malformations (ARUBA): a multicentre, non-blinded, randomised trial.** *Lancet* 2014;383:614–21
2. Stapf C, Mast H, Sciacca RR, et al; New York Islands AVM Study Collaborators. **The New York Islands AVM Study: design, study progress, and initial results.** *Stroke* 2003;34:e29–33
3. Stapf C, Mast H, Sciacca RR, et al. **Predictors of hemorrhage in patients with untreated brain arteriovenous malformation.** *Neurology* 2006;66:1350–55

4. Stapf C, Mohr JP, Choi JH, et al**. Invasive treatment of unruptured brain arteriovenous malformations is experimental therapy.** *Curr Opin Neurol* 2006;19:63–68
5. Raymond J, Darsaut TE, Molyneux AJ; TEAM Collaborative Group. **A trial on unruptured intracranial aneurysms (the TEAM trial): results, lessons from a failure and the necessity for clinical care trials.** *Trials* 2011;12:64
6. Berkhemer OA, Fransen PS, Beumer D, et al; MR CLEAN Investigators. **A randomized trial of intraarterial treatment for acute ischemic stroke.** *N Engl J Med* 2015;372:11–20
7. Zelen M. **Randomised consent trials.** *Lancet* 1992;340:375
8. Taylor KM, Margolese RG, Soskolne CL. **Physicians' reasons for not entering eligible patients in a randomized clinical trial of surgery for breast cancer.** *N Engl J Med* 1984;310:1363–70

Current and Emerging MR Imaging Techniques for the Diagnosis and Management of CSF Flow Disorders: A Review of Phase-Contrast and Time–Spatial Labeling Inversion Pulse

S. Yamada, K. Tsuchiya, W.G. Bradley, M. Law, M.L. Winkler, M.T. Borzage, M. Miyazaki, E.J. Kelly, and J.G. McComb

ABSTRACT

SUMMARY: This article provides an overview of phase-contrast and time–spatial labeling inversion pulse MR imaging techniques to assess CSF movement in the CNS under normal and pathophysiologic situations. Phase-contrast can quantitatively measure stroke volume in selected regions, notably the aqueduct of Sylvius, synchronized to the heartbeat. Judicious fine-tuning of the technique is needed to achieve maximal temporal resolution, and it has limited visualization of CSF motion in many CNS regions. Phase-contrast is frequently used to evaluate those patients with suspected normal pressure hydrocephalus and a Chiari I malformation. Correlation with successful treatment outcome has been problematic. Time–spatial labeling inversion pulse, with a high signal-to-noise ratio, assesses linear and turbulent motion of CSF anywhere in the CNS. Time–spatial labeling inversion pulse can qualitatively visualize whether CSF flows between 2 compartments and determine whether there is flow through the aqueduct of Sylvius or a new surgically created stoma. Cine images reveal CSF linear and turbulent flow patterns.

ABBREVIATIONS: CSP = cavum septi pellucidi; NPH = normal pressure hydrocephalus; PC = phase-contrast; Time-SLIP = time–spatial labeling inversion pulse; V_{enc} = velocity-encoding value

Rapid advances in imaging techniques have remarkably improved the diagnosis and treatment of CNS disorders, with MR imaging being the most recent. New MR imaging applications are continually being developed, providing improved assessment of CNS disorders and their response to treatment. One area that has received much attention, but with only limited success, is CSF movement, the alteration of which results in many clinical disorders with hydrocephalus (including normal pressure hydrocephalus), cystic CSF collections, and Chiari malformations being more common. Until now, the only MR imaging technique to visualize CSF movement is phase-contrast (PC) MR imaging. Time–spatial labeling inversion pulse (Time-SLIP) is another option, which makes it possible to noninvasively select CSF at any region in the CNS and visualize its movement for up to 5 seconds, providing information about CSF dynamics even in slow-flowing regions. Time-SLIP is expected to have widespread application for diagnosis and evaluation of response to treatment of abnormal CSF movement. The objective of this article is to review the history and findings of PC and discuss additional benefits of Time-SLIP as another technique for expanding the role of MR imaging for the care and management of CNS disorders.

From the Department of Neurosurgery (S.Y.), Toshiba Rinkan Hospital, Sagamihara, Kanagawa, Japan; Department of Radiology (K.T.), Kyorin University, Mitaka, Tokyo, Japan; Department of Radiology (W.G.B.), University of California, San Diego, San Diego, California; Department of Neuroradiology (M.L.), University of Southern California, Los Angeles, California; Steinberg Diagnostic Imaging Center (M.L.W.), Las Vegas, Nevada; Division of Neuroradiology (M.T.B.), Department of Radiology, Institute for Maternal Fetal Health, Children's Hospital Los Angeles, Los Angeles, California; Department of Biomedical Engineering (M.T.B.), USC Viterbi School of Engineering, University of Southern California, Los Angeles, California; Toshiba Medical Research Institute (M.M.), Vernon Hills, Illinois; Toshiba America Medical Systems Inc (E.J.K.), Tustin, California; Division of Neurosurgery (J.G.M.), Children's Hospital Los Angeles, Los Angeles, California; and Department of Neurological Surgery (J.G.M.), Keck School of Medicine, University of Southern California, Los Angeles, California.

Please address correspondence to Erin J. Kelly, PhD, Toshiba America Medical Systems Inc, 2441 Michelle Dr, Tustin, CA 92780; e-mail: ekelly@tams.com

Indicates open access to non-subscribers at www.ajnr.org

Indicates article with supplemental on-line appendix.

Indicates article with supplemental on-line video.

http://dx.doi.org/10.3174/ajnr.A4030

Phase-Contrast MR Imaging: Technical Review

The earliest MR imaging visualization of CSF flow through the aqueduct was not obtained through quantitative methods but was inferred through distinct MR imaging flow artifacts arising from decreased signal and magnified by increased flow velocities.[1-4] Initial methods for quantifying such flow relied on knowledge of the T1 and T2 relaxation times of the CSF or a comparison of the degree of saturation between static tissue and flowing regions.[5,6] Later a modified gradient-echo technique, using phase shifts induced by bipolar gradients programmed into the pulse sequence, improved visualization of CSF movement. Feinberg and Mark[7] implemented a velocity imaging method that combined cardiac synchronization, 2D Fourier transform phase-encoding, and high temporal resolution to measure brain motion and CSF flow. They found differences in CSF velocity patterns in patients with dilated

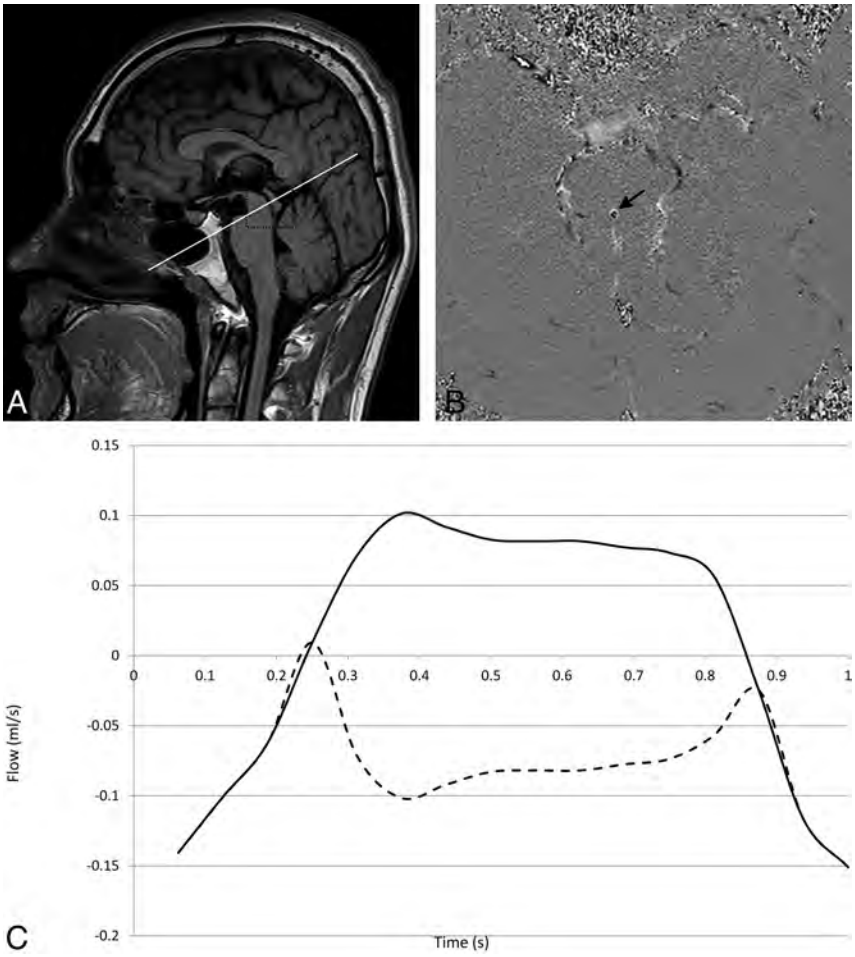

FIG 1. A 26-year-old healthy male volunteer. *A*, Geometry for the oblique-axial CSF phase-contrast scan. The section is positioned axially at a 90° angle through the aqueduct of Sylvius (*rectangle, A*). Aliasing (*B*) occurs if a phase value is greater than the maximum expected velocity, causing the phase to wrap back to a multiple of π, appearing black (*black arrow*) when it should appear white (or vice versa). Uncorrected (*dotted line*) and corrected (*solid line*) flow waveforms in milliliters per second represent bidirectional flow through the aqueduct (*C*). Aliasing can be corrected off-line by adding a multiple of $2 \times \pi \times V_{enc}$ to aliased pixels.

ventricles compared with controls, an early indication that MR velocity imaging might be useful in evaluating hydrocephalus.[7]

In PC, signal contrast between flowing and stationary spins is generated by sensitizing the phase of the transverse magnetization to the velocity of the spins.[8,9] PC collects 2 datasets, each with opposite polarity. When the 2 datasets are subtracted, accumulated phases from stationary spins cancel, but because flowing spins move from 1 position in the magnetic field gradient to another during the time between the executions of the 2 opposite polarity gradients, the moving spins accumulate a net phase proportional to the velocity of the nuclei. Because velocity is being measured as phase, the velocity values must be within $+\pi$ and $-\pi$. Aliasing occurs if a phase value is $>\pi$, causing the phase to wrap back to a multiple of π.

A parameter was developed that sets the maximum velocity that can be encoded in the pulse sequence, known as the velocity-encoding value (V_{enc}). The V_{enc} can be adjusted according to the arrangement of the bipolar gradients. PC generates the best results when maximum flow velocity is anticipated correctly through the V_{enc}. Flow velocities greater than the V_{enc} produce aliasing artifacts, and velocities much smaller than the V_{enc} result in poor image quality and weak signal.[10,11] An example of aliasing artifacts is shown in Fig 1. When aliasing occurs, the velocity information must be corrected by adding or subtracting $2 \times \pi \times V_{enc}$ during postprocessing, or the scan can be repeated with a higher V_{enc}. Magnitude and phase images are generated from 1 acquisition containing both anatomy and velocity information.

By synchronizing the acquisition with the cardiac cycle, the series of images generated contains velocity information that can be mapped to the phases of the heartbeat. From this, velocity can be plotted as a function of the cardiac cycle, providing the ability to calculate stroke volume, flow rate, mean velocity, and peak systolic/diastolic flow. Two series of velocity images are shown in Fig 2, where Fig 2*A* depicts a series of midline sagittal images and Fig 2*B* depicts a series of axial images at the level of the aqueduct. In both series, every odd phase of the 16 cardiac phases that were acquired is displayed.

PC and CSF Imaging

The SNR in PC images is highly related to the precision between the V_{enc} and the velocity being measured. Choosing the V_{enc} very close to the maximum expected velocity results in the maximum SNR in the velocity image. The V_{enc} must be lowered to achieve sufficient SNR for slow CSF flow. A setting of a V_{enc} that is too low may cause aliasing. Lowering the V_{enc} increases the gradient strength on the bipolar gradient and may increase the TR. Imaging flow throughout the cardiac cycle requires a short TR to achieve adequate temporal resolution. Therefore, PC for optimal CSF flow results requires careful fine-tuning of parameters for maximizing temporal resolution, SNR, and $V_{enc.}$ This sometimes can be problematic for patients whose CSF flow velocities are very high or very low compared with control values, with no way to individually predetermine the optimal situation. PC can only measure CSF if it is moving.

One limitation of the measurements obtained from PC acquisitions is that they result from data collected over a large number of cardiac cycles. The final velocity waveform represents an average measurement of those cycles, but it is presented as 1 cycle. For the most accurate quantitative evaluation of CSF flow, through-plane acquisition is performed perpendicular to the aqueduct, which minimizes partial volume effects.[10,11] Qualitative assessment of CSF flow can be accomplished with a midline sagittal acquisition for assessing in-plane flow. Not accounted for is the effect of respiration.

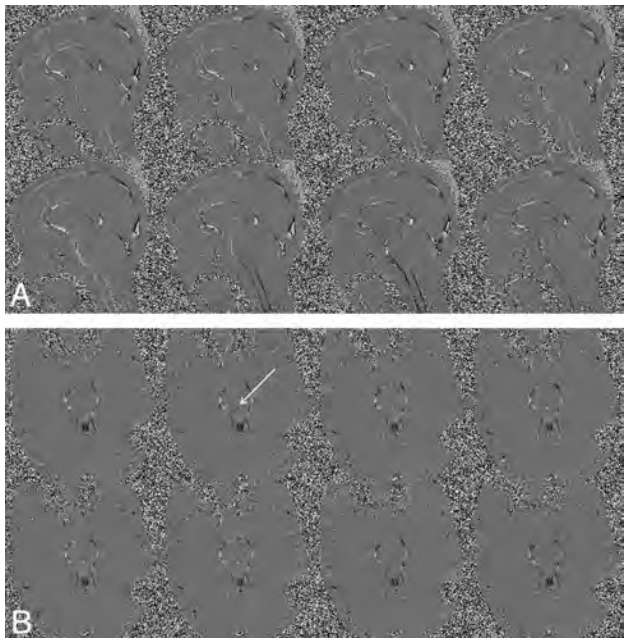

FIG 2. An 18-year-old healthy female volunteer. *A*, A series of midline sagittal images depicting pulsatile CSF flow, where flow magnitude and direction are represented as gray-scale. Flow changes from positive to negative and back to positive (white indicates peak caudal flow; black, peak cranial flow). *B*, Depiction of a series of axial images at the level of the aqueduct (*arrow*). In both series, every odd phase of the 16 cardiac phases that were acquired is displayed.

Quantitative Measurements from PC

Since the development of PC, clinical MR imaging flow studies of CSF have primarily focused on measurements in the aqueduct; however, a few studies sought to quantify flow in the prepontine cistern and craniocervical junction.[12-14] CSF pulsatility has been studied extensively by using this method[15,16] and has successfully demonstrated the ability to quantify CSF in axial locations throughout the brain. The pulsatile component moves cranially and caudally in a cyclical fashion as a function of the cardiac cycle at aqueductal peak velocity between 3 and 7 cm/s.[14] On the basis of these CSF flow studies, the brain is considered to behave as if it were being pulled in systole by the spinal cord secondary to arterial expansion.[15]

Numerous studies have documented normal aqueductal stroke volumes between 30 and 50 μL.[14,15,17,18] (The aqueductal CSF stroke volume is defined as the average of the volume flowing down during systole and up during diastole.[19]) Studies of CSF flow in hydrocephalus secondary to intracranial pressure changes demonstrated by invasive monitoring have found up to a 10-fold increased pulsatile aqueductal flow[15,17,19-24] compared with that in healthy controls. This finding has been used to build criteria for diagnosing idiopathic normal pressure hydrocephalus (NPH) based on stroke volumes of >42 μL[19] or pulsatile flow rates above a threshold of 18 mL/min, for example.[20] However, setting thresholds such as these has so far not proved to be clinically reliable. For example, Greitz[15] found, along with an increased aqueductal flow rate, a corresponding decreased flow rate through the craniocervical junction. Balédent et al,[12] in a larger study, found no such changes. To use stroke volume to diagnose hyperdynamic CSF, a measurement that some investigators have advocated for diagnosing shunt-responsive NPH,[19] one must first determine a baseline stroke volume in healthy elderly patients. Then, by using the same technique on the same machine, some have found a stroke volume twice normal to correlate with shunt responsiveness.[19]

In addition to net flow measurements, some studies have used the time-dependent features of the waveform to identify abnormal pathophysiology. One such study revealed a shorter systolic flow period of the temporal waveform for patients with communicating hydrocephalus compared with healthy controls.[12] PC measurements of CSF flow have also been used to study patients with Chiari I malformation. In these studies, the CSF flow at the craniocervical junction has been shown to exhibit changes in flow patterns, including local flow jets and bidirectional flow.[25-27] These studies have shown that patients with Chiari I malformations have significant elevations of peak CSF systolic velocity at the foramen magnum. The application of these findings to determine which patients would benefit from a craniocervical decompression has, however, proved problematic.

PC has also been used to study vascular flow timing with respect to CSF flow timing in various locations in the brain. Some studies hypothesized that vascular flow timing may be used as a measure of intracranial compliance changes in NPH and can be used as an indicator of shunt responsiveness.[28] These studies have not proved helpful because the measurements were not able to successfully predict shunt responsiveness.[29] A study of PC measurements of hydrodynamics found that the patients who responded to shunts were identical to the nonresponders in all variables measured.[29]

Prediction of improved clinical function following CSF diversion, particularly in patients thought to have NPH, has been a highly sought goal for PC CSF flow studies. In particular, the association between aqueductal stroke volume and the response to shunting has been tested numerous times.[19,21-24,30,31] Initial studies found a positive response to CSF diversion for patients with NPH whose aqueductal stroke volumes reached ≥ 42 μL.[19] However, repeat studies by Kahlon et al[32] performed in 38 patients did not find any statistical significance between stroke volume and improvement from shunting. Dixon et al[22] also failed to find an association between CSF pulsatility and clinical symptoms of NPH. Some of the variability in findings may be attributed to temporal changes that naturally occur, with PC measuring 1 point in time of a dynamically changing system. In fact, Scollato et al[33] observed a patient with unshunted hydrocephalus for 2 years and found an initial increase in aqueductal stroke volume, followed by a decrease. Therefore, this variability in pulsatility, which is still not clearly understood, makes it difficult to use a single PC measurement of stroke volume as a reliable predictor of whether a given patient will respond favorably to CSF diversion.

Time-SLIP

A New Look at CSF Movement. Historic CSF flow theories of progressive hydrocephalus propose that blockage of the arachnoid granulations increases the resistance to the absorption of CSF into the bloodstream, leading to an accumulation of CSF in the ventricles. In the pulsatile models of hydrocephalus, a "water-hammer" effect is hypothesized, in which large undampened pul-

sations produce increased pressure gradients and asymmetric pulsation distributions lead to ventricular dilation.[34,35] Enlarged pulse-wave amplitudes of CSF movement in patients with NPH have been observed and measured with MR imaging for a number of years.[1,36] This effort has attempted to improve our understanding of hydrocephalus.[14,15,36] However, it has failed to correctly identify those patients who would benefit from CSF diversion. PC cannot reliably visualize CSF flow within the ventricular or subarachnoid spaces or within cysts; this visualization can be repeatedly accomplished with Time-SLIP.[37] Bulk CSF flow (ie, drainage of CSF from the CNS) of approximately 20 mL/h, is too little and too widely dispersed to be seen with MR imaging at present.

Time-SLIP and Arterial Spin-Labeling. Time-SLIP is an arterial spin-labeling variant that can be combined with fast advanced spin-echo or steady-state free precession sequences to depict flow in any imaging orientation within a targeted region.[37,38] For vascular imaging, arterial spin-labeling magnetically tags the blood with radio frequency pulses and uses the labeled blood as a tracer to generate vascular images in a relatively simple manner. The stationary tissue signal is suppressed by an inversion pulse, and the final image contains only the contribution of the labeled flow, acquired after a deliberate delay time known by convention as the TI interval. Arterial spin-labeling has been used to evaluate blood flow in the renal, carotid, and pulmonary arteries and in the pulmonary and portal-venous systems. This technique produces high-quality angiograms by using blood as its own tracer, instead of a contrast agent.[39-44] The application of arterial spin-labeling lends itself very well to imaging CSF movement, by using CSF as its own tracer as well.

Time-SLIP and CSF. CSF is a flowing entity; therefore, a similar approach can be used to depict CSF movement, but in a unique way. Unlike PC, which is cardiac-gated and displays the visualization of the pulsatile component of CSF, 2D Time-SLIP acquisitions are incremental, allowing the linear and turbulent movement components of CSF to be seen for up to 5 seconds noninvasively for the first time. Using a 2D fast advanced spin-echo sequence as the fundamental acquisition scheme, Time-SLIP can acquire a series of single-shot images with incremental TI to visualize linear and turbulent flow.[37]

Time-SLIP: Technical Review. CSF movement viewed with Time-SLIP uses a single-shot fast advanced spin-echo technique as the underlying sequence in any sagittal, coronal, axial, or oblique plane. Technical details can be found in the article by Yamada et al.[37] While the use of arterial spin-labeling for visualization of the vasculature throughout the body is well-established, its application for CSF flow imaging is relatively new and differs from traditional applications in its use of incremental TI within the same 2D imaging sequence, thus enabling the CSF and its movement to be viewed in small incremental steps, independent of the cardiac cycle.

Distinguishing CSF Flow Patterns

Time-SLIP has enabled CSF flow to be viewed and understood in a new way that has directly benefitted patients.[45,46] On the basis of a number of studies using Time-SLIP on healthy subjects, it has showed evidence of turbulent reflux flow between the aqueduct of Sylvius and the third ventricle, something that has never been seen on PC.[37] In addition, this reflux flow was also clearly and consistently seen in the lateral ventricles because CSF flows backward from the third ventricle through the foramen of Monro into the lateral ventricle.[37]

On the basis of the results of initial baseline studies, Time-SLIP can be readily used as a screening tool to determine whether the CSF flow is typical, atypical, or not moving at all.[37] In an article by Yamada et al,[37] 2 patients with hydrocephalus did not exhibit the same reflux pattern consistently depicted in the healthy subjects. In a patient with noncommunicating hydrocephalus secondary to a posterior fossa tumor, the reflux flow into the lateral ventricle was absent from the tagged CSF in the third ventricle. A repeat study in this patient following the placement of a right lateral ventricle external CSF drain showed re-establishment of the normal reflux flow pattern consistently observed in the healthy subjects. In a patient with a left middle fossa arachnoid cyst, the CSF in the basal cistern was tagged. Before fenestration, no evidence of CSF flow into the cyst was noted. After surgical intervention, a repeat study demonstrated labeled CSF flowing into the cyst. In both cases, imaging with Time-SLIP confirmed noninvasively the anticipated restoration of CSF movement.

A recent case study reported the usefulness of Time-SLIP in evaluating a patient with an enlarging symptomatic cavum septi pellucidi (CSP), a CSF-filled cavity bounded by thin triangular vertical membranes separating the right and left anterior horns of the lateral ventricles.[47] Serial CT scans noted progressive enlargement of the CSP and lateral ventricles in this patient, who developed progressive headaches and obtundation following a subarachnoid hemorrhage. Before surgical intervention, Time-SLIP showed CSF flow between the third and lateral ventricles, but not into the CSP. Following surgical fenestration of the CSP, MR imaging with Time-SLIP demonstrated decreased ventricular and CSP size and the presence of CSF flowing between the third ventricle and the CSP, which coincided with resolution of this patient's symptoms. The Time-SLIP study in this patient supported the hypothesis of Shaw and Alvord[48] that in asymptomatic nonexpanding CSP, CSF is in free communication with the ventricular system. In fact, the study showed that when CSF communication was absent in this patient, the CSP expanded.[48] The case study is an example of the clinical usefulness of the technique in demonstrating the presence or absence of CSF communication.

The effect of respiration on CSF flow has not been adequately studied with PC because of temporal limitations. Low-resolution or indirect methods such as echo-planar imaging and real-time acquisition and evaluation of pulsatile blood flow have not been able to adequately visualize CSF movement in response to respirations either.[49] The higher intrinsic SNR and temporal resolution of Time-SLIP make it possible to visualize CSF movement in response to respiration and how the CSF flow patterns are altered by the depth of the respiratory effort.

Utility of Time-SLIP

Time-SLIP is a straightforward noninvasive method for determining whether CSF can flow between 2 spaces and whether flow has been restored after surgical intervention.[37,47] Because Time-

SLIP acquires a series of images during several seconds, the presence or absence of CSF movement from the tagged region into adjacent compartments, such as through the aqueduct of Sylvius,

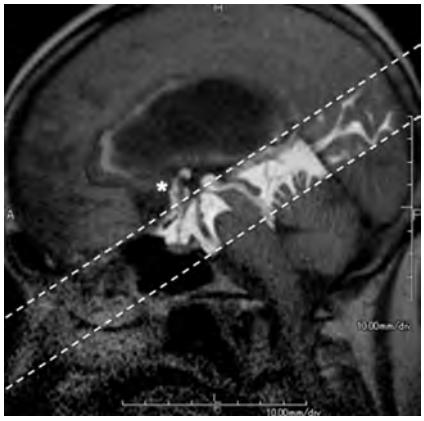

FIG 3. Hydrocephalus in a 74-year-old woman. The patient had undergone endoscopic third ventriculostomy. Patency of the fenestration on the floor of the third ventricle is readily and noninvasively confirmed postsurgery by the presence of CSF flow between the third ventricle and the basal cisterns (*asterisk*) emerging from the tagged region (*dotted lines*). (See On-line Video 1, which demonstrates postsurgical CSF flow between the third ventricle and the basal cisterns.)

confirms the presence of CSF flow or blockage, as seen in the patient depicted in Fig 3, before and after endoscopic third ventriculostomy. Time-SLIP can be used postoperatively to evaluate the patency of the fenestration by observing CSF flow between the third ventricle and the basal cisterns (Fig 3). Reflux flow from the third ventricle into the lateral ventricle has been established in adult patients without hydrocephalus; however, flow has been shown to be restricted in patients with hydrocephalus and NPH.[37] Normal reflux flow in a healthy patient is seen in Fig 4*A*, restricted in NPH (Fig 4*B*), and restored after surgical intervention (Fig 4*C*). A Chiari malformation can restrict normal CSF flow between the cranial and spinal compartments; this restriction, in turn, results in CSF accumulation within the spinal cord, producing a syrinx. Time-SLIP is a useful, noninvasive tool for evaluating pre- and postoperative craniocervical decompressive changes to CSF flow (Fig 5).

For understanding CSF flow disorders, the PC technique to quantify CSF flow velocities and Time-SLIP to visualize CSF flow characteristics, pathways, and blockages are qualitatively useful techniques in combination. Time-SLIP is especially useful in regions where it is difficult or impossible to visualize CSF flow with PC, such as in the lateral ventricles, subarachnoid spaces, or within a cyst, secondary to limitations of V_{enc}, SNR, or the absence of pulsatile flow. The Time-SLIP tag is freely selectable, and

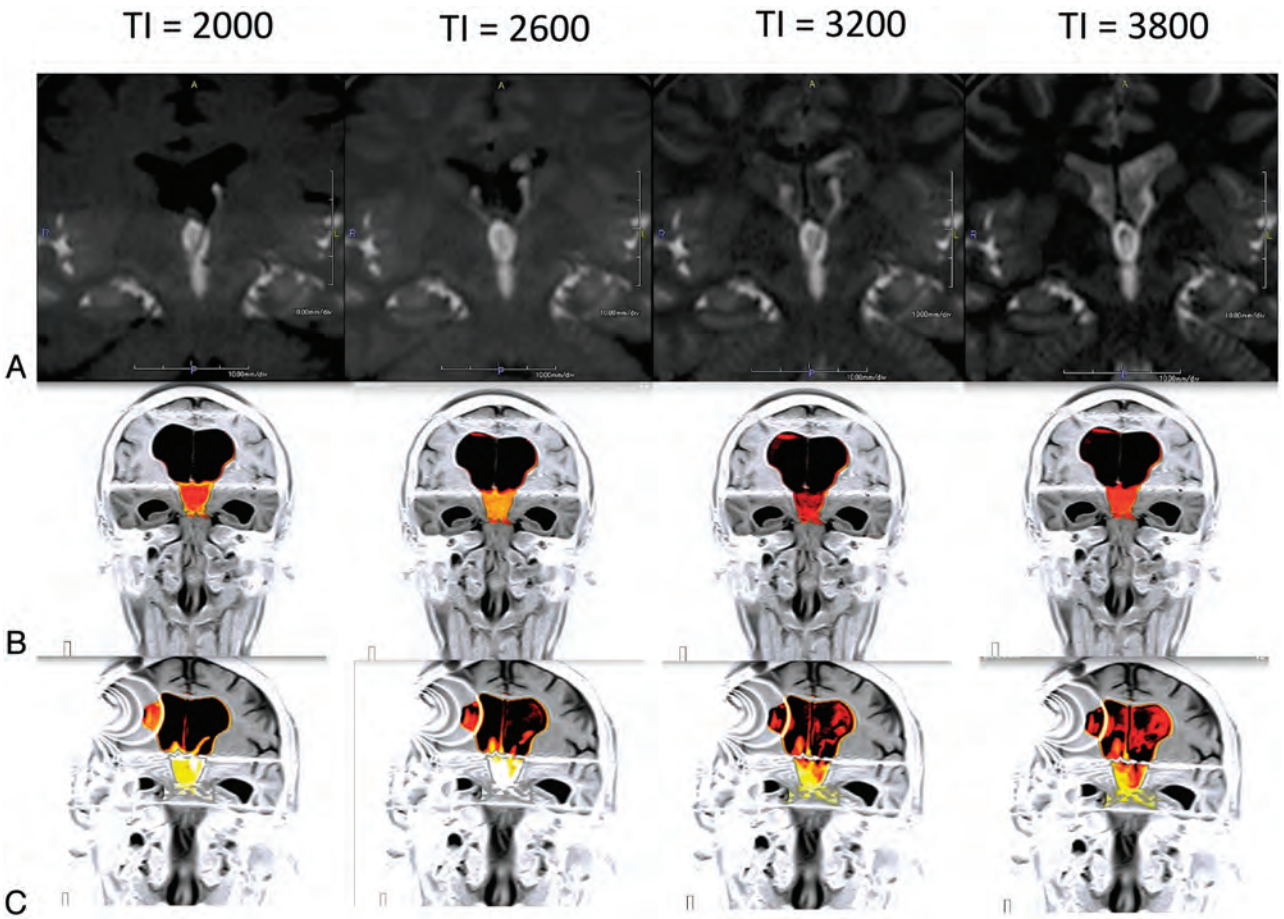

FIG 4. Idiopathic normal pressure hydrocephalus in a 78-year-old man. Time-SLIP has consistently shown the presence of reflux flow from the third ventricle into the lateral ventricle in adult patients without hydrocephalus (*A*). This flow is shown to be restricted in NPH (*B*). Time-SLIP in the same patient confirms that this flow is restored after surgical intervention by inserting a CSF diverting shunt (*C*, artifacts on the right are from the shunt valve). (See On-line Videos 2 and 3, which demonstrate restricted flow and restored flow pre- and postsurgery, respectively.)

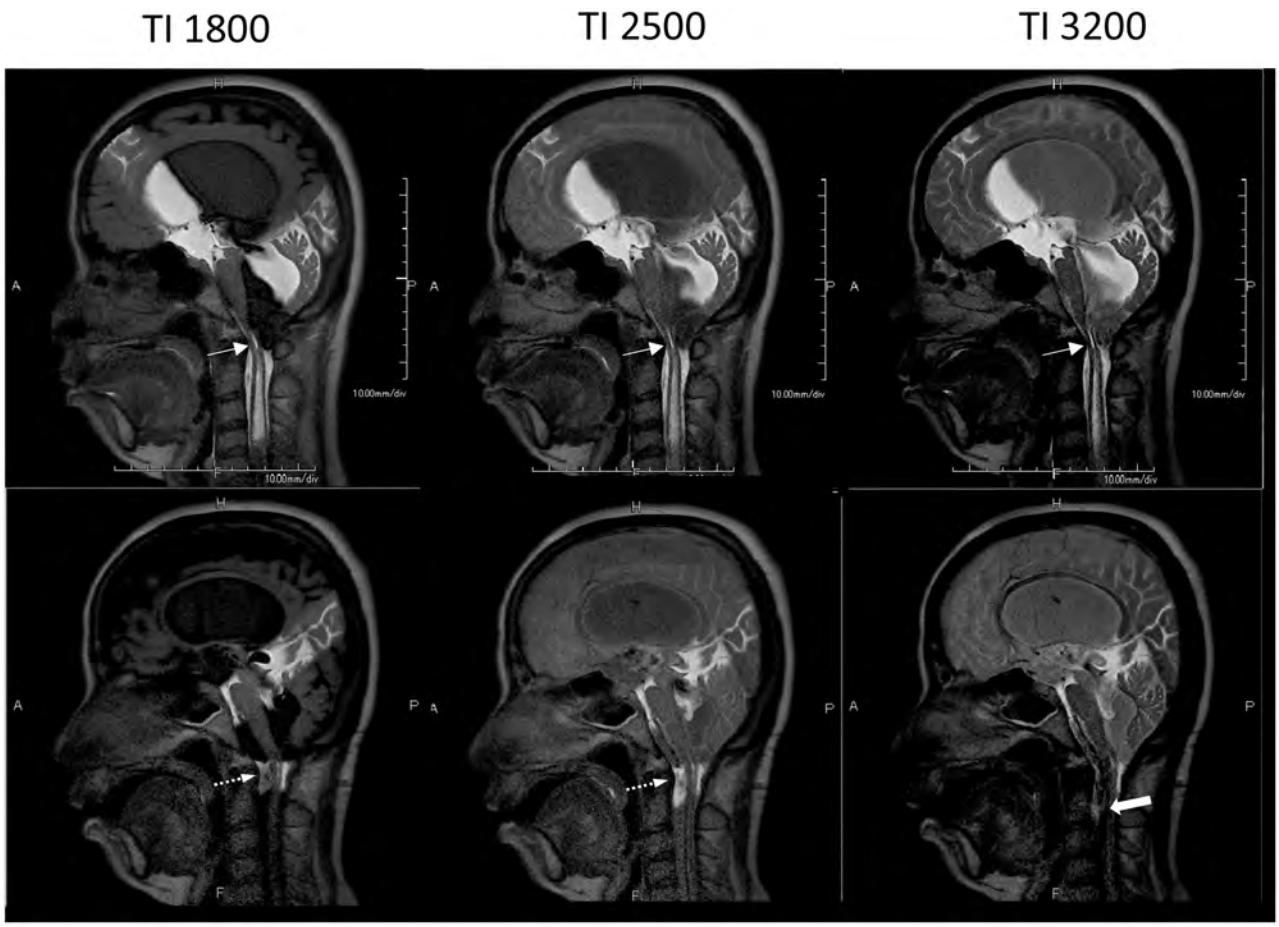

FIG 5. Chiari malformation in a 43-year-old woman pre- (top row) and post- (bottom row) surgery, shown at incremental TIs. Obliteration of the subarachnoid space at the craniocervical junction is associated with Chiari I malformation and a syrinx (top row, *arrow*). Following craniocervical decompression (bottom row, *arrow*), Time-SLIP shows CSF flow ventral to the brain stem and cervical spinal cord and a decrease in the size of the syrinx (*bold arrow*). (See On-line Videos 4 and 5, which demonstrate restricted flow and restored flow with a decrease in the size of the syrinx pre- and postsurgery, respectively.)

its orientation is easily and infinitely changed to target the region of interest, allowing CSF flow to be visualized in any direction or location.

Half of all occurrences of NPH have no known cause, and diagnosis is made primarily by clinical observations such as gait disturbances, dementia, and incontinence. Although enlarged ventricles are the expected MR imaging finding in patients with suspected NPH, the definitive diagnosis of NPH is difficult, and PC has not consistently predicted patient responsiveness to shunting. More extensive studies are currently underway to investigate whether Time-SLIP will be more predictive in diagnosing suspected NPH that is responsive to CSF diversion.

Time-SLIP can be used to determine whether CSF spaces are in communication. Following an endoscopic third ventriculostomy, a catheter is often placed in the ventricle to measure postoperative intraventricular pressure. Contrast injected into the ventricles can establish the success of the procedure by noting the distribution of the contrast with a CT scan. The use of Time-SLIP for this purpose would alleviate the need for postprocedural CT ventriculography because surgical outcomes could be assessed noninvasively.[37]

Summary and Future Work

PC was the first quantitative MR imaging tool for evaluating CSF in pathophysiologic conditions. Time-SLIP provides additional information about CSF flow patterns. Perhaps most remarkably, the typical CSF flow pathway that has been described in textbooks is actually much different from that observed noninvasively with Time-SLIP,[45] even in the normal, nonhydrocephalic brain. Larger clinical studies are expected to provide additional evidence. Possible clinical applications using Time-SLIP to visualize and monitor CSF movement are listed in the On-line Appendix.

Most treatments for hydrocephalus and related CSF flow disorders are surgical, and these are known to work well in appropriate patients. Initial Time-SLIP studies have shown that successful treatments can be attained by understanding CSF flow patterns and by restoring these flow patterns when they are abnormal.[37,45,47]

Disclosures: Shinya Yamada—*UNRELATED*: *Grants/Grants Pending*: $5000,* *Payment for Lectures (including service on Speakers Bureaus)*: $2000, *Travel or Meeting Expenses Unrelated to Activities Listed*: $2000, all from Toshiba Medical Systems. Kazuhiro Tsuchiya—*UNRELATED: Payment for Lectures (including service on Speakers Bureaus)*: *Development of Educational Presentations*: Toshiba Medical Systems. Mark L. Winkler—*RELATED*: *Other*: travel support to meetings from Toshiba Medical Systems; *UNRELATED*: *Consultancy*: Toshiba America Medical Systems. *Money paid to the institution.

REFERENCES

1. Bradley WG Jr, Kortman KE, Burgoyne B. **Flowing cerebrospinal fluid in normal and hydrocephalic states: appearance on MR images.** *Radiology* 1986;159:611–16
2. Mark AS, Feinberg DA, Sze GK, et al. **Gated magnetic resonance imaging of the intracranial cerebrospinal fluid spaces.** *Acta Radiol Suppl* 1986;369:296–99
3. Bradley WG Jr, Whittemore AR, Kortman KE, et al. **Marked cerebrospinal fluid void: indicator of successful shunt in patients with suspected normal-pressure hydrocephalus.** *Radiology* 1991; 178:459–66
4. Krauss JK, Regel JP, Vach W, et al. **Flow void of cerebrospinal fluid in idiopathic normal pressure hydrocephalus of the elderly: can it predict outcome after shunting?** *Neurosurgery* 1997;40:67–73, discussion 73–74
5. Singer JR. **Nuclear magnetic resonance blood flow measurements.** *Cardiovasc Intervent Radiol* 1986;8:251–59
6. Singer JR, Crooks LE. **Nuclear magnetic resonance blood flow measurements in the human brain.** *Science* 1983;221:654–56
7. Feinberg, DA, Mark, AS. **Human brain motion and cerebrospinal fluid circulation demonstrated with MR velocity imaging.** *Radiology* 1987;163:793–99
8. Dumoulin CL, Yucel EK, Vock P, et al. **Two- and three-dimensional phase contrast MR angiography of the abdomen.** *J Comput Assist Tomogr* 1990;14:779–84
9. Tsuruda JS, Shimakawa A, Pelc NJ, et al. **Dural sinus occlusion: evaluation with phase-sensitive gradient-echo MR imaging.** *AJNR Am J Neuroradiol* 1991;12:481–88
10. Connor SE, O'Gorman R, Summers P, et al. **SPAMM, cine phase contrast imaging and fast spin-echo T2-weighted imaging in the study of intracranial cerebrospinal fluid (CSF) flow.** *Clin Radiol* 2001;56:763–72
11. Saloner D. **The AAPM/RSNA physics tutorial for residents: an introduction to MR angiography.** *Radiographics* 1995;15:453–65
12. Balédent O, Gondry-Jouet C, Meyer ME, et al. **Relationship between cerebrospinal fluid and blood dynamics in healthy volunteers and patients with communicating hydrocephalus.** *Invest Radiol* 2004; 39:45–55
13. Greitz D, Hannerz J, Rähn T, et al. **MR imaging of cerebrospinal fluid dynamics in health and disease: on the vascular pathogenesis of communicating hydrocephalus and benign intracranial hypertension.** *Acta Radiol* 1994;35:204–11
14. Wagshul ME, Chen JJ, Egnor MR, et al. **Amplitude and phase of cerebrospinal fluid pulsations: experimental studies and review of the literature.** *J Neurosurg* 2006;104:810–19
15. Greitz D. **Cerebrospinal fluid circulation and associated intracranial dynamics: a radiologic investigation using MR imaging and radionuclide cisternography.** *Acta Radiol Suppl* 1993;386:1–23
16. Naidich TP, Altman NR, Gonzalez-Arias SM. **Phase contrast cine magnetic resonance imaging: normal cerebrospinal fluid oscillation and applications to hydrocephalus.** *Neurosurg Clin N Am* 1993;4:677–705
17. Bateman GA, Levi CR, Schofield P, et al. **The pathophysiology of the aqueduct stroke volume in normal pressure hydrocephalus: can comorbidity with other forms of dementia be excluded?** *Neuroradiology* 2005;47:741–48
18. Stoquart-ElSankari S, Balédent O, Gondry-Jouet C, et al. **Aging effects on cerebral blood and cerebrospinal fluid flows.** *J Cereb Blood Flow Metab* 2007;27:1563–72
19. Bradley WG Jr, Scalzo D, Queralt J, et al. **Normal-pressure hydrocephalus: evaluation with cerebrospinal fluid flow measurements at MR imaging.** *Radiology* 1996;198:523–29
20. Luetmer PH, Huston J, Friedman JA, et al. **Measurement of cerebrospinal fluid flow at the cerebral aqueduct by use of phase-contrast magnetic resonance imaging: technique validation and utility in diagnosing idiopathic normal pressure hydrocephalus.** *Neurosurgery* 2002;50:534–43, discussion 543–44
21. Egeler-Peerdeman SM, Barkhof F, Walchenbach R, et al. **Cine phase-contrast MR imaging in normal pressure hydrocephalus patients: relation to surgical outcome.** *Acta Neurochir Suppl* 1998;71:340–42
22. Dixon GR, Friedman JA, Luetmer PH, et al. **Use of cerebrospinal fluid flow rates measured by phase-contrast MR to predict outcome of ventriculoperitoneal shunting for idiopathic normal-pressure hydrocephalus.** *Mayo Clin Proc* 2002;77:509–14
23. Poca MA, Sahuquillo J, Busto M, et al. **Agreement between CSF flow dynamics in MRI and ICP monitoring in the diagnosis of normal pressure hydrocephalus: sensitivity and specificity of CSF dynamics to predict outcome.** *Acta Neurochir Suppl* 2002;81:7–10
24. Gideon P, Ståhlberg F, Thomsen C, et al. **Cerebrospinal fluid flow and production in patients with normal pressure hydrocephalus studied by MRI.** *Neuroradiology* 1994;36:210–15
25. Haughton VM, Korosec FR, Medow JE, et al. **Peak systolic and diastolic CSF velocity in the foramen magnum in adult patients with Chiari I malformations and in normal control participants.** *AJNR Am J Neuroradiol* 2003;24:169–76
26. Iskandar BJ, Quigley M, Haughton VM. **Foramen magnum cerebrospinal fluid flow characteristics in children with Chiari I malformation before and after craniocervical decompression.** *J Neurosurg* 2004;101(2 suppl):169–78
27. Quigley MF, Iskandar B, Quigley ME, et al. **Cerebrospinal fluid flow in foramen magnum: temporal and spatial patterns at MR imaging in volunteers and in patients with Chiari I malformation.** *Radiology* 2004;232:229–36
28. Bateman GA. **Vascular compliance in normal pressure hydrocephalus.** *AJNR Am J Neuroradiol* 2000;21:1574–85
29. Bateman GA, Loiselle AM. **Can MR measurement of intracranial hydrodynamics and compliance differentiate which patient with idiopathic normal pressure hydrocephalus will improve following shunt insertion?** *Acta Neurochir (Wien)* 2007;149:455–62, discussion 462
30. Balédent O, Henry-Feugeas MC, Idy-Peretti I. **Cerebrospinal fluid dynamics and relation with blood flow: a magnetic resonance study with semiautomated cerebrospinal fluid segmentation.** *Invest Radiol* 2001;36:368–77
31. Henry-Feugeas MC, Idy-Peretti I, Baledent O, et al. **Cerebrospinal fluid flow waveforms: MR analysis in chronic adult hydrocephalus.** *Invest Radiol* 2001;36:146–54
32. Kahlon B, Annertz M, Ståhlberg F, et al. **Is aqueductal stroke volume, measured with cine phase-contrast magnetic resonance imaging scans useful in predicting outcome of shunt surgery in suspected normal pressure hydrocephalus?** *Neurosurgery* 2007;60:124–29, discussion 129–30
33. Scollato A, Tenenbaum R, Bahl G, et al. **Changes in aqueductal CSF stroke volume and progression of symptoms in patients with unshunted idiopathic normal pressure hydrocephalus.** *AJNR Am J Neuroradiol* 2008;29:192–97
34. Egnor M, Zheng L, Rosiello A, et al. **A model of pulsations in communicating hydrocephalus.** *Pediatr Neurosurg* 2002;36:281–303
35. Branco G, Goulão A, Ferro JM. **MRI in aqueduct compression and obstructive hydrocephalus due to an ecstatic basilar artery.** *Neuroradiology* 1993;35:447–48
36. Bradley WG. **Cerebrospinal fluid dynamics and shunt responsiveness in patients with normal-pressure hydrocephalus.** *Mayo Clin Proc* 2002;77:507–08
37. Yamada S, Miyazaki M, Kanazawa H, et al. **Visualization of cerebrospinal fluid movement with spin labeling at MR imaging: preliminary results in normal and pathophysiologic conditions.** *Radiology* 2008;249:644–52
38. Miyazaki M, Lee VS. **Nonenhanced MR angiography.** *Radiology* 2008;248:20–43
39. Chen X, Xia C, Sun J, et al. **Nonenhanced renal artery MR angiography with time spatial labeling inversion pulse technology and its clinical values**[in Chinese]. *Sichuan Da Xue Xue Bao Yi Xue Ban* 2010;41:881–84
40. Hori M, Aoki S, Oishi H, et al. **Utility of time-resolved three-dimen-**

sional magnetic resonance digital subtraction angiography without contrast material for assessment of intracranial dural arterio-venous fistula. *Acta Radiol* 2011;52:808–12

41. Ishimori Y, Monma M, Kawamura H, et al. **Time spatial labeling inversion pulse cerebral MR angiography without subtraction by use of dual inversion recovery background suppression.** *Radiol Phys Technol* 2011;4:78–83
42. Kogure T, Kogure K, Iizuka M, et al. **Effective use of flow-spoiled FBI and time-SLIP methods in the diagnostic study of an aberrant vessel of the head and neck: "left jugular venous steal by the right jugular vein."** *J Magn Reson Imaging* 2010;32:429–33
43. Satogami N, Okada T, Koyama T, et al. **Visualization of external carotid artery and its branches: non-contrast-enhanced MR angiography using balanced steady-state free-precession sequence and a time-spatial labeling inversion pulse.** *J Magn Reson Imaging* 2009;30:678–83
44. Sugita R, Furuta A, Horaguchi J, et al. **Visualization of pancreatic juice movement using unenhanced MR imaging with spin labeling: preliminary results in normal and pathophysiologic conditions.** *J Magn Reson Imaging* 2012;35:1119–24
45. Yamada S, Goto T. **Understanding of cerebrospinal fluid hydrodynamics in idiopathic hydrocephalus (A) visualization of CSF bulk flow with MRI time-spatial labeling pulse method (time-SLIP)** [in Japanese]. *Rinsho Shinkeigaku* 2010;50:966–70
46. Yamada S, Shibata M, Scadeng M, et al. **MRI tracer study of the cerebrospinal fluid drainage pathway in normal and hydrocephalic guinea pig brain.** *Tokai J Exp Clin Med* 2005;30:21–29
47. Yamada S, Goto T, McComb JG. **Use of a spin-labeled cerebrospinal fluid magnetic resonance imaging technique to demonstrate successful endoscopic fenestration of an enlarging symptomatic cavum septi pellucidi.** *World Neurosurg* 2013:80:436.e15–18
48. Shaw CM, Alvord EC Jr. **Cava septi pellucid et vergae: their normal and pathological states.** *Brain* 1969;92:213–23
49. Yamada S, Miyazaki M, Yamashita Y, et al. **Influence of respiration on cerebrospinal fluid movement using magnetic resonance spin labeling.** *Fluids Barriers CNS* 2013;10:36

Critique of the Analysis of UpToDate.com on the Treatment of Painful Vertebral Compression Fractures: Time to Update UpToDate

D.P. Beall, W.P. McRoberts, S.H. Berven, J.T. Ledlie, S.M. Tutton, and B.P. Parsons

ABSTRACT

SUMMARY: The treatment of painful vertebral compression fractures has changed substantially since the introduction of vertebroplasty in the mid-1980s and balloon kyphoplasty in the late 1990s. Both procedures were widely accepted with the vertebral fractures treated reaching 150,000 per annum in 2009 prior to the publication of 2 randomized controlled trials comparing vertebroplasty with a sham treatment published in the *New England Journal of Medicine* in August 2009. Since then, there has been a flood of information on vertebral augmentation and balloon kyphoplasty. It is worth evaluating this information especially because it relates to current recommendations that are often followed blindly by medical and administrative groups unfamiliar with either the procedure or the high level of evidence surrounding vertebral augmentation. To streamline the evaluation of some current recommendations, we limited the analysis to the recommendations found on UpToDate.com. This Web site is an evidence-based, peer-reviewed source of information available for patients, doctors, health insurance companies, and population-based medical decision-making.

ABBREVIATIONS: BKP = balloon kyphoplasty; NSM = nonsurgical management; VA = vertebral augmentation; VCF = vertebral compression fracture; VP = vertebroplasty

The treatment of painful vertebral compression fractures (VCFs) has changed substantially since the introduction of vertebroplasty in the mid-1980s.[1] The advent of balloon kyphoplasty in the late 1990s represented a new variation of the procedure by using balloons to reduce the vertebral fracture and create a void within the vertebral body.[2] Both procedures were widely accepted with vertebral fractures treated reaching 150,000 per annum in 2009 before the publication of 2 randomized controlled trials comparing vertebroplasty with a sham treatment published in the *New England Journal of Medicine* in August 2009.[3–5]

The publication of the trials generated a substantial controversy because the results seemed to fly in the face of clinical experience; consequently, numerous societies and physician groups issued statements commenting on the conclusions of the studies. The Society of Interventional Radiology[6] and the North American Spine Society[7] issued statements commenting on the trials with the Society of Interventional Radiology stating that "based on the … weakness in the studies and the degree of discordance between the outcomes of these studies, prior studies and experience, we believe it is premature—and possibly incorrect—to conclude that vertebroplasty is no better than a control sham procedure" and the North American Spine Society stating that "[b]eyond the lay press releases which claim 'Vertebroplasty found to be useless for osteoporotic fracture and disk pain,' it is time for cooler heads to prevail. The medical literature thirsts for evidence. The data from these two studies must be considered carefully and thoughtfully.… More practical conclusions should be made based on a thorough and systematic review of *all* the literature to better define the subgroup of patients for which vertebroplasty might be most appropriate."

Since 2009, a flood of information has discussed vertebral augmentation (VA), a term that includes vertebroplasty (VP) and balloon kyphoplasty (BKP). This information provides valuable insight into the treatment of patients with osteoporotic VCFs. It is worth evaluating this information especially because it relates to current recommendations that are often followed blindly by medical and administrative groups unfamiliar with either the VA procedures or the high level and unpresented body of evidence surrounding VA.

To streamline the evaluation of some current recommendations, we limited the analysis to the recommendations found on

Received June 19, 2014; accepted after revision June 30.

From Radiology Services (D.P.B.), Clinical Radiology of Oklahoma, Musculoskeletal Imaging and Interventional, Oklahoma City, Oklahoma; Interventional Spine and Pain Medicine (W.P.M.), Holy Cross Hospital, Fort Lauderdale, Florida; Department of Orthopaedic Surgery (S.H.B.), University of California San Francisco, San Francisco, California; Tyler Neurosurgery (J.T.L.), Tyler, Texas; Departments of Radiology and Surgery (S.M.T.), Medical College of Wisconsin, Froedtert East Clinic, Milwaukee, Wisconsin; and Department of Radiology (B.P.P.), University of Oklahoma College of Medicine, Edmond, Oklahoma.

Please address correspondence to Douglas P. Beall, MD, Chief of Radiology Services, Clinical Radiology of Oklahoma, Musculoskeletal Imaging and Interventional, 610 NW 14th St, Oklahoma City, OK 73103; e-mail: db@clinrad.org

http://dx.doi.org/10.3174/ajnr.A4095

UpToDate.com. This Web site is an evidence-based, peer-reviewed source of information available for patients, doctors, health insurance companies, and population-based medical decision-making. Taking the recommendations point-by-point from the Web site and comparing them with evidence-based information found in the medical literature will simplify the process.

UpToDate.com on Pain Relief Benefits of Vertebroplasty

Short-term placebo-controlled (sham procedure) trials of vertebroplasty in patients with osteoporotic compression fractures have not shown a significant benefit in reducing pain.[8,9] Thus, we do not recommend vertebroplasty or kyphoplasty for the treatment of osteoporotic compression fractures.

Evidence-Based Information. The authors are basing their recommendation not to treat on 2 trials published in 2009.[4,5] These articles are vertebroplasty articles only, but the authors extrapolated their recommendation to BKP as well, it being a different procedure.

There are 1587 vertebral augmentation articles in the English language. The most recent meta-analysis published in 2012 is the first one of only level 1 and 2 data, and it evaluated 27 studies, including 8 randomized studies.[10] The authors concluded after analyzing this body of literature in great detail that both VP and BKP provide significant pain relief and a 50% reduced rate of additional fracture over nonsurgical management. They also concluded that BKP has better anatomy restoration and may be more beneficial than VP for improving quality of life and disability.

A recommendation against a procedure that has very strong support by a large body of high-quality literature is not a logical recommendation, but to extrapolate that recommendation to a procedure that has even greater support in the literature is a non sequitur.

UpToDate.com on Pain Relief and Patient Selection

In unblinded randomized trials comparing vertebroplasty with pain management, there was greater improvement in pain immediately after vertebroplasty (1 day) but not at 2 weeks,[11] 3 months,[12] or 12 months.[13] In 1 trial, the improvement in pain after vertebroplasty was significant at 1 day, 1 month, and 1 year.[14] However by the 1-month and 1-year time points, the between-group differences in the reduction in mean pain score (-2.6 and -2.0, respectively) were of uncertain clinical significance. In addition, more than half of the patients who initially qualified for the study had spontaneous reduction or resolution of pain (mean pain score, <5) during screening and therefore were not eligible for inclusion in the study.

Evidence-Based Information. The authors stated that the VERTOS trial,[11] a randomized controlled trial investigating percutaneous vertebroplasty with optimal pain medication treatment, showed no greater improvement of pain after 2 weeks. They then compared this pain measurement with 2 additional time points (3 months and 12 months) in 2 studies different from the VERTOS trial. This comparison has too much heterogeneity to allow an appropriate comparison, and the "snapshot in time" implication that there was no difference in pain levels is not what the VERTOS trial concluded. Rather, the VERTOS authors reported that "pain relief and improvement of mobility, function, and stature after VP is immediate and significantly better in the short term compared with medication treatment."[11] The additional 2 studies by Rousing et al[15,16] were 3- and 12-month follow-ups of the same patients. The authors of UpToDate.com did not mention that in these studies, the pain score before and after the operation in the VP group was 7.9 and 2.0, respectively, a significant decrease, and that assessment of back pain 1 month after discharge from the hospital showed a significantly lower Visual Analog Scale score in the VP group over the conservative group. The referenced studies are also small with a combined total of 133 patients and especially small compared with the much more highly regarded VERTOS II trial with 202 patients, which found consistent and significant pain relief at 6 different measurements at the conclusion of the study at a year.[14]

A recent meta-analysis on VP, which was the first to include all the available prospective evidence, including 9 prospective controlled trials (6 of which were randomized controlled trials), concluded that compared with nonsurgical management (NSM), VP was more effective in relieving pain and in improving the quality of life for patients with VCFs.[17] This meta-analysis was also substantially larger, quadrupling the sample size compared with previous meta-analysis.

A comment was made by the UpToDate.com authors that "more than half of the patients who initially qualified for the study had spontaneous reduction or resolution of pain (mean pain score <5) during screening and therefore were not eligible for inclusion in the study."[17] We believe that this is an entirely appropriate execution of the inclusion/exclusion criteria. VCFs can heal and often do, but when they are present, these fractures tend to cause pain that most patients would rate at least a 6 or 7 of 10.[18] When patients are included in fracture assessments that have fewer than 6 of 10 levels of pain, the pain is likely not coming from the fracture. The INVEST trial, investigational vertebroplasty safety and efficacy trial, previously referenced by the UpToDate.com authors had a pain level of ≥ 3 as an inclusion criterion, which could certainly have allowed many patients to be evaluated for the treatment of their fractures who did not have pain related to the fracture at all. Additionally, in this trial, they screened 1812 patients to enroll 131. This trial has a far greater discrepancy between screened and enrolled patients than the VERTOS trial and could certainly give rise to significant selection bias.

UpToDate.com on Timing of Vertebral Augmentation

VP and BKP are performed in an outpatient setting, though the optimal timing related to fracture acuity is unclear.[19,20]

Evidence-Based Information. A meta-analysis of all of the level 1 and 2 data shows that surgical intervention within the first 7 weeks yielded greater pain reduction than VCFs treated later.[10] The UpToDate.com authors referred to an article by Ledlie and Renfro[19] in regard to the timing of VP and BKP, but according to Dr Ledlie, the article does not address the timing of BKP and only the average age of the fractures in the series was reported. He also stated that this was a report on an historical series and not a recommendation for the timing of BKP.

The Kaufmann et al[20] reference in support of the UpToDate

statement actually concluded that "VP is a highly efficacious therapy for relief of pain and improvement in mobility, regardless of fracture age." The authors also noted that the longer the fracture had been present, the greater was the need for postprocedural anesthesia. The information determined is that painful VCFs are well-treated regardless of age and that the sooner they are treated, the less the requirement will be for postoperative pain medication.

UpToDate.com on Short- and Long-Term Benefits

The potential short-term benefit for both procedures is improvement in pain, whereas potential long-term benefits include prevention of recurrent pain at the treated levels, limitation or reversal of height loss and spinal deformity, and improved functional capability.

Evidence-Based Information. These assertions are not referenced but state that VP and BKP provide short-term benefits in pain. If all of the best level 1 data that follow a patient >6 months are analyzed, the benefit is consistent and persistent for the treated patients up to 2 years.[10,11,17] The long-term benefits are more difficult to accurately characterize because these patients are not typically followed for >2 years, but on the basis of current information, if the patient does not have an additional fracture or other spine injury, their pain relief should be durable.

UpToDate.com on Randomized Controlled Trials on Vertebroplasty

In 2 short-term, blinded trials comparing vertebroplasty with a sham procedure, there was no immediate or delayed benefit of vertebroplasty.[4,5] One of these trials compared vertebroplasty with a simulated procedure without cement in 131 patients who had 1–3 painful osteoporotic VCFs.[4] The primary outcomes were pain intensity during the previous 24 hours and disability, measured by the modified Roland-Morris Disability Questionnaire. The improvement in pain and disability scores was similar in both groups at all time points (3 days, 2 weeks, 1 month). In both groups, the greatest improvement occurred within 3 days of the procedure and was maintained at 1 month.

In these 2 trials, patients assigned to the sham procedures received the same subcutaneous and periosteal anesthetic as those assigned to the full vertebroplasty procedure. The anesthetic, rather than the vertebroplasty procedure itself, may account for some of the immediate pain relief noted in unblinded trials.[4,16]

On the basis of the available data, we do not recommend vertebroplasty for pain reduction in patients with osteoporotic compression fractures.

Evidence-Based Information. The UpToDate.com authors focused on 2 randomized controlled trials published in 2009.[4,5] There is no mention of an analysis of the total body of literature for making a treatment decision. As mentioned above, a meta-analysis published in 2012 was the first to include all available prospective evidence, including 6 randomized controlled trials.[4,5] This meta-analysis concluded that compared with NSM, vertebroplasty was more effective in relieving pain and in improving the quality of life for patients with VCFs. We believe that recommendations should be based on all of the available high-quality data, not just 2 small selected studies.

In regard to the 2 randomized controlled trials published in 2009, these studies are highly controversial and have generated a large amount of discussion. Most of the issues focus on the execution of these 2 trials. Some of the primary criticisms were that the INVEST trial was underpowered (target enrollment was 250 versus the actual enrollment of 131) and that both studies had prominent selection bias. The crossover of patients in the INVEST trial was far greater for those patients crossing over from sham to VP (51%) compared with vice versa (13%). The clinical and imaging diagnostic criteria for inclusion were very different from those in most randomized controlled trials, with patients having a pain score of ≥3 on the Visual Analog Scale being eligible for inclusion, and there was no requirement for MR imaging or nuclear bone scanning for diagnosing the VCFs. There was also no description of a clinical examination used to determine whether the pain came from the VCF itself or from another problem, and the trial of Buchbinder et al[5] assessed "overall pain" rather than spine-related pain, undermining the validity of the measurement in this population replete with potentially comorbid painful conditions. There was also criticism that the INVEST trial was not a true sham, with 63% of the patients receiving sham treatment correctly guessing that their treatment, and the injection was performed with a paraspinal injection of local anesthetic, which has been used to successfully palliate patients' pain from VCFs for up to 8 weeks.[21] Despite all of these limiting factors, if the same response rate for the 131 patients had been obtained on the originally intended 250 patients, VP would have been found to be significantly better than sham treatment at a P value of $< .01$. Despite the low enrollment of only 131 patients, if only 1 patient had reported a different response (ie, a favorable response in the VP group or an unfavorable response in the sham group), VP would have been found to be significantly better than a sham, with a P value of $< .04$. Given the near-equivocal nature of this information, it is an inappropriate trial on which to base significant population-based recommendations and, in our opinion, the quality of the assessment in these trials was far less than in other trials that had a greater number of patients.[8,9,14,16]

UpToDate.com on Kyphoplasty

Data from randomized trials are limited. In the largest trial to date, 300 patients with 1–3 acute vertebral fractures were randomly assigned to balloon kyphoplasty versus nonsurgical care (not a sham procedure as in the above vertebroplasty trials).[12] After 1 month, patients assigned to kyphoplasty had greater improvement in the Short-Form 36 physical component summary scale, a validated quality of life measurement. However, after 12 months, the difference in improvement between the 2 groups was no longer significant.

Evidence-Based Information. The authors stated that randomized controlled trials on BKP are limited. Of the 27 articles identified by Papanastassiou et al[10] in their summary of all level 1 and 2 data on VA, 18 of the studies involved BKP. All these studies by definition included >20 patients, and the BKP articles included the FREE trial, efficacy and safety of balloon kyphoplasty compared with non-surgical care for vertebral compression fracture,

with 300 patients, and a trial comparing BKP and VP with 100 patients.[12,22] The conclusion of Papanastassiou et al regarding BKP was that it decreased pain to a greater degree than VP (5.07 versus 4.55 points on the Visual Analog Scale) and resulted in significantly better improvement in the quality of life than both VP and NSM. This meta-analysis was taken from 1587 articles on vertebral augmentation, more articles than in any other area of spinal medicine. If the authors' contention is that the trials are limited for BKP, then it would follow that there is no other area of the spine that had anything but limited information. It is our contention that there is more than adequate information on which to base a decision that BKP is effective.

The UpToDate.com authors also stated that significant differences in Short-Form 36 were only short-lived, not significant after 12 months, but they did not mention any other parameters measured, ignoring the conclusion of the authors that reduction in pain, EQ-5D (a measure of health status), quality of life, patient satisfaction, and kyphotic angulation remain statistically significant at all time points throughout the 2 years measured. It is also troubling that the authors of UpToDate.com singled out the lack of statistical significance of a single time point in the Short-Form 36 physical component summary when all other time points measured up to a year were significant and all of the time points of the Short-Form 36 Bodily Pain Scale throughout the entire study were significant.

UpToDate.com on Adverse Effects of VP and BKP

Vertebroplasty and kyphoplasty are not without risk. Short-term complications occur predominantly because of extravasation of the cement and may include increased pain and damage from heat or pressure to the spinal cord or nerve roots,[22] and rarely cement embolization.[23] Extravasation has been reported in 11%–73% of vertebroplasty procedures,[24] and less commonly with kyphoplasty.

Evidence-Based Information. The authors stated that short-term complications occurring from cement extravasation may occur from heat producing damage to the nerve roots or spinal cord, and they referenced an article from Watts et al,[22] who stated directly that "theoretically, local heat might damage adjacent tissues because of the exothermic reaction, but the surrounding vascularized tissues, particularly the dura, act to reduce local heat effects. Local tissue damage has been reported only anecdotally." This finding has remained true with time, and exothermic damage to neural elements and other structures is either very rare or nonexistent. A recent randomized controlled trial of 256 patients examined the differences between traditional polymethylmethacrylate (bone cement) and Cortoss (Stryker, Kalamazoo, Michigan), an injectable, combeite glass ceramic tri-resin polymer with little to no exothermic reaction. The study showed no difference in complication rates, no evidence of adverse exothermic events with bone cement, and no difference between cements in the reduction of the patient pain levels.[13]

The authors also characterized cement embolization and extravasation as adverse effects. A better description reveals embolization and extravasation as extremely common with embolization occurring in 5%–23% of all patients and extravasation in up to 73% as stated above.[23-27] Most important, however, is the point that most embolisms and extravasation are neither symptomatic or adverse. A review of all of the level 1 and 2 data shows that most studies did not either report or encounter any serious adverse events. Overall, the literature suggests that both procedures had safe serious adverse event profiles with occasional case reports of symptomatic cement extravasation in the VP arm.[28-35]

The risk of performing VA should be balanced with the risk of withholding the procedure because these patients are typically debilitated and have a mortality rate of 8.6 times that of age-matched controls and have a 40% greater mortality after 8 years.[36,37] In the first longitudinal, population-based comparison of mortality risk between surgical and nonsurgical groups, a Medicare dataset from 2005 to 2008 comprising 858,978 patients with VCFs was analyzed.[38] This included 119,253 patients treated with BKP, 63,693 patients treated with VP, and the remainder treated with NSM. The findings at the 4-year follow-up showed that the VA treatment group was 37% less likely to die than the NSM group and that the adjusted life expectancy was 85% greater for the VA group. The adjusted life expectancy for the BKP was greater than that of VP and was increased 115% compared with the NSM group. Overall the median life expectancy was increased between 2.2 and 7.3 years across all treated groups compared with nonsurgical management. A retrospective review of the treatment of refractory osteoporotic VCFs by Gerling et al,[39] in which treatment with VA was compared with NSM in a hospital setting found a significant survival advantage ($P < .001$) for patients treated with VA over those patients treated with NSM, regardless of comorbidities, age, or the number of fractures diagnosed at the start date.

UpToDate.com on Adjacent-Level Fractures

Two retrospective reviews of patients treated with vertebroplasty found a high rate of new vertebral fractures.[40-42] In 1 report of 177 patients, 22 patients developed 36 new vertebral body fractures. Of the 36 fractures, 67% involved vertebrae adjacent to a previously treated level and 67% occurred within 30 days after the initial treatment.[32] In another study of 432 patients treated with vertebroplasty, 84 patients had new vertebral fractures occurring within 4 months of the procedure.[41]

Evidence-Based Information. If all of the level 1 and 2 data on VA are analyzed rather than focusing on particular studies, the adjacent-level fracture rate for those patients treated with VA was 11% compared with 22% for those patients treated with NSM.[10] The rate of adjacent-level fractures in untreated patients was 20%.[40,43] Not only does there appear to be no increased risk of adjacent-level fractures, but there is also very strong supporting evidence that treatment with VA reduces the rate of adjacent-level fractures by half.[10]

CONCLUSIONS

Substantial scientific contributions to the English literature on vertebral augmentation rival nearly any other topic in the spine. If the highest quality portion of that literature is analyzed, the conclusions that can be drawn are that vertebral augmentation was significantly better than nonsurgical management for decreasing pain and if the fracture was treated in the first 7 weeks, the pain reduction was better. This analysis also showed significantly fewer

additional fractures for those patients treated with vertebral augmentation rather than those treated with nonsurgical management, and those patients treated with kyphoplasty had a significantly better improvement in their quality of life than those treated with vertebroplasty.

Most of the best contributions to the literature have been relatively recent, and many of the analyses and recommendations have been based on older literature. The data show significantly higher mortality rates in those treated with nonsurgical management compared with those patients treated with vertebral augmentation; these findings emphasize the importance of offering the treatment most likely to benefit the patient. The data show these benefits to be pain reduction, fewer additional fractures, and improved quality and length of life. If all of these factors are taken into consideration, it appears that the information on UpToDate is out of date.

Disclosures: Douglas P. Beall—*RELATED*: *Consulting Fee or Honorarium*: Spineology; *UNRELATED: Board Membership*: Medtronic, Benvenue; *Consultancy*: Medtronic, Dfine, Osseon, Lilly, Smith and Nephew, VertiFlex, Synthes, Alphatech Spine, Benvenue, Convatec, Integral Spine Solutions, Medical Metrics; *Payment for Lectures (including service on Speakers Bureaus)*: Medtronic, Dfine, Osseon, Lilly, Smith and Nephew, VertiFlex, Synthes, Alphatech Spine, Benvenue, Convatec, Integral Spine Solutions, Medical Metrics; *Payment for Development of Educational Presentations*: Medtronic, Benvenue; *Stock/Stock Options*: Spineology; *Travel/Accommodations/Meeting Expenses Unrelated to Activities Listed*: Medtronic; *Other*: Medtronic, Dfine, Osseon, Lilly, Smith and Nephew, VertiFlex, Synthes, Alphatech Spine, Benvenue, Convatec, Integral Spine Solutions, Medical Metrics. Sigurd H. Berven—*UNRELATED: Board Membership*: Globus Medical, Medtronic Interventional; *Grants/Grants Pending*: National Institutes of Health,* Orthopaedic Research and Education Foundation,* AOSpine,* Globus Medical*; *Payment for Lectures (including service on Speakers Bureaus)*: Biomet, DePuy, Globus, Medtronic, Stryker; *Royalties:* Medtronic; *Stock/Stock Options*: Simpirica, Providence Medical. Sean M. Tutton—*UNRELATED: Consultancy*: Benvenue. William Porter McRoberts—*UNRELATED*: *Board Membership*: Medtronic, St. Jude, *Comments*: I sit on the scientific advisory board of these 2 companies; *Consultancy*: St. Jude, Medtronic, Axonics, Bioness, Gore Technologies, Spinal Modulation, *Comments*: I provide scientific advice to these companies; *Payment for Lectures (including service on Speakers Bureaus)*: St. Jude, *Comments*: I provide medical education for this company; *Payment for Development of Educational Presentations*: St. Jude, *Comments*: I help develop education materials surrounding neuromodulation. Jon T. Ledlie—*UNRELATED*: *Board Membership*: Alphatec Scientific Advisory Board; *Consultancy*: Medtronic; *Payment for Lectures (including service on Speakers Bureaus)*: Medtronic; *Stock/Stock Options*: Phygen stock; Phygen was bought by Alphatec and the stock converted to Alphatec; *OTHER RELATIONSHIPS*: past member of Kyphon Scientific Advisory Board. *Money paid to the institution.

REFERENCES

1. Galibert P, Deramond H, Rosat P, et al. **Preliminary note on the treatment of vertebral angioma by percutaneous acrylic vertebroplasty** [in French]. *Neurochirurgie* 1987;33:166–68
2. Voggenreiter G. **Balloon kyphoplasty is effective in deformity correction of osteoporotic vertebral compression fractures.** *Spine (Phila Pa 1976)* 2005;30:2806–12
3. Millennium Research Group. Global Markets for Minimally Invasive Vertebral Compression Fracture Treatments 2010. December 30, 2009. http://www.marketresearch.com/Millennium-Research-Group-v648/Global-Minimally-Invasive-Vertebral-Compression-2731438/. Accessed February 20, 2013
4. Kallmes DF, Comstock BA, Heagerty PJ, et al. **A randomized trial of vertebroplasty for osteoporotic spinal fractures.** *N Engl J Med* 2009;361:569–79
5. Buchbinder R, Osborne RH, Ebeling PR, et al. **A randomized trial of vertebroplasty for painful osteoporotic vertebral fractures.** *N Engl J Med* 2009;361:557–68
6. Society of Interventional Radiology. **Society of Interventional Radiology commentary on vertebroplasty and the August studies in the New England Journal of Medicine.** http://www.sirweb.org/misc/Noridian/Commentary_SIR_vertebroplasty.pdf. Published November 24, 2009. Accessed February 15, 2013
7. North American Spine Society. **Newly released vertebroplasty RCT's: a tale of two trials.** http://www.spine.org/Documents/NASS Comment_on_Vertebroplasty.pdf. Published October 13, 2009. Accessed March 5, 2013
8. Kasperk C, Hillmeier J, Nöldge G, et al. **Treatment of painful vertebral fractures by kyphoplasty in patients with primary osteoporosis: a prospective nonrandomized controlled study.** *J Bone Miner Res* 2005;20:604–12
9. Komp M, Ruetten S, Godolias G. **Minimally invasive therapy for functionally unstable osteoporotic vertebral fracture by means of kyphoplasty: prospective comparative study of 19 surgically and 17 conservatively treated patients.** *J Miner Stoffwechs* 2004;11(suppl 1):13–15
10. Papanastassiou ID, Phillips FM, Meirhaeghe JV, et al. **Comparing effects of kyphoplasty, vertebroplasty, and non-surgical management in a systematic review of randomized and non-randomized controlled studies.** *Eur Spine J* 2012;21:1826–43
11. Voormolen MH, Mali WP, Lohle PN, et al. **Percutaneous vertebroplasty compared with optimal pain medication treatment: short-term clinical outcome of patients with subacute or chronic painful osteoporotic vertebral compression fractures. The VERTOS study.** *AJNR Am J Neuroradiol* 2007;28:555–60
12. Wardlaw D, Cummings SR, Van Meirhaeghe J, et al. **Efficacy and safety of balloon kyphoplasty compared with non-surgical care for vertebral compression fracture (FREE): a randomised controlled trial.** *Lancet* 2009;373:1016–24
13. Bae H, Hatten HP Jr, Linovitz R. **A prospective randomized FDA-IDE trial comparing Cortoss with PMMA for vertebroplasty: a comparative effectiveness research study with 24-month follow-up.** *Spine (Phila Pa 1976)* 2012;37:544–50
14. Klazen CA, Lohle PN, de Vries J, et al. **Vertebroplasty versus conservative treatment in acute osteoporotic vertebral compression fractures (Vertos II): an open-label randomised trial.** *Lancet* 2010;376:1085–92
15. Rousing R, Andersen MO, Jespersen SM, et al. **Percutaneous vertebroplasty compared to conservative treatment in patients with painful acute or subacute osteoporotic vertebral fractures: three-months follow-up in a clinical randomized study.** *Spine (Phila Pa 1976)* 2009;34:1349–54
16. Rousing R, Hansen KL, Andersen MO, et al. **Twelve-months follow-up in forty-nine patients with acute/semiacute osteoporotic vertebral fractures treated conservatively or with percutaneous vertebroplasty: a clinical randomized study.** *Spine (Phila Pa 1976)* 2010;35:478–82
17. Shi MM, Cai XZ, Lin T, et al. **Is there really no benefit of vertebroplasty for osteoporotic vertebral fractures? A meta-analysis.** *Clin Orthop Relat Res* 2012;470:2785–99
18. Suzuki N, Ogikubo O, Hansson T. **The course of acute vertebral body fragility fracture: its effect on pain, disability and quality of life during 12 months.** *Eur Spine J* 2008;17:1380–90
19. Ledlie JT, Renfro MB. **Kyphoplasty treatment of vertebral fractures: 2-year outcomes show sustained benefits.** *Spine (Phila Pa 1976)* 2006;31:57–64
20. Kaufmann TJ, Jensen ME, Schweickert PA, et al. **Age of fracture and clinical outcomes of percutaneous vertebroplasty.** *AJNR Am J Neuroradiol* 2001;22:1860–63.
21. Wilson DJ, Owen S, Corkill RA. **Facet injections as a means of reducing the need for vertebroplasty in insufficiency fractures of the spine.** *Eur Radiol* 2011;21:1772–78
22. Watts NB, Harris ST, Genant HK. **Treatment of painful osteoporotic vertebral fractures with percutaneous vertebroplasty or kyphoplasty.** *Osteoporos Int* 2001;12:429–37
23. Bernhard J, Heini PF, Villiger PM. **Asymptomatic diffuse pulmonary embolism caused by acrylic cement: an unusual complication of percutaneous vertebroplasty.** *Ann Rheum Dis* 2003;62:85–86

24. Shapiro S, Abel T, Purvines S. **Surgical removal of epidural and intradural polymethylmethacrylate extravasation complicating percutaneous vertebroplasty for an osteoporotic lumbar compression fracture. Case report.** *J Neurosurg* 2003;98(1 suppl):90–92
25. Diamond TH, Champion B, Clark WA. **Management of acute osteoporotic vertebral fractures: a nonrandomized trial comparing percutaneous vertebroplasty with conservative therapy.** *Am J Med* 2003;114:257–65
26. Choe DH, Marom EM, Ahrar K, et al. **Pulmonary embolism of polymethyl methacrylate during percutaneous vertebroplasty and kyphoplasty.** *AJR Am J Roentgenol* 2004;183:1097–102
27. Duran C, Sirvanci M, Aydoğan M, et al. **Pulmonary cement embolism: a complication of percutaneous vertebroplasty.** *Acta Radiol* 2007;48:854–59
28. Kim YJ, Lee JW, Park KW, et al. **Pulmonary cement embolism after percutaneous vertebroplasty in osteoporotic vertebral compression fractures: incidence, characteristics, and risk factors.** *Radiology* 2009;251:250–59
29. Dong R, Chen L, Gu Y, et al. **Improvement in respiratory function after vertebroplasty and kyphoplasty.** *Int Orthop* 2009;33:1689–94
30. Grohs JG, Matzner M, Trieb K, et al. **Minimal invasive stabilization of osteoporotic vertebral fractures: a prospective nonrandomized comparison of vertebroplasty and balloon kyphoplasty.** *J Spinal Disord Tech* 2005;18:238–42
31. Pflugmacher R, Kandziora F, Schroder R, et al. **Vertebroplasty and kyphoplasty in osteoporotic fractures of vertebral bodies—a prospective 1-year follow-up analysis** [in German]. *Rofo* 2005;177:1670–76
32. Pflugmacher R, Taylor R, Agarwal A, et al. **Balloon kyphoplasty in the treatment of metastatic disease of the spine: a 2-year prospective evaluation.** *Eur Spine J* 2008;17:1042–48
33. Santiago FR, Abela AP, Alvarez LG, et al. **Pain and functional outcome after vertebroplasty and kyphoplasty. A comparative study.** *Eur J Radiol* 2010;75:e108–13
34. Schofer MD, Efe T, Timmesfeld N, et al. **Comparison of kyphoplasty and vertebroplasty in the treatment of fresh vertebral compression fractures.** *Arch Orthop Trauma Surg* 2009;129:1391–99
35. Grafe IA, Da Fonseca K, Hillmeier J, et al. **Reduction of pain and fracture incidence after kyphoplasty: 1-year outcomes of a prospective controlled trial of patients with primary osteoporosis.** *Osteoporos Int* 2005;16:2005–12
36. Cauley JA, Thompson DE, Ensrud KC, et al. **Risk of mortality following clinical fractures.** *Osteoporos Int* 2000;11:556–61
37. Lau E, Ong K, Kurtz S, et al. **Mortality following the diagnosis of a vertebral compression fracture in the Medicare population.** *J Bone Joint Surg Am* 2008;90:1479–86
38. Edidin AA, Ong KL, Lau E, et al. **Mortality risk for operated and nonoperated vertebral fracture patients in the Medicare population.** *J Bone Miner Res* 2011;26:1617–26
39. Gerling MC, Eubanks JD, Patel R, et al. **Cement augmentation of refractory osteoporotic vertebral compression fractures: survivorship analysis.** *Spine (Phila Pa 1976)* 2011;36:E1266–69
40. Uppin AA, Hirsch JA, Centenera LV, et al. **Occurrence of new vertebral body fracture after percutaneous vertebroplasty in patients with osteoporosis.** *Radiology* 2003;226:119–24
41. Trout AT, Kallmes DF, Kaufmann TJ. **New fractures after vertebroplasty: adjacent fractures occur significantly sooner.** *AJNR Am J Neuroradiol* 2006;27:217–23
42. Trout AT, Kallmes DF, Layton KF, et al. **Vertebral endplate fractures: an indicator of the abnormal forces generated in the spine after vertebroplasty.** *J Bone Miner Res* 2006;21:1797–802
43. Lindsay R, Silverman SL, Cooper C, et al. **Risk of new vertebral fracture in the year following a fracture.** *JAMA* 2001;285:320–23

Social Media and Research Visibility

R.T. Fitzgerald and A. Radmanesh

Assessing the value of scientific research output, an important component of academic promotion and tenure, is increasingly based on metrics such as the Impact Factor, H-index, and more recently Google Scholar, that attempt to numerically encapsulate an author's productivity and scholarly impact. The H-index, discussed by *AJNR* Editor-in-Chief Mauricio Castillo in a 2010 editorial,[1] and an expanding alphabet soup of additional measurement tools (M-index, C-index, S-index, E-index, etc) are based on article citations accumulated over time. As such, it behooves researchers to consider avenues to expand the reach and visibility of their work. It is expected that article influence will soon be used by funding entities to assign monies for research. Social media represent a potential opportunity to do so, and may be particularly important in an era in which the link between an article's citation rate and its publishing journal is in decline.[2]

A growing body of literature has examined the impact of social media on views and citations of scholarly articles. Tweets containing a link to an article, or "tweetations" have been shown to predict highly cited articles within the first 3 days after publication.[3] Randomly selected articles that are disseminated via social media (Twitter, Facebook, LinkedIn) are viewed and downloaded more frequently than unselected papers.[4] Thewall et al[5] showed a positive correlation between altmetrics (a measure of citations or mentions in specific social media services) and eventual citations, with the strongest evidence for articles posted on Twitter, Facebook wall posts, and blog entries. Other authors found a less robust correlation between tweets and citations and have suggested that these metrics may represent different yet complementary measures of an article's value.[6] Further studies are required to fully assess the long-term relationship between altmetrics and traditional measures of scholarly value.

From the Department of Radiology (R.T.F.), University of Arkansas for Medical Sciences, Little Rock, Arkansas; and Mallinckrodt Institute of Radiology (A.R.), Washington University School of Medicine, St Louis, Missouri.

Please address correspondence to Ryan T. Fitzgerald, MD, Department of Radiology, University of Arkansas for Medical Sciences, 4301 W Markham St, Little Rock, AR 72205; e-mail: fitzgeraldryant@uams.edu; @ryantfitzgerald

http://dx.doi.org/10.3174/ajnr.A4054

Despite evidence supporting the potential benefits of social media engagement for researchers, adoption of social media in academia has been slow. It is estimated that fewer than 3% of scientists are active Twitter users.[7] A study to assess the prevalence of social media mentions in 1.4 million scholarly articles published between 2010 and 2012, fewer than 10% were tweeted at least once; however, the rate of tweets increased substantially over the 3-year study period from 2.4% in 2010 to 20.4% in 2012.[6] General science and medicine journals such as *Nature* (@nature) and the *New England Journal of Medicine* (@nejm) enjoy a greater abundance of followers relative to subspecialty journals such as *AJNR*, and thus their articles are more likely to be frequently retweeted. Most journals (67%) have less than 20% of their content tweeted.[6] *AJNR* (@AmJNeuroradiol) tweets each and every article that appears in our pages. We invite *AJNR* authors to include their Twitter handles in the author contact information list of new submissions to facilitate professional networking and potential collaborations.

REFERENCES

1. Castillo M. **Measuring academic output: the H-index.** *AJNR Am J Neuroradiol* 2010;31:783–84
2. Lozano GA, Larivière V, Gingras Y. **The weakening relationship between the impact factor and papers' citations in the digital age.** *J Am Soc Inf Sci* 2012;63:2140–45
3. Eysenbach G. **Can tweets predict citations? Metrics of social impact based on Twitter and correlation with traditional metrics of scientific impact.** *J Med Internet Res* 2011;13:e123
4. Allen HG, Stanton TR, Di Pietro F, et al. **Social media release increases dissemination of original articles in the clinical pain sciences.** *PLoS One* 2013;8:e68914
5. Thelwall M, Haustein S, Larivière V, et al. **Do altmetrics work? Twitter and ten other social web services.** *PLoS One* 2013;8:e64841
6. Haustein S, Peters I, Sugimoto CR, et al. **Tweeting biomedicine: an analysis of tweets and citations in the biomedical literature.** *J Am Soc Inf Sci* 2014;65:656–69
7. Priem J, Costello KL, Dzuba T. **Prevalence and use of Twitter among scholars.** figshare. Published December 16, 2012. doi: 10.6084/m9.figshare.104629

Exposing Hidden Truncation-Related Errors in Acute Stroke Perfusion Imaging

W.A. Copen, A.R. Deipolyi, P.W. Schaefer, L.H. Schwamm, R.G. González, and O. Wu

ABSTRACT

BACKGROUND AND PURPOSE: The durations of acute ischemic stroke patients' CT or MR perfusion scans may be too short to fully sample the passage of the injected contrast agent through the brain. We tested the potential magnitude of hidden errors related to the truncation of data by short perfusion scans.

MATERIALS AND METHODS: Fifty-seven patients with acute ischemic stroke underwent perfusion MR imaging within 12 hours of symptom onset, using a relatively long scan duration (110 seconds). Shorter scan durations (39.5–108.5 seconds) were simulated by progressively deleting the last-acquired images. CBV, CBF, MTT, and time to response function maximum (Tmax) were measured within DWI-identified acute infarcts, with commonly used postprocessing algorithms. All measurements except Tmax were normalized by dividing by the contralateral hemisphere values. The effects of the scan duration on these hemodynamic measurements and on the volumes of lesions with Tmax of >6 seconds were tested using regression.

RESULTS: Decreasing scan duration from 110 seconds to 40 seconds falsely reduced perfusion estimates by 47.6%–64.2% of normal for CBV, 1.96%–4.10% for CBF, 133%–205% for MTT, and 6.2–8.0 seconds for Tmax, depending on the postprocessing method. This truncation falsely reduced estimated Tmax lesion volume by 71.5 or 93.8 mL, depending on the deconvolution method. "Lesion reversal" (ie, change from above-normal to apparently normal, or from >6 seconds to ≤6 seconds for the time to response function maximum) with increasing truncation occurred in 37%–46% of lesions for CBV, 2%–4% for CBF, 28%–54% for MTT, and 42%–44% for Tmax, depending on the postprocessing method.

CONCLUSIONS: Hidden truncation-related errors in perfusion images may be large enough to alter patient management or affect outcomes of clinical trials.

ABBREVIATIONS: MRP = MR perfusion imaging; SVD = singular value decomposition; Tmax = time-to-maximum of the deconvolved tissue response function

CT and MR perfusion (MRP) imaging are used frequently in acute ischemic stroke care and are increasingly used to determine treatment eligibility in therapeutic trials.[1-4] In both techniques, maps of regional hemodynamic parameters like CBF or CBV are derived from dynamic images that quantify the concentrations of an intravenously injected contrast agent as it passes through the brain. Clinical studies often omit consideration of the postprocessing algorithms that convert concentration measurements to perfusion maps, implicitly accepting their accuracy. However, postprocessing algorithms can produce significant errors,[5] which typically are visually undetectable during interpretation.

One type of error results from temporal truncation of concentration measurements by scan durations that are too short to adequately sample the passage of the contrast agent bolus, which occurs most often under ischemic conditions. Bolus injections typically take at least 5 seconds, and injecting the larger volumes of contrast used for CTP may take 10 seconds or longer.[6,7] After injection, the bolus travels to ischemic brain tissue via stenotic arteries and/or circuitous collateral pathways, potentially lengthening the average arm-to-brain transit time to 35 seconds or more.[8]

Received August 11, 2014; accepted after revision September 22.

From the Departments of Radiology (W.A.C., A.R.D., P.W.S., R.G.G., O.W.) and Neurology (L.H.S.), Massachusetts General Hospital and Harvard Medical School, Boston, Massachusetts.

This work was supported by National Institutes of Health grants P50NS051343, R01NS059775, and R01NS063925.

This research was presented in part at: "Perfusion MRI: Standardization, Beyond CBF and Everyday Clinical Applications," conducted by the International Society for Magnetic Resonance in Medicine Scientific Workshop, October 11–14, 2012; Amsterdam, the Netherlands.

Please address correspondence to William A. Copen, MD, Massachusetts General Hospital, Neuroradiology GRB-273A, 55 Fruit St, Boston, MA 02114; e-mail: wcopen@partners.org

Indicates open access to non-subscribers at www.ajnr.org

http://dx.doi.org/10.3174/ajnr.A4186

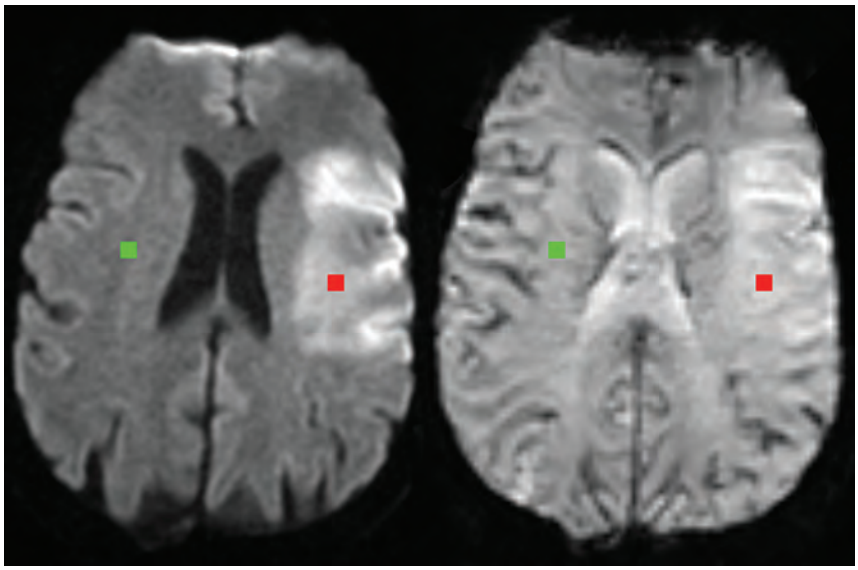

FIG 1. Region-of-interest placement. Lesion (red) and contralateral (green) regions of interest from 1 patient are superimposed on the diffusion-weighted image that was used for their placement (*left*) and the perfusion source image to which they were subsequently transferred (*right*).

Dispersion may cause some components of the bolus to arrive far later.[9] Once each part of the bolus arrives, the average time that it spends in ischemic tissue is commonly 10–20 seconds and sometimes considerably longer,[10] because autoregulatory vasodilation slows blood velocity. In comparison, CTP and MRP scans may be as short as 40 seconds.[6,11] Therefore, the parametric perfusion maps that are used for clinical interpretation may be derived from severely truncated concentration data.

A previous study showed that data truncation may result in underestimation of CBV in ischemic tissue.[12] We hypothesized that other common perfusion measurements are also prone to truncation-related errors. We retrospectively analyzed the MRP images of patients with acute stroke, which can be acquired with longer scan durations than CTP scans, without concern for ionizing radiation exposure. We simulated progressively shorter scan durations by discarding the images acquired at the final time points in each perfusion scan. We tested whether scan duration altered calculated perfusion parameters within acute infarcts, by placing regions of interest near the center of each patient's DWI lesion, and then assessing whether perfusion measurements obtained within these ROIs were altered by increasing degrees of scan truncation. We investigated perfusion within acute infarcts because especially severe ischemia might be expected to exist within infarcts, and because some studies have substituted perfusion imaging for DWI in identifying irreversibly injured tissue.[1-4,13,14] We also tested whether scan duration altered the volumes of lesions in thresholded maps of the time-to-maximum of the deconvolved residue function (Tmax), because these volumes have been used to determine eligibility for recanalization therapy in clinical trials.[3,15]

MATERIALS AND METHODS

Patient Selection

This study was approved by our institutional review board, which waived its informed consent requirement because only retrospective data analysis was performed. We reviewed hospital records and selected all patients from a 14-month period who satisfied the following criteria: 1) clinical diagnosis of new ischemic stroke; 2) MR imaging examinations, including DWI and MRP, completed within 12 hours of the time when the patient was last seen at neurologic baseline; 3) discovery of new symptoms within 15 minutes of that time; and 4) DWI-positive anterior circulation ischemic lesion. Patients were excluded if their DWI or MRP data were too motion-degraded to permit satisfactory processing, if motion correction resulted in the sections containing the DWI lesion being no longer visualized, or if the DWI lesion was too small to accommodate a region of interest measuring 5.2 × 5.2 mm.

Image Acquisition

Images were acquired on a 1.5T MR imaging scanner (Signa; GE Healthcare, Milwaukee, Wisconsin). DWI used a balanced spin-echo echo-planar pulse sequence, incorporating two 180° radiofrequency pulses to reduce eddy current–related artifacts.[16] The FOV was 22 cm, with a 128 × 128 matrix, zero-filled in *k*-space to produce 256 × 256 pixel images. TR was 5000 ms, and TE was as short as possible. There were 25 diffusion-encoding directions, with $b=1000$ s/mm^2 and 3 volumes with $b=0$ s/mm^2.

MRP used a gradient-echo echo-planar pulse sequence with a 22-cm FOV and a 128 × 128 matrix. TR and TE were 1500 and 35 ms, respectively, and the flip angle was 60°. Eighty volumes were acquired, resulting in a scan time of 2 minutes. Ten seconds after scan initiation, 20 mL of gadopentetate dimeglumine (Magnevist; Bayer HealthCare Pharmaceuticals, Wayne, New Jersey) was power-injected intravenously at 5 mL/s, followed by a similar volume of normal saline, injected at the same rate.

For both DWI and MRP, section thickness and spacing were 5 and 1 mm, respectively. DWI sections were prescribed to completely cover the brain. MRP coverage was limited to 14 or 15 sections, prescribed as a subset of DWI section locations.

Image Review

Without referring to perfusion maps, an experienced neuroradiologist placed a 5.2 × 5.2 mm region of interest in the geographic center of each patient's DWI lesion. A second, identically sized region of interest was placed in an anatomically similar location on the opposite side of the brain, to allow normalization of perfusion values in the lesion via comparison with presumably normal values. These ROIs were transferred to the corresponding anatomic locations on the raw perfusion images (Fig 1). Before generation of any postprocessed perfusion maps, the neuroradiologist reviewed the ROIs to ensure that neither included a macroscopically visible blood vessel whose "blooming" could unduly influence perfusion measurements. When this occurred, the region of interest was moved slightly. Whenever possible, each patient's ROIs were placed exclusively in gray matter or exclusively

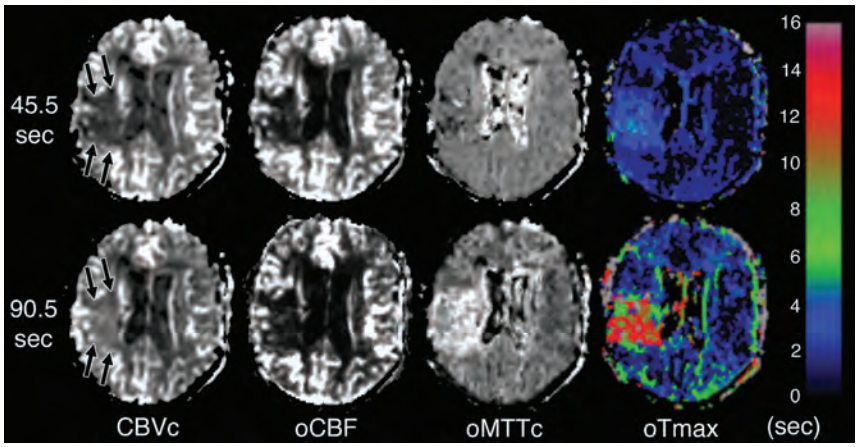

FIG 2. Visual appearance of truncation artifacts resulting from scans of different durations. Sample perfusion maps produced from a single patient's perfusion data, which have been truncated to simulate perfusion scans of 2 different durations that are similar to those in common clinical use: 45.5 seconds (*top row*) and 90.5 seconds (*bottom row*) following contrast injection. The CBV map from the shorter 45.5-second scan shows a low-CBV lesion in the right frontal lobe (*arrows*, *top row*). However, the more accurate CBV map produced from the longer scan shows elevated rather than reduced CBV (*arrows*, *bottom row*). CBF maps produced from the 2 scan durations show little appreciable difference. The MTT map from the truncated scan shows almost no lesion, but there is a sizeable lesion with prolonged MTT in the map produced from the longer scan. The Tmax maps produced from the 2 scan durations show subjectively appreciable lesions of similar sizes. However, the color legend at the right of the figure shows that the abnormal Tmax values produced by the shorter scan are <6 seconds, so this tissue would not be classified as "at risk" by studies that use that threshold, whereas the longer scan produced a large lesion with Tmax values above the 6-second threshold.

in white matter. In the few cases in which this placement was impossible, the lesion and contralateral ROIs were chosen to include similar proportions of gray and white matter.

Following the completion of region-of-interest placement, the same neuroradiologist manually measured the volumes of DWI-hyperintense lesions that were thought to reflect acute infarction, for each patient.

Image Processing

From MRP data, we calculated 4 commonly studied regional hemodynamic parameters: CBV, CBF, MTT, and the time at which the deconvolved tissue response function R(t) reached its maximum (Tmax). To assess whether different computation methods have varying vulnerabilities to truncation-related artifacts, we calculated each of these 4 parameters using several alternative algorithms, so that 11 perfusion maps were created for each patient.

Generation of 10 of the 11 perfusion maps required deriving R(t) from the tissue concentration function C(t), by using deconvolution with an arterial input function. Deconvolution was performed by in-house, fully automated software, using the following steps: First, the number of baseline images (ie, before arrival of the contrast bolus) was derived by spatially smoothing each image with a Hanning filter, averaging the signal intensity of all tissue pixels at each time point, and selecting the time point before the one exhibiting the largest incremental signal change as the final baseline image. Motion correction was performed by coregistering[17] each volume to the first baseline image, and the images were then converted to concentration-of-contrast-agent versus time curves, C(t).[18]

Arterial input function voxels were selected from the section with the largest number of high-blood-volume voxels. Candidate voxels were identified with a combination of previously described criteria,[19-23] including high CBV, early contrast agent arrival time, short relative MTT, and narrow full width at half maximum concentration values. K-means cluster analysis was then performed on the candidate voxels, and the cluster with the narrowest full width at half maximum was selected as the arterial input function. The same arterial input function was used for every simulated scan duration, though the arterial input function was truncated to the same length as the C(t).

Deconvolution was performed by using 2 alternative algorithms: standard singular value decomposition (sSVD)[24] and oscillation-index regulated singular value decomposition with a block circulant matrix (oSVD), a refined version of SVD that is insensitive to bolus arrival delay–related artifacts.[25] Hereafter, hemodynamic measurements derived from standard singular value decomposition are labeled with the prefix "s," whereas those derived from oSVD are labeled with the prefix "o."

CBV was calculated in 3 ways. One CBV measurement, hereafter called CBVc, was produced by integrating the C(t) in each image pixel. This simplest of CBV algorithms has been used in numerous MRP studies and does not require deconvolution.[20,26] The other 2 CBV measurements were produced by integrating the R(t), and will be designated sCBVr and oCBVr, to indicate which deconvolution algorithm was used. This technique is equivalent theoretically to that used by at least 1 commercially available CTP software package.[27]

CBF was calculated as the maximum value of the deconvolved response function (sCBF or oCBF), and Tmax was the time at which that maximum was reached (sTmax or oTmax). MTT was calculated as the quotient of CBVc divided by sCBF or oCBF (yielding sMTTc or oMTTc, respectively), sCBVr divided by sCBF (yielding sMTTr), or oCBVr divided by oCBF (yielding oMTTr).

To assess the effects of scan duration, we created temporally truncated datasets, simulating the data that would have been acquired if shorter scans had been performed. For example, a 90-second scan duration was simulated by discarding the images from the final 30 seconds of the full 120-second scan. Sample perfusion maps produced from a single patient's data, truncated to simulate 2 different scan durations, are shown in Fig 2.

Our MRP protocol included a 10-second delay between the beginning of image acquisition and initiation of contrast injection. To facilitate comparison with previously published results (which may not use the same preinjection delay) and to facilitate future protocol design, we will hereafter refer to our simulated scan durations in terms of their relationship to the time at which

contrast injection began (eg, the duration of the full 120-second scan was 110 seconds postinjection).

Statistical Analysis

For each patient, for every simulated scan duration, normalized CBV, CBF, and MTT measurements were obtained, by dividing the mean of the lesion region-of-interest values by the mean value in the contralateral region of interest. For the 2 Tmax measurements, sTmax and oTmax, the mean absolute regional Tmax value recorded in the lesion region of interest was recorded, without normalization.

For every simulated scan duration ranging from 39.5 to 110 seconds postinjection, the mean of each hemodynamic measurement across all patients was calculated. This minimum duration was chosen for 2 reasons: First, 39.5 seconds was the shortest scan duration for which perfusion measurements incorporated at least 9 data points for all patients, thereby avoiding noisier measurements obtained from only a few data points. Second, perfusion studies have used scan durations as short as 40 seconds postinjection,[6,11] and, with our TR of 1.5 seconds, the available scan duration closest to 40 seconds was 39.5 seconds.

Linear regression analyses were performed between each of these 11 hemodynamic measurements and scan duration, and against the base-10 logarithm of scan duration. To assess the magnitude of truncation-related errors that might be expected for an individual patient, we fit longitudinal fixed-effects models for each hemodynamic parameter, with patient-specific slopes and intercepts, incorporating observations from all durations, from all patients. For these fixed-effects regressions, measurements were included only if they were produced from at least 9 postarrival data points.

For each of the 11 measurements, we counted the number of patients for whom worsening truncation by shorter scan durations resulted in "lesion reversal," which we defined as either the false creation of an apparent lesion when no lesion was truly present, or the false disappearance of a lesion when a lesion was truly present. Our goal was to reserve the classification of "lesion reversal" for only those cases in which worsening truncation caused a sustained change from above-normal ROI values to below-normal values and to avoid labeling as "lesion reversal" cases in which image noise caused perfusion values to fluctuate randomly above and below normal levels. Therefore, to determine that lesion reversal had occurred for a particular patient and any of the 9 normalized measurements, we required that decreasing scan durations (ie, worsening truncation) resulted in above-normal measurements for at least 3 consecutive scan durations, followed by below-normal measurements for at least 3 consecutive durations, and were not followed by a subsequent return to 3 above-normal measurements. For sTmax and oTmax, which were not normalized, we defined lesion reversal as a sustained transition from values of >6 seconds to ≤6 seconds. Several recent studies have proposed 6 seconds as the Tmax threshold that best identifies tissue at risk of infarction.[3,15] For each of the 11 perfusion measurements, we tallied the proportion of patients for which lesion reversal occurred, and used logistic regression to assess whether the likelihood of lesion reversal was related to DWI lesion size.

In some clinical trials, patient eligibility for recanalization therapy was based on the existence of a sufficient volume of brain tissue with a Tmax of >6 seconds. To determine how scan duration might artifactually influence this measured volume, we measured the volumes of tissue with a Tmax of >6 seconds for each patient at each simulated duration. We assessed the effect of scan duration on lesion volume by using additional regression analyses similar to those described above.

RESULTS

The study included 57 patients, 25 women, whose ages ranged from 30.4 to 93.3 years, with a mean ± standard deviation of 68.2 ±16.8 years. DWI lesion volumes ranged from 0.29 to 178.07 mL, with a mean ± standard deviation of 31.40 ± 42.65 mL.

For all hemodynamic parameters, the logarithmic model produced higher R^2 goodness-of-fit statistics. Therefore, only the results of the logarithmic model will be discussed. The means of all 11 parameters decreased significantly ($P < .001$) as truncation increased, as shown in Fig 3. However, the calculated slopes for sCBF and oCBF were much smaller than those of the other parameters, reflecting the much smaller effect that truncation had on CBF. The calculated slopes for each parameter were the following: CBVc, 0.99/$\log_{10}$(s); sCBVr, 1.07/$\log_{10}$(s); oCBVr, 1.11/$\log_{10}$(s); sCBF, 0.09/$\log_{10}$(s); oCBF, 0.06/$\log_{10}$(s); sMTTc, 2.70/$\log_{10}$(s); sMTTr, 3.16/$\log_{10}$(s); oMTTc, 4.04/$\log_{10}$(s); oMTTr, 4.69/$\log_{10}$(s); sTmax, 15.6 s/$\log_{10}$(s); and oTmax, 18.6 s/$\log_{10}$(s). Aggregated lesion volumes of tissue with a Tmax of >6 seconds also decreased significantly with decreasing scan duration ($P < .001$), with slopes of 73.8 mL/$\log_{10}$(s) and 167.6 mL/$\log_{10}$(s) for sTmax and oTmax, respectively (Fig 4).

Results of the fixed regression models with patient-specific slopes and intercepts are presented in Table 1 for region of interest–based hemodynamic measurements and lesion reversal frequencies, and in Table 2 for volumes of lesions with a Tmax of >6 seconds. All 11 parameters decreased significantly as truncation increased ($P < .001$). Again, the calculated slopes for CBF were much smaller than those of the other parameters. To facilitate meaningful interpretation of the magnitudes of scan duration–dependent artifacts, Table 1 includes calculations of "potential truncation effect," which we define as the decrease in the calculated value of that parameter that would be expected for an individual patient if perfusion data were truncated by reducing the scan duration from 110 seconds to 40 seconds postinjection. Decreasing the scan duration from 110 to 40 seconds falsely reduced perfusion estimates by 47.6%–64.2% of normal for CBV, 1.96%–4.10% for CBF, 133%–205% for MTT, and 6.19–8.00 seconds for Tmax.

Lesion reversal frequencies for the 3 methods of computing CBV ranged between 37% and 46%, indicating that for more than one-third of patients, truncation of data by a short scan could result in the appearance of a low-CBV lesion when no such lesion was truly present. Lesion reversal frequencies for the 4 MTT calculations ranged between 28% and 54%, indicating that truncation errors could obscure high-MTT lesions for many patients. Lesion reversal frequencies for sTmax and oTmax were 42% and 44%, respectively, again showing that truncation errors could often prevent detection of tissue considered at risk of infarction.

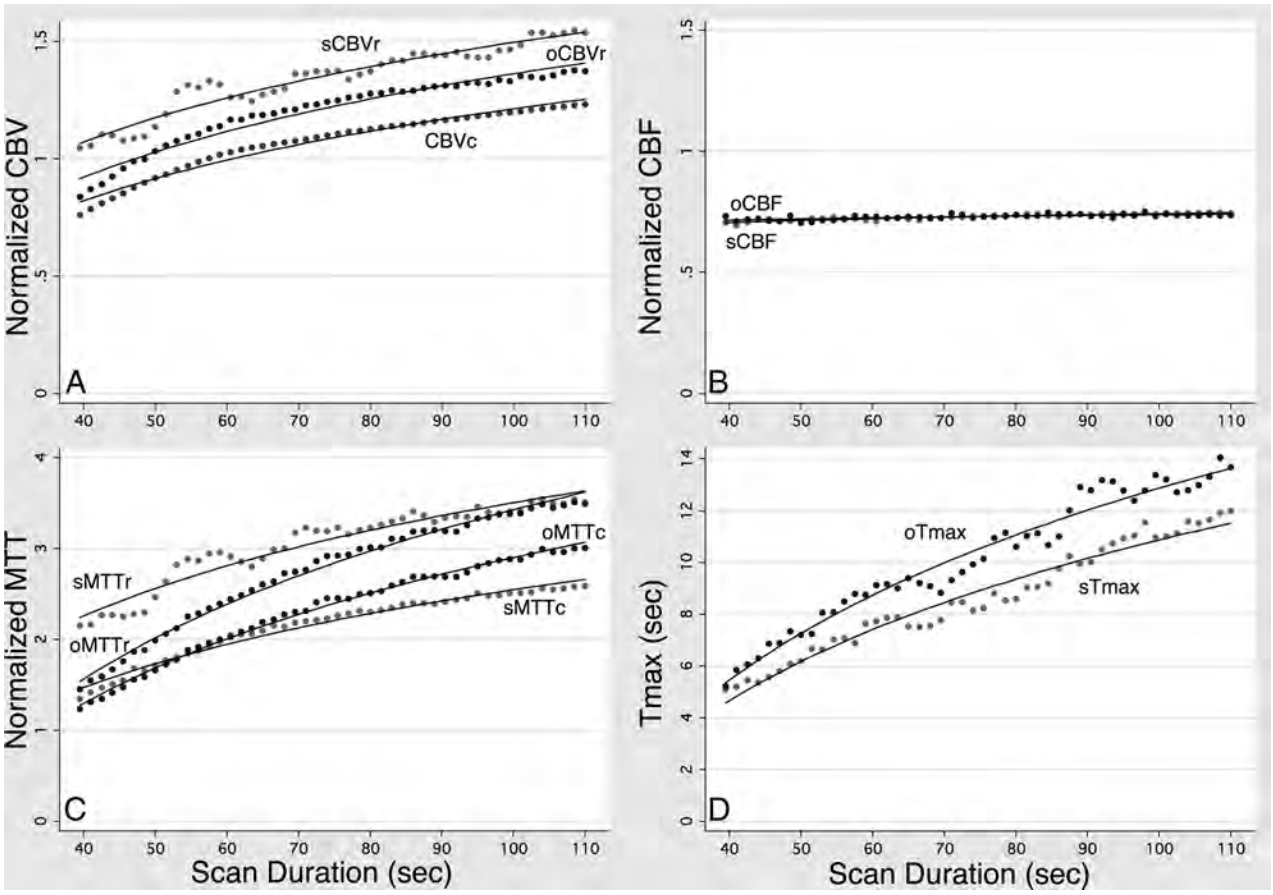

FIG 3. Quantitative measurement of truncation artifacts caused by scans of different durations. Mean values of the 3 different CBV measurements (*A*), the 2 different CBF measurements (*B*), the 4 different MTT measurements (*C*), and the 2 different Tmax measurements (*D*), averaged across all patients, for scan durations ranging from 39.5 to 110 seconds after contrast injection. The curves in each graph were fitted by logarithmic regression, which showed a significant ($P < .001$) decrease in every calculated parameter with decreasing scan time. However, the magnitude of this reduction was much smaller for CBF than for the other parameters.

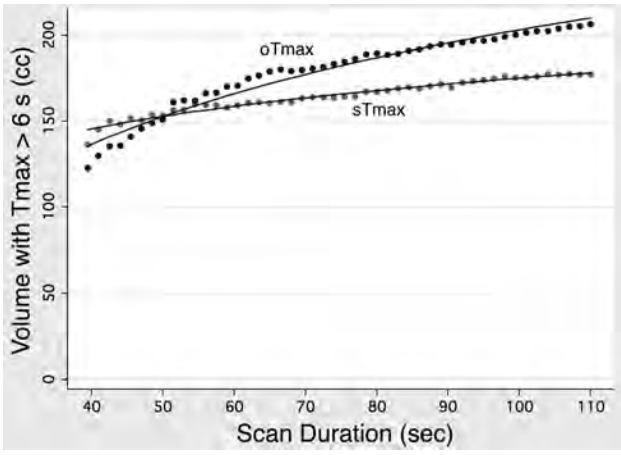

FIG 4. Artifactual effect of truncation on Tmax lesion volumes. Volumes of tissue with calculated Tmax values of >6 seconds averaged across all patients, for scan durations ranging from 39.5 to 110 seconds after contrast injection. The curves in each graph were fitted by logarithmic regression, which showed a significant ($P < .001$) reduction in both sTmax and oTmax with decreasing scan duration.

Lesion reversal was much rarer for oCBF and sCBF, with lesion reversal frequencies of 2% and 4%, respectively.

Logistic regression analysis showed no statistically significant relationship between lesion reversal frequency and DWI lesion size for any of the 11 perfusion parameters, except for sMTTc (odds ratio = 1.021/mL, $P = .03$) and sMTTr (odds ratio = 1.018/mL, $P = .02$).

Significant associations ($P < .001$) were also found between scan duration and the volume of tissue with a Tmax of >6 seconds. Truncating scan durations from 110 to 40 seconds falsely reduced the estimated Tmax lesion volume by 71.5 mL for sTmax, and 93.8 mL for oTmax (Table 2). An example of the effect of scan duration on Tmax lesion volume is shown in Fig 5.

DISCUSSION

Perfusion imaging research studies frequently provide little or no information regarding the postprocessing algorithms used, and design details of proprietary postprocessing software typically are not revealed. However, inattention to methodology may conceal errors in perfusion images that could significantly change their implications for patient care. Our results demonstrate that common perfusion postprocessing algorithms may produce very different results when scans of different durations are performed on the same patient, resulting in varying degrees of data truncation errors.

Longer scans more completely sample the passage of the contrast bolus through the brain, and presumably provide more ac-

Table 1: Regression-derived effects of scan duration on various hemodynamic measurements

Hemodynamic Measurement	Deconvolution Algorithm	Function Used for CBV Integration	*t*-statistic	Slope[a]	Potential Truncation Effect[b]	Lesion Reversal Frequency
CBVc	None	Concentration	41.53	$1.08/\log_{10}(s)$	47.6%	37% (21/57)
sCBVr	sSVD	Response	17.99	$1.46/\log_{10}(s)$	64.2%	35% (20/57)
oCBVr	oSVD	Response	16.72	$1.17/\log_{10}(s)$	51.4%	46% (26/57)
sCBF	sSVD	NA	9.62	$0.09/\log_{10}(s)$	4.10%	4% (2/57)
oCBF	oSVD	NA	3.58	$0.04/\log_{10}(s)$	1.96%	2% (1/57)
sMTTc	sSVD	Concentration	34.49	$3.03/\log_{10}(s)$	133%	47% (27/57)
sMTTr	sSVD	Response	35.57	$3.73/\log_{10}(s)$	164%	28% (16/57)
oMTTc	oSVD	Concentration	42.50	$3.79/\log_{10}(s)$	166%	54% (31/57)
oMTTr	oSVD	Response	51.15	$4.67/\log_{10}(s)$	205%	39% (22/57)
sTmax	sSVD	NA	25.91	$14.10/\log_{10}(s)$	6.19 seconds	44% (25/57)
oTmax	oSVD	NA	28.62	$18.2/\log_{10}(s)$	8.00 seconds	42% (24/57)

Note:—NA indicates not applicable.

[a] The slopes of all 11 hemodynamic parameters with respect to the logarithm of scan duration were significantly greater than zero ($P < .001$). Therefore, *t*-statistics rather than *P* values are reported.

[b] "Potential truncation effect" refers to the expected reduction in the calculated parameter value that would result from decreasing the scan duration from 110 seconds to 40 seconds postinjection. For example, if the CBVc value derived from a 110-second scan were 107.6% of normal, the expected CBVc using a 40-second scan would be 60.0% of normal.

Table 2: Regression-derived effects of scan duration on the volume of brain tissue with Tmax greater than 6 seconds

Hemodynamic Measurement	Deconvolution Algorithm	*t*-statistic	Lesion Volume Slope[a]	Potential Truncation Effect[b]
sTmax	sSVD	44.21	$162.7\ mL/\log_{10}(s)$	71.5 mL
oTmax	oSVD	47.94	$213.4\ mL/\log_{10}(s)$	93.8 mL

[a] The slopes of sTmax and oTmax lesion volumes with respect to the logarithm of scan duration were both significantly greater than zero with $P < .001$. Therefore, *t*-statistics rather than *P* values are reported.

[b] "Potential truncation effect" reflects the expected decrease in the lesion volume that would result from decreasing the scan duration from 110 seconds to 40 seconds postinjection. For example, if the volume of an oTmax lesion were measured to be 150 mL using a 110-second scan, the expected lesion volume derived from a 40-second scan would be 56.2 mL.

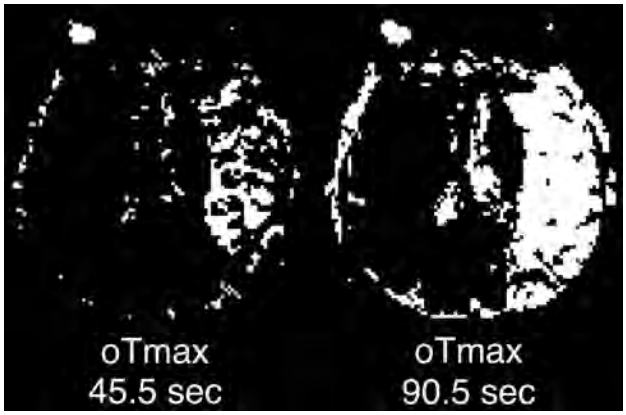

FIG 5. Change in Tmax lesion volume resulting from truncation artifacts. Tmax maps produced from a single patient's perfusion data, which have been truncated to simulate perfusion scans of 2 different durations that are similar to those in common clinical use: 45.5 seconds (*left*) and 90.5 seconds (*right*) following contrast injection. High-contrast window settings were used to depict pixels with a Tmax of >6 seconds as white and other pixels as black. The 90.5-second scan demonstrates a large lesion that would be considered "at risk" by using the 6-second criterion and could potentially make the patient eligible for thrombolytic therapy. The 45.5-second scan shows a much smaller Tmax lesion. Tmax lesion sizes measured across all image sections for this patient were 430.2 mL for the 90.5-second scan and 79.2 mL for the 45.5-second scan.

curate perfusion measurements. Shorter scans may produce perfusion maps in which CBV, MTT, Tmax, and, to a much lesser degree, CBF values are all underestimated in ischemic brain tissue to varying degrees, depending on truncation severity. Because scan durations vary widely across institutions, the severity of truncation artifacts likely varies extensively as well. Perfusion measurements reported in different studies from different institutions may not only fail to reflect the true hemodynamic status of the brain but may not even be reliably comparable with each other.

The severity of truncation artifacts is presumably most severe in stroke patients, whose arterial lesions delay the arrival of the contrast agent bolus and prolong its transit through the brain. However, truncation can also be worsened for other reasons. For example, a slower contrast injection rate, a narrower intravenous catheter, longer or larger injection tubing, or an increase in patient size could all result in increased truncation artifacts. Even if these factors were constant, moment-to-moment changes in cardiac output could change the rate at which contrast material is delivered to the brain and, therefore, the degree of truncation. Therefore, even data acquired at different times at the same institution by using the same imaging protocol may be difficult to compare if the scan duration is too short.

In acute stroke imaging, perfusion maps are often used to identify brain tissue that is putatively at risk of infarction.[4] Some studies have proposed defining tissue at risk as visibly appreciable MTT lesions. As shown in Fig 2, the truncation artifacts introduced by a shorter scan could make such lesions less conspicuous or erase them entirely. Other studies have proposed delineating at-risk tissue by using quantitative hemodynamic thresholds, for example, Tmax values of >6 seconds. In our study, calculated Tmax values changed from above that threshold to below it in nearly half of ischemic lesions, when scan durations were reduced. Our analysis estimates that truncation of perfusion data may reduce the measured volume of putative "at-risk" tissue by >70 mL, depending on truncation severity and the postprocessing algorithm used. These truncation-related errors in MTT and Tmax maps could result in failure to administer thrombolytic therapy to patients who could be eligible for treatment in clinical trials using Tmax inclusion criteria.

Some studies have also proposed that perfusion imaging can also be used to identify "core" brain tissue that has irre-

versible ischemic injury, a role usually filled by DWI, because low-CBV lesions approximate the size and location of DWI lesions.[2,13] Our results show that identifying core tissue with perfusion imaging also may be challenging, because shorter scan durations could cause CBV to appear low when it is actually elevated. If a large low-CBV lesion is presumed to reflect extensive completed infarction that would make thrombolytic therapy futile or dangerous, then truncation-related errors in the CBV calculation could result in failure to treat patients who otherwise would be eligible.

Our study is limited in that only a handful of postprocessing algorithms were tested. Although these algorithms are among the most commonly used in clinical research and practice, other algorithms potentially could be more resistant to truncation-related errors. In addition, oTmax and sTmax volumes appear to diverge with increased scan duration. However, it is more likely that both will converge to different steady-state values representing the extent of tissue with abnormal hemodynamics. This outcome is likely due to the threshold used for identifying tissue at risk being based on literature values that used SVD for deconvolution. It is possible that if a higher Tmax threshold were used, similar volumetric results would be obtained. This finding of volume dependency exemplifies the need to disclose the algorithms used for calculating perfusion maps, even those as simple as Tmax.

Another limitation of our study is our inability to achieve exactly the same proportion of gray matter and white matter in each patient's lesion and contralateral ROIs, for those patients in whom ROIs could not be placed entirely within either gray matter or white matter structures. As a result, noise may have been introduced into the ratios that were used for normalization of CBV, CBF, and MTT values. Therefore, the lesion reversal frequencies that we calculated for each parameter are best considered approximations of the frequencies that would be computed by using a larger sample size. However, because each patient's lesion and contralateral ROIs did not change positions across different scan durations, volume averaging–related errors in normalization ratios would not invalidate our finding that increasing truncation causes artifactual decreases in calculated perfusion parameters.

The most straightforward way to avoid truncation-related errors in perfusion maps is simply to use CTP and MRP scans that are as long as is feasibly possible. Unfortunately, in the case of CTP, longer scans entail increased exposure to ionizing radiation. This increase in exposure may be mitigated by combining an increase in scan duration with a decrease in sampling frequency, for example, acquisition of CTP images every 3 seconds instead of every 1 second. However, reducing sampling frequency also presumably degrades perfusion maps, causing errors whose nature and severity are dependent on the imaging technique and postprocessing algorithm used. Such artifacts are beyond the scope of the current study but have been investigated by previous studies that used methodology similar to ours, in which the effects of various sampling frequencies were tested by acquiring a scan with a high sampling frequency and then simulating lower frequencies by selectively omitting some images.[28-30]

CONCLUSIONS

Our results show that truncation of data by short perfusion scans may introduce large errors in perfusion maps of patients with acute ischemic stroke. Our findings highlight the importance of considering the vulnerabilities of different algorithms to truncation errors when choosing among them and interpreting the results of published studies that have relied on perfusion imaging. Just as stroke researchers have recognized the importance of assessing postprocessing errors related to bolus arrival delay,[31] our results show that truncation-related errors may be important as well. Testing perfusion postprocessing software for these and other shortcomings is more difficult when vendors of proprietary software do not disclose the details of their postprocessing algorithms. Therefore, our results also show the importance of transparency in revealing algorithms that may be used in clinical research or patient care.

Disclosures: Ona Wu—*RELATED*: *Grant*: National Institutes of Health/National Institute of Neurological Disorders and Stroke (R01NS059775)*; *UNRELATED*: *Consultancy*: Penumbra, *Comments*: I consulted on work unrelated to the topic of this article; *Grants/Grants Pending*: National Institutes of Health (P50NS051343, R01NS059775, R01NS082285);* *Royalties*: US Patent 7,512,435, March 31, 2009,* *Comments*: delay-compensated calculation of tissue blood flow. This patent has been licensed by GE Healthcare, Siemens, Imaging Biometrics, and Olea Medical. *Money paid to the institution.

REFERENCES

1. Hacke W, Furlan AJ, Al-Rawi Y, et al. **Intravenous desmoteplase in patients with acute ischaemic stroke selected by MRI perfusion-diffusion weighted imaging or perfusion CT (DIAS-2): a prospective, randomised, double-blind, placebo-controlled study.** *Lancet Neurol* 2009;8:141–50
2. Parsons M, Spratt N, Bivard A, et al. **A randomized trial of tenecteplase versus alteplase for acute ischemic stroke.** *N Engl J Med* 2012;366:1099–107
3. Ma H, Parsons MW, Christensen S, et al. **A multicentre, randomized, double-blinded, placebo-controlled Phase III study to investigate EXtending the time for Thrombolysis in Emergency Neurological Deficits (EXTEND).** *Int J Stroke* 2012;7:74–80
4. Kidwell CS, Jahan R, Gornbein J, et al. **A trial of imaging selection and endovascular treatment for ischemic stroke.** *N Engl J Med* 2013;368:914–23
5. Kudo K, Christensen S, Sasaki M, et al. **Accuracy and reliability assessment of CT and MR perfusion analysis software using a digital phantom.** *Radiology* 2013;267:201–11
6. Ho CY, Hussain S, Alam T, et al. **Accuracy of CT cerebral perfusion in predicting infarct in the emergency department: lesion characterization on CT perfusion based on commercially available software.** *Emerg Radiol* 2013;20:203–12
7. Murphy BD, Fox AJ, Lee DH, et al. **Identification of penumbra and infarct in acute ischemic stroke using computed tomography perfusion-derived blood flow and blood volume measurements.** *Stroke* 2006;37:1771–77
8. Chiu FY, Kao YH, Teng MM, et al. **Validation and absolute quantification of MR perfusion compared with CT perfusion in patients with unilateral cerebral arterial stenosis.** *Eur J Radiol* 2012;81:4087–93
9. Calamante F, Gadian DG, Connelly A. **Delay and dispersion effects in dynamic susceptibility contrast MRI: simulations using singular value decomposition.** *Magn Reson Med* 2000;44:466–73
10. Carrera E, Jones PS, Iglesias S, et al. **The vascular mean transit time: a surrogate for the penumbra flow threshold?** *J Cereb Blood Flow Metab* 2011;31:1027–35
11. Schramm P, Schellinger PD, Klotz E, et al. **Comparison of perfusion computed tomography and computed tomography angiography**

source images with perfusion-weighted imaging and diffusion-weighted imaging in patients with acute stroke of less than 6 hours' duration. *Stroke* 2004;35:1652–58
12. Deipolyi AR, Wu O, Macklin EA, et al. **Reliability of cerebral blood volume maps as a substitute for diffusion-weighted imaging in acute ischemic stroke.** *J Magn Reson Imaging* 2012;36:1083–87
13. Wintermark M, Flanders AE, Velthuis B, et al. **Perfusion-CT assessment of infarct core and penumbra: receiver operating characteristic curve analysis in 130 patients suspected of acute hemispheric stroke.** *Stroke* 2006;37:979–85
14. Kamalian S, Kamalian S, Maas MB, et al. **CT cerebral blood flow maps optimally correlate with admission diffusion-weighted imaging in acute stroke but thresholds vary by postprocessing platform.** *Stroke* 2011;42:1923–28
15. Lansberg MG, Straka M, Kemp S, et al. **MRI profile and response to endovascular reperfusion after stroke (DEFUSE 2): a prospective cohort study.** *Lancet Neurol* 2012;11:860–67
16. Reese TG, Heid O, Weisskoff RM, et al. **Reduction of eddy-current-induced distortion in diffusion MRI using a twice-refocused spin echo.** *Magn Reson Med* 2003;49:177–82
17. Collins DL, Neelin P, Peters TM, et al. **Automatic 3D intersubject registration of MR volumetric data in standardized Talairach space.** *J Comput Assist Tomogr* 1994;18:192–205
18. Rosen BR, Belliveau JW, Chien D. **Perfusion imaging by nuclear magnetic resonance.** *Magn Reson Q* 1989;5:263–81
19. Carroll TJ, Rowley HA, Haughton VM. **Automatic calculation of the arterial input function for cerebral perfusion imaging with MR imaging.** *Radiology* 2003;227:593–600
20. Rempp KA, Brix G, Wenz F, et al. **Quantification of regional cerebral blood flow and volume with dynamic susceptibility contrast-enhanced MR imaging.** *Radiology* 1994;193:637–41
21. Mouridsen K, Christensen S, Gyldensted L, et al. **Automatic selection of arterial input function using cluster analysis.** *Magn Reson Med* 2006;55:524–31
22. Rausch M, Scheffler K, Rudin M, et al. **Analysis of input functions from different arterial branches with gamma variate functions and cluster analysis for quantitative blood volume measurements.** *Magn Reson Imaging* 2000;18:1235–43
23. Mlynash M, Eyngorn I, Bammer R, et al. **Automated method for generating the arterial input function on perfusion-weighted MR imaging: validation in patients with stroke.** *AJNR Am J Neuroradiol* 2005;26:1479–86
24. Østergaard L, Weisskoff RM, Chesler DA, et al. **High resolution measurement of cerebral blood flow using intravascular tracer bolus passages. Part I: mathematical approach and statistical analysis.** *Magn Reson Med* 1996;36:715–25
25. Wu O, Østergaard L, Weisskoff RM, et al. **Tracer arrival timing-insensitive technique for estimating flow in MR perfusion-weighted imaging using singular value decomposition with a block-circulant deconvolution matrix.** *Magn Reson Med* 2003;50:164–74
26. Sorensen AG, Copen WA, Østergaard L, et al. **Hyperacute stroke: simultaneous measurement of relative cerebral blood volume, relative cerebral blood flow, and mean tissue transit time.** *Radiology* 1999;210:519–27
27. *CT Perfusion 4D User Guide*. Revision 2. Milwaukee: GE Healthcare Publications; 2011
28. Wintermark M, Smith WS, Ko NU, et al. **Dynamic perfusion CT: optimizing the temporal resolution and contrast volume for calculation of perfusion CT parameters in stroke patients.** *AJNR Am J Neuroradiol* 2004;25:720–29
29. Kamena A, Streitparth F, Grieser C, et al. **Dynamic perfusion CT: optimizing the temporal resolution for the calculation of perfusion CT parameters in stroke patients.** *Eur J Radiol* 2007;64:111–18
30. Abels B, Klotz E, Tomandl BF, et al. **CT perfusion in acute ischemic stroke: a comparison of 2-second and 1-second temporal resolution.** *AJNR Am J Neuroradiol* 2011;32:1632–39
31. Wintermark M, Albers GW, Alexandrov AV, et al. **Acute stroke imaging research roadmap.** *Stroke* 2008;39:1621–28

Contribution and Additional Impact of Imaging to the SPAN-100 Score

P. Krishnan, G. Saposnik, B. Ovbiagele, L. Zhang, S. Symons, and R. Aviv

ABSTRACT

BACKGROUND AND PURPOSE: Stroke Prognostication by Using Age and NIHSS score (SPAN-100 index) facilitates stroke outcomes. We assessed imaging markers associated with the SPAN-100 index and their additional impact on outcome determination.

MATERIALS AND METHODS: Of 273 consecutive patients with acute ischemic stroke (<4.5 hours), 55 were characterized as SPAN-100-positive (age +NIHSS score ≥ 100). A comprehensive imaging review evaluated differences, using the presence of the hyperattenuated vessel sign, ASPECTS, clot burden score, collateral score, CBV, CBF, and MTT. The primary outcome assessed was favorable outcome (mRS ≤ 2). Secondary outcomes included recanalization, lack of neurologic improvement, and hemorrhagic transformation. Uni- and multivariate analyses assessed factors associated with favorable outcome. Area under the curve evaluated predictors of favorable clinical outcome.

RESULTS: Compared with the SPAN-100-negative group, the SPAN-100-positive group (55/273; 20%) demonstrated larger CBVs (<0.001), poorer collaterals ($P < .001$), and increased hemorrhagic transformation rates (56.0% versus 36%, $P = .02$) despite earlier time to rtPA ($P = .03$). Favorable outcome was less common among patients with SPAN-100-positive compared with SPAN-100-negative (10.9% versus 42.2%; $P < .001$). Multivariate regression revealed poorer outcome for SPAN-100-positive (OR = 0.17; 95% CI, 0.06–0.38; $P = .001$), clot burden score (OR = 1.14; 95% CI, 1.05–1.25; $P < .001$), and CBV (OR = 0.58; 95% CI, 0.46–0.72; $P = .001$). The addition of the clot burden score and CBV improved the predictive value of SPAN-100 alone for favorable outcome from 60% to 68% and 74%, respectively.

CONCLUSIONS: SPAN-100-positivity predicts a lower likelihood of favorable outcome and increased hemorrhagic transformation. CBV and clot burden score contribute to poorer outcomes among high-risk patients and improve stroke-outcome prediction.

ABBREVIATIONS: AUC = area under curve; CBS = clot burden score; SPAN-100 = Stroke Prognostication Using Age and NIHSS

Several scores have been designed to prognosticate clinical outcomes in acute ischemic stroke and assess potential risks of intravenous thrombolysis.[1] Age and stroke severity measured by the National Institutes of Health Stroke Scale are among major independent prognostic factors for determining stroke outcome.[2,3] Stroke Prognostication Using Age and NIHSS (SPAN-100) was conceived by combining age in years and stroke severity measured by the NIHSS[4] and applying the combination to predict clinical outcome and risk of intracerebral hemorrhage. With individuals older than 80 years of age constituting a significant proportion of hospitalized patients with acute ischemic stroke, the relevance of the SPAN-100 is self-evident.[5] Moreover, the elderly also have a higher risk of fatality and longer hospitalization, necessitating the consideration of the benefit-harm ratio preceding rtPA therapy. More interestingly, most stroke predictive scores use either clinical or imaging components, and though several exist, their utility in clinical practice is somewhat restricted.[1] Multimodal imaging-selection strategies are evolving into a cornerstone for stroke management to best define target groups with salvageable tissue at risk.[6-9] Apart from excluding hemorrhage and early ischemic changes, the presence and extent of ischemic core, intravascular clot burden, and extent of collaterals are critical elements assessed by imaging, dictating management and outcome in patients with stroke.[10]

The simplicity of SPAN-100, using readily accessible information including age and NIHSS, makes it attractive for practical

Received April 6, 2014; accepted after revision October 16.

From the Division of Neuroradiology (P.K., S.S., R.A.), Department of Medical Imaging, University of Toronto and Sunnybrook Health Sciences Centre, Toronto, Ontario, Canada; Stroke Outcome Reach Center (G.S.), Division of Neurology, Department of Medicine, St. Michael's Hospital, University of Toronto, Ontario, Canada; Department of Neurosciences (B.O.), Medical University of South Carolina, Charleston, South Carolina; and Biostatistician (L.Z.), Sunnybrook Health Sciences Center, Toronto, Ontario, Canada.

P. Krishnan and G. Saposnik contributed equally to the article.

Paper previously presented at: American Society of Neuroradiology Annual Meeting and the Foundation of the ASNR Symposium, May 17–22, 2014; Montreal, Quebec, Canada.

Please address correspondence to Richard I. Aviv, MD, FRCR, Sunnybrook Health Sciences Centre, 2075 Bayview Ave, Toronto, Ontario, Canada M4N 3M5; e-mail: richard.aviv@sunnybrook.ca

http://dx.doi.org/10.3174/ajnr.A4195

use. Furthermore, imaging features accompanying SPAN-100-positivity provide insight into pathophysiologic characteristics of patients evaluated with SPAN-100. We sought to externally validate SPAN-100, document multimodal CT parameters associated with SPAN-100 status, and assess their interaction with SPAN-100 and clinical outcome.

MATERIALS AND METHODS

Study Design and Patient Cohort

A single-center retrospective study of patients presenting to a regional stroke center within 4.5 hours of anterior circulation stroke symptoms with a vessel occlusion, between October 2009 and December 2011, was performed. The institutional review board approved this study, and individual patient consent was obtained. Patients underwent clinical assessment by certified stroke neurologists and an acute CT-based stroke protocol, including CTA and CTP. Follow-up imaging included repeat CTA/CTP at 24 hours and 5- to 7-day CT or MR imaging. Presenting demographic data collected included age, sex, and cerebrovascular risk factors, including hypertension, diabetes, hypercholesterolemia, coronary artery disease, atrial fibrillation, and history of smoking and previous stroke. Baseline National Institutes of Health Stroke Scale (pre-NIHSS) and 3-month follow-up modified Rankin Scale scores were documented. Patients were not treated with intra-arterial therapies because this option was not available when these patients underwent the CT studies.

Outcome Measures. The primary outcome was favorable clinical outcome defined as mRS $\leq$ 2. Secondary outcomes included hemorrhagic transformation (by using the European Cooperative Acute Stroke Study definition), recanalization, and lack of NIHSS improvement between baseline and 24 hours (defined as $<$3-point NIHSS change).[4] Patients were divided into 2 groups: SPAN-100-positive (age + NIHSS score of $>$100) and SPAN-100-negative (age + NIHSS score of $<$100).

Image Analysis. Imaging was assessed by an experienced neuroradiologist. A comprehensive imaging review documented the presence of the hyperattenuated vessel sign, ASPECTS, early ischemic changes, clot burden score, and collateral score. CBV, CBF, and MTT volumes were measured planimetrically by using Medical Image Processing, Analysis, and Visualization, Version 4.4.1 (National Institutes of Health, Bethesda, Maryland; http://mipav.cit.nih.gov). The threshold adopted for volumetric measurements of penumbra and infarct was internally validated. Penumbral tissue was identified by using a threshold of CBF of $>$19 mL/100 g/min and relative MTT of $<$140%, whereas infarct on the CBV map was defined by CBV of $<$1.48 mL/100 g.[11] CT Perfusion software, Version 4 (GE Healthcare, Milwaukee, Wisconsin) was used to analyze data from the baseline CT perfusion study to calculate parametric maps of CBF, CBV, and MTT. A deconvolution of the arterial input curves by using the model of Johnson and Wilson was applied to calculate the parametric maps.[12] A venous output function from the anterior cerebral artery and the superior sagittal sinus was obtained to correct for partial volume averaging of the arterial input curves. Functional CT perfusions maps were analyzed by using custom software (IDL, Version 6.1; RSI-Research Systems, Chapel Hill, North Carolina). All components of the analysis were performed blinded to the clinical information to reduce interpreter bias. Pixels with CBF values of $>$100 mL/100 g/min or CBV of $>$8 mL/100 g were excluded and were not used for calculating average CBF and CBV values for regions of interest. The time from symptom onset to scan, rtPA treatment, and hemorrhagic transformation on follow-up was noted for each patient.

Clot burden score (CBS) was used to quantify the burden of intracranial thrombus in the proximal intracranial circulation. The score allocates points on a scale of 0–10 for contrast opacification of proximal intracranial vessels. Two points each were subtracted for the presence of thrombus in the supraclinoid ICA and proximal or distal M1, and 1 point each, for the infraclinoid ICA, A1, and each affected proximal M2 branch ($\leq$2 points).[12] Collateral score was used to grade the extent of collateral vascular supply to the occluded MCA distribution on a scale of 0–3. A score of zero denotes absent collateral supply; a score of 1, collateral filling of $\leq$50%; a score of 2, $>$50% but $<$100%; and a score of 3, collateral supply to 100% of the occluded MCA distribution.[12]

Scanning Protocol and Generation of Parametric Maps

The CT stroke protocol was performed on a 64-section CT scanner (LightSpeed VCT; GE Healthcare) and included pre- and postcontrast CT head scans. The parameters used were as follows: 120 kV(peak), 340 mA, 8 $\times$ 5 mm collimation, 1 s/rotation, and table speed of 15 mm/rotation. Standard CTA from the aortic arch to the vertex was performed with the following parameters: 0.7-mL/kg iodinated contrast, maximum of 90 mL (iohexol; Omnipaque, 300 mg iodine/mL; GE Healthcare), 5- to 10-second delay, 120 kVp, 270 mA, 1 s/rotation, 1.25-mm-thick sections, and table speed of 3.7 mm/rotation. CTA data comprised multiplanar 7-mm MIP reconstructions and 4-mm axial reformats on CTA source images. The biphasic CTP technique included a 45-second initial scan reconstructed at 0.5-second intervals, producing a series of 90 sequential images for each of the 8 sections, covering 4 cm from the basal ganglia to the lateral ventricles. This was followed by a second phase covering the same 8 sections, 15 seconds apart for 6 acquisitions for an additional 90 seconds as previously published.[13]

CTP scanning parameters used were the following: 80 kVp, 100 mA, 0.5-mL/g (maximum, 50-mL) iodinated contrast agent injected at 4 mL/s with a 3- to 5-second delay.

Statistical Analysis

All analyses were conducted by SAS (Version 9.3 for Windows; SAS Institute, Cary, North Carolina). We compared demographic and clinical factors between patients with SPAN-100-positivity and -negativity. The χ^2 test was used for categoric variables; the Wilcoxon rank sum test, for continuous variables with nonnormalized distribution; and the ANOVA, for those with normalized distribution. To search for the most significant clinical and imaging factors related to SPAN-100 status, we performed backward stepwise-selection logistic regression. Natural log-transformation was applied for normalization of variables when necessary. Comparison of demographic, imaging, and outcome factors was made for patients with SPAN-100-positivity and SPAN-100-negativity who did or did not receive rtPA, by using univariate logistic regression. To investigate the

Table 1: Comparing demographics/clinical factors between patients with positive SPAN-100 and patients with negative SPAN-100

	SPAN-100-Negative (n = 218)	SPAN-100-Positive (n = 55)	P Value
Age (yr)	68.2 ± 12.5	85.5 ± 5.07	<.001
NIHSS (median, IQR)	13 (7–18)	21 (17–24)	<.001
Male sex	121 (55.5%)	22 (40)	.04
SBP	157.7 (139–172)	156.04 (138–177)	.77
DBP	84.9 (71–95)	76.1 (64–87)	.01
Glucose (admission)	8.1 (5.8–8.1)	7.6 (6.0–9.0)	.18
Risk factors			
Hypertension	127 (58.26)	45 (81.8)	.001
Diabetes mellitus	43 (19.72)	10 (18.18)	.79
Hypercholesterolemia	72 (33.03)	25 (45.4)	.08
Coronary artery disease	53 (24.3)	12 (21.8)	.69
Atrial fibrillation	64 (29.36)	19 (34.5)	.45
Smoker	44 (20.1)	6 (10.9)	.11
Stroke	1 (0.46)	1 (1.82)	.29
Hyperdense sign	114 (52.53)	35 (63.64)	.13
ASPECTS (median) (IQR)	7 (6–9)	7 (5–8)	.39
Clot burden score	6 (4–9)	6 (5–9)	.29
Collateral score	2 (2–3)	2 (1–2)	<.001
CBV (median) (IQR)	14.7 (4.7–34.7)	34.7 (13.8–60.5)	<.001
CBF	101.6 (55.3–133.1)	98.2 (74.6–129.5)	.75
MTT	104.5 (58.5–133.4)	98.4 (74.7–130.5)	.69
Time and thrombolysis			
rtPA dose	63.0 (54–73)	63.0 (54–72)	.75
Onset to CT	104.0 (80–148)	108.0 (75–127)	.62
Onset to rtPA	161.7 (147)	143.0 (131)	.03
Outcome			
Recanalization	119 (55.35)	33 (61.1)	.44
mRS (at follow-up)	3 (1–4)	5 (4–6)	<.001
mRS ≤ 2	92 (42.2)	6 (10.9)	<.001
NIHSS improves >3 in 24 hours	101 (46.3)	27 (49)	.71
Hemorrhagic transformation	78 (38.6)	28 (56.0)	.02
Hemorrhage infarct	64 (29.4)	23 (41.8)	.07
Parenchymal hemorrhage	26 (11.9)	9 (16.4)	.37

Note:—IQR indicates interquartile range; SBP, systolic blood pressure; DBP, diastolic blood pressure.

association between favorable outcome and demographic/clinical factors, we performed a univariate logistic regression analysis as described above. Factors with $P < .10$ in univariate analysis were included in a backward stepwise logistic regression after adjusting for SPAN-100 status.

The additional benefit of significant clinical and radiologic factors over SPAN-100 as a null model for favorable outcome prediction was tested by using the Akaike information criterion ($AIC = L_{RES} + 2 \times k$). A lower Akaike information criterion indicates a better model fit, where L_{RES} represents the restricted maximized $-2 \times$ log-likelihood (-2 L) of the model, and k, the number of parameters in the model. The G2 likelihood ratio statistic is the difference between $-2\ L$ of the fitted model (transformed threshold) and the reference model (nontransformed threshold). A 2-sided P value was obtained from the G2 likelihood ratio χ^2 test. Similarly, the area under the curve (AUC) was calculated for each model by using receiver operator characteristic curves and was compared with pair-wise comparison. A P value < .05 was considered significant.

RESULTS

Among 273 patients with acute ischemic stroke, 55 (20.1%) were SPAN-100-positive (Table 1). Factors associated with SPAN-100-positivity included female sex ($P = .02$), hypertension ($P = .001$), and diastolic blood pressure ($P = .006$). rtPA was given to 47/55 (85.5%) of the SPAN-100-positive group and 172/218 (78.9%) of the SPAN-100-negative group ($P = .28$). The rtPA dose was comparable in both groups with a mean of 63 mg ($P = .7$), though patients with SPAN-100-positivity received rtPA earlier (143 minutes versus 161 minutes; $P = .03$).

Differences in Imaging Parameters by SPAN-100 Status

The collateral score was lower in patients with SPAN-100-positivity, consistent with worse collateral circulation ($P < .001$). Baseline CBVs were higher in patients with SPAN-100-positivity ($P = .001$) despite similar CBF/MTT volumes ($P = .7$ and .6, respectively), indicating comparable degrees of ischemia. No significant difference for median baseline ASPECTS ($P = .39$), hyperattenuated MCA sign, clot burden score, or early ischemic change was observed. Stepwise multivariate logistic regression analysis revealed that hypertension (OR = 3.1; 95% CI, 1.1–7.07; $P = .003$), female sex (OR = 0.47; 95% CI, 0.2–0.8; $P = .02$), and collateral score (OR = 0.4; 95% CI, 0.2–0.6; $P < .001$) were associated with SPAN-100-positive status. Baseline CBV did not reach clinical significance.

Primary and Secondary Outcome by SPAN-100 Status

Favorable clinical outcome was less common in patients with SPAN-100-positivity (10.9% versus 42.2%, $P < .001$). Any hemorrhage was more common in patients with SPAN-100-positivity (56% versus 38.6%, $P = .02$). Hemorrhagic transformation was the most common hemorrhagic infarction subtype (Table 1). Recanalization rate and lack of NIHSS improvement were similar ($P = .4$ and $P = .7$). In contradistinction to patients with SPAN-100-negativity, no significant demographic imaging or outcome differences were present in patients with SPAN-100-positivity with or without rtPA treatment. Patients with SPAN-100-negativity treated with rtPA were more likely than non-rtPA-treated patients to present earlier ($P = .01$), demonstrate the hyperattenuated sign ($P = .06$), undergo hemorrhagic infarction ($P = .05$), recanalization ($P = .009$), show neurologic improvement within 24 hours, and experience a good clinical outcome ($P = .06$).

Predictors of Outcome

Multiple clinical and radiologic factors were associated with favorable clinical outcome on univariate analysis (Table 2). The multivariate logistic regression showed that SPAN-100-positivity (OR = 0.17; 95% CI, 0.06–0.38; $P < .001$) and larger CBV (OR = 0.58; 95% CI, 0.46–0.72; $P < .001$) were associated with a lower

Table 2: Univariate logistic regression analysis of good clinical outcome (mRS ≤ 2) on demographic and clinical factors and imaging parameters

	mRS ≤ 2 (*n* = 98), Favorable Outcome	mRS > 2 (*n* = 175), Poor Outcome	*P* Value	OR (95% CI)
Age (yr)	67 (57–78)	76 (66–83)	<.001	0.96 (0.94–0.98)
NIHSS pre-rtPA (median, IQR)	17 (12–21)	9.0 (4–15)	<.001	0.86 (0.82–0.90)
Female sex	42 (42.86)	88 (50.29)	.23	1.35 (0.82–2.23)
SBP	151 (138.5–173.5)	155 (137–171.5)	.93	1.00 (0.99–1.01)
DBP	81 (72.5–92)	80 (70–90)	.26	1.01 (0.99–1.02)
Glucose (admission)[a]	6.4 (5.4–7.3)	6.4 (5.4–7.3)	.04	0.42 (0.17–0.92)
Risk factors				
Hypertension	54 (55.10)	118 (67.43%)	.04	0.59 (0.36–0.99)
Diabetes mellitus	15 (15.31)	38 (21.71)	.20	0.65 (0.33–1.24)
Hypercholesterolemia	29 (29.59)	68 (38.86)	.12	0.66 (0.39–1.12)
Coronary artery disease	23 (24.3)	42 (24)	.92	0.97 (0.54–1.73)
Atrial fibrillation	29 (29.59)	54 (30.86)	.82	0.94 (0.55–1.61)
Smoker	22 (22.45)	28 (16)	.18	1.52 (0.81–2.83)
Stroke	1 (1.02)	1 (0.57)	.68	1.79 (0.07–45.66)
Hyperdense sign	48 (48.98%)	101 (58.05)	.14	0.69 (0.42–1.14)
EIC	84 (85.91)	158 (90.29)	.25	0.65 (0.30–1.39)
ASPECTS (median, IQR)	8 (6–9)	7 (5–8)	.001	1.24 (1.09–1.42)
Clot burden score	7 (6–9)	6 (4–9)	.002	1.14 (1.05–1.25)
Collateral score	2 (2–3)	2 (1–3)	.02	1.46 (1.06–2.04)
CBV (median, IQR)[a]	8.77 (2.5–24.09)	25.14 (9.1–49.60)	<.001	0.58 (0.46–0.72)
CBF	88.12 (44.7–122.1)	104.17 (74.3–143.6)	<.001	0.99 (0.99–1.00)
MTT	87.96 (43.2–125.9)	105.4 (77.5–138.8)	<.001	0.99 (0.99–1.00)
Time and thrombolysis				
rtPA given (No. of the patients)	80 (81.63%)	139 (79.43%)	.66	1.15 (0.62–2.20)
rtPA dose (mg)	64.0 (50–73)	62.0 (54–72)	.94	1.00 (0.98–1.02)
Onset to CT (min) (median, IQR)[a]	102.0 (74–151)	105.0 (80.5–141.5)	.73	1.08 (0.68–1.72)
Onset to rtPA (min) (median IQR)	145 (120–179)	146 (126–175)	.70	1.00 (1.00–1.01)
Outcome				
Recanalization	119 (55.35%)	33 (61.1%)	<.001	3.58 (2.09–6.30)
Hemorrhagic transformation	28 (30.43%)	78 (48.75%)	.004	0.46 (0.26–0.78)
NIHSS improves >3 in 24 hours	101 (46.3%)	27 (49%)	.20	1.38 (0.84–2.27)
SPAN-100-positive	6 (6.12%)	49 (28%)	<.001	0.17 (0.06–0.38)

Note:—EIC indicates early ischemic changes.
[a] Natural log-transformation was applied for normalizing the distribution.

Table 3: Prediction of favorable clinical outcome and hemorrhagic transformation

	AIC	−2 (Log-Likelihood)	R^{2a}	AUC	OR	95% CI	*P* Value
Favorable clinical outcome							
Model of SPAN-100 only	316.64	312.64	0.054	0.599		0.56–0.64	
SPAN-100					0.2	0.1–0.4	
Model of SPAN-100, CBS	307.42	301.42	0.088	0.676		0.61–0.74	.004
SPAN-100					0.2	0.1–0.3	
CBS					1.2	1.1–1.3	
Model of SPAN-100, CBS, CBV	294.09	286.09	0.135	0.742		0.68–0.80	<.001
SPAN-100					0.2	0.1–0.5	
CBS					1.1	1.0–1.2	
CBV					0.6	0.5–0.8	
Hemorrhagic transformation							
Model of SPAN-100 only	342.06	338.06	0.019	0.55		0.49–0.60	
SPAN-100					2.0	1.1–3.8	
Model of SPAN-100, CBS	339.39	333.392	0.037	0.62		0.54.5–0.69	.02
SPAN-100					2.2	1.2–4.1	
CBS					0.9	0.8–0.9	

Note:—AIC indicates Akaike information criterion.
[a] R^2 is the proportion of variability in a dataset that is accounted for by the statistical model.

likelihood of a favorable outcome, whereas a higher clot burden score (OR = 1.14; 95% CI, 1.05–1.25; $P = .003$) was associated with a greater chance of a favorable outcome. No interaction was found between SPAN-100 and CBV ($P = .53$) or between SPAN-100 and clot burden score ($P = .98$), respectively. The AUC for favorable clinical outcome by using SPAN-100 alone was 60%, increasing significantly to 68% and 74% with the addition of the clot burden score and CBV, respectively (Table 3). Univariate logistic regression for any hemorrhage showed significance for NIHSS ($P < .001$), hyperattenuated sign ($P = .001$), ASPECTS ($P = .022$), collateral score ($P = .020$), CBV ($P < .001$), and SPAN-100 ($P = .027$). Stepwise logistic regression of SPAN-100, collateral score, CBV, and clot burden score demonstrated significant associations for SPAN-100 (OR = 2.17; 95% CI, 1.16–4.14; $P = .001$) and clot burden score (OR = 0.91; 95% CI, 0.84–0.99; $P = .03$) with hemorrhagic transformation. The AUC for hemorrhagic transformation by using SPAN-100 alone was 55%, increasing significantly to 62% with the addition of clot burden score (Table 3).

DISCUSSION

Early prognostication of ischemic stroke outcome is a critical component of stroke management. SPAN-100, combining age and NIHSS score, is a recently proposed simple and practical tool to estimate the clinical response and risk of hemorrhagic complications after thrombolysis.[4] Although other clinical risk scores[1] may have a better power to prognosticate stroke, the SPAN-100 index is a practical tool that may help determine patients who are more likely to achieve a good or poor outcome. The combination of a simple clinical tool with imaging parameters may help stratify patients according to their risk for receiving thrombolytic or endovascular therapy for acute stroke. We evaluated the role of imaging parameters added to the SPAN-100 score to estimate clinical outcomes. We confirmed that patients with SPAN-100-positivity were less likely to be independent irrespective of rtPA treatment, while carrying a higher risk of hemorrhagic complications. Notably, worse outcomes occurred despite earlier time to rtPA therapy. Patients with SPAN-100-positivity had lower collateral circulation and larger baseline CBVs. Extending prior studies, we explored the interaction between the SPAN-100 index and additional radiologic factors and assessed their additional predictive value over SPAN-100 status for clinical outcome. Both the clot burden score (reflecting the burden of intraluminal thrombus) and CBV (reflecting infarct core) remained significant contributors to clinical out-

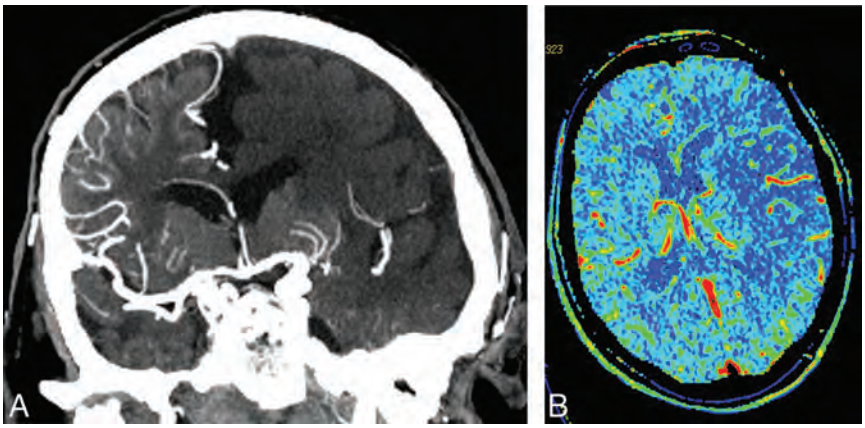

FIG 1. Coronal CTA MIP image and CBV map in a patient with SPAN-100-positivity at presentation. Coronal CTA MIP image (*A*) in this SPAN-100-positive patient with acute right-sided hemiparesis and subsequent unfavorable outcome demonstrates abrupt occlusion of the main stem left MCA with a collateral score of zero. The corresponding CBV map (*B*) demonstrates a large CBV deficit.

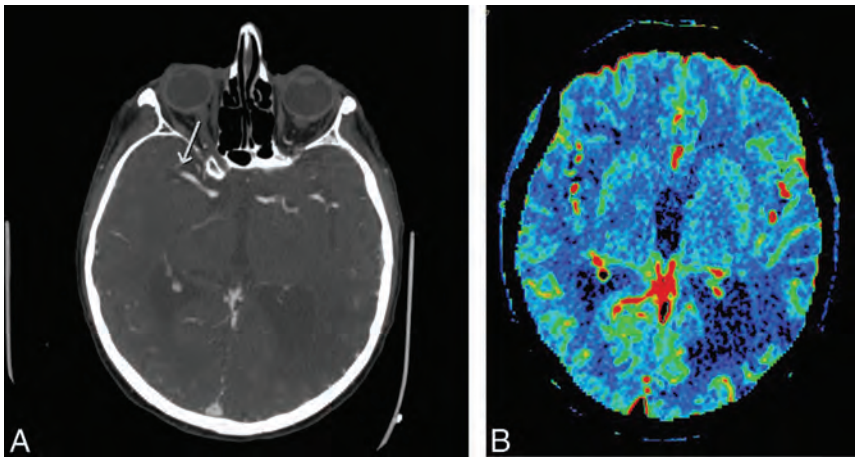

FIG 2. Axial CTA MIP image and CBV map in a patient with SPAN-100-positivity with favorable outcome. Axial CTA MIP (*A*) in this SPAN-100-positive patient with left-sided acute stroke and favorable outcome shows abrupt occlusion of the distal main stem right MCA. The extent of clot burden is low and underscores the utility of imaging in prognostication. The CBV map (*B*) shows a cortical-subcortical insular/subinsular defect in the right MCA distribution, with relative sparing of the basal ganglia. Chronic infarction is incidentally seen in the left parietal lobe.

come prediction and improved the prediction of the probability of achieving a favorable outcome at 3 months. Similarly the SPAN-100 index and clot burden score predicted hemorrhagic transformation.

In patients with SPAN-100-positivity, reduced collateral flow contributed to larger baseline CBVs manifest by its dominance within a multivariate analysis of SPAN-100 status and the loss of CBV significance. Collateral score reduction in patients with SPAN-100-positivity is supported by prior reports of diminishing functional collateral compensatory capacity with age.[14] Similarly, the CTA collateral profile is strongly associated with baseline infarct volume and long-term outcome in acute ischemic stroke.[15-17] Poor collateral flow and larger CBV, in part, explain the worse outcome in patients with SPAN-100-positivity despite an earlier time to rtPA (Fig 1). Increased intracranial hemorrhage in patients with SPAN-100-positivity may also, in part, be attributed to poorer collaterals[18] and larger baseline CBVs, with a clear association between baseline infarct volume and hemorrhage as previously described.[19,20] Despite CBV differences in SPAN-100 subgroups on univariate analysis, no significant baseline difference of ASPECTS was seen. This apparent disparity likely reflects the relatively coarse sensitivity of ASPECTS for lesion volume within the M1–6 or cortical regions compared with the significant impact of even small basal ganglia lesions on ASPECTS. Heavy weighting of ASPECTS to the basal ganglia may, in part, contribute to its modest sensitivity for outcome prediction.[21,22]

Although reduced collateral flow was also associated with unfavorable outcome on univariate analysis, CBV and the clot burden score remained dominant in the multivariate analysis in addition to SPAN-100 status. In the multivariate analysis, the imaging factors of SPAN-100 status, CBV, and clot burden scores were significantly associated with the mRS outcome (Fig 2). The lack of interaction between SPAN-100 status and clot burden score or between CBV and SPAN-100 status indicated that the probability difference on the mRS good outcome between SPAN-100-positivity and -negativity was similar with clot burden score changes or with CBV changes. For instance, in patients with a clot burden score of 6, the proportion of good mRS outcome was 6% for patients with positive SPAN-100 and 49% for patients with negative SPAN-100 (the difference was 43%). In patients with a clot burden score of 9, the difference in the proportion of good mRS outcome was 33% versus 71% for those with positive or negative SPAN-100 (the difference was 38%). These nonsignificant interaction terms might be due to the limited sample size in patients from the SPAN-100-positive group. Indeed, similar to a prior study, the AUC of SPAN-100 status alone was 60%.[23] The addition of CBV and clot burden score, however, increased predictions to 74%. A systematic review by Schiemanck et al[24] and several other studies[7,10,25] corroborated the importance of lesion volume and neurologic deficit assessed by the NIHSS score for clinical-outcome determination. Clot location and volume were both previously shown to be important independent prognostic factors of outcome.[10,12,26] Similarly, larger clot burden is associated with larger baseline infarct volumes, poorer clinical outcome, and risk of hemorrhage.[26,27]

Limitations of the present study include a retrospective data analysis with a modest sample size. CBV, though improving prognostication for outcome, is difficult to measure in real-time and complicates the purposeful simplicity of the SPAN-100 index as a

quick clinical prognostic tool. Whether rapid estimations of CBV, for example by ABC/2 (a commonly used method for volume calculation), provide benefit similar to that of a planimetric approach remains uncertain. The limited spatial resolution of CT perfusion may also underestimate complete CBV measurement. This issue is easily addressed with widely available table-toggle techniques[28,29] or 320-section scanners capable of whole-head imaging. Furthermore, the small sample of patients with SPAN-100-positivity is a limitation of this study and could have partly contributed to the lack of a significant difference in outcomes in this group. Finally, the accuracy of CTP CBV for DWI core assessment has recently been questioned,[30] though in our experience, this was largely mitigated by protocols that capture the full time-attenuation curve, thereby avoiding CBV underestimation.

Most of the predictive scores for outcome in acute stroke are inclusive of age and stroke severity scale (NIHSS), and their predictive power is moderate. Hence, consideration for rtPA treatment is currently based on clinical judgment, and clinical scores are used as an adjunct. Because the SPAN-100 index is among the more simplified prognostic scores for stroke outcome with core prognostic determinants of age and NIHSS, it would be reasonable to suggest that imaging parameters should be an integral part of the future stroke-outcome prediction scores with a need to customize for individual patients with a greater degree of precision. Our study re-emphasizes the need to incorporate imaging parameters (eg, CBV, collaterals, and clot burden scores) to provide additional predictive power.

The practical use of clinical prediction scores at present is limited in decision-making paradigms and is essentially complementary to clinical assessment. Future trials and larger retrospective studies inclusive of imaging parameters are needed to design comprehensive clinical scores with the potential to triage patients and tailor treatment options.

CONCLUSIONS

Imaging parameters improve outcome estimation in stroke prognostication when added to the clinical risk score (SPAN-100 index). Reduced collateral flow, higher clot burden, and larger cerebral blood volume deficits offer insight into the most relevant pathophysiologic parameters explaining poorer clinical outcomes among patients with SPAN-100-positivity.

The addition of imaging parameters to the SPAN-100 index improves the predictive power of stroke prognostication (ie, the prediction of favorable outcome and the risk of subsequent hemorrhage). The inherent simplicity of the SPAN-100 index and additional imaging parameters renders easy translation of this prediction score for practical use in routine clinical decision-making.

The routinely performed imaging assessment for acute stroke (multimodal CT and the parameters CBV, clot burden score, and collateral scores) could potentially add meaningful value to a well-established simplified clinical score (SPAN-100 index) for stroke prognostication.

Disclosures: Gustavo Saposnik—*UNRELATED*: *Grants/Grants Pending*: Dr Saposnik is supported by the Distinguished Clinician Scientist Award from the Heart and Stroke Foundation of Canada.

REFERENCES

1. Rabinstein A. Rundek T. **Prediction of outcome after ischemic stroke: the value of clinical scores.** *Neurology* 2013;80:15–16
2. Weimar C, Konig IR, Kraywinkel K, et al. **Age and National Institutes of Health Stroke Scale Score within 6 hours after onset are accurate predictors of outcome after cerebral ischemia: development and external validation of prognostic models.** *Stroke* 2004;35:158–62
3. König I, Ziegler A, Bluhmki E, et al. **Predicting long-term outcome after acute ischemic stroke: a simple index works in patients from controlled clinical trials.** *Stroke* 2008;39:1821–26
4. Saposnik G, Guzik A, Reeves M, et al. **SPAN 100: a practical method of stroke prognostication combining age and NIHSS after tPA.** *Neurology* 2013;80:21–28
5. Saposnik G, Cote R, Phillips S, et al. **Stroke Outcome Research Canada (SORCan) Working Group: variables associated with 7-day, 30-day, and 1-year fatality after ischemic stroke.** *Stroke* 2008;39:2522–30
6. Obach V, Oleaga L, Urra X, et al. **Multimodal CT-assisted thrombolysis in patients with acute stroke: a cohort study.** *Stroke* 2011;42:1129–31
7. Lev MH, Segal AZ, Farkas J, et al. **Utility of perfusion-weighted CT imaging in acute middle cerebral artery stroke treated with intra-arterial thrombolysis: prediction of final infarct volume and clinical outcome.** *Stroke* 2001;32:2021–18
8. Campbell BC, Weir L, Desmond PM, et al. **CT perfusion improves diagnostic accuracy and confidence in acute ischaemic stroke.** *J Neurol Neurosurg Psychiatry* 2013;84:613–18
9. Hopyan J, Ciarallo A, Dowlatshahi D, et al. **Certainty of stroke diagnosis: incremental benefit with CT perfusion over noncontrast CT and CT angiography.** *Radiology* 2010;255:142–53
10. Demchuk A, Menon B, Goyal M. **Imaging based selection in acute ischemic stroke trials: a quest for imaging sweet spots.** *Ann N Y Acad Sci* 2012;1268:63–71
11. Eilaghi A, d'Esterre CD, Lee TY, et al. **Toward patient-tailored perfusion thresholds for prediction of stroke outcome.** *AJNR Am J Neuroradiol* 2014;35:472–77
12. Tan IY, Demchuk AM, Hopyan J, et al. **CT angiography clot burden score and collateral score: correlation with clinical and radiologic outcomes in acute middle cerebral artery infarct.** *AJNR Am J Neuroradiol* 2009;30:525–31
13. Aviv RI, d'Esterre CD, Murphy BD, et al. **Hemorrhagic transformation of ischemic stroke: prediction with CT perfusion.** *Radiology* 2009;250:867–77
14. Brozici M, van der Zwan A, Hillen B. **Anatomy and functionality of leptomeningeal anastomoses: a review.** *Stroke* 2003;34:2750–62
15. Souza L, Yoo A, Chaudhry Z, et al. **Malignant CTA collateral profile is highly specific for large admission DWI infarct core and poor outcome in acute stroke.** *AJNR Am J Neuroradiol* 2012;33:1331–36
16. Lima FO, Furie KL, Silva GS, et al. **The pattern of leptomeningeal collaterals on CT angiography is a strong predictor of long-term functional outcome in stroke patients with large vessel intracranial occlusion.** *Stroke* 2010;41:2316–22
17. Liebeskind D. **Collateral perfusion: time for novel paradigms in cerebral ischemia.** *Int J Stroke* 2012;7:309–10
18. Bang O, Saver J, Kim S, et al. **Collateral flow averts hemorrhagic transformation after endovascular therapy for acute ischemic stroke.** *Stroke* 2011;42:2235–39
19. Bhatt A, Vora A, Thomas A, et al. **Lower pretreatment cerebral blood volume affects hemorrhagic risks after intra-arterial revascularization in acute stroke.** *Neurosurgery* 2008;63:874–78; discussion 878–79
20. Jain A, Jain M, Kanthala A, et al. **Association of CT perfusion parameters with hemorrhagic transformation in acute ischemic stroke.** *AJNR Am J Neuroradiol* 2013;34:1895–900
21. Dzialowski I, Hill MD, Coutts SB, et al. **Extent of early ischemic changes on computed tomography (CT) before thrombolysis: prognostic value of the Alberta Stroke Program Early CT Score in ECASS II.** *Stroke* 2006;37:973–78

22. Menon BK, Puetz V, Kochar P, et al. **ASPECTS and other neuroimaging scores in the triage and prediction of outcome in acute stroke patients.** *Neuroimaging Clin N Am* 2011;21:407–23, xii
23. Vogt G, Laage R, Shuaib A, et al. **Initial lesion volume is an independent predictor of clinical stroke outcome at day 90: an analysis of the Virtual International Stroke Trials Archive (VISTA) database.** *Stroke* 2012;43:1266–72
24. Schiemanck SK, Kwakkel G, Post MW, et al. **Predictive value of ischemic lesion volume assessed with magnetic resonance imaging for neurological deficits and functional outcome post stroke: a critical review of the literature.** *Neurorehabil Neural Repair* 2006;20:492–502
25. Murphy A, Symons SP, Hopyan J, et al. **Factors influencing clinically meaningful recanalization after IV-rtPA in acute ischemic stroke.** *AJNR Am J Neuroradiol* 2013;34:146–52
26. Sillanpää N, Saarinen JT, Rusanen H, et al. **Location of the clot and outcome of perfusion defects in acute anterior circulation stroke treated with intravenous thrombolysis.** *AJNR Am J Neuroradiol* 2013;34:100–06
27. Puetz V, Dzialowski I, Hill MD, et al. **Calgary CTA Study Group: intracranial thrombus extent predicts clinical outcome, final infarct size and hemorrhagic transformation in ischemic stroke: the clot burden score.** *Int J Stroke* 2008;3:230–36
28. Roberts HC, Roberts TP, Smith WS, et al. **Multisection dynamic CT perfusion for acute cerebral ischemia: the "toggling-table" technique.** *AJNR Am J Neuroradiol* 2001;22:1077–80
29. Youn SW, Kim JH, Weon YC, et al. **Perfusion CT of the brain using 40-mm-wide detector and toggling table technique for initial imaging of acute stroke.** *AJR Am J Roentgenol* 2008;191:W120–26
30. Lev MH. **Acute stroke imaging: what is sufficient for triage to endovascular therapies?** *AJNR Am J Neuroradiol* 2012;33:790–92

Comparing 3T and 1.5T MRI for Mapping Hippocampal Atrophy in the Alzheimer's Disease Neuroimaging Initiative

N. Chow, K.S. Hwang, S. Hurtz, A.E. Green, J.H. Somme, P.M. Thompson, D.A. Elashoff, C.R. Jack, M. Weiner, and L.G. Apostolova, for the Alzheimer's Disease Neuroimaging Initiative

ABSTRACT

BACKGROUND AND PURPOSE: Prior MR imaging studies, primarily at 1.5T, established hippocampal atrophy as a biomarker for Alzheimer disease. 3T MR imaging offers a higher contrast and signal-to-noise ratio, yet distortions and intensity uniformity are harder to control. We applied our automated hippocampal segmentation technique to 1.5T and 3T MR imaging data, to determine whether hippocampal atrophy detection was enhanced at 3T.

MATERIALS AND METHODS: We analyzed baseline MR imaging data from 166 subjects from the Alzheimer's Disease Neuroimaging Initiative-1 (37 with Alzheimer disease, 76 with mild cognitive impairment, and 53 healthy controls) scanned at 1.5T and 3T. Using multiple linear regression, we analyzed the effect of clinical diagnosis on hippocampal radial distance, while adjusting for sex. 3D statistical maps were adjusted for multiple comparisons by using permutation-based statistics at a threshold of $P < .01$.

RESULTS: Bilaterally significant radial distance differences in the areas corresponding to the cornu ammonis 1, cornu ammonis 2, and subiculum were detected for Alzheimer disease versus healthy controls and mild cognitive impairment versus healthy controls at 1.5T and more profoundly at 3T. Comparison of Alzheimer disease with mild cognitive impairment did not reveal significant differences at either field strength. Subjects who converted from mild cognitive impairment to Alzheimer disease within 3 years of the baseline scan versus nonconverters showed significant differences in the area corresponding to cornu ammonis 1 of the right hippocampus at 3T but not at 1.5T.

CONCLUSIONS: While hippocampal atrophy patterns in diagnostic comparisons were similar at 1.5T and 3T, 3T showed a superior signal-to-noise ratio and detected atrophy with greater effect size compared with 1.5T.

ABBREVIATIONS: AD = Alzheimer disease; ADNI = Alzheimer's Disease Neuroimaging Initiative; CA = cornu ammonis; CDR = Clinical Dementia Rating; MCI = mild cognitive impairment; MMSE = Mini-Mental State Examination; NC = healthy control

Alzheimer disease (AD), the most common form of dementia in the elderly, is characterized by progressive cognitive and functional decline. AD is increasingly recognized as one of the most important medical problems facing society today. In the United States alone, approximately 5.2 million people have AD. This number is predicted to rise to 13.8 million by 2050.[1] Worldwide, an estimated 35.6 million people lived with dementia in 2010. The worldwide prevalence is expected to reach 65.7 million diagnosed cases in 2030, and 115.4 million, in 2050.[2]

At the tail end of the cognitive spectrum, AD is often preceded by mild cognitive impairment (MCI), an intermediate stage between normal aging and dementia. Patients with MCI show a milder degree of cognitive impairment and preserved ability for day-to-day activities.[3] Patients with MCI are at an increased risk

Received February 28, 2014; accepted after revision October 24.

From the School of Medicine (N.C.), University of California, Irvine, Irvine, California; Oakland University William Beaumont School of Medicine (K.S.H.), Rochester Hills, Michigan; Departments of Neurology (K.S.H., S.H., L.G.A.) and Biostatistics (D.A.E.), University of California, Los Angeles, David Geffen School of Medicine, Los Angeles, California; Department of Physiology (A.E.G.), Monash University, Melbourne, Australia; Department of Neurology (J.H.S.), Cruces University Hospital, Barakaldo, Spain; Imaging Genetics Center (P.M.T.), Institute for Neuroimaging and Informatics, Keck/University of Southern California School of Medicine, Los Angeles, California; Departments of Neurology, Psychiatry, Engineering, Radiology, and Ophthalmology (P.M.T.), University of Southern California, Los Angeles, California; Department of Radiology (C.R.J.), Mayo Clinic and Foundation, Rochester, Minnesota; and Department of Radiology and Biomedical Imaging (M.W.), University of California, San Francisco, School of Medicine, San Francisco, California.

Research was conducted at Department of Neurology, David Geffen School of Medicine, University of California, Los Angeles, Los Angeles, California.

This work was generously supported by the Easton Consortium for Alzheimer Drug Discovery and Biomarkers, National Institutes of Health R01 AG040770, National Imaging Associates K23 AG026803, National Imaging Associates P50 AG16570, National Institute of Biomedical Imaging and Bioengineering EB008561, National Institute of Biomedical Imaging and Bioengineering EB01651, National Library of Medicine LM05639, National Center for Research Resources RR019771 and National Institutes of Health RR021813, and the ADNI National Imaging Associates U01AG024904.

Please address correspondence to Liana G. Apostolova, MD, MSCR, Mary S. Easton Center for Alzheimer's Disease Research, 10911 Weyburn Ave, 2nd floor, Los Angeles, CA 90095; e-mail: lapostolova@mednet.ucla.edu

http://dx.doi.org/10.3174/ajnr.A4228

for developing AD. Identifying patients during this prodromal stage allows early interventions. Noninvasive biomarkers for detecting prodromal AD are greatly needed.[4]

Hippocampal atrophy is the most established structural AD imaging biomarker to date. Hippocampal volume shrinkage is associated with AD-like postmortem hippocampal neuronal loss[5,6] and neurofibrillary tangle deposition.[7] Atrophy of the cornu ammonis (CA) 1 subfield is characteristic of both AD and MCI.[8-11] Greater involvement of CA1 is a risk factor for conversion from MCI to AD.[9,10]

High-resolution MR imaging has helped us visualize subtle anatomic changes in the brain in the initial stages of disease.[12,13] State-of-the-art analytic techniques helped us identify, quantify, and track AD-associated atrophy with great precision. The hippocampus, an area involved early in AD, has been studied via visual rating scales,[14-16] regional volumetric analysis,[10,11,17-19] and shape-deformation methods.[9,20-23] The early studies have used 1.5T, and some of the recent ones have used higher magnetic field strengths. Few studies have compared atrophy detection between 1.5T and 3T field-strength scans.[24-27] One tensor-based morphometry whole-brain study reported that analyses of 1.5T and 3T Alzheimer's Disease Neuroimaging Initiative (ADNI) data from the same subjects did not differ statistically in detecting neurodegenerative changes during 12 months.[26] Hippocampal volumes extracted from the same study cohort at 1.5T and 3T showed only 3.2% test-retest variability.[25] Similar results were reported for manual segmentations in 8 healthy subjects with 1.5T and 3T scans in an epilepsy study.[28]

Using the ADNI-1 dataset, we sought to directly compare 1.5T and 3T segmentations and to determine how well each magnetic field strength detects anatomic differences between subjects who are cognitively healthy (NC) or have MCI and AD as well as between subjects with MCI who converted from MCI to AD in 3 years (MCI converters) and those who did not (MCI nonconverters). Although distortions and intensity uniformity may be more difficult to control at 3T, 3T MR imaging offers higher contrast and signal-to-noise ratio. We hypothesized that higher field MR imaging will offer greater power to detect hippocampal atrophy in the cognitive spectrum from normal aging to AD.

MATERIALS AND METHODS

Subjects

ADNI-1[29-32] is a longitudinal multisite observational study, which started in 2004 and collected cognitive, imaging, and biomarker data from 200 NC subjects, 400 with MCI, and 200 with AD. The goals of ADNI are to determine relationships among clinical, cognitive, imaging, genetic, and biochemical biomarkers as AD evolves from normal aging to MCI to dementia, to discover biomarkers sensitive to early diagnosis, to establish standardized methods for imaging/biomarker collection, and to conduct research on methodologies that could lower the costs of clinical trials.

Our sample consisted of the 187 (22%) of the 842 subjects in ADNI-1 who underwent both 1.5T and 3T MR imaging. 1.5T and 3T brain baseline MR images and their associated clinical data were downloaded from the ADNI public data base (http://adni.loni.usc.edu). The cognitive variables we used to clinically characterize the research cohorts are the global Clinical Dementia Rating (CDR), sum-of-boxes Clinical Dementia Rating,[33,34] and the Mini-Mental State Examination (MMSE).[35,36] These are the 3 most commonly used global scales to gauge disease severity. The global CDR reflects the overall severity of dementia in which global CDR scores of 0, 0.5, 1, 2, and 3, indicate no cognitive decline, questionable cognitive decline, and very mild, mild, moderate, or severe dementia, respectively. The sum-of-boxes Clinical Dementia Rating ranges from 0 to 18 and reflects clinical deterioration in memory, orientation, judgment and problem solving, community affairs, home and hobbies, and personal care. The MMSE is a 30-point global cognitive screening instrument that evaluates orientation, registration, attention, calculation, recall, and language. All patients with AD met the National Institute of Neurological Disorders and Stroke/Alzheimer's Disease and Related Disorders Association criteria for probable AD.[37] Subjects with MCI met the criteria of Petersen et al for MCI.[3] Our MCI converter-versus-nonconverter analyses included only subjects with follow-up data for 36 months after baseline (36 were MCI converters, and 31 were MCI nonconverters).

Imaging Data Collection, Image Preprocessing, and Analysis

We acquired 1.5T and 3T scans analyzed in this study from 31 ADNI-1 sites on scanners from 3 MR imaging vendors (GE Healthcare, Milwaukee, Wisconsin; Philips Healthcare, Best, the Netherlands; or Siemens, Erlangen, Germany) with a standardized protocol developed to evaluate 3D T1-weighted sequences for morphometric analyses (http://adni.loni.usc.edu/methods/documents/mri-protocols/).[31,38] Participants with structural abnormalities such as hemispheric infarctions, white matter ischemic changes, and focal lesions were excluded from participation.[31] Of the 187 subjects who were imaged at both 1.5T and 3T, 111 (59%) subjects were scanned on GE Healthcare, 24 (13%) on a Phillips Healthcare, and 52 (28%) on Siemens 1.5T scanners. At 3T, 29 (15%) subjects were scanned on GE Healthcare, 50 (27%) were scanned on Phillips Healthcare, and 108 (58%), on Siemens scanners.

The 1.5T and 3T scanning protocols used a 3D sagittal volumetric sequence. The typical 1.5T acquisition parameters were TR = 2400 ms, minimum full TE, TI = 1000 ms, flip angle = 8°, FOV = 24 cm, with a 256 × 256 × 170 acquisition matrix in the x-, y-, and z-dimensions, yielding a voxel size of 1.25 × 1.25 × 1.2 mm^3. For 3T scans, the typical parameters were a TR = 2300 ms, minimum full TE, TI = 900 ms, flip angle = 8°, FOV = 26 cm, with a 256 × 256 × 170 acquisition matrix in the x-, y-, and z-dimensions, yielding a voxel size of 1.0 × 1.0 × 1.2 mm^3. The 3T protocol included an increased receiver bandwidth to compensate for the increase in chemical shift and susceptibility artifacts.[31] For a detailed description of the acquisition parameters for the various scanner manufacturers, please see Jack et al (2008).[31]

The ADNI MR imaging core at the Mayo Clinic preprocessed the data by using Gradwarp (GE Healthcare) for correction of geometric distortion due to gradient nonlinearity,[39] "B1-correction" for adjusting image intensity inhomogeneity,[31] "N3" bias field correction for reducing residual intensity inhomogeneity,[40] and geometric scaling for adjusting scanner- and session-specific

calibration errors.[31] The raw and preprocessed data are stored at the Laboratory of Neuroimaging at the University of Southern California and are available to the general scientific community for download (http://adni.loni.usc.edu).

MR images were automatically registered by using a 9-parameter transformation to the ICBM53 template.[41] The images were resampled in an isotropic space of 220 voxels along x-, y- and z-axes with a final voxel size of 1 mm^3.

For each field strength, a minimal deformation target was constructed from 9-parameter linearly aligned scans.[42] The minimal deformation target is an unbiased average template image created to represent common features for a group of subjects. This helps to reduce bias by using a template that deviates least from the anatomy of the subjects and to improve statistical power by using a customized template. For this study, 1.5T and 3T baseline scans were nonlinearly aligned to the minimal deformation target developed from 1.5T and 3T images of the NC group.

Two experienced raters manually traced the hippocampal formations of 21 randomly selected subjects (7 NCs, 7 with MCI, and 7 with AD) at 1.5T and 3T by using our in-house hippocampal tracing protocol[43] (intrarater reliability, Cronbach $\alpha = 0.97$; interrater reliability, Cronbach $\alpha = 0.9$). Traces included the hippocampus proper, dentate gyrus, and subiculum as previously described.[44] Tracers were blinded to subject demographics, diagnosis, and the study objective. Anatomic landmarks were followed in all 3 orthogonal viewing planes by using interactive segmentation software. The hippocampi were traced on contiguous coronal sections following a detailed well-established protocol with high intra- and interrater reliability.[45] When boundaries were ambiguous, standard neuroanatomic atlases were consulted.[46,47] Traces included the whole hippocampal head, body, and tail.

Hippocampal segmentation used AdaBoost, our automated machine-learning hippocampal segmentation algorithm, based on a statistical method called "Adaptive Boosting."[48] The technique has been previously described in detail in several publications.[49,50] Briefly, AdaBoost uses a training set (ie, a small number of representative images) to develop classification rules for hippocampal-versus-nonhippocampal tissue. Our training set for this study consisted of 21 subjects, 7 NCs, 7 with MCI, and 7 with AD, who were scanned at both 1.5T and 3T. AdaBoost analyzes the specific feature information contained in the positive and negative voxels (ie, those belonging and not belonging to the structure of interest) of the training dataset and develops segmentation rules based on the optimal combination of features. AdaBoost uses ~18,000 local features, such as image gradients, local curvature of image interfaces, tissue classification as gray or white matter, and statistical information on the likely stereotaxic position of the hippocampus. In the training phase, the algorithm applies mathematic approaches from the fields of machine learning and computer vision[51] to estimate the optimal weighting of these features in a mathematic formula that computes the probability of any given voxel for being inside the hippocampus. AdaBoost performance has been previously validated and has been found to agree with human raters as well as human raters agree with each other (ie, similar to interrater reliability).[49] After statistical rules for hippocampal segmentation are developed, the algorithm is tested in a training set and then applied to the full sample. All segmentations were visually inspected to make sure they appropriately captured the hippocampal anatomy at the given magnetic field strength.

We used an anatomic mesh modeling method called "hippocampal radial distance"[44] to match equivalent hippocampal surface points, obtained from the AdaBoost hippocampal segmentations, across subjects. To match the digitized points representing the hippocampus surface traces in each brain volume, we made the AdaBoost contours spatially uniform by modeling them as a 3D parametric surface mesh.[44] This procedure allows statistical comparisons in 3D and averaging of hippocampal surface morphology across all individuals belonging to a group. Next, to assess the pattern of regional hippocampal atrophy, a medial core, threading down the center of the hippocampus, was computed for each individual. Radial distance was assessed by measuring the distances from the hippocampal surface points to the medial core of the individual's hippocampal surface model.[44] Change in radial distance with time can, therefore, capture localized atrophy. This methodology assures that all hippocampal surfaces are represented by using the same parametric mesh structure. This allows corresponding surface traces and the associated distance measures to be matched across subjects and/or time and averaged across diagnostic groups. Distance fields indexing local expansions or contractions in hippocampal surface morphology can thus be compared statistically between groups.

An ROI was drawn over the lateral hippocampal surface (ie, the area corresponding to CA1) on the 3D hippocampal radial distance model, and the CA1 mean radial distance was computed for each subject at both 1.5T and 3T.

Statistical Methods

We used ANOVA with post hoc Bonferroni correction for multiple comparisons to examine between-group diagnostic differences in age, education, MMSE, CDR, and sum-of-boxes Clinical Dementia Rating. A χ^2 test was used to determine differences in sex distribution.

The effect of diagnosis on hippocampal radial distance was studied by using linear regression while correcting for demographic variables that showed significant between-group differences. Our 3D statistical maps were adjusted for multiple comparisons by using permutation-based statistics with a threshold of $P < .01$. A Student t test was performed for the direct comparison of 1.5T- and 3T-derived radial distance in each diagnostic group.

The observed CA1 regional differences between MCI converters and nonconverters at 3T but not at 1.5T (see "Results") were further examined by using receiver operating characteristic curves. We studied how well the mean CA1 radial distance (in millimeters) discriminated between MCI converters and nonconverters at 3T and 1.5T. We used the Mann-Whitney Wilcoxon test for independent paired samples to statistically compare the sum of the ranks for the mean CA1 radial distance at 1.5T versus 3T and the DeLong partial area under the curve test to statistically compare the area under the curve of the 2 receiver operating characteristic curves.

Demographic characteristics for the diagnostic-comparisons study

Variable	NC (n = 53)[a]	MCI (n = 76)[a]	AD (n = 37)[a]	P Value
Age (yr)	75.4 ± 4.7 (60–87)	75.2 ± 8.2 (55–88)	74.1 ± 8.7 (57–91)	.671
Education (yr)	16.1 ± 2.8 (7–20)	15.9 ± 3.2 (6–20)	14.6 ± 3.2 (7–20)	.055
Sex, M/F	18:35	47:29	13:24	.002[b]
MMSE	29.3 ± 0.9 (26–30)	26.8 ± 1.9 (23–30)	23.3 ± 2.1 (20–27)	<.0001[b]
CDR global	0 ± 0 (0)	0.50 ± 0 (1)	0.69 ± 0.25 (1)	<.0001[b]
CDR sum of boxes	1.0 ± 0.2 (1–2)	2.8 ± 1.0 (2–6)	5.1 ± 1.5 (3–9)	<.0001[b]
1.5T Left hippocampus (mm^3)	3859 ± 436 (2707–4730)	3335 ± 588 (1730–4827)	3242 ± 615 (1573–4302)	<.0001[b]
1.5T Right hippocampus (mm^3)	3734 ± 591 (2114–5441)	3254 ± 641 (850–4796)	3110 ± 668 (613–4814)	<.0001[b]
3T Left hippocampus (mm^3)	3897 ± 758 (408–5087)	3259 ± 601 (1627–4697)	3123 ± 598 (2013–4437)	<.0001[b]
3T Right hippocampus (mm^3)	3981 ± 612 (1468–5158)	3389 ± 638 (1800–5053)	3237 ± 672 (1873–4577)	<.0001[b]

[a] Data are means and ranges.
[b] Significant.

RESULTS

Demographics

Twenty-one 3T MR imaging scans failed the automated hippocampal segmentation process and were excluded from further analyses. Thus, our final sample consisted of 166 subjects in ADNI-1 (53 NCs, 76 with MCI, and 37 with AD). Demographic data are shown in the Table. Differences in sex distribution were found ($P = .002$), with the MCI group having significantly more men than women compared with the NC and AD groups. Sex was included as a covariate in the radial distance multiple regression model. As expected, the NC group had the highest MMSE score (29.3 ± 0.9) compared with MCI (26.8 ± 1.9) and AD groups (23.3 ± 2.1) ($P < .0001$). NC had the lowest CDR global score (0 ± 0), followed by MCI (0.50 ± 0) and AD (0.69 ± 0.25) ($P < .0001$). The sum-of-boxes Clinical Dementia Rating followed a similar trend: NC (1.0 ± 0.2), MCI (2.8 ± 1.0), and AD (5.1 ± 1.5) ($P < .0001$).

Hippocampal Regional Volume Differences

Predictably, NC had the largest hippocampal volumes, and the AD group had the smallest (Table). Mean hippocampal volumes at 1.5T were significantly different among NC, MCI, and AD both on the left and the right (ANOVA, $P < .0001$). Between-group differences after Bonferroni correction for multiple comparisons were significant for NC versus MCI (left and right, $P < .0001$) and NC versus AD (left and right, $P < .0001$), but they were not significant when comparing MCI with AD (left, $P = 1$; right, $P = .77$). 3T-derived left hippocampal volumes showed significant differences among NC, MCI, and AD (ANOVA, $P < .0001$). 3T-derived hippocampal volumes were significantly different between NC and MCI (left and right, $P < .0001$) and NC and AD (left and right, $P < .0001$) but not between MCI versus AD (left, $P = .90$; right, $P = .71$).

We used a paired-samples t test to directly compare 1.5T versus 3T hippocampal volumes. In the pooled sample, we observed significantly larger right ($P = .03$) but not left ($P = .50$) hippocampal volumes at 3T compared with 1.5T. The intraclass correlation coefficient between 1.5T and 3T volumes was 0.89, and the absolute mean volumetric difference was 1.8%. Within diagnostic groups, significant volumetric differences were seen in the NC group on the right (right, $P = .04$; left, $P = .43$) but not in the MCI (right, $P = .20$; left, $P = .43$) or AD groups (right, $P = .42$; left, $P = .40$).

Surface-Mapping Atrophy Patterns

Bilaterally significant atrophy in the CA1, CA2, and subiculum regions was detected for AD versus NC at both field strengths but was more extensive at 3T (1.5T: left $P_{corrected} = .0015$, right $P_{corrected} = .0015$; 3T: left $P_{corrected} = .0001$, right $P_{corrected} = .0001$; Fig 1). The pattern of atrophy seen in MCI compared with NC was similar and was similarly more extensive at 3T (1.5T: left $P_{corrected} = .0019$, right $P_{corrected} = .0020$; 3T: left $P_{corrected} = .0008$, right $P_{corrected} = .0001$). No significant differences in radial distance between AD and MCI were found (1.5T: left $P_{corrected} = .49$, right $P_{corrected} = 1.0$; 3T: left $P_{corrected} = .31$, right $P_{corrected} = .65$).

The hippocampal radial distance of MCI converters versus MCI nonconverters was not significantly different at 1.5T (left $P_{corrected} = .80$, right $P_{corrected} = .74$), yet at 3T, we observed differences in the CA1 radial distance that were significant on the right (right $P_{corrected} = .01$) and trend-significant on the left (left $P_{corrected} = .06$, Fig 2). Mann-Whitney Wilcoxon comparison of mean CA1 radial distance between MCI converters and nonconverters showed significant differences at 3T ($P = .003$) and trend-significance at 1.5T ($P = .098$).

The receiver operating characteristic analyses examining the ability of mean CA1 radial distance to discriminate MCI converters and nonconverters resulted in an area under the curve of 0.62 at 1.5T and 0.71 at 3T (Fig 3). While the absolute difference in the area under the curve between the 2 field strengths (Δ area under the curve = 0.09) was relatively large, it was not statistically significant (DeLong test, $Z = 1.5361$, $P = .125$).

DISCUSSION

The bilateral atrophy in the CA1, CA2, and subiculum regions for NC versus AD and NC versus MCI in this present study agrees with findings in prior studies.[9-11,20,52-54] At 3T, MCI converters versus nonconverters presented significant hippocampal atrophy along the lateral and medial edges of the hippocampus corresponding to the CA1 and subicular regions—in concurrence with prior reports by our group based on independent samples.[10]

To date, several groups have compared the performance of 1.5T with 3T for detecting brain atrophy. In a strictly signal-to-noise comparison study, Fushimi et al[24] reported no significant differences in signal-to-noise ratios between 1.5T and 3T in multisection images with a 0-mm gap. Applying tensor brain morphometry and Structural Image Evaluation Using Normalization

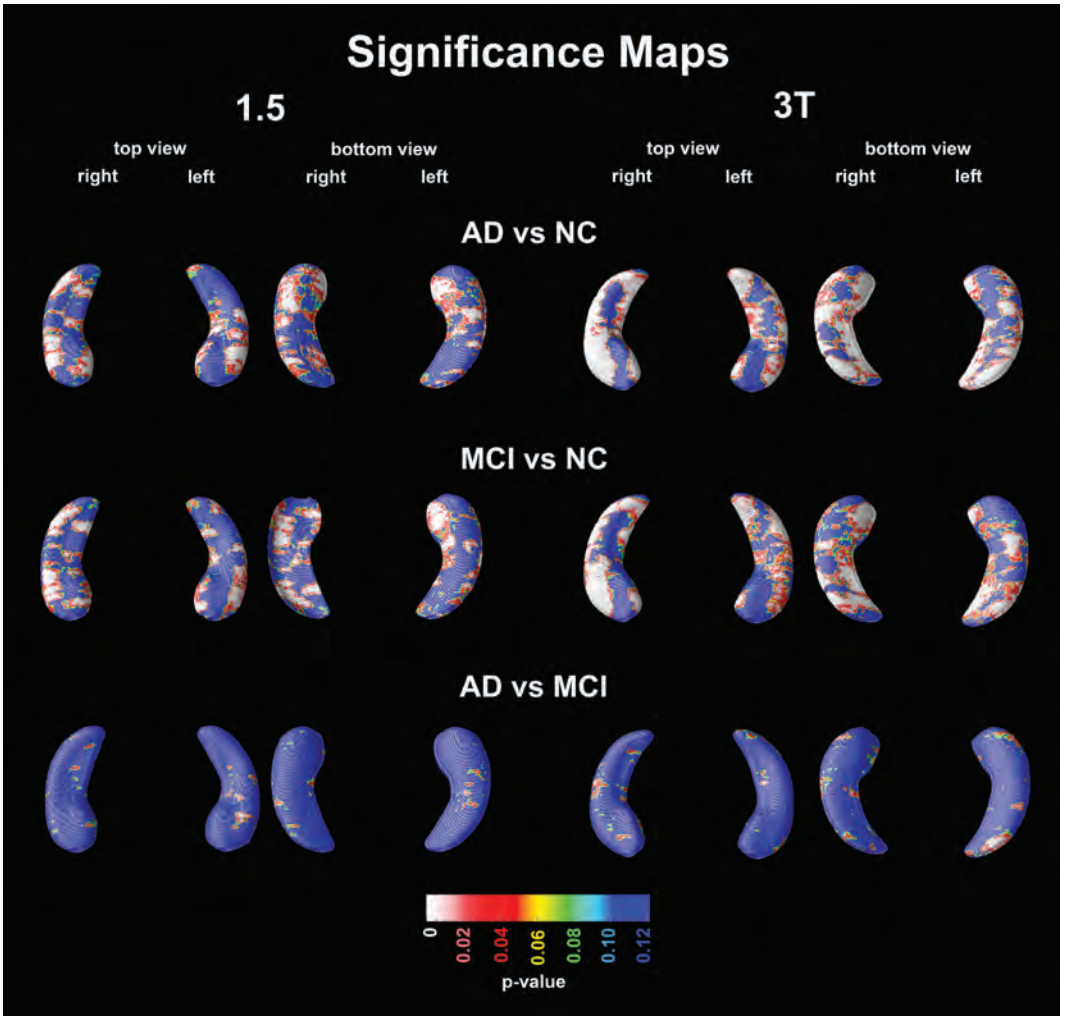

FIG 1. 3D statistical maps of diagnostic comparisons by using 1.5T and 3T. Red and white areas in the significance maps correspond to $P < .05$.

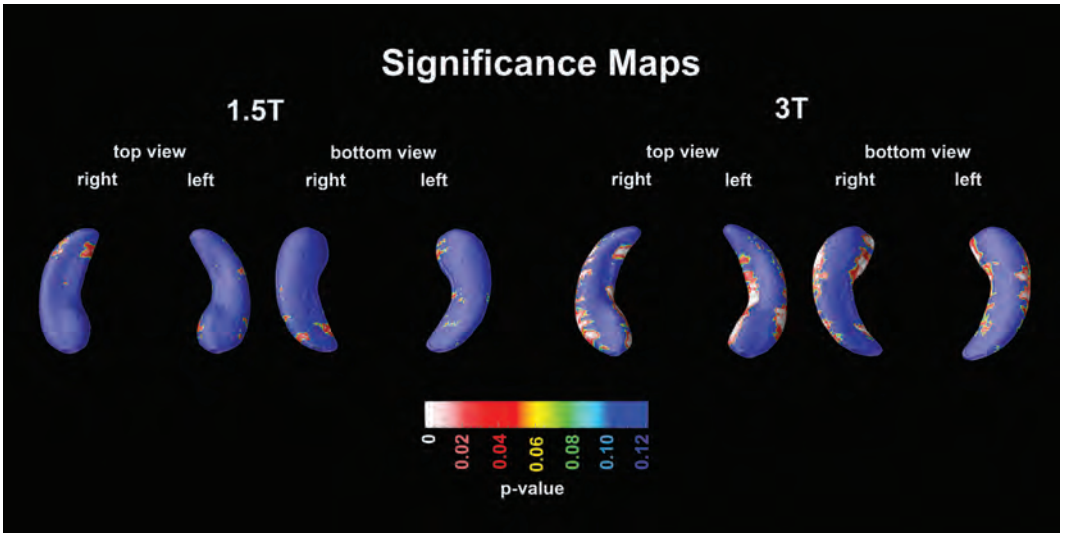

FIG 2. 3D statistical maps for MCI converters versus nonconverters at 1.5T and 3T.

of Atrophy algorithms to ADNI-1 1.5T and 3T data, Ho et al[26] reported no significant advantage of 3T over 1.5T for detecting 1-year whole-brain atrophy rates. Perhaps most importantly, 2 groups compared the performance of their automated multiatlas hippocampal segmentation techniques at 1.5T and 3T in small samples derived from ADNI-1. Lötjönen et al[25] used a sample consisting of 10 NCs, 10 subjects with MCI, and 10 subjects with AD and reported an intraclass correlation coefficient of 0.98 and

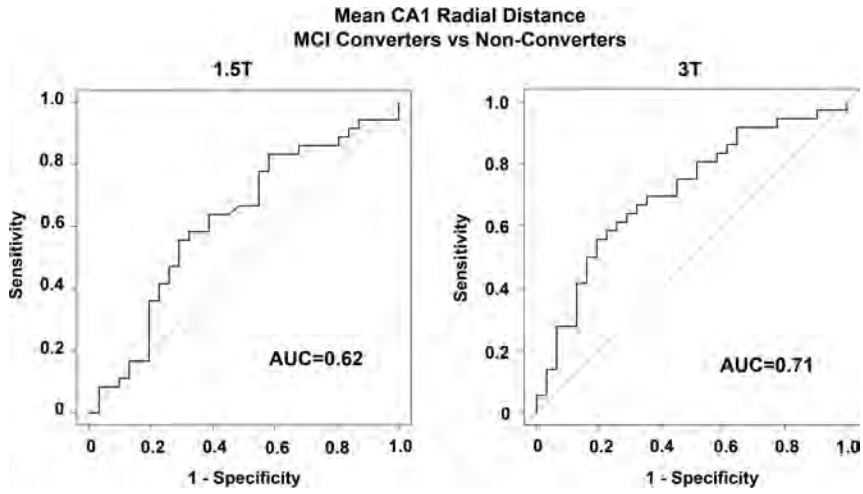

FIG 3. Receiver operator characteristic curves of the ability of mean CA1 radial distance to differentiate between MCI converters versus nonconverters at 1.5T and 3T. AUC indicates area under the curve.

an absolute volumetric difference between 1.5T and 3T of 3.2%. Macdonald et al,[27] by using 18 subjects with AD and 18 NCs from ADNI-1, reported an intraclass correlation coefficient of 0.97 between 1.5T and 3T hippocampi segmented with their hippocampal multiatlas propagation and segmentation algorithm. Here by using 166 subjects with ADNI-1 imaged at 1.5T and 3T, we report an intraclass correlation coefficient of 0.89 and a mean volumetric difference between 1.5T and 3T measurements across the sample of 1.8%. In addition, here we reveal that 3T seems to show an advantage in detecting subtle region-specific morphometric changes over 1.5T.

The strengths of this study include the large sample size from many ADNI sites across the country, standardized MR imaging protocol, systematic postacquisition analysis, and quality control of phantom-based monitoring of all scanners. Some limitations resulted from the susceptibility-induced geometric distortion and signal losses, which could increase noise, especially in the temporal lobe regions at 3T. Additionally, higher field-strength imaging is more susceptible to chemical shift artifacts.[55,56] Despite these limitations, 3T proved superior to 1.5T for shape analysis and between-group comparisons.

For this study, we had access to only 1.5T and 3T data. It is possible that even higher magnetic field[57,58] strengths such as 7T or 11T may reveal finer scale features and provide superior power for detecting between-group differences. The future directions of this study include conducting longitudinal analyses to show the progressive atrophy that occurs with the disease with time.

CONCLUSIONS

Our 1.5T and 3T hippocampal volumes obtained after automated segmentation with the AdaBoost algorithm were not significantly different between MCI and AD but were significant in NC versus MCI and NC versus AD, with the 3T segmentations resulting in larger mean hippocampal volumes in the NC group. This difference could potentially be explained by the larger CSF pool around the hippocampal formation in subjects with atrophy, which provides good contrast for hippocampal versus extrahippocampal tissue discriminability even at 1.5T—this provides a comparable segmentation in MCI and AD but not in NCs who lack large CSF pools surrounding the hippocampus in the temporal horn. Our data suggest that 3T images, with their higher contrast and higher signal-to-noise ratio, may enhance the topographic localization of atrophy.

ACKNOWLEDGMENTS

Data used in preparation of this article were obtained from the Alzheimer's Disease Neuroimaging Initiative data base (adni.loni.usc.edu). As such, the investigators within the ADNI contributed to the design and implementation of ADNI and/or provided data but did not participate in analysis or writing of this report. A complete listing of ADNI investigators can be found at: http://adni.loni.usc.edu/wp-content/uploads/how_to_apply/ADNI_Acknowledgement_List.pdf.

The ADNI was launched in 2003 by the National Institute on Aging, the National Institute of Biomedical Imaging and Bioengineering, the Food and Drug Administration, private pharmaceutical companies, and nonprofit organizations, as a $60 million, 5-year public-private partnership. The primary goal of the ADNI has been to test whether serial MR imaging, positron-emission tomography, other biologic markers, and clinical and neuropsychological assessment can be combined to measure the progression of mild cognitive impairment and early Alzheimer disease. Determination of sensitive and specific markers of very early AD progression is intended to aid researchers and clinicians in developing new treatments and to monitor their effectiveness, as well as lessen the time and cost of clinical trials.

The Principal Investigator of this initiative is Michael W. Weiner, MD, VA Medical Center and University of California, San Francisco. The ADNI is the result of effort of many coinvestigators from a broad range of academic institutions and private corporations, and subjects have been recruited from >50 sites across the United States and Canada. The initial goal of ADNI was to recruit 800 subjects, but ADNI has been followed by ADNI–Grand Opportunity and ADNI-2. To date, these 3 protocols have recruited >1500 adults, 55–90 years of age, to participate in the research, consisting of cognitively healthy older individuals, those with early or late MCI, and those with early AD. The follow-up duration of each group is specified in the protocols for ADNI-1, ADNI-2, and ADNI–Grand Opportunity. Subjects originally recruited for ADNI-1 and ADNI–Grand Opportunity had the option of being followed in ADNI-2. For up-to-date information, see www.adni-info.org.

Data collection and sharing for this project were funded by the Alzheimer's Disease Neuroimaging Initiative (National Institutes of Health Grant U01 AG024904) and the Department of Defense ADNI (Department of Defense award number W81XWH-12–2–0012). ADNI is funded by the National Institute on Aging, the National Institute of Biomedical Imaging and Bioengineering, and through generous contributions from the following: Alzhei-

mer's Association; Alzheimer's Drug Discovery Foundation; BioClinica; Biogen Idec; Bristol-Myers Squibb; Eisai; Elan Pharmaceuticals; Eli Lilly; F. Hoffmann-La Roche and its affiliated company Genentech; GE Healthcare; Innogenetics; IXICO; Janssen Alzheimer Immunotherapy Research & Development; Johnson & Johnson Pharmaceutical Research & Development; Medpace; Merck & Co; Meso Scale Diagnostics; NeuroRx Research; Novartis Pharmaceuticals; Pfizer; Piramal Imaging; Servier; Synarc; and Takeda Pharmaceutical. The Canadian Institutes of Health Research is providing funds to support ADNI clinical sites in Canada. Private sector contributions are facilitated by the Foundation for the National Institutes of Health (www.fnih.org). The grantee organization is the Northern California Institute for Research and Education, and the study is coordinated by the Alzheimer's Disease Cooperative Study at the University of California, San Diego. ADNI data are disseminated by the Laboratory for Neuro Imaging at the University of Southern California.

Disclosures: Paul M. Thompson—*RELATED*: *Grant*: We have an ADNI grant to cover costs of MRI processing.* David A. Elashoff—*RELATED*: *Grant*: National Institutes of Health. Clifford R. Jack—*RELATED*: *Grant*: National Institutes of Health*; *UNRELATED*: *Consultancy*: Janssen.* Michael Weiner—*Scientific Advisory Boards*: 2013–2014, Pfizer, Eli Lilly; *Consulting*: 2013, Alzheimer's Drug Discovery Foundation, Avid Radiopharmaceuticals, Eli Lilly, ClearView Healthcare Partners, Perceptive Informatics, Smartfish AS, Decision Resources, Araclon, Synarc, Merck, Genentech, Defined Health; *Funding for Travel*: 2013, Kenes International, Alzheimer's Disease Research Center University of California, San Diego, University of California, Los Angeles, University of California, San Diego, Sanofi-Aventis Groupe, University Center Hospital Toulouse, Araclon, AC Immune, Eli Lilly, New York Academy of Sciences; 2014, National Brain Research Center, India (for Johns Hopkins Medicine, Baltimore); *Editorial Advisory Boards*: Alzheimer's and Dementia, MRI; *Research Support from Government Entities*: Department of Defense, Veterans Administration; *Organizations Contributing to the Foundation for National Institutes of Health and Thus to the National Imaging Associates–Funded Alzheimer's Disease Neuroimaging Initiative:* Abbott, Alzheimer's Association, Alzheimer's Drug Discovery Foundation, Anonymous Foundation, AstraZeneca, Bayer Healthcare, BioClinica (ADNI 2), Bristol-Myers Squibb, Cure Alzheimer's Fund, Eisai, Elan, Gene Network Sciences, Genentech, GE Healthcare, GlaxoSmithKline, Innogenetics, Johnson & Johnson, Eli Lilly, Medpace, Merck, Novartis, Pfizer, Roche, Schering Plough, Synarc, Wyeth. Liana G. Apostolova—*RELATED*: *Grant*: National Institutes of Health R01 AG040770,* National Imaging Associates K23 AG026803,* National Imaging Associates P50 AG16570,* National Imaging Associates U01AG024904*; *UNRELATED*: *Consultancy*: Eli Lilly; *Payment for Lectures (including service on Speakers Bureaus):* Eli Lilly; *Payment for Development of Educational Presentations:* Eli Lilly. *Money paid to the institution.

REFERENCES

1. Alzheimer's Association. **2013 Alzheimer's disease facts and figures.** *Alzheimers Dement* 2013;9:208–45
2. Wortmann M. **Dementia: a global health priority—highlights from an ADI and World Health Organization report.** *Alzheimers Res Ther* 2012;4:40
3. Petersen RC, Doody R, Kurz A, et al. **Current concepts in mild cognitive impairment.** *Arch Neurol* 2001;58:1985–92
4. Appel J, Potter E, Shen Q, et al. **A comparative analysis of structural brain MRI in the diagnosis of Alzheimer's disease.** *Behav Neurol* 2009;21:13–19
5. Bobinski M, de Leon MJ, Wegiel J, et al. **The histological validation of post mortem magnetic resonance imaging-determined hippocampal volume in Alzheimer's disease.** *Neuroscience* 2000;95:721–25
6. Zarow C, Vinters HV, Ellis WG, et al. **Correlates of hippocampal neuron number in Alzheimer's disease and ischemic vascular dementia.** *Ann Neurol* 2005;57:896–903
7. Csernansky JG, Hamstra J, Wang L, et al. **Correlations between antemortem hippocampal volume and postmortem neuropathology in AD subjects.** *Alzheimer Dis Assoc Disord* 2004;18:190–95
8. Frisoni GB, Ganzola R, Canu E, et al. **Mapping local hippocampal changes in Alzheimer's disease and normal ageing with MRI at 3 Tesla.** *Brain* 2008;131:3266–76
9. Apostolova LG, Thompson PM, Green AE, et al. **3D comparison of low, intermediate, and advanced hippocampal atrophy in MCI.** *Hum Brain Mapp* 2010;31:786–97
10. Apostolova LG, Dutton RA, Dinov ID, et al. **Conversion of mild cognitive impairment to Alzheimer disease predicted by hippocampal atrophy maps.** *Arch Neurol* 2006;63:693–99
11. Apostolova LG, Dinov ID, Dutton RA, et al. **3D comparison of hippocampal atrophy in amnestic mild cognitive impairment and Alzheimer's disease.** *Brain* 2006;129:2867–73
12. Mueller SG, Laxer KD, Barakos J, et al. **Subfield atrophy pattern in temporal lobe epilepsy with and without mesial sclerosis detected by high-resolution MRI at 4 Tesla: preliminary results.** *Epilepsia* 2009;50:1474–83
13. Mueller SG, Chao LL, Berman B, et al. **Evidence for functional specialization of hippocampal subfields detected by MR subfield volumetry on high resolution images at 4 T.** *Neuroimage* 2011;56:851–57
14. Scheltens P, Launer LJ, Barkhof F, et al. **Visual assessment of medial temporal lobe atrophy on magnetic resonance imaging: interobserver reliability.** *J Neurol* 1995;242:557–60
15. Visser PJ, Verhey FR, Hofman PA, et al. **Medial temporal lobe atrophy predicts Alzheimer's disease in patients with minor cognitive impairment.** *J Neurol Neurosurg Psychiatry* 2002;72:491–97
16. Korf ES, Wahlund LO, Visser PJ, et al. **Medial temporal lobe atrophy on MRI predicts dementia in patients with mild cognitive impairment.** *Neurology* 2004;63:94–100
17. Jack CR Jr, Petersen RC, Xu YC, et al. **Prediction of AD with MRI-based hippocampal volume in mild cognitive impairment.** *Neurology* 1999;52:1397–403
18. Devanand DP, Pradhaban G, Liu X, et al. **Hippocampal and entorhinal atrophy in mild cognitive impairment: prediction of Alzheimer disease.** *Neurology* 2007;68:828–36
19. Mueller SG, Schuff N, Yaffe K, et al. **Hippocampal atrophy patterns in mild cognitive impairment and Alzheimer's disease.** *Hum Brain Mapp* 2010;31:1339–47
20. Morra JH, Tu Z, Apostolova LG, et al. **Automated 3D mapping of hippocampal atrophy and its clinical correlates in 400 subjects with Alzheimer's disease, mild cognitive impairment, and elderly controls.** *Hum Brain Mapp* 2009;30:2766–88
21. Apostolova LG, Morra JH, Green AE, et al. **Automated 3D mapping of baseline and 12-month associations between three verbal memory measures and hippocampal atrophy in 490 ADNI subjects.** *Neuroimage* 2010;51:488–99
22. Apostolova LG, Hwang KS, Andrawis JP, et al. **3D PIB and CSF biomarker associations with hippocampal atrophy in ADNI subjects.** *Neurobiol Aging* 2010;31:1284–303
23. Colliot O, Chetelat G, Chupin M, et al. **Discrimination between Alzheimer disease, mild cognitive impairment, and normal aging by using automated segmentation of the hippocampus.** *Radiology* 2008;248:194–201
24. Fushimi Y, Miki Y, Urayama S, et al. **Gray matter-white matter contrast on spin-echo T1-weighted images at 3 T and 1.5 T: a quantitative comparison study.** *Eur Radiol* 2007;17:2921–25
25. Lötjönen J, Wolz R, Koikkalainen J, et al. **Fast and robust extraction of hippocampus from MR images for diagnostics of Alzheimer's disease.** *Neuroimage* 2011;56:185–96
26. Ho AJ, Hua X, Lee S, et al. **Comparing 3 T and 1.5 T MRI for tracking Alzheimer's disease progression with tensor-based morphometry.** *Hum Brain Mapp* 2010;31:499–514
27. Macdonald KE, Leung KK, Bartlett JW, et al. **Automated template-based hippocampal segmentations from MRI: the effects of 1.5T or 3T field strength on accuracy.** *Neuroinformatics* 2014;12:405–12
28. Briellmann RS, Syngeniotis A, Jackson GD. **Comparison of hippocampal volumetry at 1.5 Tesla and at 3 Tesla.** *Epilepsia* 2001; 42:1021–24
29. Mueller SG, Weiner MW, Thal LJ, et al. **The Alzheimer's Disease**

Neuroimaging Initiative. *Neuroimaging Clin N Am* 2005;15:869–77, xi–xii
30. Mueller SG, Weiner MW, Thal LJ, et al. **Ways toward an early diagnosis in Alzheimer's disease: the Alzheimer's Disease Neuroimaging Initiative (ADNI).** *Alzheimers Dement* 2005;1:55–66
31. Jack CR Jr, Bernstein MA, Fox NC, et al. **The Alzheimer's Disease Neuroimaging Initiative (ADNI): MRI methods.** *J Magn Reson Imaging* 2008;27:685–91
32. Weiner MW, Veitch DP, Aisen PS, et al. **The Alzheimer's Disease Neuroimaging Initiative: a review of papers published since its inception.** *Alzheimers Dement* 2013;9:e111–194
33. Hughes CP, Berg L, Danziger WL, et al. **A new clinical scale for the staging of dementia.** *Br J Psychiatry* 1982;140:566–72
34. Morris JC. **The Clinical Dementia Rating (CDR): current version and scoring rules.** *Neurology* 1993;43:2412–14
35. Cockrell JR, Folstein MF. **Mini-Mental State Examination (MMSE).** *Psychopharmacol Bull* 1988;24:689–92
36. Folstein MF, Folstein SE, McHugh PR. **"Mini-mental state": a practical method for grading the cognitive state of patients for the clinician.** *J Psychiatr Res* 1975;12:189–98
37. McKhann G, Drachman D, Folstein M, et al. **Clinical diagnosis of Alzheimer's disease: report of the NINCDS-ADRDA Work Group under the auspices of Department of Health and Human Services Task Force on Alzheimer's Disease.** *Neurology* 1984;34:939–44
38. Leow AD, Klunder AD, Jack CR Jr, et al. **Longitudinal stability of MRI for mapping brain change using tensor-based morphometry.** *Neuroimage* 2006;31:627–40
39. Jovicich J, Czanner S, Greve D, et al. **Reliability in multi-site structural MRI studies: effects of gradient non-linearity correction on phantom and human data.** *Neuroimage* 2006;30:436–43
40. Sled JG, Zijdenbos AP, Evans AC. **A nonparametric method for automatic correction of intensity nonuniformity in MRI data.** *IEEE Trans Med Imaging* 1998;17:87–97
41. Mazziotta J, Toga A, Evans A, et al. **A probabilistic atlas and reference system for the human brain: International Consortium for Brain Mapping (ICBM).** *Philos Trans R Soc Lond B Biol Sci* 2001; 356:1293–322
42. Hua X, Leow AD, Parikshak N, et al. **Tensor-based morphometry as a neuroimaging biomarker for Alzheimer's disease: an MRI study of 676 AD, MCI, and normal subjects.** *Neuroimage* 2008;43:458–69
43. Narr KL, van Erp TG, Cannon TD, et al. **A twin study of genetic contributions to hippocampal morphology in schizophrenia.** *Neurobiol Dis* 2002;11:83–95
44. Thompson PM, Hayashi KM, De Zubicaray GI, et al. **Mapping hippocampal and ventricular change in Alzheimer disease.** *Neuroimage* 2004;22:1754–66
45. Narr KL, Thompson PM, Sharma T, et al. **Three-dimensional mapping of temporo-limbic regions and the lateral ventricles in schizophrenia: gender effects.** *Biol Psychiatry* 2001;50:84–97
46. Mai JK, Paxinos G, Assheuer JK. *Atlas of the Human Brain.* San Diego: Elsevier Academic Press; 2004
47. Duvernoy HM. *The Human Hippocampus: An Atlas of Applied Anatomy.* Munich: Springer Verlag; 1988
48. Freund Y, Shapire R. **A decision-theoretic generalization of online learning and an application to boosting.** *Journal of Computer and System Sciences* 1997;55:119–39
49. Morra JH, Tu Z, Apostolova LG, et al. **Validation of a fully automated 3D hippocampal segmentation method using subjects with Alzheimer's disease mild cognitive impairment, and elderly controls.** *Neuroimage* 2008;43:59–68
50. Morra JH, Tu Z, Apostolova LG, et al. **Automated mapping of hippocampal atrophy in 1-year repeat MRI data from 490 subjects with Alzheimer's disease, mild cognitive impairment, and elderly controls.** *Neuroimage* 2009;45:S3–15
51. Morra JH, Tu Z, Toga AW, et al. **Machine learning for brain image segmentation.** In: Gonzalez FA, Romero E, eds. *Biomedical Image Analysis and Machine Learning Technologies.* Hershey: Medical Information Science References; 2009
52. Wang L, Swank JS, Glick IE, et al. **Changes in hippocampal volume and shape across time distinguish dementia of the Alzheimer type from healthy aging.** *Neuroimage* 2003;20:667–82
53. Becker JT, Davis SW, Hayashi KM, et al. **Three-dimensional patterns of hippocampal atrophy in mild cognitive impairment.** *Arch Neurol* 2006;63:97–101
54. Frisoni GB, Sabattoli F, Lee AD, et al. **In vivo neuropathology of the hippocampal formation in AD: a radial mapping MR-based study.** *Neuroimage* 2006;32:104–10
55. Frayne R, Goodyear BG, Dickhoff P, et al. **Magnetic resonance imaging at 3.0 Tesla: challenges and advantages in clinical neurological imaging.** *Invest Radiol* 2003;38:385–402
56. Tanenbaum LN. **Clinical 3T MR imaging: mastering the challenges.** *Magn Reson Imaging Clin N Am* 2006;14:1–15
57. Das SR, Avants BB, Pluta J, et al. **Measuring longitudinal change in the hippocampal formation from in vivo high-resolution T2-weighted MRI.** *Neuroimage* 2012;60:1266–79
58. Mueller SG, Stables L, Du AT, et al. **Measurement of hippocampal subfields and age-related changes with high resolution MRI at 4T.** *Neurobiol Aging* 2007;28:719–26

Cerebral Microbleeds: Different Prevalence, Topography, and Risk Factors Depending on Dementia Diagnosis—The Karolinska Imaging Dementia Study

S. Shams, J. Martola, T. Granberg, X. Li, M. Shams, S.M. Fereshtehnejad, L. Cavallin, P. Aspelin, M. Kristoffersen-Wiberg, and L.O. Wahlund

ABSTRACT

BACKGROUND AND PURPOSE: Cerebral microbleeds are thought to represent cerebral amyloid angiopathy when in lobar regions of the brain and hypertensive arteriopathy when in deep and infratentorial locations. By studying cerebral microbleeds, their topography, and risk factors, we aimed to gain an insight into the vascular and amyloid pathology of dementia diagnoses and increase the understanding of cerebral microbleeds in dementia.

MATERIALS AND METHODS: We analyzed 1504 patients (53% women; mean age, 63 ± 10 years; 10 different dementia diagnoses) in this study. All patients underwent MR imaging as part of the dementia investigation, and all their clinical parameters were recorded.

RESULTS: Among the 1504 patients with dementia, 22% had cerebral microbleeds. Cerebral microbleed topography was predominantly lobar ($P = .01$) and occipital ($P = .007$) in Alzheimer disease. Patients with cerebral microbleeds were significantly older ($P < .001$), were more frequently male ($P < .001$), had lower cognitive scores ($P = .006$), and more often had hypertension ($P < .001$). Risk factors for cerebral microbleeds varied depending on the dementia diagnosis. Odds ratios for having cerebral microbleeds increased with the number of risk factors (hypertension, hyperlipidemia, diabetes, male sex, and age 65 and older) in the whole patient group and increased differently in the separate dementia diagnoses.

CONCLUSIONS: Prevalence, topography, and risk factors of cerebral microbleeds vary depending on the dementia diagnosis and reflect the inherent pathology of different dementia diagnoses. Because cerebral microbleeds are seen as possible predictors of intracerebral hemorrhage, their increasing prevalence with an increasing number of risk factors, as shown in our study, may require taking the number of risk factors into account when deciding on anticoagulant therapy in dementia.

ABBREVIATIONS: CAA = cerebral amyloid angiopathy; CMB = cerebral microbleed; ICD = International Classification of Diseases; KIDS = Karolinska Imaging Dementia Study; MMSE = Mini-Mental State Examination

Cerebral microbleeds (CMBs) are not usually seen on conventional MR imaging and CT but have been increasingly detected due to the more frequent use of the T2* and SWI MR imaging sequences, sensitive to minute amounts of blood. On MR imaging, CMBs are seen as round hypointense foci, and histologically they are represented by hemosiderin deposits in macrophages, mainly located around small vessels.[1,2] The pathology of CMBs is thought to vary depending on the location: Deep and infratentorial CMBs represent underlying hypertensive arteriopathy, whereas lobar CMBs mainly represent vascular amyloid deposition, so-called cerebral amyloid angiopathy (CAA).[3]

CAA and hypertension are common in patients with dementia. CAA is reported to be present in up to 98% of patients with Alzheimer disease in postmortem studies, and hypertension in middle-aged and elderly populations has been related to the development of dementia.[4,5] Studies have shown a higher prevalence of CMBs in patients with dementia compared with healthy populations. Alzheimer disease, for instance, is reported to have a CMB prevalence of 18%–32% versus 3%–11% in healthy populations imaged with MR field strengths of 1T–1.5T.[6-15] Consequently, CMBs are hypothesized to play an important role in the

Received September 3, 2014; accepted after revision September 16.

From the Departments of Neurobiology, Care Sciences, and Society (X.L., S.M.F., L.O.W.) and Clinical Science, Intervention, and Technology (S.S., J.M., T.G., M.S., L.C., P.A., M.K.-W.), Division of Medical Imaging and Technology, Karolinska Institute, Stockholm, Sweden; and Department of Radiology (S.S., J.M., T.G., M.S., L.C., P.A., M.K.-W.) and Division of Clinical Geriatrics (X.L., S.M.F., L.O.W.), Karolinska University Hospital, Stockholm, Sweden.

This work was supported by the Stockholm County Council and Karolinska Institute.

Please address correspondence to Sara Shams, MD, Department of Radiology, Karolinska University Hospital, SE-14186 Stockholm, Sweden; e-mail: sara.shams@ki.se

Indicates open access to non-subscribers at www.ajnr.org

Indicates article with supplemental on-line tables.

Indicates article with supplemental on-line photos.

http://dx.doi.org/10.3174/ajnr.A4176

disease mechanisms of dementia as well as being a marker of the synergistic effects between vascular and amyloid pathology.[16] Of further interest, CAA and hypertension are the most common causes of intracerebral hemorrhage, with CMBs being proposed as a possible predictor of intracerebral hemorrhage.[17]

Investigating CMBs in dementia is of importance for further understanding the disease mechanisms of different dementia diagnoses and improved clinical and therapeutic treatment. CMBs and their location may give an insight into the vascular and amyloid pathology of dementia diagnoses and thus expose different dementia characteristics. Up-to-date studies on CMBs and dementia have been conducted mainly on small cohorts, without a standardized scale for CMB rating and with a scarcity of included dementia diagnoses. Furthermore, analyses have been made on a whole-cohort basis, rather than separating different dementia diagnoses and their respective CMB characteristics. In this study, we aimed to examine the prevalence, topography, and risk factors associated with CMBs in a large and diverse dementia population with subgroup analysis. By doing so, we hoped to gain insight in the pathophysiologic mechanisms in different dementia diagnoses. We hypothesized that CMB prevalence would be dependent on risk factors, depending on the dementia diagnosis, and that vascular risk factors would be important in the development of CMBs in dementia.

MATERIALS AND METHODS

Patients

This study is part of the Karolinska Imaging Dementia Study (KIDS), a cross-sectional study on the impact of CMBs in dementia. Patients undergoing dementia investigation/follow-up from January 1, 2006 to January 1, 2012, and having undergone MR imaging with CMB sequences were included in this study. A total of 1509 patients were included. Exclusion criteria for all patients were insufficient MR imaging scan quality (3 patients excluded) and a history of traumatic brain injury (2 patients excluded), leading to a cohort of 1504 patients.

All patients included had undergone routine dementia assessment, including medical history; physical, neurologic, and cognitive examinations; laboratory tests; and, consequently, MR imaging of the brain with CMB sequences at the memory clinic/radiology department, Karolinska University Hospital. Diagnosis was based on the International Classification of Diseases (ICD)-10 criteria, by an experienced memory clinic team consisting of geriatricians, neuropsychologists, neurophysiologists, and neuroradiologists after the whole picture had been considered. All patients were subdivided into 10 diagnostic groups on the basis of the ICD-10 codes, shown in On-line Table 1. If >1 ICD code existed for a patient, the current ICD code at the dementia investigation/MR imaging scan was chosen.

Clinical data were collected for every patient during the dementia investigation. The presence of hypertension, hyperlipidemia, and diabetes was determined on the basis of prior medical diagnosis and treatment for all patients. Vascular risk factors are included for all patients in this study, and the Mini-Mental State Examination (MMSE) scores, for 1416 patients. The percentage of MMSE scores in the diagnoses was 91%–97%, except in frontotemporal lobe dementia (77%) and asymptomatic hereditary dementia (73%). The MMSE score was missing due to the following: patient too severely disoriented to participate (6%, $n = 5$; Alzheimer disease and vascular dementia only) and score registration missing in the patient notes, even though it was performed (94%, $n = 83$). Informed consent was obtained from each patient; if the patient was too confused to consent, it was obtained from a legal guardian. Ethics approval was obtained from the regional ethics board, Stockholm, Sweden.

MR Imaging Protocols

All patients underwent MR imaging of the brain at the radiology department, Karolinska University Hospital, Huddinge, Sweden. For each patient, axial SWI and/or T2* sequences and conventional MR imaging sequences, such as T1, T2, and FLAIR, were performed. Three MR imaging scanners at the radiology department, Karolinska University Hospital, Huddinge, Sweden, were used. Of all patients, 453 patients were scanned on a 1.5T Magnetom Symphony scanner (Siemens, Erlangen, Germany; T2*: TE, 25 ms; TR, 792 ms; flip angle, 20°; section thickness, 5.0 mm), 687 patients were scanned on a 1.5T Magnetom Avanto scanner (Siemens; T2*: TE, 26 ms; TR, 800 ms; flip angle, 20°; section thickness, 5.0 mm; SWI: TE, 40 ms; TR, 49 ms; flip angle, 15°; section thickness, 4.0 mm), and 364 patients were scanned on a Magnetom Trio scanner (Siemens; 3T; T2*: TE, 20 ms; TR, 620 ms; flip angle, 20°; section thickness, 4.0 mm; SWI: TE, 20 ms; TR, 28 ms; flip angle, 15°; section thickness, 1.6 mm). Scans of all patients were randomly assigned to various MR imaging scanners with 1.5T and 3T field strengths and different CMB sequences, T2* and SWI. In the whole cohort, the distribution of patients scanned at 3T with SWI sequences included is seen in On-line Table 1.

Image Analysis

All MR images first underwent routine analysis by the neuroradiologists at the radiology department, Karolinska University Hospital. In addition, all MR images were analyzed specifically for CMBs by an MD/PhD student, with 2 years of training and experience in MR imaging and neuroradiology, at the initial time of rating. The rater was blinded to clinical data and assessed the number and location of CMBs on T2* and/or SWI sequences according to the Microbleed Anatomical Rating Scale.[2] Minor modifications were made to the Microbleed Anatomical Rating Scale to increase the accuracy of CMB ratings: CMBs were not rated as probable; hypointensities in the globus pallidus were not rated to reduce the risk of calcifications and physiologic iron deposition mimicking CMBs. Furthermore, if a patient had a deep venous anomaly in the vicinity of a CMB, the CMB was not rated as definitive because deep venous anomalies increase the risk of adjacent cavernomas that, in turn, can mimic a CMB. T2-weighted images were analyzed simultaneously with the CMB sequences, to better distinguish vessels and flow voids, which might mimic CMBs.

To ensure a correct CMB rating, a senior consultant neuroradiologist rated 50 patients with CMBs with wide distributions in different locations. The 50 patients with CMBs were selected from the KIDS database established after analysis by choosing the first 10 patients with CMBs for every year from 2006 to 2010, to get a thorough representation of CMBs analyzed. Besides the 50 patients with CMBs, 50 patients without CMBs were also analyzed,

all chosen in the same manner as patients with CMBs. The second rater was blinded to clinical data and prior ratings. Interrater analysis yielded an intraclass correlation coefficient of 0.988 when the 50 patients with CMBs were taken into account and 0.987 when all analyses were considered. Both coefficients equal an excellent agreement.[18] Intrarater analysis was also performed by the MD/PhD student, rating the whole cohort for CMBs in the same manner as above (blinded to clinical data, prior ratings). Two months after the initial analysis, the first 100 patients with CMBs and the first 100 patients without CMBs were re-rated. Intraclass correlation analysis showed excellent agreement, 0.989 ($n = 200$), and 0.991 for the 100 patients with CMBs only. All neuroradiologic analyses were made on a radiologic PACS workstation with 3 radiologic monitors.

Statistical Analysis

Descriptive statistics are presented as means (±SD) for continuous variables and median and interquartile range for CMBs. Inter- and intrarater analysis was performed with the intraclass correlation coefficient on the number of CMBs and is presented in "Image Analysis." Differences in population characteristics and CMBs in the diagnoses were analyzed by using χ^2 and Fisher exact tests for categoric variables. CMBs were defined as dichotomous (present/absent). Due to our nonparametric data, the Mann Whitney *U* test was used for continuous variables. Kruskall-Wallis analysis was performed when analyzing CMB topography in the cohort, with topographies as categoric variables and CMBs as a continuous variable. The topographic analysis was performed in the 3 Microbleed Anatomical Rating Scale locations and more specific infratentorial and lobar locations. Logistic regression was performed for all diagnostic groups with CMBs (dichotomous variable: present/absent) as a dependent variable and diagnosis as an independent variable. For each diagnosis, the subjective cognitive impairment was set as a reference group. Odds ratios were adjusted for hypertension, hyperlipidemia, diabetes, sex, age, MR imaging field strength (1.5/3T), and CMB sequence (SWI/T2*). Logistic regression was further used to obtain odds ratios for CMBs, depending on the number of risk factors. CMB (dichotomous: present/absent) was a dependent variable, with the number of risk factors as an independent variable. The model was adjusted for MR imaging field strength and CMB sequence. Negative binomial regression analyses were used to determine the impact of the number of CMBs/number of CMBs in different topographies on risk factors. The number of CMBs was a dependent variable, and risk factor, an independent variable; the model was corrected for MR imaging field strength and CMB sequence. Post hoc Bonferroni correction was applied to all *P* values; thus, all significance levels presented in this article are Bonferroni-corrected, unless otherwise stated. SPSS 22.0 (IBM, Armonk, New York) was used for statistical analyses, and $P < .05$ was statistically significant.

RESULTS

Prevalence

In the 1504 recruited patients, 332 (22%) had CMBs. Patient characteristics are shown in On-line Table 2. The prevalence ($\chi^2 = 94$; $P < .001$) and number ($P < .001$) of CMBs and the presence of multiple ($\chi^2 = 25$; $P = .03$) CMBs varied significantly among the different diagnostic groups (On-line Table 2 and On-line Fig 1). The significant adjusted odds ratios for having CMBs in the different diagnoses were the following: alcohol-related dementia (OR, 4.0; 95% CI, 1.4–11.2), Alzheimer disease (OR, 2.0; 95% CI, 1.2–3.1), unspecified dementia (OR, 2.2; 95% CI, 1.0–4.4), and vascular dementia (OR, 8.7; 95% CI, 4.1–18.6) (On-line Table 2).

Topography

The most common CMB topography among all patients with CMBs ($n = 332$) was lobar; this was also true in the separate groups (On-line Table 3). Eighty-four percent had CMBs in lobar regions, followed by infratentorial topography in 30% of patients and deep topography in 27% (On-line Table 3). In patients with CMBs ($n = 332$), 487 CMBs (median, 1; interquartile range, 1–5), were found in infratentorial locations; 367, in deep locations (median, 2; interquartile range, 1–3); and 2415 CMBs, in lobar locations (median, 2; interquartile range, 1–5). Kruskall-Wallis analysis of the topographic distribution of CMBs, for all diagnoses, in infratentorial, deep, and lobar regions showed a significant lobar predominance of CMBs only in Alzheimer disease ($P = .01$). Further analysis for more detailed brain regions (brain stem; cerebellum; deep; frontal, parietal, temporal, and occipital lobes) in the diagnoses showed a significant difference among these locations only in Alzheimer disease, with most CMBs in occipital regions ($P = .007$).

Risk Factors and Associations

Comparing patients with ($n = 332$) and without CMBs ($n = 1172$), we found that CMBs were significantly more frequent in male patients ($\chi^2 = 37$; $P < .001$), older patients ($\chi^2 = 32$; $P < .001$), and those with hypertension ($\chi^2 = 23$; $P < .001$) (On-line Table 4). There was no significant association between CMBs and diabetes, hyperlipidemia, and low MMSE score (<21) in the whole cohort. Risk factors and association with CMBs for the separate groups are shown in On-line Table 4. Mann Whitney *U* analysis for the whole cohort showed lower MMSE scores with CMBs (mean MMSE score: CMB+, 24 ± 5; CMB−, 25 ± 5; $P = .02$). In the separate groups, this was only true in unspecified dementia (CMB+, 24 ± 5; CMB−, 21 ± 5; $P = .01$) and asymptomatic hereditary dementia (mean MMSE score: CMB+, 28 ± 1; CMB−, 29 ± 1; $P = .032$) before Bonferroni correction, and it was insignificant after correction.

In the separate groups, CMB prevalence was higher with hypertension in subjective cognitive impairment ($\chi^2 = 8$; $P = .02$) and higher with hyperlipidemia in mild cognitive impairment ($\chi^2 = 7$; $P = .03$). Male patients further had a higher prevalence of CMBs in Alzheimer disease ($\chi^2 = 8$; $P = .02$), mild cognitive impairment ($\chi^2 = 10$; $P = .01$), and vascular dementia ($\chi^2 = 7$; $P = .04$). Older patients, defined as 65 years and older, had a higher CMB prevalence in Alzheimer disease ($\chi^2 = 9$; $P = .01$) and mild cognitive impairment ($\chi^2 = 8$; $P = .02$) (On-line Table 4).

When we took the number of CMBs and the relation to risk factors into account, in a multivariate negative binomial regression analysis, male sex, advanced age, and hypertension showed an increasing number of CMBs in the whole cohort. A decreasing number of CMBs with hyperlipidemia and diabetes were shown.

Prevalence and odds ratios of CMBs depending on number of risk factors[a]

Diagnostic Group	0 RF[b]	1 RF		2 RF		3 RF		≥4 RF	
	Prevalence	Prevalence	OR	Prevalence	OR	Prevalence	OR	Prevalence	OR
All patients ($n = 1504$)	10 (31)	18 (92)	2.1 (1.4–3.3)[d]	28 (105)	3.8 (2.5–5.9)[c]	35 (69)	5.3 (3.3–8.5)[c]	33 (35)	4.8 (2.8–8.4)[c]
Subjective cognitive impairment ($n = 385$)	8 (13)	10 (13)	1.2 (0.5–2.8)	11 (6)	1.3 (0.5–3.8)	24 (7)	3.6 (1.3–10.2)[e]	20 (2)	3.2 (0.6–17.2)
Alzheimer disease ($n = 423$)	7 (4)	26 (37)	4.9 (1.7–14.6)[d]	37 (47)	8.2 (2.8–24.4)[c]	33 (23)	7.1 (2.3–22.2)[d]	23 (7)	3.4 (0.9–13.1)
Mild cognitive impairment ($n = 418$)	7 (5)	17 (24)	2.8 (1.0–7.7)[e]	22 (25)	3.7 (1.3–10.3)[e]	37 (21)	7.8 (2.7–22.9)[c]	35 (14)	7.2 (2.2–21.3)[d]
Vascular dementia ($n = 54$)	67 (4)	50 (3)	0.5 (0.04–6.1)	58 (11)	0.6 (0.1–4.7)	58 (7)	0.5 (0.1–4.8)	64 (7)	0.8 (0.1–7.1)

Note:—RF indicates risk factors; OR, odds ratio of CMBs in all groups; Prevalence, prevalence of CMBs in all groups.

[a] Numbers are % (No.), odds ratio (95% CI). Logistic regression analysis was performed with CMBs (present/absent) as a dependent variable and number of risk factors as an independent variable. Risk factors were defined as hypertension, hyperlipidemia, diabetes, male sex, and age 65 years and older. The model was corrected for MRI field strength (1.5T/3T) and CMB sequence (T2*/SWI). In the risk factor groups, prevalence of CMBs (number of patients) is stated to the left and odds ratios for CMBs, to the right.

[b] Patients with zero risk factors were used as a reference.

[c] $P < .001$, significant after Bonferroni correction.

[d] $P < .05$, significant after Bonferroni correction.

[e] $P < .05$, significant before Bonferroni correction.

On-line Table 5 shows the regression coefficients for the risk factors in the 4 largest diagnoses.

CMB prevalence and odds ratio for the presence of CMBs increased with the increasing number of risk factors in the whole patient group (Table). The Table shows the impact of the number of risk factors on CMB prevalence and odds ratios in the 4 largest diagnostic groups. On-line Fig 2 illustrates the increase in odds ratios for number of risk factors in the whole patient group.

The topography of CMBs and the association to risk factors were analyzed. Patients with CMBs in deep and infratentorial locations were compared with patients with CMBs in lobar regions regarding patient characteristics (hyperlipidemia, diabetes, sex, age, and MMSE score). The only difference found between the 2 groups was 62% of all patients with deep and infratentorial CMBs having hypertension, compared with 48% in patients with lobar CMBs ($\chi^2 = 10$; $P = .006$). When we took the number of CMBs into account in a multivariate negative binomial regression analysis, CMBs were associated with different risk factors in the different topographies and diagnoses (On-line Table 5).

DISCUSSION

Our study provides insight in CMBs and the relation to various dementia diagnoses. Prevalence, topography, and risk factors (hypertension, hyperlipidemia, diabetes, male sex, and older age) for CMBs vary depending on the dementia diagnosis. Prevalence and odds ratios for CMBs increase with the increasing number of risk factors in the whole patient group and increase differently in different dementia diagnoses.

To the best of our knowledge, this is the first study on CMBs and dementia in a large and diverse cohort with subgroup analysis and emphasis on risk factors for the presence of CMBs. The prevalence of CMBs detected in our study is in line with previously published results.[6-8,13-15,19,20] However, the mean age in other studies has generally been higher, therefore presumably occasionally leading to a higher CMB prevalence. Similarly, studies using higher field strengths and the SWI sequence have shown a higher prevalence of CMBs.[21]

Our findings may have several important clinical implications. The association of lobar CMBs with CAA and deep CMBs with hypertensive arteriopathy has been shown and discovered in pathologic and risk factor analysis studies and further by in vivo PET imaging with Pittsburgh compound-B.[22-29] The prevalence, topography, and risk factors of CMBs may thus give an insight in the vascular and amyloid components of different dementia diagnoses.

Our results showed a significantly predominant lobar and occipital CMB topography in Alzheimer disease, typical for CAA,[30-33] reflecting the importance of amyloid pathology in Alzheimer disease. Lobar topography of CMBs in Alzheimer disease has been reported before,[6,8,13,19,20] with occipital predominance only reported in 1 study.[6] The CMB topography in the whole cohort was predominantly lobar, with a large amount of strictly lobar CMBs compared with CMBs strictly in infratentorial and deep regions. This may reflect the predominance of CAA and further amyloid pathology in dementia, as well as increasing CAA with age. Our topographic analysis further showed CMBs in both lobar and deep and infratentorial locations across dementia diagnoses, with a relation to hypertension in both topographies, corroborating the synergistic/additive effects of amyloid and vascular disease in dementia.

The concomitant effects between amyloid and vascular pathology are further suggested in our results. Hypertension and hyperlipidemia were both accompanied by higher CMB prevalence in the whole patient group and in mild and subjective cognitive impairment. Furthermore, hypertension in subjective cognitive impairment and hyperlipidemia in mild cognitive impairment were significantly associated with an increasing number of CMBs. The association of CMBs with hypertension and hyperlipidemia in the early dementia stages may suggest a stepwise process, with vascular risk factors important early in the dementia process, later overtaken by amyloid pathology. Likewise, theories exist that hypertension may be an important risk factor for the development of Alzheimer disease.[5] The odds ratios for CMBs, adjusted for vascular risk factors, sex, and advanced age support this theory. Only alcohol-related dementia, Alzheimer disease, unspecified dementia, and vascular dementia had significant odds ratios for developing CMBs, when adjusting for vascular risk factors. This finding suggests the importance of amyloid pathology in the development of CMBs in Alzheimer disease, vascular dementia, and possibly also in alcohol-related dementia, though unreported cerebral contusions might be possible in the latter case as well.

Prevalence and number of CMBs rendered a slightly different risk factor profile across the diagnoses. In the whole cohort, the prevalence of CMBs increased with hypertension and hyperlipid-

emia, and the number of CMBs decreased with hyperlipidemia and diabetes. The decrease in CMBs with hyperlipidemia may imply that hyperlipidemia in itself merely causes or leads to the development of CMBs, without major impact on the number of CMBs. The association of diabetes with a decreasing number of CMBs and the lack of association with the prevalence of CMBs suggest that diabetes in itself may not be a strong risk factor for CMBs in dementia. Hypertension, male sex, and advanced age were associated with consistently higher prevalence/number of CMBs and are thus presumably strong risk factors for CMBs across dementia diagnoses. The MMSE score increased with an increasing number of CMBs in Alzheimer disease and mild cognitive impairment, suggesting that the number of CMBs does not directly impact cognition.

Another potentially important clinical implication of our study is the increasing CMB prevalence with number of risk factors. Odds ratios for CMBs increased with the increasing number of risk factors (vascular risk factors, male sex, and older age) in the whole patient group. Because CMBs have been suggested as predictors of intracerebral hemorrhage, the number of risk factors may be an important factor to consider, especially in patients with anticoagulant medication. However, more research is warranted to outline the role of CMBs as a predictor of intracerebral hemorrhage and thus the clinical implications of our finding.

Our study has several strengths. A large and diverse cohort, subgroup analysis, and the use of a standardized scale for CMB rating accompanied by excellent inter- and intrarater agreement are major strengths, contributing to the generalizability of our study. Limitations, on the other hand, encompass the use of different MR imaging parameters and field strengths. Nevertheless, patients were randomly assigned to different scanners, with almost equal representation of MR imaging field strength/CMB sequence across diagnoses. Furthermore, we corrected all our regression models for the potential effect of MR imaging field strength and CMB sequence.

CONCLUSIONS

Our study demonstrates the variance of CMBs in dementia, providing an insight into different dementia diagnoses. Future studies in the KIDS will focus on CSF markers in relation to CMBs and further neuroradiologic interpretations.

ACKNOWLEDGMENTS

We thank Helena Forssell and Karin Kjellsdotter for their administrative and technical assistance.

REFERENCES

1. Fazekas F, Kleinert R, Roob G, et al. **Histopathologic analysis of foci of signal loss on gradient-echo T2*-weighted MR images in patients with spontaneous intracerebral hemorrhage: evidence of microangiopathy-related microbleeds.** *AJNR Am J Neuroradiol* 1999;20:637–42
2. Gregoire SM, Chaudhary UJ, Brown MM, et al. **The Microbleed Anatomical Rating Scale (MARS): reliability of a tool to map brain microbleeds.** *Neurology* 2009;73:1759–66
3. Auer RN, Sutherland GR. **Primary intracerebral hemorrhage: pathophysiology.** *Can J Neurol Sci* 2005;32(suppl 2):S3–12
4. Jellinger KA. **Alzheimer disease and cerebrovascular pathology: an update.** *J Neural Transm* 2002:109:813–36
5. Skoog I. **The relationship between blood pressure and dementia: a review.** *Biomed Pharmacother* 1997;51:367–75
6. Pettersen JA, Sathiyamoorthy G, Gao FQ, et al. **Microbleed topography, leukoaraiosis, and cognition in probable Alzheimer disease from the Sunnybrook dementia study.** *Arch Neurol* 2008;65:790–95
7. Nakata-Kudo Y, Mizuno T, Yamada K, et al. **Microbleeds in Alzheimer disease are more related to cerebral amyloid angiopathy than cerebrovascular disease.** *Dement Geriatr Cogn Disord* 2006;22:8–14
8. Cordonnier C, van der Flier WM, Sluimer JD, et al. **Prevalence and severity of microbleeds in a memory clinic setting.** *Neurology* 2006;66:1356–60
9. Roob G, Schmidt R, Kapeller P, et al. **MRI evidence of past cerebral microbleeds in a healthy elderly population.** *Neurology* 1999;52:991–94
10. Jeerakathil T, Wolf PA, Beiser A, et al. **Cerebral microbleeds: prevalence and associations with cardiovascular risk factors in the Framingham Study.** *Stroke* 2004;35:1831–35
11. Sveinbjornsdottir S, Sigurdsson S, Aspelund T, et al. **Cerebral microbleeds in the population based AGES-Reykjavik study: prevalence and location.** *J Neurol Neurosurg Psychiatry* 2008;79:1002–06
12. Tsushima Y, Tanizaki Y, Aoki J, et al. **MR detection of microhemorrhages in neurologically healthy adults.** *Neuroradiology* 2002;44:31–36
13. Hanyu H, Tanaka Y, Shimizu S, et al. **Cerebral microbleeds in Alzheimer's disease.** *J Neurol* 2003;250:1496–97
14. Nakata Y, Shiga K, Yoshikawa K, et al. **Subclinical brain hemorrhages in Alzheimer's disease: evaluation by magnetic resonance T2*-weighted images.** *Ann N Y Acad Sci* 2002;977:169–72
15. Fukui T, Oowan Y, Yamazaki T, et al. **Prevalence and clinical implication of microbleeds in dementia with Lewy bodies in comparison with microbleeds in Alzheimer's disease.** *Dement Geriatr Cogn Dis Extra* 2013;3:148–60
16. Cordonnier C, van der Flier WM. **Brain microbleeds and Alzheimer's disease: innocent observation or key player?** *Brain* 2011:134(pt 2):335–44
17. Lee SH, Bae HJ, Kwon SJ, et al. **Cerebral microbleeds are regionally associated with intracerebral hemorrhage.** *Neurology* 2004;62:72–76
18. Landis JR, Koch GG. **The measurement of observer agreement for categorical data.** *Biometrics* 1977;33:159–74
19. Uetani H, Hirai T, Hashimoto M, et al. **Prevalence and topography of small hypointense foci suggesting microbleeds on 3T susceptibility-weighted imaging in various types of dementia.** *AJNR Am J Neuroradiol* 2013;34:984–89
20. Brundel M, Heringa SM, de Bresser J, et al. **High prevalence of cerebral microbleeds at 7Tesla MRI in patients with early Alzheimer's disease.** *J Alzheimers Dis* 2012;31:259–63
21. Nandigam RNK, Viswanathan A, Delgado P, et al. **MR imaging detection of cerebral microbleeds: effect of susceptibility-weighted imaging, section thickness, and field strength.** *AJNR Am J Neuroradiol* 2009;30:338–43
22. Dierksen GA, Skehan ME, Khan MA, et al. **Spatial relation between microbleeds and amyloid deposits in amyloid angiopathy.** *Ann Neurol* 2010;68:545–48
23. Park JH, Seo SW, Kim C, et al. **Pathogenesis of cerebral microbleeds: in vivo imaging of amyloid and subcortical ischemic small vessel disease in 226 individuals with cognitive impairment.** *Ann Neurol* 2013;73:584–93
24. Gurol ME, Dierksen G, Betensky R, et al. **Predicting sites of new hemorrhage with amyloid imaging in cerebral amyloid angiopathy.** *Neurology* 2012;79:320–26
25. Greenberg SM, Vernooij MW, Cordonnier C, et al. **Cerebral microbleeds: a guide to detection and interpretation.** *Lancet Neurol* 2009;8:165–74

26. Werring DJ, ed. *Cerebral Microbleeds: Pathophysiology to Clinical Practice.* Cambridge: Cambridge University Press; 2011
27. Poels MM, Vernooij MW, Ikram MA, et al. **Prevalence and risk factors of cerebral microbleeds: an update of the Rotterdam scan study.** *Stroke* 2010:41(10 suppl):S103–06
28. Wiegman AF, Meier IB, Schupf N, et al. **Cerebral microbleeds in a multiethnic elderly community: demographic and clinical correlates.** *J Neurol Sci* 2014;345:125–30
29. Romero JR, Preis SR, Beiser A, et al. **Risk factors, stroke prevention treatments, and prevalence of cerebral microbleeds in the Framingham Heart Study.** *Stroke* 2014;45:1492–94
30. Vinters HV, Gilbert JJ. **Cerebral amyloid angiopathy: incidence and complications in the aging brain. II. The distribution of amyloid vascular changes.** *Stroke* 1983;14:924–28
31. Biffi A, Greenberg SM. **Cerebral amyloid angiopathy: a systematic review.** *J Clin Neurol* 2011;7:1–9
32. Rosand J, Muzikansky A, Kumar A, et al. **Spatial clustering of hemorrhages in probable cerebral amyloid angiopathy.** *Ann Neurol* 2005;58:459–62
33. Attems J, Jellinger KA, Lintner F. **Alzheimer's disease pathology influences severity and topographical distribution of cerebral amyloid angiopathy.** *Acta Neuropathol* 2005;110:222–31

Aneurysmal Subarachnoid Hemorrhage Causes Injury of the Ascending Reticular Activating System: Relation to Consciousness

S.H. Jang and H.S. Kim

ABSTRACT

BACKGROUND AND PURPOSE: Little is known about the pathogenetic mechanism of impaired consciousness following subarachnoid hemorrhage. Using diffusion tensor imaging, we attempted to investigate the presence of injury of the lower portion of the ascending reticular activating system between the pontine reticular formation and the intralaminar thalamic nuclei, and the relation between this injury and consciousness level in patients with SAH.

MATERIALS AND METHODS: We recruited 24 consecutive patients with spontaneous SAH following aneurysmal rupture and 21 healthy control subjects. Consciousness level was rated by using the Glasgow Coma Scale. Using diffusion tensor tractography, we reconstructed the lower portion of the ascending reticular activating system between the pontine reticular formation and the intralaminar thalamic nuclei. Values of fractional anisotropy, apparent diffusion coefficient, and tract number of the ascending reticular activating system were measured.

RESULTS: A significant difference in the tract number was observed between the patient and control groups ($P < .05$); however, there was no significant difference in terms of fractional anisotropy and apparent diffusion coefficient values ($P > .05$). In addition, regarding the tract number of the patient group, the Glasgow Coma Scale showed strong positive correlations with the tract number on the more affected side ($r = 0.890$, $P < .05$), the less affected side ($r = 0.798$, $P < .05$), and both sides ($r = 0.919$, $P < .05$), respectively.

CONCLUSIONS: We found injury of the lower portion of the ascending reticular activating system between the pontine reticular formation and the thalamus in patients with SAH. In addition, we observed a close association between injury of the lower portion of the ascending reticular activating system and impaired consciousness in patients with SAH.

ABBREVIATIONS: ARAS = ascending reticular activating system; FA = fractional anisotropy; GCS = Glasgow Coma Scale

Subarachnoid hemorrhage, which occurs by extravasation of blood into the subarachnoid space covering the central nervous system, comprises 5% of all cases of stroke. The average fatality rate in patients with SAH is 51%.[1,2] Most deaths occur within 2 weeks after SAH, especially 25% within 24 hours, with approximately one-third of survivors needing life-long care.[1,2] Various neurologic complications are known to occur in >50% of survivors with SAH, and impaired consciousness is a common neurologic complication.[2] Two-thirds of patients with SAH have been reported to show impaired consciousness in the acute stage, and loss of consciousness is a powerful predictive factor for a poor neurologic outcome in patients with SAH.[2,3] However, the pathogenetic mechanism of impaired consciousness following SAH has not been clearly elucidated so far.[4]

Human consciousness consists of arousal and awareness, which is accomplished by action of the pathway known as the ascending reticular activating system (ARAS).[5-7] The ARAS is a complex neural network connecting from the reticular formation of the brain stem to the cerebral cortex via excitatory relays in the intralaminar nuclei of the thalamus; therefore, accurate assessment of the ARAS plays an important role in the diagnosis and management of patients with impaired consciousness.[5-8] Successful evaluation of the ARAS has been limited despite many attempts by using conventional MR imaging, functional neuroimaging, electrophysiologic assessments, MR spectroscopy, and positron-emission tomography.[9-11]

By contrast, diffusion tensor tractography, which is derived from diffusion tensor imaging, has enabled 3D reconstruction and estima-

Received October 2, 2014; accepted after revision October 30.

From the Department of Physical Medicine and Rehabilitation, College of Medicine, Yeungnam University, Taegu, Republic of Korea.

This research was supported by the Basic Science Research Program through the National Research Foundation of Korea and was funded by the Ministry of Education, Science and Technology (2012R1A1A4A01001873).

Please address correspondence to Hyo Sung Kim, MD, Department of Physical Medicine and Rehabilitation, College of Medicine, Yeungnam University 317-1, Daemyungdong, Namku, Taegu, 705-717, Republic of Korea; e-mail: aodwntjr1@naver.com

Indicates open access to non-subscribers at www.ajnr.org

http://dx.doi.org/10.3174/ajnr.A4203

Table 1: Demographic and clinical data of patients[a]

	Patient Group (n = 24)	Control Group (n = 21)
Male/female	7/17	12/9
Mean age (yr) (SD)	58.45 (8.73)	55.17 (9.70)
GCS (SD)	13.74 (1.42)	
Ruptured artery (AcomA, IC-PcomA, MCA, other ICA, BA, PA)	14, 3, 2, 2, 2, 1	
Fisher CT grade (SD)	2.75 (0.44)	
Duration from onset (week) (SD)	6.49 (2.63)	

Note:—AcomA indicates anterior communicating artery; IC-PcomA, internal carotid–posterior communicating artery; BA, basilar artery; PA, pericallosal artery.
[a] Values represent mean (SD).

tion of the ARAS in the healthy human brain.[5,6] In addition, a few studies have reported injury of the ARAS in patients with traumatic brain injury and hypoxic-ischemic brain injury by using diffusion tensor tractography.[12,13] However, no study on injury of the ARAS in patients with SAH has been reported, to our knowledge. In this study, we hypothesized that injury of the lower portion of the ARAS between the reticular formation of the brain stem and the intralaminar thalamic nuclei would be observed in patients with spontaneous SAH and that injury of the lower ARAS might be correlated with consciousness level.

In the current study using DTI, we attempted to investigate the presence of injury of the lower portion of the ARAS between the pontine reticular formation and the intralaminar thalamic nuclei and the relation between this injury and consciousness level in patients with SAH following aneurysmal rupture at the chronic stage >3 weeks after onset.

MATERIALS AND METHODS

Subjects

Twenty-four consecutive patients with spontaneous SAH (7 men, 17 women; mean age, 58.45 ± 8.73 years; range, 42–73 years) and 21 healthy control subjects (12 men, 9 women; mean age, 55.17 ± 9.70 years; range, 41–74 years) with no previous history of neurologic illness were recruited (Table 1). Inclusion criteria were as follows: 1) first-ever stroke; 2) age, 21–75 years; 3) hemorrhage in the subarachnoid space due to aneurysmal rupture confirmed by a neuroradiologist; 4) DTI scanning performed at a chronic stage (>3 weeks after onset); and 5) absence of serious medical complications affecting consciousness, such as hepatic problems or severe kidney disease, at the time of evaluation by using the Glasgow Coma Scale (GCS). Patients who had any other brain lesion, intracerebral hemorrhage, intraventricular hemorrhage, or hydrocephalus that required a shunt operation were excluded because these pathologic conditions could affect consciousness. The artery distribution of aneurysmal rupture in patients with SAH was as follows: anterior communicating artery, 14 patients (58.33%); internal carotid–posterior communicating artery, 3 patients (12.50%); middle cerebral artery: 2 patients (8.33%); other internal carotid artery, 2 patients (8.33%); basilar artery, 2 patients (8.33%); and pericallosal artery, 1 patient (4.17%). The severity of SAH, assessed by using the modified Fisher CT grade and the average Fisher CT grade, was 2.75 ± 0.44 (Table 1).[14] This study was conducted retrospectively, and the institutional review board of our hospital approved the study protocol.

Clinical Evaluation

Consciousness level was rated by using the GCS at the time of DTI scanning. The reliability and validity of the GCS are well-established.[15,16] The distribution of GCS scores was as follows: 3 patients, 11 points; 4 patients, 12 points; 2 patients, 13 points; 5 patients, 14 points; and 10 patients, 15 points.

Diffusion Tensor Tractography

DTI data were acquired at 6.49 ± 2.63 weeks (range, 3.14~13.86 weeks) by using a 6-channel head coil on a 1.5T Gyroscan Intera scanner (Phillips Healthcare, Best, the Netherlands) with single-shot echo-planar imaging. For each of the 32 noncollinear diffusion-sensitizing gradients, we acquired 67 contiguous sections parallel to the anterior/posterior commissure line. Imaging parameters were as follows: acquisition matrix = 96 × 96, reconstructed to matrix = 191 × 191, FOV = 240 × 240 mm, TR = 10,726 ms, TE = 76 ms, parallel imaging reduction factor (sensitivity encoding factor) = 2, EPI factor = 59, b=1000 s/mm^2, NEX = 1, and section thickness = 2.5 mm (acquired isotropic voxel size = 2.5 × 2.5 × 2.5 mm).

Probabilistic Fiber Tracking

Analysis of DTI data was performed by using the fMRI of the Brain Software Library (www.fmrib.ox.ac.uk/fsl). Affine multiscale 2D registration was used for correction of the head-motion effect and image distortion due to eddy current. Fiber tracking was performed by using a probabilistic tractography method based on a multifiber model and was applied in the current study using tractography routines implemented in the FMRIB Diffusion Toolbox (http://www.fmrib.ox.ac.uk/fsl/fdt/index.html) (5000 streamline samples, 0.5-mm step lengths, curvature thresholds = 0.2).[17] Advantages of probabilistic tractography, which was used in this study, include greater robustness to noise and the ability to detect pathways with sharper angles and distinguish crossing fibers.[18,19]

The pathway of the ARAS was determined by selection of fibers passing through seed regions of interest and target (termination) ROIs. A seed ROI was placed on the reticular formation of the pons at the level of the trigeminal nerve entry zone. The target ROI was given on the intralaminar nuclei of the thalamus at the level of the commissural plane.[10] In defining the intralaminar nuclei of the thalamus, we referred to a brain atlas.[20] Of 5000 samples generated from the seed voxel, results for contact were visualized at a threshold minimum of 1 streamlined through each voxel for analysis. Values of fractional anisotropy (FA), apparent diffusion coefficient, and tract number of the lower portion of the ARAS were measured. We defined the side that showed the lowest tract number as the more affected side and the other side as the less affected side (Fig 1).

Statistical Analysis

SPSS software (Version 15.0; IBM, Armonk, New York) was used for data analysis. A paired t test was used to determine the difference in values of DTI parameters of the ARAS between the patient group and control group and between the more affected side and the less affected side. The Pearson correlation test was used to determine the correlation between DTI parameters of the ARAS and the GCS. Results were considered significant when the P value

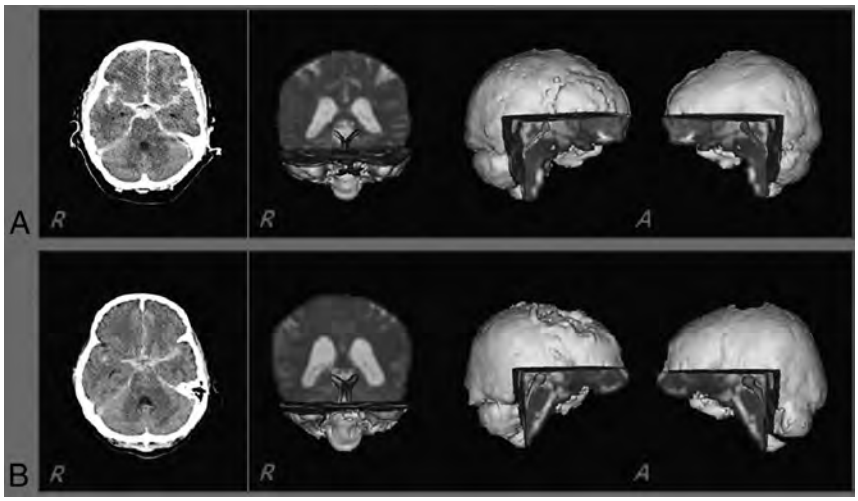

FIG 1. Brain CT (*left*) showing subarachnoid hemorrhage at onset and diffusion tensor tractography of the ascending reticular activating system between the pontine reticular formation and the intralaminar thalamic nuclei (*right*) in 2 patients (*A*, A 69-year-old woman, Glasgow Coma Scale score, 11; and *B*, A 57-year-old woman, Glasgow Coma Scale score, 15).

Table 2: Mean values for diffusion tensor imaging parameters and correlations between Glasgow Coma Scale score and diffusion tensor imaging parameters of the ascending reticular activating system[a]

	Patient Group			
	More Affected Side	Less Affected Side	Both Sides	Control Group
FA	0.40 ± 0.10 (0.150)	0.42 ± 0.03 (−0.238)	0.41 ± 0.05 (0.073)	0.41 ± 0.03
ADC	0.93 ± 0.09 (−0.079)	0.93 ± 0.08 (−0.003)	0.93 ± 0.07 (−0.052)	0.95 ± 0.12
TN	352 ± 94 (0.890[b])	441 ± 71 (0.798[b])	396.45 ± 76.04 (0.919[b])	459.13 ± 54.91

Note:—TN indicates tract number.

[a] Values represent mean ± SD (correlation coefficient) and mean average values for both sides between the right and left hemispheres.

[b] Significant differences ($P < .05$).

was < .05. A correlation coefficient of >0.60 indicated a strong correlation, a correlation coefficient between 0.40 and 0.59 indicated a moderate correlation, a correlation coefficient between 0.20 and 0.39 indicated a weak correlation, and a correlation coefficient of <0.19 indicated very weak reproducibility.[21]

RESULTS

The mean values for DTI parameters of the lower portion of the ARAS (from the pontine reticular formation to the intralaminar nuclei of the thalamus) in the patient and control groups and the correlations between DTI parameters and the GCS on the more affected side, less affected side, and both sides are shown in Table 2. A significant difference in the tract number was observed between the patient and control groups ($P < .05$); however, there was no significant difference in terms of FA and apparent diffusion coefficient values ($P > .05$). In addition, a significant difference in the tract number was observed between the more affected side and the less affected side of the ARAS in the patient group ($P < .05$). By contrast, no significant differences in terms of FA and apparent diffusion coefficient values were observed between the more affected and the less affected sides of the ARAS in the patient group ($P > .05$) (Table 2).

Regarding the tract number, the GCS showed strong positive correlations with tract number on the more affected side ($r = 0.890$, $P < .05$), the less affected side ($r = 0.798$, $P < .05$), and both sides ($r = 0.919$, $P < .05$), respectively. By contrast, no significant correlation was observed between the GCS and FA and apparent diffusion coefficient values on the more affected side, the less affected side, and both sides ($P > .05$) (Fig 2).

DISCUSSION

In this study, by using DTI, we investigated the presence of injury of the lower portion of the ARAS between the pontine reticular formation and the intralaminar thalamic nuclei and the relation of this injury and consciousness level in patients with SAH. We found that the tract number of the lower portion of the ARAS was decreased in patients with SAH, though FA and apparent diffusion coefficient values did not differ from those of healthy control subjects. In addition, the tract number of the ARAS showed strong correlation with the GCS in patients with SAH. However, no significant correlation was observed between other DTI parameters (FA and apparent diffusion coefficient) and the GCS. The FA value indicates the degree of directionality and integrity of white matter microstructures, such as axons, myelin, and microtubules; and the apparent diffusion coefficient value indicates the magnitude of water diffusion, which can increase under conditions of vasogenic or cytotoxic edema or accumulation of cellular debris from axonal injury.[22,23] By contrast, the tract number indicates the number of voxels contained within a neural tract.[24] As a result, the decrement of the tract number without a significant change of FA and apparent diffusion coefficient values of the lower ARAS suggests injury of the lower ARAS, and correlation between the tract number of the lower ARAS and GCS indicates a close relationship between the degree of injury of the lower ARAS and the consciousness level in patients with SAH.

Previous studies have reported that nearly two-thirds of deaths following SAH were due to the initial hemorrhage, and most of these deaths happened during the first 2 days.[25] Regarding acute death following SAH, increased intracranial pressure leads to overactivation of the sympathetic system, which is caused by 2 mechanisms: 1) direct effect on the brain stem, and 2) a local release of inflammatory mediators.[1,26] As a result of overactivation of the sympathetic system, life-threatening symptoms might appear rapidly, such as cardiac arrhythmias, electrocardiographic changes, and cardiac arrest after onset of SAH.[25] In addition, as a further consequence of this process, neurogenic pulmonary edema might appear, which is characterized by sudden-onset respiratory failure.[27] It is reported that the volume of initial hemorrhage and level of consciousness, which is measured by the GCS score, are strong predictors of early mortality. Thus, consciousness level following SAH is regarded as a powerful predictive fac-

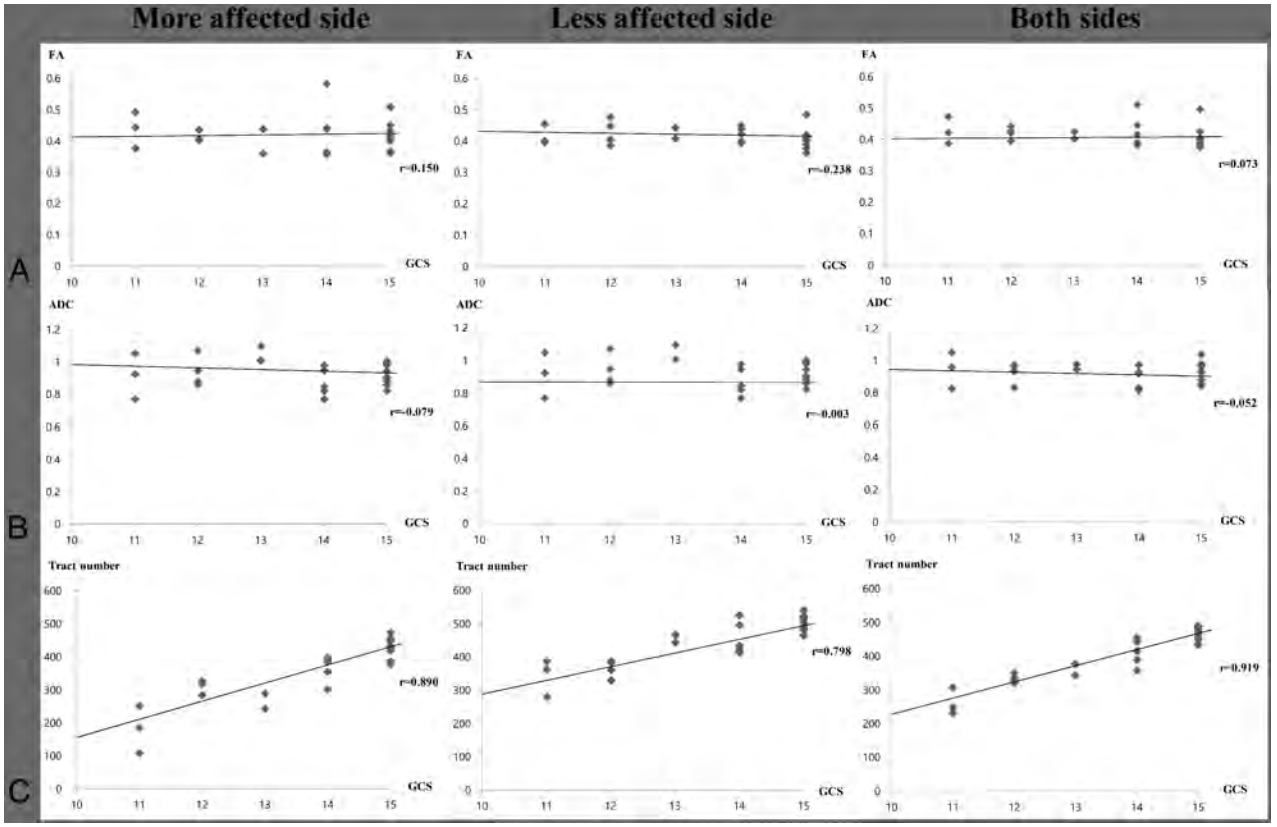

FIG 2. Correlation between the Glasgow Coma Scale score and fractional anisotropy (*A*), apparent diffusion coefficient (*B*), and tract number (*C*) of patients with subarachnoid hemorrhage on the more affected side, the less affected side, and both sides.

tor for a poor neurologic outcome in patients with SAH.[25] Although the pathogenetic mechanisms of neurologic injury following SAH have not been clearly elucidated, there are several possible mechanisms: vasospasm, cortical ischemia, microthromboemboli, hydrocephalus, free radical injury, and inflammation.[4,28-30] However, no study on the pathogenetic mechanism of injury of the lower portion of the ARAS between the reticular formation and the intralaminar thalamic nuclei following SAH has been reported.

Previous studies have reported that injury of the brain stem can be caused by hematoma in the perimesencephalic cisterns following SAH.[1,31-33] Therefore, we assume that injury of the lower portion of the ARAS might occur because of the hematoma in the subarachnoid space around the thalamus and brain stem. In addition, on the basis of previous studies suggesting the injury mechanism of periventricular white matter following intraventricular hemorrhage, we believe that this injury might be ascribed to the following mechanical or chemical mechanisms: 1) Mechanical: increased intracranial pressure or direct mass effect by intraventricular hemorrhage can cause a decrease in cerebral perfusion pressure and secondary ischemic injury to periventricular white matter; 2) chemical: a blood clot itself can cause extensive damage to the ependymal layer, subependymal layer, or periventricular tissues by release of potentially damaging substances, such as free iron, which may generate free radicals or inflammatory cytokines.[34,35]

The basis of arousal in the brain stem has been conceptualized as the ARAS, introduced by Moruzzi and Magoun in 1949[36]; they reported that electrical stimulation of the reticular formation in the brain stem evokes activation of the cerebral cortex change of electroencephalography.[36] It is now accepted that the ARAS is a complex network of neurons projecting from multiple brain stem source nuclei to the cerebral cortex via the thalamus and extrathalamic pathways.[8,37-41] Since the introduction of DTI, several studies have reported on the lower portion of the ARAS in healthy subjects and patients with brain injury.[5,6,12,13] In 2012, Edlow et al[6] reconstructed the ARAS connecting the brain stem to the thalamus, hypothalamus, and the basal forebrain in healthy subjects. In 2013, Yeo et al[5] reported a method for reconstruction of the lower portion of the ARAS from the pontine reticular formation to the thalamus in healthy subjects. Subsequently, Edlow et al in 2013[13] reported on a patient with coma who showed disruptions of white matter pathways connecting brain stem arousal nuclei to the basal forebrain and thalamic intralaminar and reticular nuclei and the pathways connecting the thalamus and basal forebrain to the cerebral cortex following traumatic brain injury. Recently, Jang et al in 2014[12] demonstrated injury of the ARAS between the pontine reticular formation and the thalamus in patients with impaired arousal after hypoxic-ischemic brain injury. As a result, to the best of our knowledge, this is the first study to demonstrate injury of the ARAS in patients with SAH. However, limitations of DTI should be considered. DTI analysis is operator-dependent, and regions of fiber complexity and crossing can prevent full reflection of the underlying fiber architecture by DTI.[42,43]

CONCLUSIONS

We found injury of the lower portion of the ARAS between the pontine reticular formation and the thalamus in patients with SAH. In addition, we found a close association between injury of the ARAS and impaired consciousness in these patients. We believe that analysis of the ARAS by using diffusion tensor tractography would be helpful in the evaluation of patients with impaired consciousness after SAH. In particular, early detection of injury of the ARAS would be helpful for prediction of prognosis and planning of rehabilitation strategies for patients with impaired consciousness following SAH. A limitation of this study is that we were not able to fully elucidate the entire ARAS system. Another limitation of this study was the relatively small number of patients. Therefore, further studies involving the entire ARAS and larger numbers of patients should be encouraged.

REFERENCES

1. van Gijn J, Kerr RS, Rinkel GJ. **Subarachnoid haemorrhage.** *Lancet* 2007;369:306–18
2. Suarez JI, Tarr RW, Selman WR. **Aneurysmal subarachnoid hemorrhage.** *N Engl J Med* 2006;354:387–96
3. Ribeiro JA, Pereira S, Basto MA, et al. **The initial loss of consciousness in spontaneous subarachnoid hemorrhage: What does it mean** [in Portuguese]? *Acta Med Port* 1998;11:1085–90
4. Rossi GF. **Physiopathology of non-traumatic subarachnoid hemorrhage: loss of consciousness** [in Italian]. *Minerva Anestesiol* 1998;64:121–23
5. Yeo SS, Chang PH, Jang SH. **The ascending reticular activating system from pontine reticular formation to the thalamus in the human brain.** *Front Hum Neurosci* 2013;7:416
6. Edlow BL, Takahashi E, Wu O, et al. **Neuroanatomic connectivity of the human ascending arousal system critical to consciousness and its disorders.** *J Neuropathol Exp Neurol* 2012;71:531–46
7. Zeman A. **Consciousness.** *Brain* 2001;124:1263–89
8. Steriade M, Glenn LL. **Neocortical and caudate projections of intralaminar thalamic neurons and their synaptic excitation from midbrain reticular core.** *J Neurophysiol* 1982;48:352–71
9. Schiff ND. **Multimodal neuroimaging approaches to disorders of consciousness.** *J Head Trauma Rehabil* 2006;21:388–97
10. Tshibanda L, Vanhaudenhuyse A, Boly M, et al. **Neuroimaging after coma.** *Neuroradiology* 2010;52:15–24
11. Bernat JL. **Chronic disorders of consciousness.** *Lancet* 2006;367:1181–92
12. Jang SH, Kim SH, Lim HW, et al. **Injury of the lower ascending reticular activating system in patients with hypoxic-ischemic brain injury: diffusion tensor imaging study.** *Neuroradiology* 2014;56:965–70
13. Edlow BL, Haynes RL, Takahashi E, et al. **Disconnection of the ascending arousal system in traumatic coma.** *J Neuropathol Exp Neurol* 2013;72:505–23
14. Frontera JA, Claassen J, Schmidt JM, et al. **Prediction of symptomatic vasospasm after subarachnoid hemorrhage: the modified Fisher scale.** *Neurosurgery* 2006;59:21–27
15. Balestreri M, Czosnyka M, Chatfield DA, et al. **Predictive value of Glasgow Coma Scale after brain trauma: change in trend over the past ten years.** *J Neurol Neurosurg Psychiatry* 2004;75:161–62
16. Teasdale G, Jennett B. **Assessment of coma and impaired consciousness: a practical scale.** *Lancet* 1974;2:81–84
17. Smith SM, Jenkinson M, Woolrich MW, et al. **Advances in functional and structural MR image analysis and implementation as FSL.** *Neuroimage* 2004;23(suppl 1):S208–19
18. Behrens TE, Berg HJ, Jbabdi S, et al. **Probabilistic diffusion tractography with multiple fibre orientations: what can we gain?** *Neuroimage* 2007;34:144–55
19. Winston GP, Mancini L, Stretton J, et al. **Diffusion tensor imaging tractography of the optic radiation for epilepsy surgical planning: a comparison of two methods.** *Epilepsy Res* 2011;97:124–32
20. Morel A. *Stereotactic Atlas of the Human Thalamus and Basal Ganglia.* New York: Informa Healthcare; 2007
21. Evans JD. *Straightforward Statistics for the Behavioral Sciences.* Pacific Grove: Brooks/Cole; 1996
22. Assaf Y, Pasternak O. **Diffusion tensor imaging (DTI)-based white matter mapping in brain research: a review.** *J Mol Neurosci* 2008;34:51–61
23. Neil JJ. **Diffusion imaging concepts for clinicians.** *J Magn Reson Imaging* 2008;27:1–7
24. Jang SH, Chang CH, Lee J, et al. **Functional role of the corticoreticular pathway in chronic stroke patients.** *Stroke* 2013;44:1099–104
25. Broderick JP, Brott TG, Duldner JE, et al. **Initial and recurrent bleeding are the major causes of death following subarachnoid hemorrhage.** *Stroke* 1994;25:1342–47
26. Banki NM, Kopelnik A, Dae MW, et al. **Acute neurocardiogenic injury after subarachnoid hemorrhage.** *Circulation* 2005;112:3314–19
27. Piazza O, Venditto A, Tufano R. **Neurogenic pulmonary edema in subarachnoid hemorrage.** *Panminerva Med* 2011;53:203–10
28. Wan H, AlHarbi BM, Macdonald RL. **Mechanisms, treatment and prevention of cellular injury and death from delayed events after aneurysmal subarachnoid hemorrhage.** *Expert Opin Pharmacother* 2014;15:231–43
29. Ayer RE, Zhang JH. **Oxidative stress in subarachnoid haemorrhage: significance in acute brain injury and vasospasm.** *Acta Neurochir Suppl* 2008;104:33–41
30. Provencio JJ, Vora N. **Subarachnoid hemorrhage and inflammation: bench to bedside and back.** *Semin Neurol* 2005;25:435–44
31. van Gijn J, van Dongen KJ, Vermeulen M, et al. **Perimesencephalic hemorrhage: a nonaneurysmal and benign form of subarachnoid hemorrhage.** *Neurology* 1985;35:493–97
32. Schwartz TH, Solomon RA. **Perimesencephalic nonaneurysmal subarachnoid hemorrhage: review of the literature.** *Neurosurgery* 1996;39:433–40; discussion 440
33. Yeo SS, Choi BY, Chang CH, et al. **Evidence of corticospinal tract injury at midbrain in patients with subarachnoid hemorrhage.** *Stroke* 2012;43:2239–41
34. Chua CO, Chahboune H, Braun A, et al. **Consequences of intraventricular hemorrhage in a rabbit pup model.** *Stroke* 2009;40:3369–77
35. Yeo SS, Choi BY, Chang CH, et al. **Periventricular white matter injury by primary intraventricular hemorrhage: a diffusion tensor imaging study.** *Eur Neurol* 2011;66:235–41
36. Moruzzi G, Magoun HW. **Brain stem reticular formation and activation of the EEG.** *Electroencephalogr Clin Neurophysiol* 1949;1:455–73
37. Perlbarg V, Puybasset L, Tollard E, et al. **Relation between brain lesion location and clinical outcome in patients with severe traumatic brain injury: a diffusion tensor imaging study using voxel-based approaches.** *Hum Brain Mapp* 2009;30:3924–33
38. Kinney HC, Samuels MA. **Neuropathology of the persistent vegetative state: a review.** *J Neuropathol Exp Neurol* 1994;53:548–58
39. Steriade M. **Arousal: revisiting the reticular activating system.** *Science* 1996;272:225–26
40. McCormick DA. **Neurotransmitter actions in the thalamus and cerebral cortex and their role in neuromodulation of thalamocortical activity.** *Prog Neurobiol* 1992;39:337–88
41. Parvizi J, Damasio A. **Consciousness and the brainstem.** *Cognition* 2001;79:135–60
42. Lee SK, Kim DI, Kim J, et al. **Diffusion-tensor MR imaging and fiber tractography: a new method of describing aberrant fiber connections in developmental CNS anomalies.** *Radiographics* 2005;25:53–65; discussion 66–68
43. Yamada K. **Diffusion tensor tractography should be used with caution.** *Proc Natl Acad Sci U S A* 2009;106:E14; author reply E15

Arterial Spin-Labeling Perfusion MRI Stratifies Progression-Free Survival and Correlates with Epidermal Growth Factor Receptor Status in Glioblastoma

X.J. Qiao, B.M. Ellingson, H.J. Kim, D.J.J. Wang, N. Salamon, M. Linetsky, A.R. Sepahdari, B. Jiang, J.J. Tian, S.R. Esswein, T.F. Cloughesy, A. Lai, L. Nghiemphu, and W.B. Pope

ABSTRACT

BACKGROUND AND PURPOSE: Glioblastoma is a common primary brain tumor with a poor but variable prognosis. Our aim was to investigate the feasibility of MR perfusion imaging by using arterial spin-labeling for determining the prognosis of patients with glioblastoma.

MATERIALS AND METHODS: Pseudocontinuous arterial spin-labeling with 3D background-suppressed gradient and spin-echo was acquired before surgery on 53 patients subsequently diagnosed with glioblastoma. The calculated CBF color maps were visually evaluated by 3 independent readers blinded to patient history. Pathologic and survival data were correlated with CBF map findings. Arterial spin-labeling values in tumor tissue were also quantified by using manual fixed-size ROIs.

RESULTS: Two perfusion patterns were characterized by visual evaluation of CBF maps on the basis of either the presence (pattern 1) or absence (pattern 2) of substantial hyperperfused tumor tissue. Evaluation of the perfusion patterns was highly concordant among the 3 readers ($\kappa = 0.898$, $P < .001$). Pattern 1 (versus pattern 2) was associated with significantly shorter progression-free survival by Kaplan-Meier analysis (median progression-free survival of 182 days versus 485 days, $P < .01$) and trended with shorter overall survival ($P = .079$). There was a significant association between pattern 1 and epidermal growth factor receptor variant III expression ($P < .01$).

CONCLUSIONS: Qualitative evaluation of arterial spin-labeling CBF maps can be used to stratify survival and predict epidermal growth factor receptor variant III expression in patients with glioblastoma.

ABBREVIATIONS: ASL = arterial spin-labeling; EGFR = epidermal growth factor receptor; EGFRvIII = epidermal growth factor receptor variant III; GBM = glioblastoma; HR = hazard ratio; OS = overall survival; PFS = progression-free survival

Glioblastomas (GBMs) are the most deadly primary tumors in the CNS, with a median survival time of only 10–15 months.[1,2] Increased perfusion of gliomas is associated with higher grade and shorter survival (even within a tumor grade).[3-9] Information on tumor perfusion and hemodynamics can be acquired by using various MR imaging techniques. For instance, numerous studies have used dynamic susceptibility-weighted perfusion-weighted imaging, a contrast-enhanced bolus-tracking method, to determine the relative cerebral blood volume within tumors.[9-12]

Arterial spin-labeling (ASL) is an MR imaging–based technique that measures blood flow and has the advantage, compared with DSC-PWI, of not requiring intravenous contrast injection. ASL scans of high quality can be acquired within 4.5 minutes, making it a practical approach to acquire MR perfusion imaging for clinical use.[13,14] ASL has proved reliable and reproducible in the assessment of CBF in various pathologic states. Correlation has been established between DSC- and ASL-derived metrics, including relative CBV and CBF.[15] It has also been reported that ASL perfusion imaging correlates with tumor blood vessel attenuation[15,16] and is predictive of glioma grade.[15,17,18] Changes in ASL-derived CBF correlate with treatment outcome for metastases following stereotactic radiosurgery. Having a completely noninvasive method, such as ASL, of determining tumor blood flow would be highly desirable, particularly if there is a correlation with survival or other outcome measures for GBM.

Tumor blood flow may also be associated with histologic markers or genetic mutations, which may impact patient prognosis and susceptibility to treatment. One such histologic marker is epidermal growth factor receptor variant III (EGFRvIII),[19] the most common type of epidermal growth factor receptor (EGFR)

Received July 11, 2014; accepted after revision September 27.

From the Departments of Radiological Sciences (X.J.Q., B.M.E., H.J.K., N.S., M.L., A.R.S., J.J.T., S.R.E., W.B.P.) and Neurology (D.J.J.W., T.F.C., A.L., L.N.), David Geffen School of Medicine at University of California, Los Angeles, Los Angeles, California; and Department of Radiology (B.J.), Second Affiliated Hospital, Zhejiang University, Hangzhou, China.

Please address correspondence to Whitney B. Pope, MD, PhD, Department of Radiological Sciences, David Geffen School of Medicine, UCLA Medical Center, 10833 Le Conte Ave, BL-428/CHS, Los Angeles, CA 90095-1721; e-mail: wpope@mednet.ucla.edu

Indicates open access to non-subscribers at www.ajnr.org

http://dx.doi.org/10.3174/ajnr.A4196

variant carrying a primary oncogene effect,[20] which is expressed with an overall prevalence of 20%–30% in GBM.[21] Although the effect of EGFRvIII on patient survival has not been fully determined,[22,23] detection of EGFRvIII expression is increasingly important as therapies that specifically target this receptor are being developed. Earlier studies showed that GBMs expressing EGFRvIII are resistant to chemotherapies.[24] The coexpression of EGFRvIII with phosphatase and tensin homolog increases GBM sensitivity to EGFR tyrosine kinase inhibitors.[25,26] The demonstrated association of DSC-PWI-derived parameters with EGFRvIII expression[19] suggests the potential for MR perfusion imaging as a promising noninvasive marker of EGFRvIII expression.

Although ASL perfusion imaging has shown promise in the evaluation of gliomas, its role as a prognostic measure for GBM has not been fully explored, and the association between ASL-derived measures and important molecular markers such as EGFRvIII is incompletely characterized. In the current study, our purpose was to determine the value of ASL perfusion imaging as a predictor of prognosis in patients with newly diagnosed GBM and as a potential marker for EGFRvIII expression.

MATERIALS AND METHODS

Patients

From an ongoing registry of patients diagnosed with GBM from July 2010 to July 2013 at Ronald Reagan–UCLA Medical Center, subjects were selected who had the following: 1) presurgical, prechemo-/radiation therapy MR imaging, including ASL and postcontrast T1-weighted images; 2) gross total or subtotal tumor resection followed by standard external beam radiation therapy (6000 ± 200 cGy, started within 3–6 weeks after surgical resection) and concomitant/adjuvant chemotherapy that included temozolomide; 3) a histologically confirmed diagnosis of GBM; 4) regular follow-up (once per 4–6 weeks) by a neuro-oncologist to monitor tumor recurrence either until the patient died or until March 31, 2014, when the study was terminated. Seventeen of the 53 total patients (32%) received bevacizumab at recurrence. All patients provided informed consent to participate in our brain tumor data base containing clinical, imaging, and pathologic patient data. This study was approved by the institutional review board and was Health Insurance Portability and Accountability Act–compliant.

Clinical and Histology Data

For all selected patients, progression-free survival data were determined per the Response Assessment in Neuro-Oncology criteria.[27] Progression-free survival (PFS) and overall survival (OS) were calculated from the date of surgery.

EGFRvIII expression status in postsurgical GBM tissue was collected from the patient's medical record based on standard testing procedures.[28,29]

MR Imaging Protocols

MR images were obtained on a 1.5T Avanto or 3T Tim Trio system (Siemens, Erlangen, Germany) by using a 12-channel head coil. The brain tumor imaging protocol included ASL, T2-weighted, FLAIR, DWI, and postcontrast T1-weighted sequences. ASL scans were obtained by using a pseudocontinuous pulse sequence with background-suppressed 3D gradient and spin-echo readout (labeling pulse duration, 1.5 seconds; postlabeling delay, 2 seconds; no flow-crushing gradient; FOV = 22 cm; matrix size = 64 × 64; twenty-six 5-mm sections; generalized autocalibrating partially parallel acquisitions = 2; TE/TR = 22/4000 ms with 30 pairs of tag and control volumes acquired within 4.5 minutes). An M0 image was acquired at the end of the ASL scan with a long postlabeling delay of 4 seconds and a TR of 8 seconds.[13,14]

ASL Postprocessing and Evaluation

ASL images were corrected for motion, pair-wise subtracted between labeled and unlabeled images and averaged to generate mean difference images and quantitative CBF maps that were calculated by using a published model.[13] Motion correction was performed retrospectively by using a custom program based on principal component analysis.[30] CBF maps of patients with GBM (n = 53) were visually evaluated by 3 independent readers (board-certified neuroradiologists with 3, 7, and 10 years of experience) blinded to patient history for focal perfusion characteristics of the tumor tissue demonstrated by conventional MR imaging, specifically postcontrast T1-weighted and T2/FLAIR sequences. Two perfusion patterns were characterized by the readers on the basis of visual evaluation of CBF maps demonstrating either the presence (pattern 1) or absence (pattern 2) of substantial and clearly recognizable areas of hyperperfused tumor tissue.

In a separate analysis, a quantitative method was applied to calculate the lesion-to-normal ratio of CBF from areas of tumor that were hyperperfused as identified by visual inspection. ROIs of 3 × 3 pixels in size (10.3 × 10.3 mm, n = 3) were manually set in the tumor area showing the maximal perfusion ($_{max}ASL_{tumor}$) by visual inspection of the CBF map, and the average value within each ROI was recorded. A second set of ROIs was drawn in the mirrored position on the contralateral hemisphere with normal brain tissue. The lesion-to-normal ratio was calculated by dividing the mean values of $_{max}ASL_{tumor}$ with the mean values of the ROIs in the normal region. We also compared average "hot spot" values from patterns 1 and 2 without normalization to contralateral normal brain.

Statistical Analysis

The interreader agreement in CBF map readings (pattern 1 versus pattern 2) from the 3 readers (n = 53 subjects times 3 readers) was assessed by using κ statistics. The κ value, also known as κ coefficient of agreement, was calculated to evaluate the degree of consensus.

A paired t test was used to compare the mean of $_{max}ASL_{tumor}$ in each subject's tumor and the mean of ASL values from ROIs in normal brain area within and between perfusion patterns (patterns 1 and 2).

ASL CBF map readings in relationship with PFS and OS were analyzed by using univariate and multivariate Cox proportional hazard models with covariates of age and sex. In cases with disagreement on CBF map readings (in which not all readers assigned the images to the same pattern), the cases were assigned to the group (hyper- versus hypoperfused) agreed on by 2 (of 3) readers. Ninety-five percent confidence intervals of the above covariates were calculated. The Kaplan-Meier graph was used to

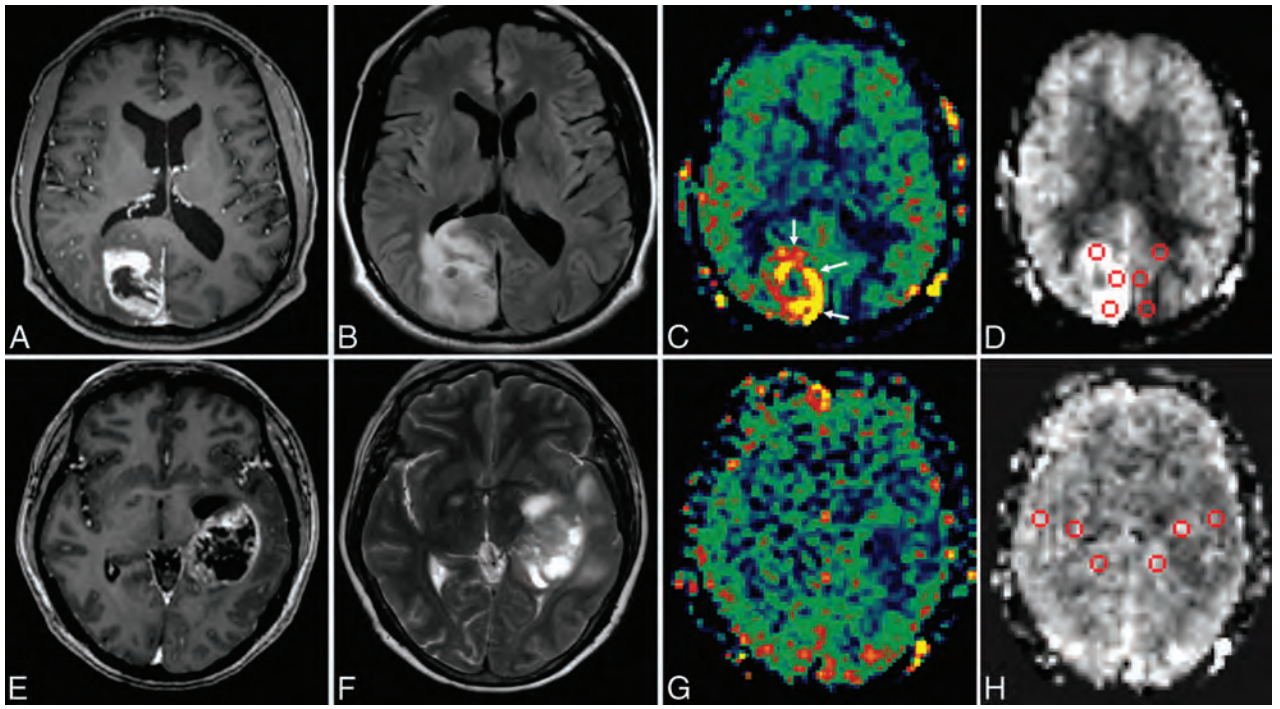

FIG 1. Qualitative and quantitative evaluation of ASL CBF maps. Conventional MR imaging (T1-weighted postcontrast imaging in *A* and *E*, T2 FLAIR in *B*, and T2 spin-echo in *F*) and ASL perfusion imaging (*C* and *G*) were visually evaluated by 3 independent readers. Two perfusion patterns can be characterized: Pattern 1 is characteristic of the presence of substantial hyperperfused tumor tissue in the CBF map, which can be identified by the bright ring-of-fire appearance (*white arrows* in *C*); in comparison, pattern 2 corresponds to the absence of easily recognizable hyperperfused tumor tissue compatible with a relatively less perfused tumor (*G*). Quantitative evaluation of ASL CBF maps is performed by applying manual ROIs in the tumoral regions with a ring-of-fire appearance and the mirrored regions in the contralateral hemisphere (*D* and *H*).

describe ASL CBF map readings at baseline to predict PFS and OS followed by the log-rank test. The correlation between CBF map readings and EGFRvIII expression was analyzed by using the Fisher exact test.

A *P* value of .05 was accepted as statistically significant. Statistical analysis was performed with STATA software (Version 12, 2012; StataCorp, College Station, Texas).

RESULTS

Patient Characteristics

The mean age of the 53 enrolled patients (28 men, 25 women) at the initial disease presentation was 60.4 ± 13.4 years, ranging from 29.3 to 82.4 years. By the time of the last assessment (March 31, 2014), 45 of the 53 patients (84.9%) had tumor progression and 40 of 53 patients (75.5%) had died.

Evaluation of ASL Maps

ASL CBF maps of patients with GBM ($n = 53$) were visually evaluated by 3 board-certified neuroradiologists blinded to patient history for focal perfusion abnormality (hyper- or hypoperfusion) in the tumor tissue. Two perfusion patterns were characterized on the basis of qualitative evaluation by the readers: Pattern 1 was characterized by the presence of substantial and easily identifiable hyperperfused tumor tissue in the CBF map, which often had a "ring-of-fire" appearance (Fig 1*A–C*); in comparison, pattern 2 corresponded to the absence of such easily identifiable hyperperfused tumor tissue and thus appeared in the CBF map as areas of lower perfusion in the region infiltrated by GBM (Fig 1*D–F*). The κ agreement test showed that evaluation of the perfusion patterns in CBF maps was highly concordant among the 3 readers ($\kappa = 0.898$, $P < .001$). On the basis of the most votes by readers, 30 of 53 patients (56.6%) had CBF maps of pattern 1, while 23 patients (43.4%) had CBF maps of pattern 2.

Table 1: Assessment of ASL values[a] in GBM by manual ROIs

	$_{max}ASL_{tumor}$[b]	Control[c]	*P* Value (*t* test)[d]	$R_{L/N}$
Pattern 1 ($n = 30$)[e]	74.53 ± 27.48	35.17 ± 10.62	<.001	2.27 ± 0.99
Pattern 2 ($n = 23$)[f]	32.51 ± 22.23	39.31 ± 17.28	.25	0.81 ± 0.37
P value (*t* test)[d]	<.001	.29	–	<.001

Note:—$R_{L/N}$ indicates lesion-to-normal brain ratio.
[a] Measured in mL/100 g/min.
[b] Maximal ASL values in the tumor tissue.
[c] ASL values taken from the contralateral hemisphere.
[d] $P < .05$ denotes statistical significance.
[e] CBF map with hyperperfused tumor tissue.
[f] CBF map with no substantial hyperperfused tumor tissue.

To confirm that the qualitative assessment of the readers corresponded to true differences in blood flow, a quantitative analysis was performed. The quantitative analysis showed that $_{max}ASL_{tumor}$ was significantly higher than ASL values of normal brain tissue in the group with the pattern 1 CBF map, but not in the group with the pattern 2 CBF map. When comparing groups of pattern 1 with those with pattern 2, there was a significant difference in the $_{max}ASL_{tumor}$ and lesion-to-normal ratio, but not in the mean values of normal brain tissue between the 2 groups (Table 1). Additionally, pattern 1 had statistically elevated CBF compared with pattern 2, without using normalized values. Thus average CBF (in milliliters/100 grams tissue/minute) for tumor was 74.8 ± 26.8 for pattern 1 compared with 32.1 ± 21.7 for pattern 2 (*t* test, $P < .001$).

Progression-Free Survival and Overall Survival

In a univariate Cox model, ASL CBF maps with pattern 1 (versus pattern 2) were predictive of shorter PFS (hazard ratio [HR] for progression = 2.23, $P = .010$) and trended with OS (HR = 1.82, $P = .084$). This predictive value was also significant for CBF maps with pattern 1 by using the log-rank test ($P = .008$) (Table 2).

The multivariate Cox model showed that patient age at the time of initial presentation (older than 50 years or younger than 50 years) was a significant predictor of PFS and OS (HR = 2.34, $P = .034$; and HR = 3.00, $P = .024$, respectively). ASL perfusion pattern (1 versus 2) remained a significant predictor of PFS (HR = 2.29, $P = .009$) and trended with OS (HR = 1.98, $P = .054$) in the multivariate analysis (Table 3).

The Kaplan-Meier method with a log-rank test showed that the perfusion patterns of ASL CBF maps stratified PFS (pattern 2 versus pattern 1, a 1.66-fold increase in median PFS; $P = .008$) and trended with OS ($P = .079$) (Fig 2).

Table 2: Univariate analysis: ASL CBF map of pattern 1 (versus pattern 2) is predictive of shorter progression-free survival and trended with overall survival

Univariate	HR (SE)	95% CI	Cox *P* Value[a]	Log-Rank *P* Value[a]
PFS ($n = 53$)	2.23 (0.70)	1.21–4.11	.010	.008
OS ($n = 50$)	1.82 (0.63)	0.92–3.58	.084	.079

Note:—SE indicates standard error.
[a] $P < .05$ denotes statistical significance.

Table 3: Multivariate Cox model for PFS and OS

Variables	HR	SE	*P* Value[a]	95% CI
Multivariate Cox model for PFS ($n = 53$)				
ASL CBF map reading[b]	2.29	0.72	.009	1.23–4.24
Patient age (yr)[c]	2.34	0.94	.034	1.06–5.13
Sex[d]	1.41	0.44	.266	0.77–2.59
Multivariate Cox model for OS ($n = 50$)				
ASL CBF map reading[b]	1.98	0.70	.054	0.99–4.00
Patient age (yr)[c]	3.00	1.46	.024	1.16–7.80
Sex[d]	1.06	0.36	.870	0.53–2.07

Note:—SE indicates standard error.
[a] $P < .05$ denotes statistical significance.
[b] By majority vote, CBF map of pattern 1 ($n = 30$) versus pattern 2 ($n = 23$).
[c] On initial presentation, older than 50 years ($n = 42$) versus younger than 50 years ($n = 11$).
[d] Male ($n = 28$) versus female ($n = 25$).

EGFRvIII Expression

Forty-one patients (in our patient cohort of 53, 77%) had EGFRvIII expression examined on postsurgical GBM tissue. Among these patients, 12 were positive for EGFRvIII expression. The Fisher exact test showed a significant association between a pattern 1 CBF map and EGFRvIII expression ($P < .01$) (Table 4).

DISCUSSION

To date, most studies of GBM perfusion have focused on the role of quantitative parameters, such as relative CBV and CBF, as markers of therapy response and clinical outcome. In the present study, a qualitative examination of CBF maps was conducted in a patient cohort with newly diagnosed GBM, and the potential for predicting tumor and the correlation with EGFRvIII expression were investigated.

We observed 2 perfusion patterns: Pattern 1 was characterized by the presence of hyperperfused tumor tissue in the CBF map, which could be identified by the bright ring-of-fire appearance; in comparison, pattern 2 corresponded to the absence of hyperperfused tumor tissue and thus appeared in the CBF map as iso- or hypoperfusion in the tumoral region. These observations were supported by not only the consistency among independent readers but also quantitative analysis by using ROI-derived ASL values from both tumor and normal brain areas. The quantitative analysis confirmed the qualitative assessment that there was increased CBF in pattern 1 compared with pattern 2. Conceivably, the dif-

Table 4: Association of CBF map of pattern 1 with EGFRvIII expression in GBM[a]

	Hyperperfusion (+)[b]	Hyperperfusion (-)[c]	Total	
EGFRvIII (+)	11	1	12	PPV: 91.67%
EGFRvIII (−)	13	16	29	NPV: 55.17%
Total	24	17	41	
Sensitivity	45.83%			
Specificity		94.12%		

Note:—PPV indicates positive predictive value; NPV, negative predictive value; +, present; −, absent.
[a] Of 53 patients, 41 had EGFRvIII expression examined on postsurgical GBM tissue. Fisher exact test *P* value = .006.
[b] CBF map with pattern 1.
[c] CBF map with pattern 2.

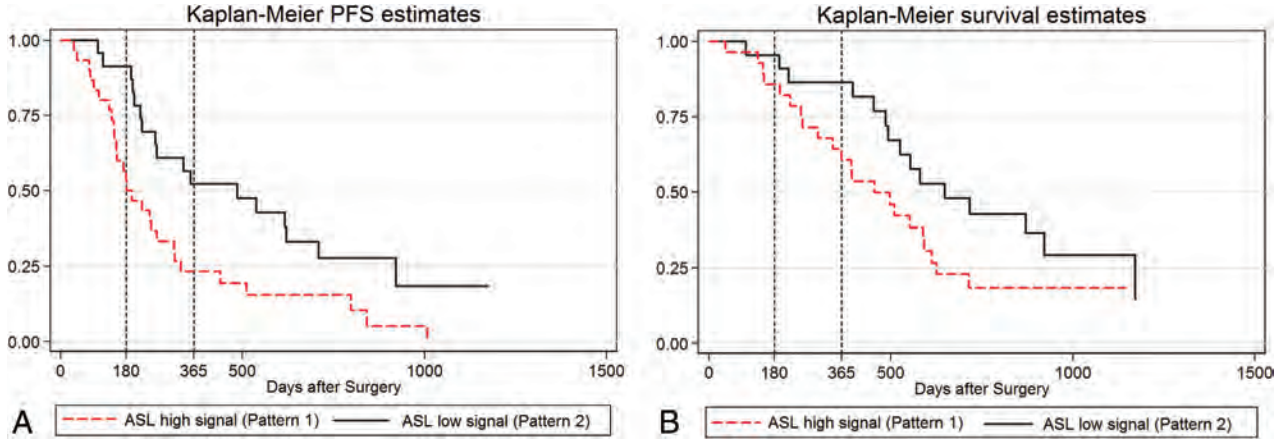

FIG 2. The Kaplan-Meier curve and log-rank test for progression-free survival and overall survival. GBM perfusion patterns are examined in their relationship to PFS (*A*) and OS (*B*). The x-axis shows days after surgery (baseline) with the vertical lines noting 6- and 12-month PFS (*A*) and 6- and 12-month OS (*B*), respectively. The y-axis represents the percentage not progressed.

ferentiation in the 2 perfusion patterns could be complicated in case of small tumors that are relatively difficult to identify by visual evaluation. However, this complication did not seem to cause a major problem for reader agreement because reading disagreements existed in only 4 of 53 cases (7.5%).

The visualization of hyperperfused tumor tissue in CBF maps could prove useful for tumor biopsy. One of the clinical challenges for brain tumor biopsy has been the underestimation of the histologic grade due to the stereotactic biopsy samples being only a small portion of the tumor. Identification and sampling from the tumor section with the highest angiogenesis and the cell proliferative rate are essential for adequate evaluation of the tumor grade. Given the correlation between ASL perfusion imaging and the attenuation of blood vessels in the tumor tissue,[15,16] it is reasonable to hypothesize that the macroscopic hyperperfused GBM tissue may represent a higher grade tumor. This hypothesis is supported by a study using DSC-PWI, which reported a significant association of tumor perfusion with the Ki67 index, a marker of cell proliferation.[6] Therefore, qualitative evaluation of the ASL CBF map may be of added value to multiparametric MR imaging (such as MR spectroscopy, apparent diffusion coefficient, and DSC) and PET/CT as a means of identifying highly proliferative tumor tissue for biopsy.

The perfusion patterns of ASL CBF maps in relation to clinical outcomes were examined by the Kaplan-Meier curve and log-rank test. ASL CBF pattern 1 (versus pattern 2) correlated with shorter PFS and trended with worse OS. Our finding is consistent with previous reports in which increased perfusion in high-grade glioma, as quantified by relative CBV derived from DSC-PWI, had significant correlation with poorer clinical outcomes.[11,31,32] Quantitative analysis that correlates parameters such as volumes and mean ASL values of the hyperperfused tumor tissue with clinical outcomes could further develop the potential value of ASL CBF maps as a predictor of tumor prognosis.

EGFRvIII is a truncated extracellular mutant of EGFR protein incapable of binding the epidermal growth factor family of ligands. However, it has been shown to be a constitutively tyrosine-phosphorylated persistent stimulation of growth activity.[20] Tykocinski et al[19] reported that relative CBV was a strong quantitative indicator of EGFRvIII expression in a study using DSC-PWI. Our study demonstrates a correlation between ASL CBF pattern 1 and EGFRvIII expression with a low sensitivity but high specificity. One possible explanation for the observed low sensitivity is that the hyperperfused tissue in GBM could be caused by effects from multiple genes and/or cross-talk between multiple cell-signaling pathways. For instance, alternative pathways are suggested by reports showing upregulation of the vascular endothelial growth factor with increased relative CBV.[19] The high specificity, however, might indicate that EGFRvIII expression alone has enough impact to generate the phenotype of macroscopic hyperperfused tissue in GBM.

The limitations of the present study include variability in therapies of the patient cohort, which may independently affect clinical outcome. However, all patients received standard therapy with radiation treatment and temozolomide, and recent data suggest that bevacizumab (which some patients received), while potentially prolonging progression-free survival by several months, has little impact on survival time.[33] Thus, the overall impact of therapy variability may be limited. Our study was also limited by a small sample size, reducing our ability to detect a potentially significant difference in overall survival (not merely progression-free survival) between patient cohorts. The potential value of ASL classifiers as a predictor of tumor prognosis and a marker of EGFRvIII expression requires verification in prospective studies. Although 2 perfusion patterns were identified in the CBF maps, a finding supported by data from quantitative analysis, potentially a more comprehensive quantitative approach, such as histogram analysis, could yield further classifiers of prognostic or predictive significance. However, our qualitative methodology has the advantage of not being reliant on extensive postprocessing, suggesting it could find utility in the real-time work flow of a busy clinical practice setting. One of the challenges for the widespread translation of ASL in clinical practice is that there is a wide range of ASL techniques and imaging protocols available from different vendors and developers. To address this issue, the recent ASL white paper[34] recommended pseudocontinuous ASL with a 3D readout and a relatively long postlabeling delay (eg, 2 seconds), which was used in the current study.

CONCLUSIONS

The qualitative evaluation of ASL CBF maps provides an expeditious method with high interobserver reliability that stratifies survival and predicts EGFRvIII expression in patients with GBM.

Disclosures: Benjamin M. Ellingson—*RELATED*: *Grant*: Genentech/Roche, Siemens. Danny JJ. Wang—*RELATED*: *Grant*: National Institutes of Health,* *Comments*: R01 EB014922/EB/NIBIB, R01 MH080892/MH/NIMH, R01 NS081077/NS/NINDS. Albert Lai—*UNRELATED*: *Consultancy*: Genentech/Roche,* *Comments*: Avastin Scientific Advisory Board. Timothy F. Cloughesy—*UNRELATED*: *Consultancy*: VBL, Proximagen, Tocagen, Genentech/Roche, Celgene, Lpath; *Expert Testimony*: Roche. *Money paid to the institution.

REFERENCES

1. Stupp R, Mason WP, van den Bent MJ, et al. **Radiotherapy plus concomitant and adjuvant temozolomide for glioblastoma.** *N Engl J Med* 2005;352:987–96
2. Van Meir EG, Hadjipanayis CG, Norden AD, et al. **Exciting new advances in neuro-oncology: the avenue to a cure for malignant glioma.** *CA Cancer J Clin* 2010;60:166–93
3. Louis DN, Ohgaki H, Wiestler OD, et al. **The 2007 WHO classification of tumours of the central nervous system.** *Acta Neuropathol* 2007;114:97–109
4. Arvinda HR, Kesavadas C, Sarma PS, et al. **Glioma grading: sensitivity, specificity, positive and negative predictive values of diffusion and perfusion imaging.** *J Neurooncol* 2009;94:87–96
5. Law M, Yang S, Wang H, et al. **Glioma grading: sensitivity, specificity, and predictive values of perfusion MR imaging and proton MR spectroscopic imaging compared with conventional MR imaging.** *AJNR Am J Neuroradiol* 2003;24:1989–98
6. Alexiou GA, Zikou A, Tsiouris S, et al. **Correlation of diffusion tensor, dynamic susceptibility contrast MRI and (99m)Tc-tetrofosmin brain SPECT with tumour grade and Ki-67 immunohistochemistry in glioma.** *Clin Neurol Neurosurg* 2014;116:41–45
7. Yoon JH, Kim JH, Kang WJ, et al. **Grading of cerebral glioma with multiparametric MR imaging and 18F-FDG-PET: concordance and accuracy.** *Eur Radiol* 2014;24:380–89
8. Weber MA, Henze M, Tüttenberg J, et al. **Biopsy targeting gliomas: do functional imaging techniques identify similar target areas?** *Invest Radiol* 2010;45:755–68
9. Hu LS, Eschbacher JM, Dueck AC, et al. **Correlations between per-**

fusion MR imaging cerebral blood volume, microvessel quantification, and clinical outcome using stereotactic analysis in recurrent high-grade glioma. *AJNR Am J Neuroradiol* 2012;33:69–76
10. LaViolette PS, Cohen AD, Prah MA, et al. **Vascular change measured with independent component analysis of dynamic susceptibility contrast MRI predicts bevacizumab response in high-grade glioma.** *Neuro Oncol* 2013;15:442–50
11. Mangla R, Ginat DT, Kamalian S, et al. **Correlation between progression free survival and dynamic susceptibility contrast MRI perfusion in WHO grade III glioma subtypes.** *J Neurooncol* 2014;116: 325–31
12. Law M, Young RJ, Babb JS, et al. **Gliomas: predicting time to progression or survival with cerebral blood volume measurements at dynamic susceptibility-weighted contrast-enhanced perfusion MR imaging.** *Radiology* 2008;247:490–98
13. Wang DJ, Alger JR, Qiao J, et al. **The value of arterial spin-labeled perfusion imaging in acute ischemic stroke: comparison with dynamic susceptibility contrast-enhanced MRI.** *Stroke* 2012;43: 1018–24
14. Wang DJ, Alger JR, Qiao J, et al. **Multi-delay multi-parametric arterial spin-labeled perfusion MRI in acute ischemic stroke— comparison with dynamic susceptibility contrast enhanced perfusion imaging.** *Neuroimage Clin* 2013;3:1–7
15. Warmuth C, Gunther M, Zimmer C. **Quantification of blood flow in brain tumors: comparison of arterial spin labeling and dynamic susceptibility weighted contrast-enhanced MR imaging.** *Radiology* 2003;228:523–32
16. Noguchi T, Yoshiura T, Hiwatashi A, et al. **Perfusion imaging of brain tumors using arterial spin-labeling: correlation with histopathologic vascular density.** *AJNR Am J Neuroradiol* 2008;29:688–93
17. Chawla S, Wang S, Wolf RL, et al. **Arterial spin-labeling and MR spectroscopy in the differentiation of gliomas.** *AJNR Am J Neuroradiol* 2007;28:1683–89
18. Kim HS, Kim SY. **A prospective study on the added value of pulsed arterial spin-labeling and apparent diffusion coefficients in the grading of gliomas.** *AJNR Am J Neuroradiol* 2007;28:1693–99
19. Tykocinski ES, Grant RA, Kapoor GS, et al. **Use of magnetic perfusion-weighted imaging to determine epidermal growth factor receptor variant III expression in glioblastoma.** *Neuro Oncol* 2012; 14:613–23
20. Zhan Y, O'Rourke DM. **SHP-2-dependent mitogen-activated protein kinase activation regulates EGFRvIII but not wild-type epidermal growth factor receptor phosphorylation and glioblastoma cell survival.** *Cancer Res* 2004;64:8292–98
21. Gan HK, Kaye AH, Luwor RB. **The EGFRvIII variant in glioblastoma multiforme.** *J Clin Neurosci* 2009;16:748–54
22. Feldkamp MM, Lala P, Lau N, et al. **Expression of activated epidermal growth factor receptors, Ras-guanosine triphosphate, and mitogen-activated protein kinase in human glioblastoma multiforme specimens.** *Neurosurgery* 1999;45:1442–53
23. Pelloski CE, Ballman KV, Furth AF, et al. **Epidermal growth factor receptor variant III status defines clinically distinct subtypes of glioblastoma.** *J Clin Oncol* 2007;25:2288–94
24. Nagane M, Levitzki A, Gazit A, et al. **Drug resistance of human glioblastoma cells conferred by a tumor-specific mutant epidermal growth factor receptor through modulation of Bcl-XL and caspase-3-like proteases.** *Proc Natl Acad Sci U S A* 1998;95:5724–29
25. Mellinghoff IK, Wang MY, Vivanco I, et al. **Molecular determinants of the response of glioblastomas to EGFR kinase inhibitors.** *N Engl J Med* 2005;353:2012–24
26. Raizer JJ. **HER1/EGFR tyrosine kinase inhibitors for the treatment of glioblastoma multiforme.** *J Neurooncol* 2005;74:77–86
27. Wen PY, Macdonald DR, Reardon DA, et al. **Updated response assessment criteria for high-grade gliomas: response assessment in neuro-oncology working group.** *J Clin Oncol* 2010;28:1963–72
28. Louis DN, Holland EC, Cairncross JG. **Glioma classification: a molecular reappraisal.** *Am J Pathol* 2001;159:779–86
29. Yoshimoto K, Dang J, Zhu S, et al. **Development of a real-time RT-PCR assay for detecting EGFRvIII in glioblastoma samples.** *Clin Cancer Res* 2008;14:488–93
30. Wang J, Alsop DC, Song HK, et al. **Arterial transit time imaging with flow encoding arterial spin tagging (FEAST).** *Magn Reson Med* 2003;50:599–607
31. Schmainda KM, Prah M, Connelly J, et al. **Dynamic-susceptibility contrast agent MRI measures of relative cerebral blood volume predict response to bevacizumab in recurrent high-grade glioma.** *Neuro Oncol* 2014;16:880–88
32. Essock-Burns E, Lupo JM, Cha S, et al. **Assessment of perfusion MRI-derived parameters in evaluating and predicting response to antiangiogenic therapy in patients with newly diagnosed glioblastoma.** *Neuro Oncol* 2011;13:119–31
33. Piccioni DE, Lai A. **Deferred use of bevacizumab for recurrent glioblastoma is not associated with diminished efficacy.** *Neuro Oncol* 2014;16:1427–28
34. Alsop DC, Detre JA, Golay X, et al. **Recommended implementation of arterial spin-labeled perfusion MRI for clinical applications: a consensus of the ISMRM perfusion study group and the European consortium for ASL in dementia.** *Magn Reson Med* 2014 Apr 8. [Epub ahead of print]

Iterative Probabilistic Voxel Labeling: Automated Segmentation for Analysis of The Cancer Imaging Archive Glioblastoma Images

T.C. Steed, J.M. Treiber, K.S. Patel, Z. Taich, N.S. White, M.L. Treiber, N. Farid, B.S. Carter, A.M. Dale, and C.C. Chen

ABSTRACT

BACKGROUND AND PURPOSE: Robust, automated segmentation algorithms are required for quantitative analysis of large imaging datasets. We developed an automated method that identifies and labels brain tumor–associated pathology by using an iterative probabilistic voxel labeling using k-nearest neighbor and Gaussian mixture model classification. Our purpose was to develop a segmentation method which could be applied to a variety of imaging from The Cancer Imaging Archive.

MATERIALS AND METHODS: Images from 2 sets of 15 randomly selected subjects with glioblastoma from The Cancer Imaging Archive were processed by using the automated algorithm. The algorithm-defined tumor volumes were compared with those segmented by trained operators by using the Dice similarity coefficient.

RESULTS: Compared with operator volumes, algorithm-generated segmentations yielded mean Dice similarities of 0.92 ± 0.03 for contrast-enhancing volumes and 0.84 ± 0.09 for FLAIR hyperintensity volumes. These values compared favorably with the means of Dice similarity coefficients between the operator-defined segmentations: 0.92 ± 0.03 for contrast-enhancing volumes and 0.92 ± 0.05 for FLAIR hyperintensity volumes. Robust segmentations can be achieved when only postcontrast T1WI and FLAIR images are available.

CONCLUSIONS: Iterative probabilistic voxel labeling defined tumor volumes that were highly consistent with operator-defined volumes. Application of this algorithm could facilitate quantitative assessment of neuroimaging from patients with glioblastoma for both research and clinical indications.

ABBREVIATIONS: BV = blood vessel; CEV = contrast-enhancing volume; DICE = Dice similarity coefficient; FHV = FLAIR hyperintensity volume; GMM = Gaussian mixture modeling; IPVL = iterative probabilistic voxel labeling; KNN = k-nearest neighbor; T1wCE = T1WI with contrast enhancement; TCIA = The Cancer Imaging Archive; TCGA = The Cancer Genome Atlas

Glioblastoma is the most common primary brain tumor and remains one of the deadliest human cancers.[1] During the past 50 years, improvement with regard to patient outcomes has been marginal.[2] A major barrier in therapeutic development is attributable to the misconception that glioblastoma constitutes a single disease. Molecular profiling has revealed that glioblastoma comprises multiple subtypes characterized by distinct molecular pathways.[3] To improve the clinical outcome of patients with glioblastoma, technologies must be developed to distinguish these subtypes.

There are compelling reasons that MR imaging may serve as a tool for dissecting the variability of glioblastoma. First, radiographic data are available for every patient because the clinical management of glioblastoma tumors is largely driven by the interpretation of MR images. Second, available data suggest that the radiographic appearance of glioblastoma is related to its physiologic state.[4,5] To better define this relationship, imaging archives with corresponding genomic profiling, such as The Cancer Imaging Archive (TCIA), have been launched (http://cancerimagingarchive.net/).

Much of the early work correlating MR imaging appearances of glioblastoma tumors with genomic profiling was performed by using manually delineated tumor volumes or qualitative assessments provided by trained clinicians.[4,5] These approaches are limited by the inherent variability of subjective interpretation, and significant

Received August 15, 2014; accepted after revision September 30.

From the Neurosciences Graduate Program (T.C.S.), School of Medicine (T.C.S., J.M.T.), Multimodal Imaging Laboratory (N.S.W., N.F., A.M.D.), Department of Radiology (N.F., A.M.D.), and Center for Theoretical and Applied Neuro-Oncology, Division of Neurosurgery, Moores Cancer Center (T.C.S., J.M.T., K.S.P., Z.T., M.L.T., B.S.C., C.C.C.), University of California, San Diego, La Jolla, California; and Weill-Cornell Medical College (K.S.P.), New York Presbyterian Hospital, New York, New York.

C.C.C. is supported by the Doris Duke Charitable Foundation Clinical Scientist Development Award, Sontag Foundation Distinguished Scientist Award, Burroughs Wellcome Fund Career Awards for Medical Scientists, Kimmel Scholar award, a Discovery Grant from the American Brain Tumor Association, and a National Cancer Institute K12 award.

Please address correspondence to Clark C. Chen, MD, PhD, Division of Neurosurgery, University of California, San Diego, 3855 Health Science Dr, #0987, La Jolla, CA 92093-0987; e-mail: clarkchen@ucsd.edu

Indicates open access to non-subscribers at www.ajnr.org

Indicates article with supplemental on-line tables.

http://dx.doi.org/10.3174/ajnr.A4171

interrater discrepancies have been reported.[6,7] Additionally, manual segmentation is time-consuming for large datasets. This limitation is particularly apparent when multiple radiographic features require segmentation. To address these deficiencies, effort has been devoted to developing automated algorithms for segmenting tumor volumes.[8-12] These algorithms include clustering,[13,14] discriminative strategies,[15] and generative approaches.[11,16,17] The success of these methods has been limited by widely differing MR imaging protocols for image acquisition and quality[18] and the significant overlap between the radiographic appearance of glioblastoma tumors and normal cerebrum on MR imaging. Although many of these methods can generate high-quality volumes from a training set, segmentation algorithms may fail when applied to images acquired by using different protocols.

We hypothesized that a probabilistic approach by using subject-specific classifiers would reliably discriminate glioblastoma from the surrounding cerebrum. In this algorithm, termed iterative probabilistic voxel labeling (IPVL), sparse, high-specificity, preliminary volumes were created for each subject by using a combination of region-growing and K-means-based tissue segmentation. Sampling of these preliminary volumes trained k-nearest neighbor (KNN) and Gaussian mixture model (GMM) classifiers by using voxel intensity and spatial coordinates. Voxel labels are assigned probabilistically by iteratively trained classifiers. Finally, each voxel is labeled as contrast-enhancing tumor volume (CEV), FLAIR hyperintensity volume (FHV), gray matter, white matter, CSF, and blood vessel (BV). Most important, our algorithm reliably segments images from the TCIA that were acquired by a variety of scanners and protocols.

MATERIALS AND METHODS

The Cancer Imaging Archive

MR images of glioblastoma tumors from The Cancer Imaging Archive were downloaded in June 2013. We identified subjects who underwent MR imaging before surgery and had a full complement of imaging, including the following: T1-weighted imaging, T1-weighted imaging with contrast enhancement (T1wCE), T2-weighted imaging, and FLAIR. Subjects were excluded when images contained a prohibitive amount of motion or distortion artifacts. Our algorithm was developed in a "pilot" set of 10 subjects from the TCIA. The algorithm was tested in 2 sets of 15 subjects selected from the TCIA that were not used during development. TCIA MR images were acquired from a number of institutions whose scanners differed by manufacturer and model and whose images varied by sequence, quality, and spatial resolution. (On-line Tables 1 and 2).

Preprocessing

Images were preprocessed by using a combination of in-house and external software including the FMRIB Software Library[19,20] (FSL, Version 5.0; http://fsl.fmrib.ox.ac.uk/fsl). Image distortions caused by gradient nonlinearity warping were corrected by using previous methods,[21-23] followed by bias-field correction by using the FMRIB Automated Segmentation Tool (FAST),[24] and were registered to the Montreal Neurological Institute-152 nonlinear sixth-generation standard brain image.[25] Affine registration was performed by using the FMRIB Linear Image Registration Tool (FLIRT).[26,27] To ensure removal of nonbrain tissues (eg, skull, optic nerve, and carotid arteries), we created a stringent brain mask from the T1WI by using a modified combination of the FSL Brain Extraction Tool[24] and the Robust Brain Extraction tool (https://www.nitrc.org/projects/robex).[28] Briefly, this method automatically compared the resultant brain with the volume derived from applying the Montreal Neurological Institute brain mask. Overestimation of >10% would adjust the fractional intensity, resulting in more restrictive brain outlines.

Preliminary Segmentation

It was crucial to generate highly specific volumes that accurately represented the range of intensity and spatial distribution for each tissue label to appropriately train our segmentation algorithm to recognize each subject's features. After skull stripping, initial tissue segmentation into preliminary WM, GM, CSF, and CEVs was performed for the available T1WI sequences by using FAST.[24] The FAST-derived initial CEV consisted of both tumor-associated CEV and BV volumes. The preliminary BV volume was distinguished from the FAST-derived CEV by performing 2 morphology-based manipulations. First, CEV objects located near the cortical surface were selectively removed by using a uniform spheric 3-mm erosion of the brain mask applied to the FAST-derived CEVs. Large vessels, such as the dural veins and carotid arteries, were removed by this operation due to their proximity to the brain surface. Second, a modified region-growing algorithm was used to identify vessels that were continuous with the venous sinuses. Region-growing was seeded in the region of the torcula (confluence of the sinuses), which was identified on the template image, to which all images were registered. Voxels identified as vessels by the combination of these methods were labeled as preliminary BV volume, while the remaining CEV was assigned to preliminary tumor-associated CEV.

The FHV preliminary volume was created by first determining and applying an automatic threshold for the FLAIR image by using the Otsu method.[29] FLAIR hyperintense regions on MR imaging may be tumor-associated or non-tumor-associated (eg, periventricular or pericortical). The non-tumor-associated hyperintense elements were excluded by using a spheric 3-mm erosion performed on the brain mask, while spheric 3-mm dilation was performed on the CSF volume. Together, these operations removed pericortical hyperintensities and the periventricular hyperintensities from the remainder of the preliminary FHVs.

Approximately 25% of voxels were labeled at this time. The voxels labeled were randomly sampled from regions that had the highest specificity to a particular volume of interest. For contrast enhancement, these included regions of contrast enhancement not continuous with the sagittal and transverse sinus. For FLAIR hyperintensity, these included regions above an intensity threshold >1.5 SDs above the mean intensity of the FLAIR image. The voxels assigned to each preliminary tissue label were used as the basis for training probabilistic classifiers (KNN and GMM). Voxels that were not classified into these categories during preliminary volume segmentation remained unassigned to avoid adding noise to the classifiers.

K-Nearest Neighbor and Gaussian Mixture Model Classifiers

The classifiers used to assign voxel membership were KNN and GMM. The KNN algorithm is a nonparametric method that assigns membership of a single datum on the basis of a number of

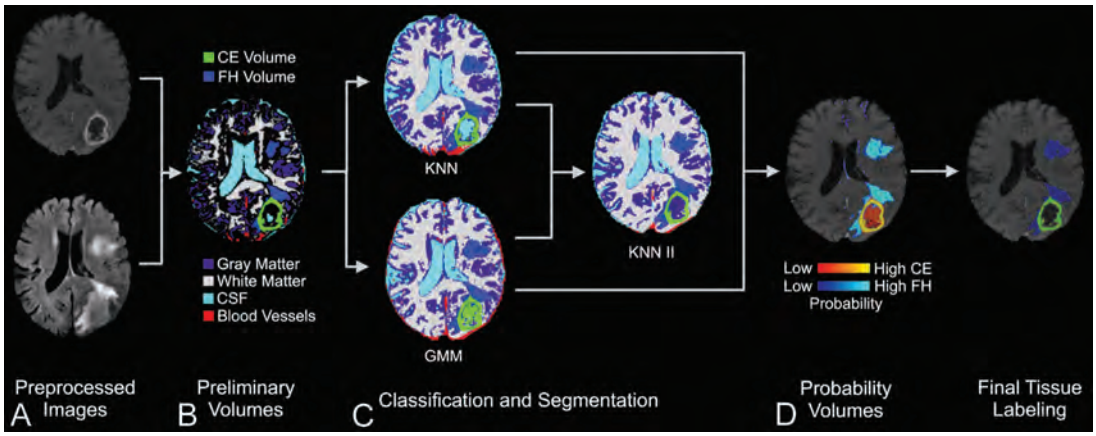

FIG 1. Work flow for iterative probabilistic voxel labeling. *A*, Downloaded TCIA images were preprocessed. *B*, Preliminary segmentation was performed to generate conservative yet highly specific preliminary volumes. *C*, In the classification step, these volumes were used to train the GMM and KNN probabilistic classifiers. The consensus of KNN and GMM classification was resampled and used to train a new classifier (KNN II), which assigned voxel tissue labels. The classifiers integrated their respective outputs to generate tissue-specific probability volumes. *D*, The voxels were assigned on the basis of their greatest probability of membership to a tissue label, and a voxel continuity filter was applied to eliminate clusters of less than 150 continuous voxels.

neighboring training examples.[30,31] GMM allows statistical clustering of data into a predefined number of Gaussian distributions, which, in this case, represent distinct imaging features. Use of these 2 probabilistic classifiers was complementary.

To expedite processing and improve accuracy, we used a weighted random sampling of the preliminary volume voxels to train both KNN and GMM classifiers. The weights for sampling reflected the relative distribution of voxels assigned to tissue labels from preliminary segmentation. Weighting was performed to avoid biasing the classifiers toward any particular tissue label caused by overrepresentation attributed to sampling error. Training was performed on a subject-by-subject basis, meaning that each patient was segmented according to his or her own subject-specific classifier by using both intensity and spatial data from each voxel to define labels. After training, all voxels, including those that were unassigned during preliminary volume creation, were classified independently by both KNN and GMM probabilistically to the 6 tissue labels: CEV, FHV, CSF, GM, WM, and BV. The probability of membership for each voxel was determined by a distance metric from classifier training. For each voxel, the greatest tissue label probability determined voxel labeling. Classifier consensus was resampled and used to re-train another iteration of KNN classification at a higher voxel sampling rate. This step had the benefit of reducing noise introduced during the creation of preliminary volumes, improving both the smoothness of the final volumes and the accuracy of the tissue labels.

Final Segmentation

Voxel label probabilities from all classifiers were summed, including the iterative KNN classification, for each tissue label, and a final segmentation volume was created by assigning voxels according to the highest probability membership to each tissue label. At this time, all voxels were probabilistically assigned. A voxel continuity filter was applied that removed discontinuous clusters of limited connectivity (fewer than 150 contiguous voxels). To address voxels that had equal probabilities of belonging to $\geq$2 tissue labels, we set priority in the following manner from greatest to least: CEV > FHV > BV to ensure that individual voxel tissue labels were mutually exclusive. This order was determined by the confidence of labeling each feature.

Segmentation Evaluation

To assess segmentation quality, we drew CEVs and FHVs manually for 2 sets of 15 subjects selected randomly from the available pool downloaded from the TCIA. These volumes were completed by 2 independent trained operators under the supervision of a neuroradiologist (N.F.) and a neurosurgeon (C.C.C.). Manual delineation of tumor-associated volumes was performed by using the software program AMIRA (http://www.vsg3d.com/amira/overview), using threshold-assisted segmentation on whole-brain T1wCE and FLAIR images that were registered to the Montreal Neurological Institute template. Operator-derived volumes were compared with IPVL-derived volumes by using the Dice similarity coefficient (DICE). This coefficient assesses the similarity between 2 volumes by dividing twice the sum of the intersection by the sum of both volumes.[32] Interoperator similarity was also compared by using this metric. A DICE equal to 1 would imply perfect similarity and overlap of 2 volumes.

Minimum Image Requirement for Adequate Segmentation

To assess the performance of our method when fewer imaging sequences were available for input, we implemented IPVL on a group of 15 subjects multiple times while removing $\geq$1 image, recapitulating common image combinations seen within the TCIA subjects. The segmentations that resulted from these image combinations were compared with operator volumes to determine their DICE similarities. FHVs were not segmented in image combinations that lacked FLAIR sequences.

RESULTS

Overview of the Automated Segmentation Algorithm

The steps of our segmentation protocol, applied to a representative case, are illustrated in Fig 1. Generally, our segmentation

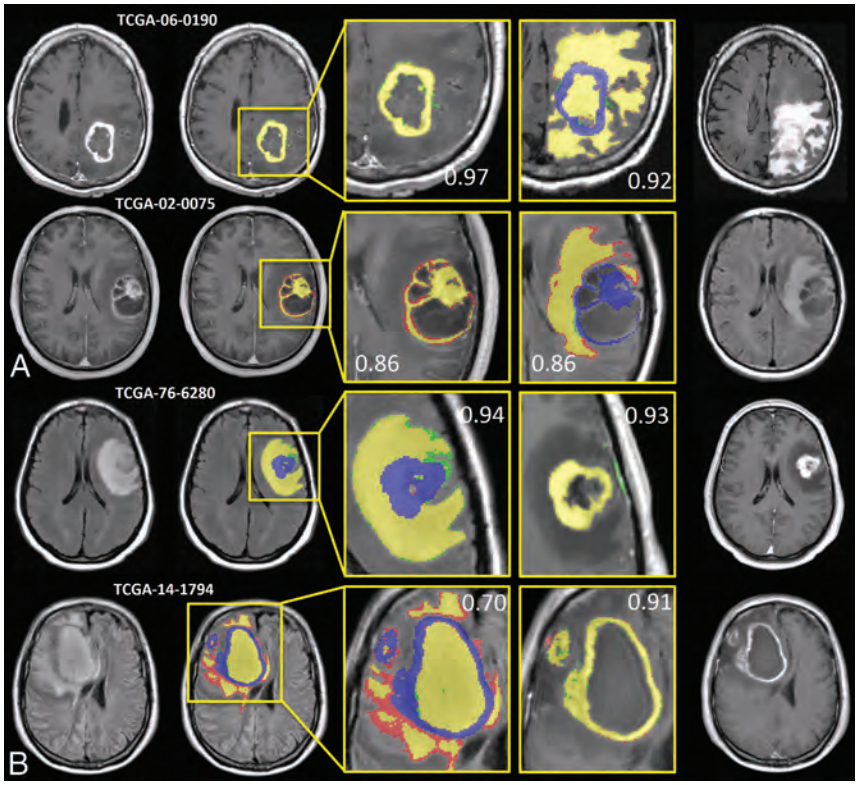

FIG 2. IPVL segment volumes that are highly analogous to operator-defined volumes. Results from 4 subjects representing the highest and lowest Dice similarity coefficient scores for CEV and FHV segmentations are shown. *A*, The highest DICE (*top*) and lowest DICE (*bottom*) examples of IPVL-segmented CEVs relative to operator-defined volumes are shown. The corresponding FHV segmentation results are shown (*right*) to demonstrate that CEV segmentations are independent of FHV segmentations. *B*, The highest DICE (*top*) and lowest DICE (*bottom*) examples of IPVL-segmented FHV relative to operator-defined volumes are shown. The corresponding CEV segmentation results are shown as well (*right*) to demonstrate that FHV segmentations are independent of CEV segmentations. Yellow indicates regions of intersection between operator and IPVL-defined volumes; red, operator-defined volume only; green, IPVL-defined volume only. Corresponding CEV segmentations are overlaid in blue on FLAIR images for clarity.

work flow was divided into 5 stages: preprocessing, preliminary segmentation, classification, probability labeling, and final segmentation. In preprocessing, images were loaded. Bias field correction, skull stripping, and registration to the template were then performed. The results of preprocessing created images in standard space to provide input for preliminary segmentation. Preliminary segmentation assigned voxel labels to CEV, FHV, BV, CSF, GM, WM, and unassigned (for voxels with ambiguous membership) by using k-means-based tissue segmentation and a region-growing algorithm. During classification, voxels sampled from these preliminary labels were used to train the GMM and KNN classifiers. All voxels were then classified to independent labels to identify CEV, FHV, BV, CSF, GM, and WM volumes. During probability labeling, each voxel was assigned a probability of membership to each tissue label. In the last step, final segmentation, voxels were labeled according to their greatest probability, and a voxel continuity filter was applied to eliminate clusters of $<$150 continuous voxels. The average time required to complete segmentation was 11.12 $\pm$ 5.63 minutes.

Manual Segmentation Comparison

Examples from 4 subjects that represented the CEVs and FHVs with the highest and lowest DICE scores relative to operator 1 are shown in Fig 2. Corresponding FHV segmentations for CEV and CEV segmentations for FHV are included to show that segmentation success for 1 feature is not necessarily correlated with segmentation success for corresponding features. Analysis showed no statistical difference among operator-derived volumes, so operator 1 was selected as the basis for image comparison ($P = .72$ for CEV interoperator, and $P = .39$ for FHV interoperator). Figure 2 demonstrates that the algorithm generates highly analogous CEVs and FHVs relative to those derived manually.

IPVL CEVs were statistically indistinguishable from volumes generated by expert operators across all subjects ($P = .93$). DICE scores, for automated CEVs, relative to operators 1 and 2, averaged 0.923 and 0.921, respectively. These DICE scores were highly comparable with those obtained from interoperator analysis (average of 0.923, Fig 3*A*). For automated FHVs, the DICE scores relative to operators 1 and 2 averaged 0.851 and 0.827, respectively. DICE scores obtained from interoperator analysis averaged 0.905 (Fig 3*B*). Analysis revealed that FHVs were slightly lower than interoperator comparison ($P = .04$). We observed that FHV DICE scores were poorer than CEV DICE scores for both the interoperator and the operator-algorithm comparisons. Overall, the DICE scores for both CEV and FHV achieved through our algorithm were improved or similar relative to those previously reported.[14-20]

To ensure that these results were generalizable, we randomly selected 15 additional subjects for analysis. The results from this analysis are highly comparable with those reported above. DICE scores for automated CEVs relative to operators 1 and 2 averaged 0.921 and 0.901, respectively. These DICE scores were highly comparable with those obtained from interoperator analysis (DICE = 0.905). For automated FHVs, the DICE scores relative to operators 1 and 2 averaged 0.846 and 0.823, respectively. DICE scores obtained from interoperator analysis averaged 0.812.

It was possible that difficult cases, including tumors with multifocal patterns, or tumors with attachment to large vessels or the brain surface, may cause errors in automatic segmentation. Of the images analyzed, 2 glioblastomas (The Cancer Genome Atlas [TCGA]-06–0139, TCGA-06–0166) were multifocal. For these subjects, IPVL-defined CEV and FHV showed mean DICE scores of 0.94 (range, 0.92–0.95) and 0.92 (range, 0.91–0.93) relative to expert defined volumes, respectively. Seven tumors (TCGA-02–0048, TCGA-06–0164, TCGA-08–0358, TCGA-76–6280, TCGA-76–6192, TCGA-76–5386, and HF1139) were located on

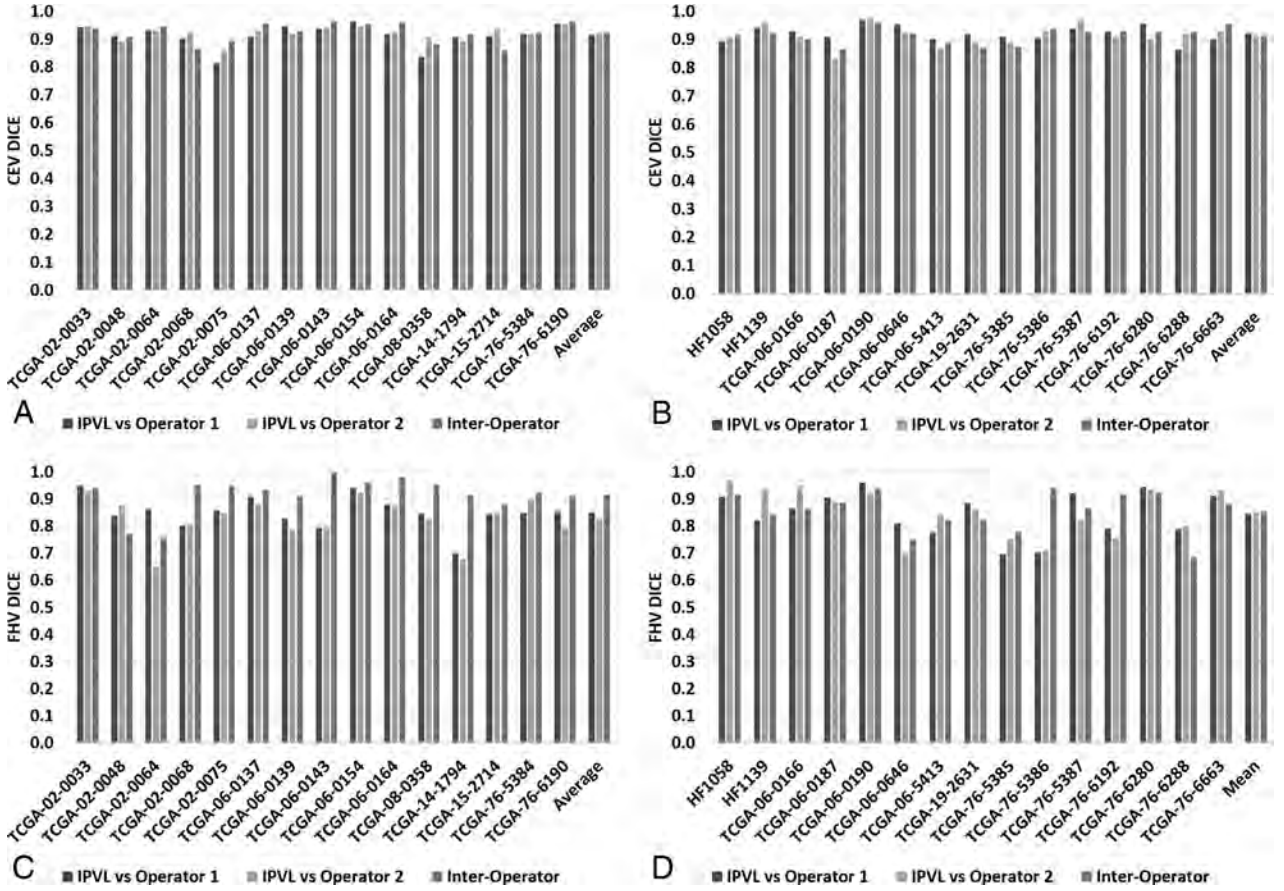

FIG 3. Quantitative comparison between IPVL-defined volumes and operator-derived volumes compared with interoperator comparisons. *A* and *B*, DICE comparisons for 2 sets of IPVL-defined and operator-defined CEVs are shown. DICE scores were calculated comparing CEVs generated by IPVL, operator 1, and operator 2. *C* and *D*, DICE score comparisons for IPVL-defined and operator-defined FHVs. DICE scores were calculated comparing FHVs generated by IPVL, operator 1, and operator 2.

the surface of the cerebrum. For these tumors, IPVL-defined CEV and FHV showed mean DICE scores of 0.92 (range, 0.84–0.96) and 0.84 (range, 0.70–0.95). One tumor (TCGA-76–5385) was attached to a major vessel (the MCA). For this tumor, IPVL-defined CEV and FHV showed mean DICE scores of 0.90 (range, 0.89–0.91) and 0.72 (range, 0.70–0.75). These results suggest that our algorithm performs adequately in anatomic locations and in difficult cases that are historically challenging to previously published algorithms.

Minimal Image Requirement for Adequate Segmentation

The TCIA and other image databases include many subjects who do not have the full complement of T1WI, T1wCE, T2WI, and FLAIR images. In the TCIA, this full set of imaging was available in only 52% of subjects. Therefore, it was of interest to determine how our algorithm would perform when limited imaging modalities were available. To this end, we examined how the sequential removal of the various image sequences impacted segmentation performance. DICE scores were determined for a subject's segmentations by using each combination of images relative to operator-defined volumes. These DICE scores were plotted compared with the DICE scores derived from segmentations by using all 4 imaging sequences.

For CEV segmentations, removal of T1WI and T2WI did not significantly affect performance. The DICE scores obtained when comparing volumes delineated by using only T1wCE and FLAIR were comparable with those obtained when all 4 imaging sequences were processed by our algorithm (Fig 4*A*). Similarly, FHV segmentations were minimally impacted by image reduction, and DICE scores by using all 4 imaging sequences were comparable with those obtained when using only T1wCE and FLAIR (Fig 4*B*).

To further characterize the impact of reducing the number of image sequences on the performance of CEV and FHV segmentations, we also plotted the range of DICE scores that resulted from removing ≥1 image series for each subject. For most subjects, removing images minimally impacted DICE scores—that is, the segmentation quality was not significantly altered (Fig 4*C* for CEV, Fig 4*D* for FHV). For FHV segmentations, removal of T2WI and T1WI did not significantly alter segmentation performance (Fig 4*D* for FHV).

Only 2 subjects, TCGA-02–0068 and TCGA-06–0164, had increased vessel contamination of the CEVs when FLAIR images were removed during image-reduction analysis. CEV segmentations for image combinations that contained at least a FLAIR and T1wCE image were highly comparable across all subjects (Fig 4*E*). While adequate CEV segmentation required only T1wCE for most cases, FLAIR images improved CEV and BV discrimination and may be required for segmentation in a subset of subjects.

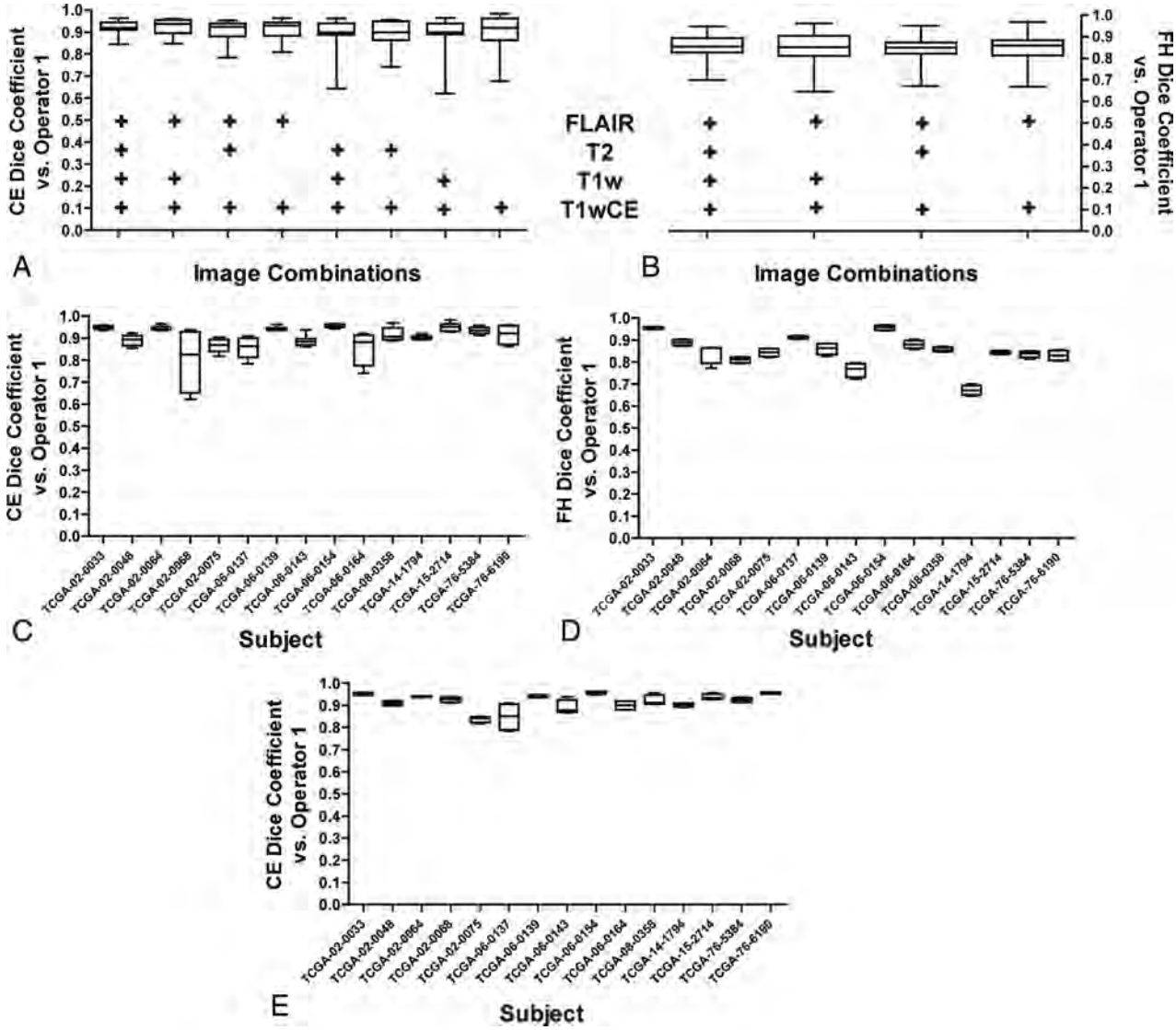

FIG 4. Effects of removing image sequences on IPVL segmentation. *A*, Select image sequences (such as T1WI) were removed before IPVL CEV segmentations for each subject. The image sequences that were available during IPVL segmentation are indicated by a plus sign. DICE scores were calculated for the resultant CEVs relative to operator 1–defined CEVs. The distribution of DICE scores across all subjects because of image sequence removal is shown as a boxplot. *B*, Select image sequences were removed before IPVL FHV segmentations. DICE scores were calculated for the resultant FHV segmentations relative to operator 1–defined FHVs. The distribution of DICE scores across all subjects due to image-sequence removal is shown as a boxplot. *C*, A boxplot demonstrates the range of DICE scores for IPVL-segmented CEVs relative to operator-defined CEVs per patient for all image combinations tested. *D*, A boxplot demonstrates the range of DICE scores for IPVL-segmented FHVs relative to operator-defined FHVs per patient for all image combinations tested. *E*, A boxplot demonstrates the range of DICE scores for IPVL-segmented CEVs relative to operator-defined CEVs per patient when only T1WI and FLAIR source images were used for IPVL segmentation.

Most surprising, CEV segmentation for T1wCE and FLAIR alone was nearly identical to CEV segmentation results that used all available imaging series. These results suggest that our algorithm requires only T1wCE and FLAIR images for robust volume segmentation of both tumor-associated CEVs and FHVs.

DISCUSSION

The success of any automated segmentation process hinges on the a priori definition of the features that constitute a volume of interest. Human vision can integrate visual data along with both experience and assumption to distinguish and classify independent features. This task is often challenging for a computer because the cross-section of data available to the computer is often simplified. We hypothesized that the complexity of image segmentation could be largely recapitulated by using iterating probabilistic classifiers trained on sparse subject-specific preliminary features. To test this hypothesis, we predefined the voxels that were most likely associated with the features of interest to generate preliminary volumes. We then used k-nearest neighbor and GMM probabilistic classifiers to refine the segmentation process. In our algorithm, these complementary probabilistic classifiers were integrated in an iterative manner to converge on a segmentation result for the various features of an MR image. Our results demonstrate that IPVL image segmentation is highly comparable with segmentations that were drawn manually.

Most important, the time required for segmentation per subject averaged 11.2 minutes when all 4 image sequences were used. In contrast, manual segmentation by experts required 1–3

hours depending on the size and complexity of the volume to be segmented. As such, our method presents an opportunity for high-throughput quantitative analysis of TCIA images and other imaging databases. The insensitivity of our algorithm to interinstitutional methodologic differences in MR imaging supports its utility for this application. Further supporting the utility of our algorithm, we demonstrated that only 2 image sequences (the T1wCE and FLAIR images) are needed for reliable segmentation of tumor CEVs and FHVs. Finally, using a common template space will provide a platform for future analyses, intersubject comparisons, and longitudinal studies.

While our study was focused on the development of an algorithm for research use in terms of radiographic biomarker discovery, reliable volume segmentation by using our algorithm may also impact clinical practice. For example, it is often difficult to detect subtle differences in the radiographic appearance of a tumor during disease progression. As a result, changes in serial MR imaging may be underappreciated until a patient becomes symptomatic. Automated segmentation and longitudinal quantitative comparison may help facilitate the detection of subtle radiographic changes, such as tumor progression, thereby allowing clinicians to perform procedures to prevent clinical deterioration in select patients. Application of these methods may also aid the evaluation of the therapeutic response in clinical trials.

Careful study of the discrepancies between the volumes generated by IPVL and expert-defined volumes revealed a few limitations. The algorithm can fail to detect tumor contrast enhancement or FLAIR hyperintensity in regions of these volumes that fall below a single voxel (~1 mm). This limitation, a result of voxel sampling and partial volume effect, could be mitigated with higher resolution imaging. In a few subjects (eg, TCGA-02–0068, TCGA-06–0154), reliable delineation of BV volume from tumor CEVs remained challenging when image combinations lacking FLAIR images were used for segmentation, leading us to conclude that FLAIR and T1wCE are required for our method. Segmentation of FLAIR volumes remains a challenge, but this challenge is shared by the human eye as demonstrated by the interobserver discrepancies reported previously. The use of higher order image processing, such as textural analysis, may facilitate the improvement of our algorithm in the near future.

CONCLUSIONS

We demonstrate that iterative probabilistic voxel labeling is a reliable and robust tool for automatic segmentation of MR images in the TCIA dataset. Application of this method could facilitate quantitative radiographic assessment of glioblastoma for both researchers and clinicians alike.

Disclosures: Anders M. Dale—*RELATED*: *Grant*: National Institutes of Health,* Department of Defense,* National Science Foundation*; *UNRELATED*: *Grants/Grants Pending*: National Institutes of Health,* Department of Defense,* National Science Foundation*; *Patents (planned, pending or issued)*: University of California, San Diego,* CorTechs,* Labs Inc*; *Stock/Stock Options*: CorTechs, Labs Inc, Human Longevity Inc, *Comments*: I hold equity in CorTechs Labs Inc and serve on its Scientific Advisory Board. I am also a member of the Scientific Advisory Board of Human Longevity Inc; the terms of these arrangements have been reviewed and approved by the University of California, San Diego, in accordance with its conflict of interest policies; *Other*: GE Healthcare,* Medtronic,* *Comments*: I receive support from GE Healthcare and Medtronic under Research Agreements with the University of California, San Diego. *Money paid to the institution.

REFERENCES

1. Omuro A, DeAngelis LM. **Glioblastoma and other malignant gliomas: a clinical review.** *JAMA* 2013;310:1842–50
2. Minniti G, Muni R, Lanzetta G, et al. **Chemotherapy for glioblastoma: current treatment and future perspectives for cytotoxic and targeted agents.** *Anticancer Res* 2009;29:5171–84
3. Brennan CW, Verhaak RG, McKenna A, et al. **The somatic genomic landscape of glioblastoma.** *Cell* 2013;155:462–77
4. Diehn M, Nardini C, Wang DS, et al. **Identification of noninvasive imaging surrogates for brain tumor gene-expression modules.** *Proc Natl Acad Sci U S A* 2008;105:5213–18
5. Gutman DA, Cooper LA, Hwang SN, et al. **MR imaging predictors of molecular profile and survival: multi-institutional study of the TCGA glioblastoma data set.** *Radiology* 2013;267:560–69
6. Deeley MA, Chen A, Datteri R, et al. **Comparison of manual and automatic segmentation methods for brain structures in the presence of space-occupying lesions: a multi-expert study.** *Phys Med Boil* 2011;56:4557–77
7. Weltens C, Menten J, Feron M, et al. **Interobserver variations in gross tumor volume delineation of brain tumors on computed tomography and impact of magnetic resonance imaging.** *Radiother Oncol* 2001;60:49–59
8. Zhu Y, Young GS, Xue Z, et al. **Semi-automatic segmentation software for quantitative clinical brain glioblastoma evaluation.** *Acad Radiol* 2012;19:977–85
9. Diaz I, Boulanger P, Greiner R, et al. **An automatic brain tumor segmentation tool.** *Conf Proc IEEE Eng Med Biol Soc* 2013;2013:3339–42
10. Harati V, Khayati R, Farzan A. **Fully automated tumor segmentation based on improved fuzzy connectedness algorithm in brain MR images.** *Comput Boil Med* 2011;41:483–92
11. Prastawa M, Bullitt E, Moon N, et al. **Automatic brain tumor segmentation by subject specific modification of atlas priors.** *Acad Radiol* 2003;10:1341–48
12. Zikic D, Glocker B, Konukoglu E, et al. **Decision forests for tissue-specific segmentation of high-grade gliomas in multi-channel MR.** *Med Image Comput Comput Assist Interv* 2012;15:369–76
13. Phillips WE 2nd, Phuphanich S, Velthuizen RP, et al. **Automatic magnetic resonance tissue characterization for three-dimensional magnetic resonance imaging of the brain.** *J Neuroimaging* 1995;5:171–77
14. Clark MC, Hall LO, Goldgof DB, et al. **Automatic tumor segmentation using knowledge-based techniques.** *IEEE Trans Medi Imaging* 1998;17:187–201
15. Lee CH, Wang S, Murtha A, et al. **Segmenting brain tumors using pseudo-conditional random fields.** *Med Image Comput Comput Assist Interv* 2008;11(pt 1):359–66
16. Prastawa M, Bullitt E, Ho S, et al. **A brain tumor segmentation framework based on outlier detection.** *Med Image Anal* 2004;8:275–83
17. Menze B, van Leemput K, Lashkari D, et al. **A generative model for brain tumor segmentation in multi-modal images.** In: Jiang T, Navab N, Pluim JW, et al, eds. *Medical Image Computing and Computer-Assisted Intervention: MICCAI 2010.* Berlin: Springer-Verlag Berlin; 2010:151–59
18. Gordillo N, Montseny E, Sobrevilla P. **State of the art survey on MRI brain tumor segmentation.** *Magn Reson Imaging* 2013;31:1426–38
19. Jenkinson M, Beckmann CF, Behrens TE, et al. **FSL.** *Neuroimage* 2012;62:782–90
20. Smith SM, Jenkinson M, Woolrich MW, et al. **Advances in functional and structural MR image analysis and implementation as FSL.** *Neuroimage* 2004;23(suppl 1):S208–19
21. Dale AM, Fischl B, Sereno MI. **Cortical surface-based analysis. I. Segmentation and surface reconstruction.** *Neuroimage* 1999;9:179–94

22. Jovicich J, Czanner S, Greve D, et al. **Reliability in multi-site structural MRI studies: effects of gradient non-linearity correction on phantom and human data.** *Neuroimage* 2006;30:436–43
23. Holland D, Kuperman JM, Dale AM. **Efficient correction of inhomogeneous static magnetic field-induced distortion in echo planar imaging.** *Neuroimage* 2010;50:175–83
24. Smith SM. **Fast robust automated brain extraction.** *Hum Brain Mapp* 2002;17:143–55
25. Grabner G, Janke AL, Budge MM, et al. **Symmetric atlasing and model based segmentation: an application to the hippocampus in older adults.** *Med Image Comput Comput Assist Interv* 2006;9(pt 2):58–66
26. Jenkinson M, Smith S. **A global optimisation method for robust affine registration of brain images.** *Med Image Anal* 2001;5:143–56
27. Jenkinson M, Bannister P, Brady M, et al. **Improved optimization for the robust and accurate linear registration and motion correction of brain images.** *Neuroimage* 2002;17:825–41
28. Iglesias JE, Liu CY, Thompson PM, et al. **Robust brain extraction across datasets and comparison with publicly available methods.** *IEEE Trans Med Imaging* 2011;30:1617–34
29. Otsu N. **A threshold selection method from gray-level histograms.** *IEEE Transactions on Systems, Man, and Cybernetics* 1979;9:62–66
30. Steenwijk MD, Pouwels PJ, Daams M, et al. **Accurate white matter lesion segmentation by k nearest neighbor classification with tissue type priors (kNN-TTPs).** *Neuroimage Clin* 2013;3:462–69
31. Anbeek P, Vincken KL, van Bochove GS, et al. **Probabilistic segmentation of brain tissue in MR imaging.** *Neuroimage* 2005;27:795–804
32. Dice LR. **Measures of the amount of ecologic association between species.** *Ecology* 1945;26:297–302

Dynamic Contrast-Enhanced Perfusion Processing for Neuroradiologists: Model-Dependent Analysis May Not Be Necessary for Determining Recurrent High-Grade Glioma versus Treatment Effect

J.D. Hamilton, J. Lin, C. Ison, N.E. Leeds, E.F. Jackson, G.N. Fuller, L. Ketonen, and A.J. Kumar

ABSTRACT

BACKGROUND AND PURPOSE: Dynamic contrast-enhanced perfusion MR imaging has proved useful in determining whether a contrast-enhancing lesion is secondary to recurrent glial tumor or is treatment-related. In this article, we explore the best method for dynamic contrast-enhanced data analysis.

MATERIALS AND METHODS: We retrospectively reviewed 24 patients who met the following conditions: 1) had at least an initial treatment of a glioma, 2) underwent a half-dose contrast agent (0.05-mmol/kg) diagnostic-quality dynamic contrast-enhanced perfusion study for an enhancing lesion, and 3) had a diagnosis by pathology within 30 days of imaging. The dynamic contrast-enhanced data were processed by using model-dependent analysis (nordicICE) using a 2-compartment model and model-independent signal intensity with time. Multiple methods of determining the vascular input function and numerous perfusion parameters were tested in comparison with a pathologic diagnosis.

RESULTS: The best accuracy (88%) with good correlation compared with pathology ($P = .005$) was obtained by using a novel, model-independent signal-intensity measurement derived from a brief integration beginning after the initial washout and by using the vascular input function from the superior sagittal sinus for normalization. Modeled parameters, such as mean endothelial transfer constant > 0.05 minutes^{-1}, correlated ($P = .002$) but did not reach a diagnostic accuracy equivalent to the model-independent parameter.

CONCLUSIONS: A novel model-independent dynamic contrast-enhanced analysis method showed diagnostic equivalency to more complex model-dependent methods. Having a brief integration after the first pass of contrast may diminish the effects of partial volume macroscopic vessels and slow progressive enhancement characteristic of necrosis. The simple modeling is technique- and observer-dependent but is less time-consuming.

ABBREVIATIONS: AUC = area under the curve; DCE = dynamic contrast-enhanced perfusion MRI; K^{trans} = endothelial transfer constant; SSS = superior sagittal sinus; VIF = vascular input function; v_p = vascular plasma volume fraction

There are over 23,000 newly diagnosed malignant brain tumors in the United States every year.[1] Glioblastoma is one of the most common and devastating brain tumors. Most patients survive <1 year from diagnosis if untreated. Despite the large number of potential treatments that have been used, only modest gains in mortality (9–12 months of life gained) have been made due to tumor recurrence.[2] A variety of treatment-related changes occur on normal brain tissues related to the effects of radiation and chemotherapy, such as temozolomide.[3] Delayed radiation-/treatment-induced brain necrosis is one of the effects that can cause an enlarging, enhancing mass. This can mimic recurrent tumor on conventional CT or MR imaging, with few clues as to the diagnosis.[4]

Delayed radiation necrosis may be a result of progressive, obliterative endarteritis resulting in hypoxia,[5] with an immune inflammatory response. Treatments include steroids, hyperbaric oxygen,[5] bevacizumab (antivascular endothelial growth factor) in resistant cases,[6,7] or surgical resection for pending herniation. With recurrent gliomas (astrocytomas and oligodendrogliomas, most commonly glioblastoma), single agent or combination chemotherapy and/or additional surgery or radiation therapy may be sought.[8]

Received September 13, 2012; accepted after revision August 27, 2014.

From the Department of Diagnostic Radiology, Section of Neuroimaging (J.D.H., C.I., N.E.L., L.K., A.J.K.), Department of Imaging Physics, Section of MRI Physics (J.L., E.F.J.), and Department of Pathology, Section of Neuropathology (G.N.F.), The University of Texas M.D. Anderson Cancer Center, Houston, Texas; Radiology Partners Houston (J.D.H.), Houston, Texas; Rice University (J.L.), Houston, Texas; and Baylor College of Medicine (J.L.), Houston, Texas.

This work was supported by the M.D. Anderson Levit Distinguished Chairman Funds.

Paper previously presented at: Annual Meeting of the American Society Neuroradiology, June 4–9, 2011; Seattle, Washington.

Please address correspondence to Jackson D. Hamilton, MD, Radiology Partners Houston, 5301 Hollister Dr, Suite 350, Houston, TX 77040; e-mail: Jackson.hamilton@radpartners.com

http://dx.doi.org/10.3174/ajnr.A4190

MR perfusion techniques, such as dynamic contrast-enhanced (DCE) and dynamic susceptibility contrast perfusion examinations, have been shown to be useful in differentiating delayed radiation-induced necrosis from recurrent glial tumor.[9-12] A combined parameter approach further improves accuracy.[13] DCE data can be either model-independent or model-dependent. Model-independent indices rely on the T1 signal intensity increase by using gadolinium contrast. In the initial first pass of contrast (vascular phase), the signal change is related to the blood volume in the tissue of interest.[9] After the concentration of gadolinium in the blood begins to equilibrate with the second and third passes of contrast, the leakage of contrast from the vessel to the interstitial space (extravascular, extracellular space) becomes an increasingly important factor in the signal-intensity enhancement. Various model-independent parameters by using the area under the curve of signal intensity with time have been proposed in the pharmacologic literature.[14]

Model-dependent indices are often derived from a 2-compartment model.[15] In this model or its derivatives, the intravascular and interstitial spaces are treated as having a certain volume fraction (eg, v_p [vascular plasma volume fraction]) with both forward (endothelial transfer constant [K^{trans}]) and backward constants to explain the kinetics across a membrane (ie, the blood-brain barrier). These values are derived from a deconvolution that compares the dynamic T1 signal changes with contrast in a region of interest with a vascular input function (VIF).[16] There is considerable variability as to the best method to choose the VIF, either by using an artery or a vein or having an algorithm that chooses the pixels by curve-fitting clusters of pixels.[17] There has been recent debate on whether simple model-independent analysis[10] of signal intensity with time may perform as well as more complex compartmental models.[9,18] The following article seeks the best DCE analysis for improving the accuracy of determining delayed radiation-induced necrosis versus recurrent glioma, by using various model-dependent and -independent parameters and VIF methodology.

MATERIALS AND METHODS

Patient Population

With institutional review board approval, the data from patients were retrospectively gathered from January 2009 to January 2012. Inclusion criteria required that the patient have the following: 1) prior diagnosis of glioma that had been previously treated, including conventional standards of radiation therapy and usually temozolomide; 2) parenchymal brain enhancement that progressed over successive imaging studies; 3) diagnostic quality protocol including a half-dose contrast agent DCE protocol (0.05 mmol/kg at rate 4 mL/s); 4) biopsy or resection within 30 days of the protocol; and 5) older than 18 years of age. Demographic and treatment data were recorded.

Imaging Acquisition

All imaging data were obtained on an HDxt 3T MR imaging scanners by using a multichannel phased array head coil (GE Healthcare, Milwaukee, Wisconsin). Following any required standard-of-care precontrast agent imaging, DCE data were acquired by using a T1-weighted 3D fast-spoiled gradient-echo technique. Images were acquired with a temporal resolution of 5.1 seconds before, during, and up to 4 minutes after administration of 0.05-mmol/kg gadopentetate dimeglumine (Magnevist; Bayer HealthCare Pharmaceuticals, Wayne, New Jersey) followed by a 20-mL saline flush. These were injected by an MR imaging–compatible automated system at 4 mL/s. Half-dose DCE was performed before subsequent full-dose dynamic susceptibility contrast perfusion imaging as part of the imaging protocol. DCE parameters included the following: TE, 1.8 ms; TR, 4 ms; 256 × 160 matrix; 24 × 18 cm FOV; sixteen 5-mm thick contiguous sections (8-cm coverage); and total scan time of approximately 5 minutes. This imaging yielded approximately 36 time points with a reconstructed voxel resolution of approximately 1.0 × 1.0 × 5.0 mm. The MR imaging examination concluded with any necessary standard-of-care postcontrast agent–enhanced imaging.

Image Processing

DCE Analysis Method 1. A 2-compartment generalized kinetic model[15] was used with the technique proposed by Murase et al,[16] including motion correction as implemented in the software package nordicICE (NordicNeuroLab, Bergen, Norway). A 3-parameter analysis was performed to yield values of endothelial transfer constant related to contrast leaving the vessel, the reflux rate constant related to contrast re-entering the vessel, and the vascular plasma volume fraction related to the percentage volume of blood vessels. The values of the extravascular, extracellular volume fraction (interstitial space) were then computed from the ratio of K^{trans} over the reflux rate constant. Recorded values included mean and maximum. In addition, model-independent parameters (ie, area under the curve [AUC], initial AUC, and maximum slope) were also computed with both scaled and unscaled values to the VIF.

Several methods for detecting the VIF were tested. With a previously described algorithm,[17] which picked 5 clusters of voxels that are expected to be vessels on the basis of the dynamic signal response, VIFs were generated from the following: 1) whole-brain images; 2) a region of interest confined to the vertical portion of the superior sagittal sinus (SSS), which avoided feeding veins causing mixing artifacts in the same section (further described in method 2 below); and 3) a region of interest surrounding the M1 to M2 bifurcation of the MCA ipsilateral to the lesion. Additionally, a fourth method was used with all pixels in a region of interest placed in the SSS. A deconvolution algorithm was used to generate maps of the parameters of interest.[16] Oval lesion ROIs were placed over the area of enhancement by a radiologist (J.D.H.) and trainee (J.L.), blinded to the pathology results. The lesion region-of-interest locations were maintained through the multiple processing options with different VIFs. The values were recorded for the axial image with the maximum K^{trans} value.

DCE Analysis Method 2. A simple, model-independent analysis evaluated the relative change in signal intensity with time. The AUC was an integration of the enhancing region of interest of the lesion divided by the VIF (Advantage Workstation, Version 4.3 or 4.4; GE Healthcare). The VIF from a ~1-cm-diameter oval region of interest was placed in the SSS. This region of interest was positioned in the vertical portion of the SSS, while avoiding feeding

veins entering the sinus at the same level, to decrease inhomogeneity from mixing artifacts. The lesion ROIs were defined by the contrast-enhancing area with the most signal change and contoured by 2 board-certified radiologists with neuroradiology fellowship training (J.D.H. and C.I.), blinded to the pathology results.

Multiple limits of the average AUC integration were evaluated. The starting time for VIF integration was the start of the first-pass contrast agent wash-in or at the end of contrast agent washout. The end time of integration was computed at 30, 60, 90, or 120 seconds after the arrival of the contrast bolus (wash-in). Additionally, an integration of just the time of the first pass of contrast agent (wash-in to washout) was used (similar timing to that of dynamic susceptibility plasma volume measurements). The region-of-interest positions were maintained across all time iterations for the AUC. Care was taken to avoid large central nonenhancing areas (due to cyst or necrosis) and medium-to-large vessels (by using source images from contrast-enhanced, T2, and gradient-echo images). The average values of the AUC for both the VIF and the user-defined area of contrast enhancement were recorded. The contrast-enhanced lesion AUC value was divided by the VIF AUC value and expressed as a percentage for each patient.

Pathologic Data

After imaging, the selected patients underwent either stereotactic biopsy or resection within 30 days of imaging as part of their clinical care. Medical records and follow-up imaging data were also followed to minimize the possibility of false pathologic results due to tissue undersampling. Pathology results were graded on a 5-point scale based on the pathology report rendered by a board-certified pathologist specializing in brain tumors. This ranged from nearly completely tumor (score = 1) to complete necrosis or other treatment-related effects (score = 5). Scores of 3 (small areas [~5 cells per high-power field] of viable tumor) and 4 (predominate necrosis with scattered atypical cells or rare mitosis, which did not progress within 6 months) were important because they delineated the categorization of recurrent tumor versus necrosis, respectively. Each pathology report was independently scored by 2 evaluators (J.D.H. and G.N.F.). In case of disagreement or an equivocal report, the pathology sample was re-evaluated by a board-certified neuropathologist (G.N.F.).

Statistics

The results of these 2 methods of perfusion analysis from the same datasets were compared with the pathology results. The Spearman nonparametric 2-tailed correlation was used to compare the perfusion data with the categoric ranked pathology grading, by using SPSS (IBM, Armonk, New York) and R, Version 3.0.1 (http://www.r-project.org). Additionally, post hoc arbitrary values were used to find optimal cutoff values for sensitivity, specificity, and accuracy, by using the cutoff in pathology grading of 3 and 4, as defined above. The Kaplan-Meier method was used to estimate the distribution of overall survival times from the time of the MR imaging examination, and groups were compared by using the log-rank test. Interrater reliability was calculated as both a percentage difference in values and κ statistics for the cutoff between grades 3 and 4 pathology reports.

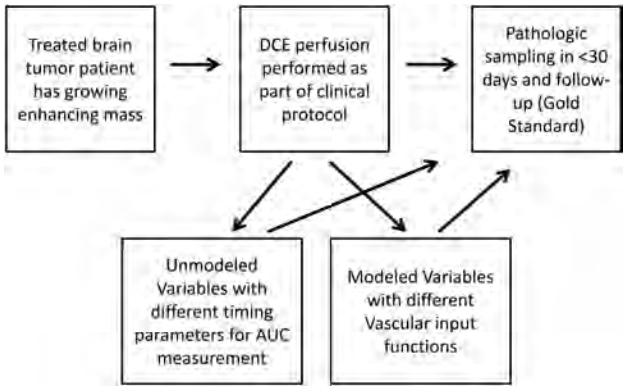

FIG 1. Overview diagram of the basic study design. This study tests the accuracy of DCE parameters in determining delayed radiation necrosis from recurrent glioma. Unmodeled parameters with varying times for the integration of DCE area under the curves and modeled parameters with varying locations/techniques for the vascular input function are tested. These are compared with the criterion standard of pathologic scoring and clinical follow-up.

RESULTS

Patient Population

Twenty-four patients met the inclusion criteria for the protocol, including biopsy within 30 days for suspicion of recurrent glioma with a progressively enhancing lesion on MR imaging. Of 200 patients evaluated with DCE under the protocol, 61 had biopsies. Twenty patients with biopsies were excluded because of a non-glioma primary tumor, no previous radiation therapy, or pathology sampling occurring >30 days after imaging. In addition, 17 patients were excluded due to a full-dose DCE examination (after an imaging protocol change). No patient was excluded due to the quality of the imaging.

There were 4 women and 20 men with an average age of 51 ± 9 years. Patients had previous diagnoses of glioblastoma (n = 15), anaplastic astrocytoma (n = 7), anaplastic oligodendroglioma (n = 1), and oligodendroglioma (n = 1). At least 3 glioblastomas were secondary by dedifferentiation, with older pathologic results showing lower grade tumor. The average time from radiation therapy completion to imaging was 2.6 ± 2.1 years, though 2 patients had the protocol within 6 months of therapy completion. Thus, in most patients, the clinical question was recurrent glioma versus delayed radiation-induced necrosis (rather than pseudoprogression). All except 1 patient had previous treatment with temozolomide. Seven patients had previous treatment with bevacizumab, with a variety of other chemotherapies and/or vaccines used in 9 patients. An overview of the study design is given in Fig 1.

Pathology Results and Follow-Up

Median follow-up was 24 months, with 1 patient having <3 months' follow-up. Of the 15 tumor recurrences (pathology score of 1–3), 13 patients (87%) had died at the time of data analysis. Nine patients had delayed radiation-induced necrosis by pathology (pathology score of 4 or 5), of which only 2 patients (22%) had died. There was a significant association between pathology

Comparison of DCE measurement with pathologic grading[a]

Measurement	Method	Nonparametric Coefficient	Significance (*P* Value)	Post Hoc Cutoff	Sensitivity	Specificity	Accuracy
Mean K^{trans}	1-Nordic	0.606	.002	$\geq$0.05 min^{-1}[b]	80%	78%	79%
Max K^{trans}	1-Nordic	0.542	.006	$\geq$0.2 min^{-1}	80%	78%	79%
Mean k_{ep}	1-Nordic	0.446	.03	$\geq$0.27 min^{-1}	47%	78%	58%
Mean v_p	1-Nordic	0.555	.005	>2[c]	71%	89%	79%
Max v_p	1-Nordic	0.513	.01	>9[c]	73%	67%	71%
Mean v_e	1-Nordic	0.566	.004	>12[c]	80%	78%	79%
Short AUC	2-Simple	0.410	.047	>12%[c]	93%	67%	84%
Intermediate AUC	2-Simple	0.478	.018	>14%[c]	93%	67%	84%
Delayed short AUC	2-Simple	0.556	.005	>20%[c,d]	93%	78%	88%

Note:—Delayed short AUC indicates ratio of AUC from the lesion over the superior sagittal sinus vascular input integrated between the end of the initial vascular washout and early progressive leakage phases; max, maximum; k_{ep}, reflux rate constant; v_e, extravascular, extracellular volume fraction.

[a] The methods given are for model-independent "simple" calculations of the signal with time (method 2) versus the pharmacokinetic model calculations using nordicICE (method 1). The pixel selection algorithm around the superior sagittal sinus was used for the latter. The nonparametric correlation to categoric ranking of pathology is given by a Spearman ρ correlation. Post hoc arbitrary cutoff values are given for the most accurate performance for determining tumor, with tumor (pathology grading of 1–3) regarded as a positive case for sensitivity and specificity.

[b] Best performing modeled variable for correlation with pathology.

[c] A relative unit.

[d] Best performing model independent variable.

score and overall survival (hazard ratio = 7.93 for tumor recurrence, $P = .002$). Both evaluators of the pathology report were within a point for all cases. One specimen was changed from a pathology score of 3 to 2 after review of the specimen. There was no disagreement between scores of 3 and 4.

Image Acquisition and Analysis

Method 1. To determine the best method for the nordicICE analysis (method 1), we tested 4 types of VIFs. The K^{trans} values from region-of-interest pixel choosing from the MCA or SSS worked better than whole-brain coverage when compared with pathology. The fourth method for defining the VIF by using the complete region of interest in the SSS was immediately excluded because some of the maximum K^{trans} values were reported as zero, which was not possible given the contrast enhancement of these areas indicating contrast escape from the vessel.

The Table demonstrates the best performing measurements for both methods 1 and 2. The best correlation to the pathologic grade by modeled values (method 1) was the mean extravascular extracellular volume fraction, the mean v_p, and the mean K^{trans} by VIF from pixel choosing in the SSS. Maximum K^{trans}, mean reflux rate constant, mean and maximum v_p, and mean AUC also had significant correlations for values with VIF from the region of the SSS but not from the region of the MCA. An example of the variation based on the VIF is given in Fig 2. The mean K^{trans} of $\geq$0.05 $minutes^{-1}$ for residual tumor from the VIF near the SSS had 2 false-positives and 3 false-negatives (sensitivity 80%, specificity 78%, and accuracy 79%). Although the model-independent values of scaled AUC and peak values did correlate to pathology, because they did not perform better than the best performing model-independent variable from method 2, they are not included in the Table.

Method 2. Of all the possible time iterations for the generation of normalized lesion AUC/VIF ratios (eg, wash-in to 90 seconds, washout to 60 seconds, and so forth), the integration from the end of the first-pass washout to 60 seconds after bolus arrival was the best model-independent measure correlated to the pathology grading (Spearman coefficient = −0.56, $P = .005$) and had the best accuracy of all measurements. The accuracy was 88% (93% sensitivity, 78% specificity) with 2 false-positives and 1 false-negative by using a cutoff value of >20% for tumor. It was termed "delayed short AUC" because it fell between the initial vascular washout and progressive leakage phases. This value correlated with mean/maximum K^{trans} (Spearman coefficient = 0.615/0.462, $P = .001/.021$) and mean/maximum v_p (Spearman coefficient = 0.570/0.441, $P = .004/.031$) by method 1. The delayed short AUC also correlated to the mean unscaled area under the curve from method 1 (Spearman coefficient = 0.487, $P = .016$); this outcome is expected because these are similar values without the use of model-dependent compartmental modeling.

The delayed short AUC outperformed the standard pharmacologic measurements of wash-in to 60 or 90 seconds (short and intermediate AUC, respectively). Graphic representations of delayed short AUC and intermediate AUC integrations used to derive these values are shown in Fig 3 in the case of tumor recurrence and Fig 4 for treatment-related necrosis. Note that the vascular input in the SSS on these figures happens to correspond to the axial image of the lesion location for ease of illustration, but this correspondence is often not the case. Also note, as explained in the legends, that the delayed short AUC by excluding the first pass of contrast is less sensitive to the large vessels, such as found in the VIF.

No additional arbitrary cutoff values for any of the parameters in method 1, with either the VIF from the SSS or MCA, performed as well as the delayed short AUC. The patients whose DCE values did not reflect pathology grading tended to have atypical treatment regimens such as prior vaccines or antivascular endothelial growth factor treatment (eg, bevacizumab). This finding is expected given the granulation tissue response, which can be created by locally delivered antitumor vaccines (false-positive) and the vascular normalizing effect of bevacizumab (false-negative).[19]

Intra- and Interreader Variability

For method 1, the second reader (J.L.) had a wide average variability of 49.8 ± 286.1% from reader 1 (J.D.H.) for mean K^{trans} (κ value of 0 for cutoff of mean $K^{trans} \geq 0.05$ min-

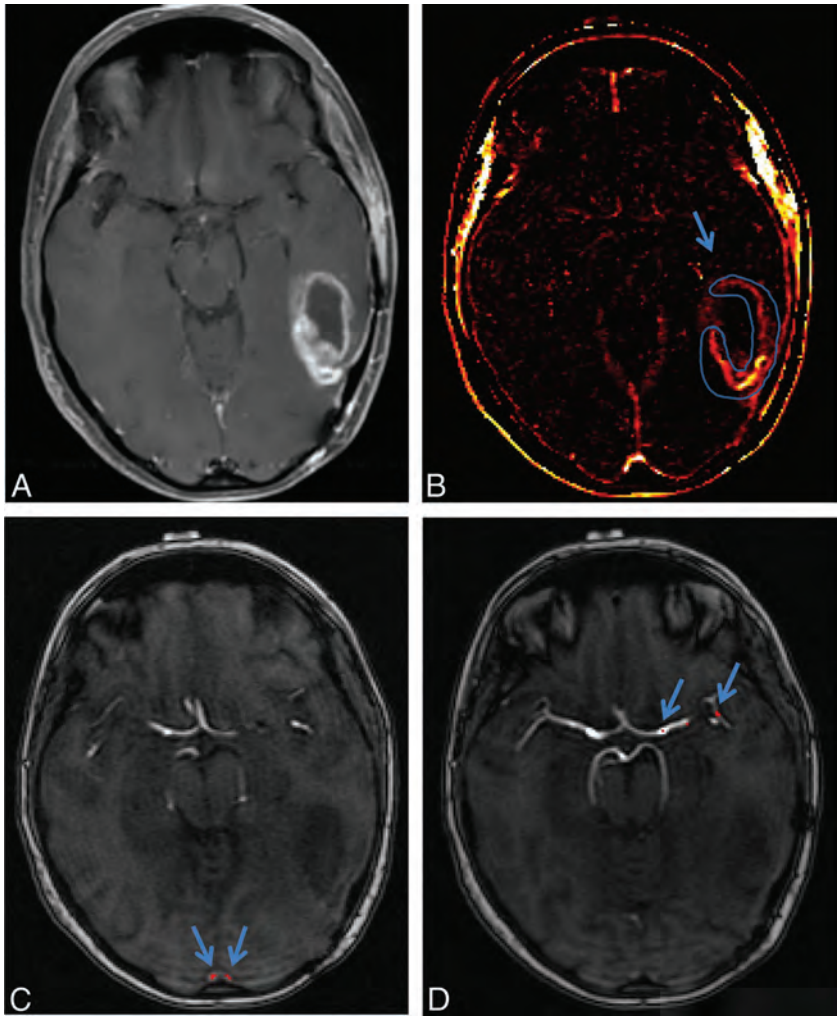

FIG 2. Example of a change in modeled values related to the location of the vascular input function. Note a left parietal ring-enhancing lesion on axial postcontrast T1 imaging (*A*) and DCE (*B*), which on subsequent pathology was recurrent glioblastoma with some superimposed treatment effects (pathology score of 2). A region of interest was drawn to cover the enhancing regions with sparing of the centrally necrotic portion. *C*, The pixels chosen by nordicICE for a region of interest in the superior sagittal sinus. *D*, The pixels chosen for the M1 and proximal M2 branches of the ipsilateral middle cerebral artery. By changing from SSS to MCA, the mean/maximum K^{trans} changed from 0.0165/0.169 to 0.283/3.003 in relative units, a 20× difference. The mean/maximum plasma volume changed from 0.652/4.94 to 5.49/34.87, a nearly 10× difference.

utes^{-11}). For method 2, the second reader (C.I.) had 14.7 ± 28.2% average variability for the short delayed AUC measurement compared with reader 1 (J.D.H). When the cutoff value of 20% was used, this yielded a κ value of 0.6, due to addition of 1 false-positive and 4 false-negatives. When the second reader repeated the measurement, there was 2.8 ± 28.8% average intrareader variability.

DISCUSSION

We compared a simple model-independent signal-intensity change analysis versus a 2-compartment pharmacokinetic model analysis, choice of vascular input function, and choice of analysis output parameters to determine the optimal method for determining delayed radiation-induced necrosis from recurrent glioma. A novel measurement based on model-independent analysis performed in a manner equivalent to the corrected 2-compartment modeling analysis for our dataset. Because method 2 was processed on the same workstation as the rest of the protocol, there was a substantial decrease in analysis time. It took ~10 minutes for method 1 with additional time required to transfer images to a separate workstation compared with ~5 minutes for method 2.

Argument for Model-Independent Modeling

There are several possible explanations for the delayed short AUC having worked well. First, not including the first pass of contrast agent results in relative resistance to the frequent issue of a large- or medium-sized vessel being within the same voxel or region of interest as the contrast-enhancing lesion (Figs 3 and 4). In some ways, this is like removing the signal usually gathered by gradient-echo dynamic susceptibility contrast perfusion on the first-pass of contrast for assessment of vascularity. Second, there is resistance to a greater value being generated primarily from the change in signal intensity occurring later due to slow progressive leakage, by having a relatively narrow range of integration (30–45 seconds). This is a characteristic of delayed radiation-induced necrosis (Fig 4). Third, by having the integration occur after the first-pass bolus and by using a venous rather than an arterial VIF, the tumor-related delay in mean transit time is less of an issue[20] (see "Vascular Input Function Importance" section). Thus, the signal in the delayed short AUC primarily is derived from the contrast escape or permeability from the vessel derived during the first pass of contrast after the contrast in the vessel has washed out. To a lesser degree, delayed short AUC corresponds to the second pass of contrast within the vessels, which relates to the microvascular attenuation/plasma volume. Thus, the observed signal change is a combination of pharmacokinetic model parameters K^{trans}, v_p, and reflux rate constant, as demonstrated by the correlation with the modeled parameters.

Our technique tried to limit variations in contrast agent bolus, with most wash-in and washout periods averaging 3–4 time points or 15–20 seconds. The average delayed short AUC measures incorporated ~9 time points (45 seconds) of data. If the bolus was slow to washout on VIF, a minimum of 30 seconds of integration time was used. Delayed short AUC differs from the initial AUC by 60–90 seconds because it does not include the first pass of the contrast agent bolus. The latter have been reported in the pharmacologic literature as robust parameters without modeling error,[14] but did not correlate as well in this study.

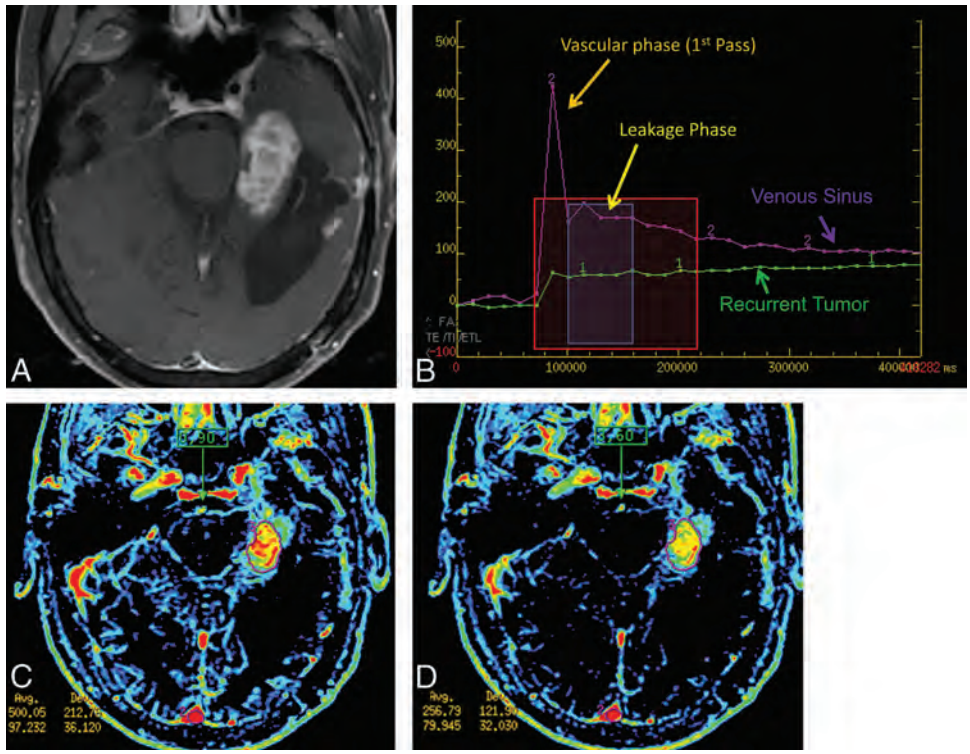

FIG 3. Example of recurrent glioblastoma by using 2 different AUC measurements. *A*, An enhancing lesion on T1WI involving the left parahippocampal region, which proved to be recurrent glioblastoma. *B*, A signal change over the time curve from the Advantage Workstation (GE Healthcare). The *pink curve* (voxel 2) is derived from the superior sagittal sinus (more inferior than normal positioning for illustration purposes) and demonstrates an initial vascular phase with the first pass of contrast washing in and then out. The *green curve* (voxel 1) demonstrates the signal change of a recurrent glioblastoma showing the initial rise of signal during the vascular phase followed by a slow rise during accumulated contrast escape or leakage of the contrast agent from the vessel. The *red box* demonstrates the time of integration for the "intermediate AUC" whose corresponding image is *C*, labeled "0.90." The *blue box* demonstrates the time of integration showing the values for the "delayed short AUC" over approximately 45 seconds, labeled "3.60." Notice in the corresponding image (*D*) that the cortical vessels are less well-seen than in *C* but the tumor remains (scaling is the same). Numerically, the vascular input decreases 49% (from an area under the curve of 500 to 257 relative units), while the tumor only decreases signal by 18% (97 to 80). Intermediate and delayed short AUC values from these data are 19% (97/500) and 31% (80/257), respectively.

Arguments against Simple Modeling

One weakness of the delayed short AUC measurement is that it is heavily dependent on user input. The values for the SSS can be widely variable if care is not taken to do the following: 1) use a large enough region of interest to reduce undersampling, 2) keep the region of interest completely within the venous sinus, and 3) pick an area that minimizes inhomogeneity due to inflow from unopacified veins or sections toward the edges of the imaging volume. For this latter point, we used the vertical portion of the superior sagittal sinus in a region that did not have a feeding vein within the axial image. The delayed short AUC measurement also helped by using the vascular information in a more steady-state compared with the volatility and regional variability in signal change of the first pass of contrast. Additionally, the user must also define the lesion region of interest on the basis of the contrast enhancement, and this region of interest will invariably differ from observer to observer.[21] These limitations are revealed in the interrater analysis, which shows wide variability and poorer performance by the second reader. Most surprising, the modeled data actually had greater variability, which may be partially attributed to the relative inexperience of the trainee. More sophisticated methods of volume rendering, segmentation, and histogram analysis have been reported,[21] which may further improve the reproducibility of mean values from the ROIs.

Of the 5 recommendations for measurement of K^{trans} or the initial area under the gadolinium concentration versus time curve made by a prior consensus group,[14] this study did not use T1 mapping and estimates of contrast agent relaxivity in tumor vasculature and tissue for converting signal-intensity change to contrast agent concentration. Our group thought these steps would add further error/inefficiency and work against the goal of obtaining a simple, time-efficient data analysis methodology. However, a VIF and power injector were used to improve reproducibility in a group of patients with heterogeneous cardiac output. Also, scanning sufficiently began before contrast arrival to establish a baseline, at least 5 time points before contrast wash-in. These steps are necessary for model-independent measurements, which are more dependent on changes in the acquisition technique compared with complex model-based analysis,[14,21] which has been our experience. The magnet strength, injection parameters, cardiac output, and so forth can all have nonlinear changes in the dynamic T1 response that make it challenging to compare results from various institutions.[14,21] Whatever the method chosen, consistency and pathologic validation are important for establishing it.

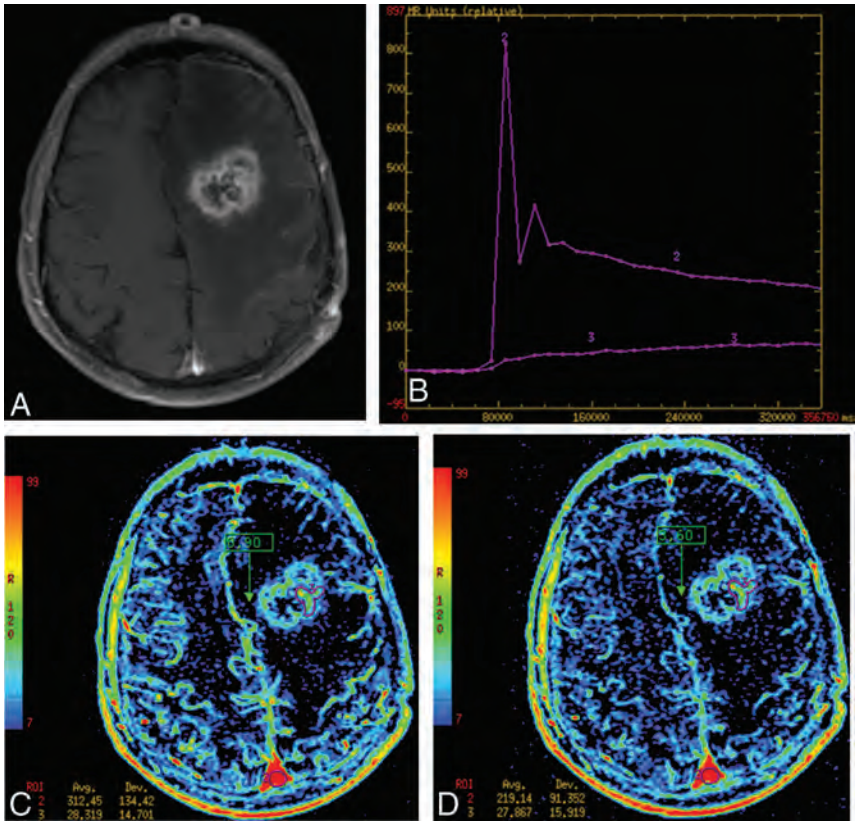

FIG 4. Example of treatment-related necrosis by using 2 different AUC measurements. *A*, An enhancing lesion on T1WI of the left frontal lobe, which was proved to be treatment-related necrosis (pathology grade = 5). *B*, A slow progressive increase in signal of the lesion compared with the vascular input and the lesion in *B*. *C* and *D*, the "intermediate AUC" and "delayed short AUC" integrations, respectively. Notice the significant drop in the superior sagittal sinus between these integrations (312 to 219 relative units) with little change in the lesion (it remains at 28). Intermediate and delayed short AUC values from these data are 9% (28/312) and 12% (28/219), respectively.

Vascular Input Function Importance

The method of VIF determination is important for determining clinically useful values. For this particular clinical question, the automated selection of pixels in a region near the superior sagittal sinus outperformed other locations for method 1. We compared the timing of wash-in and washout of the first bolus pass from the MCA and SSS regions with the image mean value. In 11 of the 24 cases, there was a delay in the start of the wash-in and/or a delay in the peak of the VIF for the SSS compared with the image mean timing. Similarly, 5 of the cases had early wash-in or peak compared with the image mean timing with VIF around the MCA. On average, the peaks were also lower for the MCA compared with the SSS (596 ± 461 versus 1457 ± 1272 in relative signal-intensity units, respectively). One possible reason that the VIF near the SSS worked better is that if there was to be a delay between the transit time of the lesion and the vein, there was still signal from contrast leakage and vascular recirculation in the enhancing lesion after the first pass. However, if the timing derived from the VIF was early, as with that derived from the MCA, this arrival may result in spuriously low-average results because the integration began before the first bolus pass reached the lesion and would have values near baseline T1. In other words, for the same increment of error in timing the VIF, there is probably less error in the measured values if it is late rather than early. The method of picking the VIF for the delayed short AUC was the least useful method when applied to method 1, because it forced the K^{trans} values to zero. This is likely because the SSS had such a large signal change that the contrast accumulation in the lesion was relatively insignificant in the model.

Further Study Limitations

A further limitation to any retrospective study is that the biopsy specimen location was not predetermined; therefore, the location could not be correlated directly back to a particular pixel or region-of-interest value. In addition, the pathology grading criteria were done retrospectively on the basis of reports and were confirmed in equivocal cases by pathology, rather than strict grading criteria, with actual percentage tumor estimations or automatic counts done prospectively. The total number of patients in this study was small. There was heterogeneity in the timing of imaging and the variety of treatments used.

CONCLUSIONS

Several methods of using DCE data were compared with the pathology for treatment-related effects versus recurrent high-grade gliomas; this comparison is relevant to clinical decision-making and survival. The results indicate that a measurement based on model-independent data analysis (delayed short AUC) performed at least as well as more complex model-based methods, with an accuracy of up to 88%. Because this measurement is technique- and observer-dependent, care must be taken to ensure reliability. Additionally, it is shown that vascular input function derived from the superior sagittal sinus is superior to that from the middle cerebral artery.

ACKNOWLEDGMENTS

We thank Dawid Schellingerhout, MB, ChB, and Kelly Duggan, The University of Texas M.D. Anderson Cancer Center; and Sandeep N. Gupta, PhD, GE Global Research Center, for their help in making this manuscript possible.

Disclosures: Claro Ison—*UNRELATED*: *Employment*: Cardinal MRI Center.

REFERENCES

1. Ostrom QT, Gittleman H, Liao P, et al. **CBTRUS statistical report: primary brain and central nervous system tumors diagnosed in the United States in 2007–2011.** *Neuro Oncol* 2014;16(suppl 4):iv1–iv63
2. Ballman KV, Buckner JC, Brown PD, et al. **The relationship between six-month progression-free survival and 12-month overall survival end points for phase II trials in patients with glioblastoma multiforme.** *Neuro Oncol* 2007;9:29–38

3. Yang I, Aghi MK. **New advances that enable identification of glioblastoma recurrence.** *Nat Rev Clin Oncol* 2009;6:648–57
4. Kumar AJ, Leeds NE, Fuller GN, et al. **Malignant gliomas: MR imaging spectrum of radiation therapy- and chemotherapy-induced necrosis of the brain after treatment.** *Radiology* 2000;217:377–84
5. Kohshi K, Imada H, Nomoto S, et al. **Successful treatment of radiation-induced brain necrosis by hyperbaric oxygen therapy.** *J Neurol Sci* 2003;209:115–17
6. Levin VA, Bidaut L, Hou P, et al. **Randomized double-blind placebo-controlled trial of bevacizumab therapy for radiation necrosis of the central nervous system.** *Int J Radiat Oncol Biol Phys* 2011;79:1487–95
7. Gonzalez J, Kumar AJ, Conrad CA, et al. **Effect of bevacizumab on radiation necrosis of the brain.** *Int J Radiat Oncol Biol Phys* 2007;67:323–36
8. Weller M, Cloughesy T, Perry JR, et al. **Standards of care for treatment of recurrent glioblastoma: are we there yet?** *Neuro Oncol* 2013;15:4–27
9. Bisdas S, Naegele T, Ritz R, et al. **Distinguishing recurrent high-grade gliomas from radiation injury: a pilot study using dynamic contrast-enhanced MR imaging.** *Acad Radiol* 2011;18:575–83
10. Narang J, Jain R, Arbab AS, et al. **Differentiating treatment-induced necrosis from recurrent/progressive brain tumor using nonmodel-based semiquantitative indices derived from dynamic contrast-enhanced T1-weighted MR perfusion.** *Neuro Oncol* 2011;13:1037–46
11. Barajas RF Jr, Chang JS, Segal MR, et al. **Differentiation of recurrent glioblastoma multiforme from radiation necrosis after external beam radiation therapy with dynamic susceptibility-weighted contrast-enhanced perfusion MR imaging.** *Radiology* 2009;253:486–96
12. Hu LS, Baxter LC, Smith KA, et al. **Relative cerebral blood volume values to differentiate high-grade glioma recurrence from post-treatment radiation effect: direct correlation between image-guided tissue histopathology and localized dynamic susceptibility-weighted contrast-enhanced perfusion MR imaging measurements.** *AJNR Am J Neuroradiol* 2009;30:552–58
13. Zeng QS, Li CF, Liu H, et al. **Distinction between recurrent glioma and radiation injury using magnetic resonance spectroscopy in combination with diffusion-weighted imaging.** *Int J Radiat Oncol Biol Phys* 2007;68:151–58
14. Leach MO, Brindle KM, Evelhoch JL, et al. **The assessment of antiangiogenic and antivascular therapies in early-stage clinical trials using magnetic resonance imaging: issues and recommendations.** *Br J Cancer* 2005;92:1599–610
15. Tofts PS, Kermode AG. **Measurement of the blood-brain barrier permeability and leakage space using dynamic MR imaging. 1. Fundamental concepts.** *Magn Reson Med* 1991;17:357–67
16. Murase K, Yamazaki Y, Miyazaki S. **Deconvolution analysis of dynamic contrast-enhanced data based on singular value decomposition optimized by generalized cross validation.** *Magn Reson Med Sci* 2004;3:165–75
17. Mouridsen K, Christensen S, Gyldensted L, et al. **Automatic selection of arterial input function using cluster analysis.** *Magn Reson Med* 2006;55:524–31
18. Sourbron S, Ingrisch M, Siefert A, et al. **Quantification of cerebral blood flow, cerebral blood volume, and blood-brain-barrier leakage with DCE-MRI.** *Magn Reson Med* 2009;62:205–17
19. Pope WB, Young JR, Ellingson BM. **Advances in MRI assessment of gliomas and response to anti-VEGF therapy.** *Curr Neurol Neurosci Rep* 2011;11:336–44
20. Bjornerud A, Sorensen AG, Mouridsen K, et al. **T1- and T2*-dominant extravasation correction in DSC-MRI: part I—theoretical considerations and implications for assessment of tumor hemodynamic properties.** *J Cereb Blood Flow Metab* 2011;31:2041–53
21. Jackson A, O'Connor JP, Parker GJ, et al. **Imaging tumor vascular heterogeneity and angiogenesis using dynamic contrast-enhanced magnetic resonance imaging.** *Clin Cancer Res* 2007;13:3449–59

Imaging the Intracranial Atherosclerotic Vessel Wall Using 7T MRI: Initial Comparison with Histopathology

A.G. van der Kolk, J.J.M. Zwanenburg, N.P. Denswil, A. Vink, W.G.M. Spliet, M.J.A.P. Daemen, F. Visser, D.W.J. Klomp, P.R. Luijten, and J. Hendrikse

ABSTRACT

BACKGROUND AND PURPOSE: Several studies have attempted to characterize intracranial atherosclerotic plaques by using MR imaging sequences. However, dedicated validation of these sequences with histology has not yet been performed. The current study assessed the ability of ultra-high-resolution 7T MR imaging sequences with different image contrast weightings to image plaque components, by using histology as criterion standard.

MATERIALS AND METHODS: Five specimens of the circle of Wills were imaged at 7T with 0.11 × 0.11 mm in-plane-resolution proton attenuation–, T1-, T2-, and T2*-weighted sequences (through-plane resolution, 0.11–1 mm). Tissue samples from 13 fiducial-marked locations (per specimen) on MR imaging underwent histologic processing and atherosclerotic plaque classification. Reconstructed MR images were matched with histologic sections at corresponding locations.

RESULTS: Forty-four samples were available for subsequent evaluation of agreement or disagreement between plaque components and image contrast differences. Of samples, 52.3% ($n = 23$) showed no image contrast heterogeneity; this group comprised solely no lesions or early lesions. Of samples, 25.0% ($n = 11$, mostly advanced lesions) showed good correlation between the spatial organization of MR imaging heterogeneities and plaque components. Areas of foamy macrophages were generally seen as proton attenuation–, T2-, and T2*- hypointense areas, while areas of increased collagen content showed more ambiguous signal intensities. Five samples showed image-contrast heterogeneity without corresponding plaque components on histology; 5 other samples showed contrast heterogeneity based on intima-media artifacts.

CONCLUSIONS: MR imaging at 7T has the image contrast capable of identifying both focal intracranial vessel wall thickening and distinguishing areas of different signal intensities spatially corresponding to plaque components within more advanced atherosclerotic plaques.

ABBREVIATIONS: CoW = circle of Willis; PD = proton-attenuation

Intracranial atherosclerosis is emerging as one of the main causes of cerebral ischemic stroke and transient ischemic attack, with a high risk of recurrent ischemic events.[1] In recent years, several MR imaging sequences have been developed on 3T and 7T field strengths that specifically visualize the intracranial arterial vessel wall, enabling direct assessment of intracranial atherosclerotic plaques.[2-8] Similar to studies of carotid artery atherosclerosis almost a decade ago, several studies have recently attempted to characterize intracranial plaque components, such as intraplaque hemorrhage,[9,10] fibrous cap,[11] and lipid components, by using MR imaging.[12,13]

For the carotid arteries, much research has already been done validating image signal heterogeneity within the vessel wall with histology, the criterion standard.[14-20] Imaging carotid artery atherosclerosis has the advantage of easy access to ex vivo atherosclerotic plaque material for validation, using carotid endarterectomy specimens. It is now possible to image calcification, fibrous cap, intraplaque hemorrhage, and lipid-rich necrotic core in the carotid artery with moderate-to-good sensitivity and specificity by

Received June 18, 2014; accepted after revision August 30.

From the Departments of Pathology (A.V., W.G.M.S.), Radiology (A.G.v.d.K., J.J.M.Z., F.V., D.W.J.K., P.R.L., J.H.), and Image Sciences Institute (J.J.M.Z.), University Medical Center Utrecht, Utrecht, the Netherlands; Department of Pathology (N.P.D., M.J.A.P.D.), Academic Medical Center Amsterdam, Amsterdam, the Netherlands; and Philips Healthcare (F.V.), Best, the Netherlands.

This research was performed within the framework of the Center for Translational Molecular Medicine (www.ctmm.nl), project PARISk (Plaque At RISk; grant 01C-202), and was supported by the Dutch Heart Foundation.

Please address correspondence to Anja G. van der Kolk, MD, PhD, Department of Radiology, University Medical Center Utrecht, Postbox 85500, 3508 GA, Utrecht, the Netherlands; e-mail: A.G.vanderKolk@umcutrecht.nl

Indicates article with supplemental on-line tables.

Indicates article with supplemental on-line photo.

http://dx.doi.org/10.3174/ajnr.A4178

using multicontrast MR imaging.[20] Although 1 recent study showed promising preliminary results of plaque characterization by using a combined T1- and T2-weighted sequence[21] compared with histology, dedicated validation with histology of intracranial vessel wall sequences with multiple image contrast weightings has not yet been performed. Therefore, whether MR imaging with multiple image contrast weightings has enough image contrast to also visualize various intracranial atherosclerotic plaque components remains a question.

Validation of MR images with histology for intracranial atherosclerosis in vivo is much more cumbersome compared with carotid plaques, because no therapies (comparable with carotid endarterectomy) exist in which intracranial atherosclerotic plaques are removed. Furthermore, intracranial arteries are smaller than carotid (or other major peripheral) arteries,[22] necessitating a high spatial resolution, and therefore high SNR, for plaque visualization. Because the SNR increases approximately linearly with field strength, 7T MR imaging might provide the spatial resolution necessary to image small atherosclerotic plaques.[22] Furthermore, several dedicated intracranial vessel wall sequences at 7T have already shown promising results in the visualization of vessel wall lesions in vivo.

In this feasibility study, ultra-high-resolution 7T MR imaging sequences with different image contrast weightings were developed and used in an ex vivo setting, to assess the ability (image contrast) of 7T MR imaging to image different intracranial atherosclerotic plaque components. For validation of our findings, results were compared with histology.

MATERIALS AND METHODS

Specimen Preparation

Five specimens of the circle of Willis (CoW) were selected from >100 postmortem cases that were performed in our institution. Material was handled in a coded manner that met the criteria of the code of conduct used in the Netherlands for the responsible use of human tissue in medical research (www.federa.org/codes-conduct), and institutional review board approval for this retrospective study was obtained. The primary selection criterion was the macroscopic presence of atherosclerosis as judged by an experienced pathologist (A.V.). Furthermore, care was taken that the specimens included the major arteries of the CoW; if specimens were damaged and therefore not complete (ie, histologic samples could not be taken from all 13 locations described below), they were excluded from our study, even when macroscopic atherosclerosis was present. All specimens had been stored in formaldehyde. After selection, the specimens were cleaned thoroughly with a lukewarm solution of polysorbate 20 (0.5% Tween-20; Sigma Aldrich, St. Louis, Missouri) dissolved in distilled water to remove blood clots within the arterial vessel lumen, reducing the chance of artifacts on MR imaging. The specimens were then individually placed within a 9.5-cm round Petri dish and embedded in a 2% agarose solution (Seakem LE Agarosel; Lonza, Rockland, Maine). During immersion in the agarose solution, care was taken to remove all air from the specimens. The embedded specimens were stored in a refrigerator at a temperature of 5°C for solidification until imaging could be performed.

To enable spatial correlation of the MR images with histologic sections, we used cactus spines as fiducials and placed them in the agarose gel, adjacent to 13 locations of histologic sampling. The 13 locations (Fig 1) included, when possible (no air within artery), all the major arteries of the CoW: vertebral arteries, basilar artery (different levels), posterior cerebral arteries, distal ICAs, MCAs, and anterior cerebral arteries.

MR Imaging Protocol

Imaging was performed on a 7T whole-body system (Achieva; Philips Healthcare, Best, the Netherlands) with two 16-channel dedicated surface coils (High density surface array; MR Coils BV, Drunen, the Netherlands) above and below the specimens for signal reception,[23] and a volume transmit/receive coil for transmission (Quad TR; Nova Medical, Wilmington, Massachusetts). Two specimens could be imaged at one time. The specimens, within their Petri dish, were placed on top of each other in the middle of a thin plastic container, by using plastic filling above and below. The container was then filled with fluorinated lubricants (Fomblin PFPE; Solvay Solexis, Bollate, Italy) until the specimens were completely submerged, to provide susceptibility matching. The two 16-channel surface coils were placed above and below the filled box, after which the whole package was placed inside the volume transmit/receive coil.

Imaging was performed at room temperature. For imaging, sequences with 4 different contrast weightings were used, resembling previous MR imaging–histologic correlation studies in the proximal ICA. Parameters of the 4 sequences can be found in On-line Table 1. After a 3D T1-weighted turbo field echo sequence with full-specimen coverage was applied, single-section proton-attenuation (PD)–weighted spin-echo-, single-section T2-weighted TSE, and single-section T2*-weighted turbo field echo sequences with identical geometric parameters were performed for each of the 13 marked locations (resulting in 1 section per image contrast per sample location), by using the T1-weighted images for planning. The PD-weighted spin-echo and T2-TSE sequences included an inversion pulse to null the signal from the agarose gel, similar to CSF suppression in a FLAIR sequence. The inversion delay of 1100 ms was regarded as long enough to limit the amount of T1-weighting in the vessel wall, which has a shorter *T1* ex vivo (approximately 300 ms; data not shown). The total scan duration for each CoW specimen was approximately 40.5 hours. To compensate for potential frequency drifts due to the long sequence durations, we used frequency navigators. For the PD-weighted spin-echo and T2-TSE, the nonselective frequency navigators were applied just before excitation and used to adjust the system frequency accordingly. For the T2*-weighted turbo field echo sequence, a navigator echo was used, as described previously.[24]

Histologic Processing

Histologic processing was performed by using an in-house-developed protocol. After imaging was performed, approximately 0.5-cm-thick tissue samples were taken from the 13 marked locations of each CoW specimen. Ink markings were then used to enable correlation of histologic sections and MR images: Black ink was used to mark the sample side next to the fiducial, while blue ink was used to mark the cranial side of the sample with respect to the

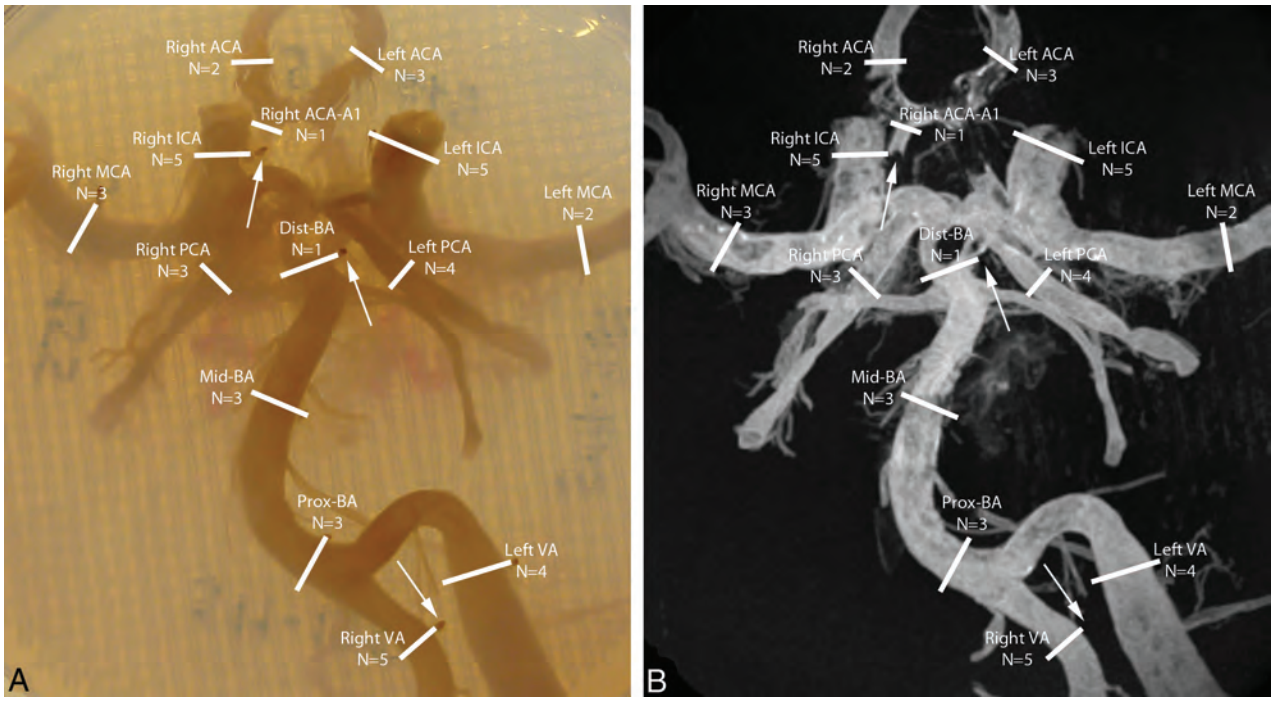

FIG 1. Photograph (*A*) and maximum intensity projection (*B*) of the 7T T1-weighted turbo field echo MR imaging sequence of the CoW specimen of an 87-year-old man embedded in a 2% agarose solution within a Petri dish. The sample locations are illustrated by *white lines*. For each sample location, care was taken to avoid sampling near a visible air bubble or sampling of a collapsed arterial segment. The *N* below each arterial segment denotes the number of samples for that location within the 44 assessed samples obtained from the 5 CoW specimens. MR images were correlated with histologic sections by using fiducials placed within the agarose solution (*arrows* in *A* and *B*). A1 indicates A1 segment of the anterior cerebral artery; Dist-BA, distal segment of the basilar artery; Mid-BA, middle segment of the basilar artery; Prox-BA, proximal segment of the basilar artery; ACA, anterior cerebral artery; VA, vertebral artery.

Petri dish. The tissue samples, placed within small plastic containers with 6 spaces, were then placed in the chelating reagent ethylenediaminetetraacetic acid 12.5% for 3–4 days to dissolve wall calcifications, to reduce the risk of damaging the samples during slicing. Ethylenediaminetetraacetic acid captures calcium ions within calcified areas but retains associated phosphate groups, which can afterward be visualized with an H&E stain. After being processed and embedded in paraffin, the samples were cut into 4-μm sections, stained with H&E and Van Gieson elastic, and assessed by using a slide scanner (Slide scanner with Dotlide software, Version 2.5; Olympus, Tokyo, Japan).

The modified American Heart Association classification by Virmani et al[25] was used to classify each sample on atherosclerotic characteristics, as follows: no anomaly; early lesions, including intimal thickening (<50% smooth-muscle cells, no lipids, inflammatory cells), fatty streak, and pathologic intimal thickening (>50% smooth-muscle cells, rich in proteoglycans, foamy macrophages); and advanced lesions, including fibrolipid plaque (>40% lipid), thin cap atheroma (<65-μm thickness), fibrous plaque (<40% lipid), fibrocalcified plaque (>40% calcified), and calcified nodule (calcified element protruding into the intima). When applicable, plaque complications, like rupture, hemorrhage, or erosion, were also assessed.

Correlation of MR Images with Histology

First, T1-weighted images were reconstructed (0.11-mm thickness) for each sample, corresponding to the orientation and location of the PD-, T2-, and T2*-weighted images at each of the 13 locations marked by the fiducials. Then, the MR images were compared with the histologic sections at the corresponding location. If the MR images did not match the corresponding histologic section due to errors in MR imaging planning or gross deformation of the sample during histologic processing, the sample was excluded from analysis. Some deformation of the samples is inevitable; however, when no correlation in shape could be identified even when the ink locations were used as additional spatial markers, the sample was excluded. Samples were also excluded from analysis in case of histologic processing errors (mixed-up/damaged/parallel, instead of perpendicular, cut samples). The resulting MR imaging histology sets were then evaluated for agreement or disagreement between plaque components and image contrast differences. First, MR images were assessed by A.G.v.d.K. for the presence of image contrast heterogeneity within the arterial vessel wall for each sample; then, the corresponding areas on the histologic sections were assessed by N.P.D. for possible atherosclerotic changes that could explain the image contrast heterogeneity seen on the MR images.

When no vessel wall atherosclerosis was present, heterogeneities on MR imaging were scored as having "no correlation." When atherosclerosis was present in the same area, the spatial organization of plaque components (eg, collagen-rich rim, areas of foamy macrophages) was compared with the spatial organization of the vessel wall MR imaging heterogeneities, scoring either "no correlation" or a correlation that was then described more specifically. Finally, samples in which no MR imaging heteroge-

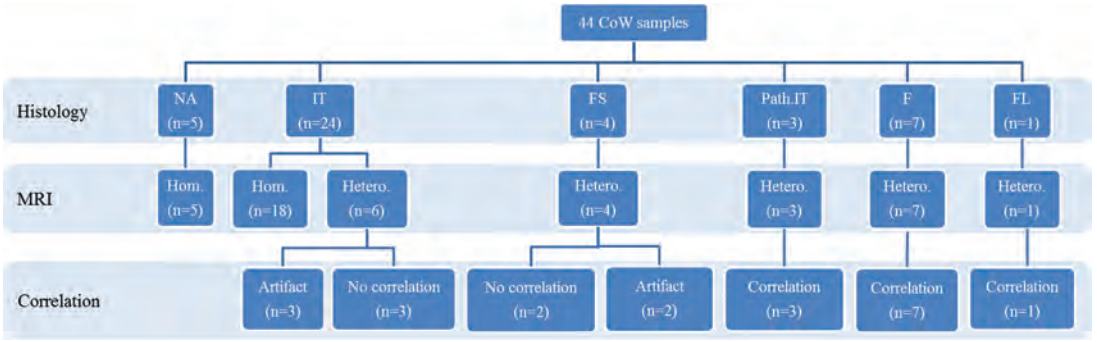

FIG 2. Overview of histologic classification and the presence of vessel wall heterogeneity on MR imaging of the 44 samples of the CoW, including correlation scoring. "Artifact" indicates intima-media artifacts; F, fibrous plaque; FL, fibrolipid plaque; FS, fatty streak; Hom., vessel wall with homogeneous signal intensity; Hetero., vessel wall with heterogeneous signal intensity; IT, intimal thickening; NA, no anomaly (no atherosclerosis); Path.IT, pathologic intimal thickening.

neity was found but where atherosclerotic changes were present were also described. Because this was a feasibility study assessing the ability of 7T MR imaging to provide sufficient image contrast for visualizing intracranial atherosclerotic plaques and characterizing its components, blinding was not performed.

RESULTS

Sample Population

Five CoW specimens from 3 men, 54 (subject 1 in figures), 71 (subject 2), and 87 years of age (subject 3), and 2 women, 65 (subject 4) and 74 years of age (subject 5), were used; although clinical information regarding disease status of these patients was not available due to the coded handling of the material, our histopathologic studies did not show characteristics of other specific diseases (vasculopathy, vasculitis) that may have adversely affected the arteries. A total of 65 samples of CoW arteries was obtained; 21 of these 65 samples (32.3%) were excluded due to either lack of correlation in shape or fiducial location ($n = 11$), air within the sample that was not seen during MR imaging planning ($n = 1$), or histologic processing errors ($n = 9$), resulting in 44 samples for assessment. Processing samples for histologic analysis was a very delicate process, due to the fragile nature of the arterial tissue in combination with the small size of the taken samples; these features sometimes led to parallel cut samples or deformation of the sample. Figure 1 illustrates the sample location and the number of samples obtained at each location.

Histologic Classification

Five samples (11.4%) had no atherosclerosis; 31 samples (70.4%) contained early atherosclerotic lesions: Twenty-four samples showed intimal thickening, 4 showed a fatty streak, and 3 showed pathologic intimal thickening. The remaining 8 samples (18.2%) showed either fibrous plaques ($n = 7$) or a fibrolipid plaque ($n = 1$). No fibrocalcific plaques, calcified nodules, or thin cap atheromas were seen; also, no plaque complications such as rupture, (intraplaque) hemorrhage, or erosion were found.

MR Image Contrast Heterogeneity

Twenty-three of 44 samples (52.3%) showed no image-contrast heterogeneity on any of the 4 MR image contrast weightings (T1-, PD-, T2-, or T2*-weightings; Fig 2 and On-line Figure). Samples within this group comprised solely no or early lesions: Five samples had no atherosclerosis; the other 18 showed intimal thickening (On-line Figure). In 21 of 44 samples (47.7%), various patterns of image contrast heterogeneity were found (Fig 2 and On-line Table 2). Eleven samples (25.0%; Fig 3) showed good correlation between the spatial organization of vessel wall MR imaging heterogeneities (areas of decreased or increased signal intensity) and the spatial organization of plaque components (eg, collagen-rich rim, areas of foamy macrophages). These 11 samples comprised 8 advanced lesions (7 fibrous plaques, 1 fibrolipid plaque) and 3 samples with pathologic intimal thickening (last stage of early lesions). Within these samples, areas of foamy macrophages and proteoglycans or areas with high levels of lipids were most often (8 of 9 plaques with these characteristics) seen as hypointense areas within the vessel wall on the PD-, T2-, and T2*-weighted sequences (Fig 3); 1 sample with foamy macrophages showed a hyperintense signal on all sequences used (distal basilar artery in a 71-year-old man, On-line Table 2). Areas of increased collagen content (present in all 11 plaques) showed more ambiguous signal intensities: Five samples showed corresponding hyperintense areas on at least T2- and T2*-weighted images (Fig 3, cases 1–3), with isointense-to-hyperintense signal on the T1- and PD-weighted images, while 5 samples showed a hypointense signal for these areas on the T2- and T2*-weighted images (Fig 3, case 4), with various signal intensities on the T1- and PD-weighted images. In 1 sample, the collagen-rich area could only be distinguished from healthy vessel wall because of the adjacent hypointense area of foamy macrophages.

Five other samples (3 with intimal thickening and 2 with fatty streaks, 11.4%) showed image-contrast heterogeneity on MR images, without corresponding plaque components on histologic sections (Fig 4). Eleven samples (25.0%, 5 with no other signal heterogeneity; Fig 4) showed a hypointense line within the vessel wall on the PD-, T2-, and T2*-weighted images, which was isointense on the T1-weighted images. Although this hypointensity corresponded with a space between the intima and media of the arterial wall on the histologic sections, it was regarded as artifacts of the specimen because of either detachment of the intima (eg, due to prolonged storage) or because of cleaning the specimens (flushing arteries with water/careful removal of blood clots). Due to these intima-media artifacts, making a distinction between ar-

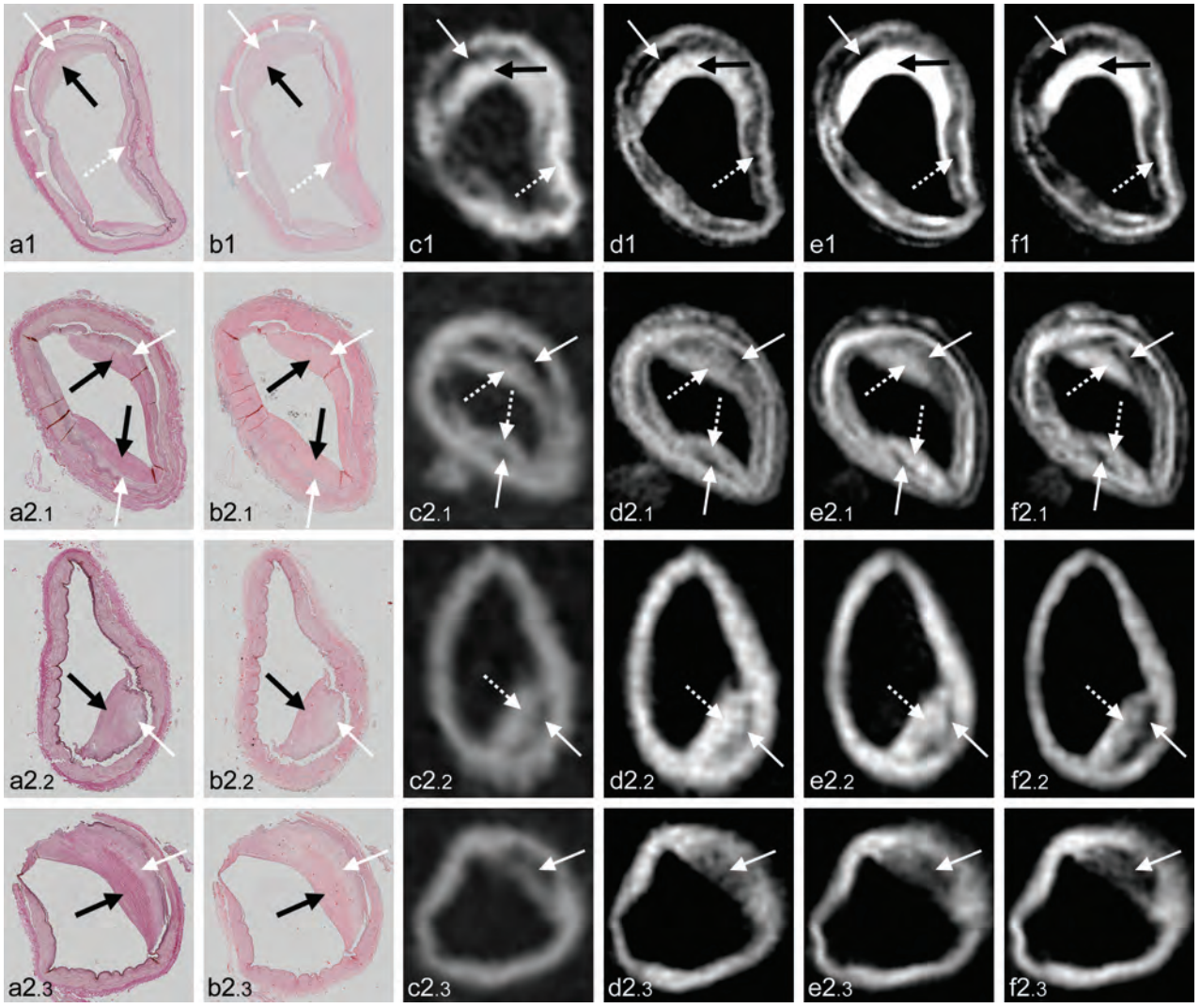

FIG 3. Four examples of atherosclerotic plaques with corresponding signal heterogeneity on 7T MR images. Histologic sections (magnification ×10) with Van Gieson elastic (*a*) and H&E (*b*) staining, with corresponding 7T MR images of T1-weighted (*c*), PD-weighted (*d*), T2-weighted (*e*), and T2*-weighted (*f*) sequences. *a1–f1,* Cross-section of the left ICA of subject 3. Histologic examination shows fibrous plaque with proteoglycans (*white arrow*, *a1–b1*) and increased collagen (*black arrow*, *a1–b1*); a patch of foamy macrophages can also be appreciated (*dashed white arrow*, *a1–b1*). On the corresponding MR images, the rim of increased collagen can be seen as hyperintense on all sequences (*black arrow*, *c1–f1*), while the small patch of foamy macrophages corresponds with a hypointense area (*dashed arrow*, *c1–f1*). Due to the intima-media artifacts, a distinction between artifacts (*arrowheads*, *a1–b1*) and proteoglycans lining the artifacts within the hypointense area on MR imaging (*white arrow*, *c1–f1*) cannot be made. *a2.1–f2.3*, Cross-sections of the right vertebral artery (*2.1*), right ICA (*2.2*), and left ICA (*2.3*) of subject 2. *a2.1–f2.1*, Histologic examination shows fibrous plaque with increasing collagen from outside (*white arrows*, *a2.1–b2.1*) to inside (*black arrows, a2.1–b2.1*); on the corresponding MR images, the area with more strongly increased collagen appears as a mostly hyperintense inner area (*dashed arrows*, *c2.1–f2.1*), compared with the area with less collagen (*white arrows*, *c2.1–f2.1*). *a2.2–f2.2*, Histologic examination shows pathologic intimal thickening with proteoglycans and foamy macrophages (*white arrow*, *a2.2–b2.2*) and increased collagen (*black arrow*, *a2.2–b2.2*); again, the collagen-rich inner area appears isointense on the MR images (*dashed white arrow*, *c2.2–f2.2*), while the area with proteoglycans and foamy macrophages appears mostly hypointense (*white arrow*, *c2.2–f2.2*). *a2.3–f2.3*, Histologic examination shows fibrous plaque with a thick inner rim of increased collagen (*black arrow*, *a2.3–b2.3*) and a thick outer rim with foamy macrophages (*white arrow*, *a2.3–b2.3*); in this case, vessel wall thickening on MR imaging has a hypointense signal, corresponding with both foamy macrophages and increased collagen (*white arrow*, *c2.3–f2.3*).

tifacts and proteoglycans/foamy macrophages lining the artifacts within the hypointense area on MR imaging was sometimes difficult (Fig 3, case 1).

DISCUSSION

In the present study, we assessed the feasibility of 7T MR imaging to characterize ex vivo intracranial atherosclerotic plaques with sufficient image contrast, by using ultra-high-resolution sequences with 4 different contrast weightings. Areas of focal arterial vessel wall thickening on ultra-high-resolution MR images corresponded with histologically determined advanced atherosclerotic lesions. In all of these more advanced lesions, signal heterogeneities on 7T MR imaging enabled the spatial differentiation of different plaque components, like foamy macrophages and collagen. In early lesions, no signal-intensity heterogeneity could be observed.

Using 7T MR imaging with dedicated surface coils made it possible to image the intracranial arterial vessel wall ex vivo with

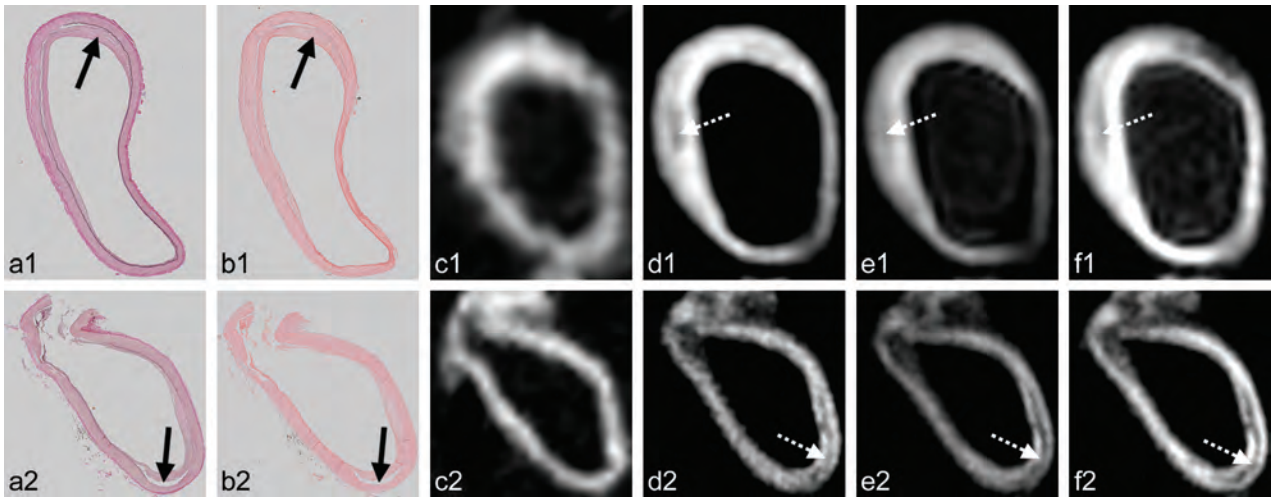

FIG 4. Two examples of discrepancies between 7T MR imaging and histology. Histologic sections (magnification ×10) with Van Gieson elastic (*a*) and H&E (*b*) staining, with corresponding 7T MR images of the T1- (*c*), PD- (*d*), T2- (*e*), and T2*-weighted (*f*) sequences. Cross-section of the right posterior cerebral artery (*a1–f1*) and left ICA (*a2–f2*) of subject 5. *a1–f1,* Histologic examination shows a fatty streak (*black arrow*, *a1–b1*), which is not seen as signal heterogeneity of the vessel wall on the MR images. A hypointense area away from the fatty streak can be appreciated on the MR images (*dashed white arrow*, *d1–f1*), but this does not correspond with any vessel wall pathology on histology, apart from intima-media artifacts. *a2–f2*, Histologic examination shows minor intimal thickening on the PD-, T2-, and T2*-weighted MR images. A hypointense line can be seen within a large part of the vessel wall (*dashed white arrow*, *d2–f2*), which corresponds to intima-media artifacts on the histologic sections (*black arrow, a2–b2*).

an acquired in-plane resolution of 0.11 × 0.11 mm. For the T1-weighted turbo field echo sequence, the images could be reconstructed in all directions by using 3D image acquisitions of 0.11 × 0.11 × 0.11 mm. With this high spatial resolution, conspicuity of the intracranial arterial vessel wall and its pathology could be obtained, though some problems of ex vivo imaging remained, such as removal of all air from the arterial lumen, that may otherwise give rise to image artifacts. An initial comparison was performed with histologic classification at specific arterial locations, similar to carotid plaque characterization studies.[26] Of the 44 arterial samples that were assessed in this study, correlation between MR imaging and histology was shown to be best in the samples with more advanced lesions. None of the 5 samples with healthy arterial vessel walls showed areas of signal hypo- or hyperintensity on MR images. This finding was also true for 18 of 24 samples (75%) with intimal thickening, suggesting that these early atherosclerotic changes are beyond the contrast-to-noise ratio obtained with the ultra-high-resolution sequences used.

Of the more advanced lesions, all 8 samples (7 with fibrous plaque, 1 with fibrolipid plaque) showed at least partial correlation between the spatial organization of the MR signal heterogeneities and the spatial organization of plaque components of the corresponding histologic sections. In this small subset, a hypointense signal on all sequences generally corresponded to the presence of foamy macrophages, increased proteoglycans, or a lipid-rich core (with or without additional intima-media artifacts). Areas of increased collagen content showed more ambiguous signal intensities ranging from hypo- to hyperintense on the same image contrast weightings. In comparison, previous studies[27-29] on plaque characterization in the carotid artery showed a lipid-rich core to be hyperintense on T1-weighted imaging and iso- to hypointense on PD- and T2-weighted imaging; a fibrous (collagen-rich) area was shown to be isointense on T1-weighted imaging, iso- to hyperintense on T2-weighted imaging, and hyperintense on PD-weighted imaging. The discrepancies in signal characteristics between these studies and our results may be due to the prolonged formalin fixation of our specimen, due to the changed contrast at ultra-high-field (where, for example, compact collagen has a shorter T2*[30]), or they may be related to the less advanced atherosclerotic status of most of our samples. For instance, we only had 1 sample with a lipid-rich core, and no samples with intraplaque hemorrhage or plaque rupture, advanced atherosclerotic characteristics on which the MR signal characteristics of these previous studies were mostly based.[27-29] Overall, the clearest histology-corresponding image contrast heterogeneity was seen on the T2- and T2*-weighted MR images (see, for instance, Fig 3*e1-f1*), followed by the T1-weighted images. The PD-weighted images showed less clear image contrast differences among different plaques components.

In 14% of the samples ($n = 6$), heterogeneity of the arterial vessel wall was found on MR imaging without histologic correlates. This could be due to the larger through-plane spatial resolution of the sequences used in this study. Although a through-plane spatial resolution of only 1 mm was used, the resolution obtained with histologic sections was still several factors above the MR imaging resolution. Partial volume effects within the obtained 1-mm-thick images resulted in a summation of signal intensities within this 1-mm-thick area, while a single histologic section of 4-μm thickness only showed pathology within that 4-μm-thick area.

This study has limitations. Although CoW specimens were selected that macroscopically contained atherosclerotic plaques, only 18% of samples contained advanced plaques with corresponding plaque components. A higher percentage of advanced plaques would have given more clear insight into the specific MR signal characteristics of different plaque components (general signal intensity on different image contrast weightings), which are

not as clearly present in early lesions. Especially, increased collagen content within atherosclerotic plaques, which showed ambiguous signal-intensity results in the current study, might benefit from inclusion of more advanced plaques. Even so, our results still show that 7T MR imaging has the image contrast to show focal thickening of the intracranial arterial vessel wall and to distinguish areas with different plaque components by using ultra-high-resolution sequences. Furthermore, in this study, 2D sections of selective areas were used for most MR imaging; a 3D approach (like the T1-weighted sequence used) with isotropic voxels would decrease exclusion of samples due to location inconsistencies between MR imaging and histology, thereby decreasing possible selection bias. Regarding technical improvements, development of quantitative MR images, like T1-, T2-, and T2* mapping, would enable quantitative plaque characterization, making qualitative scoring performed in the current study unnecessary. These improvements would not only enable more firm statements regarding the accuracy of either T1-, T2-, or T2*-weighted sequences in characterizing atherosclerotic plaque, they could also enable the development of in vivo sequences specifically designed to visualize ≥1 plaque component with high image contrast, even making very high spatial resolutions unnecessary.

A hypointense line within the vessel wall was seen in 25% of samples, corresponding to a defect between the intima and media of the vessel wall. These artifacts could be related to a prolonged storage period of the CoW specimens. Although easily identifiable, it did influence our results (On-line Table 2); because the same hypointense signal is seen in foamy macrophages/lipid-rich core, we therefore could not clearly distinguish vacant space from foamy macrophages/lipid-rich core when the artifacts were present in the histologic sections. This limitation, however, will not be present with in vivo characterization of intracranial atherosclerotic plaques. Furthermore, the current ex vivo studies will be of limited use in the validation of contrast enhancement that can be visible with in vivo MR imaging. Obviously, contrast agent injection and subsequent enhancement can only be imaged in vivo,[31] and postmortem examination in these patients is the only validation method. Finally, the very long scan duration (approximately 40 hours) of the ultra-high-resolution sequences used in this study prohibits their use in vivo in clinical practice. However, we think that our results may serve as a starting point for further histologic validation of in vivo intracranial vessel wall sequences, albeit with lower spatial resolutions.

CONCLUSIONS

Our results show that 7T MR imaging, by using ultra-high-resolution sequences with different image contrast weightings, has image contrast capable of identifying focal thickening of the intracranial arterial vessel walls and distinguishing areas of different signal intensities that spatially correspond to plaque components within more advanced intracranial atherosclerotic plaques. Additional studies that further validate signal characteristics of the specific plaque components in a quantitative manner, also for lower resolution sequences, will enable future in vivo characterization of intracranial atherosclerotic plaques.

Disclosures: Anja van der Kolk—*RELATED*: *Other:* Center for Translational Molecular Medicine,* *Comments*: This research was performed within the framework of the Center for Translational Molecular Medicine (www.ctmm.nl), project PARISk (Plaque At RISk; grant 01C-202), and was supported by the Dutch Heart Foundation. Fredy Visser—*RELATED*: *Employment*: Philips Healthcare, Best, the Netherlands. *Money paid to the institution.

REFERENCES

1. Qureshi AI, Caplan LR. **Intracranial atherosclerosis.** *Lancet* 2014;383:984–98
2. Dieleman N, van der Kolk AG, Zwanenburg JJ, et al. **Imaging intracranial vessel wall pathology using magnetic resonance imaging: current prospects and future directions.** *Circulation* 2014;130:192–201
3. Klein IF, Lavallee PC, Mazighi M, et al. **Basilar artery atherosclerotic plaques in paramedian and lacunar pontine infarctions: a high-resolution MRI study.** *Stroke* 2010;41:1405–09
4. Xu WH, Li ML, Gao S, et al. **Plaque distribution of stenotic middle cerebral artery and its clinical relevance.** *Stroke* 2011;42:2957–59
5. van der Kolk AG, Zwanenburg JJ, Brundel M, et al. **Intracranial vessel wall imaging at 7.0-T MRI.** *Stroke* 2011;42:2478–84
6. Skarpathiotakis M, Mandell DM, Swartz RH, et al. **Intracranial atherosclerotic plaque enhancement in patients with ischemic stroke.** *AJNR Am J Neuroradiol* 2013;34:299–304
7. Lou X, Ma N, Ma L, et al. **Contrast-enhanced 3T high-resolution MR imaging in symptomatic atherosclerotic basilar artery stenosis.** *AJNR Am J Neuroradiol* 2013;34:513–17
8. van der Kolk AG, Hendrikse J, Brundel M, et al. **Multi-sequence whole-brain intracranial vessel wall imaging at 7.0 Tesla.** *Eur Radiol* 2013;23:2996–3004
9. Turan TN, Bonilha L, Morgan PS, et al. **Intraplaque hemorrhage in symptomatic intracranial atherosclerotic disease.** *J Neuroimaging* 2011;21:e159–61
10. Park JK, Kim SH, Kim BS, et al. **Imaging of intracranial plaques with black-blood double inversion recovery MR imaging and CT.** *J Neuroimaging* 2011;21:e64–68
11. Chung JW, Kim BJ, Choi BS, et al. **High-resolution magnetic resonance imaging reveals hidden etiologies of symptomatic vertebral arterial lesions.** *J Stroke Cerebrovasc Dis* 2014;23:293–302
12. Natori T, Sasaki M, Miyoshi M, et al. **Evaluating middle cerebral artery atherosclerotic lesions in acute ischemic stroke using magnetic resonance T1-weighted 3-dimensional vessel wall imaging.** *J Stroke Cerebrovasc Dis* 2014;23:706–11
13. Turan TN, Rumboldt Z, Brown TR. **High-resolution MRI of basilar atherosclerosis: three-dimensional acquisition and FLAIR sequences.** *Brain Behav* 2013;3:1–3
14. Yuan C, Mitsumori LM, Ferguson MS, et al. **In vivo accuracy of multispectral magnetic resonance imaging for identifying lipid-rich necrotic cores and intraplaque hemorrhage in advanced human carotid plaques.** *Circulation* 2001;104:2051–56
15. Cai JM, Hatsukami TS, Ferguson MS, et al. **Classification of human carotid atherosclerotic lesions with in vivo multicontrast magnetic resonance imaging.** *Circulation* 2002;106:1368–73
16. Moody AR, Murphy RE, Morgan PS, et al. **Characterization of complicated carotid plaque with magnetic resonance direct thrombus imaging in patients with cerebral ischemia.** *Circulation* 2003;107:3047–52
17. Mitsumori LM, Hatsukami TS, Ferguson MS, et al. **In vivo accuracy of multisequence MR imaging for identifying unstable fibrous caps in advanced human carotid plaques.** *J Magn Reson Imaging* 2003;17:410–20
18. Cappendijk VC, Cleutjens KB, Kessels AG, et al. **Assessment of human atherosclerotic carotid plaque components with multisequence MR imaging: initial experience.** *Radiology* 2005;234:487–92
19. Narumi S, Sasaki M, Ohba H, et al. **Predicting carotid plaque char-**

acteristics using quantitative color-coded T1-weighted MR plaque imaging: correlation with carotid endarterectomy specimens. *AJNR Am J Neuroradiol* 2014;35:766–71
20. den Hartog AG, Bovens SM, Koning W, et al. **Current status of clinical magnetic resonance imaging for plaque characterisation in patients with carotid artery stenosis.** *Eur J Vasc Endovasc Surg* 2013;45:7–21
21. Majidi S, Sein J, Watanabe M, et al. **Intracranial-derived atherosclerosis assessment: an in vitro comparison between virtual histology by intravascular ultrasonography, 7T MRI, and histopathologic findings.** *AJNR Am J Neuroradiol* 2013;34:2259–64
22. Jahnke C, Dietrich T, Paetsch I, et al. **Experimental evaluation of the detectability of submillimeter atherosclerotic lesions in ex vivo human iliac arteries with ultrahigh-field (7.0 T) magnetic resonance imaging.** *Int J Cardiovasc Imaging* 2007;23:519–27
23. Petridou N, Italiaander M, van de Bank BL, et al. **Pushing the limits of high-resolution functional MRI using a simple high-density multi-element coil design.** *NMR Biomed* 2013;26:65–73
24. Versluis MJ, Peeters JM, van RS, et al. **Origin and reduction of motion and f0 artifacts in high resolution T2*-weighted magnetic resonance imaging: application in Alzheimer's disease patients.** *Neuroimage* 2010;51:1082–88
25. Virmani R, Kolodgie FD, Burke AP, et al. **Lessons from sudden coronary death: a comprehensive morphological classification scheme for atherosclerotic lesions.** *Arterioscler Thromb Vasc Biol* 2000;20:1262–75
26. Saam T, Hatsukami TS, Takaya N, et al. **The vulnerable, or high-risk, atherosclerotic plaque: noninvasive MR imaging for characterization and assessment.** *Radiology* 2007;244:64–77
27. Yuan C, Mitsumori LM, Beach KW, et al. **Carotid atherosclerotic plaque: noninvasive MR characterization and identification of vulnerable lesions.** *Radiology* 2001;221:285–99
28. Fuster V, Fayad ZA, Moreno PR, et al. **Atherothrombosis and high-risk plaque: Part II: approaches by noninvasive computed tomographic/magnetic resonance imaging.** *J Am Coll Cardiol* 2005;46:1209–18
29. Silvera SS, Aidi HE, Rudd JH, et al. **Multimodality imaging of atherosclerotic plaque activity and composition using FDG-PET/CT and MRI in carotid and femoral arteries.** *Atherosclerosis* 2009;207:139–43
30. de Jong S, Zwanenburg JJ, Visser F, et al. **Direct detection of myocardial fibrosis by MRI.** *J Mol Cell Cardiol* 2011;51:974–79
31. Portanova A, Hakakian N, Mikulis DJ, et al. **Intracranial vasa vasorum: insights and implications for imaging.** *Radiology* 2013;267:667–79

Modeling the Relationship among Gray Matter Atrophy, Abnormalities in Connecting White Matter, and Cognitive Performance in Early Multiple Sclerosis

A.F. Kuceyeski, W. Vargas, M. Dayan, E. Monohan, C. Blackwell, A. Raj, K. Fujimoto, and S.A. Gauthier

ABSTRACT

BACKGROUND AND PURPOSE: Quantitative assessment of clinical and pathologic consequences of white matter abnormalities in multiple sclerosis is critical in understanding the pathways of disease. This study aimed to test whether gray matter atrophy was related to abnormalities in connecting white matter and to identify patterns of imaging biomarker abnormalities that were related to patient processing speed.

MATERIALS AND METHODS: Image data and Symbol Digit Modalities Test scores were collected from a cohort of patients with early multiple sclerosis. The Network Modification Tool was used to estimate connectivity irregularities by projecting white matter abnormalities onto connecting gray matter regions. Partial least-squares regression quantified the relationship between imaging biomarkers and processing speed as measured by the Symbol Digit Modalities Test.

RESULTS: Atrophy in deep gray matter structures of the thalami and putamen had moderate and significant correlations with abnormalities in connecting white matter ($r = 0.39–0.41$, $P < .05$ corrected). The 2 models of processing speed, 1 for each of the WM imaging biomarkers, had goodness-of-fit (R^2) values of 0.42 and 0.30. A measure of the impact of white matter lesions on the connectivity of occipital and parietal areas had significant nonzero regression coefficients.

CONCLUSIONS: We concluded that deep gray matter regions may be susceptible to inflammation and/or demyelination in white matter, possibly having a higher sensitivity to remote degeneration, and that lesions affecting visual processing pathways were related to processing speed. The Network Modification Tool may be used to quantify the impact of early white matter abnormalities on both connecting gray matter structures and processing speed.

ABBREVIATIONS: ChaCo = Change in Connectivity; NeMo = Network Modification Tool; PLSR = partial least-squares regression; RD = radial diffusivity; SDMT = Symbol Digit Modalities Test

One of the most pressing questions in multiple sclerosis is understanding the relationship between white matter lesions and subsequent atrophy, physical disability, and cognitive impairment. MS is a neurologic disorder that has pathologic manifestations in both WM and gray matter, some of which can be detected via in vivo MR imaging. WM changes have been extensively studied in MS, by using diffusion imaging and tractography[1,2] and structural imaging.[3] Classically, MS has been seen as primarily a disease of the WM, but recent developments have identified clinically relevant GM pathologies.[4,5] The underlying cause of GM abnormalities is unclear,[6] but some have hypothesized that it may be a result of retrograde or anterograde Wallerian degeneration.[7]

There are many studies of WM pathology and networks in MS[8,9] and studies of WM/GM pathologies in tandem.[10,11] However, one must incorporate topologic information[2] to test whether connectivity plays a role in MS. Recent studies[12,13] provide evidence that networks may provide a basis for the spread of pathology in a variety of neurologic disorders; the understanding

Received June 27, 2014; accepted after revision September 2.

From the Departments of Radiology (A.F.K., M.D., A.R.) and Neurology (W.V., E.M., C.B., K.F., S.A.G.), and The Brain and Mind Research Institute (A.F.K., A.R., S.A.G.), Weill Cornell Medical College, New York, New York.

This work was supported by EMD Serono, a Leon Levy Foundation Neuroscience Fellowship, and the following National Institutes of Health grants: P41 RR023953-02, P41 RR023953-02S1, and R01 NS075425.

Paper previously presented in part at: Conference for the European Committee for Treatment and Research in Multiple Sclerosis, October 2–5, 2013; Copenhagen, Denmark; and Conference for the Organization for Human Brain Mapping, June 8–12, 2014; Hamburg, Germany.

Please address correspondence to Amy F. Kuceyeski, PhD, Weill Cornell Medical College, 515 East 71st St, S-114, New York, NY 10065; e-mail: amk2012@med.cornell.edu

Indicates open access to non-subscribers at www.ajnr.org
Indicates article with supplemental on-line appendix.
Indicates article with supplemental on-line photos.
http://dx.doi.org/10.3174/ajnr.A4165

Demographics (mean ± standard deviation) for the early MS cohort and the healthy control group

	All Subjects with MS	Subgroup of Subjects with MS with SDMT	Healthy Controls
Total No.	121	66	15
Female	77	44	9
Age (yr)	37.5 ± 9.8	36.5 ± 9.3	36.3 ± 13.2
Disease duration	2.1 ± 1.5	1.6 ± 1.5	NA
SDMT	N/A	49.8 ± 10.5	NA
EDSS	1.2 ± 1.4	1.04 ± 1.06	NA

Note:—EDSS indicates Expanded Disability Status Scale; NA, not applicable.

of this process may result in prediction of disease progression and patient disability. Tractography methods used to infer structural connectivity networks have been applied in MS[14,15]; however, practical implementation of tractography is laborious and time-consuming and requires expertise. Applying it in disease is especially challenging[16] due to increased pathology-related noise in the diffusion signal.[1,17,18] To circumvent these issues, we used the recently developed Network Modification Tool (NeMo; https://github.com/jimmyshen007/NeMo),[19] which can infer structural connectivity losses from WM abnormalities without having to perform tractography in subjects with tissue pathology.

We hypothesize that the patterns of tissue abnormalities in individuals with MS impact neurologic outcomes, due to their specific neuroanatomic locations and subsequent disruption of the relevant functional pathways within the structural network. To test this hypothesis, we used the NeMo Tool to estimate, for each patient, the impact of his or her specific WM abnormality map on the fiber connectivity network and relate this to one of the most commonly used measures of end-stage CNS injury: regional brain atrophy. Furthermore, we used partial least-squares regression (PLSR), a commonly used approach in neuroimaging,[20] to relate imaging biomarkers to processing speed. Our goal was to identify which WM imaging technique best captures physiologically relevant changes and to identify which regional imaging biomarkers are significant contributors to processing speed. To our knowledge, this study is the first to apply PLSR to structural connectivity and GM atrophy biomarkers to predict subtle cognitive changes in early MS.

MATERIALS AND METHODS

Data

Data were collected from 121 patients with early relapsing-remitting MS (Table); consent was obtained from all subjects in this institutional review board–approved retrospective study. All except 6 patients were on disease-modifying therapies for MS at the time of MR imaging, with an average treatment duration of 1.76 ± 1.78 years. All patient MRIs were acquired within 5 years of their first neurologic symptom, which is our definition of "early" MS. The following four sets of images were acquired on a 3T scanner (HDxt 16.0; GE Healthcare, Milwaukee, Wisconsin) using an 8-channel phased array coil: T1-weighted sagittal 3D-brain volume imaging (1.2 × 1.2 × 1.2 mm), T2 (0.5 × 0.5 × 3 mm), T2 FLAIR (1.2 × 0.6 × 0.6 mm), and 34-direction diffusion imaging (b=1000, 0.8 × 0.8 × 2.5 mm). All subjects that had the required imaging within 5 years of their first symptom were included; no other exclusion criterion was imposed. The same images were collected on an age- and sex-matched group of 15 healthy controls. The written version of the Symbol Digit Modalities Test (SDMT) was performed on a subgroup of 66 patients. The SDMT measures processing speed, which is known to be one of the earliest affected cognitive domains in MS, and is particularly sensitive to MS-associated impairment.[21]

GM Atrophy and T2 FLAIR Hyperintensity Lesion Masks

FreeSurfer (http://surfer.nmr.mgh.harvard.edu)[22] was used on the T1 images to produce subcortical segmentation, cortical parcellation, and tissue-type masks (WM, GM, and other tissue), which were checked and manually edited for misclassification due to WM hyperintensities and common temporal region errors. T2 images were linearly coregistered to the T1 and FreeSurfer parcellations. The T2 FLAIR images were masked with the WM segmentation and subcortical mask and thresholded to create the WM abnormality masks. The resulting WM hyperintensity masks were then overlaid on T2 and T2 FLAIR images and manually edited (W.V., S.A.G., and E.M.), after which a trained neurologist (W.V.) gave a final approval. T1 images were also acquired on 15 age-matched healthy volunteers and processed with the same pipeline for calculating atrophy (Table).

Diffusion Image Processing

Each subject's T1 was normalized via a nonlinear transformation into Montreal Neurological Institute space and segmented (GM, WM, CSF, and bone) by using the new segment toolbox (SPM8 software; http://www.fil.ion.ucl.ac.uk/spm/software/spm8).[23] A binary brain mask in T1 space was created by combining GM and WM maps and dilating and binarizing the resulting volume and subtracting the bone map (thresholded at 5%). For the diffusion data, a similar brain mask was obtained by applying the Brain Extraction Tool utility[24] to the b0 image. Diffusion tensor coefficients were computed via weighted linear least-squares regression with the fMRI of the Brain Software Library DTIFit (http://fsl.fmrib.ox.ac.uk/fsl/fsl-4.1.9/fdt/fdt_dtifit.html) utility. Maps of diffusion summary statistics, namely fractional anisotropy, axial diffusivity, mean diffusivity, and radial diffusivity (RD), were then calculated and mapped to Montreal Neurological Institute space via linear and nonlinear transforms in FSL (http://www.fmrib.ox.ac.uk/fsl). The Crawford modified t test,[25] designed for individual subject voxelwise significance testing, was implemented for each individual's diffusion measures in SPM8. A mask was applied to restrict the testing to WM voxels only (as defined by the SPM8 WM mask), and family-wise error correction was imposed, with no minimum threshold for cluster size.

The NeMo Tool

The NeMo Tool (Fig 1) infers changes to the structural connectivity network that may result from a given mask of WM alterations by referencing a data base of 73 healthy control tractograms in a common space (Montreal Neurological Institute space). The WM abnormality masks of subjects with MS were normalized to common space by using first a linear coregistration followed by nonlinear normalization in SPM8. The Change in Connectivity (ChaCo) score, defined for each GM region, is the percentage of tracts connecting to that region that pass through the WM abnor-

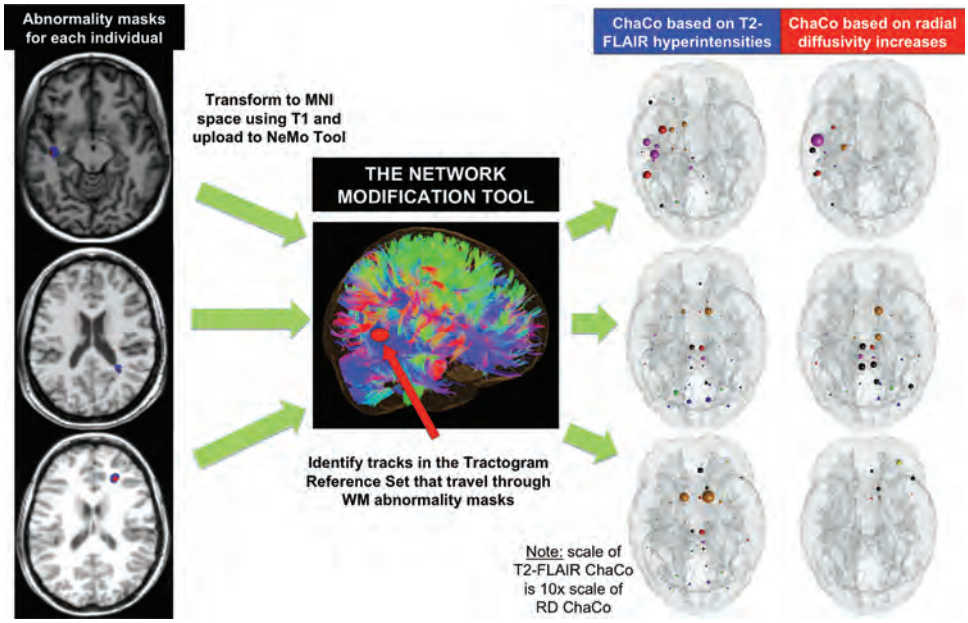

FIG 1. The workflow for the NeMo Tool and some examples. T2 FLAIR lesion (blue) and RD abnormality masks (red) were created and normalized to Montreal Neurological Institute space (*left*). The NeMo Tool was used to calculate the Change in Connectivity score that quantifies the effect of those areas of abnormality on regional structural connectivity (*middle*). ChaCo scores are shown for the T2 FLAIR lesions and RD abnormality masks for 3 particular individuals via the glass brain display (*right*). Each region in the atlas is represented by a sphere at its center whose color denotes functional membership (blue indicates visual; magenta, somatomotor; green, dorsal attention; red, ventral attention; cyan, limbic; yellow, frontoparietal; black, default mode; orange, cerebellar/subcortical) and whose size indicates the amount of connectivity abnormalities (larger indicates more connectivity abnormalities). Note that the T2 FLAIR WM lesion-based ChaCo spheres are at a scale that is 10 times that of the RD-based ChaCo spheres for visibility.

mality mask. For example, if a GM region had 1000 connecting WM tracts and 50 passed through any voxel in the WM abnormality mask, the ChaCo score for that region would be 50/1000 = 5%, or −0.05 (the negative indicating a loss of connections). The identification of tracts that go through a lesion was a binary process: Tracts that went through 1 lesion were not considered different from those that went through >1.

Statistical Analysis

Atrophy for each of 121 subjects with MS was measured by calculating standard *z* scores of thickness for 68 cortical regions and volume for 18 subcortical regions from the FreeSurfer atlas, compared against the group of 15 healthy controls who had the same scans and processing. Partial Spearman correlations (controlling for age) were calculated on a region-by-region basis (after averaging left and right hemispheres to increase signal-to-noise) to identify regions with stronger associations between the burden of WM abnormality (measured ChaCo scores) and GM loss (measured with atrophy). *P* values were false discovery rate–corrected for multiple comparisons.[26]

Partial Least-Squares Regression

PLSR[27] was used in the subgroup of 66 subjects with MS to predict SDMT on the basis of their age, ChaCo scores, and GM atrophy profiles for each of the 86 GM regions. One PLSR model for each WM imaging technique (T2 FLAIR lesions and diffusion abnormality masks) was constructed to compare their respective performances. PLSR reduces the dimensionality of the input data by finding new combinations of the input variables that have maximal correlation with the outcome variables. PLSR is advantageous in situations where you have many more input variables than you do data points because the data get reduced to a parsimonious set of statistically relevant components. PLSR is also useful when input variables may be collinear because each of the constructed components on which the subsequent regression is based is mutually independent. The final number of components was chosen via jackknife cross-validation to minimize data overfitting, and the stability of the model was assessed by using bootstrapping.[20] Confidence intervals for the regression coefficients were calculated by using the bias-corrected and accelerated percentile method.[28] If the confidence interval did not include zero, that region's ChaCo score was considered a significant predictor after correcting for multiple comparisons by using the Šidák method.[29] Further details are given in On-line Appendix A.

RESULTS

RD and mean diffusivity had a vastly higher signal than the other statistics of fractional anisotropy and axial diffusivity, which largely had little or no voxels with significant differences. The Crawford modified *t* test is rather conservative, and we did not have a large healthy control group, which could explain the lack of significant differences in the other summary statistics. What is not surprising, the mean diffusivity and RD masks identified similar WM voxels; in fact, their ChaCo scores had a Pearson correlation of 0.98 ($P < .05$). Due to the lack of signal in fractional anisotropy and axial diffusivity masks and the similarity of the mean diffusivity and RD masks, we continued the analysis with RD only. The total volume of the RD and T2 FLAIR abnormality masks were significantly and moderately correlated (Spearman $r = 0.52$, $P <$

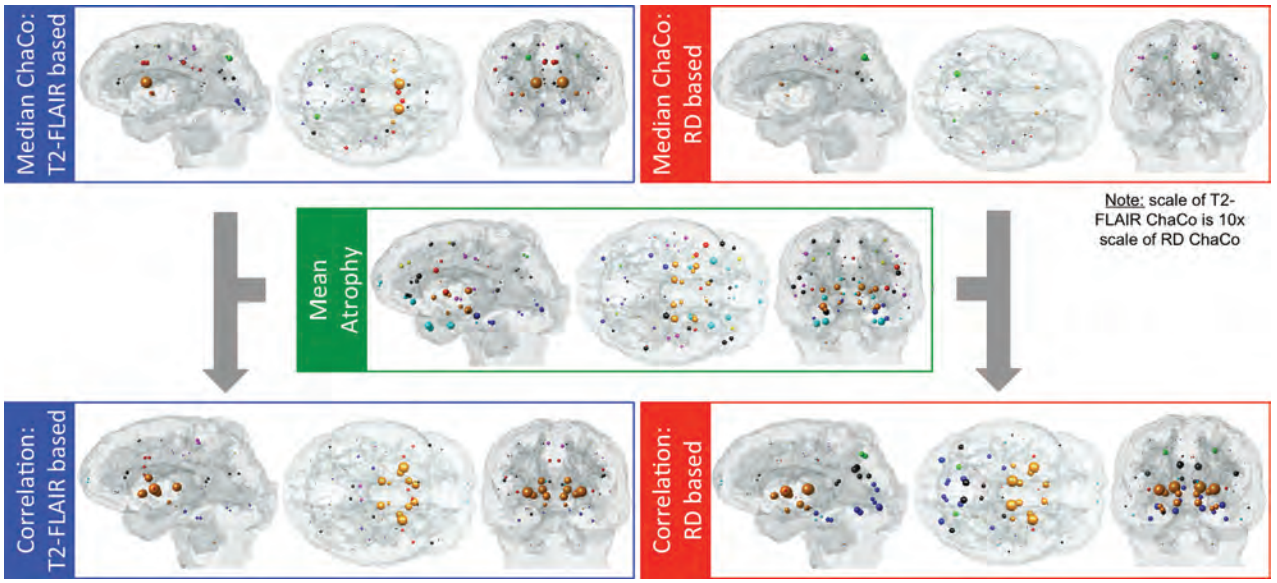

FIG 2. Median ChaCo for the 2 abnormality masks (T2 FLAIR lesions and RD abnormalities), mean atrophy, and corresponding correlation over 121 patients with MS. Each sphere indicates the center of a given gray matter region, while the color denotes functional network membership (blue indicates visual; magenta, somatomotor; green, dorsal attention; red, ventral attention; cyan, limbic; yellow, frontoparietal; black, default mode; orange, cerebellar/subcortical). Larger spheres indicate more connectivity abnormalities, more atrophy, or higher correlation, respectively. Note that the T2 FLAIR WM lesion-based ChaCo spheres are at a scale that is 10 times that of the RD-based ChaCo spheres for visibility.

.05), as were their ChaCo scores (Spearman $r = 0.51$, $P < .05$). T2 FLAIR lesion masks generally encompassed at least an order of magnitude larger volume; therefore, ChaCo was generally an order of magnitude larger. RD abnormalities were at times contained within T2 FLAIR lesions; however, 48 of 121 subjects had no overlapping voxels. Figure 1 displays the masks of T2 FLAIR hyperintensities (blue) and RD increases (red) for 3 different individuals along with the corresponding ChaCo scores via a "glass brain" display. The glass brain display has a sphere located at the center of each of the 86 GM regions, whose size is proportional to the ChaCo score of that region (larger indicates more connectivity abnormalities) and whose color indicates its functional network membership. The intersubject variability across these patients with early MS can be appreciated, as can the correspondence of the abnormality masks from the 2 imaging modalities. We did observe that the RD abnormalities in these subjects are often circumscribed by or in close proximity to the T2 FLAIR lesion masks. These locations gave us confidence that the image processing steps, including normalization of both image modalities, were adequate (On-line Fig 3 has more examples).

ChaCo Scores and Atrophy

Glass brain displays in Fig 2 show the median of the ChaCo scores across the population for the 2 abnormality masks (larger sphere indicates more connectivity abnormalities), with the mean of the atrophy in the middle row (larger sphere indicates more atrophy) and correlations between the two measures in the bottom row (larger sphere indicates higher correlation). Areas with the highest median ChaCo scores (>1.5% disconnected) for the T2 FLAIR–based masks were the bilateral caudate, caudal anterior cingulate, posterior cingulate, putamen, left superior and inferior parietal gyri, and right pericalcarine. Areas with highest median ChaCo scores for the RD-based masks were the bilateral caudate nucleus and parietal regions. Areas of highest atrophy were mainly subcortical areas, including the thalamus, and temporal pole regions. For visualization of ChaCo and atrophy values over the entire population, see On-line Fig 1.

Correlations of ChaCo with Atrophy

Over all 86 regions in each of the 121 subjects with MS, regional ChaCo from both abnormality masks had weak partial Spearman correlations (controlling for age) with atrophy (T2 FLAIR ChaCo: $r = 0.01$, $P > .05$; and RD ChaCo: $r = 0.042$, $P < .05$). Bilateral regions with significant partial Spearman correlations (controlling for age and multiple comparisons corrected) were observed between both sets of ChaCo scores and atrophy. Deep GM structures of the thalami ($r = 0.30$ and $r = 0.41$) and putamen ($r = 0.38$ and $r = 0.39$) had significant correlations of atrophy with both T2 FLAIR–based and RD-based ChaCo scores, respectively. In addition to those regions, the caudate nucleus ($r = 0.26$), globus pallidus ($r = 0.26$), and nucleus accumbens ($r = 0.28$) were correlated for T2 FLAIR on the basis of ChaCo, and the hypothalamus ($r = 0.26$) was significantly correlated for RD-based ChaCo. Finally, the temporal poles had particularly high atrophy (second highest after the thalami) and had nonsignificant correlation with both ChaCo scores. However, these results could merely reflect the difficulty of FreeSurfer in handling temporal regions.

Partial Least-Squares Regression

One subject who had a very large amount of WM damage over the whole brain relative to the rest of the population (ie, the z score of the mean T2 FLAIR lesion-based ChaCo was >5) was removed from this analysis. SDMT scores in our MS cohort were significantly lower ($P < .05$) when compared via t test with 2 different sets of healthy populations with similar age ranges.[30,31] Both models included 2 final components based on the selection criteria outlined in On-line Appendix A. The T2 FLAIR lesion-based model was more accurate ($R^2 = 0.42$) than the RD-based model

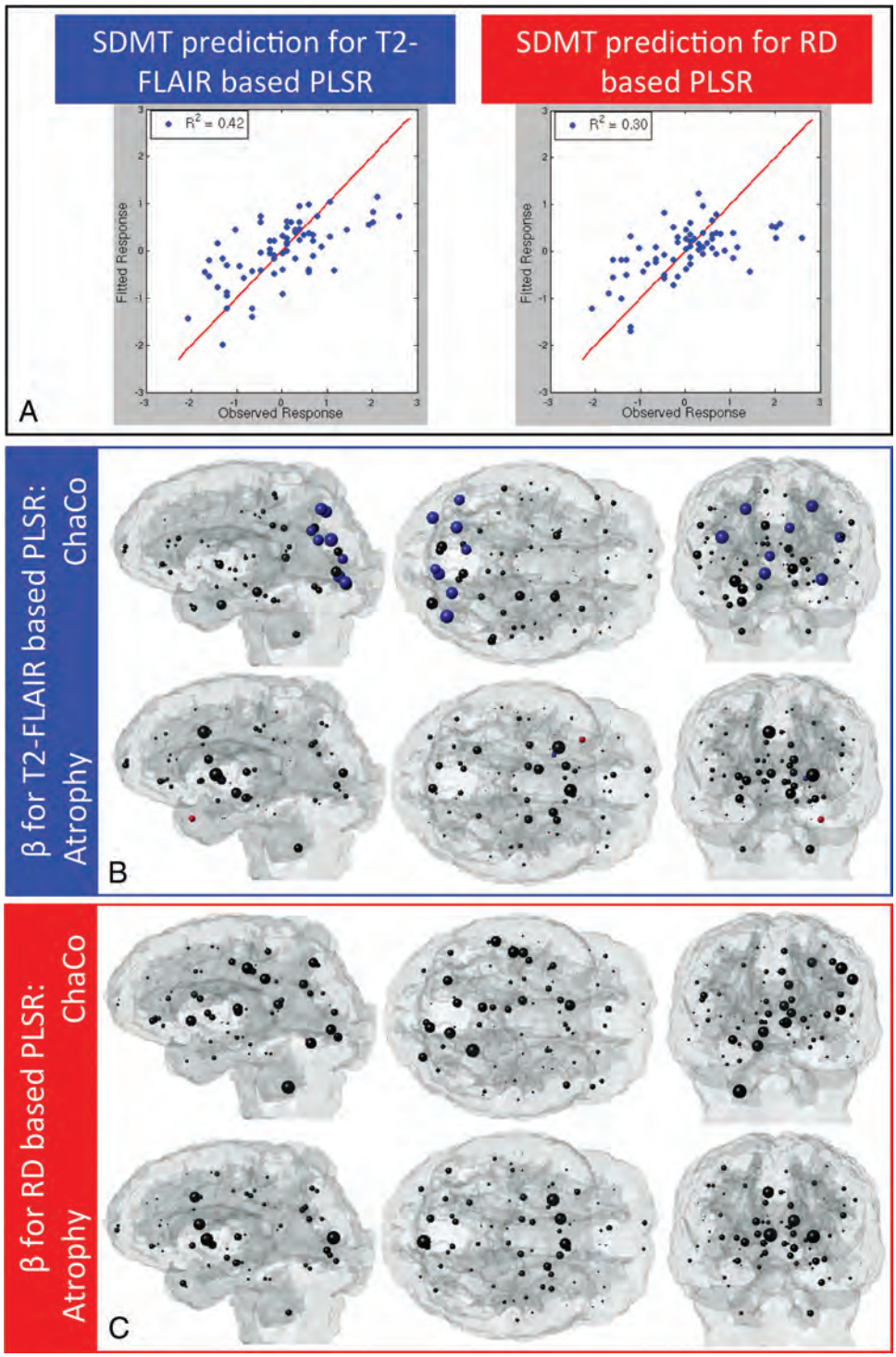

FIG 3. Partial least-squares regression results. *A*, The predicted versus actual normalized SDMT scores for the 2 models (T2 FLAIR lesion-based ChaCo and RD abnormality–based ChaCo), along with the R^2 value in the legend. The *red line* represents perfect prediction (x = y). *B*, Glass brain displays show regression coefficients for the ChaCo scores (*top row*) and atrophy (*bottom row*) of each gray matter region for the T2 FLAIR–based PLSR model. Sphere color denotes that the regression coefficient was the following: 1) nonzero and positive (blue), 2) nonzero and negative (red), or 3) not significantly different from zero (black). Sphere size is proportional to the mean of the bootstrapped sample of the regression coefficient. *C*, Same plot as in *B*, but for the RD abnormality–based PLSR model.

($R^2 = 0.30$) (Fig 3*A*). Figure 3*B*, -*C* visualizes the regression coefficients for both models. Sphere size is proportional to the mean of the bootstrapped sample, and color corresponds to the significance and direction of the coefficient (blue indicates positive and significant; red, negative and significant; and black, not significant). In the T2 FLAIR lesion-based model, the ChaCo scores of several brain regions in the occipital and parietal lobes were significant predictors of SDMT, along with subject age and GM atrophy in the right putamen (Fig 3*B*). Higher ChaCo and atrophy scores correspond to tissues that are closer to normal, so positive

regression coefficients indicate that more normal tissues corresponded to higher SDMT scores, as expected. Other subcortical areas such as the thalamus, nucleus accumbens, globus pallidus, hypothalamus, hippocampus, caudate nucleus, and the cerebellum had large positive mean regression coefficients, but none were significant. There were 2 regions whose atrophy coefficient had a significant negative relationship with SDMT; however, their values were quite small. No coefficients in the RD-based model remained significant after multiple-comparison corrections (Fig 3*C*).

On-line Fig 2 shows the component coefficients for ChaCo and atrophy scores for each of the 2 models. These are the directions on which the data are projected before performing model fitting and can be thought of as the weights in a weighted average of the input variables. These coefficients give additional information about the relative importance of each predictor to each component. The color corresponds to the sign of the coefficient (blue indicates negative; red, positive). However, sign information is not important except for relative comparison because the PLSR components are invariant to reflection. The first component represents the direction on which the data were projected to have maximal correlation with the outcome variable; the second component was the direction to achieve the next highest correlation (while maintaining independence of the first direction). The first components of both models (On-line Fig 2*A*, -*C*) emphasized the contribution of ChaCo scores over the contribution of atrophy. Their second components varied slightly: In the T2 FLAIR–based model (On-line Fig 2*B*), the second component seemed to emphasize both overall atrophy and ChaCo in the occipital and parietal areas, while the second component in the RD-based model (On-line Fig 2*D*) seemed to emphasize only overall atrophy.

DISCUSSION

Relatively weak correlations were observed between ChaCo scores and global regional atrophy, probably a result of a few factors. First, this patient population is early in the course of the disease, and there is not much appreciable atrophy in the structural MR imaging, which is only sensitive to detection of macroscopic tissue loss. Second, primary neuronal loss may also be occurring due to a mechanism independent from the one associated with WM lesions. Future studies will follow these same subjects longitudinally to better understand these mechanisms.

Most interesting, areas with significant correlation between both types of WM abnormality masks and atrophy appeared in the subcortical areas of the thalamus and putamen. Additional regions with significant correlation between ChaCo and atrophy included the caudate nucleus, globus pallidus, nucleus accumbens, and hypothalamus. These results largely suggest that deep GM areas are more sensitive to Wallerian degeneration, either retrograde or anterograde. Our results agree with other findings showing the following: 1) Striatal regions are susceptible to damage from inflammation arising in other areas[32,33]; 2) atrophy in the putamen, caudate, and thalamus is related to whole-brain T1 and T2 lesions in MS[34]; 3) thalamic atrophy can be explained in part by lesion volume and mean diffusivity in WM tracts connecting to the thalamus[35]; and 4) atrophy in deep GM regions of the caudate and pulvinar are related to ipsilateral WM lesion probability maps in highly connected regions.[36] In this cohort, overall observed atrophy was small (no regions showed significant group-wise atrophy after multiple-comparison corrections); however, regions with the most atrophy were the thalamus and other subcortical areas. Taken together, these findings indicate deep GM structures as areas of early injury in MS with a possible disease-duration-related WM injury gradient. Our current approach cannot determine the direction of a causal relationship between atrophy and WM connectivity abnormalities; however, it does support the hypothesis that deep GM regions are more related to WM abnormalities than other structures.

The PLSR results suggest that T2 FLAIR lesions in regions of the occipital and parietal lobes dealing with visual processing and integration may play an important role in subtle processing-speed dysfunction measured by the SDMT. Most interesting, our study by using similar methods in subjects with stroke, also revealed that ChaCo scores in occipital regions were significant predictors of SDMT performance (A.F.K., unpublished data, 2014). This finding, consistent across varying pathologies, populations, data acquisition techniques, and imaging parameters, provides validation of the current approach and strengthens our confidence in the visual pathways/SDMT connection. The SDMT requires close visual tracking, which may be adversely affected by abnormalities in WM connecting to the primary visual cortex and associated areas. We also observed that WM abnormalities seem to be more predictive of SDMT performance than atrophy because the ChaCo scores were emphasized by the primary component of each model. However, that this effect may be due to the relatively low amount of atrophy seen in this population with early MS cannot be ruled out. Our work adds to the growing body of literature suggesting that connectivity abnormalities of cognitively important cortical regions by injury to the interconnecting WM may provide a potential mechanism for cognitive dysfunction in MS.[37,38]

Limitations and Future Work

Tractography is a complex and error-prone process even in healthy subjects; there is currently no method that can fully capture true in vivo anatomy. The NeMo Tool uses tractography in healthy controls to determine the effects of WM abnormalities in the MS cohort. WM connections vary from individual to individual; therefore, the NeMo Tool may not be accurately representing a particular person's connectivity. Calculating average ChaCo scores over a large number of healthy subjects minimizes this drawback. See On-line Appendix B for a quantitative analysis of the influence of the variability in healthy controls on the reliability of ChaCo scores. Another limitation lies in the binary nature of tract counting: A streamline was not counted differently if it went through >1 lesion. In the future, this process will be modified to account for such situations.

Because the lesion masks are coregistered to common space by using the patient's MRI, which may contain pathologies, some errors may exist in the normalization process. Normalization was checked visually for accuracy (On-line Fig 3); furthermore, the effect of any small existing errors is again minimized by averaging over the large number of normal tractograms used in the NeMo tool.

There may be other elements of cognition affected in this cohort besides processing speed. Future studies will create a detailed picture of cognitive dysfunction in early MS. As the study expands to subjects with longer-term disease, we will also investigate functional areas other than cognition, for instance, motor impairment as measured by the Expanded Disability Status Scale. Another limitation is the relatively small number of healthy controls on which we based the *z* scores of cortical thickness, volume, and diffusion summary statistics. The size of the group is somewhat mitigated by the fact that they are age- and sex-matched to the patient population. Even so, this fact, coupled with the conservative nature of the Crawford *t* test, most likely contributed to the relatively low volume of abnormalities seen in the diffusion images, including RD maps.

Finally, future studies will focus on more sophisticated and specific imaging of both cortical lesions and WM abnormalities. Cortical lesions, which have been shown to be prevalent even in early MS,[39] are most likely occurring in this population. The fact that we are unable to detect cortical lesions with our current imaging protocol could be a source of the weak association of GM atrophy and ChaCo scores. Future studies will address the role of cortical lesions on connecting WM by using appropriate imaging, for instance, double inversion recovery or phase-sensitive inversion recovery MR imaging. In addition, T2 FLAIR and diffusion imaging are not specific to the nature of WM abnormalities in MS, being demyelination, axonal loss, and so forth. Future studies will focus on more specific measures of WM, for instance, myelin water fraction imaging.

CONCLUSIONS

This work demonstrates, in a regionally unbiased manner, that abnormalities in WM arising from demyelination and/or inflammation in MS are intimately related to atrophy in connecting deep GM regions. In addition, it was shown that T2 FLAIR abnormalities in WM connecting to areas of the brain dealing with visual integration and possibly GM atrophy in subcortical areas are related to subtle processing-speed changes in early MS, as captured by the SDMT. Successful application of the NeMo Tool indicates it has potential as an imaging-based biomarker to measure the impact of early inflammatory activity on behavioral changes and subsequent neuronal loss.

Disclosures: Ashish Raj—*RELATED*: *Grant*: Biogen Idec,* Novartis,* *Comments*: minor salary support as part of investigator-initiated research study at Weill-Cornell, which was supported by these companies; strictly academic research role. Susan A. Gauthier—*RELATED*: *Grant*: EMD Serono,* *Comments*: partially supported a study from which some of these data are derived; *UNRELATED*: *Consultancy*: Genzyme; *Grants/Grants Pending*: National Multiple Sclerosis Society,* Novartis,* Genzyme,* Biogen Idec.* *Money paid to the institution.

REFERENCES

1. Pagani E, Bammer R, Horsfield MA, et al. **Diffusion MR imaging in multiple sclerosis: technical aspects and challenges.** *AJNR Am J Neuroradiol* 2007;28:411–20
2. Gorgoraptis N, Wheeler-Kingshott CA, Jenkins TM, et al. **Combining tractography and cortical measures to test system-specific hypotheses in multiple sclerosis.** *Mult Scler* 2010;16:555–65
3. Rovaris M, Filippi M, Minicucci L, et al. **Cortical/subcortical disease burden and cognitive impairment in patients with multiple sclerosis.** *AJNR Am J Neuroradiol* 2000;21:402–08
4. Geurts JJ, Barkhof F. **Grey matter pathology in multiple sclerosis.** *Lancet Neurol* 2008;7:841–51
5. Calabrese M, Romualdi C, Poretto V, et al. **The changing clinical course of multiple sclerosis: a matter of grey matter.** *Ann Neurol* 2013;74:76–83
6. Geurts JJ, Stys PK, Minagar A, et al. **Gray matter pathology in (chronic) MS: modern views on an early observation.** *J Neurol Sci* 2009;282:12–20
7. Narayanan S, Fu L, Pioro E, et al. **Imaging of axonal damage in multiple sclerosis: spatial distribution of magnetic resonance imaging lesions.** *Ann Neurol* 1997;41:385–91
8. Shu N, Liu Y, Li K, et al. **Diffusion tensor tractography reveals disrupted topological efficiency in white matter structural networks in multiple sclerosis.** *Cereb Cortex* 2011;21:2565–77
9. Rocca MA, Valsasina P, Martinelli V, et al. **Large-scale neuronal network dysfunction in relapsing-remitting multiple sclerosis.** *Neurology* 2012;79:1449–57
10. Bodini B, Khaleeli Z, Cercignani M, et al. **Exploring the relationship between white matter and gray matter damage in early primary progressive multiple sclerosis: an in vivo study with TBSS and VBM.** *Hum Brain Mapp* 2009;30:2852–61
11. Sbardella E, Petsas N, Tona F, et al. **Assessing the correlation between grey and white matter damage with motor and cognitive impairment in multiple sclerosis patients.** *PLoS One* 2013;8:e63250
12. Raj A, Kuceyeski A, Weiner M. **A network diffusion model of disease progression in dementia.** *Neuron* 2012;73:1204–15
13. Zhou J, Gennatas ED, Kramer JH, et al. **Predicting regional neurodegeneration from the healthy brain functional connectome.** *Neuron* 2012;73:1216–27
14. Mesaros S, Rocca MA, Kacar K, et al. **Diffusion tensor MRI tractography and cognitive impairment in multiple sclerosis.** *Neurology* 2012;78:969–75
15. Hu B, Ye B, Yang Y, et al. **Quantitative diffusion tensor deterministic and probabilistic fiber tractography in relapsing-remitting multiple sclerosis.** *Eur J Radiol* 2011;79:101–07
16. Jones DK, Cercignani M. **Twenty-five pitfalls in the analysis of diffusion MRI data.** *NMR Biomed* 2010;23:803–20
17. Pierpaoli C, Barnett A, Pajevic S, et al. **Water diffusion changes in Wallerian degeneration and their dependence on white matter architecture.** *Neuroimage* 2001;13(6 pt 1):1174–85
18. Wheeler-Kingshott CA, Cercignani M. **About "axial" and "radial" diffusivities.** *Magn Reson Med* 2009;61:1255–60
19. Kuceyeski A, Maruta J, Relkin N, et al. **The Network Modification (NeMo) Tool: elucidating the effect of white matter integrity changes on cortical and subcortical structural connectivity.** *Brain Connect* 2013;3:451–63
20. Krishnan A, Williams LJ, McIntosh AR, et al. **Partial least squares (PLS) methods for neuroimaging: a tutorial and review.** *Neuroimage* 2011;56:455–75
21. Bergendal G, Fredrikson S, Almkvist O. **Selective decline in information processing in subgroups of multiple sclerosis: an 8-year longitudinal study.** *Eur Neurol* 2007;57:193–202
22. Fischl B, Sereno MI, Dale AM. **Cortical surface-based analysis. II: Inflation, flattening, and a surface-based coordinate system.** *Neuroimage* 1999;9:195–207
23. Penny WD, Friston KJ, Ashburner JT, et al, eds. *Statistical Parametric Mapping: The Analysis of Functional Brain Images.* Burlington: Academic Press; 2006:656
24. Smith SM. **Fast robust automated brain extraction.** *Hum Brain Mapp* 2002;17:143–55
25. Crawford JR, Garthwaite PH, Ryan K. **Comparing a single case to a control sample: testing for neuropsychological deficits and dissociations in the presence of covariates.** *Cortex* 2011;47:1166–78
26. Benjamini Y, Hochberg Y. **Controlling the false discovery rate: a practical and powerful approach to multiple testing.** *Journal of the Royal Statistical Society* 1995;57:289–300
27. Wold S, Sjöström M, Eriksson L. **PLS-regression: a basic tool of ch-**

emometrics. *Chemometrics and Intelligent Laboratory System* 2001; 58:109–30
28. Efron B, Tibshirani R. *An Introduction to the Bootstrap*. London: Chapman and Hall/CRC; 1994:456
29. Šidák Z. **Rectangular confidence regions for the means of multivariate normal distributions.** *J Amer Statist Assn* 1967;62:626–33
30. Centofani CC. *Selected Somatosensory and Cognitive Test Performances as a Function of Age and Education in Normal and Neurologically Impaired Adults* [dissertation]. Ann Arbor: University of Michigan; 1975
31. Bate AJ, Mathias JL, Crawford JR. **Performance on the Test of Everyday Attention and standard tests of attention following severe traumatic brain injury.** *Clin Neuropsychol* 2001;15:405–22
32. Karpuk N, Burkovetskaya M, Kielian T. **Neuroinflammation alters voltage-dependent conductance in striatal astrocytes.** *J Neurophysiol* 2012;108:112–23
33. Cappellani R, Bergsland N, Weinstock-Guttman B, et al. **Subcortical deep gray matter pathology in patients with multiple sclerosis is associated with white matter lesion burden and atrophy but not with cortical atrophy: a diffusion tensor MRI study.** *AJNR Am J Neuroradiol* 2014;35:912–19
34. Tao G, Datta S, He R, et al. **Deep gray matter atrophy in multiple sclerosis: a tensor based morphometry.** *J Neurol Sci* 2009;282: 39–46
35. Henry RG, Shieh M, Amirbekian B, et al. **Connecting white matter injury and thalamic atrophy in clinically isolated syndromes.** *J Neurol Sci* 2009;282:61–66
36. Mühlau M, Buck D, Förschler A, et al. **White-matter lesions drive deep gray-matter atrophy in early multiple sclerosis: support from structural MRI.** *Mult Scler* 2013;19:1485–92
37. Dineen RA, Vilisaar J, Hlinka J, et al. **Disconnection as a mechanism for cognitive dysfunction in multiple sclerosis.** *Brain* 2009;132(pt 1): 239–49
38. Roosendaal SD, Geurts JJ, Vrenken H, et al. **Regional DTI differences in multiple sclerosis patients.** *Neuroimage* 2009;44:1397–403
39. Lucchinetti CF, Popescu BFG, Bunyan RF, et al. **Inflammatory cortical demyelination in early multiple sclerosis.** *N Engl J Med* 2011; 365:2188–97

Bayesian Estimation of Cerebral Perfusion Using Reduced-Contrast-Dose Dynamic Susceptibility Contrast Perfusion at 3T

K. Nael, B. Mossadeghi, T. Boutelier, W. Kubal, E.A. Krupinski, J. Dagher, and J.P. Villablanca

ABSTRACT

BACKGROUND AND PURPOSE: DSC perfusion has been increasingly used in conjunction with other contrast-enhanced MR applications and therefore there is need for contrast-dose reduction when feasible. The purpose of this study was to establish the feasibility of reduced-contrast-dose brain DSC perfusion by using a probabilistic Bayesian method and to compare the results with the commonly used singular value decomposition technique.

MATERIALS AND METHODS: Half-dose (0.05-mmol/kg) and full-dose (0.1-mmol/kg) DSC perfusion studies were prospectively performed in 20 patients (12 men; 34–70 years of age) by using a 3T MR imaging scanner and a gradient-EPI sequence (TR/TE, 1450/22 ms; flip angle, 90°). All DSC scans were processed with block circulant singular value decomposition and Bayesian probabilistic methods. SNR analysis was performed in both half-dose and full-dose groups. The CBF, CBV, and MTT maps from both full-dose and half-dose scans were evaluated qualitatively and quantitatively in both WM and GM on coregistered perfusion maps. Statistical analysis was performed by using a *t* test, regression, and Bland-Altman analysis.

RESULTS: The SNR was significantly ($P < .0001$) lower in the half-dose group with 32% and 40% reduction in GM and WM, respectively. In the half-dose group, the image-quality scores were significantly higher in Bayesian-derived CBV ($P = .02$) and MTT ($P = .004$) maps in comparison with block circulant singular value decomposition. Quantitative values of CBF, CBV, and MTT in Bayesian-processed data were comparable and without a statistically significant difference between the half-dose and full-dose groups. The block circulant singular value decomposition–derived half-dose perfusion values were significantly different from those of the full-dose group both in GM (CBF, $P < .001$; CBV, $P = .02$; MTT, $P = .02$) and WM (CBF, $P < .001$; CBV, $P = .003$; MTT, $P = .01$).

CONCLUSIONS: Reduced-contrast-dose (0.05-mmol/kg) DSC perfusion of the brain is feasible at 3T by using the Bayesian probabilistic method with quantitative results comparable with those of the full-dose protocol.

ABBREVIATIONS: cSVD = block circulant singular value decomposition; FD = full-dose; HD = half-dose; SVD = singular value decomposition

DSC MR perfusion has been increasingly used to evaluate cerebral perfusion parameters in a variety of clinical applications, including acute ischemic infarction[1-3] and brain tumors.[4,5]

Most brain DSC perfusion studies are currently performed by using a gadolinium contrast dose of 0.1 mmol/kg.[6] To accomplish multi-injection protocols, one can use a double dose (0.2 mmol/kg) of gadolinium or split the current standard dose (0.1 mmol/kg) in half. Yet there are several incentives to reduce the contrast dose for brain DSC perfusion: First, the necessity to perform multiple contrast-enhanced sequences in routine neurodiagnostic MR imaging applications. For example, in patients presenting with acute ischemic stroke, a combination of contrast-enhanced MR angiography and DSC perfusion can improve the imaging-protocol acquisition speed.[7,8] In patients with brain tumors, the addition of a dynamic contrast-enhanced DSC perfusion scan may provide complementary diagnostic information.[9,10] The second incentive is the direct relationship between the risk of nephrogenic systemic fibrosis and contrast dose.[11] The third is the potential to reduce overall health care costs.

Contrast-dose reduction for DSC perfusion is challenging.[6,12,13] Some investigators have explored the possibility of dose reduction to 0.05 mmol/kg at 3T with mixed results.[14,15] The lower SNR associated with a reduced contrast dose remains a major limiting factor.[16] Deconvolution, routinely used for DSC

Received July 12, 2014; accepted after revision October 19.

From the Department of Medical Imaging (K.N., B.M., W.K., E.A.K., J.D.), University of Arizona, Tucson, Arizona; Olea Medical SAS (T.B.), La Ciotat, France; and Department of Radiological Sciences (J.P.V.), University of California, Los Angeles, Los Angeles, California.

Abstract of the preliminary results previously presented at: Annual Meeting of the American Society of Neuroradiology, May 20, 2014; Montréal, Quebec, Canada.

Please address correspondence to Kambiz Nael, MD, University of Arizona Medical Center, Department of Medical Imaging, Neuroradiology Section, 1501 N Campbell, PO Box 245067, Tucson, AZ 85724-5067; e-mail: kambiznael@gmail.com; @kambiznael

http://dx.doi.org/10.3174/ajnr.A4184

analysis, may not be an ideal methodology because small changes in the concentration time curve may dramatically influence the response residue function.[16,17] Reducing the contrast dose, with a resultant higher noise and lower SNR, can further accentuate this limitation. In contrast, the Bayesian probabilistic method is inherently less sensitive to low SNR[18] conditions and has the potential to more accurately calculate cerebral perfusion in low-dose protocols.

The purpose of this study was to establish the feasibility of reduced-contrast-dose (0.05-mmol/kg) brain DSC perfusion at 3T by using the Bayesian method and to compare the results with a block circulant singular value decomposition (cSVD)[19] analysis method, which is used routinely in clinical practice. If its potential is realized, the described protocol can add flexibility to multiinjection MR imaging protocols, such as those used for the evaluation of brain tumors and patients with stroke, without the need for additional contrast.

MATERIALS AND METHODS

Patients

Twenty consecutive patients (12 men, 8 women; mean age, 39.4 years; range, 19–74 years) who were referred for contrast-enhanced MR imaging of the brain were prospectively enrolled. All examinations were performed in accordance with institutional review board guidelines with an approved study protocol. The clinical indication for MR imaging included the following: persistent headache ($n = 7$), dizziness ($n = 4$), signs and symptoms of multiple sclerosis ($n = 4$), and staging for the evaluation of intracranial metastasis in patients with a history of underlying cancer ($n = 5$).

Image Acquisition

Imaging was performed on a clinical 3T scanner (Magnetom Skyra; Siemens, Erlangen Germany). A 16-element array coil (head, $n = 12$; neck, $n = 4$) was used for signal reception. Our routine contrast-enhanced brain MR imaging protocol includes axial and sagittal T1, axial T2, FLAIR, gradient recalled-echo, DWI, DSC perfusion, and 3D T1 postcontrast sequences. Two sets of DSC perfusion data in each patient were obtained by using a gradient recalled-echo–EPI sequence with identical sequence parameters (TR/TE, 1450/22 ms; flip angle, 90°; FOV, 22 cm; matrix size, 128 mm; 4-mm sections × 30; generalized autocalibrating partially parallel acquisition with an acceleration factor of 3, 60 dynamic frames).

A total of 0.15 mmol/kg of gadolinium contrast was used for each patient. The first DSC perfusion scan was obtained after acquisition of conventional noncontrast images and following the intravenous injection of 0.05-mmol/kg gadolinium (labeled as half-dose [HD]). After an 8-minute interval, during which axial T2WI and 3D postcontrast T1WI were acquired, the second DSC perfusion image was obtained following intravenous injection of 0.1 mmol/kg of gadolinium (labeled full-dose [FD]). Each contrast injection was flushed with 15 mL of saline. A constant injection rate of 5 mL/s was used for contrast and saline flush injections in all studies by using an electronic power injector.

Image Analysis

With FDA-approved software (Olea Sphere; Olea Medical Solutions, La Ciotat, France), the arterial input function was selected automatically by using a cluster analysis algorithm[20] and the deconvoluted perfusion parameters were calculated by using both the cSVD technique[19] and Bayesian probabilistic methods.[18]

Parametric maps of CBF, CBV, and MTT from both FD and HD were generated and available for qualitative and quantitative analysis. In addition, the Bayesian framework allows estimation of the noise SD. Hence, a univocal estimation of the SNR, defined as the ratio between the postcontrast signal over the SD, was used for quantitative analysis of SNR.

Qualitative Analysis

The CBF, CBV, and MTT maps in both HD and FD were introduced in a random order and in separate sessions to a neuroradiologist who was blinded to the type of contrast injection scheme and method of postprocessing. A 4-scale image-quality score was used to evaluate the delineation of major structures such as ventricles, thalami, basal ganglia, and brain stem with respect to susceptibility-mediated distortion at tissue interfaces, noise, and motion: 1, poor image quality, not interpretable; 2, impaired image quality with substantial distortion and noise, limiting the delineation of major structures; 3, good image quality with minimal distortion, diagnostic image quality; and 4, excellent image quality with delineation of all structures.

Quantitative Analysis

The FLAIR images, CBF, CBV, MTT, and the SNR maps from FD and HD DSC studies for each patient were coregistered by the Olea Sphere software by using a 12-*df* transformation and a mutual information cost function. This step was followed by visual inspection to ensure adequate alignment.

Quantitative analysis was performed by 1 observer by using a region-of-interest-based analysis. Using FLAIR images for accurate identification of anatomic landmarks, we placed ROIs on the precentral gyrus and centrum semiovale to represent GM and WM, respectively. The ROIs were expanded automatically to the coregistered FD and HD studies in each individual. We automatically calculated the means ± SDs of CBF, CBV, MTT, and SNR and recorded them in each region of interest in cSVD- and Bayesian-calculated maps separately.

Statistical Analysis

Statistical analysis was performed by using MedCalc for Windows, Version 12.2.1 (MedCalc Software, Mariakerke, Belgium). The image-quality grading differences between cSVD- and Bayesian-calculated maps in both HD and FD were tested by the Wilcoxon rank sum test and the Spearman rank correlation. The quantitative analysis of CBF, CBV, and MTT in the HD and FD groups was tested by regression analysis and *t* test between cSVD- and Bayesian-calculated parameters. The significance level was defined as $P < .05$ (2-sided). Bivariate scatterplots ± 95% CIs and Bland-Altman plots were also generated.

RESULTS

Qualitative Analysis

Of 20 patients, 15 had normal study findings, 2 had MR imaging findings of multiple sclerosis, 1 had an incidental meningioma, and 2 had chronic white matter ischemic changes. Table 1 sum-

Table 1: Qualitative evaluation of perfusion parametric maps in full-dose (0.1-mmol/kg) and half-dose (0.05-mmol/kg) contrast groups processed with Bayesian and cSVD methods[a]

	Bayesian	cSVD	Wilcoxon Test (*P* Value)	Spearman Rank (*r*), 95% CI
Full-dose				
CBF	4, 3–4	4, 3–4	.76	0.84, 0.63–0.93
CBV	4, 3–4	4, 3–4	.6	0.69, 0.35–0.87
MTT	4, 3–4	3, 3–4	.12	0.53, 0.32–0.76
Half-dose				
CBF	4, 3–4	3, 3–4	.27	0.66, 0.31–0.85
CBV	3, 3–4	3, 2–4	.02[b]	0.4, 0.17–0.74
MTT	3, 3–4	3, 2–3	.004[b]	0.12, 0.04–0.54

[a] Data are presented as median, range.
[b] Significant.

marizes the results of image-quality scores (median, range) in both the HD and FD groups by using cSVD and Bayesian methods.

In FD DSC studies, all (100%) CBF, CBV, and MTT maps derived from Bayesian and cSVD methods were of diagnostic image quality (score, ≥3). There was no significant difference for image quality scores between Bayesian- versus cSVD-derived CBF ($P = .76$), CBV ($P = .6$), and MTT ($P = .12$) maps. Spearman rank correlation coefficients (r) were 0.84, 0.69, and 0.53 for CBF, CBV, and MTT, respectively (Table 1).

In HD DSC studies, all (100%) Bayesian-processed perfusion maps were of diagnostic image quality (score, ≥3). While 100% of cSVD-calculated CBF maps had diagnostic image quality, CBV maps in 4 patients (20%) and MTT maps in 8 patients (40%) were rated nondiagnostic (score, 2) due to significant inhomogeneity across the FOV, obscuring delineation of major structures (Fig 1). There was a significant difference in image-quality scores for Bayesian- versus cSVD-derived CBV ($P = .02$) and MTT ($P = .004$) maps. Spearman rank correlation coefficients (r) were 0.66, 0.40, and 0.12 for CBF, CBV, and MTT, respectively (Table 1).

When we compared FD and HD, there was higher correlation in image-quality scores in Bayesian-processed data compared with cSVD. The Spearman rank correlation coefficients ± the 95% CIs for image-quality scores were $r = 0.66$, 0.30–0.85 for CBF; $r = 0.61$, 0.24–0.83 for CBV; and $r = 0.59$, 0.20–0.80 for MTT in Bayesian-processed data.

The Spearman rank correlation coefficients ± 95% CIs for image-quality scores were $r = 0.45$, 0.20–0.74 for CBF; $r = 0.40$, 0.10–0.71 for CBV; and $r = 0.08$, 0.001–0.45 for MTT in cSVD-processed data.

Quantitative Analysis

The means of SNR values in gray matter were 27.1 ± 7.8 for the FD and 18.4 ± 7.0 for the HD group (32% lower SNR in the HD group, $P < .001$). The means of SNR values in white matter were 13.5 ± 5.9 for the FD group and 8.0 ± 4.9 for the HD group (40% lower SNR in HD, $P < .001$).

Quantitative analysis of perfusion parameters obtained from Bayesian and cSVD methods in gray matter and white matter is summarized in Tables 2 and 3. cSVD-derived perfusion values were statistically significantly different between the HD and FD groups both in gray matter and white matter (Table 2). Bayesian-derived perfusion values for the FD and HD groups were statistically significantly different for CBF but not for CBV or MTT (Table 3).

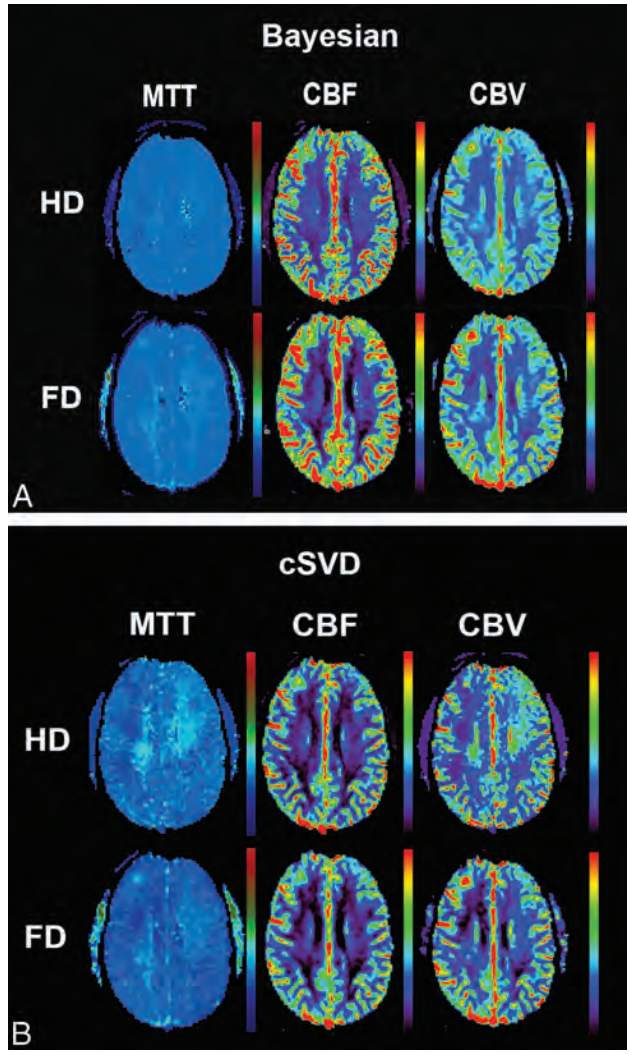

FIG 1. Coregistered and aligned MTT, CBF, and CBV maps from FD (0.1-mmol/kg) and HD (0.05-mmol/kg) DSC perfusion imaging are shown in this 40-year-old man who presented with headache. While the image quality of perfusion maps in FD scans is comparable between Bayesian and cSVD, note the heterogeneity and regional errors seen in cSVD-derived MTT and CBV maps in HD scans.

Regression analysis for quantitative perfusion values between the HD and FD groups showed significantly higher correlation in data processed with the Bayesian compared with the cSVD method. Bivariate scattergrams with 95% CI lines for comparison of HD and FD quantitative analysis between Bayesian and cSVD methods for both gray matter and white matter are summarized in Fig 2.

Correlation coefficient values (R^2) between the HD and FD groups for Bayesian-derived CBF, CBV, and MTT were 0.96, 0.71, and 0.64 in gray matter and 0.96, 0.81, and 0.85 in white matter, respectively. Correlation coefficient values (R^2) between the HD and FD groups for cSVD-derived CBF, CBV, and MTT were 0.72, 0.28, and 0.24 in gray matter and 0.60, 0.52, and 0.01 in white matter, respectively.

Bland-Altman plots for comparison of HD and FD quantitative analysis between Bayesian and cSVD methods for both gray

Table 2: cSVD-derived quantitative analysis of CBF, CBV, and MTT for gray matter and white matter in half-dose (0.05-mmol/kg) and full-dose (0.1-mmol/kg) contrast groups[a]

	cSVD-Processed DSC					
	GM		*t* Test	WM		*t* Test
Contrast Dose	FD	HD	(*P* Value)	FD	HD	(*P* Value)
CBF (mL/100 g/min)	68.7 ± 23.1	38.4 ± 19.6	<.001[b]	19.4 ± 6.4	10.8 ± 3.9	<.001[b]
CBV (mL/100 g)	2.4 ± 1	1.7 ± 0.8	.002[b]	1.3 ± 0.6	0.8 ± 0.4	<.001[b]
MTT (sec)	4.4 ± 0.9	5.5 ± 1.8	.005[b]	4.1 ± 1.7	5.9 ± 2.3	.008[b]

[a] Data are presented as mean ± SD.
[b] Significant.

Table 3: Bayesian-derived quantitative analysis of CBF, CBV, and MTT for gray matter and white matter in half-dose (0.05-mmol/kg) and full-dose (0.1-mmol/kg) contrast groups[a]

	Bayesian-Processed DSC					
	GM		*t* Test	WM		*t* Test
Contrast Dose	FD	HD	(*P* Value)	FD	HD	(*P* Value)
CBF (mL/100 g/min)	75.7 ± 27.0	62.1 ± 23.2	.001[b]	21.6 ± 7.1	17.9 ± 6.2	.037[b]
CBV (mL/100 g)	2.2 ± 0.8	1.8 ± 0.7	.090	1.3 ± 0.4	1.1 ± 0.4	.11
MTT (sec)	2.9 ± 0.9	2.7 ± 1.1	.450	4.3 ± 1.1	4.8 ± 1.2	.051

[a] Data are presented as mean ± SD.
[b] Significant.

matter and white matter are summarized in Fig 3. There was a significantly smaller mean difference and narrower range (variability) between HD and FD perfusion values when processed with Bayesian in comparison with cSVD methods (Fig 3).

DISCUSSION

Our results suggest that by using the Bayesian probabilistic method, reduced-contrast-dose brain DSC perfusion is feasible at 3T, with qualitative and quantitative results comparable with a full-dose control group. The Bayesian method outperformed the singular value decomposition (SVD)-deconvolution technique for reduced-contrast-dose DSC perfusion, in which the SNR was lower. Our data support the hypothesis that the inherent insensitivity of the Bayesian method to low SNR can provide acceptable measurement of cerebral perfusion in comparison with FD scans. This is reflected in a higher qualitative and quantitative correlation between HD and FD data in Bayesian-processed data in comparison with cSVD.

A fundamental issue in DSC processing is the conversion of the observed concentration time curve into reliable estimates of CBF, CBV, and MTT. Most processing techniques by using the indicator-dilution theory assume that the observed concentration time curve is the convolution of the arterial input function with a residue function, scaled by CBF. The residue function represents the fraction of observed tracer remaining in the observed vasculature at a certain time after its arrival.

The influence of contrast-dose reduction on deconvoluted perfusion parameters, including CBF, CBV, and MTT, has been evaluated by several investigators.[6,12,14] Hypothetically and in the absence of noise, DSC-CBF determinations should be insensitive to contrast dose. In a noise-free environment, the deconvolution process of the arterial input function is expected to eliminate the influence that a longer arterial bolus characteristic of a higher contrast dose has on the CBF calculation. Similarly, the CBV calculation should be independent of dose, because the tissue measures of contrast agent concentration are scaled against those measured in the artery and then are integrated with time. However, in reality, concentration time curves obtained by DSC perfusion do exhibit a relatively high noise level. Deconvolution of noisy concentration time curves is an ill-posed problem when small changes in magnitude can dramatically influence the residue function.[16] Reducing the contrast dose can result in a decrease in tissue relaxivity ($\Delta R2^*$) and thus a drop in the peak of arterial input function and a significant increase in noise level,[6] which, in turn, can further accentuate the inaccuracies of deconvolution-based techniques in low-SNR systems.

The use of higher magnetic fields (≥3T), with inherently higher SNR and shorter T2/T2* relaxation times, should translate into a more effective T2* reduction for a given contrast dose during capillary passage[21,22] and offset some of the low SNR limitations. However, the effect of a high magnetic field alone on reduced-contrast-dose DCS perfusion has been modest, with mixed results using 0.05 mmol/kg of gadolinium at 3T.[14,15] Another approach is to use an improved postprocessing technique that is less sensitive to low SNR. SVD-based deconvolution,[16,19] one of the most broadly used DSC processing techniques, has 2 major shortcomings: First, in SVD, the regularization is achieved by truncating the smallest singular value (threshold) that is responsible for the fast oscillation in the nonregularized residue function. This threshold parameter is fixed at a given ad hoc value, in which, ideally, it should be adapted to each voxel and determined from the perfusion data. Second, the truncated SVD method is equivalent to using a low-pass filter, which is suboptimal for estimating the residue function, known to be discontinuous.

Although improved deconvolution techniques can be obtained by using a semiadaptive threshold, as used in oscillation index SVD[19] or Gaussian process deconvolution,[23] some investigators have promoted the more robust nonparametric Bayesian technique to deal with the challenge of low SNR.[18,24] In the Bayesian method, a generative model of signal is used, applying the Bayes rule to combine experimental perfusion data and a priori information about the parameters, to compute a posteriori probability distribution functions for every parameter of interest. From those distributions, parameter estimates and errors in those estimates can be derived (eg, the mean and SD of the a posteriori distributions). The only reasonable assumption made to build the prior distribution of the residue function is that this function must be smooth. One of the advantages of this method is that it treats the regularization parameter as any other parameter. Hence, the regularization parameter is automatically estimated from the perfusion data so that the regularization is optimal for every experimental condition and set of hemodynamic parameters, without any human intervention. Furthermore, the method uses much more precise numeric approximations of the convolution product, which helps to reduce bias in the estimates. From

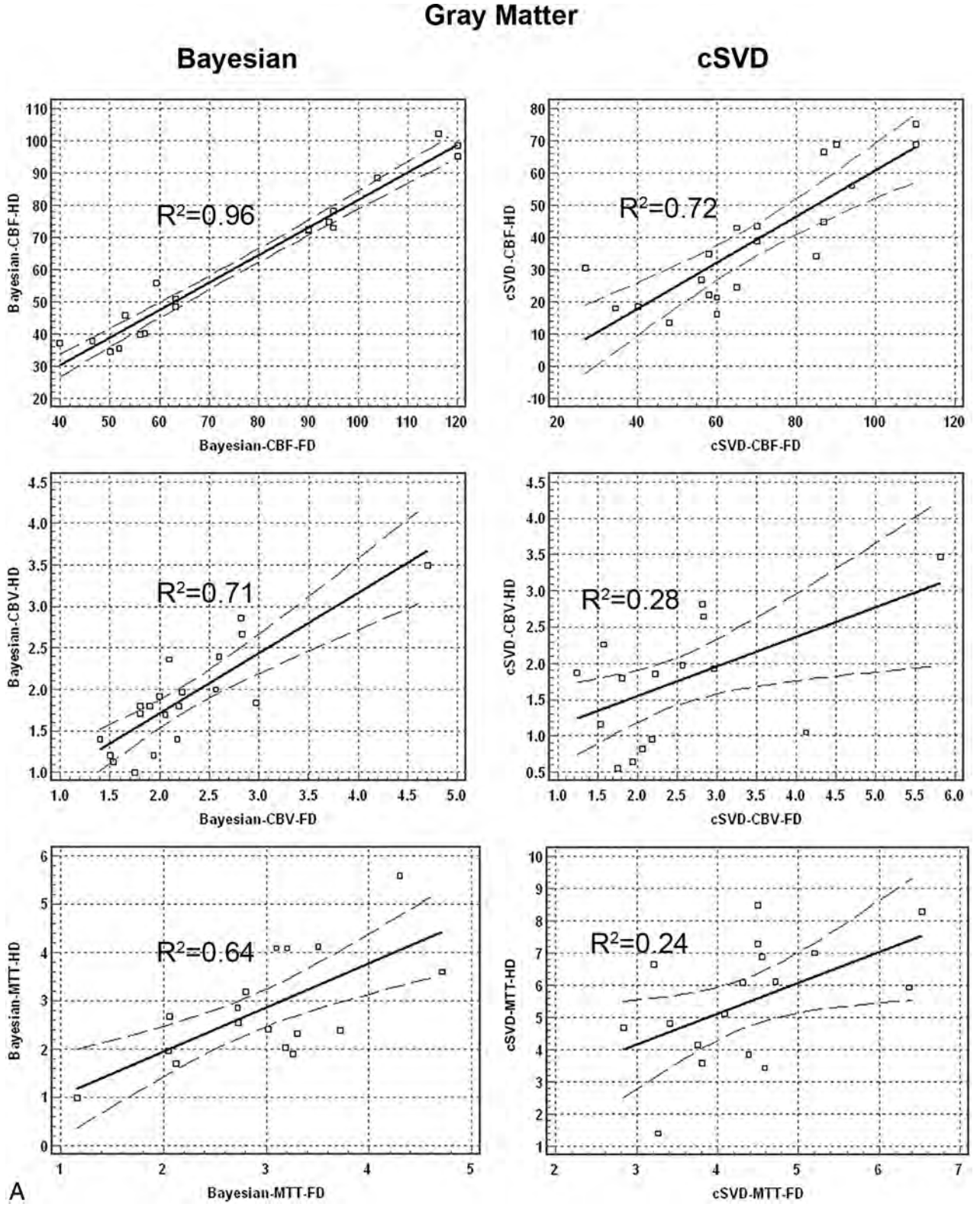

FIG 2. Bivariate regression scatterplots with 95% CI lines of quantitative analysis of CBF, CBV, and MTT derived from full-dose (0.1-mmol/kg) and half-dose (0.05-mmol/kg) DSC perfusion imaging in both gray matter and white matter. There is significantly higher correlation between HD and FD perfusion values in Bayesian- versus cSVD-processed data.

simulation studies, the method has been shown to be more precise, robust, and less sensitive to noise level.[18,24]

Our results confirm the theoretic advantages of the Bayesian method over SVD-based deconvolution to achieve a more accurate estimation of DSC perfusion parameters in low-SNR environments.[18,25] We demonstrate that by reducing the contrast dose, all Bayesian-derived perfusion maps retained diagnostic image quality, while 20% and 40% of SVD-derived CBV and MTT

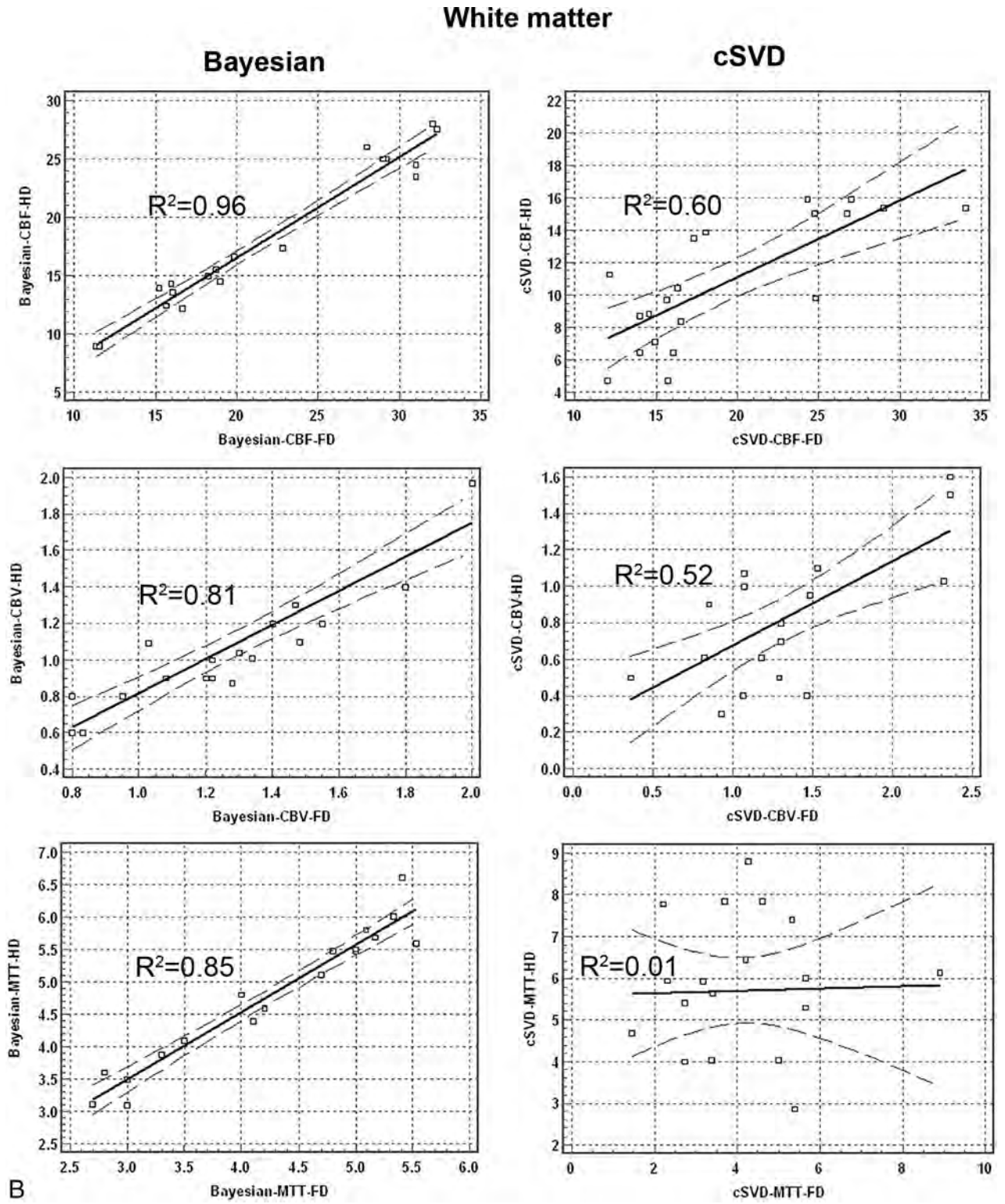

FIG 2. Continued.

maps, respectively, were nondiagnostic due to significant inhomogeneity caused by increased noise. In addition, in the reduced-contrast-dose scans, the Bayesian-processed data demonstrated quantitative perfusion values comparable with those of the FD group. Most important, the cSVD-derived quantitative values revealed an approximately 44% underestimation of CBF, 30% underestimation of CBV, and 20% overestimation of MTT in gray matter compared with the FD. This finding highlights the known limitation[16] of deconvolution techniques when dealing with noisy concentration time curves that have resulted from contrast-dose reduction. Due to an inherently lower perfusion, white matter usually receives a relatively smaller volume of contrast in comparison with gray matter.[26] This can result in a noisier environment in the cerebral white matter, as highlighted by our results, which revealed an even

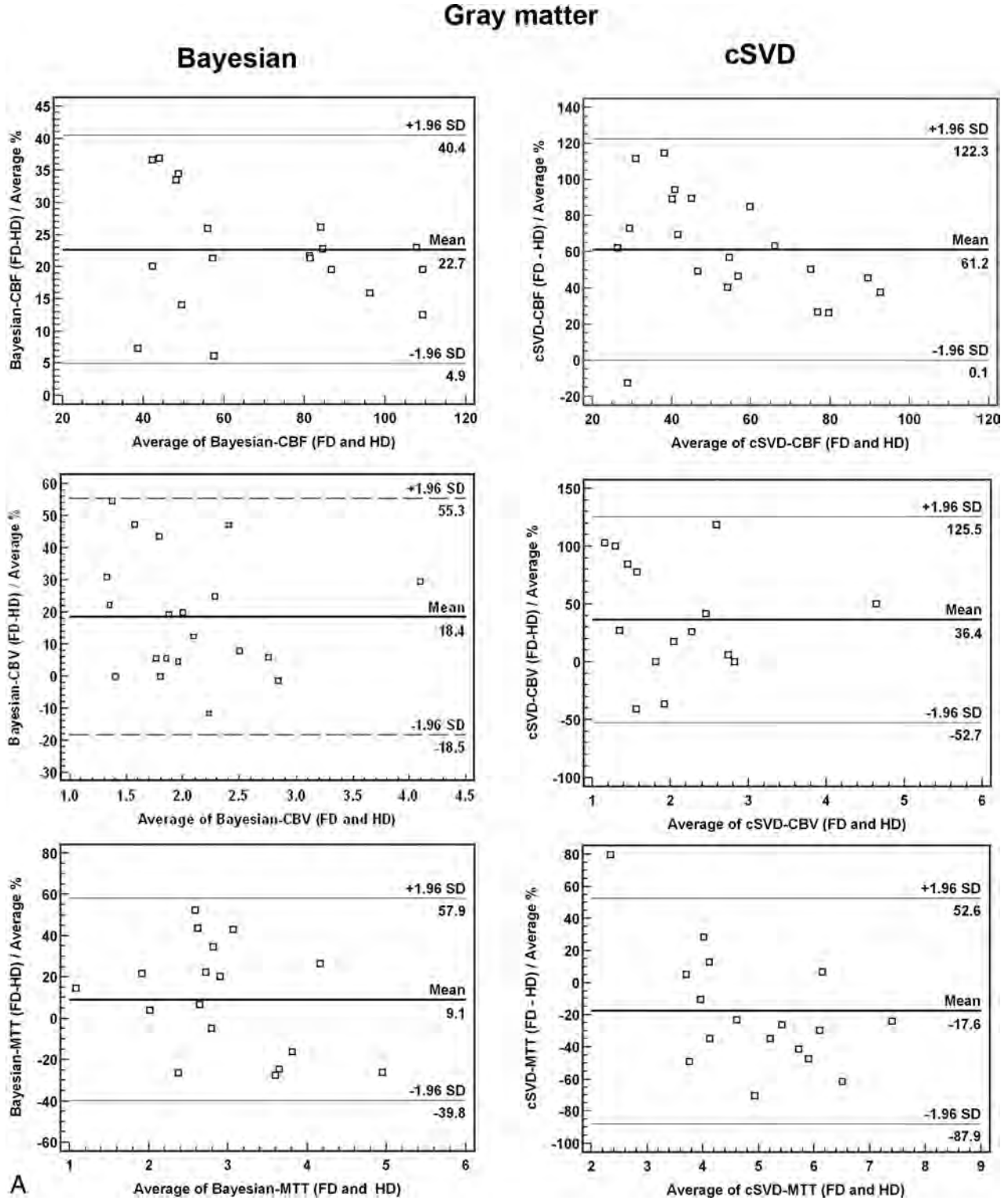

FIG 3. Bland-Altman plots of quantitative analysis of CBF, CBV, and MTT derived from full-dose (0.1-mmol/kg) and half-dose (0.05-mmol/kg) DSC perfusion in both gray matter and white matter. There is a significantly smaller mean difference and narrower range in Bayesian- versus cSVD-processed data between HD and FD perfusion values.

higher underestimation of CBV (38%) and overestimation of MTT (30%) in white matter compared with gray matter.

Our study has several limitations. First, our sample size was relatively small, which limits the power of the study. Second, we chose a rather empiric approach to assess the effect of contrast-dose reduction on DSC perfusion parameters. Besides noise, changes in contrast dose can affect many other factors, including tissue relaxivity and arterial statistical field shifts, which, in turn, can affect the DSC perfusion parameters. The possible interaction among these variables may ultimately require a more complex

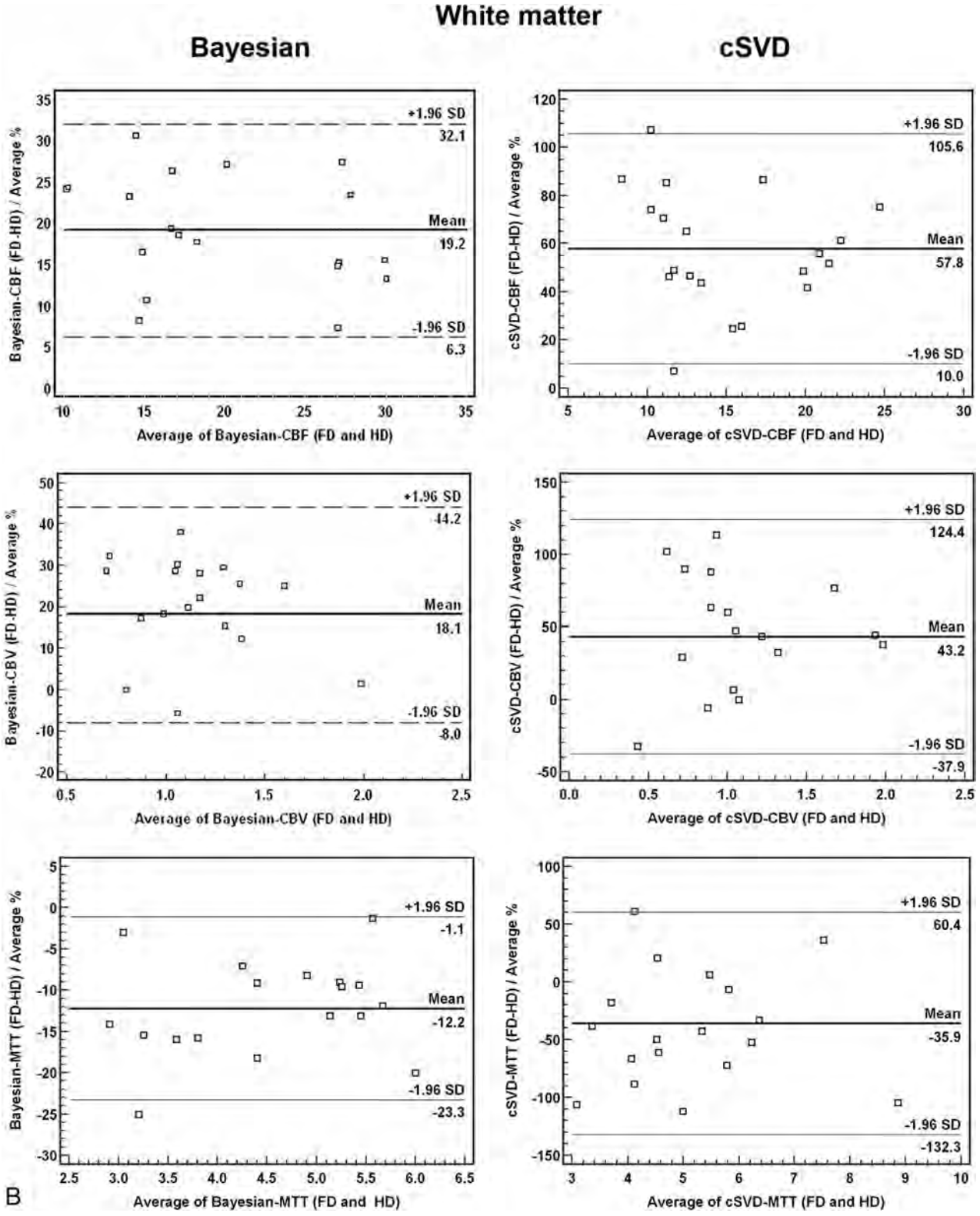

FIG 3. Continued.

model and a more systematic approach with mathematic modeling to corroborate our findings. The FD DSC perfusion was always performed after HD, and the pre-existing contrast may introduce an unknown bias. Finally, despite using an intraindividual comparison of perfusion values in the HD and FD groups, the semiquantitative nature of DSC analysis remains an inherent limitation of this technique and the results should be interpreted in this context. Identical perfusion parameters should not be expected between FD and HD groups regardless of the applied deconvolution technique. In this study, despite better correlation

and less variability in Bayesian-derived perfusion values, the perfusion values remained different between FD and HD.

CONCLUSIONS

In summary, by using a Bayesian probabilistic method, reduced-contrast-dose brain DSC perfusion is feasible at 3T with qualitative and quantitative results comparable with those of a full-dose control group. This approach can add flexibility to multi-injection-enhanced MR imaging protocols, such as concurrent implementation of DSC and dynamic contrast-enhanced MR perfusion for brain tumor and contrast-enhanced MR angiography and DSC for patients with stroke, without the need for additional contrast.

Disclosures: Kambiz Nael—*UNRELATED*: *Consultancy*: Olea Medical SAS; *Travel/Accommodations/Meeting Expenses Unrelated to Activities Listed*: Olea Medical SAS. Timothé Boutelier—*UNRELATED*: *Employment*: Olea Medical SAS. Joseph Dagher—*UNRELATED*: *Grants/Grants Pending*: Defense Advanced Research Projects Agency, role as a Research Scientist,* *Comments*: Knowledge Enhanced Compressive Measurement. *Money paid to the institution.

REFERENCES

1. Lansberg MG, Straka M, Kemp S, et al. **MRI profile and response to endovascular reperfusion after stroke (DEFUSE 2): a prospective cohort study.** *Lancet Neurol* 2012;11:860–67
2. Albers GW, Thijs VN, Wechsler L, et al. **Magnetic resonance imaging profiles predict clinical response to early reperfusion: the diffusion and perfusion imaging evaluation for understanding stroke evolution (DEFUSE) study.** *Ann Neurol* 2006;60:508–17
3. Davis SM, Donnan GA, Parsons MW, et al. **Effects of alteplase beyond 3 h after stroke in the Echoplanar Imaging Thrombolytic Evaluation Trial (EPITHET): a placebo-controlled randomised trial.** *Lancet Neurol* 2008;7:299–309
4. Hu LS, Baxter LC, Pinnaduwage DS, et al. **Optimized preload leakage-correction methods to improve the diagnostic accuracy of dynamic susceptibility-weighted contrast-enhanced perfusion MR imaging in posttreatment gliomas.** *AJNR Am J Neuroradiol* 2010;31:40–48
5. Law M, Yang S, Babb JS, et al. **Comparison of cerebral blood volume and vascular permeability from dynamic susceptibility contrast-enhanced perfusion MR imaging with glioma grade.** *AJNR Am J Neuroradiol* 2004;25:746–55
6. Alger JR, Schaewe TJ, Lai TC, et al. **Contrast agent dose effects in cerebral dynamic susceptibility contrast magnetic resonance perfusion imaging.** *J Magn Reson Imaging* 2009;29:52–64
7. Ryu CW, Lee DH, Kim HS, et al. **Acquisition of MR perfusion images and contrast-enhanced MR angiography in acute ischaemic stroke patients: which procedure should be done first?** *Br J Radiol* 2006;79:962–67
8. Nael K, Meshksar A, Ellingson B, et al. **Combined low-dose contrast-enhanced MR angiography and perfusion for acute ischemic stroke at 3T: a more efficient stroke protocol.** *AJNR Am J Neuroradiol* 2014;35:1078–84
9. Armitage PA, Schwindack C, Bastin ME, et al. **Quantitative assessment of intracranial tumor response to dexamethasone using diffusion, perfusion and permeability magnetic resonance imaging.** *Magn Reson Imaging* 2007;25:303–10
10. Weber MA, Zoubaa S, Schlieter M, et al. **Diagnostic performance of spectroscopic and perfusion MRI for distinction of brain tumors.** *Neurology* 2006;66:1899–906
11. Kanal E, Barkovich AJ, Bell C, et al. **ACR guidance document for safe MR practices: 2007.** *AJR Am J Roentgenol* 2007;188:1447–74
12. Heiland S, Reith W, Forsting M, et al. **How do concentration and dosage of the contrast agent affect the signal change in perfusion-weighted magnetic resonance imaging? A computer simulation.** *Magn Reson Imaging* 2001;19:813–20
13. Wirestam R, Thilmann O, Knutsson L, et al. **Comparison of quantitative dynamic susceptibility-contrast MRI perfusion estimates obtained using different contrast-agent administration schemes at 3T.** *Eur J Radiol* 2010;75:e86–91
14. Manka C, Traber F, Gieseke J, et al. **Three-dimensional dynamic susceptibility-weighted perfusion MR imaging at 3.0 T: feasibility and contrast agent dose.** *Radiology* 2005;234:869–77
15. Alger JR, Schaewe TJ, Liebeskind DS, et al. **On the feasibility of reduced dose dynamic susceptibility contrast perfusion MRI for stroke.** In: *Proceedings of the Annual Meeting of the International Society for Magnetic Resonance in Medicine*, Montréal, Québec, Canada. May 6–13, 2011
16. Østergaard L, Weisskoff RM, Chesler DA, et al. **High resolution measurement of cerebral blood flow using intravascular tracer bolus passages. Part I: mathematical approach and statistical analysis.** *Magn Reson Med* 1996;36:715–25
17. Carpenter TK, Armitage PA, Bastin ME, et al. **DSC perfusion MRI-quantification and reduction of systematic errors arising in areas of reduced cerebral blood flow.** *Magn Reson Med* 2006;55:1342–49
18. Boutelier T, Kudo K, Pautot F, et al. **Bayesian hemodynamic parameter estimation by bolus tracking perfusion weighted imaging.** *IEEE Trans Med Imaging* 2012;31:1381–95
19. Wu O, Østergaard L, Weisskoff RM, et al. **Tracer arrival timing-insensitive technique for estimating flow in MR perfusion-weighted imaging using singular value decomposition with a block-circulant deconvolution matrix.** *Magn Reson Med* 2003;50:164–74
20. Mouridsen K, Christensen S, Gyldensted L, et al. **Automatic selection of arterial input function using cluster analysis.** *Magn Reson Med* Mar 2006;55:524–31
21. DeLano MC, Fisher C. **3T MR imaging of the brain.** *Magn Reson Imaging Clin N Am* 2006;14:77–88
22. Patil V, Jensen JH, Johnson G. **Intravascular contrast agent T2 (*) relaxivity in brain tissue.** *NMR Biomed* 2013;26:392–99
23. Andersen IK, Szymkowiak A, Rasmussen CE, et al. **Perfusion quantification using Gaussian process deconvolution.** *Magn Reson Med* 2002;48:351–61
24. Sasaki M, Kudo K, Boutelier T, et al. **Assessment of the accuracy of a Bayesian estimation algorithm for perfusion CT by using a digital phantom.** *Neuroradiology* 2013;55:1197–203
25. Mouridsen K, Friston K, Hjort N, et al. **Bayesian estimation of cerebral perfusion using a physiological model of microvasculature.** *Neuroimage* 2006;33:570–79
26. Leenders KL, Perani D, Lammertsma AA, et al. **Cerebral blood flow, blood volume and oxygen utilization: normal values and effect of age.** *Brain* 1990;113:27–47

Altered Microstructure in Temporal Lobe Epilepsy: A Diffusional Kurtosis Imaging Study

L. Bonilha, C.-Y. Lee, J.H. Jensen, A. Tabesh, M.V. Spampinato, J.C. Edwards, J. Breedlove, and J.A. Helpern

ABSTRACT

BACKGROUND AND PURPOSE: Temporal lobe epilepsy is associated with regional abnormalities in tissue microstructure, as demonstrated by DTI. However, the full extent of these abnormalities has not yet been defined because DTI conveys only a fraction of the information potentially accessible with diffusion MR imaging. In this study, we assessed the added value of diffusional kurtosis imaging, an extension of DTI, to evaluate microstructural abnormalities in patients with temporal lobe epilepsy.

MATERIALS AND METHODS: Thirty-two patients with left temporal lobe epilepsy and 36 matched healthy subjects underwent diffusion MR imaging. To evaluate abnormalities in patients, we performed voxelwise analyses, assessing DTI-derived mean diffusivity, fractional anisotropy, and diffusional kurtosis imaging–derived mean diffusional kurtosis, as well as diffusional kurtosis imaging and DTI-derived axial and radial components, comparing patients with controls.

RESULTS: We replicated findings from previous studies demonstrating a reduction in fractional anisotropy and an increase in mean diffusivity preferentially affecting, but not restricted to, the temporal lobe ipsilateral to seizure onset. We also noted a pronounced pattern of diffusional kurtosis imaging abnormalities in gray and white matter tissues, often extending into regions that were not detected as abnormal by DTI measures.

CONCLUSIONS: Diffusional kurtosis is a sensitive and complementary measure of microstructural compromise in patients with temporal lobe epilepsy. It provides additional information regarding the anatomic distribution and degree of damage in this condition. Diffusional kurtosis imaging may be used as a biomarker for disease severity, clinical phenotypes, and treatment monitoring in epilepsy.

ABBREVIATIONS: DKI = diffusional kurtosis imaging; FA = fractional anisotropy; MD = mean diffusivity; TLE = temporal lobe epilepsy

The most common histologic finding in patients with medial temporal lobe epilepsy (TLE) is hippocampal sclerosis, which is defined as neuronal loss and gliosis involving the hippocampus.[1-3] Routine clinical MR imaging of patients with TLE can demonstrate signs associated with hippocampal sclerosis.[4,5] Recent observations suggest that hippocampal abnormalities are not the only structural injury in TLE.[6-9] Imaging studies using whole-brain quantitative morphometry have repeatedly demonstrated that TLE is associated with extrahippocampal abnormalities[6,8-13] involving perihippocampal and perilimbic structures.

However, the full extent of structural abnormalities in TLE is still unclear. Therefore, the lack of a sensitive and specific marker of extrahippocampal damage may prevent the assessment of its clinical relevance. Diffusion MR imaging techniques aimed at quantifying tissue microstructure may offer more sensitive tools for determining the extent of brain pathology in TLE. A promising new method called diffusional kurtosis imaging (DKI) can provide information about cerebral microstructural abnormalities beyond that provided by conventional diffusion tensor imaging.[14,15] In fact, by providing a more comprehensive characterization of water diffusion properties, DKI may be more suitable for detecting subtle brain damage in TLE.

In this study, we investigated the anatomical pattern of microstructural abnormalities associated with TLE by contrasting the

Received July 12, 2014; accepted after revision October 19.

From the Departments of Neurology and Neurosurgery (L.B., J.C.E.) and Radiology and Radiological Science (C.-Y.L., J.H.J., A.T., M.V.S., J.A.H.), Comprehensive Epilepsy Center (L.B., J.C.E., J.B.), and Center for Biomedical Imaging (L.B., C.-Y.L., J.H.J., A.T., M.V.S.), Medical University of South Carolina, Charleston, South Carolina.

This study was supported by the American Society of Neuroradiology (grant No. 89779-01; Principal Investigator, A. Tabesh).

Please address correspondence to Leonardo Bonilha, MD, PhD, Department of Neurology and Neurosurgery, Medical University of South Carolina, 96 Jonathan Lucas St, 3rd floor CSB, Charleston, SC 29425; e-mail: bonilha@musc.edu

Indicates article with supplemental on-line table.

http://dx.doi.org/10.3174/ajnr.A4185

voxel-based analyses of microstructure maps derived from DKI and from well-established DTI.

MATERIALS AND METHODS

Subjects

Thirty-two consecutive patients with left TLE were recruited from the Comprehensive Epilepsy Center at the Medical University of South Carolina, where they were diagnosed on the basis of a comprehensive history and neurologic evaluation. The TLE diagnosis was defined in accordance with the criteria proposed by the International League Against Epilepsy,[16] based on a history compatible with partial seizures with temporal onset, interictal epileptiform discharges on interictal electroencephalography, and hippocampal atrophy on visual inspection of MR imaging. Not all patients included in this study were surgical candidates; thus, ictal recording was not obtained in all patients. All patients exhibited a classic presentation for TLE, based on history, seizure semiology, epileptiform discharges on interictal electroencephalography, as well as routine MRI. Most patients, but not all, exhibited signs of hippocampal sclerosis on MR imaging, and a detailed description of the demographic and clinical information for patients included in this study is provided in the On-line Table.

The mean age of patients was 44.8 ± 16.7 years; 22 patients were women. We also studied a control group of healthy individuals recruited from the local community who had no history of neurologic problems and no risk factors for epilepsy (mean age, 40.4 ± 11.6 years; 24 women). Patients and controls were similar in sex ($P = .21$) and age ($P = .92$) distributions.

Image Acquisition

All patients and controls underwent the same imaging protocol performed on a 3T Magnetom Verio MR imaging scanner (Siemens, Erlangen, Germany) equipped with a 12-channel head coil. Diffusion-weighted images were obtained by using a twice-refocused echo-planar sequence with 3 diffusion weightings (b=0, 1000, and 2000 s/mm^2) along 30 diffusion-encoding directions with NEX = 1 (NEX = 10 for b=0). Other imaging parameters were TR = 8500 ms, TE = 98 ms, FOV = 222 × 222 mm^2, matrix size = 74 × 74, parallel imaging factor = 2, no partial Fourier encoding, section thickness = 3 mm, and 40 axial sections. Acquisition time was 9 minutes and 12 seconds. Structural images were obtained by using a magnetization-prepared rapid acquisition of gradient echo sequence with TR = 2250 ms, TE = 4.18 ms, TI = 900 ms, FOV = 256 × 256 mm^2, matrix size = 256 × 256, section thickness = 1 mm, and 176 sagittal sections.

Image Processing

Tissue Volume Maps. T1-weighted images were submitted to gray and white matter tissue segmentation using the VBM toolbox (http://dbm.neuro.uni-jena.de/vbm/) for SPM8 software (http://www.fil.ion.ucl.ac.uk/spm/software/spm8). Image normalization and segmentation were performed iteratively by using the symmetric tissue probability map of VBM, very light regularization, and affine regularization to the ICBM space template (European Brains; http://bmap.ucla.edu/portfolio/atlases/ICBM_Template/). Spatial normalization was performed with affine and nonlinear transformations yielding modulated normalized gray and white matter probability maps. All maps were transformed into standard space, and their averages (gray and white matter maps separately) were used to provide tissue inclusion masks for statistical analyses.

Microstructure Maps. DKI postprocessing was performed by using the in-house software Diffusional Kurtosis Estimator (http://www.nitrc.org/projects/dke),[17] which performed the following processing steps to generate diffusivity and kurtosis maps: first, motion correction through a 6-parameter rigid-body transformation to spatially align all DWIs. Second, at each voxel, the diffusion and diffusional kurtosis tensors were jointly fitted to the DWIs for b=0, 1000, and 2000 s/mm^2 for that voxel, and the mean kurtosis was calculated from the tensors. The diffusion tensor was fitted to the DWIs for b=0 and 1000 s/mm^2, and mean diffusivity and (MD) fractional anisotropy (FA) were calculated from the diffusion tensor. Axial and radial diffusion and kurtosis maps were also generated.

FA maps were nonlinearly normalized to a common space by using the fMRI of the Brain Software Library, Version 4.1.7 (http://www.fmrib.ox.ac.uk/fsl) using a symmetric FA template, and the resulting transformation was applied to normalize the other maps. The spatially normalized images were then submitted to spatial smoothing with an 8-mm Gaussian filter.

Statistical Analyses. We performed whole-brain voxelwise analyses, comparing patients with TLE and controls regarding MD, FA, mean kurtosis, axial diffusion, radial diffusion, axial kurtosis, and radial kurtosis maps. We performed comparisons using voxelwise t tests. All results were corrected for multiple comparisons using a false discovery rate threshold of $q < 0.01$.[18]

RESULTS

Gray Matter

Patients with TLE exhibited multiple cortical areas with significant increase in diffusion parameters, along with a concurrent decrease in kurtosis parameters.

Specifically, an increase in MD was observed within the orbitofrontal cortices, frontal poles, medial left temporal lobe region, and midposterior cingulate. No significant changes were observed with axial diffusion, but radial diffusion was increased in patients in the orbitofrontal regions, frontal poles, medial left temporal regions, left lateral temporal regions, and midposterior cingulate cortex.

In contrast, at the same statistical threshold level, a more diffuse pattern of significant reductions in mean kurtosis was observed, encompassing the temporopolar cortices, temporal and frontal opercula, medial temporal lobe regions (more pronounced on the left side), left lateral temporal region, prefrontal cortices and temporal poles, and cingulate and parietal regions. Overall, a higher statistical difference was noted on the left side.

Reductions in axial kurtosis were noted particularly over the frontal polar regions, left temporal pole, left lateral temporal cortex, and left precentral areas. Reductions in radial kurtosis were diffusely distributed across the entire brain but were particularly intense over the left medial temporal cortex, left temporal polar cortex, left insula, left fusiform gyrus, cingulate cortex, and left precentral regions.

These results are shown in Fig 1.

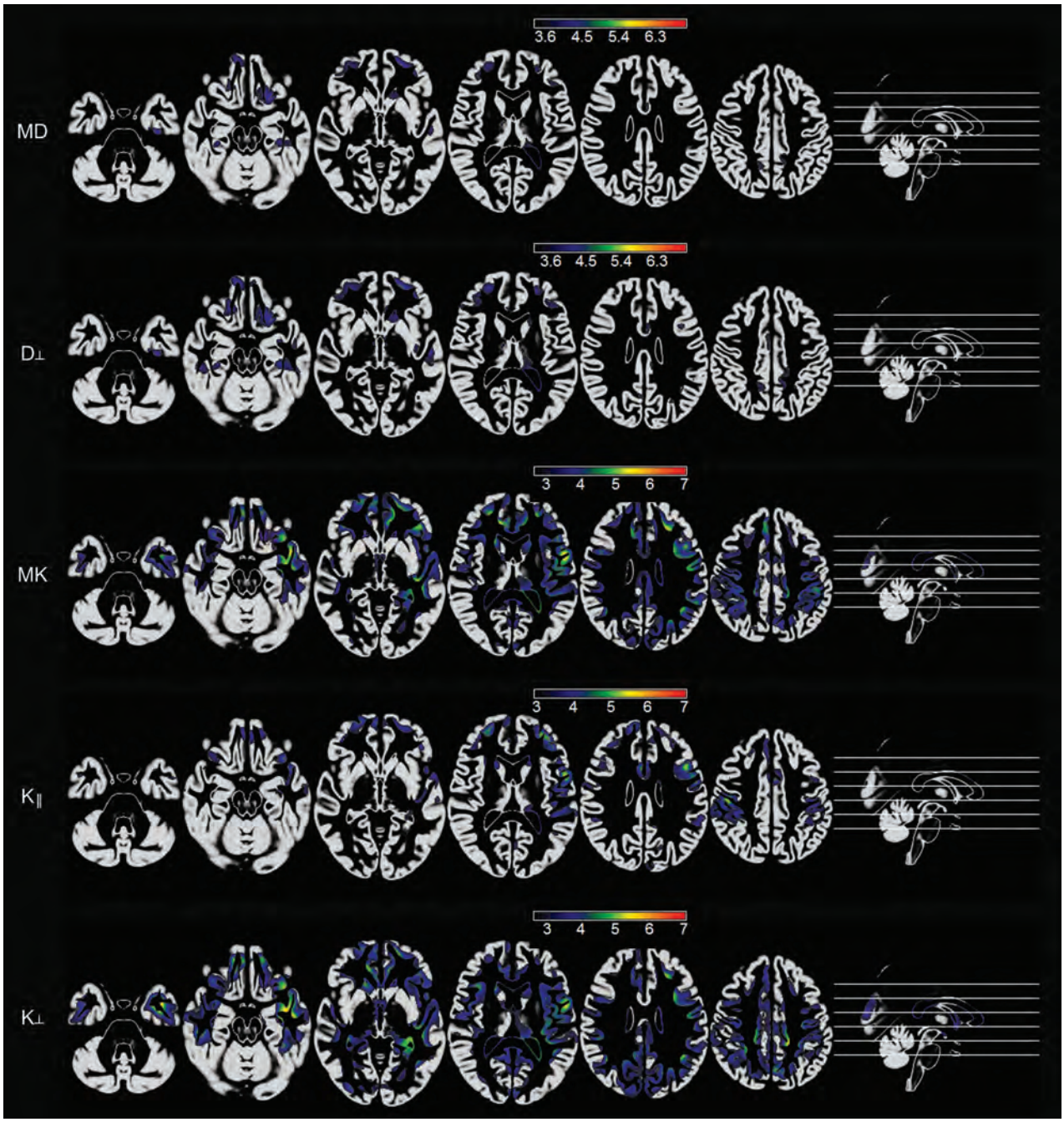

FIG 1. Voxelwise maps of cortical abnormalities in patients with TLE compared with controls. Statistical maps are overlaid on an average of probabilistic gray matter maps from all subjects. The scale bars represent absolute values of *t* scores. The first row demonstrates areas with an increase in MD in patients. The second row demonstrates areas of increased radial diffusion in patients. The third, fourth, and fifth rows demonstrate areas of reduced mean kurtosis and axial and radial kurtosis, respectively, in patients. All results were corrected for multiple comparisons by using a false discovery rate threshold of $q < 0.01$.

There were no cortical areas of reduced diffusion or increased kurtosis measures in patients.

White Matter

Patients with TLE demonstrated a significant increase in MD within the white matter in the frontal, left medial temporal, perithalamic, left occipitotemporal, and medial frontoparietal regions. There was also an increase in MD within the splenium of the corpus callosum. These abnormalities were also noted in areas of radial diffusion decrement, while axial diffusion did not demonstrate significant abnormalities between groups.

FA decrement was noted in a widespread pattern involving the medial temporal, perithalamic, orbitofrontal, left temporopolar, left occipitotemporal, and medial frontoparietal white matter regions. There was also a notable decrement in FA within the splenium of the corpus callosum, left side of the genu of the corpus callosum, and left uncinate fasciculus.

At the same statistical threshold, there was a remarkable ana-

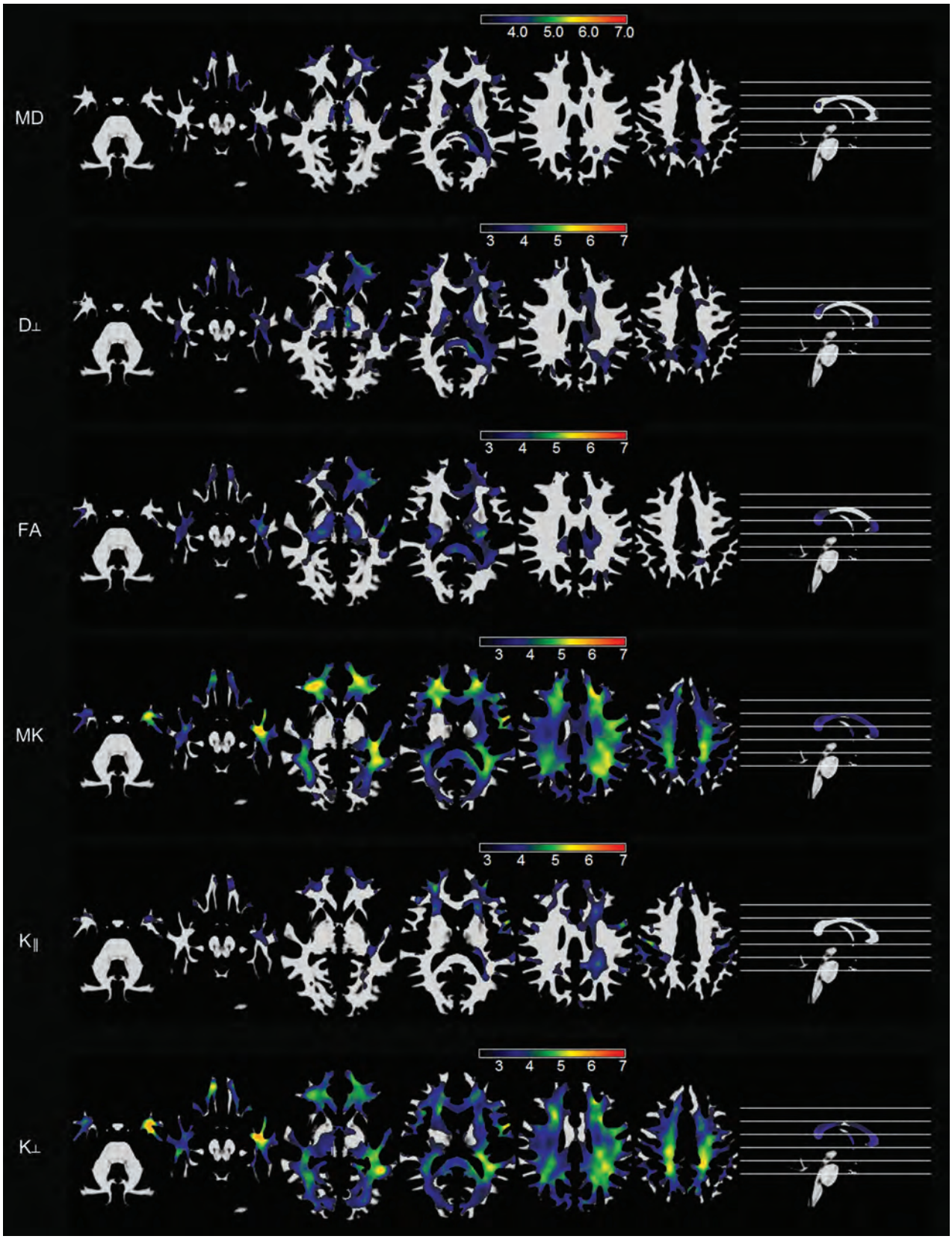

FIG 2. Voxelwise maps of white matter abnormalities in patients with TLE compared with controls. Statistical maps are overlaid on an average of probabilistic white matter maps from all subjects. The scale bars represent absolute values of *t* scores. The first and second rows demonstrate areas with an increase in MD and radial diffusion, respectively, in patients. The third row demonstrates areas with reduced FA in patients, while the fourth, fifth, and sixth rows demonstrate areas of reduced mean kurtosis, axial kurtosis, and radial kurtosis in patients, respectively. All results were corrected for multiple comparisons by using a false discovery rate threshold of $q < 0.01$.

tomical pattern of mean kurtosis reduction, which involved most of the brain white matter and was most pronounced over the left temporal, bilateral orbitofrontal, and left frontoparietal regions. These abnormalities were similar to the pattern noted with radial kurtosis decrement in patients.

These results are shown in Fig 2.

There were no areas of MD decrement, FA increase, or kurtosis increase in patients.

DISCUSSION

In this study, we investigated microstructural gray and white matter abnormalities in patients with TLE using a novel diffusion MR imaging technique called DKI. DKI is aimed at detecting changes in tissue microstructure, including those arising from non-Gaussian properties of water diffusion, thus providing a potentially more sensitive and specific tool for the evaluation of pathologic changes in TLE.[14,15] We contrasted the DKI-derived microstructural measures with the better established DTI-derived measures.

We replicated findings from several previous studies using DTI to assess microstructural abnormalities in TLE. Specifically, we demonstrated areas of increased MD and reduced FA in patients with TLE, which were preferentially located within, but not restricted to, the temporal lobe ipsilateral to the side of seizure onset.[19-29]

We observed that DKI is capable of detecting a broader anatomic pattern of microstructural abnormalities in patients with TLE, compared with conventional measures. Moreover, these results demonstrate a distribution of network abnormalities that is in direct concordance with the hypothesized network pathology related to TLE.[13,30] The presence of abnormalities demonstrated by DKI is more contiguous and anatomically plausible compared with conventional methodologies, and it is consistent with the theory of limbic and perilimbic dysfunction in TLE.[31,32]

In this study, we also corroborated the findings from Gao et al,[33] suggesting that DKI is more sensitive, compared with DTI, to detect microstructural abnormalities in the patients with TLE. Gao et al studied a population of children with TLE; nonetheless, their results are fairly equivalent to our observations from a population of adult subjects with TLE.

DKI and the Pathophysiology of TLE

The hypothesis that TLE is a disease that affects more than just the hippocampus has been corroborated by several imaging studies demonstrating abnormalities in TLE involving limbic structures.[6,8-13] However, there is considerable variability across studies regarding the extent and degree of extrahippocampal damage in TLE. These variations may be directly related to the sensitivity of the methods, as further highlighted by the observation that conventional methods are not sensitive to most extrahippocampal histologic changes.[34,35] This variability in findings precludes a better understanding of the pathophysiology of TLE.

Our results suggest that TLE is associated with extensive microstructural abnormalities, encompassing a contiguous and extensive network of extrahippocampal and extratemporal regions.

Our results were obtained from a population of consecutive patients with TLE, most of whom demonstrated signs of hippocampal sclerosis on MR imaging (On-line Table). Therefore, it is possible that the temporal and extratemporal microstructural abnormalities demonstrated by DKI are correlated with hippocampal cell loss. Future studies evaluating phenotypical differences in the distribution of DKI abnormalities may provide further insight into this subject.

Moreover, the patient population evaluated in this study was not composed exclusively of surgical candidates (ie, it included patients with relatively well-controlled epilepsy). Most interesting, our strong statistical results suggest that microstructural abnormalities were widespread across all subjects. While these findings support DKI as exquisitely sensitive to abnormalities associated with TLE, it is still unclear whether DKI can provide further information regarding classification into subgroups, particularly as it relates to pharmacologic or surgical treatment outcomes. This study provides initial evidence of DKI as a biomarker of TLE, and we believe that future studies could address the impact of DKI as a clinical biomarker.

DKI as a Biomarker

The results of this study suggest that DKI may provide a sensitive and specific biomarker of TLE. Specifically, it may be a powerful tool for determining the degree of abnormality in cortical regions, which may be related to the clinical or neuropsychological profiles, and for quantifying the burden of overall network abnormalities on clinical progression. Specifically, extrahippocampal microstructural tissue abnormalities may be related to epileptogenesis in some individuals with TLE.[31,36,37] These microstructural changes may represent a complex interaction among multiple pathologic mechanisms such as cell loss, inflammation, and axonal and dendritic reorganization, which are known to occur in epilepsy.[38]

Clinical Feasibility of DKI

DKI provides a convenient platform for the evaluation of microstructural abnormalities related to TLE and is one form of advanced diffusion MR imaging.[39] However, DKI may be advantageous to other methods due to its feasibility in routine clinical practice. Other modalities require significantly longer scan times and/or custom hardware. Conversely, DKI can be acquired with a high signal-to-noise ratio in approximately 6–10 minutes, depending on the scanner.

Future Applications

This study provides preliminary evidence in support of the utility of DKI for characterization of microstructural abnormalities in TLE. Our results suggest that DKI–defined microstructural abnormalities are pervasive in the hippocampal, temporal, and extratemporal regions. Future studies should further investigate the histologic correlates of these abnormalities and their relationship with the clinical and neuropsychological profiles in patients with medial temporal lobe epilepsy.

CONCLUSIONS

This study demonstrates the added value of kurtosis measures in the assessment of microstructural alterations in adult patients with TLE. The results of this study confirm our hypothesis that

DKI may provide complementary information regarding the location and magnitude of structural abnormalities in TLE.

Disclosures: Leonardo Bonilha—*RELATED*: *Grant*: American Society of Neuroradiology (grant No. 89779-01, Principal Investigator, A. Tabesh).* Jens H. Jensen—*OTHER RELATIONSHIPS*: Siemens owns a royalty-free nonexclusive license for diffusional kurtosis imaging with the pending patent held by New York University. I am one of the inventors. Maria V. Spampinato—*UNRELATED*: *Grants/Grants Pending*: Bracco,* *Comments*: clinical trial on 2 FDA-approved contrast agents. Ali Tabesh—*RELATED*: *Grant*: American Society of Neuroradiology,* *Comments*: 2013 Research Scientist Award. *Money paid to the institution.

REFERENCES

1. Sendrowski K, Sobaniec W. **Hippocampus, hippocampal sclerosis and epilepsy.** *Pharmacol Rep* 2013;65:555–65
2. Blümcke I, Coras R, Miyata H, et al. **Defining clinico-neuropathological subtypes of mesial temporal lobe epilepsy with hippocampal sclerosis.** *Brain Pathol* 2012;22:402–11
3. Babb TL, Brown WJ. **Pathological findings in epilepsy.** In: Engel JJ, ed. *Surgical Treatment of the Epilepsies.* New York: Raven; 1987: 511–40
4. Cendes F, Andermann F, Gloor P, et al. **MRI volumetric measurement of amygdala and hippocampus in temporal lobe epilepsy.** *Neurology* 1993;43:719–25
5. Lencz T, McCarthy G, Bronen RA, et al. **Quantitative magnetic resonance imaging in temporal lobe epilepsy: relationship to neuropathology and neuropsychological function.** *Ann Neurol* 1992;31: 629–37
6. Bernasconi N, Duchesne S, Janke A, et al. **Whole-brain voxel-based statistical analysis of gray matter and white matter in temporal lobe epilepsy.** *Neuroimage* 2004;23:717–23
7. Bonilha L, Kobayashi E, Rorden C, et al. **Medial temporal lobe atrophy in patients with refractory temporal lobe epilepsy.** *J Neurol Neurosurg Psychiatry* 2003;74:1627–30
8. Keller SS, Mackay CE, Barrick TR, et al. **Voxel-based morphometric comparison of hippocampal and extrahippocampal abnormalities in patients with left and right hippocampal atrophy.** *Neuroimage* 2002;16:23–31
9. McDonald CR, Hagler DJ Jr, Ahmadi ME, et al. **Regional neocortical thinning in mesial temporal lobe epilepsy.** *Epilepsia* 2008;49: 794–803
10. Bonilha L, Rorden C, Castellano G, et al. **Voxel-based morphometry of the thalamus in patients with refractory medial temporal lobe epilepsy.** *Neuroimage* 2005;25:1016–21
11. Bonilha L, Rorden C, Castellano G, et al. **Voxel-based morphometry reveals gray matter network atrophy in refractory medial temporal lobe epilepsy.** *Arch Neurol* 2004;61:1379–84
12. Bernasconi N, Bernasconi A, Caramanos Z, et al. **Mesial temporal damage in temporal lobe epilepsy: a volumetric MRI study of the hippocampus, amygdala and parahippocampal region.** *Brain* 2003; 126:462–69
13. Keller SS, Roberts N. **Voxel-based morphometry of temporal lobe epilepsy: an introduction and review of the literature.** *Epilepsia* 2008;49:741–57
14. Jensen JH, Helpern JA. **MRI quantification of non-Gaussian water diffusion by kurtosis analysis.** *NMR Biomed* 2010;23:698–710
15. Jensen JH, Helpern JA, Ramani A, et al. **Diffusional kurtosis imaging: the quantification of non-Gaussian water diffusion by means of magnetic resonance imaging.** *Magn Reson Med* 2005;53: 1432–40
16. **Proposal for revised classification of epilepsies and epileptic syndromes: Commission on Classification and Terminology of the International League Against Epilepsy.** *Epilepsia* 1989;30:389–99
17. Tabesh A, Jensen JH, Ardekani BA, et al. **Estimation of tensors and tensor-derived measures in diffusional kurtosis imaging.** *Magn Reson Med* 2011;65:823–36
18. Genovese CR, Lazar NA, Nichols T. **Thresholding of statistical maps in functional neuroimaging using the false discovery rate.** *Neuroimage* 2002;15:870–78
19. Keller SS, Ahrens T, Mohammadi S, et al. **Voxel-based statistical analysis of fractional anisotropy and mean diffusivity in patients with unilateral temporal lobe epilepsy of unknown cause.** *J Neuroimaging* 2013;23:352–59
20. Keller SS, Ahrens T, Mohammadi S, et al. **Microstructural and volumetric abnormalities of the putamen in juvenile myoclonic epilepsy.** *Epilepsia* 2011;52:1715–24
21. Concha L, Beaulieu C, Collins DL, et al. **White-matter diffusion abnormalities in temporal-lobe epilepsy with and without mesial temporal sclerosis.** *J Neurol Neurosurg Psychiatry* 2009;80:312–19
22. Gong G, Concha L, Beaulieu C, et al. **Thalamic diffusion and volumetry in temporal lobe epilepsy with and without mesial temporal sclerosis.** *Epilepsy Res* 2008;80:184–93
23. Gross DW, Concha L, Beaulieu C. **Extratemporal white matter abnormalities in mesial temporal lobe epilepsy demonstrated with diffusion tensor imaging.** *Epilepsia* 2006;47:1360–63
24. Concha L, Beaulieu C, Gross DW. **Bilateral limbic diffusion abnormalities in unilateral temporal lobe epilepsy.** *Ann Neurol* 2005;57: 188–96
25. Thivard L, Lehericy S, Krainik A, et al. **Diffusion tensor imaging in medial temporal lobe epilepsy with hippocampal sclerosis.** *Neuroimage* 2005;28:682–90
26. Kimiwada T, Juhasz C, Makki M, et al. **Hippocampal and thalamic diffusion abnormalities in children with temporal lobe epilepsy.** *Epilepsia* 2006;47:167–75
27. Focke NK, Yogarajah M, Bonelli SB, et al. **Voxel-based diffusion tensor imaging in patients with mesial temporal lobe epilepsy and hippocampal sclerosis.** *Neuroimage* 2008;40:728–37
28. Nilsson D, Go C, Rutka JT, et al. **Bilateral diffusion tensor abnormalities of temporal lobe and cingulate gyrus white matter in children with temporal lobe epilepsy.** *Epilepsy Res* 2008;81:128–35
29. Bonilha L, Edwards JC, Kinsman SL, et al. **Extrahippocampal gray matter loss and hippocampal deafferentation in patients with temporal lobe epilepsy.** *Epilepsia* 2010;51:519–28
30. Spencer SS. **Neural networks in human epilepsy: evidence of and implications for treatment.** *Epilepsia* 2002;43:219–27
31. Bonilha L, Martz GU, Glazier SS, et al. **Subtypes of medial temporal lobe epilepsy: influence on temporal lobectomy outcomes?** *Epilepsia* 2012;53:1–6
32. Richardson MP. **Large scale brain models of epilepsy: dynamics meets connectomics.** *J Neurol Neurosurg Psychiatry* 2012;83:1238–48
33. Gao Y, Zhang Y, Wong CS, et al. **Diffusion abnormalities in temporal lobes of children with temporal lobe epilepsy: a preliminary diffusional kurtosis imaging study and comparison with diffusion tensor imaging.** *NMR Biomed* 2012;25:1369–77
34. Eriksson SH, Free SL, Thom M, et al. **Quantitative grey matter histological measures do not correlate with grey matter probability values from in vivo MRI in the temporal lobe.** *J Neurosci Methods* 2009;181:111–18
35. Eriksson SH, Thom M, Symms MR, et al. **Cortical neuronal loss and hippocampal sclerosis are not detected by voxel-based morphometry in individual epilepsy surgery patients.** *Hum Brain Mapp* 2009;30:3351–60
36. Rorden C, Bonilha L, Nichols TE. **Rank-order versus mean based statistics for neuroimaging.** *Neuroimage* 2007;35:1531–37
37. Wennberg R, Arruda F, Quesney LF, et al. **Preeminence of extrahippocampal structures in the generation of mesial temporal seizures: evidence from human depth electrode recordings.** *Epilepsia* 2002; 43:716–26
38. Thom M, Eriksson S, Martinian L, et al. **Temporal lobe sclerosis associated with hippocampal sclerosis in temporal lobe epilepsy: neuropathological features.** *J Neuropathol Exp Neurol* 2009;68: 928–38
39. Wedeen VJ, Hagmann P, Tseng WY, et al. **Mapping complex tissue architecture with diffusion spectrum magnetic resonance imaging.** *Magn Reson Med* 2005;54:1377–86

Extra-Aneurysmal Flow Modification Following Pipeline Embolization Device Implantation: Focus on Regional Branches, Perforators, and the Parent Vessel

G. Gascou, K. Lobotesis, H. Brunel, P. Machi, C. Riquelme, O. Eker, A. Bonafé, and V. Costalat

ABSTRACT

BACKGROUND AND PURPOSE: Flow-diverter technology has proved to be a safe and effective treatment for intracranial aneurysm based on the concept of flow diversion allowing parent artery and collateral preservation and aneurysm healing. We investigated the patency of covered side branches and flow modification within the parent artery following placement of the Pipeline Embolization Device in the treatment of intracranial aneurysms.

MATERIALS AND METHODS: Sixty-six aneurysms in 59 patients were treated with 96 Pipeline Embolization Devices. We retrospectively reviewed imaging and clinical results during the postoperative period at 6 and 12 months to assess flow modification through the parent artery and side branches. Reperfusion syndrome was assessed by MR imaging and clinical evaluation.

RESULTS: Slow flow was observed in 13 of 68 (19.1%) side branches covered by the Pipeline Embolization Device. It was reported in all cases of anterior cerebral artery coverage, in 3/5 cases of M2-MCA coverage, and in 5/34 (14.7%) cases of ophthalmic artery coverage. One territorial infarction was observed in a case of M2-MCA coverage, without arterial occlusion. One case of deep Sylvian infarct was reported in a case of coverage of MCA perforators. Two ophthalmic arteries (5.9%) were occluded, and 11 side branches (16.2%) were narrowed at 12 months' follow-up; patients remained asymptomatic. Parent vessel flow modification was responsible for 2 cases (3.4%) of reperfusion syndrome. Overall permanent morbidity and mortality rates were 5.2% and 6.9%, respectively. We did not report any permanent deficit or death in case of slow flow observed within side branches.

CONCLUSIONS: After Pipeline Embolization Device placement, reperfusion syndrome was observed in 3.4%, and territorial infarction, in 3.4%. Delayed occlusion of ophthalmic arteries and delayed narrowing of arteries covered by the Pipeline Embolization Device were observed in 5.9% and 16.2%, respectively. No permanent morbidity or death was related to side branch coverage at midterm follow-up.

ABBREVIATIONS: ACA = anterior cerebral artery; PED = Pipeline Embolization Device

Flow-diversion systems appear to be promising tools for the treatment of giant, wide-neck, or fusiform intracranial aneurysms.[1-8] It allows not only the exclusion of the aneurysm sac but the treatment of the diseased arterial segment located on either side of the device by changing the hemodynamic conditions.[9,10] Blood flow is supposed to be disrupted in the aneurysm sac, while parent artery and collateral branches remain permeable. Modification of intra-aneurysmal flow after the implantation of flow diverters has been described as well in experimental and computational models,[11-13] but extra-aneurysmal flow modifications have rarely been explored. Clinical complications such as delayed aneurysm rupture,[14-16] delayed intraparenchymal hematoma,[17] and slow flow or occlusion of collateral branches covered by the device[18] have been reported, with sparse knowledge, considering the frequency.

The purpose of this study was to focus on hemodynamic changes induced by the Pipeline Embolization Device (PED; Covidien, Irvine, California) in collateral branches, perforators, and the parent artery.

MATERIALS AND METHODS

Patient Selection

We retrospectively analyzed the clinical and radiologic data of all consecutive patients treated with the PED from July 2009 to June 2012 in 2 large French neuroscience centers.

Therapeutic options were discussed by a multidisciplinary team. Patients were treated with endovascular reconstruction if they had wide-neck aneurysms (neck size, ≥4 mm, or dome-to-

Received June 20, 2014; accepted after revision September 19.

From the Department of Neuroradiology (G.G., P.M., C.R., O.E., A.B., V.C.), CHU Gui de Chauliac, Montpellier, France; Department of Imaging (K.L.), Imperial College Healthcare NHS Trust, Charing Cross Hospital, United Kingdom; and Department of Neuroradiology (H.B.), CHU La Timone, Marseille, France.

Please address correspondence to G. Gascou, MD, CHU Montpellier, Department of Neuroradiology, Av Augustin Fliche, Montpellier, France; e-mail: g-gascou@chu-montpellier.fr

http://dx.doi.org/10.3174/ajnr.A4191

neck ratio, <2) and/or if therapy was not feasible by conventional techniques (coils with or without remodeling or surgical clipping). The aneurysms treated were blister-like, fusiform, large, and giant aneurysms. The study was conducted following approval by an ethics committee, and written informed consent was obtained from every patient.

Endovascular Procedure

Medication. All patients were treated under general anesthesia and premedicated with clopidogrel (300 mg the day before). Platelet function was evaluated by using a VerifyNow P2Y12 assay (Accumetrics, San Diego, California) in the angiography suite just before the procedure.[19] Procedures were performed with the patient under systemic heparinization with an activated clotting time between 250 and 300 seconds. At the end of the procedure, each patient was given an intravenous bolus of 250–500 mg of aspirin, and heparin anticoagulation was maintained for 24 hours. Dual antiplatelet medication was then introduced (clopidogrel, 75 mg, and aspirin, 75 or 160 mg) and was maintained for at least 6 months following the procedure. At 6 months, clopidogrel was stopped and aspirin was maintained life-long.

Technique. All procedures were performed by a senior interventional neuroradiologist with experience in stent-placement techniques. The PED was implanted via a femoral artery approach across the aneurysmal segment; then, the delivery was via a 0.027-inch internal diameter microcatheter (Marksman; Covidien) that requires a 6F guide catheter support.

Morphologic characteristics of the aneurysm (morphology, volume, and neck size) and parent artery (diameter of the proximal and distal segment and collateral branches) were analyzed by using 2D and 3D reconstructed images to select the optimal device size and length.

Postoperative Management and Follow-Up. A neurologic examination was performed after the procedure. In the absence of a significant abnormality, patients were discharged after 72 hours. In cases with complications, a brain CT or MR imaging was performed. In the absence of clinical adverse events, patients were clinically followed by a stroke practitioner postdischarge at 6 and at 12 months after the procedure. All clinical adverse events (stroke, SAH, headache, nerve palsy, mass effect, or visual deficit) were documented in our prospectively populated data base before the procedure and then were re-evaluated during follow-up.

Follow-up included an MR imaging or conventional angiography at 6 and 12 months. We retrospectively analyzed flow modifications within side branches covered by the device. This assessment was made on the angiogram obtained immediately after the stent deployment, by using the same acquisition parameters (volume injected, speed, x-ray delay) as those obtained immediately before the implantation of the device. Flow modification was subjectively assessed by using a 3-point scale: 1) no modification (if the flow was the same as that before device deployment), 2) slow flow (if the contrast material became slower within the covered vessel), and 3) occlusion (if no contrast material entered the vessel). During the follow-up imaging, patency of side branches covered by the device was determined and the vessel size was reported as unchanged, narrowed, or occluded.

Table 1: Baseline characteristics

Characteristics	Value	%
Patients	59	
Age (mean, yr)	53.7	
Female sex	46	78
Aneurysms	66	
Morphology		
Saccular	44	66.7
Dissecting	16	24.2
Blister	2	3
Fusiform	4	6.1
Size (mean, mm)	10.7	
Size (maximum diameter)		
<10 mm (small)	38	57.6
>10–25 mm (large)	23	34.8
>25 mm (giant)	5	7.6
Neck ≥4 mm	50	75.8
Dome-to-neck ratio <2	36	54.5
Location		
Anterior circulation	54	81.8
CCA	25	37.9
COA	16	24.2
MCA	7	10.6
ACA	2	3
PcomA	4	6.1
Posterior circulation	12	18.2
BA	2	3
VA	7	10.7
PCA	2	3
PICA	1	1.5

Note:—CCA indicates cavernous carotid artery; COA, carotico-ophthalmic artery; BA, basilar artery; VA, vertebral artery; PcomA, posterior communicating artery; PCA, posterior cerebral artery; PICA, posterior inferior cerebellar artery.

All conventional angiograms and MRIs were reviewed by 2 neuroradiologists and adjudicated in cases of disagreement.

In addition to patency of collateral branches, baseline characteristics including patient age, aneurysms morphology, size, and location were also reported.

RESULTS

Patient Population and Aneurysm Characteristics

Between July 2009 and June 2012, 66 aneurysms in 59 patients were treated with the PED in 2 French neuroscience centers (Table 1). Fifty patients were treated by 3 operators in Montpellier, and 9 patients were treated by 1 operator in Marseille without any significant imbalance between these 2 centers.

PED Procedures

A total of 96 devices were used to treat 66 intracranial aneurysms (1.5 device per aneurysm). PED deployment was achieved in 92 cases (95.8%). Four devices (4.2%) could not be deployed. No parent artery occlusion was reported during the perioperative period.

Coils were deployed in 7 aneurysms (10.6%), including 2 ruptured aneurysms. Coils were not used in cases of potential risk of side branch occlusion. PED implantation alone was performed in 59 aneurysms (89.4%). Patients were treated with 1–5 PEDs (the number of PEDs implanted was 1 in 48 cases, 2 in 10 cases, 3 in 2 cases, 4 in 3 cases, and 5 in 2 cases). Multiple PEDs were used with telescopic reconstruction in cases of large-neck aneurysms or to treat different aneurysms in the same arterial segment.

Table 2: Hemodynamic modifications within visible side branches covered by the PED and consequences

Side Branches	No. of PEDs Implanted	No. of Side Branches	Slow Flow within Side Branches	Transient or Permanent Neurologic Deficits[a]	Territorial Ischemic Lesions on MRI	Stenosis at 12-Mo Follow-Up	Occlusion at 12-Mo Follow-Up
Ophthalmic artery	1	25	3	0	NA	2	1
	2	5	1	0	NA	1	0
	3	1	0	0	NA	0	1
	4	3	1	0	NA	0	0
Anterior choroidal artery	1	11	0	3	0	0	0
	2	1	0	0	0	0	0
ACA	1	5	5	3	0	5	0
Callosomarginal artery	1	1	0	0	0	0	0
MCA	1	5	3	2	1	1	0
PcomA	1	2	0	0	0	0	0
PICA	1	5	0	0	0	2	0
	2	1	0	0	0	0	0
SCA	3	1	0	0	0	0	0
PCA	3	1	0	0	0	0	0
Anterior spinal artery	1	1	0	0	0	0	0
Total		68	13 (19.1%)	8	1	11	2
Perforators							
Sylvian perforators	1	4	NA	3	1	NA	NA
	2	1	NA	0	0	NA	NA
BA perforators	3	1	NA	0	0	NA	NA
	5	1	NA	0	0	NA	NA
Total		7	NA	3	1	NA	NA

Note:—SCA indicates superior cerebellar artery; NA, not available; BA, basilar artery; PcomA, posterior communicating artery; PCA, posterior cerebral artery; PICA, posterior inferior cerebellar artery.

[a] Related to the side branch covered.

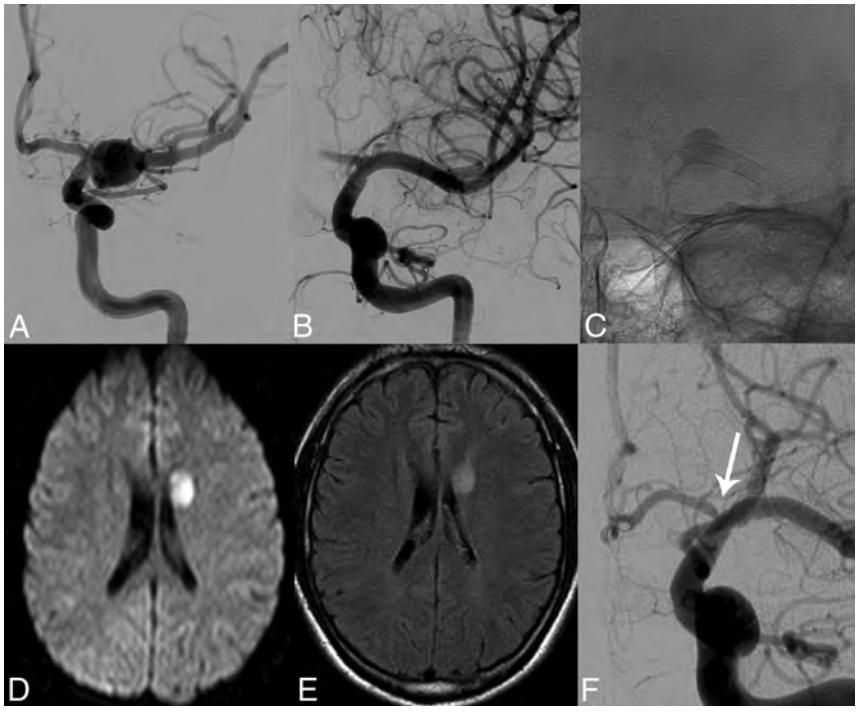

FIG 1. Perforator infarction following PED placement and arterial narrowing of the covered artery on a 12-month follow-up angiogram. *A*, Anteroposterior view shows the dissecting aneurysm of the left proximal M1 segment. *B*, Anteroposterior view after PED placement shows absence of filling of the aneurysm and slow flow within the A1 segment. The acquisition was performed with the same parameters but in a later phase to see the A1 segment. *C*, Single PED placement within the left M1 segment results in contrast stagnation within the aneurysm sac. *D* and *E*, DWI and FLAIR sequences performed 2 days later because of transient right brachiofacial hemiparesis demonstrate basal ganglial infarction. *F*, Twelve-month follow-up angiogram shows the ostial narrowing of the covered collateral branches (*arrow*).

Side Branches and Perforators Covered by the PED

Sixty-eight visible side branches were covered by the device. Immediately after PED placement, slow flow was angiographically identified within 13 branches (19.1%), including 5 of 34 (14.7%) ophthalmic arteries (Table 2), 5 of 5 (100%) anterior cerebral arteries (ACAs), and 3 of 5 (60%) M2-MCAs. In all cases of ACA coverage, the anterior communicating artery was functional. No side branch occlusion was demonstrated on the immediate angiography. Five patients presented with transient neurologic deficits. Four had multiple side branch coverage. Territorial ischemic lesions on MR imaging were reported in 2 cases: The first case was a 30-year-old man (patient 3) treated for a left dissecting ruptured MCA aneurysm. The covered branches were the ACA and MCA perforators, and an MR imaging performed the following day demonstrated a deep MCA infarct (Fig 1). The second case was a 60-year-old woman (patient 22) treated for an incidental MCA bifurcation aneurysm with a branch originating from the sac. On the final angiographic runs, slow flow was observed within the anterior MCA bifurcation branch (Fig 2). After extubation, the patient presented with mild aphasia, and MR imaging identified an MCA infarct. The patient was discharged without a significant deficit. Two patients with basilar artery PED placement died, one patient, in unclear circumstances, probably secondary to a delayed rup-

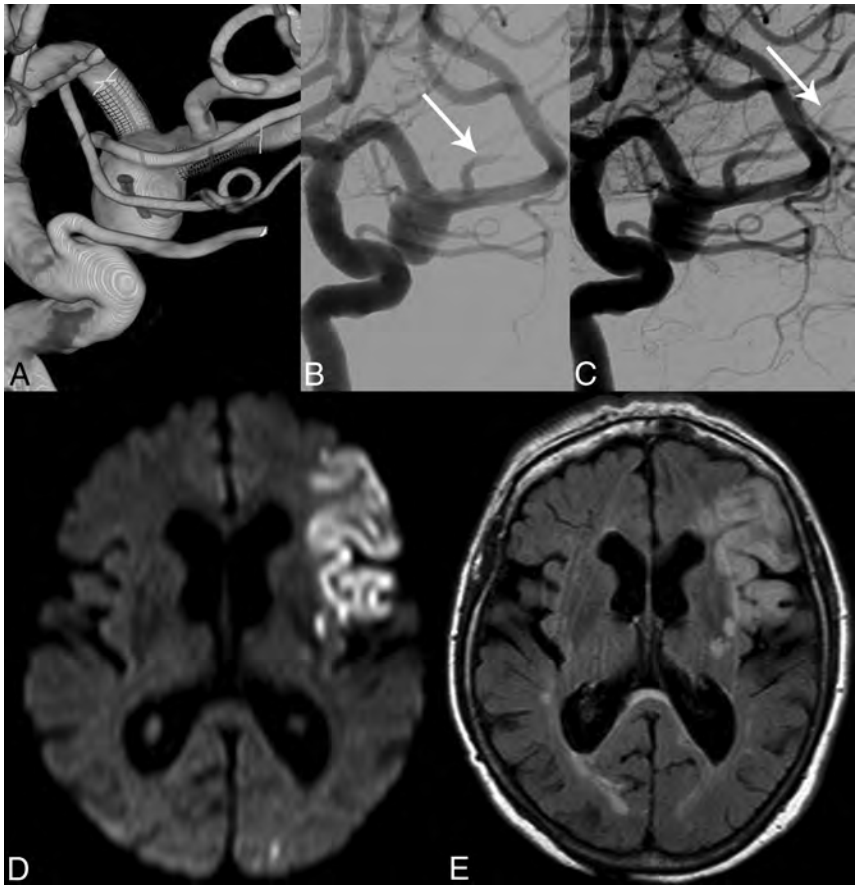

FIG 2. Slow flow within MCA side branch. *A*, Left MCA aneurysm treated with a PED covering the prefrontal branch. *B* and *C*, Slow flow within the covered side branch (*arrows*). *D* and *E*, MR imaging performed on day 1 after the procedure shows acute left anterior MCA infarct.

ture (patient 11), and the second following in-stent thrombosis (patient 24) related to premature discontinuation of antiplatelet therapy.

During follow-up angiography, 66 of 68 (97%) visible side branches covered by the PED remained patent with normal blood flow. We reported 2 cases (5.9%) of ophthalmic artery occlusion on the 12-month follow-up angiogram. Eleven cases (16.2%) of collateral branches remained patent but had an arterial narrowing, which was observed in all cases of ACA coverage. In all these cases of occlusion or narrowing, patients did not have transient or permanent deficits. The 2 patients with delayed ophthalmic artery occlusion had no flow modification on the angiogram immediately after PED placement. The 13 side branches with slow flow noted just after the procedure remained patent at 1-year follow-up.

The mean number of PEDs implanted in cases of occluded side branches was 2 (range, 1–3) versus 1.35 (range, 1–4) in cases of normal blood flow within side branches.

Clinical Follow-Up

Among 59 patients initially included in the study, 1 patient was lost to follow-up. Fifty-eight patients with 65 intracranial aneurysms underwent PED placement and discharge evaluation. During the hospitalization, we reported 19 (32.3%) minor reversible clinical adverse events: Six (10.3%) patients had headache, 5 (8.6%) had femoral puncture hematomas, and 8 (13.8%) had transient neurologic deficits. Two patients (1 man and 1 woman; respectively, 82 and 78 years of age) treated for a large carotid cavernous aneurysm presented with transient hemiplegia within 5 hour after the procedure. In both patients, flow decrease was not observed during the procedure, and blood pressure was stable around 90 mm Hg without evidence of tensional disturbance during the procedure. On the MR imaging performed (Fig 3), there was no evidence of new ischemic or hemorrhagic lesions and the intracranial arteries remained patent. FLAIR images showed leptomeningeal hyperintensity without enhancement on the postgadolinium images. On the PWI sequence, there was no hyperperfusion seen. The neurologic deficit improved during several days, and the follow-up MR imaging performed 5–7 days after the procedure showed complete resolution of the leptomeningeal signal change.

At 12 months' follow-up, the overall morbidity rate was 5.2%, and the mortality rate was 6.9% (overall morbimortality rate of 12.1%). The rate of mortality was 27.3% in the posterior circulation and 2.1% in the anterior circulation. Three patients died during follow-up, at days 10, 15, and 25. Deaths were related to in-stent thrombosis in 1 case and delayed aneurysm rupture in 2 cases. Delayed aneurysm rupture occurred in an 86-year-old woman treated for a large basilar artery aneurysm in 1 case and a 56-year-old woman treated for a large carotico-ophthalmic aneurysm in the other case. One other patient died during further treatment performed 13 months after the initial therapeutic phase because of persistent aneurysm filling. No permanent morbidity or death was related to side branch coverage.

DISCUSSION

Side Branches and Perforators Covered by the PED

In our overall cohort, delayed occlusion of the ophthalmic artery, covered by the PED, occurred in 2 cases (5.9%) but was clinically silent. In the literature, patency of collateral branches is rarely reported. Concerning the ophthalmic artery, Szikora et al[6] reported immediate occlusion in 1 case, resulting in a retinal branch occlusion and a small visual field deficit, and delayed occlusion at 6 months in 2 other cases, which were clinically silent. This finding is consistent with a rate of delayed ophthalmic artery occlusion of 11.7%. More recently, Puffer et al[18] observed that 21% of the ophthalmic artery covered by a PED appeared occluded in subsequent angiographic follow-up. All reported cases of ophthalmic artery occlusion were clinically silent, perhaps due to the good collateral circulation.[18] In another study, Yu et al[20] did not report any occlusions among 107 ophthalmic arteries covered by the PED. Overall, the placement of 1 or multiple PEDs across the ophthalmic artery appears safe.

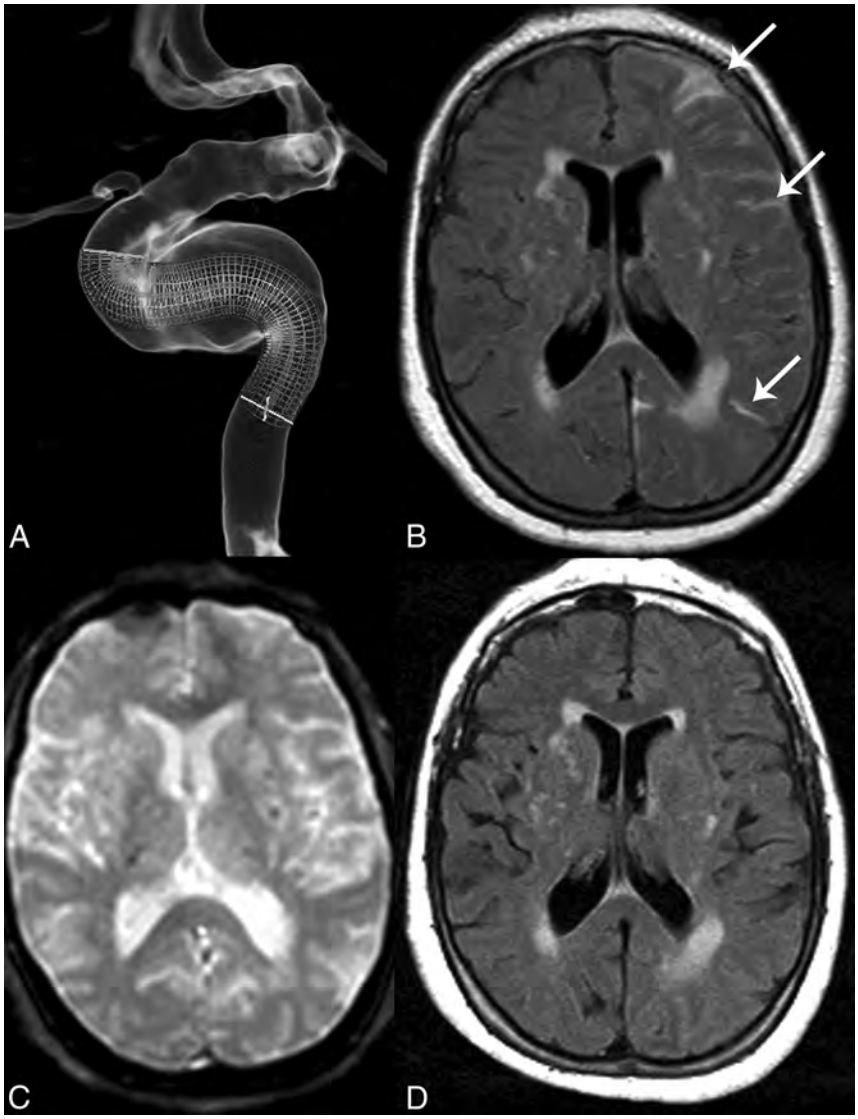

FIG 3. Imaging findings in a patient presenting with cerebral reperfusion syndrome. The patient was treated for a large left carotid cavernous aneurysm with the implantation of 2 overlapped PEDs (*A*). Seven hours after the procedure, the patient had severe headache and mild aphasia. *B* and *C*, FLAIR images show leptomeningeal hyperintensities in the left hemisphere (*arrows*) without evidence of hemorrhage on T2 gradient-echo (*C*). *D*, FLAIR performed 24 hours after the procedure shows complete reversibility of leptomeningeal hyperintensities.

In our study, as well as in the article by Szikora et al,[6] we did not report other side branch occlusions (anterior choroidal artery, posterior inferior cerebellar artery, superior cerebellar artery, posterior communicating artery, anterior spinal artery, ACA, or MCA). Brinjikji et al[21] reported an occlusion rate of 27% in cases of posterior communicating artery coverage without neurologic deficit. In all these cases, the P1 segment was patent on the initial angiogram.

In our series, slow flow was observed immediately after PED implantation in all cases of ACA coverage and in 3 of 5 cases of M2-MCA coverage. Most interesting, territorial infarction resulting in a transient aphasia was observed in only 1 case of M2-MCA slow flow.

In our series, 16.2% of collateral branches covered by the PED had arterial narrowing on the 12-month follow-up angiogram. In no case was it associated with a neurologic deficit. All cases of ACA coverage presented with delayed arterial narrowing. All patients had a patent anterior communicating artery and contralateral A1 on the initial imaging. Late narrowing or occlusion was observed in 38% (5/13) after initial slow flow and was observed in only 14.5% (8/55) when slow flow was not reported just after stent placement ($P < .05$), suggesting that peroperative slow flow is a strong predictor of late branch occlusion. In the literature, narrowing of collateral branches is rarely reported. Preclinical studies[9,22-26] reported that flow within collateral arteries was maintained after the placement of a flow diverter. However, these arteries were considered end vessels without distal collaterals. In a clinical study, Brinjikji et al[21] observed a decreased flow in 18% of posterior communicating arteries covered by a flow diverter with a patent P1. These findings suggest that the placement of a flow diverter is probably responsible for a vascular and hemodynamic remodeling of regional branches covered by the device, which can lead to arterial narrowing at midterm follow-up. This vascular remodeling is probably favored by flow competition from communicating arteries. The narrowing or occlusion of such arteries remains clinically silent due to good collaterality. In our practice, we now check the patency of the anterior communicating artery before placing a flow diverter in this segment.

Among the 5 cases of lenticulostriate coverage, we reported 1 case of infarction. This patient was treated for a dissecting MCA aneurysm with the placement of 1 PED, and it is not possible to conclude whether the infarct was due to extension of the dissection to the lenticulostriate arteries or due to the device. Overall, PED placement across perforating lenticulostriate arteries remains safe, probably due to the discrepancy between the wire size of the PED (30 μm) and the diameter of lenticulostriate arteries (mean, 480 μm; range, 100-1280 μm).[27] Furthermore, in a computational model, Appanaboyina et al[25] observed that the coverage of 90% of the perforating vessel ostium reduced <10% of the flow through the inlet. These data suggest that even if 3 wires cross a perforator ostium with a diameter of 100 μm, the coverage of the orifice area will never be >90%. However, tiny thrombi can develop on the surface of the PED and then migrate distally. A recent in vitro study observed that flow reduction within side branches was higher in cases of tight mesh or overlapping stents[24]; however, previous preclinical studies[9,22,28] did not observe side branch occlusion in rabbit models even when small branches, similar in diameter to human perforating arteries, were covered by 1 or multiple overlapped

PEDs. In our study, the number of overlapped PEDs implanted covering the lenticulostriate arteries was not a predictor of perforator infarction. Patency of perforating arteries in human clinical studies is rarely reported in the literature. van Rooij and Sluzewski[29] observed a case of perforator infarction in the territory of the lenticulostriate arteries covered by the flow diverter. Phillips et al[30] reported 3 cases of perforator infarction in the vertebrobasilar territory. Overall, the risk of occlusion of perforating arteries appears low, assuming an effective antiplatelet therapy.

Parent Artery Flow Modification

We did not observe any cases of delayed intraparenchymal hemorrhage,[17] but we reported 2 cases of reperfusion cerebral syndrome. In both cases, the patients were older than 75 years (78 and 82 years of age) and the aneurysms treated were large (13 and 15 mm) and involved a tortuous carotid artery. This syndrome has been described as a minor manifestation of the classic cerebral hyperperfusion syndrome.[31] This syndrome is a rare but well-described phenomenon occurring after a carotid endarterectomy, angioplasty, stent placement,[32] or aneurysm clipping.[33-35] It is related to a sudden increase in regional cerebral blood flow secondary to loss of cerebrovascular autoregulation.[31,32,36] The symptoms can range from headache and neurologic deficit (without any ischemic lesion on MR imaging) to intracerebral hemorrhage.[37] Several risk factors have been reported, including hypertension, diabetes, age older than 75 years, recent carotid surgery/intervention within 3 months, high-grade ipsilateral or contralateral stenosis, female sex, vascular malformation, and cerebrovascular reactivity.[32]

Recently, Chiu and Wenderoth[38] reported a case of hyperperfusion syndrome following flow-diverter treatment of a large paraclinoid aneurysm for which the clinical presentation and MR imaging findings were similar to those of our patients except that in this case, there was hyperperfusion on CT perfusion. In our study, there was no evidence of hyperperfusion on PWI-MR imaging; hence, we have to use the term "reperfusion syndrome".[31,39] Murakami et al[40] hypothesized that before treatment, giant aneurysms are responsible for the reduction in blood flow through the distal parent artery and might cause relative hypoperfusion in the ipsilateral cerebral cortex. Following aneurysm clipping, blood flow through the parent vessel suddenly increases, exceeding cerebral autoregulatory abilities, leading to cerebral hyperperfusion. One may hypothesize a similar phenomenon in aneurysms treated by surgical clipping or flow diverters, in which the stent redirects most of the blood flow into the parent artery. These data were reported in a computational fluid dynamics model,[41] in which an increase in blood flow was observed in the parent artery after PED placement. As in previous studies,[17,42] we hypothesized that these hemodynamic modifications after flow diversion could lead to delayed intraparenchymal hemorrhage.

Two patients died in unclear circumstances, and we strongly suspect delayed aneurysm rupture. These fatal events occurred a few days or weeks following flow diversion. Similar events have already been reported for the PED and Silk flow diverter (Balt Extrusion, Montmorency, France).[14-16,43,44] The reason for delayed aneurysm rupture is still uncertain. In computational models, Cebral et al[14] observed, after the placement of a flow diverter, an increase of intra-aneurysmal pressure, which could lead to rupture, especially in cases of giant aneurysms, tortuous vessels, or pre-existing proximal parent artery stenosis. Most of these ruptures have been described in cases of large or giant aneurysms treated by flow diverters alone. Hence, some authors recommend the combined use of coils[15,43] for large and giant aneurysms and suggest a modest reduction of systemic blood pressure in the postoperative period.

Limitations

A limitation of this study is the relatively small number of aneurysms treated and side branches covered by the device, which can diminish the differences between groups. Thus, we did not perform any statistical analyses. Another limitation is the follow-up period, which may be too short to assess the long-term patency of side branches, especially those with narrowing on the midterm follow-up.

CONCLUSIONS

After PED placement, reperfusion syndrome was observed in 3.4%; slow flow within side branches, in 19.1%; and territorial infarction, in 3.4%. Delayed occlusion of the ophthalmic arteries and delayed narrowing of arteries covered by the PED were observed in 5.9% and 16.2%, respectively. No permanent morbidity or death was related to side branch coverage at midterm follow-up.

Disclosures: Alain Bonafé—*UNRELATED: Consultancy*: Covidien. Vincent Costalat—*UNRELATED: Consultancy*: Sequent Medical, MicroVention, Codman, Stryker; *Payment for Lectures (including service on Speakers Bureaus)*: Stryker, Sequent Medical, Balt Extrusion; *Payment for Development of Educational Presentations*: Covidien, Stryker, MicroVention.

REFERENCES

1. Deutschmann HA, Wehrschuetz M, Augustin M, et al. **Long-term follow-up after treatment of intracranial aneurysms with the Pipeline embolization device: results from a single center.** *AJNR Am J Neuroradiol* 2012;33:481–86
2. Fischer S, Vajda Z, Aguilar Perez M, et al. **Pipeline embolization device (PED) for neurovascular reconstruction: initial experience in the treatment of 101 intracranial aneurysms and dissections.** *Neuroradiology* 2012;54:369–82
3. Lubicz B, Collignon L, Raphaeli G, et al. **Pipeline flow-diverter stent for endovascular treatment of intracranial aneurysms: preliminary experience in 20 patients with 27 aneurysms.** *World Neurosurg* 2011;76:114–19
4. McAuliffe W, Wenderoth JD. **Immediate and midterm results following treatment of recently ruptured intracranial aneurysms with the Pipeline embolization device.** *AJNR Am J Neuroradiol* 2012;33:487–93
5. Nelson PK, Lylyk P, Szikora I, et al. **The Pipeline embolization device for the intracranial treatment of aneurysms trial.** *AJNR Am J Neuroradiol* 2011;32:34–40
6. Szikora I, Berentei Z, Kulcsar Z, et al. **Treatment of intracranial aneurysms by functional reconstruction of the parent artery: the Budapest experience with the Pipeline embolization device.** *AJNR Am J Neuroradiol* 2010;31:1139–47
7. Chalouhi N, Tjoumakaris S, Starke RM, et al. **Comparison of flow diversion and coiling in large unruptured intracranial saccular aneurysms.** *Stroke* 2013;44:2150–54
8. Becske T, Kallmes DF, Saatci I, et al. **Pipeline for uncoilable or failed aneurysms: results from a multicenter clinical trial.** *Radiology* 2013;267:858–68

9. Kallmes DF, Ding YH, Dai D, et al. **A second-generation, endoluminal, flow-disrupting device for treatment of saccular aneurysms.** *AJNR Am J Neuroradiol* 2009;30:1153–58
10. D'Urso PI, Lanzino G, Cloft HJ, et al. **Flow diversion for intracranial aneurysms: a review.** *Stroke* 2011;42:2363–68
11. Kojima M, Irie K, Fukuda T, et al. **The study of flow diversion effects on aneurysm using multiple Enterprise stents and two flow diverters.** *Asian J Neurosurg* 2012;7:159–65
12. Roszelle BN, Gonzalez LF, Babiker MH, et al. **Flow diverter effect on cerebral aneurysm hemodynamics: an in vitro comparison of telescoping stents and the Pipeline.** *Neuroradiology* 2013;55:751–58
13. Shobayashi Y, Tateshima S, Kakizaki R, et al. **Intra-aneurysmal hemodynamic alterations by a self-expandable intracranial stent and flow diversion stent: high intra-aneurysmal pressure remains regardless of flow velocity reduction.** *J Neurointerv Surg* 2013;5(suppl 3):iii38–42
14. Cebral JR, Mut F, Raschi M, et al. **Aneurysm rupture following treatment with flow-diverting stents: computational hemodynamics analysis of treatment.** *AJNR Am J Neuroradiol* 2011;32:27–33
15. Hampton T, Walsh D, Tolias C, et al. **Mural destabilization after aneurysm treatment with a flow-diverting device: a report of two cases.** *J Neurointerv Surg* 2011;3:167–71
16. Siddiqui AH, Kan P, Abla AA, et al. **Complications after treatment with Pipeline embolization for giant distal intracranial aneurysms with or without coil embolization.** *Neurosurgery* 2012;71:E509–13
17. Velat GJ, Fargen KM, Lawson MF, et al. **Delayed intraparenchymal hemorrhage following Pipeline embolization device treatment for a giant recanalized ophthalmic aneurysm.** *J Neurointerv Surg* 2012;4:e24
18. Puffer RC, Kallmes DF, Cloft HJ, et al. **Patency of the ophthalmic artery after flow diversion treatment of paraclinoid aneurysms.** *J Neurosurg* 2012;116:892–96
19. Lee DH, Arat A, Morsi H, et al. **Dual antiplatelet therapy monitoring for neurointerventional procedures using a point-of-care platelet function test: a single-center experience.** *AJNR Am J Neuroradiol* 2008;29:1389–94
20. Yu SC, Kwok CK, Cheng PW, et al. **Intracranial aneurysms: midterm outcome of Pipeline embolization device–a prospective study in 143 patients with 178 aneurysms.** *Radiology* 2012;265:893–901
21. Brinjikji W, Lanzino G, Cloft HJ, et al. **Patency of the posterior communicating artery after flow diversion treatment of internal carotid artery aneurysms.** *Clin Neurol Neurosurg* 2014;120:84–88
22. Dai D, Ding YH, Kadirvel R, et al. **Patency of branches after coverage with multiple telescoping flow-diverter devices: an in vivo study in rabbits.** *AJNR Am J Neuroradiol* 2012;33:171–74
23. Lopes DK, Johnson AK. **Evaluation of cerebral artery perforators and the Pipeline embolization device using optical coherence tomography.** *J Neurointerv Surg* 2012;4:291–94
24. Roszelle BN, Babiker MH, Hafner W, et al. **In vitro and in silico study of intracranial stent treatments for cerebral aneurysms: effects on perforating vessel flows.** *J Neurointerv Surg* 2013;5:354–60
25. Appanaboyina S, Mut F, Löhner R, et al. **Computational modelling of blood flow in side arterial branches after stenting of cerebral aneurysms.** *Int J Comut Fluid Dyn* 2008;22:669–76
26. Sadasivan C, Cesar L, Seong J, et al. **Treatment of rabbit elastase-induced aneurysm models by flow diverters: development of quantifiable indexes of device performance using digital subtraction angiography.** *IEEE Trans Med Imaging* 2009;28:1117–25
27. Djulejić V, Marinkovic S, Malikovic A, et al. **Morphometric analysis, region of supply and microanatomy of the lenticulostriate arteries and their clinical significance.** *J Clin Neurosci* 2012;19:1416–21
28. Kallmes DF, Ding YH, Dai D, et al. **A new endoluminal, flow-disrupting device for treatment of saccular aneurysms.** *Stroke* 2007;38:2346–52
29. van Rooij WJ, Sluzewski M. **Perforator infarction after placement of a Pipeline flow-diverting stent for an unruptured A1 aneurysm.** *AJNR Am J Neuroradiol* 2010;31:E43–44
30. Phillips TJ, Wenderoth JD, Phatouros CC, et al. **Safety of the Pipeline embolization device in treatment of posterior circulation aneurysms.** *AJNR Am J Neuroradiol* 2012;33:1225–31
31. Cho AH, Suh DC, Kim GE, et al. **MRI evidence of reperfusion injury associated with neurological deficits after carotid revascularization procedures.** *Eur J Neurol* 2009;16:1066–69
32. Lieb M, Shah U, Hines GL. **Cerebral hyperperfusion syndrome after carotid intervention: a review.** *Cardiol Rev* 2012;20:84–89
33. Kuroki K, Taguchi H, Yukawa O. **Hyperperfusion syndrome after clipping of an unruptured aneurysm: case report.** *Neurol Med Chir (Tokyo)* 2006;46:248–50
34. Maruya J, Nishimaki K, Minakawa T. **Hyperperfusion syndrome after neck clipping of a ruptured aneurysm on a dolichoectatic middle cerebral artery.** *J Stroke Cerebrovasc Dis* 2011;20:260–63
35. Sugino T, Ohtaki M, Wanibuchi M, et al. **Hyperperfusion syndrome after clipping an unruptured cerebral aneurysm: two case reports.** *Neurol Med Chir (Tokyo)* 2010;50:306–09
36. Aubert S, Sellal F, Rouyer O, et al. **Reperfusion syndrome with cerebral vasogenic edema after carotid artery endarterectomy** [in French]. *Rev Neurol (Paris)* 2007;163:840–44
37. Narita S, Aikawa H, Nagata S, et al. **Intraprocedural prediction of hemorrhagic cerebral hyperperfusion syndrome after carotid artery stenting.** *J Stroke Cerebrovasc Dis* 2013;22:615–19
38. Chiu AH, Wenderoth J. **Cerebral hyperperfusion after flow diversion of large intracranial aneurysms.** *J Neurointerv Surg* 2013;5:e48
39. Karapanayiotides T, Meuli R, Devuyst G, et al. **Postcarotid endarterectomy hyperperfusion or reperfusion syndrome.** *Stroke* 2005;36:21–26
40. Murakami H, Inaba M, Nakamura A, et al. **Ipsilateral hyperperfusion after neck clipping of a giant internal carotid artery aneurysm: case report.** *J Neurosurg* 2002;97:1233–36
41. Levitt MR, McGah PM, Aliseda A, et al. **Cerebral aneurysms treated with flow-diverting stents: computational models with intravascular blood flow measurements.** *AJNR Am J Neuroradiol* 2014;35:143–48
42. Cruz JP, Chow M, O'Kelly C, et al. **Delayed ipsilateral parenchymal hemorrhage following flow diversion for the treatment of anterior circulation aneurysms.** *AJNR Am J Neuroradiol* 2012;33:603–08
43. Kulcsár Z, Houdart E, Bonafe A, et al. **Intra-aneurysmal thrombosis as a possible cause of delayed aneurysm rupture after flow-diversion treatment.** *AJNR Am J Neuroradiol* 2011;32:20–25
44. Velat GJ, Fargen KM, Lawson MF, et al. **Delayed intraparenchymal hemorrhage following Pipeline embolization device treatment for a giant recanalized ophthalmic aneurysm.** *J Neurointerv Surg* 2012;4:e24

Experimental Testing of a New Generation of Flow Diverters in Sidewall Aneurysms in Rabbits

Y.H. Ding, T. Tieu, and D.F. Kallmes

ABSTRACT

BACKGROUND AND PURPOSE: The development of new generation flow-diverting devices will improve the result of flow diversion in challenging aneurysms. The Flow-Redirection Endoluminal Device system is a dual-layer flow-diversion device. The purpose of this study was to evaluate the effectiveness and safety of the Flow-Redirection Endoluminal Device in a sidewall aneurysm model and in the abdominal aorta in rabbits.

MATERIALS AND METHODS: Single Flow-Redirection Endoluminal Devices were implanted in the right common carotid artery across sidewall, vein-pouch aneurysms and within the abdominal aorta in 22 New Zealand white rabbits and followed for 1 ($n = 5$), 3 ($n = 5$), 6 ($n = 4$), and 12 months ($n = 8$). Aneurysm occlusion was graded on a 3-point scale based on digital subtraction angiography (grade I, complete occlusion; grade II, near-complete occlusion; and grade III, incomplete occlusion). Toluidine blue and basic fuchsin staining was used for the evaluation of thrombus organization within the aneurysm and neck coverage with neointima. A scanning electron microscope was used for confirmation of the patency of branch vessels along with DSA.

RESULTS: Grades I and II occlusion rates were noted in 19 (86%) and 3 (14%) aneurysms, respectively, which indicated a 100% rate of complete or near-complete occlusion. No parent artery and branch artery occlusion was shown on DSA. Histologic images indicated partial or complete intraluminal thrombus organization and neointima coverage across the aneurysm neck. A scanning electron microscope indicated that all the vessel branches along the length of the device remained patent.

CONCLUSIONS: The Flow-Redirection Endoluminal Device in experimental aneurysms demonstrated high rates of progressive and complete aneurysm occlusion while preserving the patency of branch vessels.

ABBREVIATIONS: FRED = Flow-Redirection Endoluminal Device; RCCA = right common carotid artery; SEM = scanning electron microscope

Flow diverters have become important tools in the treatment of intracranial aneurysms as a recent disruptive technology. The Pipeline Embolization Device (Covidien, Irvine, California) is designed as a flexible microcatheter-delivered self-expanding cylindric construct composed of 48 braided strands of cobalt chromium and platinum. The Silk flow diverter (Balt Extrusion, Montmorency, France) is a retrievable device attached to a high-friction delivery system with a 200-cm steel plunger with a 15-mm-long radiopaque floppy portion that extends beyond the stent with a 45° tip. The retrievability, visibility, and flexibility remain to be improved.[1,2] Surpass (Stryker Neurovascular, Kalamazoo, Michigan) is a cobalt-chromium, low-porosity (metal surface area coverage, 30%), self-expanding tubular mesh structure with high-pore attenuation.[3] The high occurrence of neurologic deficits indicates that it is necessary to keep improving the performance of current flow-diverter devices. The Flow-Redirection Endoluminal Device (FRED; MicroVention, Tustin, California) was designed to increase the visibility of the device, improve its performance in patients, and reduce the occurrence of the neurologic complications.

In this study, we created a sidewall aneurysm model in rabbits and tested the FRED by combining the angiographic, histologic, and scanning electron microscope (SEM) findings at different follow-up time points.

MATERIALS AND METHODS

The FRED device is a self-expanding nickel-titanium, compliant closed-cell design compatible with a 0.027-inch Headway micro-

Received July 10, 2014; accepted after revision September 29.

From the Neuroradiology Research Laboratory (Y.H.D., D.F.K.), Department of Radiology, Mayo Clinic, Rochester, Minnesota; and MicroVention (T.T.), Tustin, California.

This work was funded by MicroVention.

Abstract previously presented at: Annual Meeting of the American Society of Neuroradiology and the Foundation of the ASNR Symposium, May 17–22, 2014; Montreal, Quebec, Canada.

Please address correspondence to Tai Tieu, MicroVention, Inc, 1311 Valencia Ave, Tustin, CA 92780; e-mail: tai.tieu@microvention.com

http://dx.doi.org/10.3174/ajnr.A4167

FIG 1. FRED flow-diverter system demonstrating a dual-layer design with the working section marked with a radiopaque helix to provide fluoroscopic visibility. Distal and proximal markers are evenly dispersed on its outer layer ends.

catheter (MicroVention). The FRED system has a unique dual-layer design composed of a low-porosity inner flow-diverter mesh with 48 braided nitinol strands and a high-porosity outer stent with 16 nitinol struts. This dual-layer coverage is designed to put the working layer (inner part) mainly at the neck, particularly at the inflow zone of the aneurysm and to create a flow-diversion effect. The outer part, which determines the total length, serves as a protection for the inner stent. The outer stent is 3 mm longer than the inner flow-diverter mesh at each end so that the proximal and distal parts of the FRED can be used to cover the adjacent perforating arteries or small branches of the parent vessel with the advantage of high porosity. The FRED has 4 radiopaque markers on each end of the outer stent and 2 interwoven helical marker strands that attach to the inner and outer stents and run the entire length of the inner stent. It can be resheathed up to 85% deployment of its total length (Fig 1).

All animal procedures were performed at ISIS Services, San Carlos, California. Following approval from the Institutional Animal Care and Use Committee of ISIS, sidewall aneurysms were created in the right common carotid artery (RCCA) in 22 New Zealand white rabbits. Details of the creation procedure have been published previously.[4] Briefly, anesthesia was induced by intravenous administration of xylazine (1 mg/kg) and ketamine (10 mg/kg) and was maintained with isoflurane (2%–3%) in oxygen (2 L/min). Using a sterile technique, we made an 8-cm paramedian incision in the neck. The RCCA and right external jugular vein were exposed and dissected. After permanent ligation of the proximal and distal sides of the right external jugular vein, a 1-cm vein pouch was harvested between the 2 sides (right external jugular vein proximal and distal). A 5-mm arteriotomy of the RCCA was made, and ligation was performed to temporarily occlude the proximal and distal sides of the arteriotomy. Heparin (150 U/kg) was injected intravenously through the ear vein before anastomosis. An end-to-side anastomosis between the vein pouch and the RCCA by using an 8–0 Prolene suture (Ethicon, Cincinnati, Ohio) was performed.

Three weeks after creation, patency of all the aneurysms and parent arteries was confirmed by DSA before FRED deployment. The detailed procedure has been published before.[5,6] Briefly, a 5F sheath was advanced on 1 side of the femoral artery via cutdown, followed by a 5F Chaperon guiding catheter (MicroVention). A Headway 27 microcatheter (MicroVention) was advanced into the distal end of parent artery (RCCA) over a Traxcess 14EX microguidewire (MicroVention) through the guide catheter. The first FRED (3.5 mm outer stent diameter × 17/11 mm) was deployed across the aneurysm neck within the RCCA. The second device (4.0 mm outer stent diameter × 18/12 mm) was deployed within the abdominal aorta crossing multiple lumbar arteries. DSA was performed through the guide catheter immediately after deployment. Aspirin (10 mg/kg) and clopidogrel (10 mg/kg) were given daily 2 days before implantation and were continued until 90 days after treatment.

Follow-up DSA was performed at 1 month ($n = 5$), 3 months ($n = 5$), 6 months ($n = 4$), and 12 months ($n = 8$) after treatment. Animals were sacrificed with a lethal injection of pentobarbital at each time point after DSA follow-up. The RCCA, including the aneurysm sac and abdominal aorta with lumbar arteries, was immediately fixed in 10% neutral buffered formalin.

Degrees of intra-aneurysmal flow disruption immediately after device deployment and before sacrifice were graded on a 3-point scale based on DSA images, including grade I (complete flow cessation, no flow within the aneurysm), grade II (near-complete flow, <10% residual flow), and grade III (incomplete occlusion, ≥10% residual flow).[7] The degree of aneurysm occlusion at follow-up was compared with the immediate postembolization images by using another 3-point scale, including stable aneurysm occlusion, progressive aneurysm occlusion, and aneurysm recanalization. Patency of parent artery and lumbar artery branches was also evaluated.

Carotid aneurysm samples were dehydrated in a graded series of ethanol and embedded in methyl methacrylate plastic. After polymerization of the plastic, 2- to 3-mm transverse sections were sawed from the proximal and distal ends of the FREDs and from the area of the aneurysm neck. The sections were ground to a thickness of 42–50 μm by using Linear Grinding technology (Exakt Technologies, Oklahoma City, Oklahoma), polished, and stained with toluidine blue and basic fuchsin. All sections containing the aneurysm sac and aneurysm neck were evaluated by light microscopy to score histologic changes on the basis of specific parameters. The tissues within the aneurysm were categorized as unorganized or organized connective tissue. The degree of endothelialized neointima across the neck was also assessed.

DSA and a scanning electron microscope were used to evaluate the patency of the lumbar arterial branch ostia on the aortic luminal surface. Before processing, the samples were opened longitudinally to expose the luminal surface and the FRED implants were photographed. The sample was rinsed in 0.1-mol/L sodium phosphate buffer and then postfixed in 1% osmium tetroxide for 30 minutes. The samples were then dehydrated in a graded series of ethanol. After critical point drying, the tissue was mounted and sputter coated with gold; the sample was visualized by using a scanning electron microscope (magnification range X15-X600; Hitachi, Tokyo, Japan). Tissue processing and the histopathology report (including SEM results) were offered by CVpath Institute, Gaithersburg, Maryland.

Histologic sections containing the proximal, mid-, and distal sections were analyzed with a National Institute of Standards and Technology calibrated microscope system (IP Lab software, Rockville, Maryland) under a BX51 light microscope (Olympus, Melville, New York). The average value of each histologic factor at the above 3 locations was calculated. The cross-sectional areas (internal elastic lamina [IEL] and lumen) of each stented section were measured. The percentage of luminal narrowing was calculated with the following formula:

$$\% \text{ Stenosis} = [1 - (\text{Lumen Area}/\text{IEL Area})] \times 100.$$

The extent of stenosis was classified as 4 categories: minimal (<20%), mild (20%–35%), moderate (>35% to <50%), and marked (≥50%).

Neointima formation and endothelial coverage was semiquantified and expressed as the percentage of the lumen circumference covered by neointima and endothelium, respectively. Their different extents were categorized as the following: minimal (<25% of the luminal surface, score: 1), mild (25%–50% of the luminal surface, score: 2), moderate (51%–75% of the luminal surface, score: 3), and marked (>75% of the luminal surface, score: 4).

RESULTS

Mean aneurysm sizes (including the aneurysm neck, width, and height) of the 22 aneurysms are shown in Table 1. There was no significant difference in aneurysm neck, width, and height among groups at different time points ($P > .05$).

Five rabbits were sacrificed at 1 month after FRED deployment: Four aneurysms demonstrated incomplete occlusion immediately after device deployment and 1 aneurysm showed near-complete occlusion. One month after treatment, 4 (4/5, 80%) aneurysms (including the aneurysm shown as having near-complete occlusion immediately after treatment) were completely occluded and 1 aneurysm showed near-complete occlusion (Fig 2*A*–*C*).

Table 1: Mean aneurysm sizes at different time points

Time	Neck (mm)	Width (mm)	Height (mm)
1 Mo	4.1 ± 1.1	6.5 ± 2.1	7.0 ± 1.7
3 Mo	3.5 ± 1.0	5.5 ± 1.6	5.5 ± 1.2
6 Mo	3.7 ± 1.1	6.3 ± 1.7	5.9 ± 1.4
12 Mo	3.6 ± 1.0	5.5 ± 1.5	6.0 ± 1.4

In the next follow-up group, 4 aneurysms were incompletely occluded immediately after device deployment, and 1 aneurysm showed near-complete occlusion. Three months after treatment, complete occlusion was shown in 4 (4/5, 80%) aneurysms (including the aneurysm shown as having near-complete occlusion immediately after treatment) and near-complete occlusion was indicated in 1 aneurysm.

Four aneurysms at the 6-month point indicated incomplete occlusion immediately after device deployment. Six months posttreatment, all (4/4, 100%) aneurysms were completely occluded.

Eight aneurysms were included at the 12-month point: Seven aneurysms were incompletely occluded immediately after device deployment and 1 aneurysm showed near-complete occlusion. Twelve months after treatment, 7 (7/8, 88%) aneurysms (including the aneurysm shown as having near-complete occlusion immediately after treatment) were completely occluded, while 1 aneurysm showed near-complete occlusion (Fig 3*A*–*C*).

In total, 19 (86%) of 22 aneurysms were completely occluded (grade I) during follow-up and 3 (14%) of 22 aneurysms showed near-complete occlusion (grade II). Thus 100% of the aneurysms indicated complete or near-complete occlusion. All aneurysms

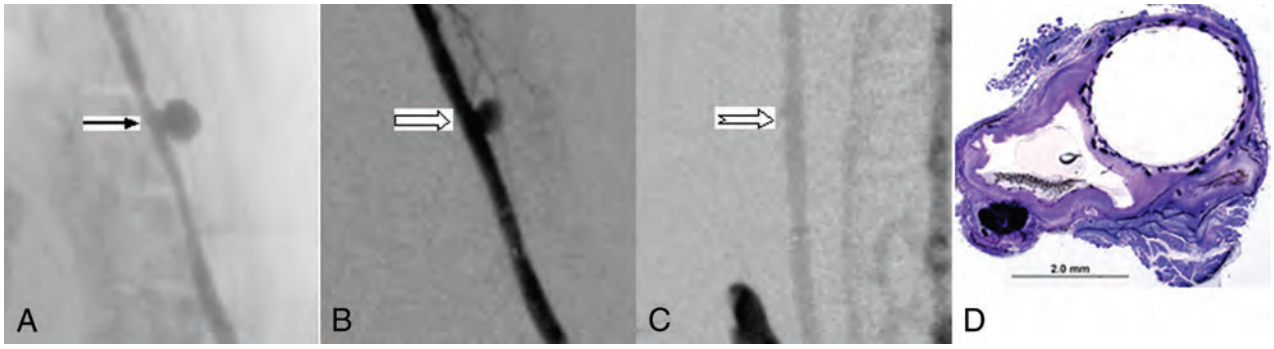

FIG 2. *A*, Anteroposterior digital subtraction angiogram shows the aneurysm (*arrow*) before treatment. *B*, DSA image immediately after device deployment shows aneurysm partial occlusion (*block arrow*). *C*, DSA image at 1 month shows complete aneurysm occlusion (*notched arrow*). *D*, Photomicrograph stained with toluidine blue and basic fuchsin shows an empty aneurysm sac completely sealed with neointimal growth incorporating the FRED struts and mesh spanning the neck, magnification 15×.

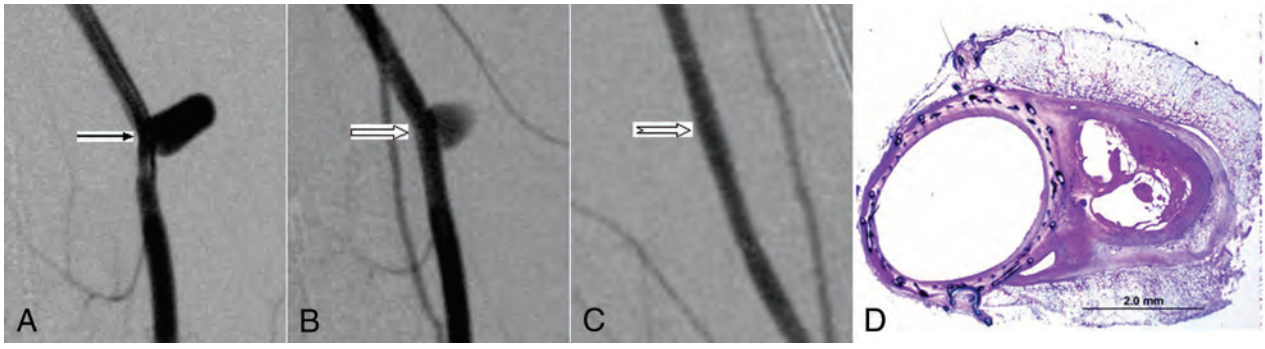

FIG 3. *A*, Anteroposterior digital subtraction angiogram shows the aneurysm (*arrow*) before treatment. *B*, DSA image immediately after device deployment shows partial aneurysm occlusion (*block arrow*). *C*, DSA image at 12 months shows complete aneurysm occlusion (*notched arrow*). *D*, Photomicrograph stained with toluidine blue and basic fuchsin shows partially organized thrombus within the aneurysm sealed with complete neointima incorporating the FRED struts and mesh across the neck, magnification 15×.

showed progressive occlusion when follow-up imaging was compared with imaging immediately after treatment (Table 2). Parent arteries remained patent in all cases.

Partially or completely organized thrombus, unorganized fibrin, and an empty aneurysm cavity were shown at each time point. Neointimal growth incorporated the device and completely excluded the aneurysm neck in 19 aneurysms, which included 2 of the 3 incompletely occluded aneurysms shown on DSA. Incomplete neointima across the neck was indicated in 3 aneurysms, of which 2 were completely occluded as shown on DSA (Figs 2*D* and 3*D*).

Nineteen (86%) cases showed marked neointima formation and endothelial coverage. Two cases (1 in the 3-month group and 1 in 12-month group) had both mild neointima formation and endothelial coverage. One case in the 12-month group showed moderate neointima formation and mild endothelial coverage. The average stenosis percentage in each group was <30%, which indicated only mild intima hyperplasia (Table 3).

All lumbar arteries remained patent in 4 groups during the follow-up period; the patency was confirmed by DSA before sacrifice and with an SEM (Fig 4).

Table 2: Aneurysm occlusion summary

	Immediately after Treatment		Before Sacrifice	
	Incomplete	Near-Complete	Complete	Near-Complete
1-Mo group ($n = 5$)	4	1	4	1
3-Mo group ($n = 5$)	4	1	4	1
6-Mo group ($n = 4$)	4	0	4	0
12-Mo group ($n = 8$)	7	1	7	1

Table 3: Histologic data at different time points

	Neointima Formation	Endothelial Coverage	Stenosis Percentage
1-Mo group	4 ± 0	4 ± 0	28.7 ± 7.0
3-Mo group	3.6 ± 0.9	3.6 ± 0.9	22.9 ± 3.9
6-Mo group	4 ± 0	4 ± 0	20.0 ± 6.0
12-Mo group	3.6 ± 0.7	3.5 ± 0.9	23.2 ± 4.0

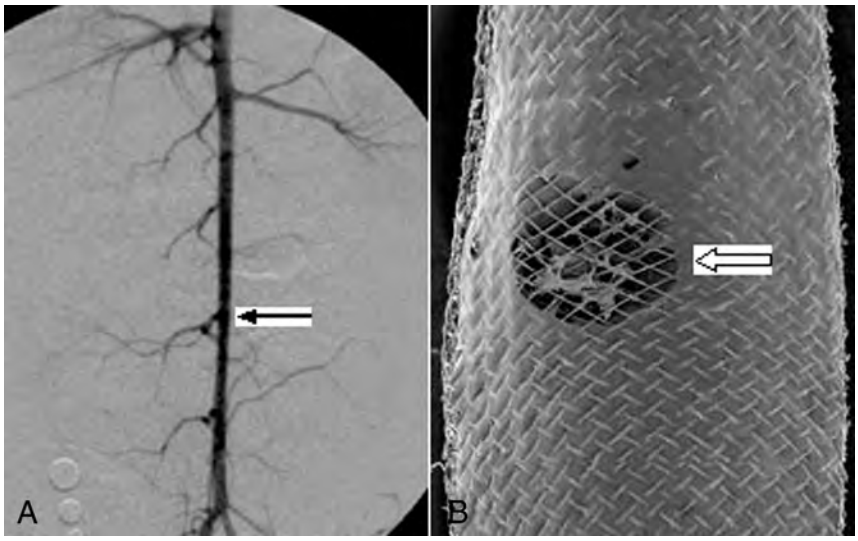

FIG 4. *A*, DSA 12 months after device deployment across the lumbar arteries (*arrow*), indicating patent lumbar arteries. *B*, SEM shows the open orifice of the lumbar artery (*block arrow*), magnification 15×.

DISCUSSION

In this study, we tested the FRED in sidewall aneurysms in rabbits. A high rate of complete aneurysm occlusion was achieved up to 12 months following implantation. Histologic findings showed that aneurysms were filled with unorganized or organized thrombus with the neck sealed by neointimal incorporation within the FRED struts and meshes. In a vein patch sidewall aneurysm model, the device demonstrated high rates of progressive and complete aneurysm occlusion while also preserving the patency of small arteries arising from the abdominal aorta.

Using a rabbit elastase-induced aneurysm model in rabbits, our group tested the performance of the Pipeline and reported the angiographic and histologic features at different periods after deployment. The aneurysm lumen was filled with unorganized, partial, or completely organized thrombus. Endothelial cells were found to cover the device struts across the aneurysm neck, and they were contiguous with the endothelium of the parent artery or aorta. Parent arteries and small, adjacent branch vessels remained patent; the patency was also confirmed by a scanning electric microscope. The rate of complete or near-complete aneurysm occlusion were 88%,[5] which was lower than that in this study (100%) by using a surgical sidewall aneurysm model. In addition, moderately thick intimal hyperplasia was noted at the distal stent portion of the parent artery in the elastase-induced aneurysm model, which is mainly because the devices were relatively oversized in the distal aspect of the parent artery. In the sidewall surgical aneurysm model, because the proximal and distal sides of parent artery have similar sizes, no obvious difference of neointimal hyperplasia in the proximal and distal parent artery was shown.[5]

Other researchers reported their initial clinical experience with the FRED, and the preliminary results are encouraging. In 33 patients with 37 aneurysms with up to 12 months' follow-up, the complete aneurysm occlusion rate was 80% (4/5) at 4–6 months and 100% (8/8) at 7–12 months after FRED deployment. Both the mortality and permanent morbidity rates were 0%.[8] A high aneurysm complete occlusion rate (7/8, 88%) was achieved at 3-month follow-up in another report.[9]

This study had several limitations. We included only a small number of subjects at each time point. In addition, although there were no significant differences of aneurysm sizes (neck, width, and height) among different groups, aneurysm shapes were not similar in some cases; these shapes might explain the difference in healing in various aneurysms.

CONCLUSIONS

In a vein patch sidewall aneurysm model, the FRED demonstrated high rates of progressive and complete aneurysm occlusion with minimal parent artery stenosis and preservation of small arterial branches arising from the abdominal aorta.

ACKNOWLEDGMENTS

The authors thank ISIS Services, San Carlos, California, led by the Chief Scientific Officer/Founder Jorge Garcia for professional management from Amy Valera, Project Manager; and technical support from Victor Avalos, Surgical Specialist; Benigno Mills, Surgical Specialist; Adam Loo, operating room technician; and Eric Chu, operating room technician, for the laboratory animal testing.

Disclosures: Tai Tieu—*RELATED*: MicroVention, *Comments*: I am a full-time employee of MicroVention Inc; thus, I receive a salary from MicroVention. My employment with MicroVention is not dependent on any publication. I receive a salary from MicroVention regardless of whether this work is published; *UNRELATED*: *Patents (planned, pending, or issued)*: MicroVention, *Comments*: All patents are the right of MicroVention. For pending or issued patents, I receive less than $1000 from MicroVention. David F. Kallmes—*RELATED*: *Grant*: MicroVention,* *Comments*: support for research personnel; *Support for Travel to Meetings for the Study or Other Purposes*: MicroVention,* *Comments*: travel to lab for device implant; *UNRELATED*: *Board Membership:* GE Healthcare (Cost-Effectiveness Board); *Consultancy*: ev3,* Medtronic,* *Comments*: planning and implementation of clinical trials; *Grants/Grants Pending*: MicroVention,* Codman,* Surmodics,* Sequent,* ev3,* *Comments*: preclinical and clinical research; *Royalties*: University of Virginia Patent Foundation (Spine Fusion). *Money paid to the institution.

REFERENCES

1. Tan LA, Keigher KM, Munich SA, et al. **Thromboembolic complications with Pipeline embolization device placement: impact of procedure time, number of stents and pre-procedure P2Y12 reaction unit (PRU) value.** *J Neurointerv Surg* 2015;7:217–21
2. Cirillo L, Leonardi M, Dall'olio M, et al. **Complications in the treatment of intracranial aneurysms with Silk stents: an analysis of 30 consecutive patients.** *Interv Neuroradiol* 2012;18:413–25
3. De Vries JD, Boogaarts J, Norden AV, et al. **New generation of flow diverter (Surpass) for unruptured intracranial aneurysms: a prospective single-center study in 37 patients.** *Stroke* 2013;44:1567–77
4. Ding YH, Tieu T, Kallmes DF. **Creation of sidewall aneurysm in rabbits: aneurysm patency and growth follow-up.** *J Neurointerv Surg* 2014;6:29–31
5. Kallmes DF, Ding YH, Dai D, et al. **A new endoluminal, flow-disrupting device for treatment of saccular aneurysms.** *Stroke* 2007;38:2346–52
6. Kallmes DF, Ding YH, Dai D, et al. **A second-generation, endoluminal, flow-disrupting device for treatment of saccular aneurysms.** *AJNR Am J Neuroradiol* 2009;30:1153–58
7. Brinjikji W, Lanzino G, Cloft HJ, et al. **Patency of the posterior communicating artery after flow diversion treatment of internal carotid artery aneurysms.** *Clin Neurol Neurosurg* 2014;120:84–88
8. Kocer N, Islak C, Kizilkilic O, et al. **Flow Re-direction Endoluminal Device in treatment of cerebral aneurysms: initial experience with short-term follow-up results.** *J Neurosurg* 2014;120:1158–71
9. Poncyljusz W, Sagan L, Safranow K, et al. **Initial experience with implantation of novel dual layer flow-diverter device FRED.** *Wideochir Inne Tech Malo Inwazyjne* 2013;8:258–64

Artery Length Sensitivity in Patient-Specific Cerebral Aneurysm Simulations

S. Hodis, S. Kargar, D.F. Kallmes, and D. Dragomir-Daescu

ABSTRACT

BACKGROUND AND PURPOSE: The reconstruction of aneurysm geometry is a main factor affecting the accuracy of hemodynamics simulations in patient-specific aneurysms. We analyzed the effects of the inlet artery length on intra-aneurysmal flow estimations by using 10 ophthalmic aneurysm models.

MATERIALS AND METHODS: We successively truncated the inlet artery of each model, first at the cavernous segment and second at the clinoid segment. For each aneurysm, we obtained 3 models with different artery lengths: the originally segmented geometry with the longest available inlet from scans and 2 others with successively shorter artery lengths. We analyzed the velocity, wall shear stress, and the oscillatory shear index inside the aneurysm and compared the 2 truncations with the original model.

RESULTS: We found that eliminating 1 arterial turn resulted in root mean square errors of <18% with no visual differences for the contours of the flow parameters in 8 of the 10 models. In contrast, truncating at the second turn led to root mean square errors between 18% and 32%, with consistently large errors for wall shear stress and the oscillatory shear index in 5 of the 10 models and visual differences for the contours of the flow parameters. For 3 other models, the largest errors were between 43% and 55%, with large visual differences in the contour plots.

CONCLUSIONS: Excluding 2 arterial turns from the inlet artery length of the ophthalmic aneurysm resulted in large quantitative differences in the calculated velocity, wall shear stress, and oscillatory shear index distributions, which could lead to erroneous conclusions if used clinically.

ABBREVIATIONS: BV = bleb volume; BW = aneurysmal bleb walls; CFD = computational fluid dynamics; OSI = oscillatory shear index; PN = a cross-section plane at the aneurysm neck; PO = a cross-section plane parallel with the PN and offset toward the middle of the aneurysm; PP = a plane perpendicular to the PN and passing near the middle of the aneurysm; PU = a cross-section plane located approximately 2 inlet diameters upstream from the aneurysm; RMS = root mean square; WSS = wall shear stress

Computational fluid dynamics (CFD) simulations of patient-specific cerebral aneurysms provides a valuable tool for understanding the hemodynamic environment. The geometry of the aneurysm needs to be accurately represented, and the computational model needs to account for the main properties of blood flow physics to obtain realistic and accurate flow solutions. When one reconstructs the computational geometry from imaging data, such as CT angiography or MR angiography, the extent of the surrounding vasculature that must be included to obtain rigorous flow solutions is not a priori known. Inclusion of small-diameter surrounding vessels usually does not affect the flow solution results but could add significant computational effort.[1] On the other hand, exclusion or severe truncation of larger vessels might change the flow estimations, usually resulting in nonrealistic flow patterns. The operator-dependent segmentation of radiologic images of aneurysms leads to model geometries that showed errors as large as 60% in the estimated hemodynamic parameters.[2-5] However, there is no published sensitivity study designed to analyze the effect of the arterial inlet length on the intra-aneurysmal flow estimates, to our knowledge. Due to the lack of accurate, clinically measured velocity profiles and cross-sectional geometries, many current studies use generic, mathematically generated blood flow boundary conditions and short arterial lengths.

As a rule of thumb, an inlet length of at least 10 artery diameters upstream of the aneurysm must be used in hemodynamic CFD simulations. In addition, the inlet boundary conditions used

Received June 30, 2014; accepted after revision September 29.

From the Department of Mathematics (S.H.), Texas A&M University, Kingsville, Texas; and College of Medicine (S.K., D.F.K., D.D.-D.), Department of Radiology (S.H., D.F.K.), and Division of Engineering (D.D.-D.), Mayo Clinic, Rochester, Minnesota.

Please address correspondence to Dan Dragomir-Daescu, PhD, Division of Engineering, Mayo Clinic, 200 First St SW, Rochester, MN 55905; e-mail: DragomirDaescu.Dan@mayo.edu

http://dx.doi.org/10.3174/ajnr.A4179

in the literature, usually velocity profiles, are taken as fully developed and axisymmetric.[1,4,6-8] These assumptions are valid only for flow in straight tubes, which is very different from flow in patient arteries, where the flow is not fully developed even in the common carotid artery, the location where measurements are more readily available. Therefore, using the fully developed axisymmetric velocity profile on a short artery inlet may result in unrealistic flow estimates in the aneurysm. In the absence of physiologic measurements of arterial cross-sectional velocity distributions, it is generally safer to include a longer anatomic inlet artery to let the flow solution develop realistically on the basis of the tortuosity of the arterial geometry.[9] Thus, we hypothesized that including a longer inlet artery will minimize the effect of the inlet boundary conditions.

The aim of this study was to assess the effect of truncating the arterial inlet length proximal to the aneurysm on the local intra-aneurysmal hemodynamics of ophthalmic aneurysms. The goal was to find a sufficient artery length such that the values of velocity, wall shear stress (WSS), and oscillatory shear index (OSI) in the aneurysm are less affected by the arterial length when using the same boundary conditions and fluid properties.

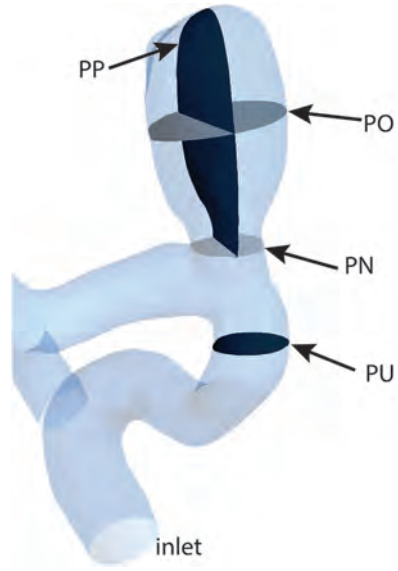

FIG 1. Aneurysm geometry showing the 4 planes chosen for velocity distributions analysis: upstream plane, neck plane, offset plane, and perpendicular plane.

MATERIALS AND METHODS

Geometries

Ten cerebral aneurysms located on the ophthalmic segment with a feeding artery starting around the lacerum segment were included in the study. The computational geometries were segmented from the 3D rotational angiography data by using Mimics (Materialise, Leuven, Belgium). For each aneurysm model, we generated 3 model truncations (T): T_0 had the longest possible inlet artery obtained from the scan imaging data, T_1 was truncated orthogonal to the artery axis after the first major arterial turn at the cavernous segment, and T_2 was truncated after the second major arterial turn, at the clinoid segment. For each patient model, the arterial outlets lengths were kept constant at >5 times the artery diameter[7,10,11] for each of the 3 arterial inlet truncations. When the outlet was near a bifurcation, we truncated even further to allow a more remote outlet boundary condition.

CFD Simulation

For each truncation, we generated uniform hex-core grids by using ICEM CFD (ANSYS, Canonsburg, Pennsylvania) with an average node-spacing of 0.12 mm and we used 5 layers in the boundary layer with a first layer thickness of 0.01 mm and an inflation factor of 1.25. These values were previously shown to lead to grid-independent velocity and pressure estimations.[7] Pulsatile flow solutions were generated with Fluent 14.0 (ANSYS) by using a second-order implicit solver. The Quadratic Upstream Interpolation for Convective Kinematics scheme was used for the convective term, with the Least Squares Cell-Based method for gradient estimation of the diffusion term at the cell faces. To handle pressure-velocity coupling, we adopted the Semi-Implicit Method for Pressure-Linked Equations algorithm. Iterative convergence was achieved when the normalized root mean square residuals for continuity and momentum equations became less than 10^{-5}. For the inlet boundary conditions, we specified a fully developed Womersley velocity profile[11] at the morphed circular inlet surface with the transient waveform given by Zamir[12] and used in Naughton et al[8] and Hodis et al,[7,10,13-15] with an average flow rate of 4 mL/s[1,5] and a maximum value of approximately 8 mL/s at peak systole. A viscosity of 0.035 poise and a density of 1050 kg/m^3 were used for physical properties. At the outlets, we applied the outflow boundary conditions derived from the stress continuity at outlet surfaces by specifying zero pressure.[16] At the lumen boundaries, we imposed a no-slip boundary condition, with zero velocity. The period of the cardiac cycle was assumed to be 1 second. To eliminate transient numeric errors, we solved the equations for 4 cardiac cycles by using 10,000 time-steps per cardiac cycle. We observed that third and fourth cardiac cycles produced almost identical results, thus confirming that the results were mathematically converged.

Hemodynamic Parameters

In this study, we compared the 3 main parameters used by researches to describe the intra-aneurysmal flow: velocity, WSS, and OSI.[1,5,17-19] Velocity and pressure are the 2 primary hemodynamic parameters that are determined from the incompressible Navier-Stokes equations in vector form[12]:

$$1) \qquad \begin{cases} \nabla \cdot \vec{v} = 0 \\ \rho\left(\dfrac{\partial \vec{v}}{\partial t} + \vec{v} \cdot \nabla \vec{v}\right) = -\nabla p + \mu \Delta \vec{v}, \end{cases}$$

where $\vec{v}$ is the velocity vector, p is the pressure scalar, and the symbols $\cdot$, ∇, and Δ are dot product, gradient, and Laplacian vector operators, respectively.

In a Newtonian fluid, the WSS vector is the force that acts tangential to the wall surface and is defined as the gradient at the wall of the tangential velocity[12,16,19,20]:

$$2) \qquad \overrightarrow{WSS} = \mu \frac{\partial(\vec{v} - (\vec{v} \cdot \vec{n})\vec{n})}{\partial \vec{n}},$$

where $\vec{n}$ is the wall outward normal.

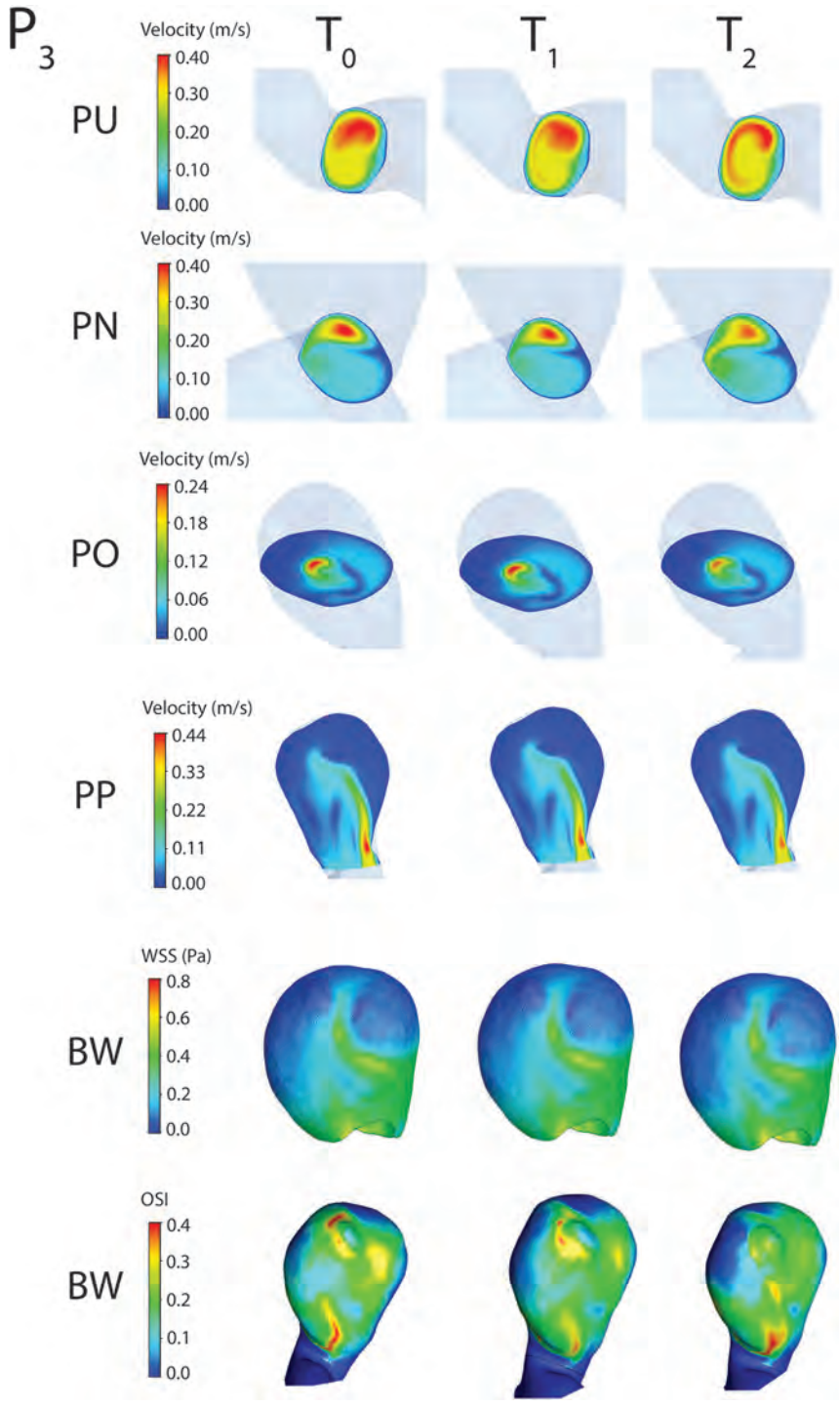

FIG 2. Velocity magnitude contour plots on the 4 planes: PU, PN, PO, and PP and WSS and OSI magnitude contours on BW for model P_3.

The OSI parameter was defined as in Ku et al.[20] A maximum value of 0.5, shows that $\overrightarrow{WSS}$ is fully changing the direction during the cardiac cycle, which usually describes a complex pulsatile flow.[21] We analyzed the velocity and WSS parameters at peak systole in the fourth cardiac cycle and the OSI during the entire fourth cycle. We chose the peak systole for the error analysis because of the larger errors compared with other time points in the cardiac cycle.[12] To compare the results for the 3 truncations, we considered 6 locations. First, we evaluated the velocity distributions in the entire aneurysm bleb volume (BV, location 1). Second, we calculated the velocity distributions on 4 cross-section planes: a cross-section plane located approximately 2 inlet diameters upstream from the aneurysm (PU), a cross-section plane at the aneurysm neck (PN), a cross-section plane parallel with PN and offset toward the middle of the aneurysm (PO), and a plane perpendicular to PN and passing near the middle of the aneurysm (PP, locations 2–5) (Fig 1). Third, WSS and OSI were both evaluated at all points on the aneurysmal bleb walls (BW, location 6). WSS and OSI are, along with vorticity, gradient oscillatory number, or relative residence time, some of the most frequently analyzed quantities in recent CFD literature of cerebral aneurysm blood flow.[22]

Quantitative Analysis

To better quantify the differences among the 3 truncations, we used a normalized error that measures the difference between 2 parameters with respect to the mean value of the 2 parameters, defined as follows:

$$3)\quad \epsilon_n^{(i)} = 100 \times \frac{2|v_0^{(i)} - v_n^{(i)}|}{v_0^{(i)} + v_n^{(i)}},$$

$$for\ n = 1,\ 2\ and\ i = 1,..,\ N,$$

where $v_0^{(i)}$ is the hemodynamic variable v at the grid point i, for the truncation T_0, N is the total number of grid points on a sample plane or surface, and $v_n^{(i)}$ is the hemodynamic variable V, at the grid point i for the truncation T_n, $n = 1, 2$.

Therefore, $\epsilon_n^{(i)}$ is an unbiased error measure relative to the mean value of T_0 and T_n ($n = 1, 2$) truncations.[23] In the results to follow, we calculated the root mean square (RMS) of the errors, over all points in the sample plane, surface, or volume, as follows:

$$4)\quad \mathrm{RMS} = \sqrt{\frac{1}{N}\sum_{i=1}^{N}(\epsilon_n^{(i)})^2},\quad n = 1,\ 2.$$

To avoid calculating errors for parameters on a specific location with magnitudes that can approach zero, we expressly eliminated from the analysis all the grid points on which the magnitudes were <10% of the maximum value. Therefore, the errors for velocity, WSS, and OSI were not recorded when their absolute values were too small.

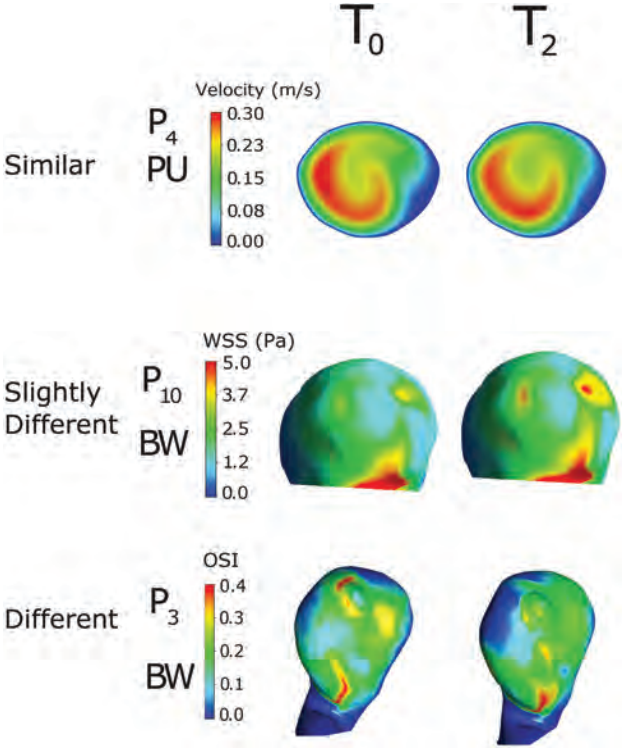

FIG 3. T_0 versus T_2 comparison illustrating similar contours (velocity on PU in P_4), slightly different contours (WSS on BW in P_{10}), and different contours (OSI on BW in P_3).

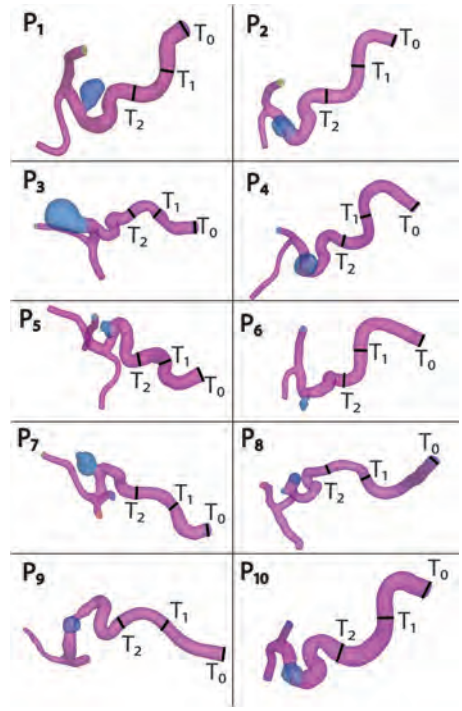

FIG 4. Ten ophthalmic aneurysm geometries showing the locations of the truncation planes: T_0 is the original model obtained from the patient clinical images (full FOV), T_1 is the first truncation at the cavernous segment, and T_2 is the second truncation, at the clinoid segment.

Qualitative Analysis

Most of the CFD analysis results presented in the literature use direct observations of isosurfaces or contour plots for a specific hemodynamic parameter. To compare observations of generated isosurfaces, we also plotted velocity contours on the 4 cross-section planes, the WSS contours on the aneurysm wall, all at peak systole, and the distributions of OSI on BW for the fourth cardiac cycle (Fig 2). Next we assessed the graphic results by visually comparing the contours between T_0 and T_1 and between T_0 and T_2 by using a trichotomous scale: similar, slightly different (Fig 3), and different and associated the qualitative results with the errors defined in Equations 3 and 4.

RESULTS

Model Truncations

The 10 segmented ophthalmic aneurysm models showing the 3 locations of inlet artery truncations are presented in Fig 4. The original model truncation, T_0, included the entire arterial length segmented from the acquired images and, depending on patient blood vessel geometry, resulted in arterial lengths ranging from 58 to 86 mm. The first user truncation, T_1, was made at the cavernous segment after the major ICA turn and resulted in arterial lengths of 33–58 mm, whereas the second user truncation, T_2, was made at the clinoid segment after the next arterial turn, with inlet arterial lengths ranging from 21 to 37 mm. The arterial inlet lengths were approximately between 14 and 18 mean arterial diameters for T_0, between 8 and 12 diameters for T_1, and between 5 and 8 diameters for T_2.

Quantitative Analysis

For the quantitative analysis, we used the errors defined in Equations 3 and 4 for the velocity vector, the WSS, and the OSI magnitudes. The results for the error RMS (Equation 4) are shown in the Table for the 6 locations: planes PU, PN, PO, and PP; the BW; and the BV. In general, the errors for the T_2 truncations were higher than the errors for the T_1 truncations, and the larger errors were observed in the PU plane and the BW location.

For 8 models (P_2, P_4, P_5, P_6, P_7, P_8, P_9, and P_{10}), the error RMS values for the T_1 to T_0 comparison were <18% (which was the threshold value for which most of the graphic plots started to look dissimilar). For the other 2 models (P_1 and P_3), the errors were as large as 32%.

In contrast, the error RMS values between the T_2 and T_0 truncations were <18% for all quantities in only 2 models (P_4 and P_8). For 5 models (P_2, P_6, P_7, P_9, and P_{10}), the errors were between 18% and 32%. In the remaining 3 models (P_1, P_3, and P_5), some of the errors were even larger, reaching 43%–55% for OSI on the BW as shown in the Table.

Overall, the T_2 truncation errors are significantly larger than T_1 truncation errors for all 10 models, as shown by a Bland-Altman plot in Fig 5.

Meaningful Error

To associate the quantitative description with the qualitative observations and define a meaningful error, we compared the contours plots with the error RMS (Equation 4) of the scatterplots representing the magnitudes of T_0 versus T_1 and T_0 versus T_2. As an example, Fig 6 shows the results of the WSS on BW for model

Percent error RMS values calculated with Equation 4 for the 10 models[a]

Models	PU Velocity		PN Velocity		PO Velocity		PP Velocity		BV Velocity		BW WSS		BW OSI	
	ϵ_1	ϵ_2	ϵ_1	ϵ_2	ϵ_1	ϵ_2	ϵ_1	ϵ_2	ϵ_1	ϵ_2	ϵ_1	ϵ_2	ϵ_1	ϵ_2
P_1	10	19	4	13	9	22	5	26	13	26	17	31	23	43
P_2	3	20	3	3	3	4	3	3	4	4	6	7	7	15
P_3	10	18	12	33	7	20	7	17	6	16	5	11	32	55
P_4	1	10	1	2	1	2	1	1	2	2	7	8	4	7
P_5	14	23	4	22	3	14	4	23	4	18	5	23	18	54
P_6	4	6	2	2	2	2	2	2	2	3	2	3	18	26
P_7	5	20	4	25	1	15	2	10	3	31	8	20	4	28
P_8	2	2	<1	1	<1	1	<1	1	<1	1	<1	2	2	2
P_9	3	52	<1	10	<1	9	<1	8	<1	11	<1	18	2	21
P_{10}	3	25	6	16	3	21	2	12	3	17	9	25	18	26

[a] ϵ_1 is the error between T_0 and T_1 truncations, while ϵ_2 is the error between T_0 and T_2 truncations, both calculated with Equation 3. The values for ϵ_1 and ϵ_2 shown in the table are the percent RMS values of the errors.

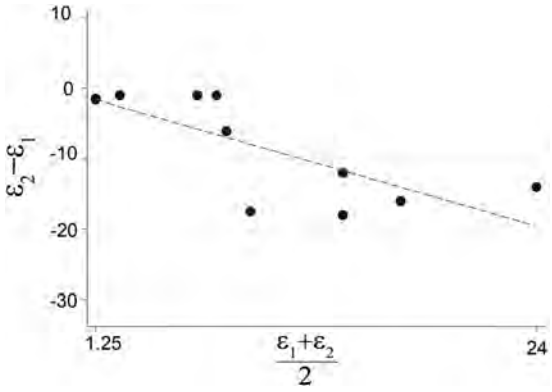

FIG 5. Bland-Altman plots of the WSS on BW for the T_0 versus T_2 and T_0 versus T_1 comparison, illustrating significantly higher error for the T_2 truncation compared with T_1 truncation for all 10 models.

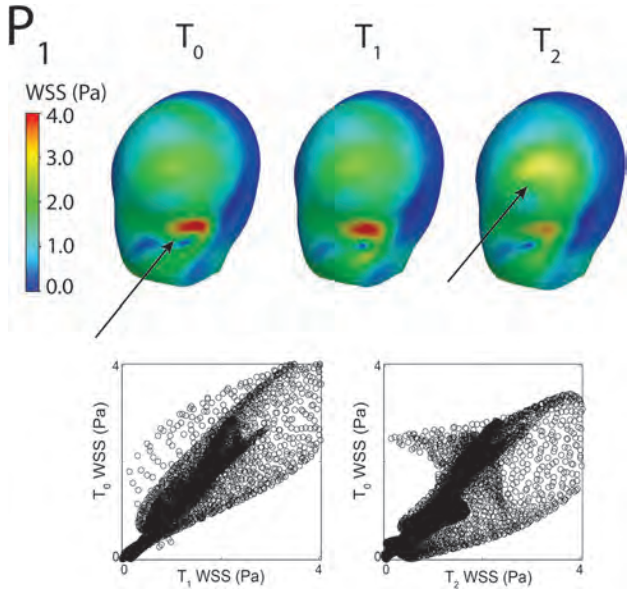

FIG 6. WSS magnitude contour plots for the 3 truncations (upper panel) and WSS magnitude scatterplots for the T_0 versus T_1 comparison and for the T_0 versus T_2 comparison, respectively (lower panels) for the model P_1. The error RMSs defined by Equation 4 corresponding to the 2 scatterplots are 17% and 31%, respectively. The *arrows* indicate the locations where the area with maximum WSS values diminishes from truncation T_0 to truncation T_2 and a new area with a local maximum forms in truncation T_2.

P_1. Here, the contours are visually similar between the T_0 and T_1 truncations, but slightly different (almost at the border of being different) for the T_0 and T_2 truncations. In addition, the scatterplot for the aneurysm bleb surface WSS magnitude for the T_0 to T_1 comparison (Fig 6, lower left) is spread along the 45° diagonal starting from the origin with an error RMS of approximately 17%. The scatterplot for the T_0 to T_2 comparison for WSS magnitudes on BW (Fig 6, lower right) is more spread out about the diagonal, with an error RMS value of 31%.

Another quantitative-qualitative analysis is presented in Fig 7, which shows the contour plots of OSI on BW for model P_5 and the scatterplot of OSI values for T_0 versus T_1 and T_0 versus T_2 comparisons. In this example, the contours are only borderline slightly different for the T_0 to T_1 comparison, which is also confirmed quantitatively by the tighter scatterplot of the T_0 versus T_1 comparison (lower left), with an error RMS of approximately 18%. However, the T_2 contour plot is visually different from the T_0 contour plot difference, which was more precisely quantified in the scatterplot (lower right), where the points are more widely spread out for higher OSI values with an error RMS value of approximately 54%. The large error RMS could be explained by the location of maximum OSI shifting from the area between the 2 aneurysm blebs in the T_0 truncation to an area near the common neck location of the 2 blebs in the T_2 truncation (shown with the arrows in Fig 7).

To find the numeric value of a visually observed meaningful error for all 10 aneurysms, we compared the contour plot results with the error RMS defined in Equation 4, and we found that contour plots with a relative error RMS of <18% could be generally considered qualitatively similar, whereas those with a relative error RMS >32% were associated with qualitatively different contours. Errors between truncations with magnitudes between 18% and 32% were observed to lead to slightly different contours.

DISCUSSION

This is the first study to assess the quantitative differences in the intra-aneurysmal blood flow parameters when truncating the length of the main artery leading to the aneurysm bleb in models of ophthalmic aneurysms and to provide a meaningful error, by associating the quantitative analysis with the qualitative description of hemodynamics results. Usually, visual observations are the standard

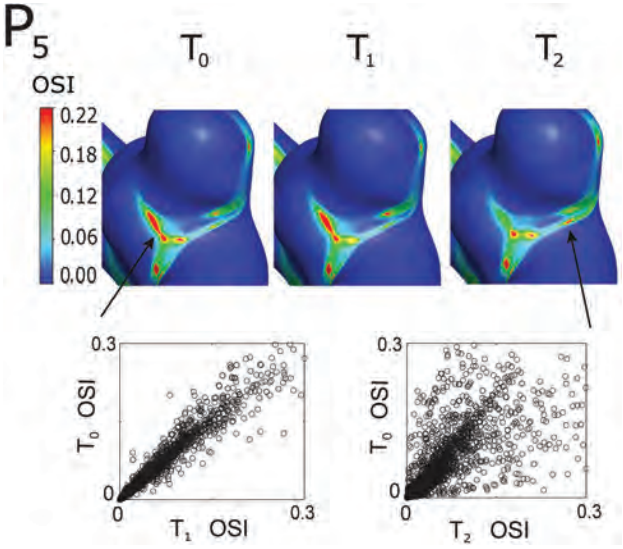

FIG 7. OSI magnitude contour plots on the aneurysm bleb surface for the 3 truncations (upper panels) and OSI magnitude scatterplots on the aneurysm bleb (lower panels). The error RMS defined by Equation 4 corresponding to the 2 scatterplots are 18% and 54%, respectively. The *arrow* on the T_0 contour plot indicates the location of the maximum OSI values, which shifts from the area between the 2 aneurysm blebs in the T_0 truncation to an area near the common neck location of the 2 blebs in the T_2 truncation.

way to compare the CFD results between models, which can potentially obscure important quantitative differences. To estimate the effect of the arterial length on the flow behavior in the aneurysm bleb, we analyzed the main flow parameters for 10 models, each with 3 truncations: the original maximum length obtained from the patient medical images and 2 user-defined truncations obtained by cutting the ICA artery after each of 2 major turns.

Qualitatively, the visual differences were observed to be small for most of the models when the ICA artery was truncated at the cavernous site (T_1 truncations). As such, a simple comparison of the contour plots with our quantitative results showed that the contours could be visually similar for the T_0 to T_1 comparison, but quantitatively, the average errors could still be relatively large, for example 17% different for WSS in P_1 (Fig 6). Because the quantitative differences account for both the location and the magnitude of the hemodynamic parameter investigated, a shifting location of the maximum value on the contour map can be much better assessed with a quantitative description of errors, but it can be sometimes misjudged by visual observation.

When the qualitative differences in the contour plots were compared with the quantitative errors presented in the Table, we observed that errors of less than approximately 18% resulted in visually similar contours for 8 models for the T_0 to T_1 comparisons. In contrast, for the T_0 to T_2 comparisons, larger errors were observed for 8 of the 10 models, which resulted in slightly different or different contour plots of the hemodynamic parameters.

In summary, we found that a short arterial truncation, such as T_2, at the clinoid segment could generate large quantitative errors and qualitative differences. However, an inlet artery starting at the cavernous segment, as in the T_1 truncation, seems to produce qualitatively similar flow behavior, but even for this more modest truncation, the quantitative errors can be too large compared with the flow parameters analyzed for the original model, T_0.

CONCLUSIONS

When one assesses the accuracy of a computational model for patient-specific aneurysms, quantitative analysis of the hemodynamic parameters must be considered along with visual analysis of the graphic representation of flow quantities. The present study showed that excluding 2 arterial turns from the artery resulted, most of the time, in large quantitative differences of the hemodynamics parameters inside the ophthalmic aneurysm blebs, which could lead to erroneous conclusions if used clinically.

Disclosures: David F. Kallmes—*UNRELATED*: *Board Membership*: GE Healthcare, *Comments*: Cost Effectiveness Board; *Consultancy:* ev3, Medtronic, *Comments*: planning and implementation of clinical trials; *Grants/Grants Pending:* ev3,* Sequent,* Surmodics,* Codman,* MicroVention*; *Royalties*: University of Virginia Patent Foundation (Spine Fusion). *Money paid to the institution.

REFERENCES

1. Cebral JR, Castro MA, Appanaboyina S, et al. **Efficient pipeline for image-based patient-specific analysis of cerebral aneurysm hemodynamics: technique and sensitivity.** *IEEE Trans Med Imaging* 2005;24:457–67
2. Karmonik C, Diaz O, Klucznik R, et al. **Quantitative comparison of hemodynamic parameters from steady and transient CFD simulations in cerebral aneurysms with focus on the aneurysm ostium.** *J Neurointerv Surg* 2014 April 10. [Epub ahead of print]
3. Ernemann UU, Gronewaller E, Duffner FB, et al. **Influence of geometric and hemodynamic parameters on aneurysm visualization during three-dimensional rotational angiography: an in vitro study.** *AJNR Am J Neuroradiol* 2003;24:597–603
4. Hoi Y, Woodward S, Kim M, et al. **Validation of CFD simulations of cerebral aneurysms with implication of geometric variations.** *J Biomech Eng* 2006;128:844–51
5. Moore JA, Steinman DA, Ethier CR. **Computational blood flow modelling: errors associated with reconstructing finite element models from magnetic resonance images.** *J Biomech* 1998;31:179–84
6. Cebral JR, Lohner R. **Efficient simulation of blood flow past complex endovascular devices using an adaptive embedding technique.** *IEEE Trans Med Imaging* 2005;24:468–76
7. Hodis S, Uthamaraj S, Smith AL, et al. **Grid convergence errors in hemodynamic solution of patient-specific cerebral aneurysms.** *J Biomech* 2012;45:2907–13
8. Naughton NM, Plourde BD, Stark JR, et al. **Impacts of waveforms on the fluid flow, wall shear stress, and flow distribution in cerebral aneurysms and the development of a universal reduced pressure.** *J Biomed Sci Eng* 2014;71002:7–14
9. Moyle KR, Antiga L, Steinman DA. **Inlet conditions for image-based CFD models of the carotid bifurcation: is it reasonable to assume fully developed flow?** *J Biomech Eng* 2006;128:371–79
10. Hodis S, Kallmes DF, Dragomir-Daescu D. **Adaptive grid generation in a patient-specific cerebral aneurysm.** *Phys Rev E Stat Nonlin Soft Matter Phys* 2013;88:052720
11. Womersley JR. **Oscillatory flow in arteries: the constrained elastic tube as a model of arterial flow and pulse transmission.** *Phys Med Biol* 1957;2:178–87
12. Zamir M. *The Physics of Coronary Blood Flow.* New York: Springer-Verlag; 2005
13. Hodis S, Uthamaraj S, Lanzino G, et al. **Computational fluid dynamics simulation of an anterior communicating artery ruptured during angiography.** *J Neurointerv Surg* 2014;6:e14
14. Hodis S, Zamir M. **Pulse wave velocity as a diagnostic index: the pitfalls of tethering versus stiffening of the arterial wall.** *J Biomech* 2011;44:1367–73
15. Hodis S, Zamir M. **Mechanical events within the arterial wall under the forces of pulsatile flow: a review.** *J Mech Behav Biomed Mater* 2011;4:1595–602

16. Versteeg H, Malalaseker W. *An Introduction to Computational Fluid Dynamics: The Finite Volume Method.* London: Pearson PLC; 2007
17. Shojima M, Oshima M, Takagi K, et al. **Magnitude and role of wall shear stress on cerebral aneurysm: computational fluid dynamic study of 20 middle cerebral artery aneurysms.** *Stroke* 2004;35:2500–05
18. Valen-Sendstad K, Steinman DA. **Mind the gap: impact of computational fluid dynamics solution strategy on prediction of intracranial aneurysm hemodynamics and rupture status indicators.** *AJNR Am J Neuroradiol* 2014;35:536–43
19. Cebral JR, Putman CM, Alley MT, et al. **Hemodynamics in normal cerebral arteries: qualitative comparison of 4D phase-contrast magnetic resonance and image-based computational fluid dynamics.** *J Eng Math* 2009;64:367–78
20. Ku DN, Giddens DP, Zarins CK, et al. **Pulsatile flow and atherosclerosis in the human carotid bifurcation: positive correlation between plaque location and low oscillating shear stress.** *Arteriosclerosis* 1985;5:293–302
21. Nordgaard H, Swillens A, Nordhaug D, et al. **Impact of competitive flow on wall shear stress in coronary surgery: computational fluid dynamics of a LIMA-LAD model.** *Cardiovasc Res* 2010;88:512–19
22. Cebral JR, Raschi M. **Suggested connections between risk factors of intracranial aneurysms: a review.** *Ann Biomed Eng* 2013;41:1366–83
23. Van Houten EE, Viviers D, McGarry MD, et al. **Subzone based magnetic resonance elastography using a Rayleigh damped material model.** *Med Phys* 2011;38:1993–2004

The Maze-Making and Solving Technique for Coil Embolization of Large and Giant Aneurysms

T. Ohta, I. Nakahara, R. Ishibashi, S. Matsumoto, M. Gomi, H. Miyata, H. Nishi, S. Watanabe, and I. Nagata

ABSTRACT

BACKGROUND AND PURPOSE: Despite major progress in treating aneurysms by coil embolization, the complete occlusion of aneurysms of >10 mm in diameter (large/giant aneurysms) remains challenging. We present a novel endovascular treatment method for large and giant cerebral aneurysms called the "maze-making and solving" technique and compare the short-term follow-up results of this technique with those of conventional coil embolization.

MATERIALS AND METHODS: Eight patients (65 ± 11.5 years of age, 7 women) with large/giant unruptured nonthrombosed cerebral aneurysm (mean largest aneurysm dimension, 19 ± 4.4 mm) were treated by the maze-making and solving technique, a combination of the double-catheter technique and various assisted techniques. The coil-packing attenuation, postoperative courses, and recurrence rate of this maze group were compared with 30 previous cases (conventional group, 65.4 ± 13.0 years of age; 22 women; mean largest aneurysm dimension, 13.4 ± 3.8 mm).

RESULTS: Four maze group cases were Raymond class 1; and 4 were class 2 as indicated by immediate postsurgical angiography. No perioperative deaths or major strokes occurred. Mean packing attenuation of the maze group was significantly higher than that of the conventional group (37.4 ± 5.9% versus 26.2 ± 5.6%). Follow-up angiography performed at 11.3 ± 5.4 months revealed no recurrence in the maze group compared with 39.2% in the conventional group.

CONCLUSIONS: The maze-making and solving technique achieves high coil-packing attenuation for efficient embolization of large and giant cerebral aneurysms with a low risk of recurrence.

Substantial progress in the endovascular treatment of cerebral aneurysms, such as balloon- and stent-assisted coil embolization, has resulted in the widespread use of these techniques with relatively high efficacy and safety. However, large and giant aneurysms remain difficult to treat by using assist techniques and bioactive coils,[1,2] possibly because the requisite coil-packing attenuation is often not achieved. We recently developed a "maze-making and solving" technique to occlude these large/giant aneurysms by achieving high packing attenuation. Here, we present the technical details of this procedure and compare the clinical outcomes and recurrence rates between large/giant aneurysm cases treated by the maze technique and matched cases treated by conventional coil embolization.

Received August 18, 2014; accepted after revision October 23.

From the Department of Neurosurgery, Kokura Memorial Hospital, Fukuoka, Japan.

Please address correspondence to Tsuyoshi Ohta, MD, Department of Neurosurgery, Kokura Memorial Hospital, 3-2-1 Asano, Kokurakita-ku, Kitakyushu, Fukuoka, Japan; e-mail: tsuyoshi@ya2.so-net.ne.jp

http://dx.doi.org/10.3174/ajnr.A4198

MATERIALS AND METHODS

This was a retrospective study of 42 patients with a large or giant (diameter, >10 mm),[3] nonthrombosed, unruptured aneurysm who received endovascular treatment at our hospital between February 2007 and December 2013. Eight of these 42 patients were treated after large-diameter coils became available in November 2012 and were treated with the "maze-making and solving" technique (the maze group). Thirty of the previous 34 patients were treated by other techniques (the conventional group). The 4 patients treated by endovascular trapping were excluded. Clinical outcomes were compared between maze and conventional groups.

Angiographic Evaluation

Aneurysmal location was defined at the origin of the neck on the basis of the classification of Bouthillier et al.[4] Angiographic findings were evaluated according to the Raymond classification[5] immediately after surgery and at follow-up. Aneurysm dimensions and volumes were measured by 3D reformatted images derived from rotational catheter angiograms[6] by using the Allura 3D-RA workstation (Philips Healthcare, Best, the

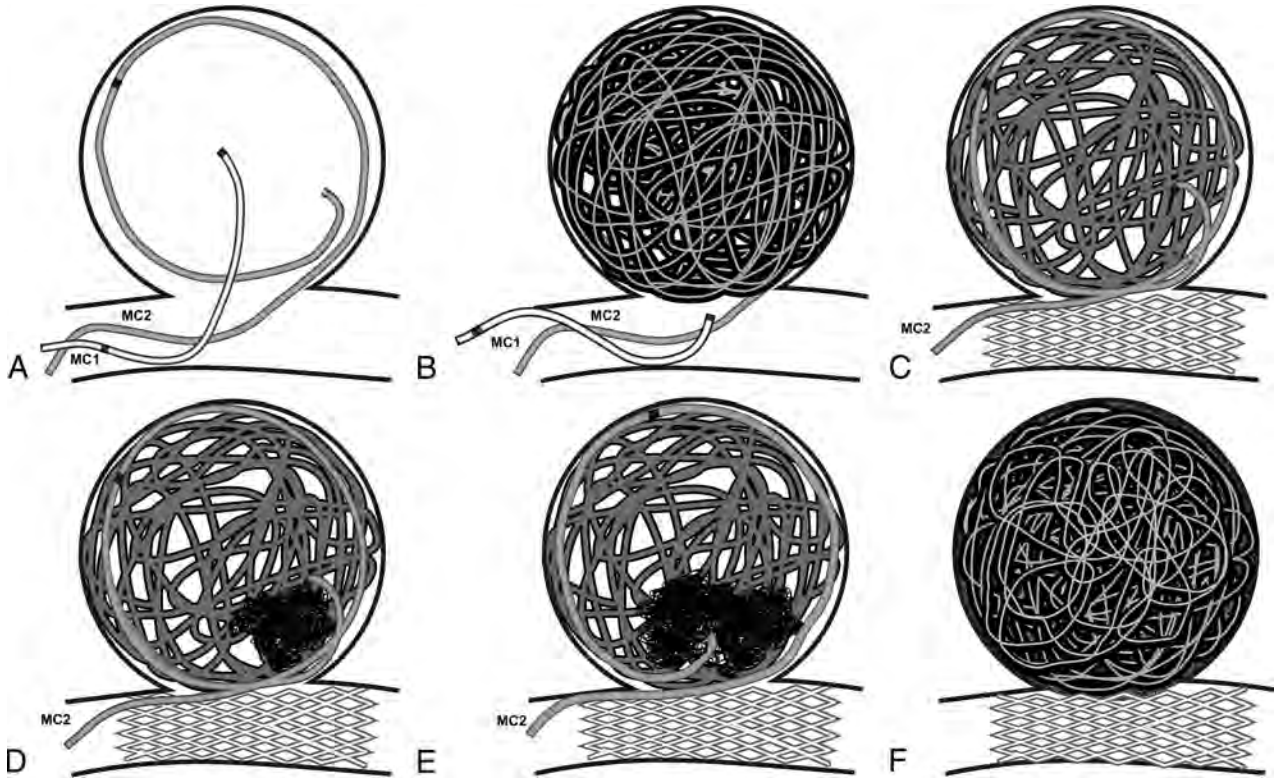

FIG 1. The concept of the maze-making and solving technique. The microcatheter for larger diameter coils (MC1) is placed in the center of the aneurysm, and the catheter for traditional coils (MC2) is placed following the aneurysmal wall to reach beyond the orifice (*A*). As many as possible larger diameter coils are inserted (*B*). Cross-section illustrations reveal random interspaces still left unembolized and the movement of MC2 (*C–E*). Note the elevation of MC2 by stent placement and the second marker of MC2 buried in larger diameter coils (*C*). Traditional coils from MC2 fill the dead space left unembolized (*D*). After sufficient filling, the microcatheter is moved back to follow the wall and finds a new space. Note the altered position of the tip and the course of MC2 (*E*). If we repeat these dead space–filling and wall-follower methods in a stepwise fashion, the aneurysm is tightly embolized (*F*).

Netherlands). Angiographic recurrence was defined as any worsening of the Raymond classification or enlargement of the residual aneurysm. Angiographic follow-up was performed at 3 months and annually after treatment. When an angiographic recurrence was considered progressive and large enough to embolize again, reintervention was performed. The follow-up period was defined as the number of months postsurgery to recurrence or to the latest angiogram.

Packing Attenuation

The total volume of the coils deployed into each aneurysm was calculated by multiplying the total length of the coils by the cross-sectional area.[7] Full circumferential expansion was assumed to calculate the volume of hydrogel coils.[8] Packing attenuation was calculated as the ratio of the total coil volume to the total aneurysm volume.

Clinical Assessment

Perioperative complications were defined as any new neurologic deficits, serious adverse events extending hospitalization, or death occurring within 30 days after the operation. Periprocedural death and major stroke (mRS $\geqq$ 2) were defined as serious perioperative complications. Clinical follow-up was performed at 1, 3, and 6 months and annually after treatment. Each patient was evaluated by the mRS[9] at follow-up, and any worsening was recorded as chronic neurologic deterioration.

Technical Details of the Maze-Making and Solving Technique

Patients were prescribed aspirin, 100 mg, and clopidogrel, 75 mg, at least 7 days before their treatment. All treatments were performed with the patient under general anesthesia and systemic heparinization, with an activated clotting time of approximately 300–350 seconds. This technique is a combination of the double-catheter technique, the "one and a half round microcatheterization technique,"[10] and various assist techniques. Two microcatheters for aneurysms, 1 balloon catheter and 1 microcatheter for stent placement, are required. One is a microcatheter for larger diameter coils (0.0145–0.020 inches), such as Penumbra Coil 400 (Penumbra, Alameda, California) or HydroFrame 18 (Terumo, Tokyo, Japan) coils. The other is a microcatheter for traditional coils of <0.014 inches in diameter. The microcatheter for larger diameter coils is placed in the center of the aneurysm, and the other, for traditional coils, is placed along the aneurysmal wall to reach beyond the orifice (Fig 1*A*). Using balloon assistance, we inserted as many larger diameter coils as possible (Fig 1*B*). To avoid uneven filling, we inserted larger diameter coils with the movement of the microcatheter by using balloon assistance. This process yields a higher packing attenuation while forming a stable internal frame to support the aneurysm. However, this structure of the larger diameter coils still contains substantial coil-free dead space, leaving much of the aneurysmal space unembolized (Fig 1*C*).

An aneurysm containing only larger diameter coils resem-

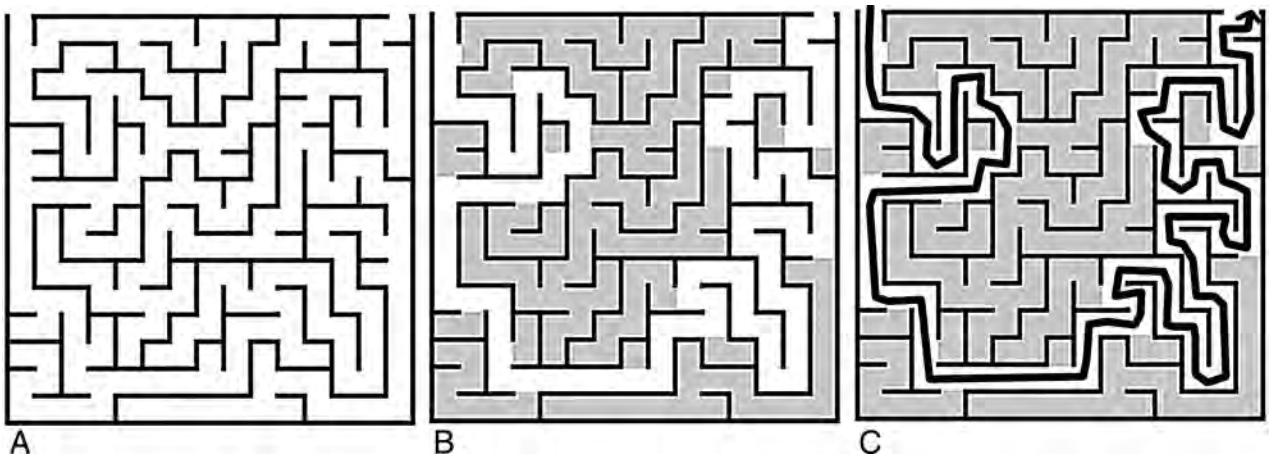

FIG 2. Maze-solving algorithms. The dead space–filling algorithm changes a complex maze (*A*) to a simple path to reach a goal (*B*). In combination with the dead space–filling algorithm, the wall-follower algorithm can fill all the spaces inside the maze.

Table 1: Patient characteristics

Case	Age/ Sex	Position[a]	Size (mm)	Vol (mL)	Symptoms	Raymond Class (Immediate)	Postoperative Course	PA		Follow-Up AG (mo)
								Larger Coils	Total	
1	77/F	L-ICA (C7)	20 × 14 × 15	1.528	None	1	Cerebral infarction (mild hemiparesis and dysesthesia), mRS 1	34.5	41.2	12
2	72/F	L-ICA (C4/5)	24 × 15 × 7	3.522	Chronic oculomotor nerve palsy	2	mRS 0	29.1	30.4	12
3	55/F	R-ICA (C4)	17 × 16 × 13	1.574	None	2	mRS 0	35.7	38.8	19
4	55/F	L-ICA (C6)	25 × 24 × 21	4.991	Progressive visual disturbance	2	Cerebral infarction (temporary dysarthria), worsening of visual disturbance, mRS 1	26.4	32.5	17
5	80/M	L-ICA (C7)	16 × 12 × 11	0.865	None	1	mRS 0	24.6	40	12
6	53/F	L-ICA (C5)	15 × 14 × 11	0.921	None	1	mRS 0	20.2	33.9	12
7	73/F	R-ICA (C7)	13 × 10 × 9	0.748	None	2	Transfusion (hemorrhage from puncture site), mRS 0	29.3	33.8	3
8	54/F	L-ICA (C4/5)	22 × 14 × 15	2.116	None	1	mRS 0	37.5	48.6	3

Note:—R indicates right; L, left; PA, packing attenuation; Vol, volume; AG, angiography.
[a] The ICA segments are defined according to the classification of Bouthillier et al.[4]

bles a maze with complex random interspaces that could be filled with smaller and softer coils. A maze-solving algorithm was applied to fill up the "maze" (Fig 2*A*) as much as possible. To solve the maze, we used dead space filling (Fig 2*B*) and a wall-follower (Fig 2*C*) algorithm. Leaving the microcatheter for traditional coils in place, we exchanged the balloon catheter with a microcatheter for stent placement and then positioned a stent to cover the aneurysm neck. Stent stabilization contributes to the controlled movement of the other microcatheter left inside the aneurysm. As shown by a cross-section illustration (Fig 1*D*), traditional smaller coils can be inserted into the dead space between the larger diameter coils. After sufficient filling, the microcatheter is moved back along the wall of the aneurysm to fill another space left unembolized (Fig 1*E*). However, the movement of these traditional coils cannot be visualized clearly, and the second marker of the microcatheter is usually hidden inside the already packed aneurysm. Thus, the first traditional coils inserted should have infiltrating capacity and be equipped with a monopolar detachment system that can indicate detachment by sound. We usually start with ED Coil-10 Infini Extra Soft coils (Kaneka Medix, Osaka, Japan), which have both features.[11,12] These coils are very soft and have high plasticity and a stretch-resistant structure, allowing them to fit within small irregular spaces.[10] If we repeat the dead space–filling and wall-follower steps, the maze is finally "solved" to achieve the highest possible coil-packing attenuation (Fig 1*F*).

Statistical Analysis

The Fisher exact test or Student *t* test, as appropriate, was used to compare group means. The Fisher exact test was used for categoric data such as sex, location, angiographic recurrence, perioperative complications, periprocedural death, major stroke, or reintervention. The Student *t* test was used for continuous variables such as packing attenuation, maximum diameter, aneurysm volume, and number of coils. A P value $< .05$ was considered significant. The P value is expressed as 2 significant figures; if the value is $<.01$, then it is expressed as $P < .01$. All analyses were performed by using js-STAR 2012 (www.kisnet.or.jp/nappa/software/star).

RESULTS

Comparison between the Maze Group and the Conventional Group

Characteristics of Patients and Aneurysms. All 8 aneurysms treated by the maze-making and solving technique were located along the ICA. Two patients had symptoms of cranial nerve palsy due to a mass effect, one chronic and the other acute. A detailed summary of patient demographic and clinical characteristics is presented in Table 1.

Table 2: Comparison between the maze and the conventional groups

	Maze Group (n = 8)	Conventional Group (n = 30)	Conventional Group Using Intracranial Stents (n = 15)	P Value between Maze Group and Conventional Group	P Value between Maze Group and Conventional Group Using Intracranial Stents
Age	65 ± 11.5	65.4 ± 13.0	68.3 ± 13.2	.93	.56
Sex (male:female)	1:7	8:22	3:12	.29	.41
Location (ICA:others)	8:0	20:10	8:7	.064	.026[a]
Packing attenuation (%)	37.4 ± 5.9	26.2 ± 5.6	27.9 ± 4.6	<.01[a]	<.01[a]
Maximum diameter (mm)	19 ± 4.4	13.4 ± 3.8	13.9 ± 5.0	<.01[a]	.02[a]
Aneurysm volume (mL)	2.03 ± 1.40	1.09 ± 1.52	1.38 ± 2.12	.13	.41
No. of coils	33.3 ± 16.1	15.5 ± 10.1	18.7 ± 12.4	.017[a]	.047[a]
Angiographic recurrence	0	11	3	.036[a]	.26
Perioperative complications	3	2	5	.31	.34
Periprocedural death or major stroke	0	5	3	.28	.26
Reintervention	0	4	2	.34	.41

[a] Significant P value.

The conventional group included 30 patients, 15 treated by balloon-assisted coil embolization and the remaining 15, by stent-assisted coil embolization. Mean age did not differ between maze and conventional groups (65 ± 11.5 years versus 65.4 ± 13.0 years), though the conventional group included more men (12.5% versus 26.7%) and patients with aneurysms outside the ICA (0% versus 33.3%). Mean maximum aneurysm diameter of the maze group was significantly larger than that of the conventional group (19 ± 4.4 mm versus 13.4 ± 3.8 mm) (Table 2).

Clinical Outcomes. In the maze group, perioperative complications occurred in 3 cases (37.5%), including 1 case of cerebral infarction with minor hemiparesis and dysesthesia (case 1), 1 case of cerebral infarction with dysarthria and worsening of visual symptoms due to an increased mass effect (case 4), and 1 case requiring blood transfusion due to hemorrhage at the puncture site (case 7). By 1 month postsurgery, most neurologic symptoms had improved, with the remaining sequelae including minor dysesthesia (case 1, mRS 1) and slightly worsened visual symptoms (case 4, mRS 1). All patients were able to resume their previous lives (mRS 0 or 1). No patient showed chronic neurologic deterioration.

In the conventional group, perioperative complications occurred in 12 patients (40%), including 6 cases of cerebral infarction, 1 case of cerebral infarction and subarachnoid hemorrhage, 2 cases of subarachnoid hemorrhage, 1 case of massive hematoma at the puncture site, 1 case of progressive dementia, and 1 case of delayed allergic vasculitis against platinum coils. Four cases showed serious perioperative complications, including 2 deaths due to immediate postoperative subarachnoid hemorrhage and massive cerebral infarction.

Angiographic Outcomes. Four "maze" treatments resulted in complete obliteration of the aneurysm (Raymond class 1), and 4 patients were left with a residual neck (Raymond class 2) as revealed by angiograms obtained immediately after surgery. The mean total number of coils inserted was 33.3 ± 16.1. The mean packing attenuation after the insertion of the larger diameter coils was 29.7 ± 5.9%, and the mean total packing attenuation following insertion of the smaller coils was 37.4 ± 5.9%. Angiographic follow-up at 11.3 ± 5.4 months after the operation revealed that the aneurysms were well-secured with no recurrences.

In the conventional group, mean packing attenuation was 26.2 ± 5.6% and the mean number of coils inserted was 15.5 ± 10.1. Treatment resulted in complete obliteration of the aneurysm (class 1) in 17 cases, a residual neck (class 2) in 10 cases, and residual aneurysm (class 3) in 3 cases as revealed by immediate postsurgical angiography. Of the remaining 28 patients, excluding 2 deaths, from the group of 30 patients, angiographic recurrence was observed in 11 (39.3%) at 5.2 ± 3.2 months and reintervention was performed in 4 patients (14.3%).

Although the mean maximum aneurysm diameter and volume were smaller in the conventional group ($P < .01$ and $P = .13$, respectively), we achieved significantly higher packing attenuation in the maze group ($P < .01$). While there was no significant difference in the rate of reintervention ($P = .35$), there was a significantly lower rate of recurrence in the maze group as revealed by angiography ($P = .036$).

Comparison between the Maze Group and the Conventional Group Using Intracranial Stents

Because the conventional group included 15 cases of coil embolization that were not assisted by a stent, we compared the results between the maze group and the conventional group for cases using intracranial stents ($n = 15$, Table 2). Mean age (65 ± 11.5 years in the maze group versus 68.3 ± 13.2 years in the conventional group using intracranial stents) and sex ratio (male/female = 1:7 versus 3:12) did not differ between the groups, though the conventional group included significantly more patients with aneurysms outside the ICA (0% versus 46.7%, $P = .026$) than the maze group. Packing attenuation (37.4 ± 5.9% versus 27.9 ± 4.6%, $P < .01$), maximum diameter (19 ± 4.4 mm versus 13.9 ± 5.0 mm, $P = .02$), and number of coils (33.3 ± 16.1 versus 18.7 ± 12.4, $P = .047$) were significantly larger in the maze group than in the conventional group using intracranial stents. The aneurysm volume (2.03 ± 1.40 mL versus 1.38 ± 2.12 mL) and the rates of perioperative complications (37.5% versus 33.3%), periprocedural death or major stroke (0% versus 20%), and reintervention (0% versus 13.3%) did not differ between the groups. Angiographic recurrence (0% versus 20%) was more common in the conventional group using intracranial stents, but this difference was not significant ($P = .26$).

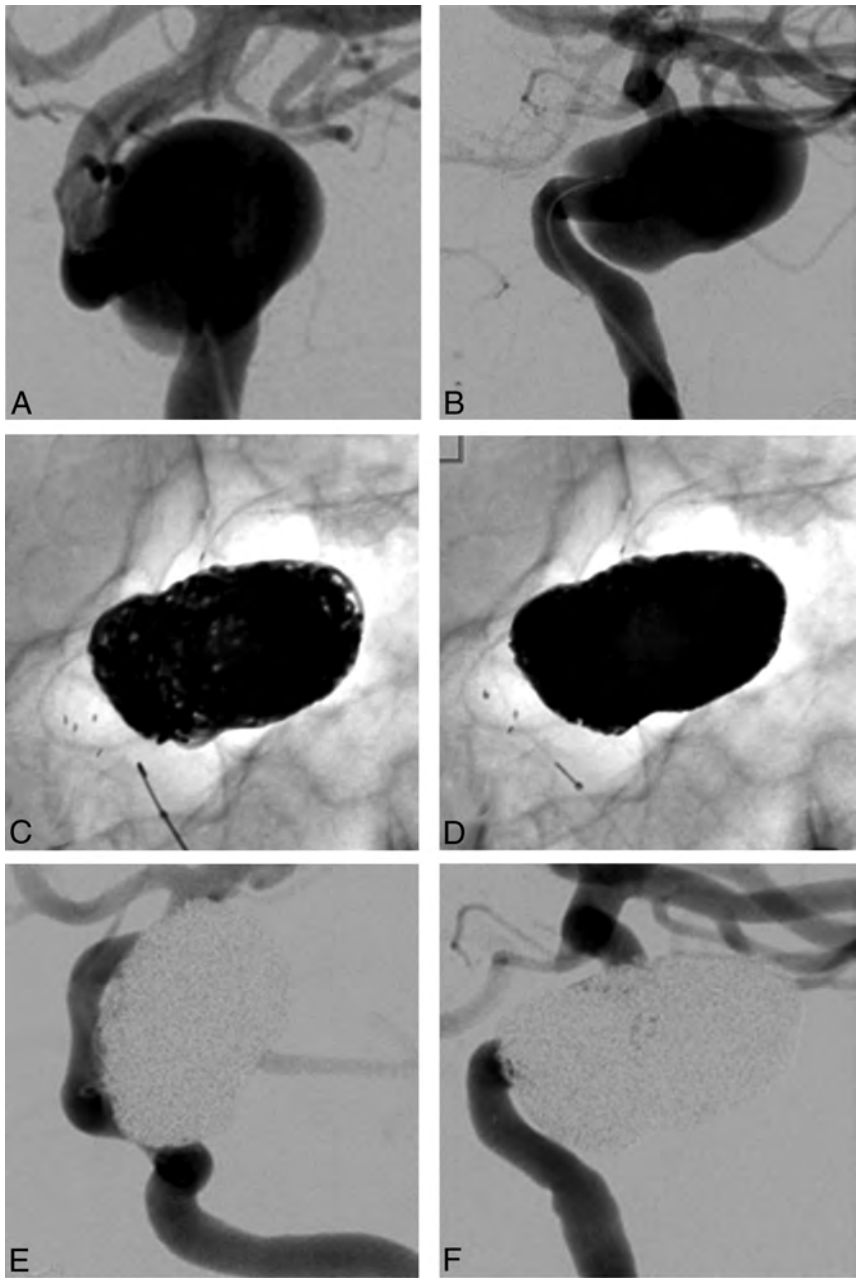

FIG 3. Representative case. Cerebral angiography reveals a left internal carotid artery large aneurysm in anteroposterior (*A*) and lateral (*B*) views. The Penumbra Coil 400 makes a maze with random interspaces between the coils (*C*), which is solved by the addition of traditional coils (*D*). Postoperative cerebral angiography reveals complete obliteration in anteroposterior (*E*) and lateral (*F*) views.

Representative Case

A large aneurysm (maximum diameter, 22 mm) was found along the left ICA (Fig 3*A*, -*B*) in a 54-year-old woman during examination for head injury. After thorough discussion, she opted for surgical intervention. After a 14-day treatment with aspirin, 100 mg, and clopidogrel, 75 mg, an 8F sheath was placed in her right femoral artery under general anesthesia and injected with heparin to reach >300-seconds activated clotting time. An 8F guiding catheter was advanced in the left ICA, and a 15-mm balloon catheter was positioned to cover the neck of the aneurysm. A PX Slim Delivery Microcatheter (45° shape; Penumbra) was placed in the center of the aneurysm, and the other microcatheter for traditional coils was positioned to reach beyond the orifice and follow the aneurysm wall. Using the balloon-assisted technique, we inserted 11 Penumbra Coil 400 coils, resulting in a packing attenuation of 37.5%, and the PX Slim microcatheter was retracted from the aneurysm into the ICA (Fig 3*C*). To stabilize the other microcatheter still inside the aneurysm, we placed a 20-mm stent over the orifice. From the other microcatheter inside the aneurysm, 26 ED Coil-10 Infini Extra Soft coils were inserted until the second marker was visible again on angiography. An additional 9 traditional coils were added (Fig 3*D*) to reach a packing attenuation of 48.6% and complete aneurysm obliteration (Raymond class 1) as revealed by angiography (Fig 3*E*, -*F*). She returned to her previous life without any complications. Angiographic findings at 3 months and MRA at 6 months postsurgery showed no recurrence.

DISCUSSION

The maze-making and solving technique enabled a higher coil-packing attenuation in large and giant aneurysms than that achieved by conventional balloon- or stent-assisted coil placement, possibly accounting for the significantly lower angiographic recurrence rate.

The natural course of an unruptured cerebral aneurysm is influenced by size,[13,14] and larger cerebral aneurysms have a poor prognosis, with a high risk of subarachnoid hemorrhage or progressive symptoms due to a mass effect.[15] In addition, large and giant aneurysms often have thicker atheromatous walls that prevent simple neck clipping.[16] Several treatment strategies, such as parent vessel occlusion, selective aneurysmal occlusion, and application of a flow-diverting stent, have been used for the treatment of large and giant aneurysms. In some cases, parent vessel occlusion may be the best choice. However, de novo aneurysm formation has been reported after carotid artery occlusion.[17] When the patient cannot tolerate parent vessel occlusion, bypass surgery should be performed. However, bypass surgery requires exceptional surgical skills, and the incidence of operative complications resulting in neurologic deficits or death was reported to be as high as 13%.[18]

Almost all previous studies of selective coiling of large and giant aneurysms have reported some reopening due to low packing attenuation.[15] Selective occlusion with Onyx (Covidien, Ir-

vine, California) has also been used[19,20]; however, the outcomes were no better than selective coil occlusion, and the immediate and delayed complication rate was considered higher than that in the present study.

In the case series, a flow-diverting stent was not an option because our government has not yet authorized this treatment. Flow-diverting stent placement is a promising therapy for challenging intracranial aneurysms, including large and giant aneurysms. However, permanent morbidity and mortality were reported to be 5.6%–10.8%.[6,21] Moreover, flow-diverting stent surgery for posterior circulation aneurysms resulted in more patients with ischemia due to perforator occlusion[22]; therefore, a more effective strategy is required, particularly for large and giant posterior circulation aneurysms.

Some practitioners have reported that moderate packing attenuation (12%–22%) should be sufficient, but this may apply only to stent-assisted coil embolization of smaller aneurysms.[23] Most aneurysms packed to approximately ≥25% remain stable at follow-up.[24] Initial studies of Penumbra Coil 400 insertion into smaller aneurysms reported packing attenuation as high as 33.7%[25] and 36.8%.[26] Our procedure also attained such high attenuation (37.4%) but on large and giant aneurysms for which higher packing attenuation has proved difficult to achieve. When we used the maze-making and solving technique, higher coil-packing attenuation was facilitated by the addition of traditional smaller coils (7.7%), following the insertion of larger diameter coils (29.7%).

Of the 8 patients treated by this new technique, 3 showed postoperative morbidity. However, all cases were minor, with 1 at mRS 0 and 2 at mRS 1. Moreover, no deaths were observed. After the augmentation of intraoperative anticoagulation therapy, we did not encounter further ischemic complications. One patient had postoperative worsening of optic nerve dysfunction, which resolved only slightly within 6 months. A previous study found that the selective coiling of unruptured large and giant carotid artery aneurysms presenting with cranial nerve palsy was as effective as parent artery occlusion and was associated with a greater chance of symptom improvement.[27]

The basic principle behind the maze-making and solving technique is to first construct a complex framework of larger diameter coils inside the aneurysm and then to fill the unembolized spaces within this large coil framework with traditional (smaller) coils by using a second microcatheter left inside the aneurysm. Although larger diameter coils occupy more volume than traditional coils, they also leave larger interspaces. However, larger diameter coils support the aneurysm; such a structure is less likely to collapse. While a new microcatheter cannot enter the aneurysm, the microcatheter already inside is unlikely to dislodge due to support by the coils and the subsequently introduced stent. The double-microcatheter technique is used to produce satisfactory occlusion by bracing 2 coils within the aneurysm,[28] but that does not discriminate the role of each microcatheter. The "one and a half round microcatheterization technique"[10] is used to position the second microcatheter for maze-solving. This technique alone may produce a high packing attenuation. However, controlling the movement of the microcatheter can be difficult, and the microcatheter may easily fall to the edge of the stent. If this technique is used after forming the maze, the complexity of the structure will prevent unnecessary movement of the second microcatheter and drop-out from the aneurysm. Solving this large coil maze by wall-following and dead space–filling algorithms allowed higher coil-packing attenuation. The order of insertion is important. If traditional coils were used for making the maze, they could not provide enough volume, whereas larger diameter coils cannot fill the interspaces left by smaller coils. Thus, the specific combination of large- and smaller-diameter coils is necessary for the success of this technique.

A long-term follow-up study indicated that using stents in endovascular treatments provided high rates of complete occlusion with low rates of recurrence[29]; therefore, the positive results observed in the maze group in the present study may be due to intracranial stents. We also analyzed the maze and the conventional groups using intracranial stents separately. Although angiographic recurrence rates did not reach significant differences, the maximum diameter and packing attenuation were significantly larger in the maze group than in the conventional group using intracranial stents. This outcome indicates that the contribution of stents is apparent but partial. In a particularly large or giant aneurysm, the maze-making and solving technique can be a better choice to reach a higher packing attenuation than with intracranial stents alone.

The major limitations of our study are the short follow-up period (11.3 ± 5.4 months) and small number of patients. However, recurrence in the conventional group occurred at 5.2 ± 3.2 months postsurgery; therefore, we monitored the patients in the maze group beyond the period of highest recurrence risk. In addition, because ED coils are for sale only in Japan, the selection of the smaller coils for the second microcatheter may be more difficult in other countries. This technique also requires more coils and thus increases the cost, but this extra surgical cost is justified if recurrence is reduced. Our technique may be applicable to aneurysms in other regions, such as the treatment of posterior circulation aneurysms. However, our cases included only anterior circulation aneurysms.

CONCLUSIONS

By the maze-making and solving technique, we attained high coil-packing attenuation for coil embolization of large and giant aneurysms. Moreover, we observed low recurrence rates compared with the traditional coil embolization of large or giant aneurysm without any significant increases in perioperative complications. This is a promising treatment method and may result in longer stability to avoid further intervention.

ACKNOWLEDGMENTS

We express our gratitude to Drs Takuya Okata, Kazutaka Sonoda, and Junpei Koge for useful and constructive comments and suggestions.

Disclosures: Tsuyoshi Ohta—*UNRELATED*: *Consultancy*: Terumo, Kaneka, *Comments*: None exceeds the criteria for self-reported conflict of interest disclosure according to the Ethical Guidelines for Clinical Research (Ministry of Labor, Health, and Welfare of Japan); *Payment for Lectures (including service on Speakers Bureaus)*: Stryker, Kaneka, Cordis, Mochida, Otsuka, *Comments*: None exceeds the criteria for self-reported conflict of interest disclosure according to the Ethical Guidelines for Clinical Research (Ministry of Labor, Health, and Welfare of Japan).

Ichiro Nakahara—*UNRELATED: Consultancy*: Terumo, Covidien, Johnson & Johnson, Kaneka, *Comments*: Consultant fee was paid to me by each neurointerventional device company. Each fee was less than $10,000 per year and did not meet the criteria for declaration of conflict of interest by the Japanese Society of Neurosurgery and Japanese Society for Neuroendovascular Therapy. Hidehisa Nishi—*UNRELATED: Payment for Lectures (including service on Speakers Bureaus)*: Boehringer Ingelheim, *Comments*: None exceeds the criteria for self-reported conflict of interest disclosure according to the Ethical Guidelines for Clinical Research (Ministry of Labor, Health, and Welfare of Japan).

REFERENCES

1. McDougall CG, Johnston SC, Gholkar A, et al. **Bioactive versus bare platinum coils in the treatment of intracranial aneurysms: the MAPS (Matrix and Platinum Science) trial.** *AJNR Am J Neuroradiol* 2014;35:935–42
2. Raymond J, Klink R, Chagnon M, et al. **Patients prone to recurrence after endovascular treatment: periprocedural results of the PRET randomized trial on large and recurrent aneurysms.** *AJNR Am J Neuroradiol* 2014;35:1667–76
3. Choi IS, David C. **Giant intracranial aneurysms: development, clinical presentation and treatment.** *Eur J Radiol* 2003;46:178–94
4. Bouthillier A, van Loveren HR, Keller JT. **Segments of the internal carotid artery: a new classification.** *Neurosurgery* 1996;38:425–32; discussion 432–33
5. Roy D, Milot G, Raymond J. **Endovascular treatment of unruptured aneurysms.** *Stroke* 2001;32:1998–2004
6. Becske T, Kallmes DF, Saatci I, et al. **Pipeline for uncoilable or failed aneurysms: results from a multicenter clinical trial.** *Radiology* 2013;267:858–68
7. Bendok BR, Parkinson RJ, Hage ZA, et al. **The effect of vascular reconstruction device-assisted coiling on packing density, effective neck coverage, and angiographic outcome: an in vitro study.** *Neurosurgery* 2007;61:835–40; discussion 840–41
8. Speirs JW, Burke TH, Lee SY, et al. **The next generation HydroCoil: initial clinical experience with the HydroFill embolic coil.** *J Neurointerv Surg* 2013;5(suppl 3):iii72–75
9. Banks JL, Marotta CA. **Outcomes validity and reliability of the modified Rankin Scale: implications for stroke clinical trials—a literature review and synthesis.** *Stroke* 2007;38:1091–96
10. Miyachi S, Matsubara N, Izumi T, et al. **The 'one and a half round microcatheterization technique' for stent-assisted coil embolization of intracranial aneurysm: technical case series.** *J Neurointerv Surg* 2014;6:357–62
11. Harada K, Morioka J. **Initial experience with an extremely soft bare platinum coil, ED coil-10 Extra Soft, for endovascular treatment of cerebral aneurysms.** *J Neurointerv Surg* 2013;5:577–81
12. Fukuda H, Miyake K, Kunieda T, et al. **Endovascular treatment of sphenoid wing dural arteriovenous fistula with pure cortical venous drainage.** *J Stroke Cerebrovasc Dis* 2014;23:1730–35
13. Morita A, Kirino T, Hashi K, et al, for the UCAS Japan Investigators. **The natural course of unruptured cerebral aneurysms in a Japanese cohort.** *N Engl J Med* 2012;366:2474–82
14. Wiebers DO, Whisnant JP, Huston J 3rd, et al. **Unruptured intracranial aneurysms: natural history, clinical outcome, and risks of surgical and endovascular treatment.** *Lancet* 2003;362:103–10
15. van Rooij WJ, Sluzewski M. **Endovascular treatment of large and giant aneurysms.** *AJNR Am J Neuroradiol* 2009;30:12–18
16. Nussbaum ES, Nussbaum LA. **A novel aneurysm clip design for atheromatous, thrombotic, or previously coiled lesions: preliminary experience with the "compression clip" in 6 cases.** *Neurosurgery* 2010;67:333–41
17. Arambepola PK, McEvoy SD, Bulsara KR. **De novo aneurysm formation after carotid artery occlusion for cerebral aneurysms.** *Skull Base* 2010;20:405–08
18. Brilstra EH, Rinkel GJ, Klijn CJ, et al. **Excimer laser-assisted bypass in aneurysm treatment: short-term outcomes.** *J Neurosurg* 2002;97:1029–35
19. Molyneux AJ, Cekirge S, Saatci I, et al. **Cerebral Aneurysm Multicenter European Onyx (CAMEO) trial: results of a prospective observational study in 20 European centers.** *AJNR Am J Neuroradiol* 2004;25:39–51
20. Weber W, Siekmann R, Kis B, et al. **Treatment and follow-up of 22 unruptured wide-necked intracranial aneurysms of the internal carotid artery with Onyx HD 500.** *AJNR Am J Neuroradiol* 2005;26:1909–15
21. Berge J, Biondi A, Machi P, et al. **Flow-diverter Silk stent for the treatment of intracranial aneurysms: 1-year follow-up in a multicenter study.** *AJNR Am J Neuroradiol* 2012;33:1150–55
22. Brinjikji W, Murad MH, Lanzino G, et al. **Endovascular treatment of intracranial aneurysms with flow diverters: a meta-analysis.** *Stroke* 2013;44:442–47
23. Chalouhi N, Dumont AS, Hasan D, et al. **Is packing density important in stent-assisted coiling?** *Neurosurgery* 2012;71:381–86; discussion 386–87
24. Sluzewski M, van Rooij WJ, Slob MJ, et al. **Relation between aneurysm volume, packing, and compaction in 145 cerebral aneurysms treated with coils.** *Radiology* 2004;231:653–58
25. Milburn J, Pansara AL, Vidal G, et al. **Initial experience using the Penumbra Coil 400: comparison of aneurysm packing, cost effectiveness, and coil efficiency.** *J Neurointerv Surg* 2014;6:121–24
26. Mascitelli JR, Polykarpou MF, Patel AA, et al. **Initial experience with Penumbra Coil 400 versus standard coils in embolization of cerebral aneurysms: a retrospective review.** *J Neurointerv Surg* 2013;5:573–76
27. van Rooij WJ, Sluzewski M. **Unruptured large and giant carotid artery aneurysms presenting with cranial nerve palsy: comparison of clinical recovery after selective aneurysm coiling and therapeutic carotid artery occlusion.** *AJNR Am J Neuroradiol* 2008;29:997–1002
28. Baxter BW, Rosso D, Lownie SP. **Double microcatheter techniques for detachable coil treatment of large, wide-necked intracranial aneurysms.** *AJNR Am J Neuroradiol* 1998;19:1176–78
29. Geyik S, Yavuz K, Yurttutan N, et al. **Stent-assisted coiling in endovascular treatment of 500 consecutive cerebral aneurysms with long-term follow-up.** *AJNR Am J Neuroradiol* 2013;34:2157–62

Carotid Plaque Characterization Using 3D T1-Weighted MR Imaging with Histopathologic Validation: A Comparison with 2D Technique

S. Narumi, M. Sasaki, T. Natori, M. Yamaguchi Oura, K. Ogasawara, M. Kobayashi, Y. Sato, Y. Ogasawara, J. Hitomi, and Y. Terayama

ABSTRACT

BACKGROUND AND PURPOSE: 3D FSE T1WI has recently been used for carotid plaque imaging, given the potential advantages in contrast and spatial resolutions. However, its diagnostic performance remains unclear. Hence, we compared the ability of this technique to readily assess plaque characteristics with that of conventional images and validated the results with histologic classification.

MATERIALS AND METHODS: We prospectively examined 34 patients with carotid stenosis who underwent carotid endarterectomy by using 1.5T scanners and obtained 3D-FSE T1WI and 2D spin-echo T1WI scans. After generating reformatted images obtained from the 3D-FSE T1-weighted images, we calculated the contrast ratios for the plaques and the adjacent muscles and compared these findings with the pathologic classifications.

RESULTS: Carotid plaques were histologically classified as types VII, VIII, IV–V, or VI. With 3D-FSE T1WI, the range of contrast ratios for each classification was the following: 0.94–0.97 (median, 0.95), 0.95–1.29 (median, 1.10), 1.33–1.54 (median, 1.42), and 1.53–2.12 (median, 1.80), respectively. With 2D imaging, the range of contrast ratios for each classification was the following: 0.79–1.02 (median, 0.90), 0.88–1.19 (median, 1.01), 1.17–1.46 (median, 1.23), and 1.55–2.51 (median, 2.07), respectively. Results were significantly different among the 4 groups ($P < .001$). Sensitivity and specificity for discriminating vulnerable plaques (IV–VI) from stable plaques (VII, VIII) were both 100% for the 3D technique and 100% and 91%, respectively, for the 2D technique.

CONCLUSIONS: 3D-FSE T1WI accurately characterizes intraplaque components of the carotid artery, with excellent sensitivity and specificity compared with those of 2D-T1WI.

ABBREVIATIONS: CR = contrast ratio; SE = spin-echo

Cervical carotid stenosis is an important cause of cerebral infarction and transient ischemic attack. Carotid endarterectomy or carotid artery stent placement is performed to prevent future stroke events but may also cause embolic complications during the surgery, especially if the plaque contains substantial vulnerable components such as intraplaque hemorrhage or lipid.[1,2] Therefore, establishing a method for characterizing intraplaque components is an important prerequisite for predicting perisurgical complications.

Several modalities have been used for plaque characterization, including ultrasonography and MR imaging. Although ultrasonography is widely used, the interpretation is typically subjective and may be impossible in the presence of extensive calcification or a high-positioned carotid bifurcation. Although gray-scale median and integrated backscatter have been introduced as quantitative metrics, previous reports suggest that they are unsuitable for evaluating intraplaque components.[3,4] MR plaque imaging is another popular method for assessing plaque characteristics. Although various imaging techniques have been used, a 2D spin-echo (SE) T1WI technique with appropriate scanning parameters has been reported to accurately quantify intraplaque components, compared with other conventional techniques.[5-8] Recently, a 3D T1WI FSE technique has been adopted for this purpose because it can minimize partial volume effects and motion artifacts, as well as enhance black-blood effects, while maintaining T1WI contrast. However, whether the 3D-FSE technique can more accurately discriminate among intraplaque components than the more conventional techniques, such as 2D-SE T1WI,

Received August 4, 2014; accepted after revision October 2.

From the Departments of Neurology and Gerontology (S.N., T.N., M.Y.O., Y.T.), Neurosurgery (K.O., M.K., Y.S., Y.O.), and Anatomy (J.H.), and Institute for Biomedical Sciences (M.S.), Iwate Medical University, Morioka, Japan.

This work was partly supported by Grants-in-Aid for Strategic Medical Science Research (S1491001, 2014–2018) and for Scientific Research (25861122) from the Ministry of Education, Culture, Sports, Science, and Technology of Japan.

Please address correspondence to Shinsuke Narumi, MD, PhD, Department of Neurology, Iwate Medical University, 19-1 Uchimaru, Morioka 020-8505, Japan; e-mail: snarumi@iwate-med.ac.jp

http://dx.doi.org/10.3174/ajnr.A4197

Table 1: Histologic classification of plaque specimens excised by carotid endarterectomy

Type[a]	Description	No. (%)	[Symptomatic/Asymptomatic]
I–II	Near-normal wall thickness without calcification	0 (0%)	
III	Diffuse intimal thickening or small eccentric plaque without calcification	0 (0%)	
IV–V	Lipid-rich or necrotic core surrounded by fibrous tissue with possible calcification	6 (19%)	[5/1]
VI	Complex plaque with possible surface defect, hemorrhage, or thrombus	14 (45%)	[14/0]
VII	Calcified lesion	2 (7%)	[1/1]
VIII	Fibrotic plaque without a lipid core and with possible small calcifications	9 (29%)	[5/4]

[a] Modified American Heart Association classification.

remains unknown. Hence, in the present study, we investigated whether the diagnostic accuracy of 3D-FSE T1WI, in terms of carotid plaque characterization, is comparable with that of 2D-SE T1WI, by using pathologic specimens excised from carotid endarterectomy as our validation standards.

MATERIALS AND METHODS

Patients

From July 2012 to December 2013, we prospectively examined 34 consecutive patients (age range, 58–79 years [mean, 70.4 years]; 31 men and 3 women) with substantial stenosis of the cervical internal carotid artery, all of whom underwent carotid endarterectomy. Of these patients, 26 had symptomatic stenosis of 50%–95%, according to the method of the North American Symptomatic Carotid Endarterectomy Trial,[9] and 8 had asymptomatic stenosis of 70%–90%. The clinical profiles of the patients included hypertension ($n = 28$), hyperlipidemia ($n = 27$), and diabetes mellitus ($n = 11$). The institutional review board approved the study protocol, and written informed consent was obtained from all patients.

Imaging Protocol

Presurgery sagittal 3D-T1WI of the bilateral carotid bifurcation was performed by using a 1.5T MR imaging scanner (Signa HDxt; GE Healthcare, Milwaukee, Wisconsin) with an 8-channel neurovascular coil. The pulse sequence parameters were as follows: flow-sensitized 3D-FSE with variable flip angles; TR/TE, 500/18.3 ms; echo-train length, 24; b-value of the flow-sensitized gradients along 3 axes, 2.2 s/mm^2; FOV, 25 × 19 cm^2; matrix size, 512 × 512 (after zero-fill interpolation); section interval, 0.5 mm (after zero-fill interpolation); partitions, 248; voxel size, 0.5 × 0.5 × 0.5 mm^3; parallel imaging factor, 2; NEX, 1; fat suppression, chemical shift selective suppression; and acquisition time, 3 minutes 54 seconds. Motion-sensitized gradients of 2.2 s/mm^2 were used as the black-blood technique.

In addition, axial 2D-T1WI of the affected carotid bifurcation was performed by using a 1.5T MR imaging scanner (Echelon Vega; Hitachi Medical Corporation, Tokyo, Japan) with an 8-channel neurovascular coil. The section direction was carefully set in a plane perpendicular to the long axis of the carotid bifurcation by using sagittal 2D phase-contrast MR angiographic imaging. The pulse sequence parameters were as follows: conventional SE with a radial *k*-space acquisition technique with self-navigation, which is similar to the periodically rotated overlapping parallel lines with enhanced reconstruction method[10]; TR/TE, 500/12 ms; FOV, 18 cm; matrix size, 512 × 512 (after zero-fill interpolation); NEX, 2; section thickness, 4.0 mm with intersection gaps of 1.0 mm; number of sections, 9; fat suppression, chemical shift selective suppression; and acquisition time, 6 minutes 46 seconds. Nonselective saturation pulses were used as the black-blood technique.

Histologic Preparation

Specimens were excised en bloc from the affected carotid arteries and submitted for histologic evaluation. The specimens were fixed in formaldehyde, and transverse sections of the carotid bifurcations were carefully cut to correspond in direction and position to the 2D-MR images. During histologic preparation, hematoxylin-eosin, Masson trichrome, and anti-Glycophorin-A stains were applied to paraffin-embedded, 7-μm-thick sections. The sections of carotid plaque were classified into 6 types, according to the modified American Heart Association classification (Table 1).[11]

Data Processing and Statistical Analyses

After using the 3D-FSE images to generate reformatted axial images that corresponded to the 2D-SE images, we measured the signal intensity of the carotid plaque and the adjacent sternomastoid muscle by using the image with the largest plaque size. The images were randomized, and a blinded author (S.N.) manually traced the plaque and muscle 3 times, by using the polygon cursor of a free software package (zioTerm 2009; Ziosoft, Tokyo, Japan). The resulting signal intensity values were averaged, and the contrast ratio (CR) was calculated by dividing the average signal intensity of the plaque by that of the muscle.

Differences in the CRs of plaques among the various histologic types were examined by using the Kruskal-Wallis test, followed by the post hoc Mann-Whitney test. Differences between the 3D-FSE and 2D-SE techniques and those between the asymptomatic and symptomatic patients were examined by using the Wilcoxon signed rank test and the Mann-Whitney test, respectively. In addition, receiver operating characteristic curve analyses were performed to evaluate the sensitivity and specificity of the ability of the techniques to differentiate plaques containing substantial vulnerable components from those containing stable components. Vulnerable components were defined as lipid, necrosis, and/or hemorrhage (IV–V, VI), while stable components were defined as calcification and fibrous tissue (I–II, III, VII, VIII). Receiver operating characteristic curve analysis was also performed to evaluate the abilities of the techniques to differentiate hemorrhagic complex plaques (VI) from other plaques. Cutoff values were determined by using the Youden index, and differences in the areas under the receiver operating characteristic curves were examined by using the DeLong test. The intraclass correlation coefficient was used to evaluate intraoperator agreements for the manual measurements. The α level used was .05.

Table 2: Contrast ratios of various carotid plaques on T1-weighted images using 3D FSE and 2D-SE techniques[a]

	Plaque Type (Modified AHA Classification)				
	VII (*n* = 2)	VIII (*n* = 9)	IV–V (*n* = 6)	VI (*n* = 14)	*P* Value[b]
3D-FSE	0.94–0.97 (0.95)	0.95–1.29 (1.10)	1.33–1.54 (1.42)	1.53–2.12 (1.80)	<.001
2D-SE	0.79–1.02 (0.90)	0.88–1.19 (1.01)	1.17–1.46 (1.23)	1.55–2.51 (2.07)	<.001
P value[c]	.655	.139	.028	.013	

Note:—AHA indicates American Heart Association.
[a] Contrast ratios are presented as range (median).
[b] Kruskal-Wallis test.
[c] Wilcoxon signed rank test.

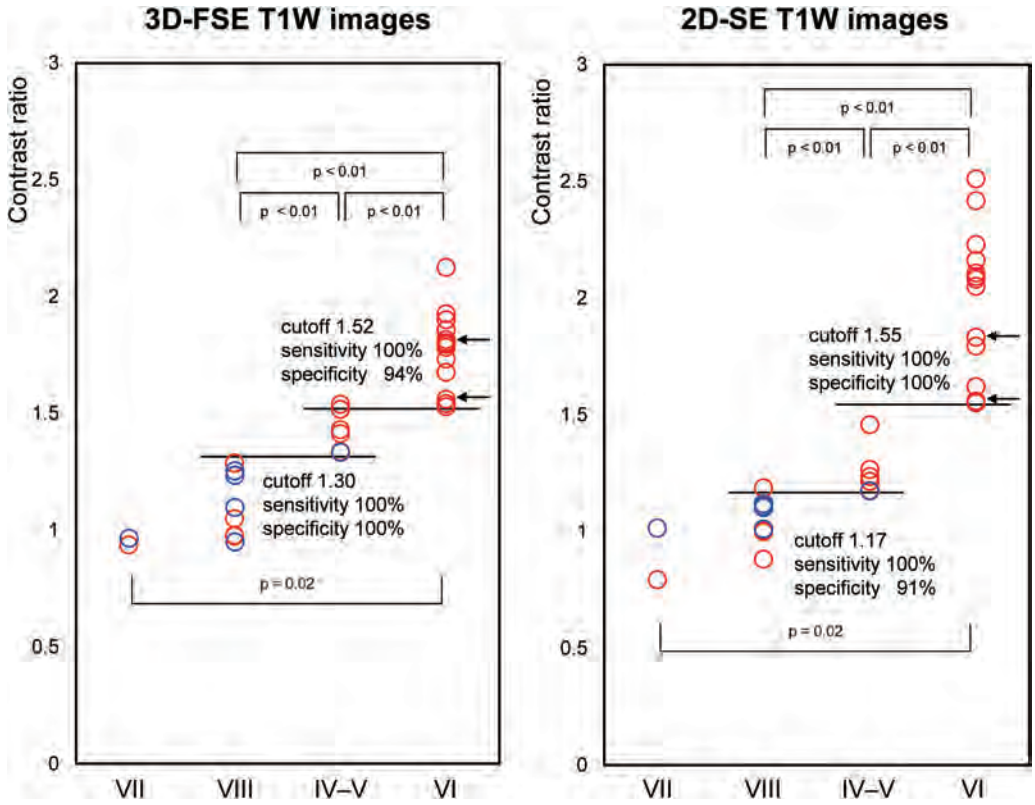

FIG 1. Contrast ratios of carotid plaques with various compositions, by using 3D-FSE and 2D-SE T1WI. Contrast ratios of type VI plaques (characterized according to the modified American Heart Association criteria) are significantly higher than those of other plaque types, by using both 3D-FSE and 2D-SE images. In addition, CRs of type IV–V plaques are significantly higher than those of types VII and VIII and are significantly higher on 3D-FSE images than on 2D-FSE images. Sensitivity and specificity for discriminating between vulnerable plaques (IV–V and VI) and stable plaques (VII and VIII) were both 100%, by using the 3D-FSE images, and 100% and 91%, respectively, by using the 2D-SE images. *Red circles* indicate symptomatic patients; *blue circles*, asymptomatic patients; and *arrows*, patients showing ischemic events during surgery.

RESULTS

Three patients were excluded because their carotid endarterectomy was postponed for >3 months after their MR imaging examinations. The remaining 31 patients were considered eligible for further quantitative analyses. Patient characteristics are as follows: age, ranging from 58 to 79 years (mean, 70.8 years); 28 men and 3 women; and interval between MR imaging and carotid endarterectomy, ranging from 1 to 82 days (median, 28 days). The number and type of carotid plaques, as determined by histopathologic examination, are shown in Table 1. Ischemic stroke events during the surgery occurred in the 2 symptomatic patients with carotid plaque type VI.

With 3D-FSE T1WI, the CR range and median values of the plaques that were histologically confirmed as types VII, VIII, IV–V, and VI were 0.94–0.97 (0.95), 0.95–1.29 (1.10), 1.33–1.54 (1.42), and 1.53–2.12 (1.80), respectively. The CR range and median value by using 2D-SE T1WI were 0.79–1.02 (0.90), 0.88–1.19 (1.01), 1.17–1.46 (1.23), and 1.55–2.51 (2.07), respectively. These values were significantly different among the groups, by using both the 3D-FSE and 2D-SE images ($P < .001$, Kruskal-Wallis test; Table 2 and Fig 1). Among the CRs of carotid plaques with various compositions, there were significant differences among all combinations of types VIII, IV-V, and VI, which tended to show isointensity to the muscle, mild hyperintensity, and marked hyperintensity, respectively, on both the 3D-FSE and 2D-SE images ($P < .01$, post hoc Mann-Whitney test; Figs 1 and 2). The CRs of types IV–V plaques on the 3D images were significantly higher than those on the 2D images ($P = .028$, Wilcoxon signed rank test), while the CRs of the type VI plaques on the 3D images were significantly lower than those on the 2D images ($P = .013$, Wilcoxon signed rank test; Table 1). Furthermore, the CRs of the plaques in the symptomatic patients were significantly higher than those in the asymptomatic patients both on the 3D images (0.94–2.12 [median, 1.54] and 0.95–1.33 [median, 1.17], respectively; $P = .004$, Mann-Whitney test) and on the 2D images

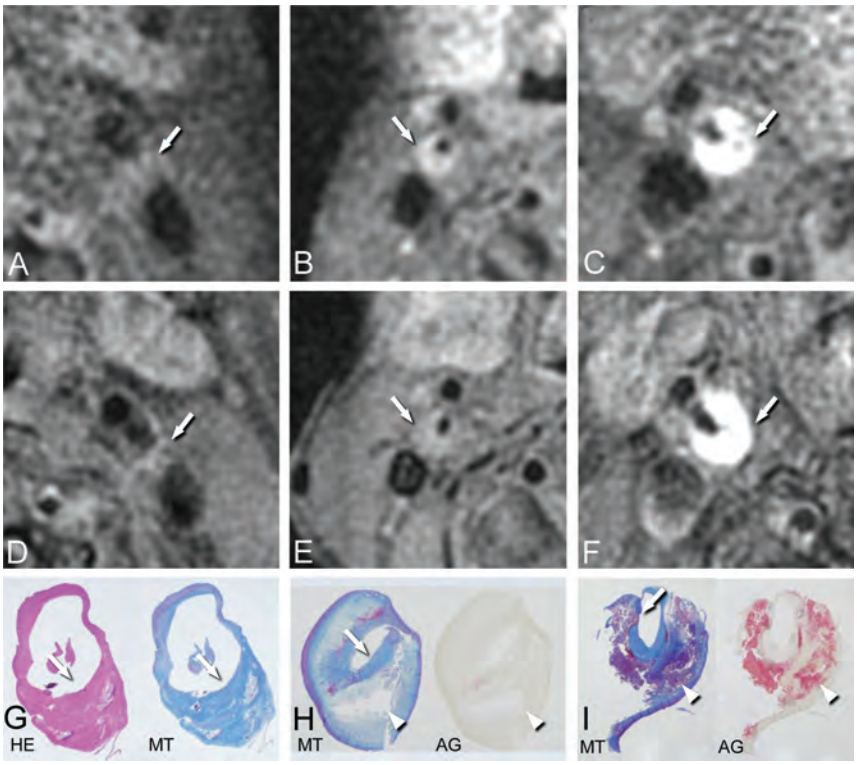

FIG 2. Imaging findings of the carotid plaques by using 3D-FSE and 2D-SE T1WI. *A–C*, 3D-FSE T1WI. *D–F*, 2D-SE T1WI. *G–I*, Histologic specimens. AG indicates anti-Glycophorin-A staining; HE, hematoxylin-eosin staining; MT, Masson trichrome staining. *G* and *H*, 2× magnification; *I*, 1.5× magnification.

A 74-year-old man with symptomatic left carotid stenosis (*A*, *D*, and *G*). The carotid plaque is isointense to the adjacent muscles on both 3D-FSE and 2D-SE T1WI (*arrows*, *A* and *D*), with CRs of 0.97 and 1.00, respectively. Histologic findings show that the plaque was primarily composed of fibrous tissue with minimal calcification, which is therefore classified as type VIII (*arrows*, *G*).

A 69-year-old man with symptomatic right carotid stenosis (*B*, *E*, and *H*). The plaque shows moderate hyperintensity on the 3D-FSE image (*arrow*, *B*) and only subtle hyperintensity on the 2D-SE image (*arrow*, *E*), with CRs of 1.52 and 1.27, respectively. Histologic findings show a lipid-rich plaque consisting of foamy cells (*arrowheads*, *H*) with a thick fibrous cap (*arrow*, *H*), which is therefore classified as types IV–V.

A 72-year-old man with symptomatic right carotid stenosis (*C*, *F*, and *I*). The plaque shows evident hyperintensity on both the 3D-FSE and 2D-SE images (*arrows*, *C* and *F*), with CRs of 1.93 and 2.23, respectively. Histologic findings show massive hemorrhage (*arrowheads*, *I*) with a partially ruptured thin fibrous cap (*arrow*, *I*), which is therefore classified as type VI.

(0.79–2.51 [median, 1.56] and 1.01–1.17 [median, 1.11], respectively; $P = .023$, Mann-Whitney test).

Receiver operating characteristic analyses revealed that the areas under the receiver operating characteristic curves for the 3D-FSE images were 1.000 (95% CI, 0.888–1.000), and the areas under the receiver operating characteristic curves for the 2D-SE images were 0.991 (95% CI, 0.871–1.000), indicating that both could discriminate between vulnerable plaques (types IV–V and VI) and stable plaques (types VII and VIII). No significant difference was detected between the 2 techniques ($P = .41$, DeLong test). The sensitivities and specificities were both 100% for the 3D images (cutoff value, 1.30) and 100% and 91%, respectively, for the 2D images (cutoff value, 1.17; Fig 1). Furthermore, in discriminating complex plaques (type VI) from other plaques, the areas under the receiver operating characteristic curves for the 3D and 2D images were 0.996 (95% CI, 0.880–1.000) and 1.00 (95% CI, 0.888–1.000), respectively, with no significant difference between the 2 techniques ($P = .48$, DeLong test). The sensitivities and specificities were 100% and 94%, respectively, for the 3D images (cutoff value, 1.52), and 100% sensitivity and specificity was determined for the 2D images (cutoff value, 1.55; Fig 1).

The intraclass correlation coefficient value for the measurements of the plaque CRs was 0.997, indicating excellent intraoperator agreements.

DISCUSSION

Unstable carotid plaques comprise lipid-rich, necrotic, and/or intraplaque hemorrhage materials, enclosed by a thin fibrous cap, which is prone to rupture and subsequently releases embolic materials into the distal blood flow. As a result, unstable plaques cause more ischemic stroke events than stable plaques, which consist mainly of fibrous tissue and/or calcification.[12,13] Unstable plaques are also thought to be one of the risk factors for embolic complications during carotid endarterectomy and carotid artery stenting.[1,2] Therefore, accurate characterization of intraplaque components can help predict stroke events and complications during surgery. In this study, we successfully demonstrated that the 3D-FSE T1WI technique can readily discriminate among histologic subtypes of carotid plaques and can differentiate unstable plaques from stable ones, with excellent sensitivity and specificity. These results were comparable with those obtained by using the 2D-SE T1WI technique.

In general, unstable carotid plaques tend to show hyperintensity on T1WI.[5,6,14-17] However, various imaging techniques have been applied to T1WI, with varying results, including conventional 2D-SE/FSE,[5,8] cardiac-gated multiple inversion-recovery black-blood 2D-FSE,[6] MPRAGE,[16,18,19] and source images of 3D time-of-flight MR angiography.[15,20,21] A recent study performing direct comparisons among these techniques found that 2D-SE imaging could more readily discriminate among fibrous, lipid-rich, necrotic, and hemorrhagic plaques because the T1 contrast can be maximized and stabilized under the appropriate scanning parameter settings.[7] In addition, the 2D-SE T1WI could accurately estimate intraplaque composition and could monitor temporal changes during medical treatment.[22,23] However, the 2D-SE technique is also prone to various technical limitations, such as substantial partial volume effects, susceptibility to motion artifacts, and prolonged acquisition time. The 3D-FSE technique has been introduced recently for plaque imaging and can theoretically overcome these limitations, while still maintaining appropriate T1 contrast.

In the present study, the 3D-FSE T1WI technique could accurately discriminate among histologically validated plaque types and could also differentiate the vulnerable plaques (types IV–V and VI) from the stable plaques (types VII and VIII) with excellent

sensitivity and specificity. In particular, the CRs of lipid-rich/necrotic plaques (types IV–V) on 3D-FSE images were significantly higher than those on 2D-SE images obtained with the identical TR. The contrast improvement of the lipid/necrotic plaques by using the 3D-FSE technique is thought to be caused by a shortened longitudinal recovery time after the last echo. This augments T1-related contrast, allowing detection of vulnerable plaques that might otherwise have been overlooked. In contrast, the CRs of hemorrhagic plaques (type VI) on 3D-FSE images were significantly lower than those on 2D-SE images, resulting in less accuracy in differentiating hemorrhagic plaques from other plaques, presumably due to the inherent T2 dependency of the 3D-FSE technique caused by its prolonged effective TE. However, this result appears to hardly affect discrimination between unstable and stable plaques because the CRs of hemorrhagic plaques remained remarkably higher than those of stable plaques.

This study includes several limitations. First, although the 3D-FSE technique provides potential advantages in terms of partial volume effects, motion artifacts, and multidirectional capability, we did not directly compare these issues between the 2 techniques because our aim was to determine whether 3D-FSE had better contrast for use in plaque characterization than 2D-SE imaging. In general, 3D techniques are suitable for assessment of carotid plaques because the carotid artery is tortuous and pulsatile and the plaques are typically small, complex in shape and composition, and elongated in the superoinferior direction. Hence, 2D imaging is not ideal for visualizing carotid plaque characteristics in detail, given their limited section direction, thickness, and coverage, as well as their susceptibility to motion artifacts. 3D imaging, including 3D-FSE T1WI, might be able to overcome these limitations. Second, we examined CRs of the plaques by using only the section with the maximum plaque size. In this study, we had to abandon the idea of evaluating the whole plaque because only a single section was available for direct comparisons among the 3D images, 2D images, and corresponding histologic sections due to partial volume effects of the 2D images and difficulties in histologic preparation for the appropriate sections. Evaluation of the entire plaque may further improve the diagnostic performance, particularly for the 3D-FSE technique. Third, we could not simultaneously obtain the 3D-FSE and 2D-SE images by using the same scanner because these advanced sequences were implemented in distinct scanners. Hence, the images used for the comparisons may not have been obtained under identical conditions, which might have affected our results, though the intervals between the scans were 2–7 days in almost all patients. Fourth, we did not perform automated analyses that we reported previously,[23] because appropriate cutoff values for differentiating plaque types on the 3D-FSE images were not known, though they were eventually elucidated in this study.

CONCLUSIONS

3D-FSE T1WI can accurately characterize carotid plaque composition mainly due to contrast improvement of the lipid-rich plaques and can differentiate vulnerable plaques from stable plaques with excellent sensitivity and specificity, being comparable with 2D-SE T1WI.

Disclosures: Shinsuke Narumi—*RELATED*: *Grant*: Grants-in-Aid for Scientific Research (25861122) from the Ministry of Education, Culture, Sports, Science and Technology of Japan. Makoto Sasaki—*RELATED*: *Consulting Fee or Honorarium*: Hitachi Medical; *UNRELATED*: *Grants/Grants Pending*: Hitachi Medical*; Japanese Ministry Education, Culture, Sports, Science and Technology; *Payment for Lectures (including service on Speakers Bureaus)*: Daiichi Sankyo, Eisai, Sanofi, Tanabe, Johnson & Johnson, Bayer, AstraZeneca, Kowa, Fuji Film, GE Healthcare. *Money paid to the institution.

REFERENCES

1. Gaunt ME, Brown L, Hartshorne T, et al. **Unstable carotid plaques: preoperative identification and association with intraoperative embolisation detected by transcranial Doppler.** *Eur J Vasc Endovasc Surg* 1996;11:78–82
2. Altaf N, Beech A, Goode SD, et al. **Carotid intraplaque hemorrhage detected by magnetic resonance imaging predicts embolization during carotid endarterectomy.** *J Vasc Surg* 2007;46:31–36
3. Waki H, Masuyama T, Mori H, et al. **Ultrasonic tissue characterization of the atherosclerotic carotid artery: histological correlates or carotid integrated backscatter.** *Circ J* 2003;67:1013–16
4. Sztajzel R, Momjian S, Momjian-Mayor I, et al. **Stratified gray-scale median analysis and color mapping of the carotid plaque: correlation with endarterectomy specimen histology of 28 patients.** *Stroke* 2005;36:741–45
5. Narumi S, Sasaki M, Ohba H, et al. **Prediction of carotid plaque characteristics using non-gated MR imaging: correlation with endarterectomy specimens.** *AJNR Am J Neuroradiol* 2013;34:191–97
6. Watanabe Y, Nagayama M, Suga T, et al. **Characterization of atherosclerotic plaque of carotid arteries with histopathological correlation: vascular wall MR imaging vs. color Doppler ultrasonography (US).** *J Magn Reson Imaging* 2008;28:478–85
7. Saito A, Sasaki M, Ogasawara K, et al. **Carotid plaque signal differences among four kinds of T1-weighted magnetic resonance imaging techniques: a histopathological correlation study.** *Neuroradiology* 2012;54:1187–94
8. Narumi S, Sasaki M, Ohba H, et al. **Altered carotid plaque signal among different repetition times on T1-weighted magnetic resonance plaque imaging with self-navigated radial-scan technique.** *Neuroradiology* 2010;52:285–90
9. North American Symptomatic Carotid Endarterectomy Trial Collaborators. **Beneficial effect of carotid endarterectomy in symptomatic patients with high-grade carotid stenosis.** *N Engl J Med* 1991;325:445–53
10. Pipe JG. **Motion correction with PROPELLER MRI: application to head motion and free-breathing cardiac imaging.** *Magn Reson Med* 1999;42:963–69
11. Cai JM, Hatsukami TS, Ferguson MS, et al. **Classification of human carotid atherosclerotic lesions with in vivo multicontrast magnetic resonance imaging.** *Circulation* 2002;106:1368–73
12. Altaf N, MacSweeney ST, Gladman J, et al. **Carotid intraplaque hemorrhage predicts recurrent symptoms in patients with high-grade carotid stenosis.** *Stroke* 2007;38:1633–35
13. Takaya N, Yuan C, Chu B, et al. **Association between carotid plaque characteristics and subsequent ischemic cerebrovascular events: a prospective assessment with MRI–initial results.** *Stroke* 2006;37:818–23
14. Cappendijk VC, Cleutjens KB, Kessels AG, et al. **Assessment of human atherosclerotic carotid plaque components with multisequence MR imaging: initial experience.** *Radiology* 2005;234:487–92
15. Chu B, Kampschulte A, Ferguson MS, et al. **Hemorrhage in the atherosclerotic carotid plaque: a high-resolution MRI study.** *Stroke* 2004;35:1079–84
16. Yamada N, Higashi M, Otsubo R, et al. **Association between signal hyperintensity on T1-weighted MR imaging of carotid plaques and ipsilateral ischemic events.** *AJNR Am J Neuroradiol* 2007;28:287–92
17. Yoshida K, Narumi O, Chin M, et al. **Characterization of carotid atherosclerosis and detection of soft plaque with use of black-blood MR imaging.** *AJNR Am J Neuroradiol* 2008;29:868–74
18. Moody AR, Murphy RE, Morgan PS, et al. **Characterization of compli-**

cated carotid plaque with magnetic resonance direct thrombus imaging in patients with cerebral ischemia. *Circulation* 2003;107:3047–52
19. Ota H, Yarnykh VL, Ferguson MS, et al. **Carotid intraplaque hemorrhage imaging at 3.0-T MR imaging: comparison of the diagnostic performance of three T1-weighted sequences.** *Radiology* 2010;254:551–63
20. Yoshimura S, Yamada K, Kawasaki M, et al. **High-intensity signal on time-of-flight magnetic resonance angiography indicates carotid plaques at high risk for cerebral embolism during stenting.** *Stroke* 2011;42:3132–37
21. Qiao Y, Etesami M, Malhotra S, et al. **Identification of intraplaque hemorrhage on MR angiography images: a comparison of contrast-enhanced mask and time-of-flight techniques.** *AJNR Am J Neuroradiol* 2011;32:454–59
22. Yamaguchi M, Sasaki M, Ohba H, et al. **Quantitative assessment of changes in carotid plaques during cilostazol administration using three-dimensional ultrasonography and non-gated magnetic resonance plaque imaging.** *Neuroradiology* 2012;54:939–45
23. Narumi S, Sasaki M, Ohba H, et al. **Predicting carotid plaque characteristics using quantitative color-coded T1-weighted MR plaque imaging: correlation with carotid endarterectomy specimens.** *AJNR Am J Neuroradiol* 2014;35:766–71

Feasibility Analysis of the Parametric Response Map as an Early Predictor of Treatment Efficacy in Head and Neck Cancer

A.H. Baer, B.A. Hoff, A. Srinivasan, C.J. Galbán, and S.K. Mukherji

ABSTRACT

BACKGROUND AND PURPOSE: Estimating changes in the volume transfer constant, normalized area under the contrast-enhancement time curve at 60 seconds, and fractional blood plasma volume by using dynamic contrast-enhanced MR imaging may be useful in predicting tumor response to chemoradiation. We hypothesized that the parametric response map, a voxel-by-voxel analysis of quantitative dynamic contrast-enhanced MR imaging maps, predicts survival in patients with head and neck cancer.

MATERIALS AND METHODS: Ten patients with locoregionally advanced head and neck squamous cell carcinoma underwent definitive concurrent chemoradiation therapy. For each patient, dynamic contrast-enhanced MR imaging data were collected before and 2 weeks after treatment initiation. Change in perfusion parameters within the primary tumor volume with time was analyzed by parametric response mapping and by whole-tumor mean percentage change. Outcome was defined as overall survival. The perfusion parameter and metric most predictive of outcome were identified. Overall survival was estimated by the log-rank test and Kaplan-Meier survival curve.

RESULTS: The volume transfer constant and normalized area under the contrast-enhancement time curve at 60 seconds were predictive of survival both in parametric response map analysis (volume transfer constant, $P = .002$; normalized area under the contrast-enhancement time curve at 60 seconds, $P = .02$) and in the percentage change analysis (volume transfer constant, $P = .04$; normalized area under the contrast-enhancement time curve at 60 seconds, $P = .02$). Blood plasma volume predicted survival in neither analysis.

CONCLUSIONS: Parametric response mapping of MR perfusion biomarkers could potentially guide treatment modification in patients with predicted treatment failure. Larger studies are needed to determine whether parametric response map analysis or percentage signal change in these perfusion parameters is the stronger predictor of survival.

ABBREVIATIONS: DCE = dynamic contrast-enhanced; HNSCC = squamous cell carcinoma of the head and neck; K^{trans} = volume transfer constant; $NAUC_{60}$ = normalized area under the contrast-enhancement time curve at 60 seconds; PRM = parametric response map; V_p = blood plasma volume

It is estimated that >50,000 new cases of head and neck cancer were diagnosed in the United States in 2013, accounting for 3% of all new cancer diagnoses.[1] Worldwide, the disease burden is even greater, with an estimated 5% of all cancers being those of the head and neck.[2] Squamous cell carcinoma of the head and neck (HNSCC) accounts for approximately 90% of primary malignancies in that anatomic region.[3-6] The overall incidence and rate of death are in decline, but HNSCC continues to present formidable diagnostic and therapeutic challenges.[7,8]

Most HNSCC is advanced (stage III and IV) at the time of diagnosis.[9] Treatment of locoregionally advanced HNSCC (stages III and IVA/B) commonly involves surgery followed by radiation therapy, surgery followed by concurrent chemoradiation, definitive concurrent chemoradiation therapy, or sequential therapy involving induction chemotherapy followed by concurrent chemoradiation therapy.

Initial posttreatment imaging is performed to identify residual disease, to evaluate the effect of treatment, and to establish a baseline for future comparison. Imaging is generally performed 2–3 months after completion of chemoradiation because transient changes in MR signal characteristics related to acute inflamma-

Received June 18, 2014; accepted after revision September 16.

From the Department of Radiology (A.H.B., B.A.H., A.S., C.J.G.), University of Michigan Health System, Ann Arbor, Michigan; and Department of Radiology (S.K.M.), Michigan State University, East Lansing, Michigan.

This work was supported by the William N. Hanafee, MD, Research Seed Grant (2011–2012) and the following National Institutes of Health grants: P50CA093990, P01CA059827, P01CA085878.

Paper previously presented in the William N. Hanafee, MD, Research Seed Grant research progress presentation at: Annual Meeting of the American Society of Head and Neck Radiology, October 3–12, 2012; Miami Beach, Florida; and Annual Meeting of the American Society of Functional Neuroradiology, February 17–19, 2014; Miami Beach, Florida.

Please address correspondence to Aaron H. Baer, MD, Massachusetts General Hospital, Division of Neuroradiology, Gray 2, Room 273A, 55 Fruit St, Boston, MA 02114; e-mail: aaronbaer@gmail.com

Indicates open access to non-subscribers at www.ajnr.org

http://dx.doi.org/10.3174/ajnr.A4296

Table 1: Subject demographics and disease status at the time of analysis

Subject	Age (yr)/Sex	Primary Location	Stage	Status	Survival (mo)	Outcome
1	62/M	Tonsil	T1 N2a	NED	75.4	Survivor
2	65/F	Soft palate	T2 N3	LF	3.5	Nonsurvivor
3	58/M	Hypopharynx	T4 N2b	LF/RF/DF	10.3	Nonsurvivor
4	83/M	Larynx	T4 N0	LF	2.0	Nonsurvivor
5	43/M	Tongue base/tonsil	T4 N2c	DF	4.6	Nonsurvivor
6	61/F	Tonsil	T2 N3	RF	66.1	Survivor
7	55/M	Piriform sinus	T2 N2b	Unknown	33.5	Survivor
8	43/M	Tonsil	T2 N2b	DF	18.9	Nonsurvivor
9	57/M	Nasopharynx	T2 N2b	NED	56.4	Survivor
10	60/M	Tongue base	T3 N0	NED	64.9	Survivor

Note:—NED indicates no evidence of disease; LF, local failure; RF, regional failure; DF, distant failure.

tion are considerable in the early postradiotherapy period.[10] While such an approach is valuable in monitoring treatment response, the delay between initiation of therapy and assessment of response precludes early treatment modification (eg, radiation therapy intensification for poorly responding tumors).[11] A tool that accurately predicts outcome soon after treatment initiation would allow initiation of alternative treatment regimens, reduce unnecessary treatment-related toxicity, and reduce the unnecessary expense of ineffective treatment regimens.

In 2005, the functional diffusion map was introduced, currently termed the parametric response map (PRM).[12,13] The PRM is a voxel-based approach to analyzing MR imaging data that allows segmentation of a tumor volume on the basis of regional intratumoral changes in the MR signal.[12-14] The tool was initially applied to ADC maps, but PRM can be applied to any imaging study. PRM analysis may uncover regional intratumoral signal changes that could be masked in whole-tumor mean signal-change calculations.

Dynamic contrast-enhanced (DCE) MR imaging and dynamic-susceptibility contrast MR imaging are techniques capable of estimating tumor vascular permeability, blood volume, blood flow, and extracellular extravascular space. The aims of this study were to prospectively collect DCE MR imaging data from patients with locoregionally advanced HNSCC before and during treatment and to examine the value of PRM analysis and whole-tumor mean change of perfusion parameters in predicting survival.

MATERIALS AND METHODS

Patients

All adult patients (18 years of age or older) presenting to the University of Michigan Health System for treatment of unresectable, locoregionally advanced, biopsy-proved, primary HNSCC for whom radiation therapy was recommended were eligible for inclusion.[15] Patients were enrolled during a 2-year period under the supervision of a faculty member of the department of radiation oncology. Informed consent was obtained from all patients, and the study was approved by the internal review board at our institution. Patients who were pregnant at the time of diagnosis or who had known contraindications to MR imaging (eg, ferromagnetic prostheses) were excluded from the study. Patients with dermal or subcutaneous HNSCC involvement were also excluded due to potential susceptibility effects at air-tissue interfaces. Of the 24 patients initially considered for this study, 4 were excluded because of metallic dental hardware noted on CT that was expected to result in unacceptable susceptibility artifacts, 2 patients were excluded after MR imaging for unacceptable susceptibility artifacts that were not anticipated by CT, 1 patient was excluded because of an incomplete treatment course, and 7 patients were excluded due to incomplete or corrupt datasets at the time of analysis. Datasets of 10 patients were analyzed for this study. Table 1 details patient demographics, disease characteristics, and survivorship.

Treatment

Each patient underwent definitive treatment with fractionated radiation therapy and concurrent chemotherapy. Radiation therapy involved 70 Gy to the primary gross tumor volume and involved lymph nodes for 7 weeks by 3D conformational or intensity-modulated radiation therapy. Initial chemotherapy regimens for the analyzed patients were as follows: 5 patients received weekly carboplatin (area under the curve of 1) and paclitaxel (20 mg/m^2 or 30 mg/m^2), 2 patients received cisplatin (40 mg/m^2) weekly, 1 patient received cisplatin (12 mg/m^2) daily for 5 days and 5-fluorouracil (600-mg/m^2 continuous infusion) for 5 days on weeks 1 and 5 of radiation therapy, 1 patient received carboplatin (area under the curve of 4) every 3 weeks, and 1 patient received cetuximab with a loading dose of 400 mg/m^2 followed by a weekly dose of 250 mg/m^2. Follow-up involved clinic visits every 6 weeks for the first 24 months, every 3 months for months 25–36, and every 6 months from month 37 onward.

Perfusion MR Imaging Acquisition

Using a 3T Philips Achieva magnet (Philips Healthcare, Best, the Netherlands), we obtained MR images at 2 time points for each participant—before treatment (t_0) and 2 weeks after initiation of chemoradiation (t_1). Sequences included DCE T1-weighted, pre- and postcontrast axial T1-weighted, axial T2-weighted FLAIR, axial T2-weighted with fat saturation, and diffusion-weighted. Each DCE acquisition included 32 dynamic volumes acquired by a 3D gradient-echo pulse sequence following the intravenous administration of 0.1 mL/kg of gadopentetate dimeglumine. DCE data were acquired in the sagittal plane to include the entire primary tumor volume and suspected metastatic lymph nodes in the same FOV, while minimizing the acquisition time and the FOV itself. We used the following acquisition parameters: TR = 5.1 ms, TE = 1.1 ms, flip angle = 20°, voxel size = 2 × 2 × 2 mm.

Defining Tumor Volumes

Primary gross tumor volumes of interest were manually defined on t_0 DCE MR imaging data by using masking software developed

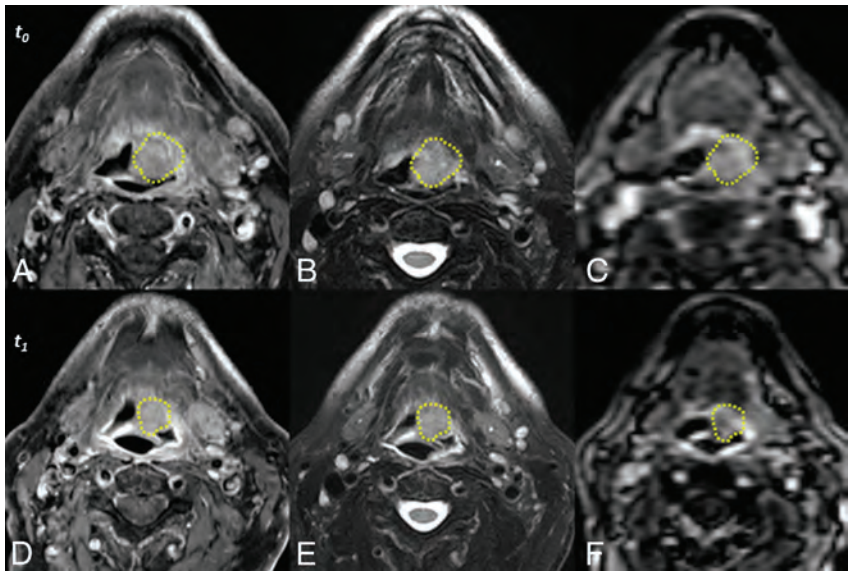

FIG 1. Unregistered sequences of a representative subject acquired before treatment (t_0, *top row*) and 2 weeks after initiation of therapy (t_1, *bottom row*). Acquisitions include postcontrast T1-weighted with fat-saturation (*A* and *D*), T2-weighted with fat-saturation (*B* and *E*), and DCE MR imaging (*C* and *F*). Manually defined primary gross tumor volumes are depicted for each time point (*yellow lines*). The images above are those of subject 10, a survivor at follow-up.

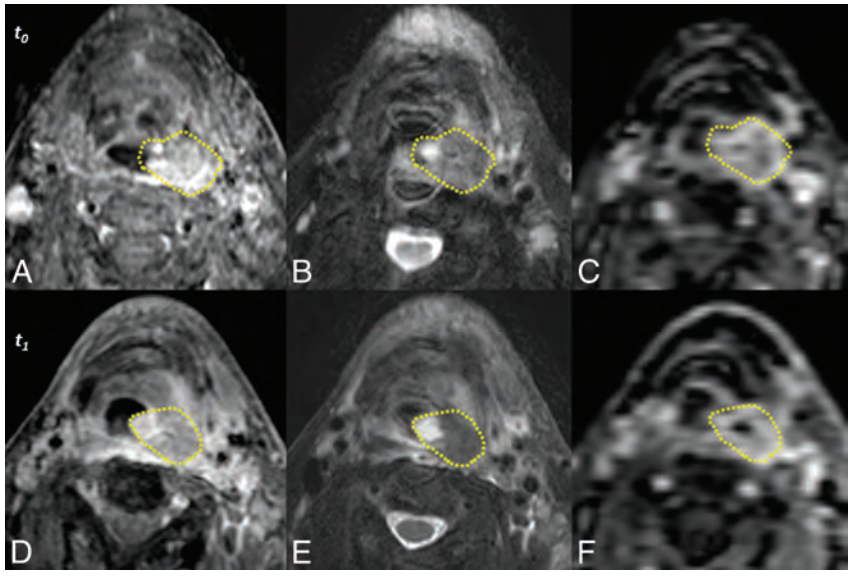

FIG 2. Unregistered sequences of a representative subject acquired before treatment (t_0, top row) and 2 weeks after initiation of therapy (t_1, bottom row). Acquisitions include postcontrast T1-weighted with fat-saturation (*A* and *D*), T2-weighted with fat-saturation (*B* and *E*), and DCE MR imaging (*C* and *F*). Manually defined primary gross tumor volumes are depicted for each time point (*yellow lines*). The images above are those of subject 3, a nonsurvivor at follow-up.

at our institution. Lymph nodes and major vascular structures were excluded from the volumes of interest. Postcontrast T1-weighted fat-saturated and T2-weighted fat-saturated sequences were referenced to assist in defining the primary tumor volumes (Figs 1 and 2). For volume-of-interest definition and for comparison with conventional MR images, the DCE MR imaging volumes were reformatted into the axial plane.

Extraction of Perfusion Parameters

To determine the arterial input function, we sampled the DCE MR imaging signal from the internal carotid artery ipsilateral to the primary tumor, and samples without clear arterial waveforms were manually excluded from the calculation. The modified Tofts model was used to extract perfusion parameters from the DCE MR imaging data at both t_0 and t_1 time points.[16] For the purposes of this study, parameters of interest include the volume transfer constant (K^{trans}), the normalized area under the contrast-enhancement time curve at 60 seconds ($NAUC_{60}$), and blood plasma volume (V_p).

Whole-Tumor Change in Perfusion Parameters

Signal values were extracted from each voxel of the primary gross tumor volume, and averaging these provided whole-tumor mean signal values. The percentage signal change was then calculated by subtracting the whole-tumor mean signal of t_0 and t_1 and dividing by that of t_0. This process was completed for each perfusion parameter (K^{trans}, $NAUC_{60}$, and V_p) of each patient. With the parameter K^{trans} as an example, the resulting whole-tumor mean signal change was reported as a percentage increase ($\%\Delta_{Ktrans+}$) or percent decrease ($\%\Delta_{Ktrans-}$).

Parametric Response Mapping

Coregistration of DCE MR imaging data from t_0 and t_1 time points was executed by using the Mutual Information for Automatic Multimodality Image Fusion software package developed at our institution. In brief, t_0 and t_1 DCE MR imaging data for each patient were spatially aligned by using thin-plate splines as the deformable registration interpolant. Registration was initiated by manually defined control points in the t_1 dataset that corresponded to regions within the primary tumor volume as defined on the t_0 dataset. The automatic algorithm then iteratively optimized the solution by using mutual information as the objective function.

Following coregistration, the temporally resolved DCE MR imaging data occupy the same 3D space, with each voxel consisting of a pair of parameter values at the 2 discrete time points. Individual voxels were classified on the basis of the change in the voxel parameter values. Those voxels with a significant increase in parameter X, which may be K^{trans}, $NAUC_{60}$, or V_p, were color-coded red, voxels with a significant decrease were blue, and those without a significant change in X were green. Global PRM mea-

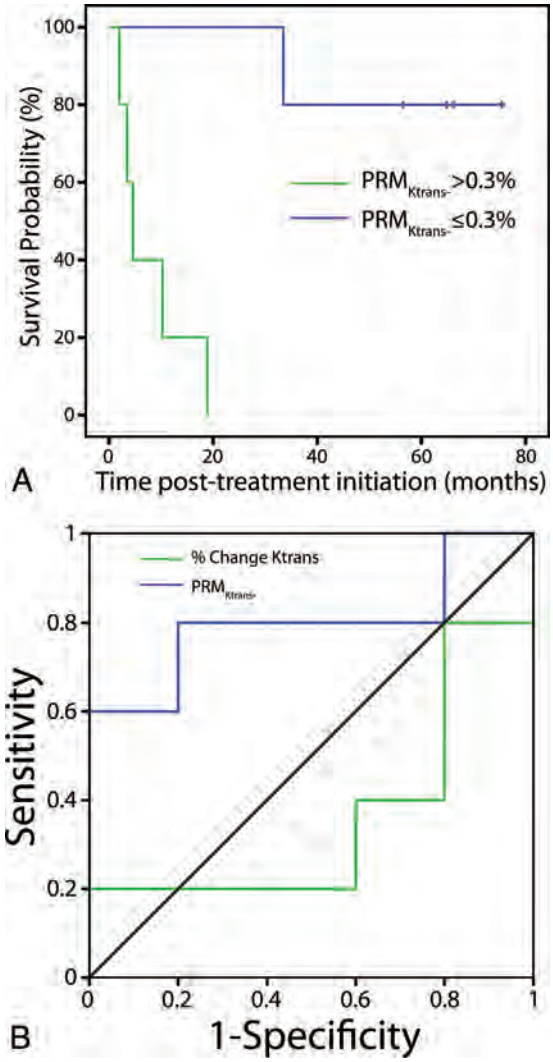

FIG 3. ROC curves for $PRM_{Ktrans-}$ (*blue line*) and $PRM_{Ktrans0}$ (*green line*) at 2 weeks after treatment initiation (*A*). Kaplan-Meier survival plots for overall survival as a function of stratification by $PRM_{Ktrans-}$ (the perfusion parameter most predictive of survival) at 2 weeks after treatment initiation (*B*). The *blue line* represents $PRM_{Ktrans-} \leq$ the cutoff. The *green line* represents $PRM_{Ktrans-} >$ the cutoff.

sures were determined by summing all parameter voxels within a classification and normalizing by the total tumor volume. These measures are presented in PRM_{X+} for increasing, PRM_{X-} for decreasing, and PRM_{X0} for unchanged.

Statistical Analysis

Outcome was defined as overall survival, the duration of which was calculated from the day of pretreatment MR imaging to the time of data analysis. An optimal "responder cutoff" was identified by using a receiver operating characteristic analysis for each parameter (K^{trans}, $NAUC_{60}$, and V_p), analyzed by using either PRM or the percentage change in the mean, and the parameter value most predictive of outcome was identified. Overall survival was estimated by the log-rank test and Kaplan-Meier survival curve (Fig 3).

RESULTS

At the time of analysis, 5 patients were survivors (50%) and 5 were nonsurvivors (50%). For survivors, median survival duration was 64.9 months (range, 33.5–75.4 months); for nonsurvivors, median survival duration was 4.6 months (range, 2.0–18.9 months).

Table 2: Statistical significance of analysis type and perfusion parameter in predicting survival

	K^{trans}		V_p		$NAUC_{60}$	
	PRM-	% Change	PRM-	% Change	PRM-	% Change
Overall survival	.002[a]	.041[a]	.308	.068	.022[a]	.024[a]

[a] Statistically significant at $\alpha = .05$.

Table 2 details the statistical significance of each analysis type for each metric in predicting overall survival. For the parameter K^{trans}, both PRM analysis ($PRM_{Ktrans-}$, $P = .002$) and percentage change analysis ($\%\Delta_{Ktrans-}$, $P = .04$) were predictive of survival. Similar results were observed for $NAUC_{60}$ ($PRM_{NAUC60-}$, $P = .02$; $\%\Delta_{NAUC60-}$, $P = .02$). Irrespective of analytical technique, V_p was not found to be predictive of survival (PRM_{Vp-}, $P = .31$; $\%\Delta_{Vp-}$, $P = .07$). The sample size was insufficient to determine whether PRM analysis or percentage change in perfusion parameters provided a stronger predictor of survival. Figure 4 depicts sample sections from PRM_{Ktrans} in a representative survivor and nonsurvivor.

DISCUSSION

Recently, PRM analysis of perfusion data has been examined as a surrogate biomarker for early cancer treatment response. In 2009, Galbán et al[17] compared PRM analysis with whole-tumor mean percentage analysis of CBV and CBF in predicting treatment response in high-grade gliomas. Results indicated that PRM analysis of CBV and CBF within the tumor were highly predictive of survival after 1 week of treatment, whereas percentage change analysis was not predictive. Furthermore, PRM of CBV was more predictive of overall survival than baseline CBV. In 2010, Tsien et al[18] examined PRM analysis of perfusion data to distinguish between disease progression and pseudoprogression in high-grade gliomas undergoing concurrent chemoradiation therapy. The study found that at week 3 of therapy, patients with progressive disease had a significant decrease in PRM of CBV compared with patients with pseudoprogression. In 2012, Wang et al[19] evaluated an analysis method known as "fuzzy clustering" to identify HNSCC tumor subvolumes in DCE MR imaging data related to treatment outcomes. Results suggested that tumor subvolumes with low blood volume that persisted from pretreatment to intratreatment (week 2 of concurrent chemoradiation therapy) time points were greater in patients with local treatment failure than in those with local control.

In our study, both $PRM_{Ktrans-}$ and $\%\Delta_{Ktrans-}$ were predictive of survival when measured early after treatment initiation. Patients with a large percentage of the primary gross tumor volume that decreased in K^{trans} (ie, a measure of endovascular permeability) were more likely to have significantly reduced survival. Similarly, findings suggest that patients with a large percentage of the primary gross tumor volume that decreased in $NAUC_{60}$ (a general measure of perfusion) were more likely to have significantly reduced survival. These findings are consistent with those previously described.

The clinical implication of our findings is that PRM is feasible and may identify, early into definitive treatment, those patients whose primary tumors will have an unfavorable response to stan-

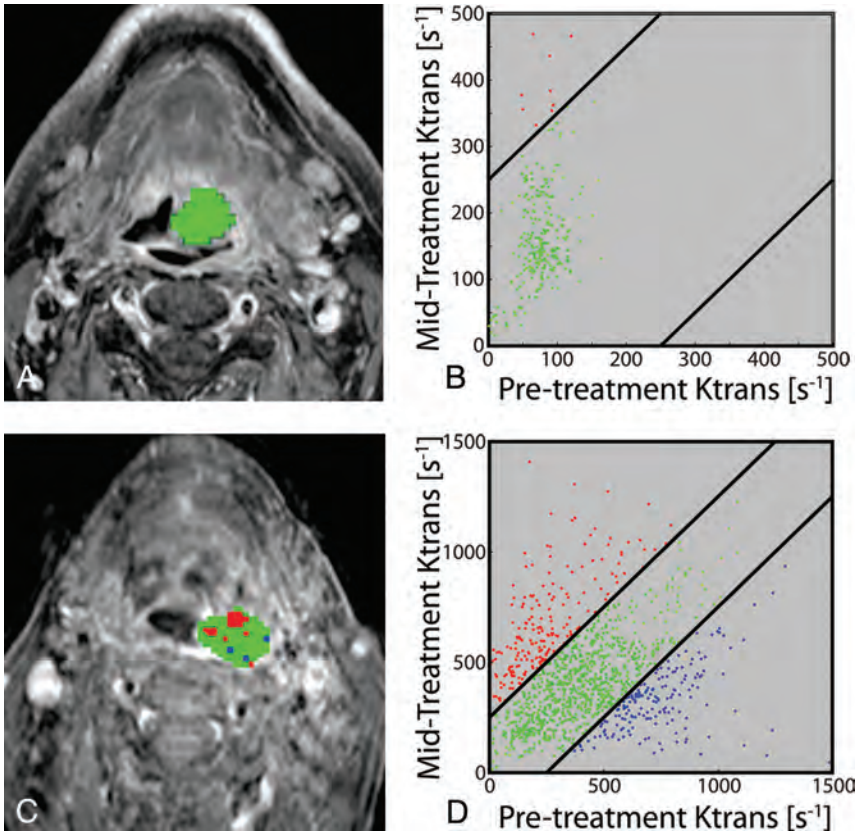

FIG 4. Representative patients with HNSCC stratified by $PRM_{Ktrans-}$ as survivor (*top row*, median survival time, 64.9 months) or nonsurvivor (*bottom row*, median survival time, 10.3 months) at the time of analysis. PRM_{Ktrans} color-coded ROIs are superimposed on pretreatment T1-weighted gadolinium contrast-enhanced images (*A* and *C*). The scatterplots illustrate the distribution of changes in K^{trans} throughout the entire volumes of interest (*B* and *D*). The 95% confidence intervals within the scatterplots are represented by the *black lines*. Voxels with significantly increasing, decreasing, or unchanged K^{trans} are coded as *red*, *blue*, and *green dots*, respectively.

dard chemoradiation regimens. Perhaps even more useful, PRM provides spatial information regarding the location of unresponsive tumor subvolumes, which may aid in selecting targets for radiation therapy intensification. The converse may also be true—tumor subvolumes with a predicted favorable response to standard radiation doses may have a similarly favorable response to a reduced dose.

Study Limitations

The processing requirements of the PRM metric are not trivial, and the modeling of DCE MR imaging data has yet to be standardized. A critical question when considering implementation of such an analysis is whether the PRM metric provides a stronger predictor of survival than percentage whole-tumor mean signal change, a simpler and less time-consuming analysis. The sample size of this feasibility study is insufficient for the multivariate analysis needed to determine which analysis type produces a stronger predictor of outcome.

A 128 × 128 in-plane matrix size was used for the DCE MR imaging acquisition in this study because using large matrices in the 32-phase sequence is inherently time-consuming. The resulting low spatial resolution may have compromised accurate manual definition of primary gross tumor volumes of interest, particularly for smaller lesions. To avoid inclusion of voxels that were subject to volume averaging in the analysis, we used conservative margins in defining the volumes of interest. This use likely resulted in undersampling signal in the periphery of the primary tumor volumes.

Data collection for this study was part of a larger investigation involving conventional and diffusion MR images. The perfusion technique had motion in some individuals, was incomplete in others due to scanner failure, and was corrupted in others likely during transfer to network storage. These issues were addressed and are not anticipated in planned future trials.

Finally, measuring the arterial input function remains a substantial source of error in the estimation of perfusion parameters with DCE-MR imaging. The optimal method of reproducibly estimating the arterial input function (eg, cohort average versus measured patient-specific) remains the subject of debate.[20]

CONCLUSIONS

The results of this retrospective analysis of prospectively collected data suggest that PRM analysis of perfusion biomarkers could potentially guide early modification of chemoradiation treatment regimens. Specifically, subvolumes of tumors with predicted treatment failure may benefit from radiation therapy intensification early in the treatment course. A prospective investigation is currently taking place at our institution to examine targeted radiation therapy intensification with the application of our technique. Larger studies are also needed to validate these findings and to determine whether PRM analysis or whole-tumor percentage signal change analysis provides a stronger predictor of survival.

ACKNOWLEDGMENTS

We gratefully acknowledge Dr Thomas Chenevert for his invaluable assistance in the preparation of this article.

Disclosures: Aaron H. Baer—*RELATED*: *Grant and Provision of Writing Assistance, Medicines, Equipment or Administrative Support*: The American Society of Head and Neck Radiology supported the study described in the article through the William N. Hanafee research seed grant ($15,000).* The funds were used for the purchase of equipment used in the study and as salary support for 2 of the coauthors, Benjamin A. Hoff and Craig J. Galbán. Ashok Srinivasan—*Royalties*: Amirsys (for book chapters). Benjamin A. Hoff—*RELATED*: *Grant*: National Institutes of Health.* Craig J. Galbán—*RELATED*: *Grant*: National Institutes of Health (P50CA093990, P01CA059827, P01CA085878)*; *UNRELATED*: *Patents (planned, pending or issued)*: University of Michigan (coinvestor of this technology); *Royalties*: University of Michigan, Imbio, *Comments*: As a coinventor of this technology, I may receive royalties from the licensing of this technology to Imbio from the University of Michigan. Suresh K. Mukherji—*RELATED*: *Grant*: American Society of Head and Neck Radiology (Hanafee Award).* *Money paid to the institution.

REFERENCES

1. Siegel R, Naishadham D, Jemal A. **Cancer statistics, 2013.** *CA Cancer J Clin* 2013;63:11–30
2. Ferlay J, Shin HR, Bray F, et al. **Estimates of worldwide burden of cancer in 2008: GLOBOCAN 2008.** *Int J Cancer* 2010;127:2893–917
3. Crozier E, Sumer BD. **Head and neck cancer.** *Med Clin North Am* 2010;94:1031–46
4. Cohan DM, Popat S, Kaplan SE, et al. **Oropharyngeal cancer: current understanding and management.** *Curr Opin Otolaryngol Head Neck Surg* 2009;17:88–94
5. Lin DT, Cohen SM, Coppit GL, et al. **Squamous cell carcinoma of the oropharynx and hypopharynx.** *Otolaryngol Clin North Am* 2005;38:59–74, viii
6. Osborne RF, Brown JJ. **Carcinoma of the oral pharynx: an analysis of subsite treatment heterogeneity.** *Surg Oncol Clin N Am* 2004;13:71–80
7. American Cancer Society. **Cancer Facts & Figures 2010.** http://www.cancer.org/research/cancerfactsstatistics/cancerfactsfigures2010/index. Accessed February 3, 2014
8. Jemal A, Siegel R, Xu J, et al. **Cancer statistics, 2010.** *CA Cancer J Clin* 2010;60:277–300
9. Monnerat C, Faivre S, Temam S, et al. **End points for new agents in induction chemotherapy for locally advanced head and neck cancers.** *Ann Oncol* 2002;13:995–1006
10. Hermans R. **Post-treatment imaging of head and neck cancer.** *Cancer Imaging* 2004;4(Spec No A):S6-15
11. Cao Y. **The promise of dynamic contrast-enhanced imaging in radiation therapy.** *Semin Radiat Oncol* 2011;21:147–56
12. Hamstra DA, Chenevert TL, Moffat BA, et al. **Evaluation of the functional diffusion map as an early biomarker of time-to-progression and overall survival in high-grade glioma.** *Proc Natl Acad Sci U S A* 2005;102:16759–64
13. Moffat BA, Chenevert TL, Lawrence TS, et al. **Functional diffusion map: a noninvasive MRI biomarker for early stratification of clinical brain tumor response.** *Proc Natl Acad Sci U S A* 2005;102:5524–29
14. Galbán CJ, Mukherji SK, Chenevert TL, et al. **A feasibility study of parametric response map analysis of diffusion-weighted magnetic resonance imaging scans of head and neck cancer patients for providing early detection of therapeutic efficacy.** *Transl Oncol* 2009;2:184–90
15. Srinivasan A, Chenevert TL, Dwamena BA, et al. **Utility of pretreatment mean apparent diffusion coefficient and apparent diffusion coefficient histograms in prediction of outcome to chemoradiation in head and neck squamous cell carcinoma.** *J Comput Assist Tomogr* 2012;36:131–37
16. Tofts PS, Brix G, Buckley DL, et al. **Estimating kinetic parameters from dynamic contrast-enhanced T(1)-weighted MRI of a diffusable tracer: standardized quantities and symbols.** *J Magn Reson Imaging* 1999;10:223–32
17. Galbán CJ, Chenevert TL, Meyer CR, et al. **The parametric response map is an imaging biomarker for early cancer treatment outcome.** *Nat Med* 2009;15:572–76
18. Tsien C, Galbán CJ, Chenevert TL, et al. **Parametric response map as an imaging biomarker to distinguish progression from pseudoprogression in high-grade glioma.** *J Clin Oncol* 2010;28:2293–99
19. Wang P, Popovtzer A, Eisbruch A, et al. **An approach to identify, from DCE MRI, significant subvolumes of tumors related to outcomes in advanced head-and-neck cancer.** *Med Phys* 2012;39:5277–85
20. Lavini C, Verhoeff JJ. **Reproducibility of the gadolinium concentration measurements and of the fitting parameters of the vascular input function in the superior sagittal sinus in a patient population.** *Magn Reson Imaging* 2010;28:1420–30

Quantitative Diffusion-Weighted MRI Parameters and Human Papillomavirus Status in Oropharyngeal Squamous Cell Carcinoma

C.S. Schouten, P. de Graaf, E. Bloemena, B.I. Witte, B.J.M. Braakhuis, R.H. Brakenhoff, C.R. Leemans, J.A. Castelijns, and R. de Bree

ABSTRACT

BACKGROUND AND PURPOSE: Patients with human papillomavirus–positive oropharyngeal squamous cell carcinomas have a better survival rate than those with human papillomavirus–negative oropharyngeal squamous cell carcinomas. DWI characterizes biologically relevant tumor features, and the generated ADC may also provide prognostic information. We explored whether human papillomavirus status and ADC values are independent tumor characteristics.

MATERIALS AND METHODS: Forty-four patients with oropharyngeal squamous cell carcinomas underwent pretreatment DWI. ADC values for the primary tumors were determined by using 3 b-values in an ROI containing the largest area of solid tumor on a single section of an axial DWI image. Human papillomavirus status was determined with p16 immunostaining, followed by high-risk human papillomavirus DNA detection on the p16-positive cases.

RESULTS: Twenty-two patients were human papillomavirus–positive (50.0%). ADC values were not significantly different between human papillomavirus–negative (ADC_{mean} = 1.56 [1.18–2.18] × 10^3 mm^2/s) and human papillomavirus–positive tumors (ADC_{mean} = 1.46 [1.07–2.16] × 10^3 mm^2/s).

CONCLUSIONS: No significant association between ADC and human papillomavirus status was found in oropharyngeal squamous cell carcinomas. In our study population, differences in genetic and histologic features between human papillomavirus–positive and human papillomavirus–negative oropharyngeal squamous cell carcinomas did not translate into different ADC values. Long-term follow-up studies are needed to establish whether ADC has prognostic value and whether this is independent of the human papillomavirus status.

ABBREVIATIONS: HNSCC = head and neck squamous cell carcinoma; HPV = human papillomavirus; OPSCC = oropharyngeal squamous cell carcinoma

Head and neck squamous cell carcinoma (HNSCC) is the sixth most common cancer worldwide.[1] During the past decades, it has been well-established that besides tobacco smoking and alcohol consumption, human papillomavirus (HPV) is an important etiologic factor in the development of HNSCC, in particular squamous cell carcinomas in the oropharynx (OPSCC). HPV-positive and HPV-negative OPSCCs are different disease entities.[2] Patients with HPV-positive OPSCC show higher response rates to treatment and have a better overall survival compared with those with HPV-negative OPSCC, despite the more often regionally advanced disease presentation in patients with HPV-positive OPSCC.[3,4] In addition, the genetic route to cancer is different for HPV-positive OPSCC,[5,6] and HPV-related tumors have distinct histologic features.[7,8] In this context, traditional prognostic factors such as tumor size and lymph node invasion may be insufficient to fully classify patients into risk groups. Identification of other prognostic tumor characteristics may lead to an improved patient selection and, as a result, higher responses to treatment and probably less treatment-induced morbidity.

DWI is a noninvasive functional technique that characterizes tissue on the basis of the random motion of water molecules, which is mainly influenced by the volume of extracellular space and the presence of cell membranes. Differences in water mobility can be quantified with the ADC: Hypocellular or necrotic tissue or both are characterized by a high ADC, whereas hypercellular tissue is characterized by a low ADC. Hence, parameters from DWI, such as ADC, could indicate biologic dissimilarities among tumors. Furthermore, studies in breast cancer have demonstrated that the ADC value significantly correlates with the expression of specific bi-

Received September 16, 2014; accepted after revision October 8.

From the Departments of Otolaryngology–Head and Neck Surgery (C.S.S., B.J.M.B., R.H.B., C.R.L., R.d.B.), Radiology and Nuclear Medicine (P.d.G., J.A.C.), Pathology (E.B.), and Epidemiology and Biostatistics (B.I.W.), VU University Medical Center, Amsterdam, the Netherlands; and Department of Oral and Maxillofacial Surgery/Oral Pathology (E.B.), VU University Medical Center/Academic Center for Dentistry Amsterdam, Amsterdam, the Netherlands.

Paper previously presented at: Dutch National Otolaryngology Conference, April 24–25, 2014; Nieuwegein, the Netherlands.

Please address correspondence to R. de Bree, MD, Department of Otolaryngology–Head and Neck Surgery, VU University Medical Center, De Boelelaan 1117, 1081 HV Amsterdam, the Netherlands; e-mail: r.bree@vumc.nl

http://dx.doi.org/10.3174/ajnr.A4271

ologic markers of disease, such as estrogen receptor and progesterone receptor.[9,10] ADC is a possible prognostic factor in HNSCC; several studies have shown that HNSCC with relatively low pretreatment ADC values responds better to chemoradiotherapy than tumors with higher pretreatment ADC values.[11-14] Additionally, HPV-positive OPSCC often has a different histology from HPV-negative OPSCC, characterized by ovoid-to-spindle-shaped hyperchromatic cells without keratinization and without a stromal response,[15] and it can by hypothesized that these histologic characteristics translate into low pretreatment ADC values; if so, this hypothesis would support the general notion that low ADC correlates with a better response to chemoradiotherapy. Limited information is available on the relation between HPV involvement and ADC values.[16]

In this study, we investigated the possible association between ADC values derived from DWI and the presence of biologically active HPV in patients with OPSCC.

MATERIALS AND METHODS

Patients and Study Design

The study was approved by the institutional review board of VU University Medical Center. We identified patients with a histopathologically proved OPSCC who had undergone DWI for diagnosis and treatment planning between January 2010 and December 2013. Patients with T1 oropharyngeal tumors were excluded because a reliable ROI could not be drawn. Fifty-seven patients could be evaluated. Medical records were reviewed for clinical characteristics, including smoking and alcohol intake, tumor node metastasis stage, and oropharyngeal subsite. Three patients were excluded due to insufficient quality of the DWI. In 2 other patients, the primary tumor was outside the range of obtained MR diffusion images; therefore, they were excluded. Eight more patients were excluded because DWI was performed with only 2 b-values. Thus, 44 patients were enrolled in the DWI analysis.

HPV Analysis

HPV testing was performed on all tumors by using a previously defined and validated algorithm for HPV detection.[17,18] In short, formalin-fixed and paraffin-embedded tumor tissue was stained by immunohistochemistry for p16 (the product of the cyclin-dependent kinase inhibitor 2A); and on the p16-immunopositive cases, high-risk HPV DNA was detected with general primer 5+/6+ polymerase chain reaction. Only the cases that were positive in the latter assay were classified as HPV-positive.

DWI

All MR imaging examinations were performed by using a 1.5T MR imaging system (Signa HDx; GE Healthcare, Milwaukee, Wisconsin) with a head coil combined with a phased array spine and neck coil. After an axial STIR series with 7-mm sections covering the entire neck area, subsequent images were centered on the area of interest containing the primary tumor and enlarged lymph nodes. Axial images (22 sections of 4-mm section thickness and 0.4-mm gap) were obtained with STIR (TR/TE/T1 = 6600/60/160 ms, 2 averages, in-plane pixel size of 0.7 × 1.1 mm) and T1WI spin-echo (TR/TE = 500/14 ms, 2 averages, no fat saturation, in-plane pixel size of 0.5 × 0.5 mm) before and after the intravenous injection of contrast material: Dotarem (0.2 mL/kg of gadoteric acid; Guerbet, Aulnay-sous Bois, France) or Gadovist (0.1 mL/kg of gadobutrol; Bayer Schering Pharma, Berlin, Germany).

DWI by using a PROPELLER technique was performed for 16 sections at the same section positions as the axial STIR and T1WI. Parameters for PROPELLER DWI were the following: TR/TE = 3500/83.87 ms; in-plane pixel size = 2 × 2 mm; and b-values = 0, 750, and 1000 s/mm^2 (3 averages). ADC maps were calculated online or off-line, respectively, by using the software of the scanner.

DWI scans were analyzed with AEGIS (Aegis Web, Version 3.2.4; Hologic, Bedford, Massachusetts), which allowed viewing of multiple MR images. The primary tumors were first identified on conventional MR images. ADC values were measured by drawing an ROI on a single section of an axial high-b-value DWI containing the largest area of solid tumor, excluding any necrotic regions with the aid of postcontrast MR images. If artifacts within the lesion were present, a smaller ROI was placed only over the undistorted area of the lesion. Subsequently, the ROIs were copied to the corresponding ADC maps. ADC was obtained as $ADC_{minimum}$ (lowest tumor voxel value within the ROI) and ADC_{mean} (mean ADC within the ROI). The ROIs were outlined by C.S.S. (MD, PhD candidate) and confirmed by a board-certified head and neck radiologist with 5 years of experience in head and neck radiology (P.d.G). Clinical information about the tumor node metastasis stage was known, but the interpreters were blinded to HPV status.

Statistical Analysis

Statistical analyses were performed by using the SPSS software package (Version 20.0; IBM, Armonk, New York). The level of significance was set at $P < .05$, and hypotheses were tested 2-sided. Analyses for differences in patient characteristics between the HPV-positive and HPV-negative groups were performed with the Pearson χ^2 test for categoric data and the Fisher exact test when appropriate. A Bonferroni correction was used to compare subgroups. The Mann-Whitney *U* test was used to compare continuous data.

RESULTS

The total study group consisted of 33 men and 11 women, with a mean age at the time of diagnosis of 58.8 years (range, 45–78). Patient characteristics by HPV status are shown in Table 1. Patients who were HPV-positive were more likely to present with a T2 primary tumor and N-positive disease. Patients who were HPV-negative were more likely to have a history of heavy smoking and excessive alcohol consumption.

With DWI, ROI areas for OPSCC ranged from 20.0 to 770.0 mm^2. The median ROI area for HPV-positive and HPV-negative OPSCCs was 165.0 mm^2 (range, 40–450 mm^2) and 160.0 mm^2 (range, 20–770 mm^2), respectively. The ROI area did not significantly differ between patients who were HPV-positive and those who were HPV-negative ($P = .77$). Examples of a DWI scan from a patient who was HPV-negative and one who was HPV-positive are shown in Figs 1 and 2, respectively. The results did not demonstrate significant differences between ADC_{mean} and $ADC_{minimum}$ in the HPV-negative and HPV-positive groups: ADC_{mean} and $ADC_{minimum}$ were 1.46 (1.07–2.16) × 10^{-3} mm^2/s (median [range]) and 1.01 (0.62–1.55) × 10^{-3} mm^2/s for patients who were HPV-positive and 1.56 (1.18–2.18) × 10^{-3} mm^2/s and 1.07 (0.62–1.51) × 10^{-3} mm^2/s for patients who were HPV-negative ($P = .51$ and $P = .67$, respectively) (Table 2).

Table 1: General patient characteristics

Characteristic	HPV-Positive (*n* = 22) (50%)	HPV-Negative (*n* = 22) (50%)	*P* Value
Sex			.30
Male	18 (81.8%)	15 (68.2%)	
Female	4 (18.2%)	7 (31.8%)	
Age at diagnosis (yr)			.92
Median (range)	57 (47–78)	60.5 (45–71)	
Oropharyngeal subsite			.29
Tonsil	12 (54.4%)	10 (45.5%)	
Base of tongue	8 (36.4%)	6 (27.3%)	
Oropharynx nos	2 (9.1%)	6 (27.3%)	
Smoking[a]			.01
Never (0–5 pack years)	8 (36.4%)	0 (0%)	
Moderate (6–24 pack years)	5 (22.7%)	5 (22.7%)	
Heavy (>24 pack years)	9 (40.9%)	17 (77.3%)	
Alcohol consumption[b]			.02
Never (0)	3 (13.6%)	0 (0%)	
Moderate (1–149 U years)	15 (68.2%)	10 (45.5%)	
Heavy (>149 U years)	4 (18.2%)	12 (54.5%)	
T-stage			.03
T2	12 (54.5%)	5 (22.7%)	
T3–4	10 (45.5%)	17 (77.3%)	
N-stage			.04
N0	0 (0%)	5 (22.7%)	
N1–3	22 (100%)	17 (77.3%)	
M-stage			NA
M0	22 (100%)	22 (100%)	
M1	0 (0%)	0 (0%)	

Note:—NA indicates not applicable; Oropharynx nos, oropharynx not otherwise specified.

[a] Smoking was defined in pack years (1 pack year = 20 cigarettes a day during 1 year).

[b] Alcohol consumption was defined in unit years (1 U year = 1 alcohol-containing consumption a day during 1 year).

DISCUSSION

OPSCCs may have a heterogeneous response to treatment, and survival varies among different groups of patients.[3,4,19] Tobacco smoking, alcohol consumption, and HPV play a role in this heterogeneity, and in particular, an HPV infection is a strong independent prognostic factor for survival in OPSCC.[4] Because traditional prognostic factors such as tumor size and lymph node involvement may be inadequate to classify patients into risk groups, identification of new prognostic tumor characteristics that may select patients for more or less aggressive treatment regimens becomes of interest. DWI may have prognostic value in HNSCC.[11-14] It is not known, however, whether the relatively low pretreatment ADC values, which are associated with better response to chemoradiotherapy in these studies, could be attributed to HPV status. This study shows that imaging parameters derived from DWI are not significantly associated with the OPSCC HPV status. Therefore, HPV status and ADC values may be factors that independently determine the prognosis of a patient with OPSCC.

HPV-related OPSCC is a clinically and histopathologically distinct disease entity.[20,21] In this study, we also found significant differences in clinical presentation, depending on HPV status; HPV-patients were more likely to have a T2 primary tumor but positive N-stage. Histopathologically, HPV-related tumors often have distinct features, characterized by a nonkeratinizing morphology and showing excessive mitoses and comedo-type necrosis, while HPV-negative OPSCC shows large polygonal cells and typical keratin formation.[8,15,20-22] In general, HPV-positive OPSCC is more poorly differentiated.[23] Characteristics of poorly differentiated squamous cell carcinomas, such as a higher cell attenuation

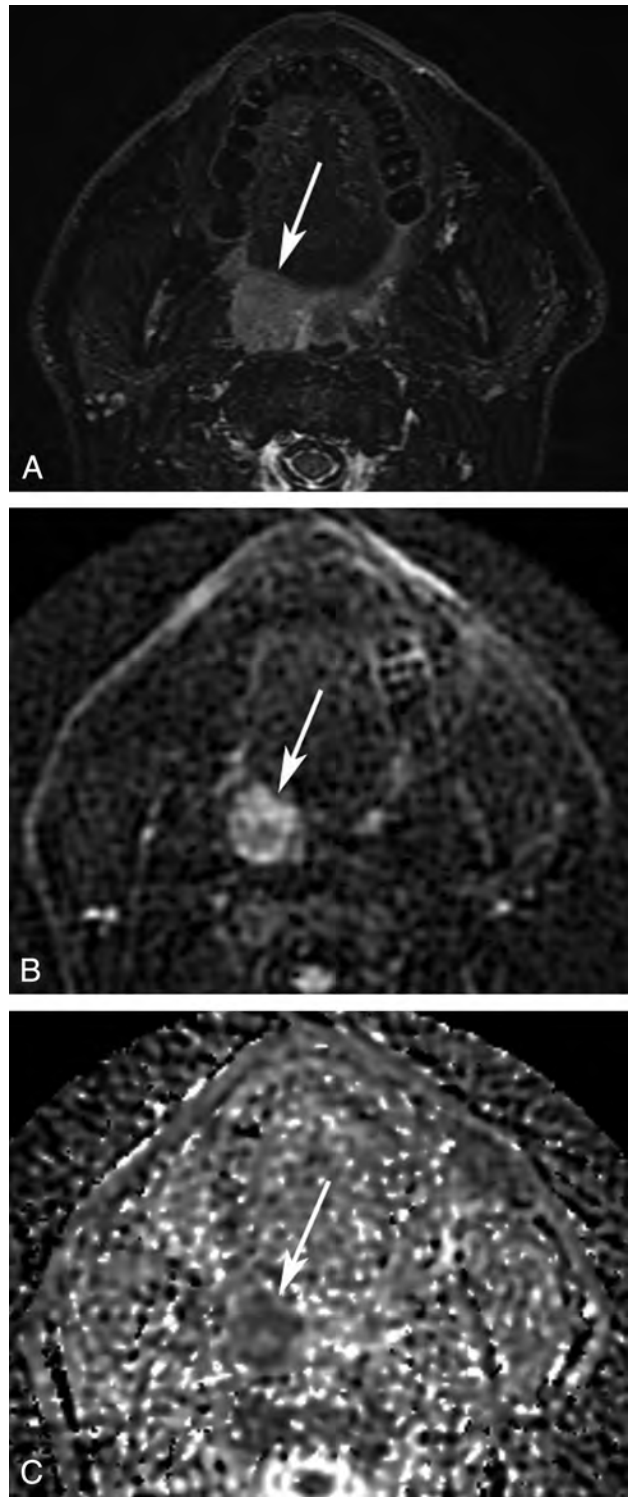

FIG 1. Axial MR images of an HPV-positive OPSCC. A 48-year-old patient was diagnosed with an OPSCC in the right palatine tonsil. *A*, STIR MR image shows a hyperintense mass in the palatine tonsil (*arrow*). A b=750 diffusion-weighted image (*B*) and an ADC map (*C*) show decreased ADC. An ROI was drawn on the b=750 diffusion-weighted image and copied to the ADC map. In this ROI, $ADC_{minimum}$ measured 0.992×10^{-3} mm^2/s.

and an increased nuclear-to-cytoplasmic ratio, reduce extracellular space and thereby the diffusion space of water protons, which could result in relatively low ADC values.[24,25] Indeed, Wang et al[24] found lower ADC values in poorly differentiated carcinomas

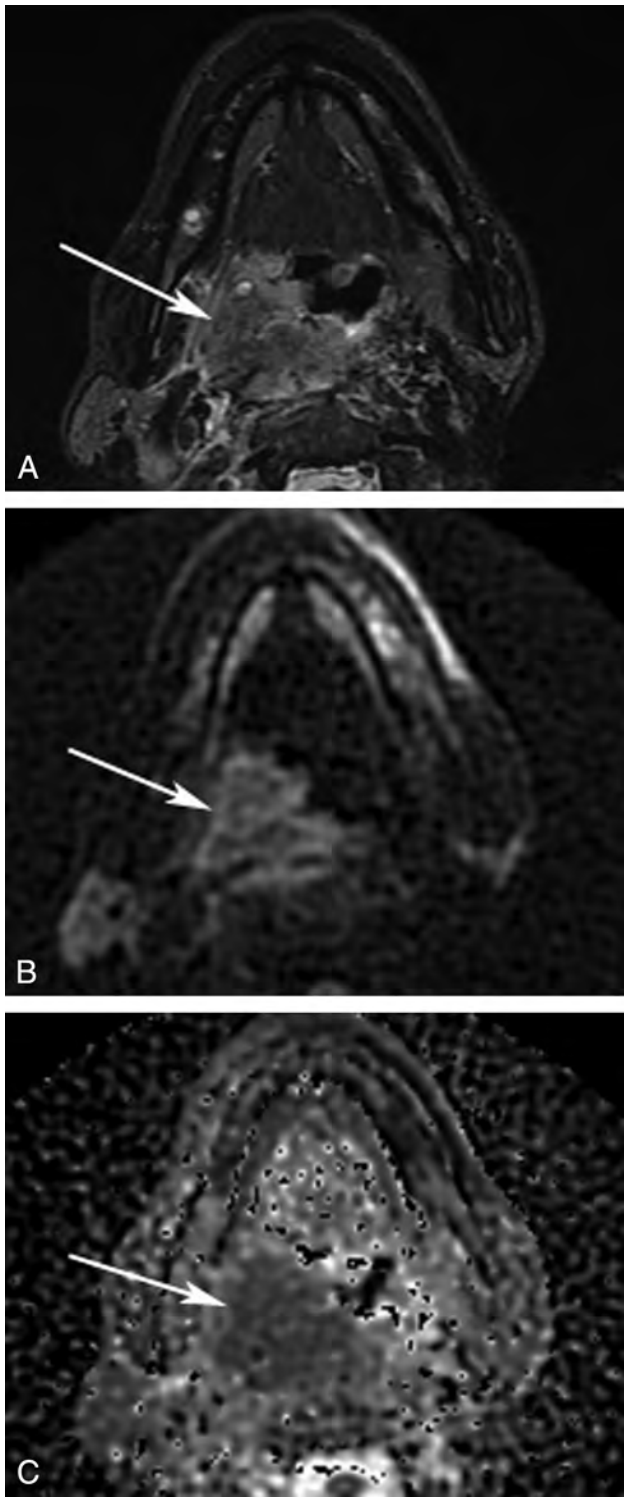

FIG 2. Axial MR images of an HPV-negative OPSCC. A 54-year-old patient was diagnosed with an OPSCC in the right palatine tonsil. *A*, STIR MR image shows a large hyperintense mass in the oropharynx (*arrow*). A $b=750$ diffusion-weighted image (*B*) and an ADC map (*C*) show decreased ADC. An ROI was drawn on the $b=750$ diffusion-weighted image and copied to the ADC map. In this ROI, $ADC_{minimum}$ measured 0.826×10^{-3} mm^2/s.

compared with well- or moderately differentiated carcinomas. It can be hypothesized that the distinct histologic features of HPV-positive and HPV-negative OPSCC may translate in different pretreatment ADC values. If this is the case, it would support the general opinion that low ADC values correlate with a better response to chemoradiotherapy.[11-14] Apparently, viable cells in a highly proliferating tumor (with low pretreatment ADC values) respond more favorably to chemoradiotherapy, probably related to the better vascularization that increases the exposure to chemotherapeutic agents.[12,26] This response is in contrast to tissues with high levels of necrosis (with high ADC values), leading to a detrimental effect on treatment efficacy.[27]

Table 2: Imaging DWI parameters in relation to HPV status[a]

	No.	ADC_{min} ($\times 10^3$ mm^2/s)	*P* Value	ADC_{mean} ($\times 10^3$ mm^2/s)	*P* Value
HPV			.67		.51
Positive	22	1.01 (0.62–1.55)		1.46 (1.07–2.16)	
Negative	22	1.07 (0.62–1.51)		1.56 (1.18–2.18)	

Note:—min indicates minimum.
[a] Values are presented as median (range).

In previous studies,[11-14] an association was reported between treatment response and pretreatment ADC values. This reported association could partly or even completely be attributed to the HPV status because patients with an HPV-positive OPSCC respond better to chemoradiotherapy than those who are HPV-negative. Unfortunately, the HPV status of the OPSCC studied was not included in the analyses. As outlined before, HPV-positive OPSCC has a different histology, and HPV involvement could translate into different ADC values. We found no association between pretreatment ADC and HPV status, and this finding suggests that ADC value and HPV status are independent characteristics in patients with OPSCC, each with their own prognostic value.

Currently, limited data are available regarding the association between HPV status and ADC in patients with OPSCC. Our data are in contrast to those of Nakahira et al,[16] who found significant lower pretreatment mean and minimum ADC values for HPV-positive than for HPV-negative OPSCCs. In their series of 26 patients, they used p16 protein overexpression as a surrogate marker for HPV infection. However, p16 immunohistochemistry is not an ideal surrogate marker for an HPV infection because a considerable percentage of patients are p16-positive but HPV-negative.[17,28] The application of p16 protein overexpression as a surrogate marker for HPV infection could have affected their results. In our institution, we use a validated algorithm for HPV detection: p16 immunostaining, followed by a general primer 5+/6 polymerase chain reaction on the p16-immunopositive cases. This algorithm showed an accuracy of 98%.[18] In addition, the conflicting data may also be explained by DWI factors; the choice of DWI-technique, the use of different b-values, and pulse sequences.

We acknowledge several limitations to this study. First, due to the retrospective study design that only included patients with an MR imaging with PROPELLER DWI, selection bias may have occurred. Second, the number of patients included was relatively small, and the study was performed in a single center. Finally, DWI studies were performed with a PROPELLER technique. DWI studies in HNSCC are most commonly performed with an echo-planar imaging sequence.[11,29,30] DWI of the head and neck area is particularly difficult, because this region is very inhomogeneous and susceptible to artifacts. If artifacts are too detrimental, a non-EPI technique, such as PROPELLER, may be a better alternative. Nevertheless, in some primary lesions, artifacts were present. Consequently, a smaller ROI was placed over only the undistorted area of the lesion.

CONCLUSIONS

Patients with HPV-positive OPSCC have a better survival rate compared with HPV-negative OPSCC. ADC values of DWI may also have prognostic value. In this study, we investigated a possible association between HPV status and ADC values in OPSCC. No significant associations were found between quantitative imaging parameters from DWI and HPV status in OPSCC. The differences in histologic features between HPV-positive and HPV-negative OPSCC did not translate into different pretreatment ADC values in our study cohort. Long-term follow-up studies are needed to investigate whether ADC values and HPV status are independent prognostic factors in patients with OPSCC treated by chemoradiotherapy.

ACKNOWLEDGMENTS

The authors thank M.M. Rietbergen and S. Hakim (Department of Otolaryngology–Head and Neck Surgery, VU University Medical Center, Amsterdam) for their assistance in retrieving HPV statuses and clinical characteristics. We also thank Daniel P. Noij (Department of Radiology and Nuclear Medicine, VU University Medical Center, Amsterdam) for assisting with ADC measurements.

Disclosures: Ruud Brakenhoff—*UNRELATED*: *Grants/Grants Pending*: European Union grants*; *Patents (planned, pending or issued)*: tumor-specific lethal microRNAs.* *Money paid to the institution.

REFERENCES

1. Ferlay J, Shin HR, Bray F, et al. **Estimates of worldwide burden of cancer in 2008: GLOBOCAN 2008.** *Int J Cancer* 2010;127:2893–917
2. Leemans CR, Braakhuis BJ, Brakenhoff RH. **The molecular biology of head and neck cancer.** *Nat Rev Cancer* 2011;11:9–22
3. Fakhry C, Westra WH, Li S, et al. **Improved survival of patients with human papillomavirus-positive head and neck squamous cell carcinoma in a prospective clinical trial.** *J Natl Cancer Inst* 2008;100:261–69
4. Ang KK, Harris J, Wheeler R, et al. **Human papillomavirus and survival of patients with oropharyngeal cancer.** *N Engl J Med* 2010;363:24–35
5. Braakhuis BJ, Snijders PJ, Keune WJ, et al. **Genetic patterns in head and neck cancers that contain or lack transcriptionally active human papillomavirus.** *J Natl Cancer Inst* 2004;96:998–1006
6. Smeets SJ, Brakenhoff RH, Ylstra B, et al. **Genetic classification of oral and oropharyngeal carcinomas identifies subgroups with a different prognosis.** *Cell Oncol* 2009;31:291–300
7. Thariat J, Badoual C, Faure C, et al. **Basaloid squamous cell carcinoma of the head and neck: role of HPV and implication in treatment and prognosis.** *J Clin Pathol* 2010;63:857–66
8. Chernock RD, El-Mofty SK, Thorstad WL, et al. **HPV-related nonkeratinizing squamous cell carcinoma of the oropharynx: utility of microscopic features in predicting patient outcome.** *Head Neck Pathol* 2009;3:186–94
9. Martincich L, Deantoni V, Bertotto I, et al. **Correlations between diffusion-weighted imaging and breast cancer biomarkers.** *Eur Radiol* 2012;22:1519–28
10. Choi SY, Chang YW, Park HJ, et al. **Correlation of the apparent diffusion coefficiency values on diffusion-weighted imaging with prognostic factors for breast cancer.** *Br J Radiol* 2012;85:e474–79
11. Kim S, Loevner L, Quon H, et al. **Diffusion-weighted magnetic resonance imaging for predicting and detecting early response to chemoradiation therapy of squamous cell carcinomas of the head and neck.** *Clin Cancer Res* 2009;15:986–94
12. Srinivasan A, Chenevert TL, Dwamena BA, et al. **Utility of pretreatment mean apparent diffusion coefficient and apparent diffusion coefficient histograms in prediction of outcome to chemoradiation in head and neck squamous cell carcinoma.** *J Comput Assist Tomogr* 2012;36:131–37
13. Chawla S, Kim S, Dougherty L, et al. **Pretreatment diffusion-weighted and dynamic contrast-enhanced MRI for prediction of local treatment response in squamous cell carcinomas of the head and neck.** *AJR Am J Roentgenol* 2013;200:35–43
14. Hatakenaka M, Nakamura K, Yabuuchi H, et al. **Pretreatment apparent diffusion coefficient of the primary lesion correlates with local failure in head-and-neck cancer treated with chemoradiotherapy or radiotherapy.** *Int J Radiat Oncol Biol Phys* 2011;81:339–45
15. Chernock RD, Lewis JS Jr, Zhang Q, et al. **Human papillomavirus-positive basaloid squamous cell carcinomas of the upper aerodigestive tract: a distinct clinicopathologic and molecular subtype of basaloid squamous cell carcinoma.** *Hum Pathol* 2010;41:1016–23
16. Nakahira M, Saito N, Yamaguchi H, et al. **Use of quantitative diffusion-weighted magnetic resonance imaging to predict human papilloma virus status in patients with oropharyngeal squamous cell carcinoma.** *Eur Arch Otorhinolaryngol* 2014;271:1219–25
17. Smeets SJ, Hesselink AT, Speel EJ, et al. **A novel algorithm for reliable detection of human papillomavirus in paraffin embedded head and neck cancer specimen.** *Int J Cancer* 2007;121:2465–72
18. Rietbergen MM, Leemans CR, Bloemena E, et al. **Increasing prevalence rates of HPV attributable oropharyngeal squamous cell carcinomas in the Netherlands as assessed by a validated test algorithm.** *Int J Cancer* 2013;132:1565–71
19. Lassen P, Eriksen JG, Hamilton-Dutoit S, et al. **Effect of HPV-associated p16INK4A expression on response to radiotherapy and survival in squamous cell carcinoma of the head and neck.** *J Clin Oncol* 2009;27:1992–98
20. Gillison ML, Koch WM, Capone RB, et al. **Evidence for a causal association between human papillomavirus and a subset of head and neck cancers.** *J Natl Cancer Inst* 2000;92:709–20
21. El-Mofty SK, Patil S. **Human papillomavirus (HPV)-related oropharyngeal nonkeratinizing squamous cell carcinoma: characterization of a distinct phenotype.** *Oral Surg Oral Med Oral Pathol Oral Radiol Endod* 2006;101:339–45
22. El-Mofty SK, Zhang MQ, Davila RM. **Histologic identification of human papillomavirus (HPV)-related squamous cell carcinoma in cervical lymph nodes: a reliable predictor of the site of an occult head and neck primary carcinoma.** *Head Neck Pathol* 2008;2:163–68
23. Mendelsohn AH, Lai CK, Shintaku IP, et al. **Histopathologic findings of HPV and p16 positive HNSCC.** *Laryngoscope* 2010;120:1788–94
24. Wang J, Takashima S, Takayama F, et al. **Head and neck lesions: characterization with diffusion-weighted echo-planar MR imaging.** *Radiology* 2001;220:621–30
25. Sumi M, Sakihama N, Sumi T, et al. **Discrimination of metastatic cervical lymph nodes with diffusion-weighted MR imaging in patients with head and neck cancer.** *AJNR Am J Neuroradiol* 2003;24:1627–34
26. Kim S, Loevner LA, Quon H, et al. **Prediction of response to chemoradiation therapy in squamous cell carcinomas of the head and neck using dynamic contrast-enhanced MR imaging.** *AJNR Am J Neuroradiol* 2010;31:262–68
27. Tatum JL, Kelloff GJ, Gillies RJ, et al. **Hypoxia: importance in tumor biology, noninvasive measurement by imaging, and value of its measurement in the management of cancer therapy.** *Int J Radiat Biol* 2006;82:699–757
28. Rietbergen MM, Snijders PJ, Beekzada D, et al. **Molecular characterization of p16-immunopositive but HPV DNA-negative oropharyngeal carcinomas.** *Int J Cancer* 2014;134:2366–72
29. Vandecaveye V, Dirix P, De Keyzer F, et al. **Predictive value of diffusion-weighted magnetic resonance imaging during chemoradiotherapy for head and neck squamous cell carcinoma.** *Eur Radiol* 2010;20:1703–14
30. King AD, Mo FK, Yu KH, et al. **Squamous cell carcinoma of the head and neck: diffusion-weighted MR imaging for prediction and monitoring of treatment response.** *Eur Radiol* 2010;20:2213–20

MRI Findings in Patients with a History of Failed Prior Microvascular Decompression for Hemifacial Spasm: How to Image and Where to Look

M.A. Hughes, B.F. Branstetter, C.T. Taylor, S. Fakhran, W.T. Delfyett, A.M. Frederickson, and R.F. Sekula Jr

ABSTRACT

BACKGROUND AND PURPOSE: A minority of patients who undergo microvascular decompression for hemifacial spasm do not improve after the first operation. We sought to determine the most common locations of unaddressed neurovascular contact in patients with persistent or recurrent hemifacial spasm despite prior microvascular decompression.

MATERIALS AND METHODS: Eighteen patients with a history of a microvascular decompression presented with persistent hemifacial spasm. All patients underwent thin-section steady-state free precession MR imaging. Fourteen patients underwent repeat microvascular decompression at our institution. Images were evaluated for the following: the presence of persistent vascular compression of the facial nerve, type of culprit vessel (artery or vein), name of the culprit artery, segment of the nerve in contact with the vessel, and location of the point of contact relative to the existing surgical pledget. The imaging findings were compared with the operative findings.

RESULTS: In 12 of the 18 patients (67%), persistent vascular compression was identified by imaging. In 11 of these 12 patients, the culprit vessel was an artery. Compression of the attached segment (along the ventral surface of the pons) was identified in most patients (58%, 7/12). The point of contact was proximal to the surgical pledget in most patients (83%, 10/12). The imaging interpretation was concordant with the surgical results regarding artery versus vein in 86% of cases and regarding the segment of the nerve contacted in 92%.

CONCLUSIONS: In patients with persistent hemifacial spasm despite microvascular decompression, the unaddressed vascular compression is typically proximal to the previously placed pledget, usually along the attached segment of the nerve. Re-imaging with high-resolution T2-weighted MR imaging will usually identify the culprit vessel.

ABBREVIATIONS: AICA = anterior inferior cerebellar artery; HFS = hemifacial spasm; MVD = microvascular decompression; PICA = posterior inferior cerebellar artery; SSFP = steady-state free precession

Hemifacial spasm (HFS) is characterized by unilateral spasms of the facial musculature.[1] While not life-threatening, the disease can profoundly reduce quality of life. It has an annual incidence of approximately 1 in 100,000 people per year.[2] HFS is most commonly the result of vascular compression of the facial nerve.[3] Microvascular decompression (MVD) of the facial nerve is a well-established treatment for HFS with success rates exceeding 90% for the initial operation.[4] Patients who have persistent HFS despite undergoing MVD pose a challenge for both neuroradiologists and neurosurgeons. However, many patients with unabated HFS despite prior MVD can and do benefit from repeat operations.[5,6] Failure to identify persistent vascular compression of the facial nerve can discourage reoperation and potential cure. The purpose of this article was to determine whether MR imaging could identify unaddressed neurovascular contact in patients with ongoing HFS despite prior MVD and to report the frequency and most common locations of this residual neurovascular contact.

Received August 5, 2014; accepted after revision September 30.

From the Departments of Radiology (M.A.H., B.F.B., C.T.T., S.F., W.T.D.), Neurosurgery (A.M.F., R.F.S.), and Otolaryngology (B.F.B.), University of Pittsburgh Medical Center, Pittsburgh, Pennsylvania.

Paper previously presented at: American Society of Neuroradiology Annual Meeting and the Foundation of the ASNR Symposium, May 17–22, 2014; Montreal, Quebec, Canada.

Please address correspondence to Raymond F. Sekula Jr, MD, University of Pittsburgh Medical Center, Department of Neurological Surgery, 200 Lothrop St, Suite B-400, Pittsburgh, PA 15213; e-mail: sekularf@upmc.edu

http://dx.doi.org/10.3174/ajnr.A4174

MATERIALS AND METHODS

Study Population

This retrospective review was approved by the institutional review board at the University of Pittsburgh Medical Center and was Health Insurance Portability and Accountability Act–compliant.

MVD imaging protocol[a]

Sequence and Plane	Flip Angle	FOV (cm)	TR/TE (ms)	Section Thickness (mm)	Spacing (mm)	Matrix
SSFP-axial	65°	18	Default to minimum	1	0.5	384 × 256
SSFP-coronal	65°	18	Default to minimum	1	0.5	384 × 256
SSFP-sagittal	65°	20	Default to minimum	1	0.5	384 × 256

[a] Also includes routine whole-brain sagittal T1-weighted, axial FLAIR, and diffusion sequences.

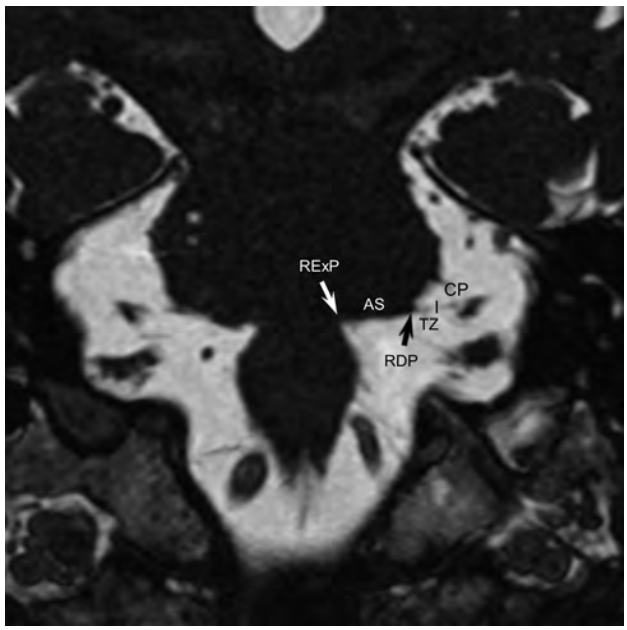

FIG 1. Facial nerve anatomy. Coronal SSFP image shows the expected locations of the root exit point (RExP, *white arrow*), the attached segment (AS) along the undersurface of the pons, and the root detachment point (RDP, *black arrow*). The transition zone (TZ) extends for approximately 3–4 mm anterolateral to the root detachment point. The cisternal portion of the facial nerve (CP) extends laterally toward the porous acusticus.

Patients presenting with persistent HFS despite prior MVD between January 2011 and December 2013 to a single neurosurgeon specializing in cranial nerve disorders were included in this study. Inclusion criteria were the following: history of a prior MVD, persistent HFS, availability of a thin-section steady-state free precession (SSFP) MR imaging performed after the date of the unsuccessful prior MVD, and having undergone a repeat MVD at our institution.

MR Imaging Technique

Patients with HFS who are being considered for repeat MVD undergo MR imaging at our institution tailored to delineate the facial nerve and adjacent vessels.[7] Studies are performed on either 1.5T or 3T MR imaging scanners (Optima and Discovery; GE Healthcare, Milwaukee, Wisconsin) and include whole-brain sagittal T1, axial FLAIR, and DWI sequences. Thin-section axial, coronal, and sagittal SSFP images through the brain stem are obtained. The imaging protocol is summarized in the Table.

Anatomic Terms

We used anatomic terms initially proposed by Tomii et al[8] in 2003 and expanded by Campos-Benitez and Kaufmann.[9] The facial nerve emerges from the brain stem within the pontomedullary sulcus at the root exit point. The facial nerve then adheres to the ventral surface of the pons for 8–10 mm, which is called the attached segment. It then separates from the pons at the root detachment point. The next segment is the transition zone of the facial nerve, which is an approximately 4-mm segment of the facial nerve where the central glial myelin transitions into the peripheral myelin created by Schwann cells. The central glial myelin does not exceed a point 4-mm distal to the root detachment point of the facial nerve.[8] After the transition zone, the cisternal portion of the nerve extends anterolaterally to the porous acusticus. The component of the nerve within the internal auditory canal is the canalicular segment. These anatomic/histologic segments can be approximated on thin-section SSFP MR imaging (Fig 1). The relevant facial nerve segments are also depicted in Fig 2.

Neurosurgical Clinical Evaluation

All patients were evaluated by a neurosurgeon (R.F.S.) who has 9 years of experience specializing in cranial nerve disorders and has performed >500 MVD operations for HFS. The diagnosis of persistent HFS was based on history and clinical evidence of persistent HFS on examination and was supported by electromyography.

Image Interpretation

Blinded to the surgical results, a single Certificate of Added Qualification–certified neuroradiologist (M.A.H.) reviewed the imaging to identify the following: the presence of a vessel contacting the facial nerve; whether the contacting vessel was an artery, vein, or both; which artery was responsible; which segment of the nerve was contacted; and whether this point of contact was proximal or distal to the existing pledget. A single neurosurgeon (R.F.S.) performed all repeat MVDs, and the imaging results were compared with his operative notes and detailed drawings performed after each case. Descriptive statistics were tabulated.

Surgical Technique

MVD was performed in the manner previously described.[10,11] In brief, the cerebellopontine angle was accessed through a retromastoid craniectomy measuring approximately 2 × 1.5 cm without the use of fixed retraction. The centrally myelinated portion of the facial nerve, from the root exit point to 4 mm distal to the root detachment point, was inspected for residual compression. Monopolar stimulation was used to assist in identifying the nerve along the attached segment. Any vascular compression found along this portion of the facial nerve was decompressed by using shredded Teflon (Dupont, Wilmington, Delaware) pledgets of varying sizes. On occasion, the previously achieved decompression was bolstered with additional pledgets. Of note, the presence of scarring and adhesions typically makes operative exposure of the facial nerve more difficult in repeat MVD operations, sometimes adding an additional hour to the operative time.

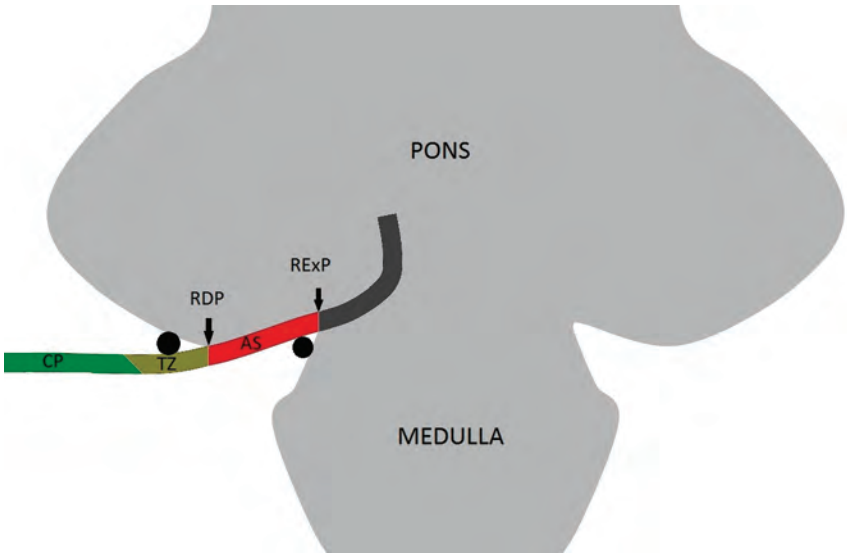

FIG 2. Coronal drawing demonstrates the facial nerve exiting the brain stem at the root exit point (RExP) in the pontomedullary sulcus. The attached segment (AS) of the nerve then runs along the pons until the nerve separates from the brain stem at the root detachment point (RDP). The transition zone (TZ) is the 3- to 4-mm segment of the facial nerve where the central glial myelin transitions into the peripheral myelin. The cisternal portion (CP) of the facial nerve is noted laterally. *Black circles* demonstrate common points of arterial compression of the facial nerve.

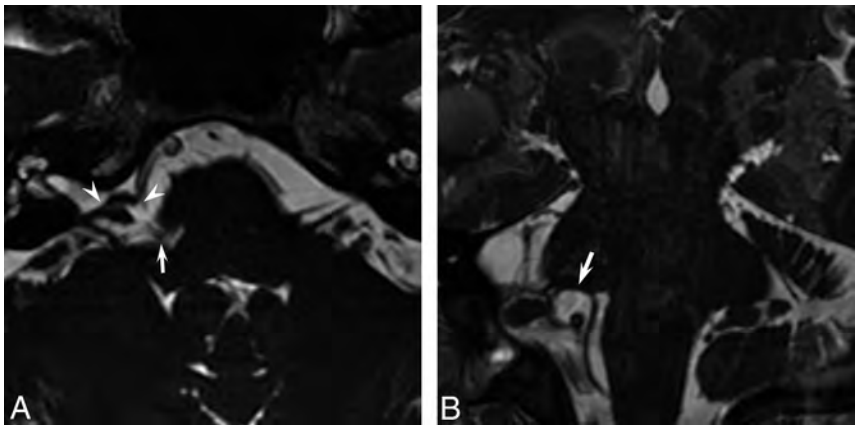

FIG 3. *A*, Axial SSFP image demonstrates the low-signal Teflon pledget (*white arrowheads*) in the right cerebellopontine angle, indicating a prior surgical decompression of the cisternal portion of the facial nerve. The right PICA is located medial to the pledget in the pontomedullary sulcus (*white arrow*). *B*, On a coronal SSFP image, the right PICA is noted to contact and deform the undersurface of the pons along the attached segment of the facial nerve (*white arrow*). This culprit vessel was confirmed and treated surgically, with complete resolution of facial spasms.

Clinical Follow-Up

Patients were contacted postoperatively via phone by a disinterested observer (A.M.F.). He administered a detailed questionnaire that addressed the presence or absence of HFS. Patients were asked to characterize their outcome after each procedure as complete spasm relief, >75% spasm relief, >50% spasm relief, or <50% spasm relief. To better assess quality of life following repeat MVD for HFS, patients were asked, "Would you elect to undergo the same procedure again if you found yourself in similar circumstances?"[12]

RESULTS

Eighteen patients with a history of a prior MVD presented with persistent HFS. Fourteen patients were offered and subsequently underwent a repeat MVD at our institution. Twelve of the 14 patients had their initial operation at an outside institution. The age range of patients at the time of the operation was 27–65 years; mean, 49 years. Ten patients were women and 4 were men. The persistent HFS was right-sided in 9 patients and left-sided in 5 patients.

Of the 14 patients included in our study, 12 (86%) had imaging evidence of persistent vascular compression of the facial nerve. The posterior inferior cerebellar artery (PICA) was the sole culprit vessel in 5 patients (42%, 5/12), the anterior inferior cerebellar artery (AICA) was the sole culprit vessel in 5 patients (42%, 5/12), and both the AICA and PICA contacted the facial nerve in 1 patient (8%, 1/12). A vein was identified contacting the facial nerve in 1 patient (8%, 1/12). No neurovascular contact was seen on MR imaging in 2 patients. Of the patients with vascular contact, the location was the following: the attached segment in 7 patients (58%, 7/12), the root detachment point in 1 patient (8%, 1/12), and the transition zone in 4 patients (33%, 4/12). The point of contact was proximal to the pledget in 10 patients (83%, 10/12) and distal to the pledget in 2 patients (17%, 2/12). Thus, persistent neurovascular contact was along the more proximal portion of the facial nerve in most patients. Imaging examples demonstrating proximal unaddressed vascular compression of the facial nerve following the first MVD are presented in Figs 3 and 4.

Three patients without imaging evidence of arterial compression on retrospective imaging review underwent repeat surgical decompression. Intraoperatively, only small arterioles were noted contacting the attached segment of the facial nerve in 2 of these patients (Fig 5). In the third patient, the AICA was identified contacting the attached segment intraoperatively, but only a vein was identified contacting the facial nerve on imaging.

Four patients were not offered repeat decompression. Three of these patients had no evidence of persistent vascular compression, and 1 patient had arterial contact of the cisternal portion (peripherally myelinated segment) of the facial nerve, distal to the existing pledget.

The imaging interpretation was concordant with the surgical results regarding artery versus vein in 12 patients (86%, 12/14). In 1 patient, a vein contacting the transition zone was identified by imaging, but intraoperatively, the AICA was noted to contact the attached segment. In the other patient, the AICA was noted con-

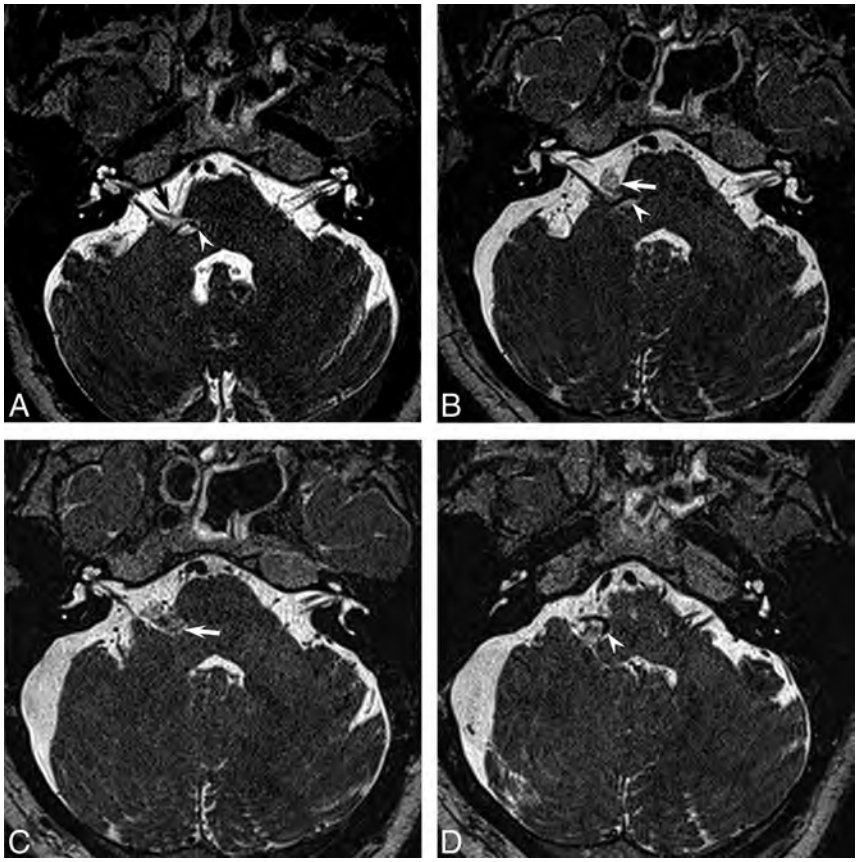

FIG 4. *A*, Preoperative axial image demonstrates 2 points of arterial contact of the facial nerve: The right AICA contacts the transition zone of the facial nerve (*black arrow*) and the right PICA contacts the attached segment of the nerve (*white arrowhead*). *B*, Postoperative axial image following the initial MVD demonstrates a Teflon pledget (*white arrow*) lateral to the pons, which decompressed the AICA from the transition zone of the facial nerve. Note that the PICA along the attached segment (*white arrowhead*) remains unaddressed. The patient had no significant reduction in spasms following this operation. *C* and *D*, Postoperative axial images following the second MVD demonstrate an additional pledget (*white arrow*, *C*) decompressing the attached segment of the nerve and displacing the PICA inferiorly (*white arrowhead*, *D*). The patient was spasm-free following the second MVD.

tacting the transition zone but intraoperatively only venous contact of the facial nerve was noted. In the 11 patients with arterial contact of the facial nerve identified by imaging who underwent repeat MVD, the radiologist's naming of the vessel was concordant with the surgeon's findings in 7 patients (63% 7/11). In the 12 patients with neurovascular contact identified by imaging (either arterial or venous), the imaging findings regarding the segment of the nerve contacted were concordant with the surgical findings in 11 patients (92%, 11/12).

Of the 14 patients who underwent repeat MVD, 12 were successfully contacted via phone and questioned regarding continued symptoms. The follow-up range was 4.0–35.9 months following the repeated MVD, with a median follow-up duration of 12.7 months. Nine of 12 patients were either spasm-free (7 patients) or had >75% reduction in their spasm frequency (2 patients). Two patients had no improvement in the frequency of their spasms, and 1 patient reported a <50% reduction, specifically a 20% reduction in spasms. Ten patients (83%, 10/12) contacted said that they would repeat the operation if they found themselves in similar circumstances. Of the 2 patients with no improvement in spasms, 1 had arterial contact along the most distal aspect of the transition zone where the centrally myelinated portion of the nerve transitions into the more resistant peripherally myelinated portion, and the other patient had only venous contact of the facial nerve identified by imaging and was also 1 of the 2 patients in whom the imaging and surgical results regarding artery versus vein were discordant.

DISCUSSION

MVD is the only permanent treatment of HFS and has a high success rate of approximately 90% for the initial surgery in experienced hands.[5,13-15] Reasons for an unsuccessful MVD include not identifying the true culprit vessels and incomplete vascular decompression.[16] Additionally, a subpopulation of <10% of patients do not improve despite undergoing a technically successfully procedure, possibly due to a central mechanism.[5,13-16] The existing literature regarding surgical success rates for repeat MVD in the setting of persistent HFS is less extensive. The anatomic location along the facial nerve where persistent vascular compression was identified in repeat MVD surgeries has not been well-described in the existing literature. Engh et al[6] performed 41 repeat MVDs for HFS and reported a favorable outcome in 82.4% of patients; however, the sites of persistent compression of the facial nerve relative to the prior surgical decompression site were described in only 2 cases. Zhong et al[13] reported results on 30 patients who underwent repeat MVD for persistent HFS, with all patients demonstrating improvement postoperatively. The authors reported that the failed first MVD was because the true culprit vessel was more proximal than expected. The authors further described the culprit artery as rostral to the facial nerve in 9 patients, between the seventh and eighth nerve in 9 patients, along the cisternal portion in 7 patients, and in the pontomedullary fissure in 15 patients. Wang et al[16] reported the surgical outcome of 33 patients who underwent repeat MVD, with 85% of patients experiencing long-term relief, but they did not delineate the sites of persistent compression.

Unknown by many physicians and of critical importance is that the location of neurovascular contact resulting in HFS is often along the attached segment of the facial nerve along the ventral surface of the pons. In a study of 115 patients undergoing their first MVD for HFS, the contact location in most patients (64%) was the attached segment.[9] In our study, persistent neurovascular contact along the attached segment was identified by imaging in 50% (7/14) of all patients and in 58% (7/12) of patients with radiologically identifiable culprit vessels. Thus, the attached seg-

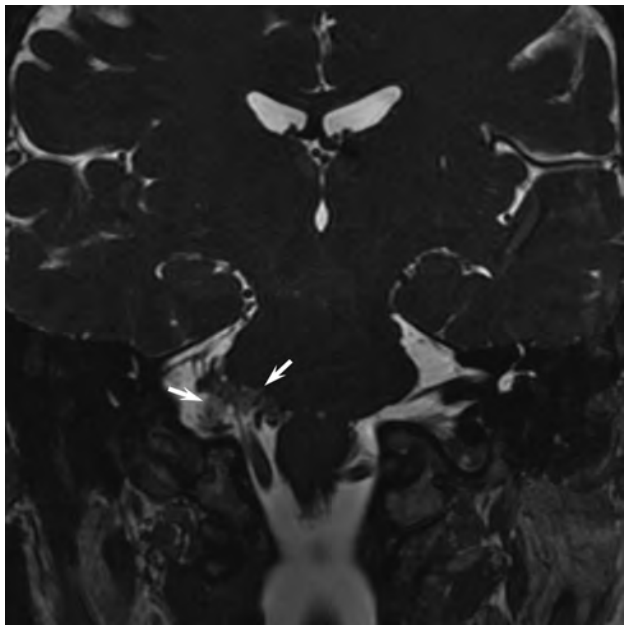

FIG 5. Coronal SSFP image demonstrates a large pledget (*white arrow*) along the attached segment of the facial nerve. No residual vascular compression of the nerve was identified by imaging. Intraoperatively, the previously placed pledget was removed and a small arteriole was identified contacting the attached segment of the nerve. The arteriole was addressed, and the patient was spasm-free postoperatively. This case illustrates how difficult it can be to interpret these imaging studies in the setting of prior pledget placement.

ment of the facial nerve extending along the ventral surface of the pons must be carefully scrutinized in all patients with HFS, including those who have undergone prior MVD. With improved MR imaging techniques, there is increasing reliance on imaging to identify vascular compression before both the first MVD and on any subsequent repeat operations. If a radiologist does not identify a site of persistent compression when present and instead reports that the facial nerve is well-decompressed, a patient may not be offered surgery and thus be denied a potential cure.

Historically, neurosurgeons have used MR imaging in the evaluation of patients with HFS to rule out confounding diagnoses such as neoplasms, vascular malformations, and multiple sclerosis.[14] However, improvements in MR imaging have led to an increased interest in its use for evaluating vascular compression of the cranial nerves.[17-20] The use of SSFP imaging has been shown to predict vascular compression of the facial nerve with sensitivities of 75%–93% and specificities of 29%–75% for blinded observers.[21] In light of this higher sensitivity and lower specificity, the decision to operate is supported by imaging, but imaging results are never the sole factor in determining whether to offer MVD to a patient. Specifically, at our institution, an operation is typically not offered to a clinically unfavorable candidate even if imaging demonstrates vascular compression of the facial nerve. However, a clinically favorable candidate will be warned that MVD has a lower chance of success if imaging does not clearly demonstrate a compressive vessel.

This study was limited by being a single-center retrospective study with a small number of patients. HFS is a rare disease that has a high surgical cure rate with initial surgeries, so the potential number of patients with persistent HFS following MVD is low. A single neuroradiologist reviewed the images retrospectively; the original reports of the studies were not used because as neuroradiologists, our understanding of the proximal facial nerve anatomy and in particular the more susceptible centrally myelinated portions of the nerve has increased rapidly during the past 2 years after a neurosurgeon specializing in cranial nerve disorders joined our institution. Many of the initial reports described vascular contact of the facial nerve only along its cisternal portion. Finally, preoperative SSFP imaging before the initial MVD was not available in most of our patients (86%, 12/14). This fact limits our ability to definitively confirm the original point of neurovascular contact.

CONCLUSIONS

Patients with persistent HFS despite prior MVD often have identifiable persistent neurovascular compression along the centrally myelinated susceptible portion of the facial nerve when imaged with dedicated thin-section SSFP sequences. In most patients, this compression occurs proximal to the existing surgical pledget. The attached segment of the facial nerve must be closely scrutinized to identify persistent neurovascular contact and thus guide the surgical management of these patients.

REFERENCES

1. Tan NC, Chan LL, Tan EK. **Hemifacial spasm and involuntary facial movements.** *QJM* 2002;95:493–500
2. Auger RG, Whisnant JP. **Hemifacial spasm in Rochester and Olmsted County, Minnesota, 1960 to 1984.** *Arch Neurol* 1990;47:1233–34
3. Jannetta PJ, Abbasy M, Maroon JC, et al. **Etiology and definitive microsurgical treatment of hemifacial spasm: operative techniques and results in 47 patients.** *J Neurosurg* 1977;47:321–28
4. Miller LE, Miller VM. **Safety and effectiveness of microvascular decompression for treatment of hemifacial spasm: a systematic review.** *Br J Neurosurg* 2012;26:438–44
5. Sekula RF Jr, Frederickson AM, Arnone GD, et al. **Microvascular decompression for hemifacial spasm in patients >65 years of age: an analysis of outcomes and complications.** *Muscle Nerve* 2013; 48:770–76
6. Engh JA, Horowitz M, Burkhart L, et al. **Repeat microvascular decompression for hemifacial spasm.** *J Neurol Neurosurg Psychiatry* 2005;76:1574–80
7. Hughes MA, Branstetter BF, Frederickson AM, et al. **Imaging hemifacial spasm.** *Neurographics* 2015;5:2–8
8. Tomii M, Onoue H, Yasue M, et al. **Microscopic measurement of the facial nerve root exit zone from central glial myelin to peripheral Schwann cell myelin.** *J Neurosurg* 2003;99:121–24
9. Campos-Benitez M, Kaufmann AM. **Neurovascular compression findings in hemifacial spasm.** *J Neurosurg* 2008;109:416–20
10. Sekula RF Jr, Bhatia S, Frederickson AM, et al. **Utility of intraoperative electromyography in microvascular decompression for hemifacial spasm: a meta-analysis.** *Neurosurg Focus* 2009;27:E10
11. Wilson CB. *Neurosurgical Procedures: Personal Approaches to Classic Operations*. Baltimore: Lippincott Williams & Wilkins; 1992
12. Linskey ME, Ratanatharathorn V, Penagaricano J. **A prospective cohort study of microvascular decompression and gamma knife surgery in patients with trigeminal neuralgia.** *J Neurosurg* 2008; 109(suppl):160–72
13. Zhong J, Li ST, Zhu J, et al. **A clinical analysis on microvascular decompression surgery in a series of 3000 cases.** *Clin Neurol Neurosurg* 2012;114:846–51
14. Barker FG 2nd, Jannetta PJ, Bissonette DJ, et al **Microvascular decompression for hemifacial spasm.** *J Neurosurg* 1995;82:201–10
15. McLaughlin MR, Jannetta PJ, Clyde et al. **Microvascular decompression of cranial nerves: lessons learned after 4400 operations.** *J Neurosurg* 1999;90:1–8

16. Wang X, Thirumala PD, Shah A, et al. **Microvascular decompression for hemifacial spasm: focus on late reoperation.** *Neurosurg Rev* 2013; 36:637–43; discussion 643–44
17. Sheth S, Branstetter BF 4th, Escott EJ. **Appearance of normal cranial nerves on steady-state free precession MR images.** *Radiographics* 2009;29:1045–55
18. Raslan AM, DeJesus R, Berk C, et al. **Sensitivity of high-resolution three-dimensional magnetic resonance angiography and three-dimensional spoiled-gradient recalled imaging in the prediction of neurovascular compression in patients with hemifacial spasm.** *J Neurosurg* 2009;111:733–36
19. Iijima K, Horiguchi K, Yoshimoto Y. **Microvascular decompression of the root emerging zone for hemifacial spasm: evaluation by fusion magnetic resonance imaging and technical considerations.** *Acta Neurochir (Wien)* 2013;155:855–62
20. Kanoto M, Toyoguchi Y, Hosoya T, et al. **Visualization of the trochlear nerve in the cistern with use of high-resolution turbo spin-echo multisection motion-sensitized driven equilibrium.** *AJNR Am J Neuroradiol* 2013;34:1434–37
21. Sekula RF Jr, Frederickson AM, Branstetter BF, et al. **Thin-slice T2 MRI imaging predicts vascular pathology in hemifacial spasm: a case-control study.** *Mov Disord* 2014;29:1299–303

Association of Superior Oblique Muscle Volumes with the Presence or Absence of the Trochlear Nerve on High-Resolution MR Imaging in Congenital Superior Oblique Palsy

H.K. Yang, D.S. Lee, J.H. Kim, and J.-M. Hwang

ABSTRACT

BACKGROUND AND PURPOSE: Congenital superior oblique palsy is known to relate to trochlear nerve absence and a variable degree of superior oblique muscle hypoplasia. The purpose of this study was to determine whether superior oblique muscle volume predicts trochlear nerve absence in congenital superior oblique palsy.

MATERIALS AND METHODS: A retrospective study of high-resolution MR imaging to evaluate the presence of the trochlear nerve and to measure superior oblique muscle areas and volumes with the image analysis tools of a PACS was performed in 128 consecutive patients with unilateral congenital superior oblique palsy and 34 age-matched healthy controls.

RESULTS: Of the 128 patients with congenital superior oblique palsy, 88 had an ipsilateral trochlear nerve absence (absent group) and 40 had both trochlear nerves (present group). In patients with congenital superior oblique palsy, the paretic side superior oblique muscle volume was significantly smaller compared with the normal side only in the absent group ($P < .001$). The left and right side superior oblique muscle volumes were not significantly different in controls ($P = .750$), and the paretic and normal side superior oblique muscle volumes were not significantly different in the present group ($P = .536$). The cutoff value of the paretic/normal side superior oblique muscle volume ratio for diagnosing trochlear nerve absence was ≤0.75 (sensitivity 98.9%, specificity 95.0%) in patients with congenital superior oblique palsy.

CONCLUSIONS: The ratio of paretic/normal side superior oblique muscle area and volume has an excellent predictability in diagnosing trochlear nerve absence in congenital superior oblique palsy.

ABBREVIATIONS: AUC = area under the receiver operating characteristic curve; SO = superior oblique muscle; SOP = superior oblique palsy

Advanced imaging modalities and functional anatomy have helped us understand the etiology and pathophysiology of superior oblique palsy (SOP).[1-12] Previous studies of SOP by using MR imaging have consistently shown a variable degree of hypoplasia of the paretic superior oblique muscle (SO) and variable trochlear nerve absence.[1-5] In our recent study of patients with congenital SOP, 73% had ipsilateral trochlear nerve absence and a variable degree of SO hypoplasia, while the remaining 27% had a normal-appearing SO and trochlear nerve on both sides, suggesting a different etiology.[3]

Consistent identification of the trochlear nerve, however, requires high-resolution MR imaging with at least a 3T system, 0.25-mm section thickness, a scanning plane set to an oblique axial direction parallel to the course of the trochlear nerve, and experienced interpretation. Thus, it may not be practical to perform high-resolution MR imaging in many institutions. On the other hand, the cross-sectional area of the SO is easily determined in the coronal plane of the most commonly used orbital MR imaging sequences, or CT. Therefore, it would be useful to be able to predict trochlear nerve absence by the degree of SO hypoplasia. Nevertheless, a quantified volumetric evaluation of the SO and its relationship to the presence or absence of the trochlear nerve has

Received August 30, 2014; accepted after revision October 26.

From the Departments of Ophthalmology (H.K.Y., D.S.L., J.-M.H.) and Radiology (J.H.K.), Seoul National University College of Medicine, Seoul National University Bundang Hospital, Seongnam, Korea.

H.K. Yang and D.S. Lee contributed equally to this work.

This work was supported by the Basic Science Research Program through the National Research Foundation of Korea funded by the Ministry of Education, Science and Technology (2013R1A1A2010606) and the Interdisciplinary Research Initiatives Program by College of Engineering and College of Medicine, Seoul National University (2012).

Please address correspondence to Jeong-Min Hwang, MD, Department of Ophthalmology, Seoul National University College of Medicine, Seoul National University Bundang Hospital, 166 Gumiro, Bundang-gu, Seongnam, Gyeonggi-do 463-707, Korea; e-mail: hjm@snu.ac.kr; and Jae Hyoung Kim, MD, Department of Radiology, Seoul National University College of Medicine, Seoul National University Bundang Hospital, 166 Gumiro, Bundang-gu, Seongnam, Gyeonggi-do 463-707, Korea; e-mail: jaehkim@snubh.org

http://dx.doi.org/10.3174/ajnr.A4202

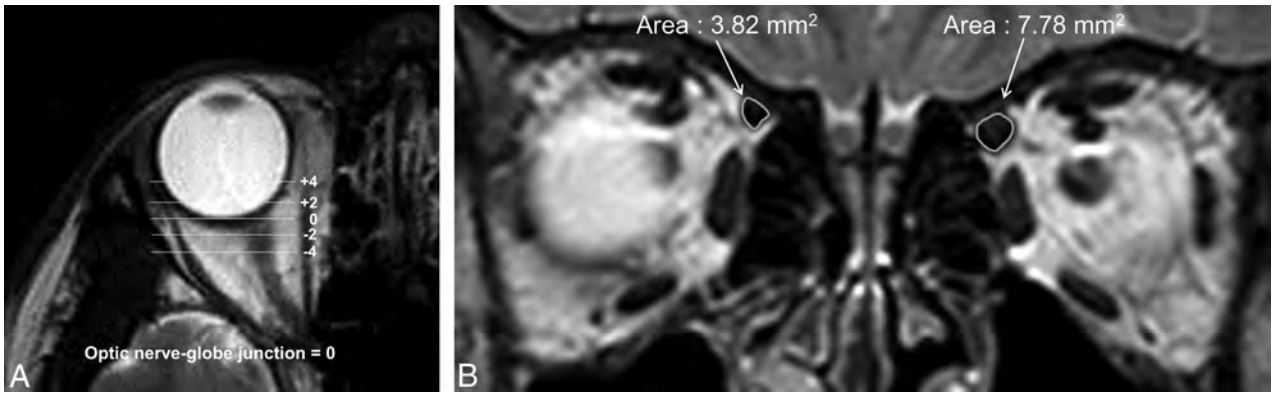

FIG 1. MR imaging in a patient with right superior oblique muscle palsy. *A*, The optic nerve–globe junction was defined as the standard plane (plane "0"), and SO areas were measured in the coronal sections of 5 contiguous planes, including the standard plane and planes that were 2 and 4 mm anterior or posterior to the standard plane. *B*, T2-weighted coronal image of the orbit and SO. The right SO is hypoplastic compared with the left. The area surrounded by the curvilinear line was measured in 5 different planes, by using DTU-710 (Wacom) and PACS software, which provides automatic measurements for area. The volume of the SO was defined as the sum of SO areas at the 5 planes multiplied by 2 mm.

not yet been determined, to our knowledge. In this study, we measured the cross-sectional areas and volume of the SO by using MR imaging and determined the ability of SO volumetry to predict trochlear nerve absence in patients with congenital SOP.

MATERIALS AND METHODS

A retrospective review of medical records was performed for 128 consecutive patients diagnosed with unilateral congenital SOP and 34 age-matched controls who had undergone thin-section MR imaging at the brain stem level at Seoul National University Bundang Hospital between August 2009 and June 2012. Patients were included if they showed the typical signs of congenital SOP, including apparent underdepression and overelevation in adduction on the affected side, positive head tilt test results, large fusional amplitudes of vertical deviation, and a history or photographic evidence of long-standing strabismus or anomalous head posture dating to infancy. Patients who had primary overaction of the inferior oblique muscle on the affected side, any evidence of acquired disease, a history of head or ocular trauma, or other potential causes, such as plagiocephaly, skew deviation, myasthenia gravis, or the ocular tilt reactions, were excluded. Subjects without strabismus and patients with simple horizontal strabismus without oblique muscle dysfunction were enrolled as the control group. Patient characteristics noted included sex, age at examination, and laterality of the paretic side. Approval to conduct this study was obtained from the institutional review board of Seoul National University Bundang Hospital.

Superior Oblique Muscle Volumetry

MR imaging was performed by using a 3T system (Intera Achieva; Philips Healthcare, Best, the Netherlands) with an 8-channel sensitivity encoding head coil, initially with T2-weighted imaging of the entire brain and the orbit and subsequently with high-resolution imaging of cranial nerves and the brain stem.[3] The initial orbital imaging to evaluate the extraocular muscles was performed, without the use of visual targets for fixation, with the turbo spin-echo technique. The sequence protocol was same as that in our previous studies.[3,4]

The SO area was measured on T2-weighted coronal images of the orbit. The optic nerve–globe junction was defined as the standard plane (plane "0"), and SO areas were measured in 5 contiguous coronal image planes, including the standard plane and the planes that were 2 mm and 4 mm anterior or posterior to the standard plane (Fig 1). We measured the area of the SO by using DTU-710 (Wacom, Saitama, Japan) and PACS software, which provides automatic measurement for area. The volume of the SO was defined as the sum of SO areas at the 5 planes multiplied by 2 mm. Measurement of the SO area on the 5 planes, SO volume, ratios of paretic/normal side SO area, and volume (left/right for controls, paretic/nonparetic for those with SOP) were investigated. Three individual interpreters measured the data, blinded to the patient's clinical status and trochlear nerve image. Measurements were repeated 3 times for each examiner, and the average of the 9 values was used for the comprehensive analysis.

Statistical Analyses

Statistical analyses were performed by using SPSS software for Windows, Version 18.0 (IBM, Armonk, New York). We compared groups by using the ANOVA with a Bonferroni post hoc test and the Pearson χ^2 test. The sensitivity and the specificity of SO area and SO volume for predicting trochlear nerve absence were determined by receiver operating characteristic curves and area under the receiver operating characteristic curves (AUCs). The interobserver intraclass correlation coefficients and their 95% confidence intervals were calculated among the measurements.

RESULTS

Patient Characteristics

Of the 128 consecutive patients diagnosed with unilateral congenital SOP (88 patients with an ipsilateral trochlear nerve absence and 40 patients with normal anatomy of the trochlear nerve on both sides), 3 were excluded due to poor quality of MR images, with obscured SO margins in the midst of surrounding soft tissues and motion artifacts, or with an SO tendon extending more posteriorly than the optic nerve–globe junction in both eyes. Hence, MR imaging measurements of the SO were performed on 125 patients with unilateral congenital SOP and 34 age-matched healthy controls. Of the 125 patients with unilateral congenital

Patient characteristics and the superior oblique muscle area and volume measured in controls and patients with congenital superior oblique palsy without (absent group) and with (present group) an ipsilateral trochlear nerve

	Control (n = 34)	Absent Group (n = 87)	Present Group (n = 38)	P Value
Age at time of imaging (yr)	16.1 ± 20.7 (1–69)	15.2 ± 17.9 (1–64)	11.5 ± 13.0 (1–58)	.896[a]
Age of onset (yr)		10.8 ± 16.9 (0–63)	7.7 ± 13.4 (0–58)	.317[b]
Interval between onset and imaging (yr)		3.8 ± 6.4 (0–44)	3.8 ± 4.8 (0–23)	.967[b]
Male sex	16 (47.0%)	55 (63.2%)	21 (55.3%)	.283[c]
Paretic side				
Right		48 (55.2%)	17 (44.7%)	.085[c]
Left		39 (44.8%)	21 (55.3%)	
SO area "0" (P)	4.58 ± 1.05 (2.68–6.89)	2.12 ± 0.96 (0.34–4.59)	5.01 ± 1.02 (3.39–7.78)	<.001[a]
SO area "0" (N)	4.43 ± 1.23 (2.41–8.53)	5.34 ± 1.31 (2.17–10.45)	4.87 ± 1.11 (3.11–8.17)	.001[a]
SO area "0" ratio (P/N)[d]	1.06 ± 0.18 (0.78–1.42)	0.40 ± 0.15 (0.05–0.75)	1.04 ± 0.10 (0.86–1.21)	<.001[a]
SO volume (P)[e]	41.57 ± 8.15 (27.03–61.17)	21.53 ± 8.69 (3.92–40.12)	46.99 ± 9.50 (28.52–75.99)	<.001[a]
SO volume (N)[f]	40.94 ± 9.87 (24.16–73.10)	49.31 ± 11.15 (27.93–94.04)	46.76 ± 9.60 (30.95–76.00)	.001[a]
SO volume ratio (P/N)[d]	1.03 ± 0.15 (0.84–1.54)	0.44 ± 0.15 (0.07–0.74)	1.03 ± 0.10 (0.79–1.20)	<.001[a]

Note:—P indicates paretic side; N, normal side; "0", measured at the optic nerve-globe junction (standard plane).
[a] P value by ANOVA.
[b] P value by independent t test.
[c] P value by Pearson χ^2.
[d] Left-to-right ratio for controls and paretic side to normal side ratio for patients with congenital SOP in the absent and present group.
[e] Left side for controls.
[f] Right side for controls.

SOP, 87 (69.6%) were found with an ipsilateral trochlear nerve absence (absent group) and 38 (30.4%) had normal anatomy of the trochlear nerve on both sides (present group). Controls without SOP had normal anatomic features of the trochlear nerves on both sides (control group). The mean age and sex distribution were not significantly different among the groups (P = .896, 0.283, respectively). There was no significant difference in the laterality of SOP between the absent and present group (P = .085) (Table).

Superior Oblique Muscle Area and Volume

In patients with congenital SOP with an absent trochlear nerve, the paretic side SO areas at all 5 contiguous coronal image planes and SO volume were significantly smaller compared with the normal side SO (P < .001 by a paired t test). However, there was no significant difference between the paretic and normal side SO areas and volume in the present group (P = .536), and there was no difference in both sides of SO areas and volume in controls (P = .750). The paretic/normal side ratios of SO areas and SO volume were significantly smaller in the absent group compared with other groups (P < .001) (Table and Fig 2). The calculated interobserver intraclass correlation coefficient of the measured SO area was 0.770 (95% CI, 0.747–0.790, P < .001).

The paretic side SO areas in the absent group were smaller than those of the present group and those of the left sides in the controls in all 5 planes (P < .001 by ANOVA, post hoc Bonferroni correction). The paretic side SO areas in the present group were not significantly different from those of the left sides in the controls (P > .05 for all 5 planes). The normal side SO areas and volume in congenital SOP were larger than those in controls (P < .001 by ANOVA), but those of the absent group and present group did not show a significant difference (P > .05 by ANOVA, post hoc Bonferroni correction).

Predictability of Trochlear Nerve Absence by SO Area and Volume

Among the receiver operating characteristic curves for predicting trochlear nerve absence (paretic side SO areas, paretic side SO volume, ratios of paretic/normal side SO areas and volume), AUC was largest for the paretic/normal side ratio of SO volume and SO area at the optic nerve–globe junction (AUC > 0.950) (Fig 3). The cutoff value of the ratio of paretic/normal side SO volume and SO area at the optic nerve–globe junction for diagnosing trochlear nerve absence was ≤0.75 (sensitivity 98.9%, specificity 95.0%) in patients with congenital SOP.

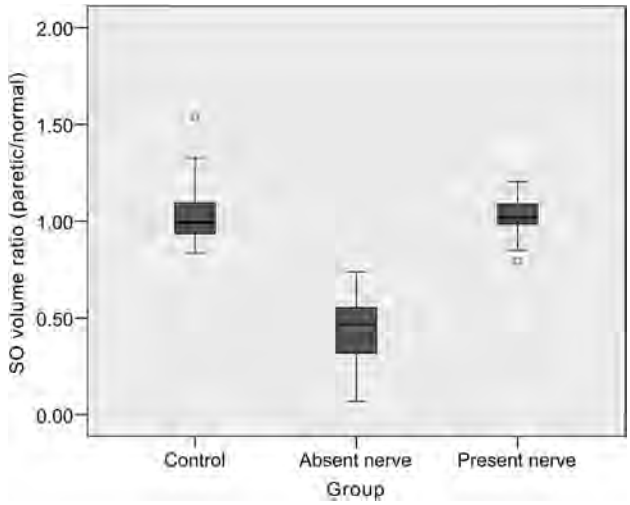

FIG 2. Boxplots of the superior oblique muscle volume ratio of the paretic-to-normal side in patients with congenital superior oblique palsy without (absent group) and with (present group) an ipsilateral trochlear nerve compared with controls. The SO volume ratio was significantly smaller in the absent group (P < .001) compared with controls. There was no significant difference of the SO volume ratio between controls and the present group.

DISCUSSION

In this study, a strong relation was found between the quantitative evaluation of SO volume and the presence or absence of the trochlear nerve in patients with clinically diagnosed congenital SOP. The main findings are as follows: First, the cross-sectional area and volume of the paretic side SO were significantly smaller com-

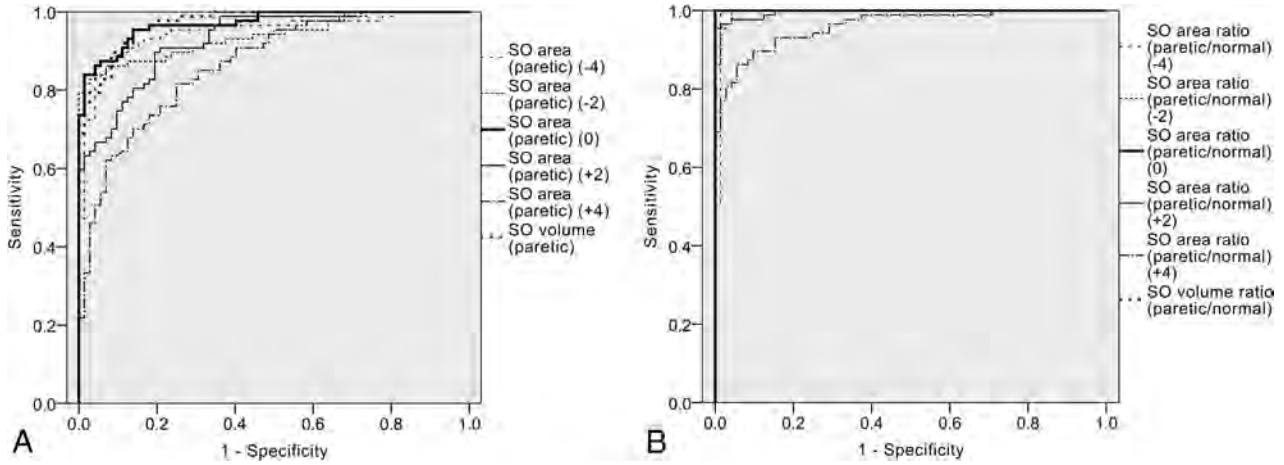

FIG 3. Receiver operating characteristic curves of paretic side SO areas, SO volume, paretic/normal side ratios of the SO area and SO volume for predicting trochlear nerve absence. The area under the receiver operating characteristic curves was largest for the paretic/normal side ratios of SO volume and SO area at the optic nerve–globe junction, with an AUC value of >0.950. AUCs of the paretic side SO areas were much smaller at the anterior planes (+4, +2) compared with the standard plane (0) or posterior planes (−2, −4).

pared with the normal side in the absent group of congenital SOP. Second, the ratio of paretic/normal side SO volume and area near the optic nerve–globe junction was ≤0.75 in patients with SOP without the trochlear nerve. Finally, SO area and volume of the contralateral normal side were larger in both groups of patients with congenital SOP than in controls.

Hypoplasia of the ipsilateral SO has been the major finding on MR imaging of patients with congenital or idiopathic SOP.[1-5] However, the extent of SO hypoplasia compared with the contralateral side varied widely from 0% to 100% in previous reports.[1-3] Sato[1] stated that in congenital SOP, there were 2 peaks in the distribution of the percentage volume of muscle size compared with the contralateral normal side: one between 20% and 40% and the other between 90% and 100%. These 2 groups correspond well to the absent group and present group of congenital SOP in our study because the mean ratio of paretic/normal side SO volume was 43% in the absent group and 103% in the present group—that is, the paretic side SO volume was abnormally small only in the patients with an absent trochlear nerve. As we have demonstrated in our previous study, the 2 groups classified by the absence or presence of the trochlear nerve in congenital SOP account for the 2 main etiologies of congenital SOP.[3] The first is based on abnormalities of the muscle and its innervations associated with SO hypoplasia and trochlear nerve absence and the other is based on the pathologic features of the tendon or heterotopic muscle pulleys.[1,13]

The ratio of paretic/normal side SO volume and SO area at the optic nerve–globe junction demonstrated excellent predictability for trochlear nerve absence. On the basis of the quantitative results of our study, we may expect that patients with congenital SOP with a significant SO hypoplasia of ≤75% compared with the contralateral normal side are likely to have trochlear nerve absence. As the coronal image plane moved anterior from the optic nerve–globe junction (plane +2, +4), however, the predictability of the SO area and the ratio of paretic/normal side SO area significantly decreased compared with the optic nerve–globe junction (plane "0") or posterior planes (plane −2, −4) (Fig 3)—that is, SO hypoplasia of the paretic side compared with the normal side was less apparent in the anterior planes. This difference can be inferred from the fact that the anterior part of the SO ends in a rounded tendon, which acts in a fibrocartilaginous pulley attached to the trochlear fovea of the frontal bone. On the other hand, the predictability of the posterior planes (−2, −4) was also lower than that of the optic nerve–globe junction, probably owing to the fusiform structure of the SO. Considering the individual variations in orbital depth and position of the SO muscle/tendon transition, the best plane for evaluating SO hypoplasia should be adjusted to the image plane having the greatest cross-sectional area of the SO.[14] Previous studies have shown that despite the individual variation, the coronal section at the nearest location posterior to the globe and optic nerve junction may be suitable for evaluating hypoplasia of the extraocular muscles.[2,7] This finding was consistent with our results, because SO hypoplasia and associated trochlear nerve absence were best predicted by the cross-sectional area of the SO near the optic nerve–globe junction. The SO volume and the sum of the SO areas at 5 planes also demonstrated good predictability of SO hypoplasia and trochlear nerve absence. However, the cross-sectional area of the SO in the plane nearest the optic nerve–globe junction was sufficient for this purpose.

The SO area and volume of the contralateral normal side were larger in patients with congenital SOP than in controls. Although it has been reported that the average maximum SO cross-section for the fellow eyes was not significantly different from those in healthy controls,[14] more recent reports showed a larger size and supernormal contractility of the normal contralateral SO compared with that in controls in patients with SOP.[7] Contralateral SO hypertrophy corresponds to the clinical finding of contralateral overdepression in adduction and may be suggestive of an adaptive change, change of fiber type distribution, or innervational change.[7] On the other hand, because we did not control fixation during imaging, variable positions of the eyeball could have affected the muscle size. The normal fellow eye of patients with congenital SOP may show a relatively downward displacement compared with that in healthy controls, and downward dis-

placement leads to a larger cross-section of the SO and inferior rectus muscle.[14]

The results of our study should be limited to congenital SOP and cannot be applied to acquired or idiopathic SOP. Acquired SOP may also show variable atrophy of the SO muscle, as in the absent group of congenital SOP.[15] A significant volume loss of the SO muscles in acquired trochlear nerve palsies has also been reported, and the nerve may also "regress" and die back, becoming severely hypoplastic.[16] The trochlear nerve may regress or become hypoplastic after perinatal injury or, in older patients, from diabetes or a developing small mass along the tentorial incisura.[17] Thus, just because the volume of the SO is significantly decreased, we cannot conclude that the etiology is from nerve absence. In addition, variable degrees of SO muscle atrophy can be found in both congenital and acquired cases with no significant difference in the appearance of the SO muscle between acquired and congenital SOP groups.[15] Moreover, the Bielschowsky head tilt test is not specific and may lead to erroneous results.[17] The presence of large vertical fusional amplitudes does not necessarily imply a congenital etiology because vertical fusional vergence may increase in adults within weeks or months after an acquired vertical strabismus.[17] Therefore, the diagnosis of congenital or acquired SO palsy cannot be concluded solely by imaging or ocular motor examination, but a thorough history and clinical examination are necessary. In these cases, the clinical features are quite different, such as the age of onset, facial asymmetry, and trochlear nerve status. Congenital SOP would be diagnosed mostly in early childhood with significant head tilt or with facial asymmetry in adulthood. In patients with severe SO muscle atrophy, trochlear nerve imaging with high-resolution MR imaging revealing an absent nerve would favor a congenital etiology, while a relatively normal trochlear nerve would suggest acquired SOP.[3]

There are certain limitations to our study. First, this is a retrospective study, not free of unintended confounding issues and a bias toward selecting severely affected patients in a tertiary referral center. Second, patients were excluded if they had poor-quality MR images: motion artifacts, obscured SO margins, or SO tendons extending more posteriorly than the optic nerve–globe junction, applicable to 3 patients of the total 162 study participants. Third, variable positions of the eyeball could have affected the muscle size. MR imaging sequences with higher resolutions by using fixation targets during imaging could overcome these problems.

CONCLUSIONS

The ratio of paretic/normal side SO area near the optic nerve–globe junction and SO volume has an excellent predictability for diagnosing trochlear nerve absence in congenital SOP. SO hypoplasia of ≤75% compared with the contralateral normal side suggests trochlear nerve absence as the etiology of congenital SOP.

Disclosures: Jeong-Min Hwang—*RELATED: Grant*: Basic Science Research Program through the National Research Foundation of Korea funded by the Ministry of Education, Science and Technology (2013R1A1A2010606) and the Interdisciplinary Research Initiatives Program by College of Engineering and College of Medicine, Seoul National University (2012).

REFERENCES

1. Sato M. **Magnetic resonance imaging and tendon anomaly associated with congenital superior oblique palsy.** *Am J Ophthalmol* 1999; 127:379–87
2. Uchiyama E, Matsuo T, Imai S, et al. **Paretic side/normal side ratios of cross-sectional areas of the superior oblique muscle vary largely in idiopathic superior oblique palsy.** *Am J Ophthalmol* 2010;149: 508–12
3. Yang HK, Kim JH, Hwang JM. **Congenital superior oblique palsy and trochlear nerve absence: a clinical and radiological study.** *Ophthalmology* 2012;119:170–77
4. Kim JH, Hwang JM. **Absence of the trochlear nerve in patients with superior oblique hypoplasia.** *Ophthalmology* 2010;117:2208–13.e1–2
5. Kim JH, Hwang JM. **MR imaging of familial superior oblique hypoplasia.** *Br J Ophthalmol* 2010;94:346–50
6. Choi BS, Kim JH, Jung C, et al. **High-resolution 3D MR imaging of the trochlear nerve.** *AJNR Am J Neuroradiol* 2010;31:1076–79
7. Kono R, Demer JL. **Magnetic resonance imaging of the functional anatomy of the inferior oblique muscle in superior oblique palsy.** *Ophthalmology* 2003;110:1219–29
8. Jiang L, Demer JL. **Magnetic resonance imaging of the functional anatomy of the inferior rectus muscle in superior oblique muscle palsy.** *Ophthalmology* 2008;115:2079–86
9. Clark RA, Demer JL. **Enhanced vertical rectus contractility by magnetic resonance imaging in superior oblique palsy.** *Arch Ophthalmol* 2011;129:904–08
10. Demer JL, Kung J, Clark RA. **Functional imaging of human extraocular muscles in head tilt dependent hypertropia.** *Invest Ophthalmol Vis Sci* 2011;52:3023–31
11. Chan TK, Demer JL. **Clinical features of congenital absence of the superior oblique muscle as demonstrated by orbital imaging.** *J AAPOS* 1999;3:143–50
12. Kono R, Okanobu H, Ohtsuki H, et al. **Absence of relationship between oblique muscle size and Bielschowsky head tilt phenomenon in clinically diagnosed superior oblique palsy.** *Invest Ophthalmol Vis Sci* 2009;50:175–79
13. Helveston EM, Krach D, Plager DA, et al. **A new classification of superior oblique palsy based on congenital variations in the tendon.** *Ophthalmology* 1992;99:1609–15
14. Demer JL, Miller JM. **Magnetic resonance imaging of the functional anatomy of the superior oblique muscle.** *Invest Ophthalmol Vis Sci* 1995;36:906–13
15. Ozkan SB, Aribal ME, Sener EC, et al. **Magnetic resonance imaging in evaluation of congenital and acquired superior oblique palsy.** *J Pediatr Ophthalmol Strabismus* 1997;34:29–34
16. Horton JC, Tsai RK, Truwit CL, et al. **Magnetic resonance imaging of superior oblique muscle atrophy in acquired trochlear nerve palsy.** *Am J Ophthalmol* 1990;110:315–16
17. Glaser JS, Siatkowski RM. **Infranuclear disorders of eye movement.** In: Duane TD. *Duane's Clinical Ophthalmology*. Vol 2. Philadelphia: Lippincott Williams & Wilkins; 2006

Open-Angle Glaucoma and Paraoptic Cyst: First Description of a Series of 11 Patients

A. Bertrand, C. Vignal, F. Lafitte, P. Koskas, O. Bergès, and F. Héran

ABSTRACT

SUMMARY: We report 11 patients who were referred to our institution for severe open-angle glaucoma who had a paraoptic cyst on MR imaging. All cysts were extraoptic and retrolaminar; most were deforming the adjacent optic nerve. Cysts had a high signal on T2 and FLAIR sequences, and a variable signal on T1 and variable echogenicity, suggesting different proteinaceous content. Arterial vascularization of the optic nerve was normal. Cyst volumes were inversely correlated with the severity of glaucoma on the same eye ($P < .01$–$.05$, Spearman correlation coefficient). We hypothesized that such cysts may reflect a valve mechanism, which would allow preservation of the translamina cribrosa pressure and thus could preserve visual function. The rarity of this association, together with the frequent mass effect of the cyst on the optic nerve, stresses the necessity of long-term follow-up in these patients.

ABBREVIATIONS: MD = mean deviation; OCT = optical coherence tomography; PSD = pattern standard deviation; US = ultrasound

Primary open-angle glaucoma, a chronic optic neuropathy characterized by a progressive excavation of the optic nerve and an associated loss of visual field sensitivity, affects approximately 2% of the population older than 40 years of age and represents a leading cause of irreversible blindness worldwide.[1] The pathogenic mechanisms of open-angle glaucoma are still a matter of debate.[2-4] Until the 1970s, primary open-angle glaucoma was considered the consequence of a single cause, the increase in intraocular pressure; but it is now recognized that approximately one-third of patients with glaucomatous neuropathy have normal intraocular pressure.[5] Recently, some authors have proposed that open-angle glaucoma may be driven not by the increased intraocular pressure but by an increased translamina cribrosa pressure gradient (ie, an increased difference of pressure between the intraocular compartment and the retrobulbar compartment [CSF compartment]).[6] This hypothesis is supported by recent experimental and clinical data showing an association between the occurrence of normal-pressure glaucoma and decreased CSF pressure.[6-9]

In this work, we present 11 patients referred to our institution for severe open-angle glaucoma in whom MR imaging demonstrated the presence of a retrolaminar paraoptic cyst at the head of the optic nerve. We collected the ophthalmologic reports of these patients, together with the results of MR imaging of the optic nerves and, when available, high-resolution MR imaging and Doppler ultrasound (US) examination of the optic nerves. We describe the morphologic characteristics of these cysts and discuss associated morphologic, vascular, and/or functional signs of optic neuropathy to determine their pathophysiologic significance.

MATERIALS AND METHODS

Case Series

Patients. We retrospectively collected the cases of 11 patients who were referred to our institution for severe open-angle glaucoma who were diagnosed on MR imaging of the optic nerves as having a paraoptic cyst from 2005 to 2011. We estimate that during this period, approximately 200 patients underwent brain MR imaging for the same indication. This retrospective study was approved by our institutional review board. Explicit informed consent was waived according to French legislation because all imaging and clinical data were generated during routine clinical work-up and were retrospectively extracted for this study.

Ophthalmologic Examinations. For 9 patients (10 cysts), we collected the results of visual field tests (24–2) on both eyes; the 2 other patients had no records in our institution. Defects on visual

Received March 5, 2014; accepted after revision September 28.

From the Departments of Diagnostic Neuroradiology (A.B., F.L., P.K., O.B., F.H.) and Ophthalmology (C.V.), Fondation Ophtalmologique Adolphe de Rothschild, Paris, France; and Department of Diagnostic and Functional Neuroradiology (A.B.), Pitié-Salpétrière Hospital, Paris, France.

Paper previously presented at: Annual Meeting of the American Society of Neuroradiology, April 21–26, 2012; New York, New York.

Please address correspondence to Françoise Héran, MD, Department of Neuroradiology, Fondation Adolphe de Rothschild, 25 rue Manin, 75019 Paris, France; e-mail: fheran@fo-rothschild.fr

Indicates article with supplemental on-line table.

http://dx.doi.org/10.3174/ajnr.A4194

field tests were retrospectively analyzed qualitatively by an ophthalmologist (C.V.) with 20 years' experience and quantitatively by using the values of mean deviation (MD) and pattern standard deviation (PSD). MD is the mean difference in decibels between the patient's measured field of vision and a normal reference field model. PSD is the sum of the deficits in decibels on the patient's measured field of vision; an impairment of the visual field corresponds to decreased MD and an increased PSD. Seven patients (8 cysts) also underwent an optical coherence tomography (OCT) on both eyes. OCT is a noninvasive optical imaging technique that allows the measurement of the nerve fiber thickness at the head of the optic nerve.[10]

MR Imaging Examinations. All patients had a standard MR imaging examination of the optic nerves. Standard MR imaging was performed on a 1.5T Gyroscan ACS-NT scanner (Philips Healthcare, Best, the Netherlands) with an 8-channel head coil and always included a 2-mm-thick coronal T2-weighted sequence perpendicular to the optic nerves. Seven patients also had high-resolution MR imaging of the optic nerves. High-resolution MR imaging was performed on the same magnet by using a surface coil placed on the eyes and comprised a 3D driven equilibrium sequence acquired in the axial plane (TR/TE = 1500/250 ms, voxel size = 0.51 × 0.65 × 1.6 mm^3), a coronal T1-weighted sequence (TR/TE = 500/20 ms, voxel size = 0.69 × 0.87 × 2 mm^3), a coronal T2-weighted sequence (TR/TE = 2975/100 ms, voxel size = 0.59 × 0.81 × 2 mm^3), and a coronal turbo-FLAIR sequence (TR/TE/inversion recovery time = 11,000/155/2800 ms, TSE factor = 50, voxel size = 0.59 × 0.75 × 2 mm^3). Cyst volumes were measured on coronal 2D-T2 in all 11 patients and on 3D driven equilibrium in the 7 patients who underwent high-resolution MR imaging. Volume measurement was done by image-by-image manual delineation, by using OsiriX Imaging Software, Version 5.5.2 (http://www.osirix-viewer.com).

US and Doppler Examinations. US and Doppler examination of the optic nerves were available in 9 patients (10 cysts). Doppler examination included the bilateral measurement of the resistance index in the ophthalmic, central retinal, nasal short posterior ciliary, and temporal short posterior ciliary arteries of both eyes. For every patient, the radiologist performing the Doppler US examination (O.B., F.L., or P.K.) was guided by the MR images of the patient's cyst.

Statistical Analysis. Data gathering and analysis were performed by A.B. Given our small sample size, only nonparametric tests were used in this study. MD, PSD, and OCT values were compared between the side of the cyst and the opposite side in the 8 patients with unilateral cysts; and available visual field tests and OCT, by using the Wilcoxon matched pair test. Arterial resistance indices were compared between the side of the cyst and the opposite side in the 7 patients who had a unilateral cyst and available US imaging, by using the Wilcoxon matched pair test. Correlation between the size of the cysts on the one hand and the indicators of glaucoma severity on the side of the cyst on the other hand (MD and PSD on visual field, thickness of the nerve fiber layer on OCT) was assessed by using the Spearman correlation coefficient.

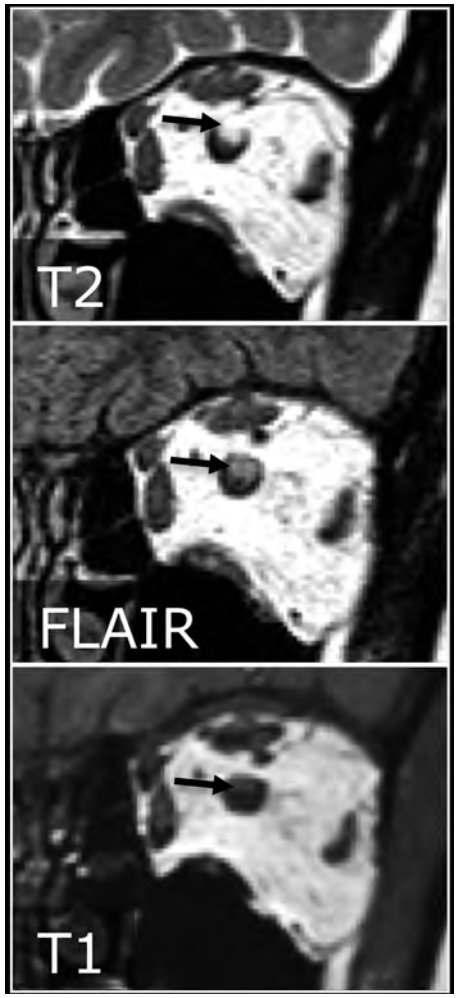

FIG 1. High-resolution MR images of a paraoptic cyst. The cyst is superolateral, causing a mass effect on the optic nerve, which is displaced inward and inferiorly. The content of the cyst appears hyperintense on T2WI and moderately hyperintense on FLAIR and T1WI.

RESULTS

Patient Characteristics

Patients were 4 men and 7 women, 48–82 years of age (median, 70 years). All patients were previously diagnosed with open-angle glaucoma; 4 had normal-pressure glaucoma (On-line Table).

Cyst Morphology

All cysts were located at the level of the optic nerve head in the retrolaminar area. In 5 patients, the cyst was located on the right optic nerve; in 5 patients, on the left optic nerve; and 1 patient had bilateral cysts. All cysts were located outside the optic nerve, and all except 2 were associated with a mass effect on the adjacent optic nerve. Cysts were located inferior (n = 1), inferolateral (n = 3), superolateral (n = 2), or superior (n = 6) to the optic nerve (On-line Table). All cysts were hyperintense on T2WI. On high-resolution MR images, the signal of the cysts was always high on T2WI, always high on FLAIR-weighted imaging, and variable on T1WI (hyperintense in 1 case, hypointense in 1 case, and of mixed intensities in the remaining cases) (Fig 1). Cyst volume ranged from 4 to 54 mm^3 on coronal T2 sequences (median, 18) and from 10 to 58 mm^3 on 3D-CISS sequences (median, 21). Among the 8

patients who underwent US imaging, 5 cysts were visible, either as a simple enlargement of the optic nerve ($n = 3$) or as an iso- to slightly hyperechoic formation, with a location and shape similar to those observed on MR imaging ($n = 2$) (Fig 2).

Doppler US

No hemodynamic perturbation of the blood supply to the optic nerve head was observed on Doppler examination. There was no statistically significant difference between the resistance indices measured on the side of the cyst and those on the opposite side, for the ophthalmic, central retinal, nasal short posterior ciliary, and temporal short posterior ciliary arteries (Table).

Correlation between Cyst Characteristics and Optic Neuropathy

Absence of Correlation between Cyst Location and Topography of Optic Neuropathy. One ophthalmologist (C.V.) qualitatively assessed the correlation between the location of the cyst on MR images and the location of visual field defects on the retina. This correlation could only be qualitative because the examiner needed to take into account the uneven spatial distribution of optic fibers from the head of the optic nerve toward the retina. In 2 cases, there was complete correlation between the location of the cyst and the visual field defects; in 5 cases, this correlation was only partial; and in the last 3 cases, there was no correlation between the location of the cyst and the visual field defects (On-line Table). Moreover, there was no statistical difference in MD and PSD values in the eye with the cyst and the eye without a cyst (paired *t* test, $P = .38$ and .47, respectively; data not shown). We also quantitatively assessed the correlation between the location of the cyst and the severity of nerve fiber loss on OCT. This correlation was unbiased and quantitative because the OCT technique gives a direct estimation of the number of fibers at the head of the optic nerve, where the cysts are located. We calculated the percentage of fiber loss on OCT in the 4 quadrants (nasal, temporal, superior, and inferior). For 4 cysts, the location of the cyst matched the quadrant of greatest fiber loss; in the 4 other cysts, the location of the cyst was in another quadrant. There was no statistical difference between fiber thickness in the quadrant where the cyst was located and in the same quadrant on the contralateral eye (Wilcoxon signed rank test, $P = .44$; data not shown).

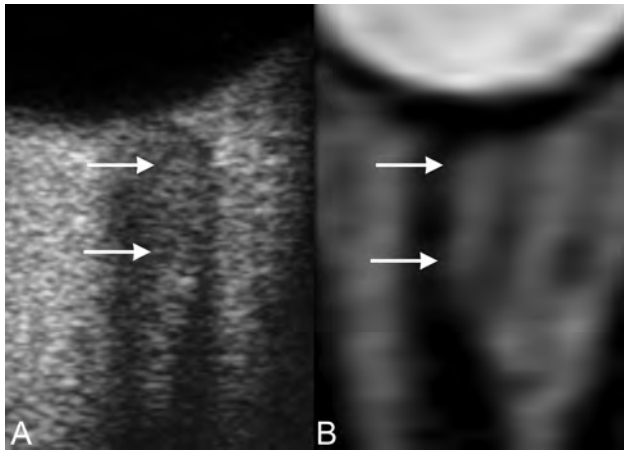

FIG 2. Axial image on US (*A*) shows a lateral paraoptic cyst, well-limited and isoechogenic. Axial-reformatted 3D-CISS in the same patient (*B*) shows a similar image of an oval hyperintense cyst.

Correlation between Cyst Size and Severity of the Optic Neuropathy. We quantitatively correlated the volume of the cysts and the severity of the glaucomatous neuropathy in the 6 patients (7 cysts) who underwent high-resolution MR imaging and for whom ophthalmologic reports were available. There was no correlation between the volume of the cyst in 3D-CISS and the thickness of the optic nerve fibers on OCT (Spearman correlation coefficient: $r = -0.25$, $P = .59$; Fig 3*A*). However, we noted a statistically significant correlation between the volume of the cyst in 3D-CISS and the severity of visual impairment in the same eye, estimated by the MD and PSD: The more voluminous the cyst was, the less impaired the visual field was (Fig 3*B*, -*C*). As estimated by linear regression, we would expect a PSD = 0 for a cyst measuring 82 mm^3 on 3D driven equilibrium; similarly, we would expect an MD = 0 for a cyst measuring 67 mm^3 on 3D driven equilibrium. No significant correlation was observed between the volume of the cyst estimated on 2D-T2 and the MD or the PSD (On-line Table).

DISCUSSION

MR imaging examination of the orbit is not typically integrated into the systemic work-up in patients with open-angle glaucoma, but it is recommended when visual deficits are severe and/or rapidly increasing, to rule out a compressive tumor or other structural pathology of the anterior visual pathways.[5] We report the association between open-angle glaucoma and paraoptic cysts.

Comparison of arterial resistance index values between the side of the cyst and the contralateral eye (Wilcoxon matched pair test)

	Central Retinal Artery		Temporal Short Ciliary Artery		Nasal Short Ciliary Artery		Ophthalmic Artery	
Case No.	Cyst Side	Contra.	Cyst Side	Contra.	Cyst Side	Contra.	Cyst Side	Contra.
1	0.59	0.67	0.65	0.58	0.52	0.48	0.76	0.75
3	0.59	0.6	0.53	0.56	0.61	0.5	0.66	0.68
4a	0.62	NA	0.64	NA	0.65	NA	0.62	NA
4b	0.63	NA	0.56	NA	0.5	NA	0.67	NA
6	0.64	0.71	NA	NA	0.59	0.63	0.66	0.74
8	0.54	0.69	0.59	0.52	0.55	0.56	0.66	0.66
9	0.64	0.61	0.64	0.6	0.61	0.61	0.77	0.82
10	0.77	0.77	0.69	0.77	0.74	0.75	0.75	0.73
11	0.6	0.58	0.48	0.44	0.48	0.53	0.7	0.7
Mean (SD)	0.62 (0.06)	0.66 (0.3)	0.6 (0.21)	0.58 (0.3)	0.58 (0.08)	0.58 (0.27)	0.69 (0.05)	0.73 (0.32)
Paired *t* test	$P = .18$		$P = .49$		$P = .79$		$P = .25$	

Note:—Contra. indicates contralateral.

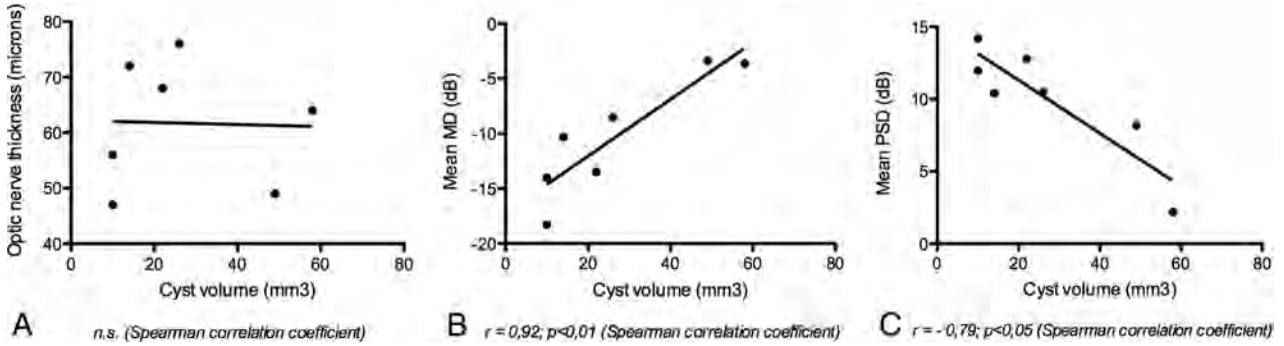

FIG 3. Correlation between cyst volumes on 3D-CISS and optic nerve fibers on OCT (*A*), MD (*B*), and PSD (*C*).

This association remains quite rare: We estimate that approximately 200 patients were referred to our institution for brain MR imaging because of severe open-angle glaucoma during a 6-year period; thus, we estimate the prevalence of these cyst to be at approximately 5% in patients with severe open-angle glaucoma. Other differential diagnoses of a paraoptic mass would include arachnoid cyst, coloboma, and pilocytic astrocytoma; however, the high signal of the cysts on FLAIR images was not in favor of a subarachnoid cyst, and the cyst location, distinct from both the optic nerve and the ocular globe, was not in favor of a tumor arising from the optic nerve, nor of a coloboma.

In our series of 11 patients, the presence of a cyst was not associated with a greater fiber loss in the head of the optic nerve, but it was associated with relatively preserved visual function. This goes against a mechanism of compression of the optic nerve by the cyst and does not suggest that surgical removal of the cyst would be of any benefit. Instead, it would suggest that for a given level of fiber loss, the cyst has some protective effect on visual function. It has been recently proposed that primary open-angle glaucoma could be driven not only by increased ocular pressure but, more generally, by an increase in translamina cribrosa pressure, either caused by elevated intraocular pressure or a diminished CSF pressure. In light of this pathogenic hypothesis, paraoptic cysts may represent a valve mechanism, by which a leakage of fluid from the ocular compartment to the optic nerve compartment would allow stabilization of the translamina cribrosa pressure and, consequently, relative preservation of visual function. However, this hypothesis remains speculative. The observed mass effect of the cyst on the optic nerve does not favor the idea that such cysts are purely protective. In addition, given the rarity of this association, our findings may not be generalized to all forms of open-angle glaucoma. It is also conceivable that distinct mechanisms underlie open-angle glaucoma with elevated pressure and open-angle glaucoma with normal pressure. In our small series, we did not observe different characteristics in these 2 groups, but this feature may simply be related to the small sample size. Consequently, long-term follow-up is warranted in patients with this MR imaging finding, to evaluate the long-term effects of these paraoptic cysts on visual function.

Disclosures: Catherine Vignal—*UNRELATED*: *Consultancy*: GenSight.

REFERENCES

1. Friedman DS, Wolfs RC, O'Colmain BJ, et al. **Prevalence of open-angle glaucoma among adults in the United States.** *Arch Ophthalmol* 2004;122:532–38
2. Rieck J. **The pathogenesis of glaucoma in the interplay with the immune system.** *Invest Ophthalmol Vis Sci* 2013;54:2393–409
3. Mozaffarieh M, Flammer J. **New insights in the pathogenesis and treatment of normal tension glaucoma.** *Curr Opin Pharmacol* 2013;13:43–49
4. Venkataraman ST, Flanagan JG, Hudson C. **Vascular reactivity of optic nerve head and retinal blood vessels in glaucoma: a review.** *Microcirculation* 2010;17:568–81
5. Kwon YH, Fingert JH, Kuehn MH, et al. **Primary open-angle glaucoma.** *N Engl J Med* 2009;360:1113–24
6. Ren R, Zhang X, Wang N, et al. **Cerebrospinal fluid pressure in ocular hypertension.** *Acta Ophthalmol* 2011;89:e142–48
7. Ren R, Jonas JB, Tian G, et al. **Cerebrospinal fluid pressure in glaucoma: a prospective study.** *Ophthalmology* 2010;117:259–66
8. Berdahl JP, Allingham RR, Johnson DH. **Cerebrospinal fluid pressure is decreased in primary open-angle glaucoma.** *Ophthalmology* 2008;115:763–68
9. Ren R, Wang N, Zhang X, et al. **Trans-lamina cribrosa pressure difference correlated with neuroretinal rim area in glaucoma.** *Graefes Arch Clin Exp Ophthalmol* 2011;249:1057–63
10. Kotowski J, Wollstein G, Folio LS, et al. **Clinical use of OCT in assessing glaucoma progression.** *Ophthalmic Surg Lasers Imaging* 2011; 42(suppl):S6–14

Susceptibility-Weighted Imaging in Pediatric Arterial Ischemic Stroke: A Valuable Alternative for the Noninvasive Evaluation of Altered Cerebral Hemodynamics

R.M. Polan, A. Poretti, T.A.G.M. Huisman, and T. Bosemani

ABSTRACT

BACKGROUND AND PURPOSE: SWI provides information about blood oxygenation levels in intracranial vessels. Prior reports have shown that SWI focusing on venous drainage can provide noninvasive information about the degree of brain perfusion in pediatric arterial ischemic stroke. We aimed to evaluate the influence of the SWI venous signal pattern in predicting stroke evolution and the development of malignant edema in a large cohort of children with arterial ischemic stroke.

MATERIALS AND METHODS: A semiquantitative analysis of venous signal intensity on SWI and diffusion characteristics on DTI was performed in 16 vascular territories. The mismatch between areas with SWI-hypointense venous signal and restricted diffusion was correlated with stroke progression on follow-up. SWI-hyperintense signal was correlated with the development of malignant edema.

RESULTS: We included 24 children with a confirmed diagnosis of pediatric arterial ischemic stroke. Follow-up images were available for 14/24 children. MCA stroke progression on follow-up was observed in 5/6 children, with 2/8 children without mismatch between areas of initial SWI hypointense venous signal and areas of restricted diffusion on DTI. This mismatch showed a statistically significant association ($P = .03$) for infarct progression. Postischemic malignant edema developed in 2/10 children with and 0/14 children without SWI-hyperintense venous signal on initial SWI ($P = .07$).

CONCLUSIONS: SWI-DTI mismatch predicts stroke progression in pediatric arterial ischemic stroke. SWI-hyperintense signal is not useful for predicting the development of malignant edema. SWI should be routinely added to the neuroimaging diagnostic protocol of pediatric arterial ischemic stroke.

ABBREVIATIONS: ACA = anterior cerebral artery; AIS = arterial ischemic stroke; ASL = arterial spin-labeling; $CMRO_2$ = cerebral metabolic rate of oxygen; mIP = minimum intensity projection; OEF = oxygen extraction fraction; PAIS = pediatric arterial ischemic stroke; PSI = prediagnostic symptomatic interval

Acute arterial ischemic stroke (AIS) affects 2–5/100,000 children every year and is associated with high mortality and morbidity.[1] The mortality rate is estimated at 5%–13%, and moderate-to-severe neurologic deficits or epilepsy occur in >50% of children after AIS.[2,3] The *Chest* and American Heart Association guidelines support the use of anticoagulation in acute pediatric arterial ischemic stroke (PAIS) despite of the absence of large-scale clinical trials.[4,5] Antithrombotic therapy aims to prevent early propagation of the thrombus, inhibit the formation of new thrombus, and promote early recanalization to save hypoperfused tissue at risk of irreversible ischemic infarction. However, the diagnosis of PAIS should be made first, and tissue at risk for infarction should be detected. The diagnosis of PAIS is frequently delayed or missed.[6] DWI/DTI is a highly sensitive MR imaging sequence in detecting early ischemic regions and is the diagnostic criterion standard for imaging acute PAIS.[7] Neuroimaging techniques that allow early, reliable, noninvasive identification of potentially salvageable hypoperfused brain tissue—the so called ischemic penumbra—are imperative to guide treatment.

SWI is a high-spatial-resolution, gradient-echo MR imaging sequence that accentuates the magnetic properties of various substances such as blood, blood products, nonheme iron, and calcification.[8] In addition, SWI accentuates magnetic susceptibility differences between deoxygenated hemoglobin in the vessels and adjacent oxygenated tissues. A few previous reports have shown that SWI-hypointense signals in veins draining hypoperfused brain areas provide indirect evaluation of critically perfused tissue by focusing on venous drainage.[9-12] In addition, SWI-hyperin-

Received September 9, 2014; accepted after revision October 13.

From the Section of Pediatric Neuroradiology, Division of Pediatric Radiology, Russell H. Morgan Department of Radiology and Radiological Sciences, The Johns Hopkins University School of Medicine, Baltimore, Maryland.

Please address correspondence to Thangamadhan Bosemani, MD, Section of Pediatric Neuroradiology, Division of Pediatric Radiology, Russell H. Morgan Department of Radiology and Radiological Science, The Johns Hopkins University School of Medicine, Charlotte R. Bloomberg Children's Center, Sheikh Zayed Tower, Room 4173, 1800 Orleans St, Baltimore, MD 21287-0842; e-mail: tbosema1@jhmi.edu

Indicates article with supplemental on-line tables.

http://dx.doi.org/10.3174/ajnr.A4187

tense signal was reported to detect regions of hyperperfusion and to be associated with an increased risk of developing postischemic malignant edema.[13] SWI may consequently serve as a valuable alternative sequence to evaluate the hemodynamics of brain tissue in PAIS.

The aims of this retrospective study were to evaluate the potential of acute SWI to identify potentially salvageable brain tissue and to predict the development of postischemic malignant edema in the largest cohort of PAIS reported so far, to our knowledge. We hypothesized that hypointense venous signal on acute SWI may identify brain tissue at risk of infarction progression by focusing on venous drainage and that the presence of SWI-hyperintense venous signal may predict the development of postischemic malignant edema.

MATERIALS AND METHODS

This retrospective study was approved by our institutional review board.

Patients

The inclusion criteria for this study were the following: 1) a confirmed diagnosis of PAIS (clinical and acute neuroimaging findings including DWI/DTI); 2) the availability of at least 1 MR imaging study of diagnostic quality including at least 3D-T1WI, axial T2WI, FLAIR images, DWI/DTI, and SWI; 3) a prediagnostic symptomatic interval (PSI) of <8 days; and 4) age at MR imaging of 18 years or younger. Children with hemorrhagic or metabolic stroke and children with acute outside neuroimaging who were transferred to our hospital were excluded from this study. Data from eligible patients were obtained through an electronic search of our pediatric neuroradiology data base covering January 1, 2009, through June 1, 2014.

Clinical histories of patients were reviewed for stroke etiology, symptoms, and clinical findings on admission; PSI; time between diagnosis and neuroimaging follow-up; development of postischemic malignant edema; and acute thrombolytic therapy. PSI was defined as the time interval between onset of symptoms and the neuroimaging diagnosis of PAIS. The presence of a postischemic malignant edema was defined by the presence of neurologic deterioration within 48–72 hours after acute PAIS and uncal or transtentorial herniation on neuroimaging and/or the need for neurosurgical decompression.

Image Acquisition

All MR imaging studies were acquired on a 1.5T clinical MR imaging scanner (Avanto; Siemens, Erlangen, Germany) by using our standard departmental protocol for PAIS, including 3D isotropic T1WI, axial T2WI, FLAIR images, DTI, SWI, arterial spin-labeling (ASL), and MRA.

A single-shot spin-echo echo-planar imaging axial DTI sequence with diffusion gradients along 20 noncollinear directions was performed. An effective high b-value of 1000 s/mm^2 was used for each of the 20 diffusion-encoding directions. An additional measurement without diffusion-weighting (b = 0 s/mm^2) was also performed. Acquisition parameters were the following: TR = 7100 ms, TE = 84 ms, section thickness = 2.5 mm, FOV = 240 × 240 mm, and matrix size = 192 × 192. An integrated parallel acquisition technique = 2 with generalized autocalibrating partially parallel acquisition reconstruction was used. Diffusion trace and ADC maps were automatically calculated by the vendor-specific software on the MR imaging scanners.

For the SWI sequence, we used the following parameters: TR = 48 ms, TE = 40 ms, flip angle = 15°, bandwidth = 80 kHz, section thickness = 1.2 mm with 128 sections per slab, FOV = 146 × 180 mm, and matrix size = 256 × 512. Integrated parallel acquisition technique factor 2 was used. Minimum intensity projection (mIP) images were automatically reconstructed by the vendor-specific software on the MR imaging scanners. An effective mIP thickness of 8 mm was used for neonates, and 16 mm, for older patients. The smaller effective mIP thickness of 8 mm was used in neonates to limit partial volume effects due to small brain size and any subsequent anatomic misregistration of vessels that might masquerade as pathology.

Image Analysis

Analysis of all images was performed in consensus by R.M.P., a medical student, A.P., a pediatric neurologist with vast experience in pediatric neuroimaging research, and T.B., a pediatric neuroradiology attending physician. For each cerebral hemisphere, we defined the following vascular territories: anterior cerebral artery (ACA) territory, posterior cerebral artery territory, and 6 cortical regions of the MCA territory (M1–3 at the level of the basal ganglia and M4–6 at the level rostral to the ganglionic structures) according to the Alberta Stroke Program Early CT Score.[14]

Diffusion was graded for each arterial territory as normal or restricted on the basis of ADC maps. SWI signal intensity of the sulcal veins for each arterial territory was graded as hyperintense, isointense, mildly hypointense, or markedly hypointense. In addition, SWI signal intensity of the intramedullary veins in the MCA territories was evaluated and graded in a manner similar to the grading of the sulcal veins. mIP SWI were used for the evaluation. Finally, perfusion in each vascular territory was graded as normal, decreased, or increased. Perfusion was evaluated on relative CBF maps for ASL. The final extent of infarction was evaluated on follow-up neuroimaging as the absence or presence of gliosis or encephalomalacia in each vascular territory.

To identify brain tissue at risk of infarction, mismatch was determined between the number of vascular territories showing restricted diffusion and the number of vascular territories showing mildly and markedly SWI-hypointense venous signal. The number of territories with SWI-hypointense venous signal was graded as greater than, equal to, or less than the number of territories with restricted diffusion. In addition, the number of territories with SWI-hypointense venous signal was compared with the number of territories with abnormal (increased or decreased) perfusion.

To identify infarct progression, the number of vascular territories with restricted diffusion on the initial MR imaging study was compared with the number of vascular territories with gliosis or encephalomalacia on the follow-up neuroimaging study. Infarct progression was defined as a higher number of involved territories with gliosis or encephalomalacia on follow-up imaging

Table 1: SWI, DWI/DTI, and PWI findings in 24 children with AIS

		SWI Findings (n = 24)				DWI/DTI Findings (n = 24)		ASL Findings (n = 7)		
		Iso	Hyper	Mildly Hypo	Markedly Hypo	Normal	Decreased	Normal	Perfusion ↓	Perfusion ↑
ACA	R	18	4	1	1	20	4	6	1	0
	L	16	5	2	1	20	4	7	0	0
MCA										
M1	R	16	2	4	2	17	7	7	0	0
	L	15	4	4	1	17	7	6	1	0
M2	R	14	2	6	2	17	7	6	1	0
	L	14	2	6	2	15	9	6	1	0
M3	R	18	2	2	2	20	4	6	1	0
	L	20	2	1	1	16	8	7	0	0
M4	R	17	2	3	2	16	8	6	1	0
	L	15	4	3	2	16	8	6	0	1
M5	R	13	3	6	2	13	11	6	1	0
	L	13	2	5	4	13	11	5	0	2
M6	R	18	3	1	2	16	8	6	1	0
	L	19	2	2	1	18	6	7	0	0
IMV	R	17	0	6	1					
	L	20	0	2	2					
PCA	R	15	4	3	2	20	4	5	2	0
	L	12	6	5	1	18	6	4	1	2

Note:—IMV indicates intramedullary veins; Iso, isointense; Hyper, hyperintense; Hypo, hypointense; ↑, increased; ↓, decreased; R, right; L, left; PCA, posterior cerebral artery.

compared with the initial DTI. For each patient, the extent of the infarcted tissue on follow-up imaging was graded as progression or none.

Statistical Analysis

The Pearson χ^2 test was used to compare the ability of the DTI-SWI hypointense venous signal mismatch to predict stroke progression within the 6 cortical regions of the MCA territory and the ability of SWI-hyperintense venous signal to predict the development of malignant edema. ASPECTS vascular territories were used to better define the extent of MCA stroke on initial imaging and to detect progression on subsequent imaging. Analyses were performed by using STATA software, Version 12.1 (StataCorp, College Station, Texas). Observed differences were considered statistically significant if the P value was $<.05$.

RESULTS

Twenty-four children (10 girls) were included in our study (On-line Table 1). The median age of patients at acute stroke presentation was 4.7 years (range, 2 days to 17 years). Risk factors for PAIS were present in 18 children (75%). The most common risk factors were congenital heart disease in 5 (21%) and Moyamoya syndrome in 4 (17%) children. The average PSI was 2 days (range, 0–7 days). None of the patients had acute thrombolytic therapy.

The results of the semiquantitative evaluation of acute DTI, SWI, and ASL data are shown in Table 1. ASL data were available for 7 children. Follow-up neuroimaging studies were available for 15 children (63%) and were performed, on average, 47 days after acute neuroimaging (range, 1 day to 8 months). Areas of gliosis or encephalomalacia were seen in 14/24 children, including all vascular territories. In the acute neuroimaging studies, a mismatch between SWI and DWI/DTI was found in 22 patients (92%). The number of vascular territories with SWI-hypointense venous signal was greater than the number of vascular territories with restricted diffusion in 15 children (63%) and smaller in 7 children (29%). In 2 children (8%), the vascular territories with SWI-hypointense venous signal and restricted diffusion matched. A mismatch between SWI and ASL was found in 6/7 patients (86%). The vascular territories with SWI-hypointense venous signal were greater than the vascular territories with abnormal perfusion in 3 children and smaller in 3 children. In 1 child, the vascular territories with SWI-hypointense venous signal and reduced perfusion matched perfectly.

Table 2: SWI/DWI mismatch in the MCA territories predicts stroke evolution on follow-up imaging in 14 children with AIS[a]

SWI/DWI	No Stroke Progression on Follow-Up	Stroke Progression on Follow-Up	Total
SWI = DWI	6	2	8
SWI > DWI	1	5	6
Total	7	7	14

[a] Pearson χ^2 test = 0.03.

The results of the semiquantitative evaluation of acute DTI, SWI, and ASL data of 14 children with a stroke within at least 1 of the 6 cortical regions of the right or left MCA territory are shown in On-line Table 2. Follow-up images were available for all 14 children included in the statistical analysis. A mismatch between SWI hypointense veins with vascular territories greater than those on DTI was found in 6 children (Table 2), of which 5 children showed infarct progression. This mismatch between SWI and DTI was significantly associated with stroke progression on follow-up imaging ($P = .03$) (Figs 1 and 2).

Malignant edema developed in 2 of 24 children (8%). In both patients, brain edema was diffuse and SWI-hyperintense venous signal involved the right ACA and MCA territories in the first patient (Fig 3) and the bilateral MCA and left posterior cerebral artery territories in the other. In both patients, ASL data were not available. SWI-hyperintense venous signal was found in 8 children with AIS who did not develop postischemic malignant edema. The presence of SWI-hyperintense venous signal was not significantly associated with the development of postischemic malignant edema ($P = .07$) (Table 3).

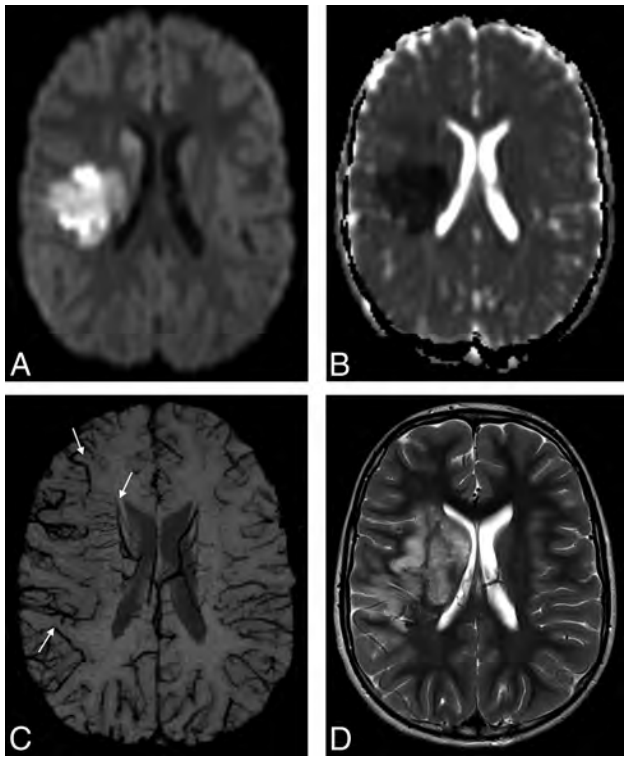

FIG 1. An 8-year-old boy with elevated lipoprotein A and AIS involving the right MCA territory. Trace of diffusion (*A*) and ADC (*B*) maps show areas of restricted diffusion in the right basal ganglia and part of the subcortical white matter and cortical gray matter in the right MCA territory, representing acute ischemia. *C*, mIP-SWI map shows markedly hypointense sulcal and intramedullary veins within the larger right MCA territory (*arrows*). *D*, Follow-up axial T2-weighted image 6 days after AIS shows hyperintense signal in the infarcted brain tissue that extends beyond the vascular territories with restricted diffusion and matches the area with SWI-hypointense veins on acute neuroimaging.

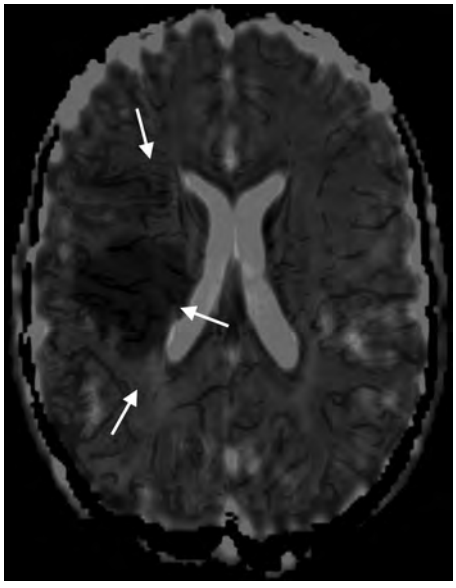

FIG 2. Fused axial ADC and mIP-SWI map images for the same child as in Fig 1 show that markedly hypointense sulcal and intramedullary veins on SWI are draining an area that extends beyond the region of restricted diffusion on the ADC map in the right MCA territory.

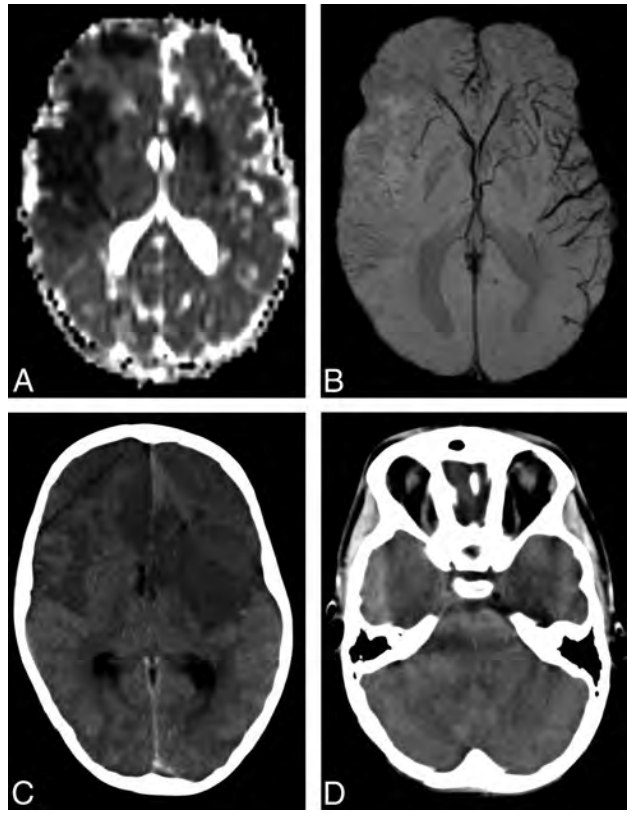

FIG 3. A 7-year-old boy with AIS involving the right ACA and partial bilateral MCA territories. *A*, ADC map shows areas of restricted diffusion in the right ACA, M1, M2, M4, and M5 territories as well as the left M2, M4, and M5 territories. *B*, mIP-SWI shows markedly hyperintense sulcal veins in the right ACA, M1, M2, M4, and M5 territories and hypointense sulcal veins in the left M1, M2, M4, and M5 territories. *C* and *D*, Follow-up axial CT image 2 days after AIS shows stroke evolution in the right ACA, M1, M2, M4, and M5 as well as in the left M2, M4, and M5 territories. In addition, there is increasing mass effect with effacement of both frontal horns of the lateral ventricles, the third and fourth ventricles, and prepontine cistern, compatible with malignant edema.

Table 3: SWI hyperintense venous signal does not predict the occurrence of postischemic malignant edema in 24 children with AIS[a]

Venous Signal Intensity on SWI	No Malignant Edema	Malignant Edema	Total
Hypointense (only)	14	0	14
Hyperintense	8	2	10
Total	22	2	24

[a] Pearson χ^2 test = 0.07.

DISCUSSION

SWI has been increasingly shown to be a useful non-contrast-enhanced imaging sequence in the evaluation of AIS.[9-13,15] SWI may do the following: 1) detect hemorrhagic components within infarcted tissue with higher sensitivity than other MR imaging sequences or imaging modalities,[16] 2) demonstrate hypointense signals in the veins draining hypoperfused areas and evaluate the ischemic penumbra by focusing on the venous drainage,[9-12] 3) show hyperintense signal in the veins draining regions of hyperperfusion or luxury perfusion indicating an increased risk of developing postischemic malignant edema,[13] 4) detect acute occlusive arterial thromboemboli,[17,18] 5) quantify microhemorrhages and predict hemorrhagic transformation before thrombolytic

therapy is initiated,[19] and 6) detect early hemorrhagic complications after intra-arterial thrombolysis.[17] Currently, most studies focus on adults, and literature on the role of SWI in PAIS is scant, based mostly on case reports or small case series. This is the largest study on SWI in PAIS to date.

Ischemic penumbra is characterized by hypoperfused brain tissue with the potential for functional recovery without morphologic damage.[20] This is possible if local blood flow can be reestablished at a sufficient level within a certain time interval. The identification of the ischemic penumbra is important because it represents tissue that could potentially be salvaged with the use of thrombolytic therapy. Although the benefit of thrombolytic therapy in PAIS has yet to be demonstrated in prospective clinical trials, retrospective studies show that at least a subset of children with AIS may potentially benefit from it.[21,22] Several tertiary pediatric centers have developed standardized systematic strategies to diagnose and treat PAIS, for participation in the ongoing Thrombolysis in Pediatric Stroke trial.[21,22] Ischemic penumbra can be depicted as a mismatch between reduced perfusion and normal diffusion by combining PWI and DWI/DTI.[23] In children, however, the routine application of PWI outside research protocols and tertiary care centers is still limited. DSC-PWI requires a rapid bolus injection of intravenous paramagnetic contrast agents that may delay acute antithrombotic therapy. ASL is a non-contrast-enhanced PWI method capable of measuring tissue perfusion by using blood as an endogenous "contrast" agent. ASL is not routinely performed in the acute setting because of the low SNR and limited spatial resolution. In addition, changes in signal intensity on ASL may be determined by factors other than reduced flow or ischemia, and knowledge of ASL-related artifacts is crucial for accurate interpretation.

The relationship between CBF and the oxygen extraction fraction (OEF) has been shown in both animal stroke models and humans by using PET, and 4 patterns have been observed in focal brain ischemia.[24,25] In the first pattern, an increase in CBV was observed to maintain CBF in response to physiologic conditions or demands (autoregulation). The second pattern is an increase of OEF to maintain a stable cerebral metabolic rate of oxygen ($CMRO_2$) in response to a reduction of CBF. The third pattern is characterized by an increase of OEF in brain regions with reduction of both CBF and $CMRO_2$ and represents ischemic penumbra. The fourth pattern represents the infarct core and is characterized by very low CBF and $CMRO_2$ with poor OEF. SWI accentuates the magnetic susceptibility differences between deoxygenated hemoglobin in the vessels and adjacent oxygenated tissues and is an ideal MR imaging sequence to depict changes in OEF noninvasively. In a retrospective study including 15 adult patients with nonlacunar ischemic stroke, Kao et al[10] showed that both SWI-DWI and PWI (MTT)-DWI mismatches were significantly associated with a higher incidence of infarct progression and had a similar ability to predict stroke evolution. In addition, they showed that semiquantitative evaluation of SWI patterns and MTT values correlated best in the MCA territories. The authors concluded that SWI is an alternative to PWI to assess ischemic penumbra and predict stroke evolution. In children, the role of SWI in depicting the ischemic penumbra was previously shown only in a small case series and a few case reports.[9,12,26] In our present study, we found a mismatch between vascular territories with SWI-hypointense venous signal and restricted diffusion in 6 children. In 5 of them, stroke progression was observed at follow-up. By contrast, stroke progression on follow-up was found in only 2 of 8 children without SWI-DTI mismatch. Our results show that a mismatch between vascular territories with SWI-hypointense venous signal and restricted diffusion is significantly associated with infarct progression in PAIS.

Postischemic malignant edema is a life-threatening early complication of PAIS and is defined as a space-occupying AIS with severe brain swelling and mass effect, which may cause transtentorial herniation and brain death.[27,28] Impaired autoregulation in patients with stroke has been shown to lead to a rise in regional CBF followed by increased extravasation of fluid into the brain tissue and edema.[29] This process is enhanced by disruption of the blood-brain barrier.[30] The increase in CBF results in reduction of OEF and subsequently in a higher concentration of oxygenated hemoglobin and SWI-hyperintense venous signal. In 1 child with AIS, SWI was shown to determine regions of hyperperfusion or luxury perfusion, which contributed to an increased risk of developing malignant edema.[13] To test our second hypothesis, we compared the occurrence of postischemic malignant edema in children with and without hyperintense venous signal on acute SWI. Our results show that hyperintense venous signal on acute SWI is not significantly associated with the development of malignant edema in PAIS.

Although this is the largest cohort of PAIS studied by SWI published to date, we are aware of several limitations of our study: the retrospective nature of the study resulting in the absence of follow-up neuroimaging studies in 10 children; the availability of ASL data in only 7 children; the semiquantitative analysis of the images, which is investigator-dependent though performed by consensus; differences in section thickness between ADC maps and mIP-SWI possibly having caused partial misregistration of some images; and no attempt to adjust for potential confounders with multiple logistic regression due to the rather small number of patients.

CONCLUSIONS

Our study shows that a mismatch between vascular territories with SWI-hypointense venous signal and restricted diffusion predicts infarct progression in PAIS, while hyperintense venous signal on acute SWI does not predict the development of malignant edema. SWI provides valuable information in PAIS and may guide early treatment options to prevent infarct progression and should be added to the neuroimaging diagnostic protocol of PAIS. Prospective studies with a larger cohort of children, a standardized follow-up interval, and ASL as part of the acute neuroimaging protocol are needed to further validate the value of SWI in PAIS.

REFERENCES

1. Amlie-Lefond C, Sébire G, Fullerton HJ. **Recent developments in childhood arterial ischaemic stroke.** *Lancet Neurol* 2008;7:425–35
2. deVeber GA, MacGregor D, Curtis R, et al. **Neurologic outcome in survivors of childhood arterial ischemic stroke and sinovenous thrombosis.** *J Child Neurol* 2000;15:316–24

3. Ganesan V, Hogan A, Shack N, et al. **Outcome after ischaemic stroke in childhood.** *Dev Med Child Neurol* 2000;42:455–61
4. Monagle P, Chalmers E, Chan A, et al. **Antithrombotic therapy in neonates and children: American College of Chest Physicians Evidence-Based Clinical Practice Guidelines (8th Edition).** *Chest* 2008; 133(6 suppl):887S–968S
5. Roach ES, Golomb MR, Adams R, et al. **Management of stroke in infants and children: a scientific statement from a Special Writing Group of the American Heart Association Stroke Council and the Council on Cardiovascular Disease in the Young.** *Stroke* 2008;39: 2644–91
6. Rafay MF, Pontigon AM, Chiang J, et al. **Delay to diagnosis in acute pediatric arterial ischemic stroke.** *Stroke* 2009;40:58–64
7. Gadian DG, Calamante F, Kirkham FJ, et al. **Diffusion and perfusion magnetic resonance imaging in childhood stroke.** *J Child Neurol* 2000;15:279–83
8. Bosemani T, Poretti A, Huisman TA. **Susceptibility-weighted imaging in pediatric neuroimaging.** *J Magn Reson Imaging* 2014;40: 530–44
9. Chalian M, Tekes A, Meoded A, et al. **Susceptibility-weighted imaging (SWI): a potential non-invasive imaging tool for characterizing ischemic brain injury?** *J Neuroradiol* 2011;38:187–90
10. Kao HW, Tsai FY, Hasso AN. **Predicting stroke evolution: comparison of susceptibility-weighted MR imaging with MR perfusion.** *Eur Radiol* 2012;22:1397–403
11. Kesavadas C, Thomas B, Pendharakar H, et al. **Susceptibility weighted imaging: does it give information similar to perfusion weighted imaging in acute stroke?** *J Neurol* 2011;258:932–34
12. Meoded A, Poretti A, Benson JE, et al. **Evaluation of the ischemic penumbra focusing on the venous drainage: the role of susceptibility weighted imaging (SWI) in pediatric ischemic cerebral stroke.** *J Neuroradiol* 2014;41:108–16
13. Bosemani T, Poretti A, Orman G, et al. **Pediatric cerebral stroke: susceptibility-weighted imaging may predict post-ischemic malignant edema.** *Neuroradiol J* 2013;26:579–83
14. Pexman JH, Barber PA, Hill MD, et al. **Use of the Alberta Stroke Program Early CT Score (ASPECTS) for assessing CT scans in patients with acute stroke.** *AJNR Am J Neuroradiol* 2001;22:1534–42
15. Santhosh K, Kesavadas C, Thomas B, et al. **Susceptibility weighted imaging: a new tool in magnetic resonance imaging of stroke.** *Clin Radiol* 2009;64:74–83
16. Wycliffe ND, Choe J, Holshouser B, et al. **Reliability in detection of hemorrhage in acute stroke by a new three-dimensional gradient recalled echo susceptibility-weighted imaging technique compared to computed tomography: a retrospective study.** *J Magn Reson Imaging* 2004;20:372–77
17. Mittal S, Wu Z, Neelavalli J, et al. **Susceptibility-weighted imaging: technical aspects and clinical applications, part 2.** *AJNR Am J Neuroradiol* 2009;30:232–52
18. Verschuuren S, Poretti A, Buerki S, et al. **Susceptibility-weighted imaging of the pediatric brain.** *AJR Am J Roentgenol* 2012;198: W440–49
19. Akter M, Hirai T, Hiai Y, et al. **Detection of hemorrhagic hypointense foci in the brain on susceptibility-weighted imaging clinical and phantom studies.** *Acad Radiol* 2007;14:1011–19
20. Astrup J, Siesjö BK, Symon L. **Thresholds in cerebral ischemia: the ischemic penumbra.** *Stroke* 1981;12:723–25
21. Bernard TJ, Rivkin MJ, Scholz K, et al. **Emergence of the primary pediatric stroke center: impact of the Thrombolysis in Pediatric Stroke Trial.** *Stroke* 2014;45:2018–23
22. Marecos C, Gunny R, Robinson R, et al. **Are children with acute arterial ischaemic stroke eligible for hyperacute thrombolysis? A retrospective audit from a tertiary UK centre.** *Dev Med Child Neurol* 2015;57:181–86
23. Albers GW. **Expanding the window for thrombolytic therapy in acute stroke. The potential role of acute MRI for patient selection.** *Stroke* 1999;30:2230–37
24. Baron JC. **Mapping the ischaemic penumbra with PET: implications for acute stroke treatment.** *Cerebrovasc Dis* 1999;9:193–201
25. Baron JC, Rougemont D, Soussaline F, et al. **Local interrelationships of cerebral oxygen consumption and glucose utilization in normal subjects and in ischemic stroke patients: a positron tomography study.** *J Cereb Blood Flow Metab* 1984;4:140–49
26. Meoded A, Poretti A, Tekes A, et al. **Clinical vignette: role of susceptibility-weighted imaging in predicting stroke evolution.** *Neurographics* 2013;3:159–63
27. Ramaswamy V, Mehta V, Bauman M, et al. **Decompressive hemicraniectomy in children with severe ischemic stroke and life-threatening cerebral edema.** *J Child Neurol* 2008;23:889–94
28. Rahme R, Jimenez L, Bashir U, et al. **Malignant MCA territory infarction in the pediatric population: subgroup analysis of the Greater Cincinnati/Northern Kentucky Stroke Study.** *Childs Nerv Syst* 2013;29:99–103
29. Dohmen C, Bosche B, Graf R, et al. **Identification and clinical impact of impaired cerebrovascular autoregulation in patients with malignant middle cerebral artery infarction.** *Stroke* 2007;38:56–61
30. Treadwell SD, Thanvi B. **Malignant middle cerebral artery (MCA) infarction: pathophysiology, diagnosis and management.** *Postgrad Med J* 2010;86:235–42

Computer-Assisted Volumetric Measurement of Core Infarct Volume in Pediatric Patients: Feasibility for Clinical Use and Development of Quantitative Metrics for Outcome Prediction

C.G. Filippi, A.M. El-Ali, V.Z. Miloushev, D.S. Chow, X. Guo, and B. Zhao

ABSTRACT

BACKGROUND AND PURPOSE: Infarct volume may predict clinical outcome in acute stroke, but manual segmentation techniques limit its routine use. We hypothesized that computer-assisted volumetric analysis to quantify acute infarct volume will show no difference compared with manual segmentation but will show increased speed of performance and will correlate with outcome.

MATERIALS AND METHODS: Patients with acute stroke younger than 18 years were included. Infarct volume on diffusion-weighted imaging was quantified by using computer-assisted volumetric and manual techniques. The Pediatric Stroke Outcome Measure scored clinical outcome. Computer-assisted volumetric and manual techniques were compared with correlation coefficients. Linear regression analysis compared Pediatric Stroke Outcome Measure with core infarct volume and percentage volume of brain infarction.

RESULTS: Twenty-three patients were analyzed (mean age, 4.6 years). Mean infarct volume from computer-assisted volumetric and manual approaches was 65.6 and 63.7 mL, respectively ($P = .56$). Concordance correlation between methods was 0.980, and between users, 0.968. The mean times for segmentation between computer-assisted volumetric and manual techniques were <1 minute and 7.3 minutes ($P < .001$). The mean infarct volumes for good and poor outcome groups were 7.4 and 75.7 mL ($P < .007$). The mean percentages of infarcted brain parenchyma for good and poor outcome groups were 0.6% and 10.4% ($P < .006$). Volumes of 32 mL and 3% for infarcted brain were associated with poor outcome in all patients.

CONCLUSIONS: Computer-assisted volumetric quantification of infarct volume is reproducible, is significantly faster than manual techniques, and may have important applications for future clinical workflow. Core infarct volumes and infarct percentage correlated with outcome severity.

ABBREVIATIONS: CAV = computer-assisted volumetry; PSOM = Pediatric Stroke Outcome Measure

Stroke in the pediatric population is occurring at increasingly younger ages with an increasing incidence estimated at 3–5 per 100,000 according to the US Nationwide Inpatient Sample (http://www.healthdata.gov/data/dataset/hcup-nationwide-inpatient-sample-nis), which showed annual increases in acute ischemic stroke admissions from 1995 to 2008.[1-6] However, pediatric stroke remains under-recognized among health care providers; a lack of evidence-based treatment and management guidelines specific to the pediatric population further complicates this problem.[7,8] This represents a critical health care problem, given the potential cost to society in terms of life-years of disability and life-years lost in the face of increasing incidence of acute ischemic arterial infarction of children.[6,7,9,10]

Recent studies support infarct volume quantification as a potential tool in the pediatric population for predicting clinical outcome.[11-13] For example, Ganesan et al[14] observed that infarcts of >10% parenchymal volume on T2-weighted imaging were associated with poor outcomes. Additionally, Domi et al[15] reported that reduced diffusion in the corticospinal tract was a predictor of motor outcomes. Furthermore, investigations in adults have suggested that core infarct volume quantification correlates best with long-term outcome; this finding lends credibility to a similar approach in pediatric stroke.[16-19]

Currently, the criterion standard for volumetric assessment involves manual segmentation, which can be time-consuming and technically challenging. These impediments may limit its use

Received June 4, 2014; accepted after revision September 28.

From the Department of Radiology, Columbia University Medical Center, New York, New York.

Alexander M. El-Ali, MD, is a recipient of Radiological Society of North America Medical Student Seed Grant 2013–2014.

Paper previously presented as an oral abstract at: Annual Meeting of the American Society of Neuroradiology, May 17–22, 2014; Montreal, Quebec, Canada.

Please address correspondence to C.G. Filippi, MD, Columbia University Medical Center, Department of Radiology, 177 Fort Washington Ave, MHB 3-111, New York, NY 10032; e-mail: sairaallapeikko@gmail.com

http://dx.doi.org/10.3174/ajnr.A4183

in the emergency setting, where time is critical for management. For these reasons, computer-assisted volumetry (CAV) applied to diffusion-weighted imaging may represent a potential tool to aid in the detection of core infarct volume in the pediatric population. With regard to neuroimaging, CAV has recently been used in the examination of recurrent glioblastoma with high reproducibility and speed compared with conventional manual approaches.

The purpose of this study was to describe a novel CAV technique for assessment of core infarct volume within the pediatric population. Specifically, we describe the reliability and feasibility of this technique compared with traditional manual approaches in patients with acute stroke. Additionally, the relationship between infarct volume and clinical outcomes by using the Pediatric Stroke Outcome Measure (PSOM) scale will be obtained.[20,21]

MATERIALS AND METHODS

Subjects

After institutional review board approval of this Health Insurance Portability and Accountability Act–compliant retrospective study, a query of the neuroradiology department data base for pediatric patients with acute arterial ischemic infarct at our institution from January 2011 to November 2012 was conducted. Acute arterial ischemic infarct was defined as an acute neurologic deficit in a patient with an MR imaging abnormality on DWI consistent with infarction and corresponding hypointense signal on the apparent diffusion coefficient map. Inclusion criteria were pediatric patients defined as younger than 18 years of age. Imaging inclusion criteria were MR imaging with DWI performed within 72 hours of admission to the hospital. Exclusion criteria were hypoxic-ischemic encephalopathy, intraparenchymal hemorrhage, prior infarcts, incomplete imaging, or poor image quality (motion degradation) and incomplete follow-up. Additionally, patients without medical records sufficient to obtain PSOM scores were also excluded.

Imaging Techniques

All imaging was performed on a 1.5T MR imaging system (Signa; GE Healthcare, Milwaukee, Wisconsin) with an 8-channel head-array coil (Signa HDxt; GE Healthcare). We performed the following sequences: sagittal T1-weighted (TR, 450 ms/TE, 6.5 ms; 5-mm thickness; echo-train length, 4; FOV, 24 cm; 256 × 224 matrix); axial T1-weighted (TR, 433 ms/TE 6.5 ms; 5-mm thickness; echo-train length, 4; FOV, 24 cm; 256 × 224 matrix); axial T2-weighted (TR, 5000 ms/TE, 90 ms; 5-mm thickness; echo-train length, 28; FOV, 24 cm; 320 × 320 matrix); and axial FLAIR imaging (TR, 8800 ms/TE, 120 ms; TI, 1650 ms; echo-train length, 1.0; 5-mm thickness; FOV, 24 cm; 256 × 192 matrix). Axial diffusion-weighted imaging (TR, 8000 ms/TE 88 ms; echo-train length, 1.0; 5-mm thickness; 128 × 128 matrix; FOV, 24 cm) was performed by using 2 b-values (0 and 1000 s/mm^2) and 3 diffusion-encoding gradient directions. Corresponding ADC maps were generated by commercial scanner software (FuncTool software; GE Healthcare).

Core Infarct Volume Segmentation

Two radiologists, including 1 with a Certificate of Added Qualification in neuroradiology, performed CAV analysis. The boundary of acute infarct was delineated on DWI sequences by using a proprietary segmentation algorithm developed in the Laboratory for Computational Image Analysis in the Department of Radiology, Columbia University Medical Center.[22,23] The computer-assisted algorithm was originally developed for liver lesions and has since been adapted for different applications, including, most recently, the volume of enhancing tumor in glioblastoma multiforme.[24-26] For the first step of the volume measurement, the entire infarct volume was separated from surrounding anatomic structures by using a segmentation algorithm that combines the image analysis techniques of active contours and a level set approach. Once the segmentation was completed on an image, the infarct contour was propagated to its neighboring images, serving as an initial region of interest for subsequent segmentations on the neighboring images. This process was continued iteratively until all the infarct images were segmented. Once the segmentation was finalized, infarct volumes were automatically calculated (Fig 1).

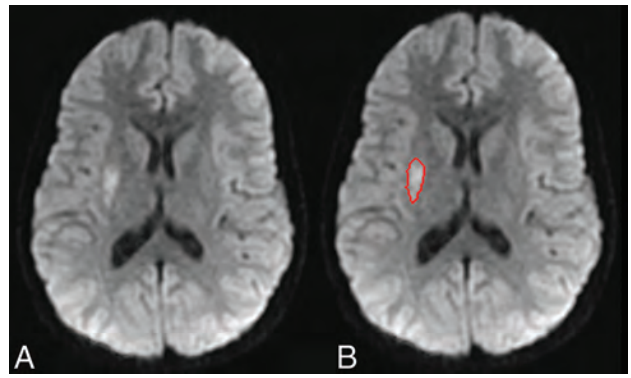

FIG 1. *A*, Reduced diffusivity within the right putamen consistent with an area of acute infarction. *B*, The contour derived from the semiautomated computer segmentation software that is used to derive infarct volume.

Table 1: Demographics of patients

Variable	No. (%)
Sex	
Male	12 (52.2)
Female	11 (47.8)
Ethnicity (No., %)	
White	4 (17.4)
Black	2 (8.7)
Asian	0 (0.0)
Hispanic	2 (8.7)
Other	15 (65.2)
Stroke risk factors (No., %)	
No risk factors	5 (21.7)
Single risk factors	11 (47.8)
Multiple risk factors	7 (30.4)
Risk factor distribution[a] (No., %)	
Hematologic	9 (39.1)
Vascular	7 (30.4)
Cardiac	4 (17.4)
Infection	3 (11.1)
Ingestion	1 (4.3)
Metabolic	1 (4.3)
Therapy (No., %)	
Anticoagulation	4 (17.4)
Antiplatelet	9 (39.1)
Anticonvulsant	14 (60.9)
Surgery	3 (13.0)

[a] Patients may have >1 risk factor.

For brain volume, we determined the contour of the brain cortical surface from which ventricular volume is subtracted by contouring the ventricular lining.

The same 2 radiologists, both of whom were blinded to the patients' prior CAV volumes and clinical outcomes, performed manual segmentation of infarct volume. Segmentation was performed by manual tracing of regions of reduced diffusion on DWI sequences. All manual segmentations were performed at a dedicated workstation (Advantage Workstation, Version 4.3; GE Healthcare). To reduce bias from prior CAV analysis, we performed manual measurements 3 months after the initial CAV analysis. All measurements were recorded in milliliters, and the time required to perform CAV and manual segmentation for core infarct volume was noted.

Table 2: Patient outcomes and stroke characteristics

Outcome Measures	(No.) (%)
Good[a]	5 (21.7)
Poor[b]	18 (78.3)
Mortality	5 (21.7)
Infarct circulation	
Anterior circulation only	20 (87.0)
Posterior circulation only	0 (0)
Both circulations	3 (13.0)
Infarct involvement	
Bilateral	11 (47.8)
ACA	8 (34.8)
MCA	23 (100.0)
PCA	12 (52.2)
Basal ganglia	9 (39.1)

Note:—ACA indicates anterior cerebral artery; PCA, posterior cerebral artery.
[a] "Good outcome" defined as healthy or mild disability using the Pediatric Stroke Outcome Measure.
[b] "Poor outcome" defined as moderate or severe disability using the Pediatric Stroke Outcome Measure or death.

Table 3: Stroke characteristics and patient outcomes

Category	Mean	Range	95% Confidence Interval		Standard Error
			Lower Limit	Upper Limit	
Total brain volume (mL)	936.6	392.0–1387.0	815.7	1057.5	61.67
Stroke volume (mL)	60.9	0.1–229.0	31.7	90.0	14.88
Stroke volume (%)	8.2	0.1–48.4	3.6	12.9	2.35
Good outcome[a]					
Stroke volume (mL)	7.4	0.08–31.63	0.97	26.12	5.48
Stroke volume (%)	0.6	0.01–2.64	0.05	2.12	0.45
Poor outcome[b]					
Stroke volume (mL)	75.7	0.40–229.00	47.28	115.43	16.80
Stroke volume (%)	10.4	0.05–48.42	6.35	17.57	2.71

[a] "Good outcome" defined as healthy or mild disability using the Pediatric Stroke Outcome Measure.
[a] "Poor outcome" defined as moderate or severe disability using the Pediatric Stroke Outcome Measure or death.

Correlation with Clinical Outcomes

Clinical outcome was scored by using the PSOM, which uses neurologic evaluation to examine sensorimotor function bilaterally, productive and receptive language, and cognitive and behavioral development.[20,21] The PSOM is typically scored as good (healthy or mild deficit) and poor (moderate or severe), and validity of the PSOM is not significantly affected when performed retrospectively.[20] Clinical data and PSOM were determined from chart review by using the examination findings of a pediatric neurologist. All patients were evaluated by a neurology attending physician following stroke, which was confirmed through chart review. Two neuroradiologists performed chart review.

Statistical Analysis

Mean manual and semiautomated volumetric measurements and segmentation times were compared by using a paired *t* test. Concordance correlation coefficients with corresponding confidence intervals between semiautomated and manual volumetric measurements were obtained. For analysis of clinical outcomes, core infarct volumes and the percentage of infarcted parenchymal volumes were compared among patients with good and poor outcomes by using the Wilcoxon rank sum test. Linear regression analysis was performed comparing the PSOM with core infarct volume and percentage volume of brain infarction. All statistical analysis was performed by using MedCalc for Windows, Version 12.2.1.0 (MedCalc Software, Mariakerke, Belgium). For this study, a P value of $< .05$ was considered statistically significant.

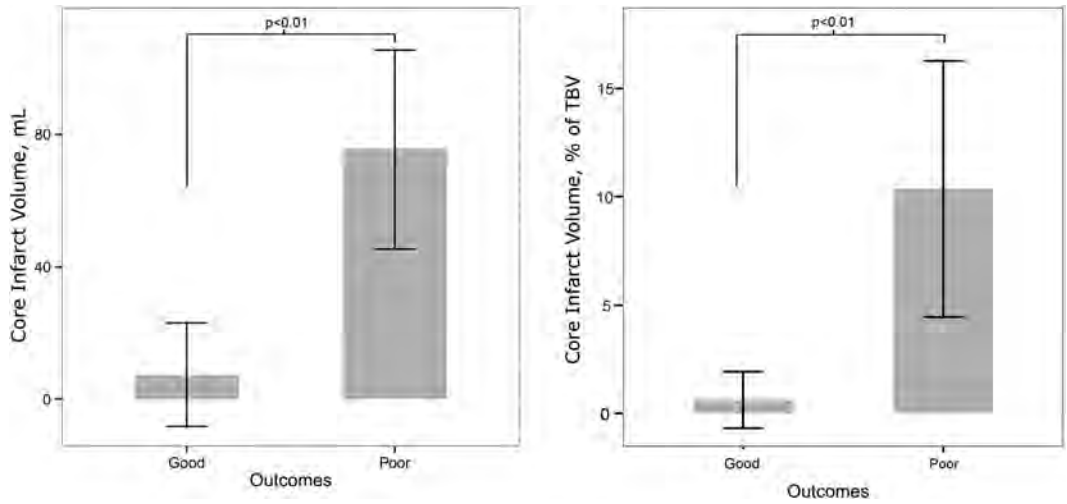

FIG 2. Graphic representation of the correlation of core infarct volume and percentage brain infarction with the Pediatric Stroke Outcome Measure. TBV indicates total brain volume.

RESULTS

Subjects

In total, 29 patients were identified, of which 79.3% (23/29) met the inclusion criteria. Patient demographics are listed in Table 1. These included 12 male and 11 female patients (age range, 0–17.6 years; mean age, 4.6 years) presenting with acute stroke. Clinical follow-up ranged from 0.8 to 19.3 months (mean, 5.1 months). Six patients were excluded. One had hypoxic-ischemic encephalopathy rather than acute stroke, 1 had marked intraparenchymal hemorrhage and prior infarcts, 1 had incomplete imaging with poor image quality (motion degradation), and another had incomplete clinical follow-up. An additional 2 patients did not have all test items in their medical records to calculate a PSOM score and were excluded.

Comparison between Manual and CAV Analysis

The mean core infarct volumes obtained for CAV and manual approaches were 65.6 and 63.7 mL, respectively ($P = .56$). The mean total brain volume was 936.6 mL. The concordance correlation between the methods was 0.980 (95% CI, 0.956–0.991). The concordance correlation for CAV measurements between 2 users was 0.968 (95% CI, 0.935–0.985). The concordance correlation for manual segmentation between 2 users was 0.978 (95% CI, 0.964–0.989). The concordance for mild and large infarcts with CAV measurements was 0.999 (95% CI, 0.994–1.000) and 0.962 (95% CI, 0.915–0.983), respectively. The concordance for mild and large infarcts with manual measurements was 0.976 (95% CI, 0.943–0.990) and 0.976 (95% CI, 0.953–0.983), respectively.

The mean times for segmentation between computer-assisted and manual techniques (including times for opening and saving images) were <1 minute and 7.3 minutes, respectively ($P < .01$).

Table 4: Infarct volume versus Pediatric Stroke Outcome Measure

	Regression Coefficient[a]	Standard Error	*P* Value
Infarct by percentage	0.150	0.067	.039
Infarct by absolute volume	0.028	0.010	.011

[a] Coefficient calculated with linear regression.

Correlation with Clinical Outcomes

Patient outcomes and stroke territory involvement are listed in Table 2, and patient outcomes with respect to stroke characteristics, including corresponding confidence intervals, are listed in Table 3. With regard to outcomes, 78.3% (18/23) had poor outcomes, and 21.7% (5/23) had good outcomes by the PSOM scores. Mortality was observed in 21.7% (5/23) cases. Mean core infarct volumes for the good and poor outcome groups were 7.4 and 75.7 mL, respectively ($P < .007$). Mean percentages of infarcted brain parenchyma for the good and poor outcome groups were 0.6% and 10.4%, respectively ($P < .006$). There was a significant correlation between PSOM and infarct volume ($P < .01$) and percentage of brain parenchymal infarction ($P < .04$). This is displayed graphically in Fig 2 and summarized in Table 4. Core infarct volumes of >32 mL and percentage of infarcted brain parenchyma of >3% had poor outcomes in all cases. Examples of segmentation results from CAV and manual approaches for infarcts in poor and good outcome cohorts are provided in Fig 3.

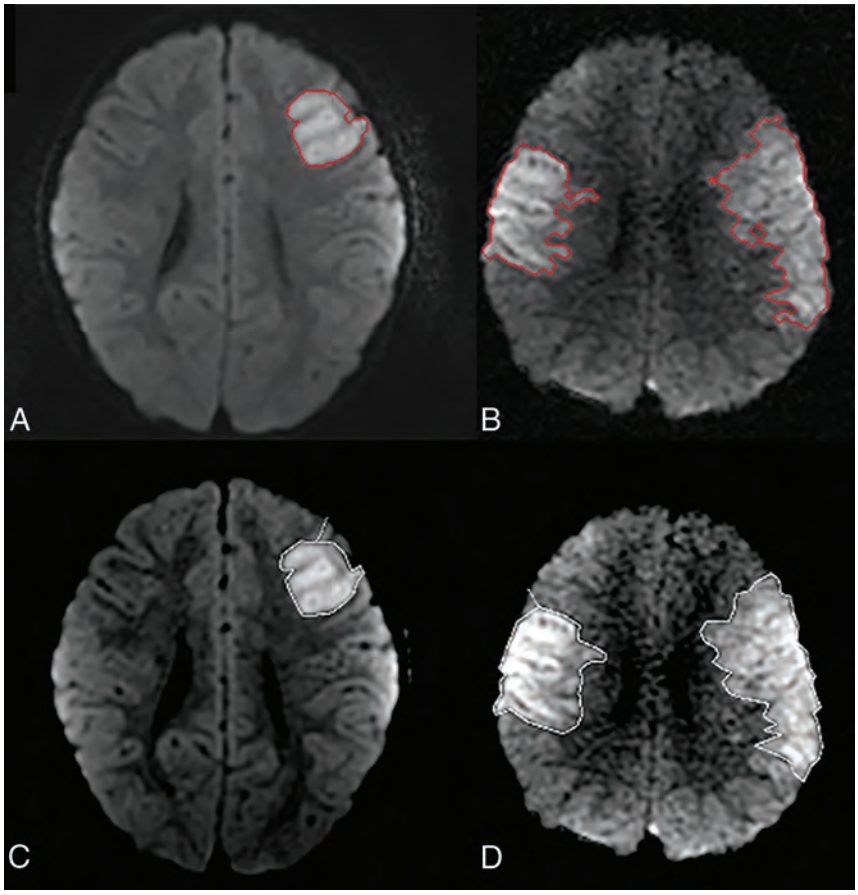

FIG 3. *A* and *B*, CAV segmentation results from patients in good and poor outcome groups, respectively. *C* and *D*, Manual segmentation results from the same respective patients.

DISCUSSION

Quantification of core infarct volume within the pediatric stroke population may provide assistance in clinical decision-making and prognostic information. However, challenges in manual segmentation currently limit its utility in an acute stroke setting because it can be prohibitively time-consuming. Additionally, while the present study did not find significant variability for manual measurements, prior work has suggested that manual determination of core infarct volume is a source of variance.[27] In the present study, we compared the quantification of infarct volume and the percentage of infarcted brain parenchyma by using a semiautomated, computer-assisted approach with a traditional, manual approach and observed no significant difference in

measured infarct volumes. CAV assessment showed high correlation between users, but the CAV was significantly faster compared with the manual approach, taking seconds to perform. The rapidity of computer-assisted quantification of infarct volume allows its real-time integration into a routine, clinical workload and its use in investigative research.

The development of quantitative neuroimaging biomarkers is needed to inform treatment planning, management, and prognostication in the setting of acute ischemic infarct in children as well as clinical trials, which need objective metrics for the assessment of clinical outcomes and cost effectiveness. Several prior studies have shown a correlation between final infarct volume and worse neurologic outcome. Zecavati et al[11] observed that core infarct volumes in pediatric patients, as determined on DWI, that exceed 10% of brain parenchymal volume were associated with poor neurologic outcome at 30 days; however, the authors used the Glasgow Outcome Score, which, unlike the PSOM, has not been specifically validated in the pediatric population. The PSOM is based on a standardized, neurologic examination; is currently the best validated outcome measure; and has shown excellent interobserver correlation and validity and reproducibility when used retrospectively to analyze neurologic examinations or in prospective longitudinal research.[20,21,28] In our study, we assessed the correlation between core infarct volume and clinical outcome by using the Pediatric Stroke Outcome Measure and observed that both infarct volume and the percentage of infarcted brain parenchyma correlated significantly with outcome. Specifically, cutoff values above 32 mL for core infarct volume and 3% for percentage of infarcted brain parenchymal volume were always associated with a bad outcome.

The CAV approach is robust; it is applicable to cases of solitary and multiple lesions and may represent an advance over qualitative vascular territory-based stroke scales. In addition, the software easily delineates total brain parenchymal volume excluding extra-axial CSF so that the percentage of infarcted brain parenchyma can be easily quantified. Beyond its utility in normalizing the infarct volume, CAV can be used independently for assessing total parenchymal or ventricular volume and may have additional applications in pediatric neuroradiology. Incorporation of CAV methods in standard clinical workflow has profound implications for the relevance of the radiologic consultation. In the context of pediatric stroke, CAV may identify children who would benefit from more aggressive therapy. CAV may quantify volumetric thresholds that could be used as end points for future clinical trials in pediatric stroke, and semiautomated methods may facilitate translation of these results from clinical trials into clinical practice.

When considering our results, several limitations should be kept in mind. First, we conducted a retrospective study, and our cohort of 23 patients is modest in size, which limits evaluation for confounders. Second, inclusion of neonates could be an additional confounder because longer follow-up may be needed because there may be a delay in the appearance of deficits after neonatal stroke, given that subtle sequelae may be difficult to delineate on neurologic examination in an incompletely myelinated, immature brain.[20,28] However, the average age in our study was almost 5 years. Because our study was based at a tertiary referral center, the poor outcome category could have been overrepresented. Children with associated neurologic disorders are included because stroke occurs with increased incidence in this group and gives the results wider applicability, and other investigators have validated the inclusion of children with neurologic disorders.[28] Additionally, our study is based on calculation of infarct volume on DWI sequences in the acute setting within 72 hours of diagnosis. However, Ebinger et al[12] have shown that subacute reduced diffusion volume in adults tightly correlated with final neurologic outcome assessed with the National Institutes of Health Stroke Scale, but most studies have shown stable DWI lesion evolution from 36 hours to 2 weeks.[12,29]

CONCLUSIONS

CAV quantification of core infarct volume in acute arterial ischemic infarct in pediatric patients provides a reproducible and significantly faster result comparable with manual techniques, which allows its easy integration into routine, clinical workflow. In our study, cutoff values above 32 mL for core infarct volume and 3% for percentage of infarcted brain parenchymal volume were associated with a poor outcome in all patients.

Disclosures: Christopher G. Filippi—*RELATED*: *Grant*: Radiological Society of North America Medical Student Seed Grant,* *Comments*: At the time of the study, coauthor Alexander El-Ali was a medical student; he is now a doctor, having graduated in May; *UNRELATED*: *Consultancy*: Regeneron Pharmaceuticals, Syntactx; *Grants/Grants Pending*: National Institutes of Health, *Comments*: 7/01/2012 to 4/30/2017; "Chronic Convection-Enhanced Delivery of Topotecan in Malignant Glioblastoma Multiforme"; Collaborator: C.G. Filippi (10% effort); Principal Investigator: Jeffrey Bruce; National Institutes of Health/National Cancer Institute; 1R01CA161404-01A; *Other:* advisor to resident and medical student as a research mentor,* *Comments*: Medical student and radiology residents have Radiological Society of North America grants for which I am scientific mentor, but this is unrelated to this work because it deals with T1 ρ MR imaging. *Money paid to the institution.

REFERENCES

1. deVeber G, Roach ES, Riela AR, et al. **Stroke in children: recognition, treatment, and future directions.** *Semin Pediatr Neurol* 2000;7:309–17
2. Carandang R, Seshadri S, Beiser A, et al. **Trends in incidence, lifetime risk, severity, and 30-day mortality of stroke over the past 50 years.** *JAMA* 2006;296:2939–46
3. Kissela BM, Khoury JC, Alwell K, et al. **Age at stroke: temporal trends in stroke incidence in a large, biracial population.** *Neurology* 2012;79:1781–87
4. George MG, Tong X, Kuklina EV, et al. **Trends in stroke hospitalizations and associated risk factors among children and young adults, 1995–2008.** *Ann Neurol* 2011;70:713–21
5. Fox CK, Fullerton HJ. **Recent advances in childhood arterial ischemic stroke.** *Curr Atheroscler Rep* 2010;12:217–24
6. Sultan S, Elkind MS. **Stroke in young adults: on the rise?** *Neurology* 2012;79:1752–53
7. Gardner MA, Hills NK, Sidney S, et al. **The 5-year direct medical cost of neonatal and childhood stroke in a population-based cohort.** *Neurology* 2010;74:372–78
8. Simma B, Holiner I, Luetschg J. **Therapy in pediatric stroke.** *Eur J Pediatr* 2013;172:867–75
9. Engelmann KA, Jordan LC. **Outcome measures used in pediatric stroke studies: a systematic review.** *Arch Neurol* 2012;69:23–27
10. Lequin MH, Dudink J, Tong KA, et al. **Magnetic resonance imaging in neonatal stroke.** *Semin Fetal Neonatal Med* 2009;14:299–310
11. Zecavati N, Singh R, Farias-Moeller R, et al. **The utility of infarct volume measurement in pediatric ischemic stroke.** *J Child Neurol* 2013;29:811–17
12. Ebinger M, Christensen S, De Silva DA, et al. **Expediting MRI-based**

proof-of-concept stroke trials using an earlier imaging end point. *Stroke* 2009;40:1353–58
13. Yoo AJ, Chaudhry ZA, Nogueira RG, et al. **Infarct volume is a pivotal biomarker after intra-arterial stroke therapy.** *Stroke* 2012;43:1323–30
14. Ganesan V, Ng V, Chong WK, et al. **Lesion volume, lesion location, and outcome after middle cerebral artery territory stroke.** *Arch Dis Child* 1999;81:295–300
15. Domi T, deVeber G, Shroff M, et al. **Corticospinal tract pre-Wallerian degeneration: a novel outcome predictor for pediatric stroke on acute MRI.** *Stroke* 2009;40:780–87
16. Beaulieu C, de Crespigny A, Tong DC, et al. **Longitudinal magnetic resonance imaging study of perfusion and diffusion in stroke: evolution of lesion volume and correlation with clinical outcome.** *Ann Neurol* 1999;46:568–78
17. Baird AE, Lövblad KO, Dashe JF, et al. **Clinical correlations of diffusion and perfusion lesion volumes in acute ischemic stroke.** *Cerebrovasc Dis* 2000;10:441–48
18. Tong DC, Yenari MA, Albers GW, et al. **Correlation of perfusion- and diffusion-weighted MRI with NIHSS score in acute (<6.5 hour) ischemic stroke.** *Neurology* 1998;50:864–70
19. Lövblad KO, Baird AE, Schlaug G, et al. **Ischemic lesion volumes in acute stroke by diffusion-weighted magnetic resonance imaging correlate with clinical outcome.** *Ann Neurol* 1997;42:164–70
20. Kitchen L, Westmacott R, Friefeld S, et al. **The Pediatric Stroke Outcome Measure: a validation and reliability study.** *Stroke* 2012;43:1602–08
21. deVeber GA, MacGregor D, Curtis R, et al. **Neurologic outcome in survivors of childhood arterial ischemic stroke and sinovenous thrombosis.** *J Child Neurol* 2000;15:316–24
22. Guo X, Zhao B. **A method and apparatus for infarct segmentation.** *Columbia University Invention Report IR* #CU15049. http://innovation.columbia.edu/technologies/2906_cumc-radiology-imaging-lab-available-technologies. Accessed November 24, 2014
23. Guo X, Zhao B, Schwartz LH. **Methods and systems for segmentation of organs and tumors and objects.** US Patent application PCT/US13/36166. April 1, 2013
24. Guo X, Schwartz LH, and Zhao B. **Semi-automated segmentation of multimodal brain tumor using active contours.** In: *Proceedings of NCI-MICCAI BRATS,* Nagoya, Japan. September 22–26, 2013:17–30
25. De Marchis GM, Filippi CG, Guo X, et al. **Brain injury visible on early MRI after subarachnoid hemorrhage might predict neurological impairment and functional outcome.** *Neurocritic Care* 2014 Jul 11. [Epub ahead of print]
26. Chow DS, Qi J, Guo X, et al. **Semiautomated volumetric measurement on postcontrast MR imaging for analysis of recurrent and residual disease in glioblastoma multiforme.** *AJNR Am J Neuroradiol* 2014;35:498–503
27. Rafay MF, Pontigon AM, Chiang J, et al. **Delay to diagnosis in acute pediatric arterial ischemic stroke.** *Stroke* 2009;40:58–64
28. deVeber G, Andrew M, Adams C, et al. **Cerebral sinovenous thrombosis in children.** *N Engl J Med* 2001;345:417–23
29. Lansberg MG, O'Brien MW, Tong DC, et al. **Evolution of cerebral infarct volume assessed by diffusion-weighted magnetic resonance imaging.** *Arch Neurol* 2001;58:613–17

Normal Fetal Posterior Fossa in MR Imaging: New Biometric Data and Possible Clinical Significance

R. Ber, O. Bar-Yosef, C. Hoffmann, D. Shashar, R. Achiron, and E. Katorza

ABSTRACT

BACKGROUND AND PURPOSE: Posterior fossa malformations are a common finding in prenatal diagnosis. The objectives of this study are to re-evaluate existing normal MR imaging biometric data of the fetal posterior fossa, suggest and evaluate new parameters, and demonstrate the possible clinical applications of these data.

MATERIALS AND METHODS: This was a retrospective review of 215 fetal MR imaging examinations with normal findings and 5 examinations of fetuses with a suspected pathologic posterior fossa. Six previously reported parameters and 8 new parameters were measured. Three new parameter ratios were calculated. Interobserver agreement was calculated by using the intraclass correlation coefficient.

RESULTS: For measuring each structure, 151–211 MR imaging examinations were selected, resulting in a normal biometry curve according to gestational age for each parameter. Analysis of the ratio parameters showed that vermian lobe ratio and cerebellar hemisphere ratio remain constant with gestational age and that the vermis-to-cisterna magna ratio varies with gestational age. Measurements of the 5 pathologic fetuses are presented on the normal curves. Interobserver agreement was excellent, with the intraclass correlation coefficients of most parameters above 0.9 and only 2 parameters below 0.8.

CONCLUSIONS: The biometry curves derived from new and existing biometric data and presented in this study may expand and deepen the biometry we use today, while keeping it simple and repeatable. By applying these extensive biometric data on suspected abnormal cases, diagnoses may be confirmed, better classified, or completely altered.

ABBREVIATIONS: ICC = intraclass correlation coefficient; CHR = cerebellar hemisphere ratio; CMS = cisterna magna cross-sectional area; PF = posterior fossa; TCD = transcerebellar diameter; VCMR = vermis-to-cisterna magna ratio; VLR = vermian lobe ratio; VP = vermian perimeter; VS = vermian cross-sectional area

The posterior cranial fossa is located between the foramen magnum, which forms its caudal boundary, and the tentorium cerebelli, which form its cephalad boundary. It includes the 3 parts of the brain stem: medulla oblongata, pons, and midbrain; the cerebellum with its vermis; and the fluid-filled spaces: the fourth ventricle and cisterna magna. The structures of the posterior fossa (PF) develop from the mesencephalon of the neural tube (midbrain and vermis), the metencephalon part of the rhombencephalon (pons and cerebellar hemispheres), and the myelencephalon part of the rhombencephalon (medulla oblongata), starting at the fourth gestational week. Normally, by the 18th gestational week, the PF consists of a developed vermis and cerebellum, a developed pons, and a fourth ventricle fully covered by the caudal part of the vermis, and the fluid-filled spaces are connected by the foramina of Luschka and Magendie.[1,2]

During the development of the structures and fluid-filled spaces of the PF, a wide spectrum of malformations of these structures is often observed. The variety of these malformations, isolated or part of a syndrome, and of their outcomes makes it difficult to classify the different pathologies.[3,4] During the past decade, attempts to classify the PF malformations have been made, to help physicians and radiologists diagnose and give an accurate prognosis for fetuses with a pathologic PF.[5-7]

The different classifications and the possible diagnoses are mainly on the basis of the morphology of the fetal PF and its biometric data. Formerly, normal biometric data were taken

Received August 4, 2014; accepted after revision September 22.

From the Departments of Obstetrics and Gynecology (R.B., D.S., R.A., E.K.), Pediatric Neurology (O.B.-Y.), and Diagnostic Imaging (C.H.), Chaim Sheba Medical Center, Tel Hashomer, Tel-Aviv University, Tel-Aviv, Israel.

Please address correspondence to Roee Ber, Department of Obstetrics and Gynecology, Chaim Sheba Medical Center, Tel Hashomer, Tel-Aviv University, Tel-Aviv, Israel; e-mail: berlerner@gmail.com

Indicates article with supplemental on-line tables.

Indicates article with supplemental on-line photos.

http://dx.doi.org/10.3174/ajnr.A4258

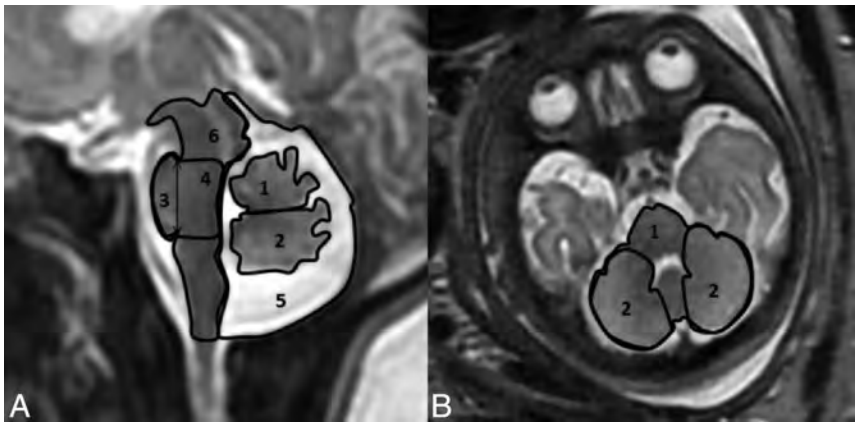

FIG 1. New parameters measured. *A*, Sagittal section of the PF: 1) vermian anterior lobe cross-sectional area, 2) vermian posterior lobe cross-sectional area, 3) pontine height, 4) pontine cross-sectional area, 5) cisterna magna cross-sectional area, 6) brain stem cross sectional area. *B*, Axial section of the PF: 1) cerebellar cross-sectional area and perimeter, and 2) cerebellar hemisphere cross-sectional areas.

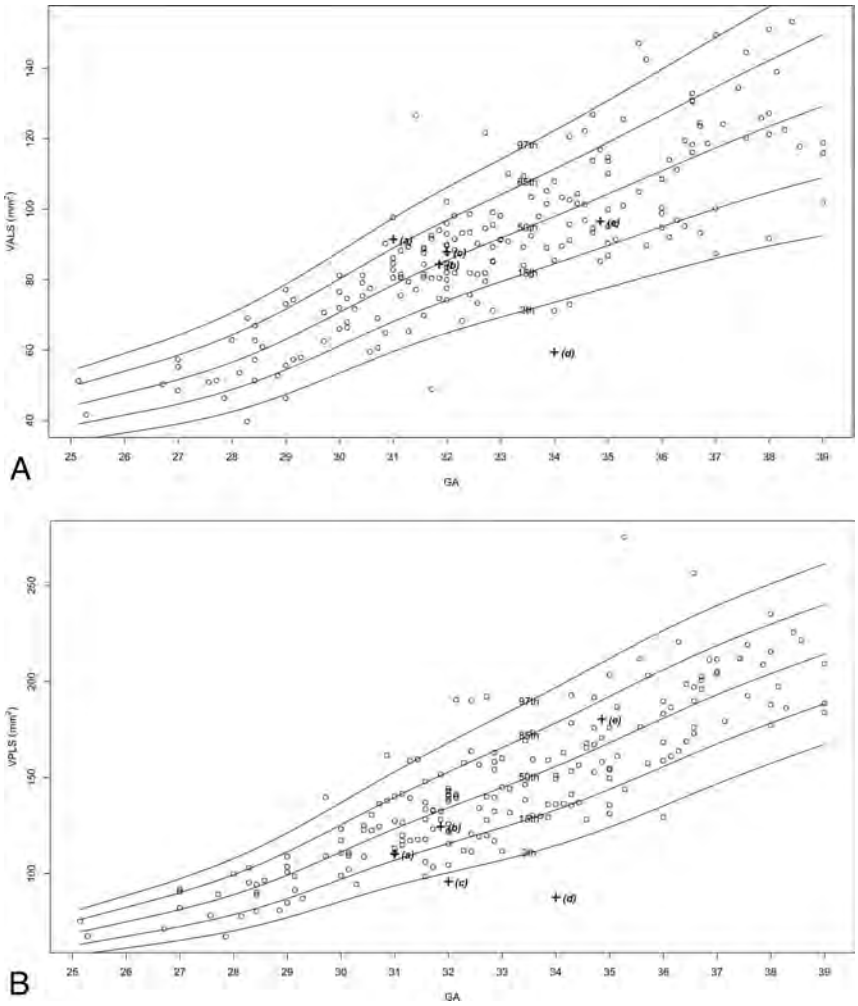

FIG 2. Percentile curves for new parameters. *A*, Vermian anterior lobe cross-sectional area. *B*, Vermian posterior lobe cross-sectional area.

mainly from studies of PF biometry in ultrasonographic imaging.[8-12] However, MR imaging has advantages over sonography when assessing fetal PF, such as better accuracy when evaluating the vermis and better contrast resolution, which enable evaluation of the brain stem.[13,14] Therefore, during the past 2 decades, MR imaging has become an important tool to prenatally evaluate the morphology of the PF, and many studies have been published to supply valid MR imaging biometric data.[15-17] However, because using MR imaging prenatally is still not a common procedure and is usually performed on suspected abnormal fetuses, re-evaluation is still needed. In addition, the high resolution of MR images makes it possible to measure structures that could not be measured before.

In this study, we re-evaluated existing normal MR imaging biometric data of PF structures in a large cohort. In addition, we suggest new biometric data, that, to our knowledge, were not measured in previous studies, to help correctly diagnose suspected pathologic fetuses. We demonstrate the potential clinical use of these data by retrospectively evaluating 5 different suspected pathologic cases.

MATERIALS AND METHODS

Population

We performed a retrospective review of 215 fetal MR imaging examinations in the Chaim Sheba Medical Center between 2007 and 2013. The included examinations were selected according to the following criteria: 25th–39th gestational week (the distribution of the number of fetuses examined by gestational week is presented in On-line Fig 1), no PF findings, and mild-to-no cerebral findings. Examinations of fetuses with isolated extracranial anomalies or maternal cytomegalovirus infection with no intracranial anomalies were also included. Eighty percent of the fetuses had no abnormal findings, and 20% had a mild lateral ventricular asymmetry or ventriculomegaly. The list of examination indications and findings is presented in On-line Table 1. For each structure measured, only satisfactory images in terms of quality and alignment were selected to be measured.

In addition, 5 fetuses with a suspected pathologic PF were selected for re-evaluation according to the new reference data generated in this study. The same structures were measured for these fetuses with the same procedure performed for healthy fetuses and detailed below.

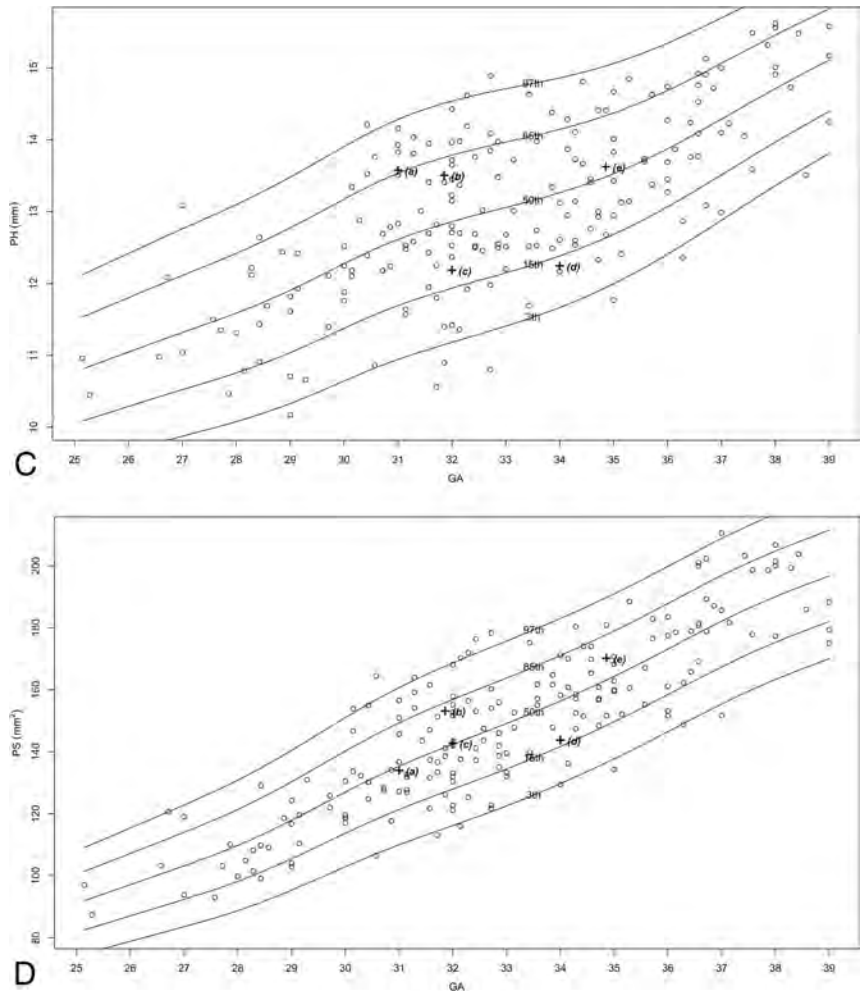

FIG 2. Continued. *C*, Pontine height. *D*, Pontine cross-sectional area.

MR Imaging Technique

In our institution, we perform fetal brain MR imaging by using a 1.5T system (Optima; GE Healthcare, Milwaukee, Wisconsin). Single-shot fast spin-echo T2-weighted sequences in 3 orthogonal planes were performed by using a half Fourier technique (NEX = 0.53) with the following parameters: section thickness, 3–4 mm; no gap; flexible coil (8-channel cardiac coil); matrix, 320/224; TE, 90 ms; and TR, 1298 ms. The FOV was determined by the size of the fetal head: 24 cm for the smaller fetuses and up to 30 cm for the larger fetuses. T1 fast-spoiled gradient-echo sequences were performed only in the axial plane with a larger FOV (400 mm); section thickness, 4 mm; gap, 0.5 mm; TR, 160 ms; and TE, 2.3 ms. The in-plane resolution of the T1 fast-spoiled gradient-recalled images was the following: sagittal—matrix, 256 × 160; FOV, 30 × 30; voxel, 1.17 × 1.875 mm; and coronal: matrix, 256 × 160; FOV, 36 × 36; voxel, 1.4 × 2.25 mm.

MR imaging was followed by a DWI sequence performed with a 40-cm FOV and b-values of 0 and 1000 or 700 ms. The ADC calculation map was added.[18]

Measurements

All measurements were performed manually by a single operator (R.B.) on a PACS reading workstation. Twenty-five random fetuses were remeasured by another operator (E.K.) to evaluate interobserver agreement for each structure. For each examination, 9 parameters were measured in the midsagittal section and 5, in the axial section. Axial section parameters were measured slightly above the base of skull in the plane of the following landmarks: the fastigium of the fourth ventricle, pons, anterior part of the temporal lobes, and eyeballs, with a symmetric presentation of the temporal lobes and eyeballs. Previously reported parameters measured in the midsagittal section included the anteroposterior diameter of the vermis, vermian height, vermian perimeter (VP), vermian cross-sectional area (VS), and pontine anteroposterior diameter. Previously reported parameters measured in the axial section included transcerebellar diameter (TCD). New parameters measured in the midsagittal section are presented in Fig 1*A* and included the vermian anterior lobe cross-sectional area, vermian posterior lobe cross-sectional area, pontine height, pontine cross-sectional area, brain stem cross-sectional area, and cisterna magna cross-sectional area (CMS). New parameters measured in the axial section are presented in Fig 1*B* and included the cerebellar perimeter and cerebellar cross-sectional area.

We calculated the following additional parameter ratios: the ratio between the cross-sectional areas of the vermian lobes (VLR), the ratio between the VS and CMS (VCMR), and the ratio between the cross-sectional areas of the cerebellar hemispheres (CHR). Previously reported biometric parameters (anteroposterior diameter of the vermis, vermian height, VS, VP, pontine anteroposterior diameter, TCD) were measured according to common methodology.[15,19] New parameters introduced in this study were measured as follows.

Sagittal Section Measurements. Vermian anterior lobe cross-sectional area and vermian posterior lobe cross-sectional area were measured as the cross-sectional area of the corresponding lobe of the vermis, with a separation line between the fourth ventricle fastigium and the vertex of the primary fissure of the vermis (Fig 1*A*). The posterolateral fissure, which separates the vermis from the nodule, is difficult to recognize in most images; therefore, the nodule of the vermis was included in the vermian posterior lobe cross-sectional area (Fig 1*A*).

Pontine height was measured as the height between the upper notch created between the pons and the cerebral peduncle and the lower notch created by the pontomedullary angle (Fig 1*A*).

The pontine cross-sectional area was measured as the area be-

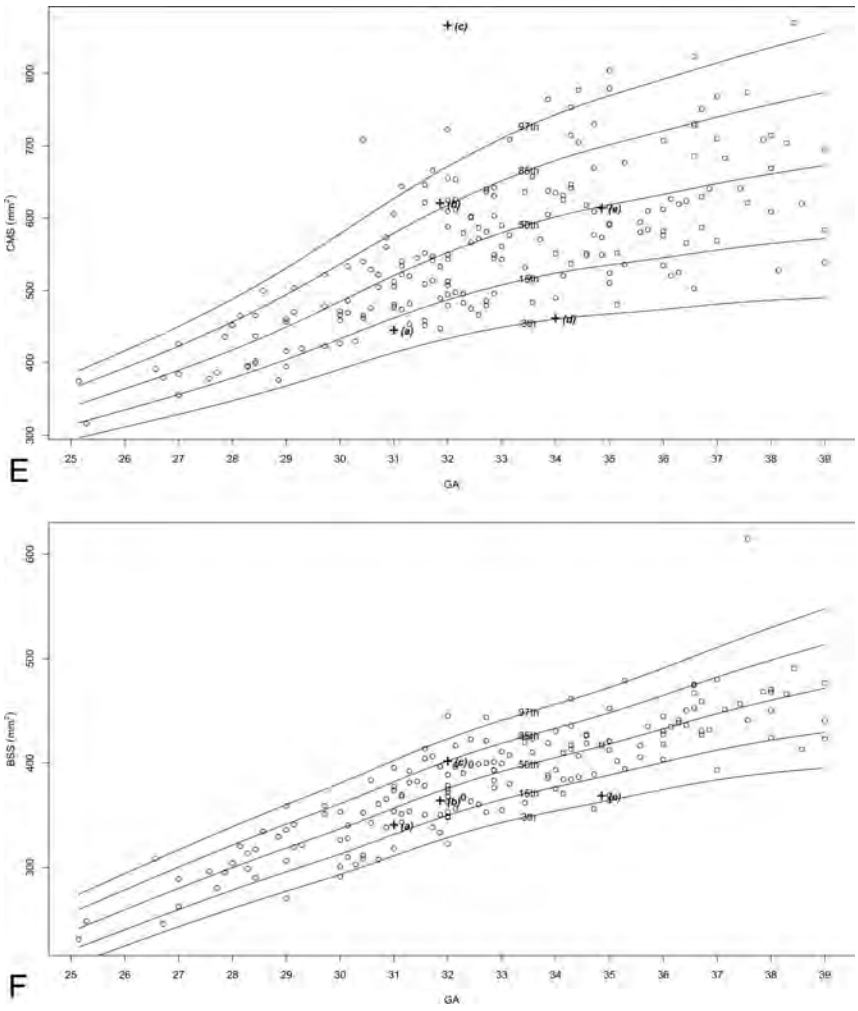

FIG 2. Continued. *E*, Cisterna magna cross-sectional area. *F*, Brain stem cross-sectional area.

tween 2 lines stretched from the pontopeduncular notch and the pontomedullary notch described above to the posterior boundary of the brain stem and orthogonal to its axis (Fig 1*A*).

CMS was measured as the area whose boundaries were the tentorium cerebelli, the posterior boundary of the brain stem, and the foramen magnum. The vermis, the fourth ventricle, and the cisterna magna were included in the CMS (Fig 1*A*).

Brain stem cross-sectional area was measured as the cross-sectional area of the medulla, the pons, and the midbrain with the tectum of the midbrain included (Fig 1*A*).

Axial Section Measurements. The cerebellar perimeter and cerebellar cross-sectional area were measured as the perimeter and area, respectively, encircling the cerebellum and the pons (Fig 1*B*).

Cross-sectional areas of the cerebellar hemispheres were measured as the area of right and left hemispheres of the cerebellum alone, excluding the vermis (Fig 1*B*).

Statistical Analysis

All statistical analysis was performed by using R, Version 3.0.1 (R statistical computing software; http://www.r-project.org). The reference intervals were estimated by using the Generalized Additive Models for Location, Scale, and Shape model,[20] the suggested method of the World Health Organization.[21] In our study, the model for centile q at gestational age t was $C_q = \mu_t + \sigma_t Z_q$, where μ_t and σ_t were the mean and SD at age t, measured in days, and Z_q was the q centile of the standard normal distribution. The functions μ_t and σ_t were estimated and smoothed by using the Rigby and Stasinopoulos algorithm[20] with a cubic spline smoothing. The normality assumption was slightly inadequate, but the resulting curves were almost identical to those achieved by assuming the Box-Cox t distribution (with 4 parameters) recommended.[21] In addition, we found the skewness and kurtosis parameters of the Box-Cox t distribution to be nonsignificant for all response variables; this finding supports our decision to simply use the normal distribution without any transformation.

For the ratio variables (VCMR, VLR, CHR), we examined the hypothesis $\mu_t = \mu$, to assess the independence of the ratios with gestational age. The hypothesis was tested by using the Generalized Additive Models for Location, Scale and Shape.

Intraclass correlation coefficient (ICC) and limit of agreement were used to study the reliability of measurements across measurers, and 25 subjects were measured by 2 measurers for this purpose. Results were defined as poor for ICC < 0.6, satisfactory for $0.6 <$ ICC < 0.8, good for $0.8 <$ ICC < 0.9, and excellent for ICC > 0.9.

Ethics Approval

The research was approved by the hospital research ethics board.

RESULTS

Normal Biometric Reference Data

Two hundred fifteen MR imaging examinations were selected for measurement, of which 151–211 images were selected as adequate for measuring in terms of quality and alignment, for each structure. The number of images per structure is presented in On-line Table 2. Normal percentile curves of biometric reference data previously reported (anteroposterior diameter of the vermis, vermian height, VS, VP, pontine anteroposterior diameter, TCD) are presented in On-line Fig 2. Normal percentile curves of new biometric reference data (vermian anterior lobe cross-sectional area, vermian posterior lobe cross-sectional area, pontine height, pontine cross-sectional area, CMS, brain stem cross-sectional area, cerebellar perimeter, cerebellar cross-sectional area) are presented in Fig 2. Normal percentiles for each parameter by gestational age are presented in On-line Tables 3–16.

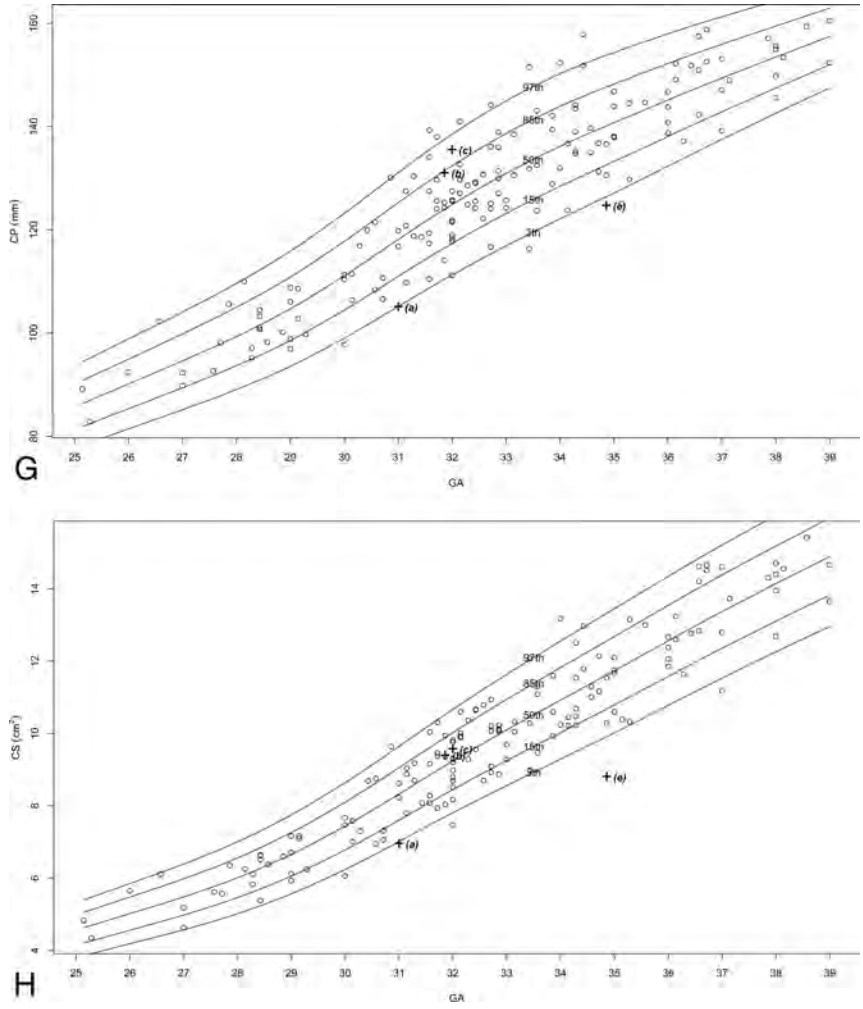

FIG 2. Continued. *G*, Cerebellar perimeter. *H*, Cerebellar cross-sectional area.

Abnormal measurements of pathologic cases

Case	Gestational Age (weeks)	Indication for MRI	Abnormal Measurements
A	31.0	Cerebellar asymmetry	CHR, TCD, CS, and CP below 3rd percentile
B	31.6	Enlarged cisterna magna	No abnormal measurements
C	32.0	Suspected abnormal vermis	VS, VPLS, and VCMR below 3rd percentile; CMS and VLR above 97th percentile
D	34.0	Suspected abnormal vermis	APDV, VH, VS, VP, VALS, and VPLS below 3rd percentile
E	32.0	Low TCD measurements and suspected abnormal brain stem	TCD, CS, and CP below 3rd percentile

Note:—APDV indicates anteroposterior diameter of the vermis; VH, vermian height; VALS, vermian anterior lobe cross-sectional area; CP, cerebellar perimeter; CS, cerebellar cross-sectional area; VPLS, vermian posterior lobe cross-sectional area.

Pathologic Cases Biometry

We obtained abnormal measurements for cases A, C, D, and E, according to new and previously reported biometric data. Case B had no abnormal measurements according to the parameters measured in this study. A list of the pathologic cases, their indication for MR imaging examination, and their abnormal biometry findings (measurements exceeding 2 SDs) is presented in the Table. The images of these fetuses are presented in Fig 3, and the measurements of images are presented on the normal curves in On-line Fig 2 and Fig 2 and are labeled according to their case number in the Table.

Normal Parameter Ratios

For VCMR, we obtained a highly significant result ($P < 10^{-10}$), implying that VCMR is not constant with gestational age. The normal percentile curves for VCMR are presented in On-line Fig 3, and the normal percentiles for VCMR are presented in On-line Table 17. For VLR and CHR, we obtained $P = .09$ and $P = .59$, respectively, and concluded that these ratios are constant with gestational age. Normal percentiles for VLR and CHR are presented in On-line Table 18.

Interobserver Agreement

Agreement between the 2 operators for each structure showed excellent correlation (ICC > 0.9) between measurers in 8 parameters, good correlation (0.8 < ICC < 0.9) in 4 parameters, and satisfactory correlation in only 2 parameters, VP and pontine height. The results are presented in On-line Table 19.

DISCUSSION

Malformations of the posterior fossa are a common finding in prenatal diagnosis and include a wide variety of pathologies and a wide spectrum of prognoses.[1,11,22] Therefore, the exact diagnosis and accurate prognosis given to the soon-to-be parents are crucial for the their understanding of the consequences of these malformations. The establishment of a diagnosis of PF malformation is based on several parameters, including anatomy, morphology, and biometry.[7] Insufficient biometry and reliance on examiners' subjective assessments may lead to a wrong diagnosis and wrong prognosis, including under- or overdiagnosis of different pathologies.[23,24]

Existing 2D MR imaging biometric data of the PF are limited to only a few parameters, which reduce the ability to analyze dynamic components such as the PF structures. Thus, the physician evaluating the fetus must rely on his or her subjective evaluation with limited objective tools. Furthermore, some previously reported studies showed no benefit in diagnosing PF malformations by using MR imaging compared with ultrasound.[4,22,25] However, the increasing use of fetal MR imaging examinations after ultrasound screening to diagnose cerebral pa-

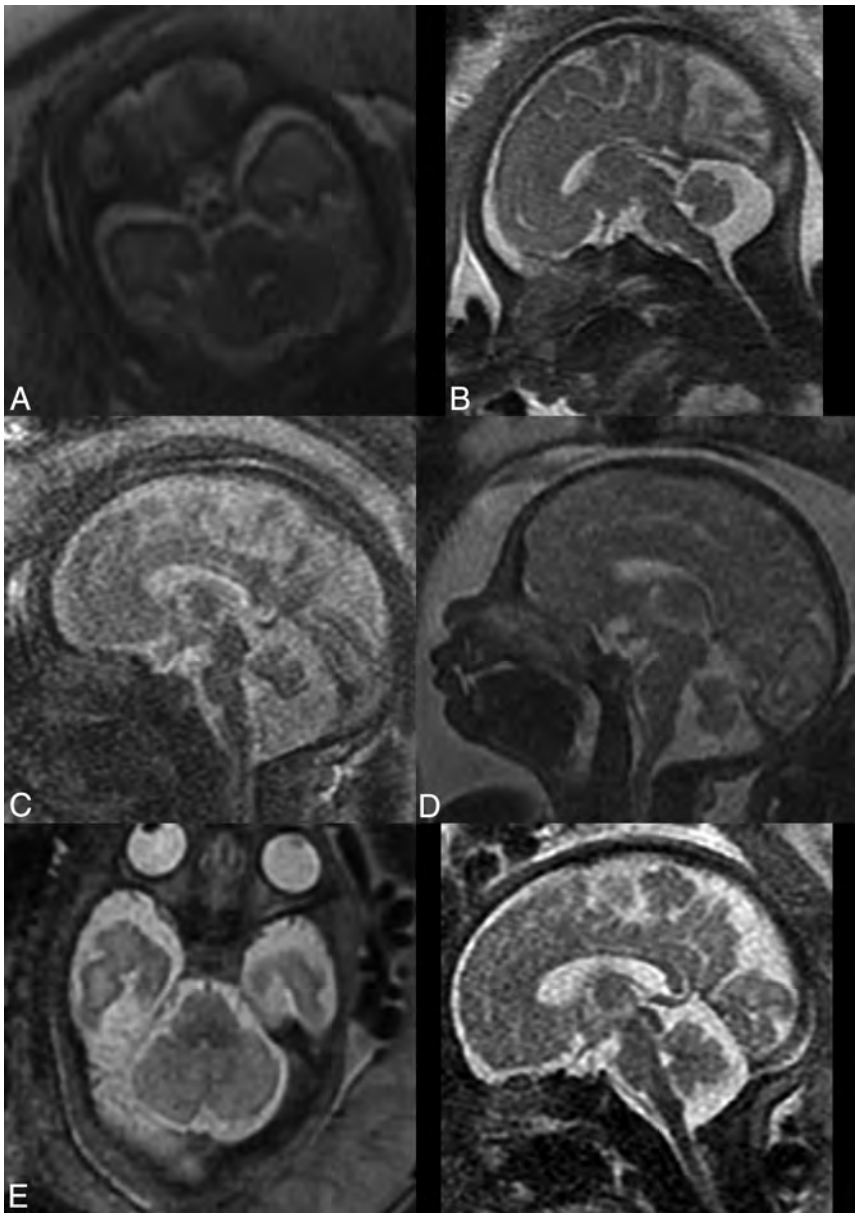

FIG 3. Pathologic cases indicated for MR imaging examinations. *A*, Cerebellar asymmetry. *B*, Enlarged cisterna magna. *C*, Suspected abnormal vermis. *D*, Suspected abnormal vermis. *E*, Low TCD measurements in axial (left) and saggital (right) planes.

thologies enables us to expand our biometric data to finer structures such as the vermian lobes and the brain stem. The vermian primary fissure is difficult to recognize by using ultrasound, making it difficult to differentiate between the vermian lobes. The brain stem is considered difficult to depict by using ultrasound techniques, and only limited biometric data are available.[10] MR imaging allows better evaluation of these structures and possible biometric assessment that might reinforce the role of MR imaging after ultrasound screening. Recent studies suggest a challenging approach to this issue by developing the technology to expand to 3D MR imaging biometry.[26-29] However, this approach has not matured and is not yet in clinical use.

In this study, we suggest that a more comprehensive yet technologically simple 2D biometry, including biometric relations between structures, can be a more thorough and accurate objective tool for diagnosing PF malformations. We performed measurements on a large cohort of 215 fetuses from the 25th to 39th gestational week. We measured 6 previously reported parameters[15,19] (anteroposterior diameter of the vermis, vermian height, VS, VP, pontine anteroposterior diameter, TCD) that are routinely used as biometric data. These parameters, together with morphologic analysis by the physician, support the diagnosis of PF malformations. To these existing data, we added 8 new biometric parameters and 3 new ratio parameters. We provided normal curves of these parameters and third, 15th, 50th, 85th, and 97th percentiles. We also showed the reproducibility of these measurements by evaluating interobserver agreement. Only 2 parameters, VP and pontine height, showed a satisfactory agreement. This could be explained by the difficulty in recognizing small fissures of the vermis in the case of VP and the difficulty in determining the location of the pontomedullary angle in the case of pontine height. The rest of the parameters measured showed good-to-excellent interobserver agreement. These expanded biometric data may replace the subjective morphologic assessment and allow further objective investigation of the pathologies.

Case A is an example of the possible clinical significance of the new parameters. Cerebellar asymmetry is a pathology diagnosed by the physician by morphologically evaluating the fetal cerebellum, along with measuring a small TCD. The cerebellar hemisphere ratio parameter, introduced in this study, may help the physician determine whether the asymmetry between lobes is within normal limits. In this case, the CHR was measured as 1.52, which exceeds normal limits and validates the subjective diagnosis of cerebellar asymmetry. By these data, we turn subjective analysis into an objective biometry-based analysis.

"Mega cisterna magna" is historically defined as a cisterna magna diameter exceeding 10 mm.[30] Previous studies have reported this definition to be inaccurate, and it has been shown to vary with gestational age.[31,32] The cisterna magna is a fluid-filled space that is normally continuous with the subarachnoid space of the entire PF, between the foramen magnum and the tentorium cerebelli. We measured the cross-sectional area of the entire fluid-filled space in the midsagittal section (CMS) and the ratio between the vermian cross-sectional area and the CMS. As reported and seen in Figs 2, both CMS and VCMR change according to gestational age but at different rates due to the change in VS. Case B was referred for

MR imaging due to an enlarged cisterna magna on ultrasound examination; the cisterna magna was measured as >10 mm on MR imaging. However, the new parameters, CMS and VCMR, were normal for this case. We believe that these curves may suggest a different approach for diagnosing mega cisterna magna, both isolated and as part of a more complex PF malformation. Perhaps by redefining the criteria for mega cisterna magna according to the new parameters, CMS and VCMR, we may avoid overdiagnosis of mega cisterna magna.

Cases C and D were both referred for MR imaging examination due to a suspected abnormal vermis on ultrasound. As seen in Fig 3, both cases present a rotated and small vermis. Indeed, VS parameters for the 2 cases are below the third percentile. Nevertheless, when we applied the new parameter measurements, a differentiation between those cases could be achieved. Case C presented with an abnormal ratio between the vermian lobes, VLR above the 97th percentile, with a small posterior lobe. This finding may imply that the posterior lobe of the vermis either developed abnormally or experienced mass effect by the fluid below it. This case also presented with an enlarged cisterna magna with CMS above the 97th percentile and VCMR below the third percentile. Case D, on the other hand, presented with a normal VLR, with 2 vermian lobe areas below the third percentile. This case did not present with an enlarged cisterna magna. The 2 seemingly similar cases morphologically are now 2 different cases biometrically. This result may help us avoid misinterpretations and overdiagnoses that were previously reported among entities such as partial vermian agenesis, inferior vermian hypoplasia, Blake pouch, and arachnoid cyst.[19] The primary fissure may be difficult to detect in cases of a rotated vermis, such as in Dandy-Walker malformation, and this is a limitation of the new measurements. However, in borderline cases such as C and D, it should be possible to recognize the primary fissure.

Case E was referred for MR imaging examination due to a small TCD and a suspected abnormal cerebellum and brain stem. As seen in Fig 3, one might suspect an asymmetry between cerebellar lobes and the brain stem looks relatively normal. When one applies the new biometric data, this case presents with a normal CHR, lowering the suspicion of asymmetry. The brain stem had relatively small biometric measurements (pontine anteroposterior diameter and brain stem cross-sectional area) below the 15th percentile. The cerebellum had all measurements (TCD, cerebellar cross-sectional area, and cerebellar perimeter) below the third percentile. These data help us describe the biometry of the PF accurately: a cerebellum that is small for gestational age, a brain stem that is relatively small, and a normal vermis and cisterna magna. This biometry may help us support or lower the suspicion of pontocerebellar dysplasia, for example.

The main limitation of this study is that we demonstrated the possible clinical significance of the new data only by applying it on selected pathologic cases. We did not compare the diagnoses we made by using these data with the previous evaluations of the pathologic cases, postnatal imaging, and their clinical outcomes. Another limitation is that we evaluated the interobserver agreement on measurements of normal cases. The results of this agreement are not necessarily valid for measurements of abnormal cases. We also did not assess the sex effect on PF measurements. This effect was previously reported to be significant statistically but insignificant clinically.[17]

CONCLUSIONS

Diagnosis of fetal pathologies of the PF are based mainly on biometry and morphology of the different structures. The expanding usage of MR imaging in prenatal screening enables us to expand the biometry we use in sonography screening. In this study, we presented comprehensive normative data, including the biometry of previously reported and new parameters and parameter ratios, in MR imaging, while keeping them simple and repeatable. We suggest that applying these new data may help further classify posterior fossa malformations, confirm borderline diagnoses, and avoid over- and underdiagnoses.

REFERENCES

1. Adamsbaum C, Moutard ML, Andre C, et al. **MRI of the fetal posterior fossa.** *Pediatr Radiol* 2005;35:124–40
2. Shekdar K. **Posterior fossa malformations.** *Semin Ultrasound CT MR* 2011;32:228–41
3. Guibaud L. **Practical approach to prenatal posterior fossa abnormalities using MRI.** *Pediatr Radiol* 2004;34:700–11
4. Malinger G, Lev D, Lerman-Sagie T. **The fetal cerebellum. Pitfalls in diagnosis and management.** *Prenat Diagn* 2009;29:372–80
5. Tortori-Donati P, Fondelli MP, Rossi A, et al. **Cystic malformations of the posterior cranial fossa originating from a defect of the posterior membranous area: mega cisterna magna and persisting Blake's pouch—two separate entities.** *Childs Nerv Syst* 1996;12:303–08
6. Patel S, Barkovich AJ. **Analysis and classification of cerebellar malformations.** *AJNR Am J Neuroradiol* 2002;23:1074–87
7. Guibaud L, des Portes V. **Plea for an anatomical approach to abnormalities of the posterior fossa in prenatal diagnosis.** *Ultrasound Obstet Gynecol* 2006;27:477–81
8. Snijders RJ, Nicolaides KH. **Fetal biometry at 14–40 weeks' gestation.** *Ultrasound Obstet Gynecol* 1994;4:34–48
9. Zalel Y, Seidman DS, Brand N, et al. **The development of the fetal vermis: an in-utero sonographic evaluation.** *Ultrasound Obstet Gynecol* 2002;19:136–39
10. Achiron R, Kivilevitch Z, Lipitz S, et al. **Development of the human fetal pons: in utero ultrasonographic study.** *Ultrasound Obstet Gynecol* 2004;24:506–10
11. Bertucci E, Gindes L, Mazza V, et al. **Vermian biometric parameters in the normal and abnormal fetal posterior fossa: three-dimensional sonographic study.** *J Ultrasound Med* 2011;30:1403–10
12. Ginath S, Lerman-Sagie T, Haratz Krajden K, et al. **The fetal vermis, pons and brainstem: normal longitudinal development as shown by dedicated neurosonography.** *J Matern Fetal Neonatal Med* 2013;26:757–62
13. Tilea B, Delezoide AL, Khung-Savatovski S, et al. **Comparison between magnetic resonance imaging and fetopathology in the evaluation of fetal posterior fossa non-cystic abnormalities.** *Ultrasound Obstet Gynecol* 2007;29:651–59
14. Blondiaux E, Garel C. **Fetal cerebral imaging–ultrasound vs. MRI: an update.** *Acta Radiol* 2013;54:1046–54
15. Garel C. **Fetal cerebral biometry: normal parenchymal findings and ventricular size.** *Eur Radiol* 2005;15:809–13
16. Triulzi F, Parazzini C, Righini A. **MRI of fetal and neonatal cerebellar development.** *Semin Fetal Neonatal Med* 2005;10:411–20
17. Tilea B, Alberti C, Adamsbaum C, et al. **Cerebral biometry in fetal magnetic resonance imaging: new reference data.** *Ultrasound Obstet Gynecol* 2009;33:173–81
18. Hoffmann C, Weisz B, Yinon Y, et al. **Diffusion MRI findings in monochorionic twin pregnancies after intrauterine fetal death.** *AJNR Am J Neuroradiol* 2013;34:212–16

19. Garel C, Fallet-Bianco C, Guibaud L. **The fetal cerebellum: development and common malformations.** *J Child Neurol* 2011;26:1483–92
20. Rigby RA, Stasinopoulos DM. **Generalized additive models for location, scale and shape.** *Appl Statist* 2005;54(part 3):507–54
21. Borghi E, de Onis M, Garza C, et al. **Construction of the World Health Organization child growth standards: selection of methods for attained growth curves.** *Stat Med* 2006;25:247–65
22. Gandolfi Colleoni G, Contro E, Carletti A, et al. **Prenatal diagnosis and outcome of fetal posterior fossa fluid collections.** *Ultrasound Obstet Gynecol* 2012;39:625–31
23. Limperopoulos C, Robertson RL, Estroff JA, et al. **Diagnosis of inferior vermian hypoplasia by fetal magnetic resonance imaging: potential pitfalls and neurodevelopmental outcome.** *Am J Obstet Gynecol* 2006;194:1070–76
24. Limperopoulos C, Robertson RL Jr, Khwaja OS, et al. **How accurately does current fetal imaging identify posterior fossa anomalies?** *AJR Am J Roentgenol* 2008;190:1637–43
25. Malinger G, Lev D, Lerman-Sagie T. **Is fetal magnetic resonance imaging superior to neurosonography for detection of brain anomalies?** *Ultrasound Obstet Gynecol* 2002;20:317–21
26. Andreas T, Wedegartner U, Tchirikov M, et al. **Fetal brain volume measurements by magnetic resonance imaging.** *Ultrasound Obstet Gynecol* 2006;27:588–89
27. Ioannou C, Sarris I, Salomon LJ, et al. **A review of fetal volumetry: the need for standardization and definitions in measurement methodology.** *Ultrasound Obstet Gynecol* 2011;38:613–19
28. Scott JA, Hamzelou KS, Rajagopalan V, et al. **3D morphometric analysis of human fetal cerebellar development.** *Cerebellum* 2012;11:761–70
29. Vatansever D, Kyriakopoulou V, Allsop JM, et al. **Multidimensional analysis of fetal posterior fossa in health and disease.** *Cerebellum* 2013;12:632–44
30. Mahony BS, Callen PW, Filly RA, et al. **The fetal cisterna magna.** *Radiology* 1984;153:773–76
31. Garel C. **Posterior fossa malformations: main features and limits in prenatal diagnosis.** *Pediatr Radiol* 2010;40:1038–45
32. Brown RN. **Reassessment of the normal fetal cisterna magna during gestation and an alternative approach to the definition of cisterna magna dilatation.** *Fetal Diagn Ther* 2013;34:44–49

Characterizing the Location of Spinal and Vertebral Levels in the Human Cervical Spinal Cord

D.W. Cadotte, A. Cadotte, J. Cohen-Adad, D. Fleet, M. Livne, J.R. Wilson, D. Mikulis, N. Nugaeva, and M.G. Fehlings

ABSTRACT

BACKGROUND AND PURPOSE: Advanced MR imaging techniques are critical to understanding the pathophysiology of conditions involving the spinal cord. We provide a novel, quantitative solution to map vertebral and spinal cord levels accounting for anatomic variability within the human spinal cord. For the first time, we report a population distribution of the segmental anatomy of the cervical spinal cord that has direct implications for the interpretation of advanced imaging studies most often conducted across groups of subjects.

MATERIALS AND METHODS: Twenty healthy volunteers underwent a T2-weighted, 3T MRI of the cervical spinal cord. Two experts marked the C3–C8 cervical nerve rootlets, C3–C7 vertebral bodies, and pontomedullary junction. A semiautomated algorithm was used to locate the centerline of the spinal cord and measure rostral-caudal distances from a fixed point in the brain stem, the pontomedullary junction, to each of the spinal rootlets and vertebral bodies. Distances to each location were compared across subjects. Six volunteers had 2 additional scans in neck flexion and extension to measure the effects of patient positioning in the scanner.

RESULTS: We demonstrated that substantial variation exists in the rostral-caudal position of spinal cord segments among individuals and that prior methods of predicting spinal segments are imprecise. We also show that neck flexion or extension has little effect on the relative location of vertebral-versus-spinal levels.

CONCLUSIONS: Accounting for spinal level variation is lacking in existing imaging studies. Future studies should account for this variation for accurate interpretation of the neuroanatomic origin of acquired MR signals.

ABBREVIATION: PMJ = pontomedullary junction

Advanced MR imaging techniques of the human spinal cord are critical to understanding the pathophysiology of conditions such as traumatic injury, degenerative spondylosis, or neuroinflammatory conditions such as multiple sclerosis. These techniques provide the opportunity to assess subclinical changes in spinal cord structure and function. For example, diffusion tensor imaging and magnetization transfer can be used to follow the integrity of white matter tracts in specific regions of the human spinal cord[1]; fMRI can be used to track the spinal response to a particular stimulus, reflecting the integrity of specific functional circuits.[2] Recently, the microstructure of the corticospinal motor pathway was mapped; imaging characteristics of this map correlated with clinical function.[3] The ultimate goal of early detection of subclinical recovery or deterioration should be to personalize treatment strategies in both the acute and chronic phases of injury.

A prerequisite to accurate interpretation of advanced imaging data is appreciating the neuroanatomic origin of the acquired signal. An imaging atlas brings prior spatial knowledge to an imaging dataset. Advanced brain imaging has benefited from the design and improvement of brain atlases that allow registration of various functional and structural imaging studies.[4,5] Atlases of the spinal cord are not as developed. Despite recent initiatives for creating a generic template of the spinal cord,[6] most previous templates have been created by individual research groups to meet the objectives of specific studies. For example, manually segmented templates have been created on the basis of specific anatomic information of the nerve rootlet position.[2] Perhaps most common is to infer neuroanatomic positions within the spinal

Received August 12, 2014; accepted after revision October 1.

From the Department of Surgery, Division of Neurosurgery (D.W.C., A.C., J.R.W., M.G.F.), Department of Computer Science (D.F., M.L.), and Department of Medical Imaging, Division of Neuroradiology (D.M.), University of Toronto, Toronto, Ontario, Canada; Toronto Western Hospital (D.W.C., D.M., N.N., M.G.F.), University Health Network, Toronto, Ontario, Canada; and Institute of Biomedical Engineering (J.C.-A.), Ecole Polytechnique de Montréal, Montreal, Quebec, Canada.

Please address correspondence to Michael G. Fehlings, MD, Division of Neurosurgery, Toronto Western Hospital, 399 Bathurst St, Suite 4WW-449, Toronto, Ontario M5T2S8, Canada; e-mail: michael.fehlings@uhn.ca; @DrFehlings

Indicates open access to non-subscribers at www.ajnr.org

http://dx.doi.org/10.3174/ajnr.A4192

cord by counting the adjacent vertebral bodies and stating that, for example, the C6 spinal cord segment is adjacent to the C5 vertebral body.[7] This latter approach coincides with widely accepted neuroanatomy textbooks, but the error associated with vertebral body measurements to predict the immediate caudal spinal cord segment has not been investigated. The diversity of human anatomy offers 2 principal sources of variability: 1) intersubject differences in spinal column anatomy, and 2) intersubject differences in spinal cord segments relative to a fixed point in the brain stem. The work presented here considers these 2 sources of diversity across a cohort of healthy individuals and presents a unique solution, a "spinal level map," which can be applied in advanced MR imaging assessment of the human cervical cord.

In this work, we impart a neuroanatomic context to single-subject high-resolution images of the cervical spine by delineating the location of vertebral bodies and spinal cord segments down the central axis of the spinal cord. Thus, we account for the personal anatomy of single subjects. Using expert markings as ground truth data, we report the distribution of vertebral and spinal cord segments across our cohort of 20 subjects. To the best of our knowledge, this is the first article that presents a quantitative, accurate solution to delineate the anatomic variability of the human cervical spinal cord. We anticipate that this approach will dramatically enhance the accuracy of quantitative MR imaging–based assessment of the normal and diseased spinal cord.

MATERIALS AND METHODS

Study Design

In this work, we investigated 20 healthy volunteers (7 men; mean age, 30.5 years; range, 19–52 years) to delineate the segmental structural anatomy of the human cervical spine. We describe the spatial relationships of both intrasubject segmental anatomy and intersubject differences in relative anatomic locations. Informed consent was obtained in all cases, and approval to conduct this work was granted by our institutional ethics review board. Demographic information of participants is listed in Table 1.

Table 1: Demographic information of study participants

Participant No.	Age (yr)	Sex	Height (cm)
1	32	F	163
2	44	M	181
3	28	F	168
4	47	M	170
5	23	F	171
6	52	F	170
7	31	F	157
8	29	M	182
9	21	M	179
10	34	F	164
11	25	F	175
12	22	F	186
13	19	M	180
14	27	F	173
15	22	M	162
16	28	F	159
17	34	F	169
18	30	F	168
19	25	F	176
20	36	M	174

MR Imaging Acquisition

All imaging data were acquired on a 3T HDx MR imaging system (GE Healthcare, Milwaukee, Wisconsin) at the Toronto Western Hospital by using an 8-channel neurovascular array coil. Subjects were carefully positioned to limit head movement and were requested not to move. A T2-weighted acquisition was obtained to optimize visualization of cervical nerve rootlets emerging from the spinal cord in a segmental fashion. We used a FIESTA-C sequence (T2-weighted): matrix, 512 × 512; NEX, 1.0; FOV, 200 mm; section thickness, 0.3 mm resulting in a voxel size of 0.3906 × 0.3906 × 0.3000 mm, without interpolation, collected in the coronal plane. Total scanning time was approximately 12 minutes.

In a subset of individuals ($n = 6$), we acquired 3 volumes: 1 in a neutral position, 1 in neck flexion, and 1 in neck extension. Although neck flexion and extension are limited within the confines of the imaging environment, we obtained roughly 6°–10° of either flexion or extension by placing extra padding under the occiput (neck flexion) or under the shoulders (neck extension). This range represents the normal positions that one might expect in the imaging environment.

Measurements along the Spinal Cord Axis

To accurately measure distances from a common point in the brain stem, the pontomedullary junction (PMJ), to any set of nerve rootlets or vertebrae along the spinal cord, we used custom algorithms written in the Python language. First, the centerline of the cord was estimated by using manual markings in 3DSlicer (http://www.slicer.org/). These points were used as the initial control points of a Catmull-Rom spline, representing the centerline of the spinal cord.[8] A 2D template-matching algorithm, by using ground truth data from several manually segmented spinal cord images, was used to segment the cervical spinal cord. The segmented volume was then used to determine a more precise centerline, which became new control points for the spline. Using the adjusted/centered spline, we identified the center point of the spinal cord at all distances from the PMJ to the lower cervical spinal cord, caudal to the C8 spinal cord segment, yielding the spinal cord centerline. Using this centerline, we then defined the arc-length axis of each individual's spinal cord and used this axis to perform measurements. Briefly, the arc-length axis can be defined as the longitudinal distance from the pontomedullary junction down the spinal cord. This reference system is unique in that it avoids the use of a Cartesian (x, y, z) coordinate system, which would be less accurate in defining distances down the spinal cord, given the variation in spinal curvature across individuals. The generation of this arc-length central spinal cord axis is illustrated in Fig 1.

Nerve Rootlet and Vertebral Body Localization

We used the C3 through C8 spinal nerve rootlets as a surrogate marker for the segmental anatomy of the spinal cord in an individual subject. To determine the distance from the PMJ to each set of spinal nerve rootlets, 2 individuals with specialized knowledge of spinal cord anatomy manually marked the dorsal nerve rootlets of segments C3–C8 at the edge of the spinal cord where the rootlets meet the CSF by using 3DSlicer. To perform these

markings, we visualized the spinal cord and cervical nerve rootlets in 3 planes (axial, sagittal, and coronal) and followed these nerve rootlets as they transition into cervical nerve roots and traverse the respective intervertebral foramen. For example, the C3 nerve rootlets transition into the C3 nerve root and emerge through the intervertebral foramen between the C2 and C3 vertebrae. After we confirmed that specific nerve rootlets had transitioned from a specific nerve root, individual dorsal nerve rootlets were marked in 3DSlicer. The most rostral and caudal extents of the C3–C7 vertebral bodies were also marked on a midsagittal section of each subject. The selected nerve rootlet and vertebrae points were then projected onto the spinal cord centerline by orthogonal projection at the midpoint of the rostral and caudal extents of either structure. A combination of MR images and artist illustration is used in Fig 2 to show how these markings were performed.

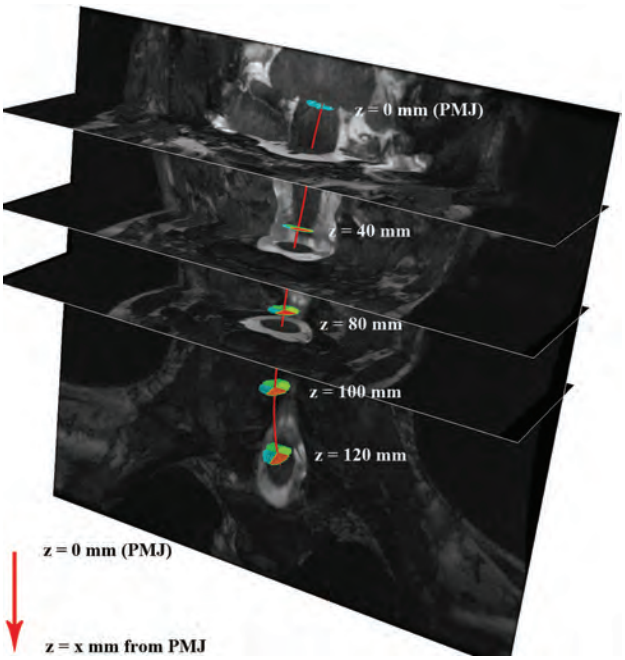

FIG 1. Results of spinal cord centerline extraction in 1 subject. The *red line* represents the spinal cord centerline. Distance from the PMJ is calculated along this centerline (z, in millimeters), for measuring the absolute location of the vertebral and spinal levels.

Interobserver Reproducibility in Identifying Cervical Nerve Rootlets and Vertebral Bodies

The interobserver reliability of both nerve rootlet and vertebral body measurements was assessed by obtaining the intraclass correlation coefficient values comparing the assessments of 2 independent observers. These coefficients were obtained by using a 2-way mixed-effects model in the SPSS statistics package, Version 21 (IBM, Armonk, New York).

Are Vertebral Bodies a Reliable Surrogate Marker for Spinal Cord Segments?

To determine whether vertebral bodies are a reliable surrogate marker for spinal cord segments, we determined the amount of overlap between the 2. This was accomplished by determining the most rostral and caudal distances of the vertebrae and spinal cord segment in question, relative to the PMJ, and calculating the percentage of the spinal cord segment that falls within the vertebral segment area. For example, for 1 subject, the C6 vertebral body lies at a distance between 116 and 128 mm from the PMJ. The C7 spinal cord segment for the same individual lies between 110 and 118 mm from the PMJ. The overlap in this case is 2 mm at the rostral end of the vertebrae and caudal end of the spinal cord segment. The percentage overlap is calculated as overlap divided by the total length of the vertebral body, in this case 2/12 mm, or 17%.

Does Patient Positioning within the MR Imaging Environment Exacerbate Differences between Vertebral and Spinal Cord Segments?

Patient positioning for neck flexion and extension is described above. To calculate the degree of neck flexion or extension, we compared the tangent of the spinal cord in the sagittal plane at 2 points along the spinal cord. In previous work, the angle was measured as the difference in vertebrae angles at C2 and C7.[9,10] The angle between these 2 vertebrae is calculated by drawing a line parallel to the posterior edge of the vertebral body, which runs parallel to the spinal cord, and calculating the angle between those 2 lines.

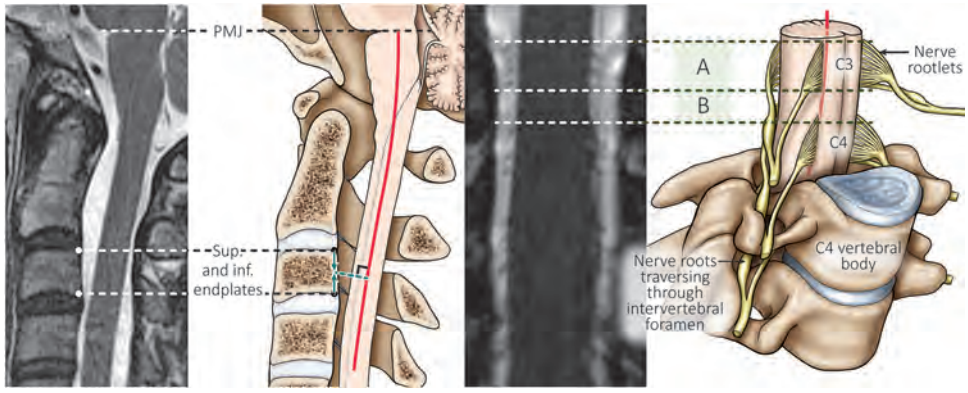

FIG 2. From left to right: T2-weighted MR image with the PMJ and superior (Sup.) and inferior (inf.) endplates of the C3 vertebral body marked with *dashed white lines*. Immediately adjacent to this, an artist's illustration demonstrates how person-specific markings are positioned relative to the individualized arc-length axis of the spinal cord (*red line*). Thus, distances can be compared across individuals along their personalized spinal cord axes. The T2-weighted coronal image depicts spinal rootlets (A) and the gap between adjacent segmental rootlets (B), delineated by *dashed white lines*. The far right artist's illustration depicts segmental rootlets and the formation of a spinal nerve root that emerges from the intervertebral foramen. To accurately localize segmental nerve rootlets, we followed the spinal nerve root that emerges from the intervertebral foramen of the respective vertebral body.

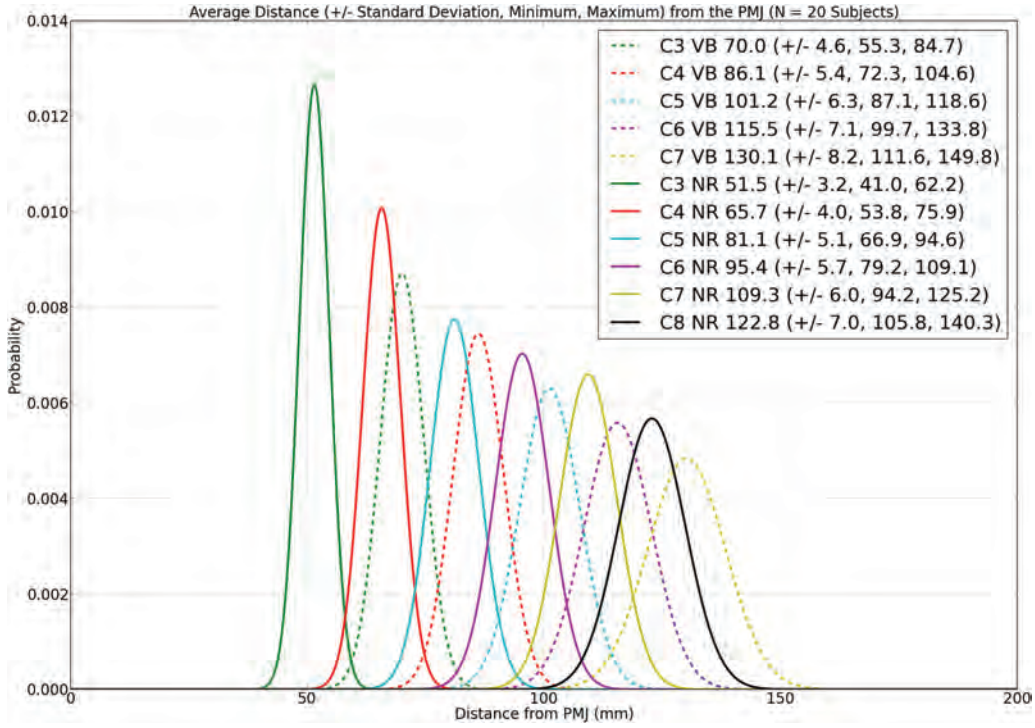

FIG 3. Nerve rootlet (NR, *solid lines*) and vertebral body (VB, *dashed lines*) distributions across our cohort of 20 individuals. The x-axis of this line graph represents the distance from the PMJ along the spinal cord axis, where zero is the PMJ and the increasing numbers are millimeter distances down the curved axis of the spinal cord to the midpoint of either the vertebral body or spinal cord segment as demarcated by nerve rootlets. The *y*-axis of the line graph represents the probability of finding either NR (*solid line*) or VB (*dashed line*) at a given distance down the curved spinal cord. The spinal cord segments and vertebral bodies represented by the *colored lines* are shown in the graph inset as distances in millimeters to the midpoint of either the vertebral bodies or spinal cord segments (as represented by nerve rootlets), projected orthogonally onto the spinal cord centerline, SDs, and range. The rostral-caudal extent of nerve rootlets corresponding to each spinal segment was relatively consistent across all spinal cord segments. The average length of spinal cord segments are the following: C3, 10.5 mm; C4, 9.9 mm; C5, 10.5 mm; C6, 9.7 mm; C7, 9.4 mm; and C8 9.6 mm.

Our method uses the spinal cord axis of each subject to measure these angles rather than relying on manually drawing parallel lines. We measured the angle of the tangent of the spinal cord axis at all locations relative to an imaginary horizontal line that lies across the sagittal plane. By subtracting any of these 2 points at different locations along the spinal cord, we are able to attain the relative angle.

To determine whether patient positioning within the MR imaging environment (slight neck flexion or extension) has an effect on the discrepancy between vertebral and spinal cord segments, we compared this discrepancy across neutral, flexion, and extension conditions. Vertebral-spinal discrepancy is defined as the difference between the midpoint of a given spinal and vertebral segment along the arc length of the spinal cord axis, reported in millimeters. Taken alone, this measurement is expected to vary across both segmental level and subject. However, if neck flexion or extension has no effect on the discrepancy between vertebral and spinal cord levels, then the difference between flexion and extension markings should be similar to the difference associated with independent observers marking vertebral and spinal cord segments across subjects. To this effect, we report each of the following: 1) the vertebral-spinal discrepancy reported for each segmental level, in millimeters, across 2 independent observers; 2) the vertebral-spinal discrepancy between neutral and flexion positioning; and 3) the vertebral-spinal discrepancy between neutral and extension positioning. In all cases, the mean and SD across all study participants are reported.

RESULTS

The adult human spinal cord is roughly the shape of a curved cylinder that extends from the cervicomedullary junction at the foramen magnum to approximately the level of the first lumbar vertebral body. The cervical spinal cord typically follows the slight lordotic curvature of the bony spinal column (the convexity of the curve points anteriorly and the concavity points posteriorly), but this varies among individuals. To account for this variability, we measured distances (arc length in millimeters) down the spinal cord from a fixed point in the brain stem, the PMJ, of 20 healthy volunteers. Figure 1 illustrates the result of spinal cord centerline extraction, for 1 subject, from the T2-weighted volume.

Imparting Neuroanatomic Context to Spinal Imaging

To provide neuroanatomic context to each individual's spinal images, we manually marked the position of vertebral bodies and segmental nerve rootlets as they emerged from the spinal cord; this is illustrated in Fig 2. The common thread among all individual datasets is the personalized spinal cord axis originating at the PMJ and continuing down the spinal cord. By conducting measurements along this personalized axis, we could compare the distribution of vertebral body and segmental rootlet positions down the rostral-caudal length of an individual's spinal cord with others in our cohort.

There are distinct gaps in the position of cervical nerve rootlets (see the MR image and illustration in Fig 2), a natural boundary

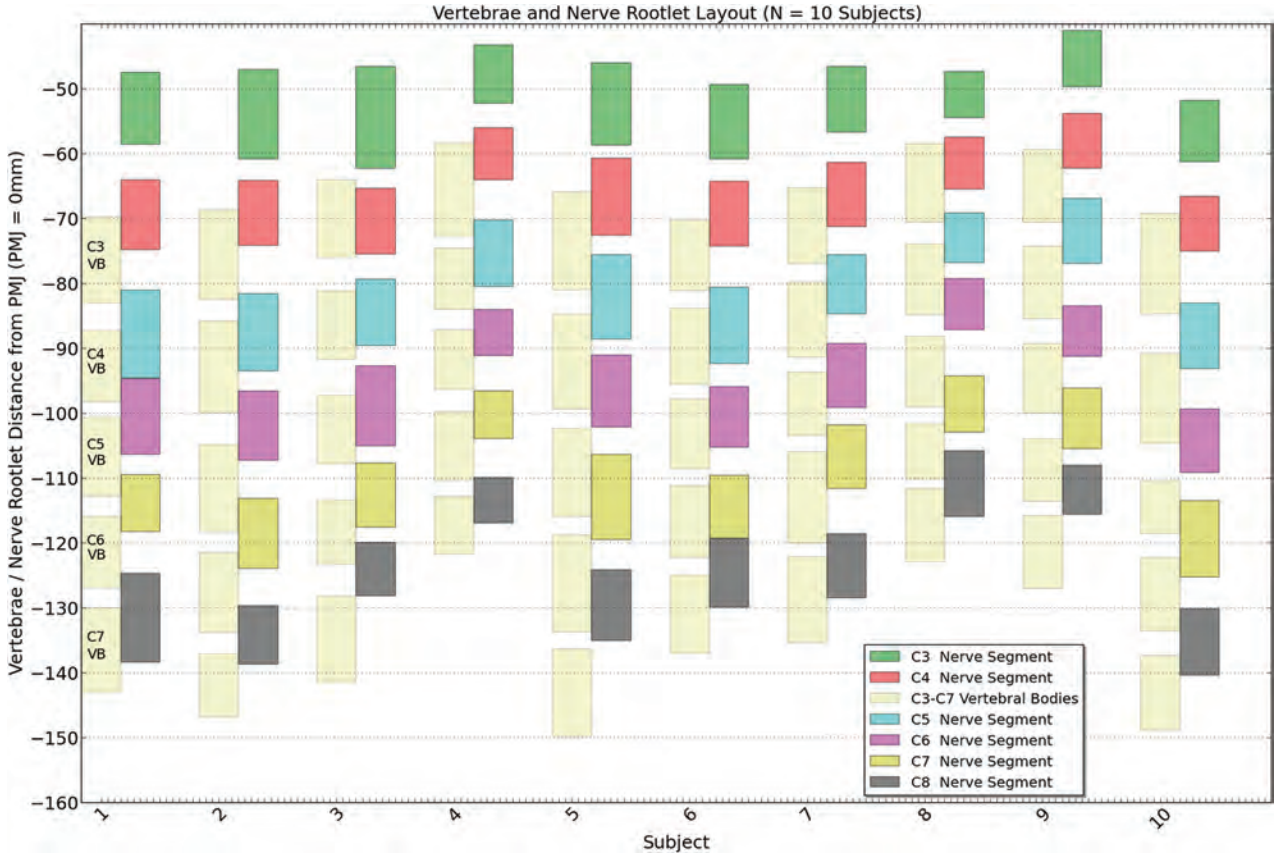

FIG 4. Vertebral body and spinal cord segment location across 10 subjects enrolled in this study. Vertebral bodies are represented for each subject by *light-shaded bars*, whereas spinal cord segments are represented by *colored bars* (see graph inset).

for segmental information before the predominant somatotopic representation in the brain. The distribution of the C3 through C8 spinal cord segments along the curved spinal cord axis is shown as solid lines and reported within the graph inset in Fig 3. A second, independent observer marked a subset of datasets ($n = 15$) yielding an interclass correlation coefficient of 1.0, $P < .01$, indicating the high degree of reproducibility with which a qualified individual can identify segmental nerve rootlets.

The distribution of vertebral bodies along the curved longitudinal spinal cord axis is shown as dashed lines and is reported in the graph inset in Fig 3. A second, independent observer marked a subset of datasets ($n = 15$) yielding an interclass correlation coefficient of 1.0, $P < .01$, indicating the high degree of reproducibility with which a qualified individual can identify the vertebral bodies.

The rostral-caudal extent of nerve rootlets corresponding to each spinal segment was relatively consistent across the C3 through C8 spinal levels. The rostral-caudal length of rootlet groups are the following (mean): C3, 10.5 ± 2.2 mm; C4, 9.9 ± 1.3 mm; C5, 10.5 ± 1.5 mm; C6, 9.7 ± 1.6 mm; C7, 9.4 ± 1.4 mm; and C8, 9.6 ± 1.4 mm.

Accounting for Interindividual Differences in Spinal Anatomy

The results presented above and illustrated in Fig 3 provide a neuroanatomic context to spinal imaging. The differences among individuals have implications for imaging studies conducted across a cohort of subjects; to account for these differences and improve the accuracy with which interpretations are drawn from imaging studies, we next considered the effect of using vertebral bodies as a surrogate for spinal segments and whether patient positioning within the MR imaging environment can exacerbate differences between vertebral and spinal cord segments.

Are Vertebral Bodies a Reliable Surrogate Marker for Spinal Cord Segments? Given the heterogeneity in spinal column and spinal cord anatomy across even a small sample of the human population, we illustrate how this might affect the spatial interpretation of imaging data by using the vertebral bodies as a rough indication of spinal cord segmental anatomy; this is illustrated in Fig 4, showing a subset of 10 subjects. As a first approximation, we illustrate the effect of assuming that a certain vertebral body is immediately adjacent to the corresponding spinal cord segment (eg, the C7 vertebral body is adjacent to the C7 spinal segment). If we apply this methodology to all 20 subjects in this study, then 0% of the C7 spinal cord segment volume is captured in the selected range. The root-mean-square error between locations of the superior endplate of the vertebral bodies and their corresponding spinal cord segments, averaged over 20 subjects and 5 groups of nerve rootlets (C3–C7), is 20.33 mm.

Neuroanatomic textbooks suggest that a more accurate landmark for predicting spinal cord segments is using the vertebral body rostral to the given spinal cord segment.[11] This assumes, for example, that the C7 spinal cord segment lies adjacent to the C6 vertebral body. Using the same 10 subjects shown in Figs 4 and 5

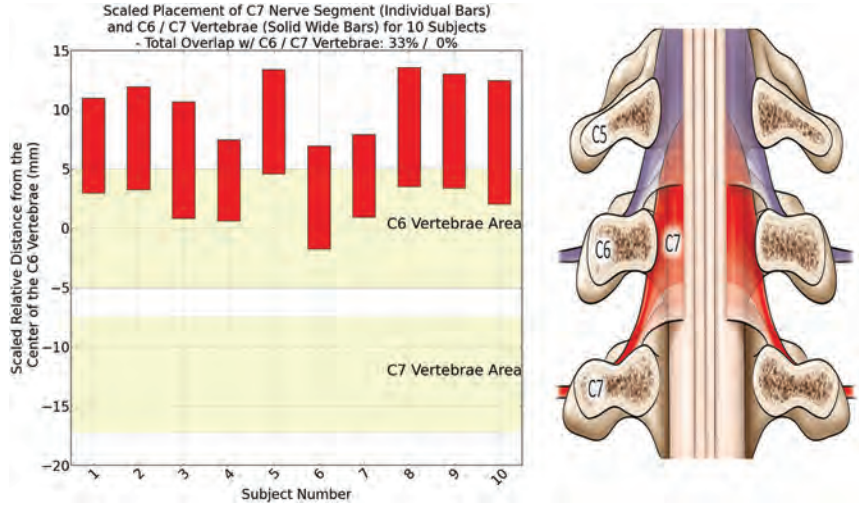

FIG 5. Left: scaled relative distance of the C7 spinal cord segments (*red bars*) from the C6 (*upper light-brown-shaded area*) and C7 (*lower light-brown-shaded area*) vertebral bodies. When we visualize an individual's cervical spine MR imaging, we tend to hold the vertebral bodies constant. This figure illustrates that the position of the seventh cervical spinal cord segment varies relative to the position of the vertebral body across a cohort of individuals. If one were to assume that the C7 spinal segments are immediately adjacent to the C7 vertebral body, then 0% of the actual segments would be captured in such an analysis. Similarly, if one were to assume that the C7 spinal cord segments are 1 vertebral body length rostral to the C7 body, then one would capture 33% of the corresponding spinal segments for the 10 subjects shown, or 44% of the corresponding spinal segments across all 20 subjects. Depending on the goals of the imaging experiment, one should pay careful attention to the relative position of spinal segments and vertebral bodies across a cohort of individuals. Assuming that spinal segments are constant may lead to false-positive or false-negative results. Right: an artist's depiction shows the range in spinal cord segments relative to the vertebral bodies; *light-shaded areas* represent areas of population level overlap.

illustrates that 33% of the intended spinal cord segment would be captured in the targeted volume. Using all 20 subjects studied, 44% of the intended spinal cord segment volume would be captured in the targeted volume. The root-mean-square error between locations of spinal cord segments and the superior endplate of the vertebral body rostral to the corresponding spinal cord segment in this case is 3.39 mm for all 20 subjects. We also note that root-mean-square error depends on the subject, ranging from 0.86 to 6.42 mm among the 20 subjects.

Does Patient Positioning within the MR Imaging Environment Exacerbate Differences Between Vertebral and Spinal Cord Segments? A subset ($n = 6$) of our initial cohort underwent imaging in slight neck flexion (by placing an extra cushion under the occiput) and slight neck extension (by placing an extra cushion under the shoulders) to determine the effect of patient positioning on the discrepancy between vertebral level and spinal segments. Measurements of flexion and extension from a neutral position are shown in Fig 6, illustrating that positioning with an extra cushion results in roughly 10°–15° of flexion or extension from a neutral position.

Vertebral-spinal discrepancy varies substantially across subjects as is illustrated in Fig 4. However, the discrepancy can be compared either within a subject in neutral position (to determine the error associated with marking vertebral and spinal segments) or within a subject between neutral and either flexion or extension positions. The error associated with determining vertebral-spinal discrepancy varied across spinal levels and was the following: C3, 1.0 mm; C4, 1.3 mm; C5, 1.3 mm; C6, 0.9 mm; and C7, 1.1 mm.

If the patient is positioned in slight flexion, the vertebral-spinal discrepancies are as follows: C3, 1.3 mm; C4, 0.7 mm; C5, 1.2 mm; C6, 0.8 mm; and C7, 1.9 mm.

If the patient is positioned in slight extension, the vertebral-spinal discrepancies are as follows: C3, 1.4 mm; C4, 0.7 mm; C5, 1.0 mm; C6, 1.0 mm; and C7, 1.0 mm.

These results are summarized in Table 2. They suggest that flexion or extension that is possible within the confines of the MR imaging environment and measured to be between 10° and 15° (Fig 5) does not affect the relative positions of vertebral and spinal cord segments.

DISCUSSION

In this work, we characterized the location of spinal and vertebral levels in humans and addressed the intersubject variability, which is a current limitation in spinal cord MR imaging studies.[12] To perform this characterization, we used the longitudinal axis of the brain stem–spinal cord to perform measurements, therefore accounting for the unique anatomy of a single subject. A detailed understanding of a single subject's anatomy is an important aspect of using advanced MR imaging–based metrics (such as diffusion- or magnetization transfer–based measurements) to refine the diagnosis of spinal cord pathology and follow the effect of novel therapeutic agents. For example, it has been demonstrated that any incremental preservation of axons after traumatic injury to the spinal cord results in a concomitant and exponential increase in clinical function.[13] With novel treatment strategies aimed at either neuroprotection or remyelination of axons, it will be extremely beneficial to use MR imaging–based biomarkers to follow the degree of change to the spinal cord structure and function in the appropriate anatomic region. Visualizing these changes may aid in the design of more efficient clinical trials and the ability to test a greater number of novel therapeutic agents within a limited patient population.[14,15] On the basis of user-defined markings of segmental nerve rootlets as ground truth data, we identified the position of spinal segments relative to the PMJ. For the first time, we report a population distribution of the segmental anatomy of the cervical spine and demonstrate that substantial variation exists in the rostral-caudal position of spinal cord segments among individuals.

Limitations of this work include the fact that measurements were obtained from a relatively small sample size of healthy controls. While this number of subjects is adequate to establish the fact that differences exist between individuals, adding a greater number of subjects of different ages and ethnic backgrounds and including those with pathologies of the spinal column would be a welcome addition in future works.

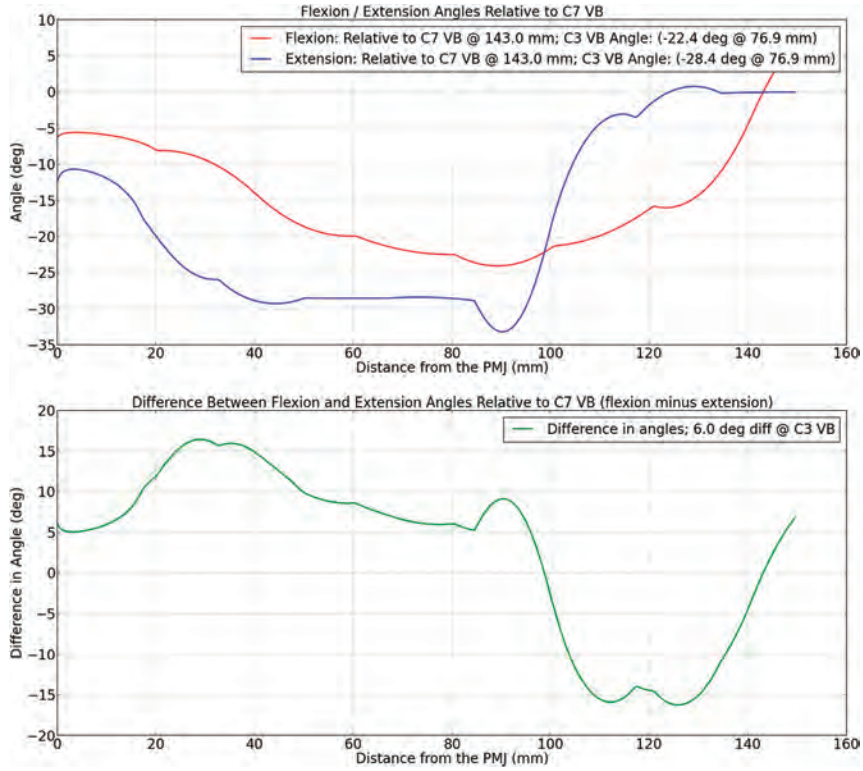

FIG 6. Automated analysis of the degree of neck flexion/extension of a subject. Top: the angle between the tangent of the spinal cord at any point and tangent at the C7 vertebral body for 1 subject with the neck in flexion (red) and extension (blue). Bottom: the difference between the flexion and extension curves or the maximum extent of curvature of the spinal cord at various locations down the longitudinal axis of the spinal cord (x-axis). VB indicates vertebral body; deg, degree; deg diff, degree difference.

Table 2: Vertebral-spinal discrepancy reported in neutral position across 2 independent observers, between neutral and flexion positions and neutral and extension positions[a]

	C3	C4	C5	C6	C7
Neutral position across 2 independent reviewers (mm)	1.0	1.3	1.3	0.9	1.1
Neutral flexion (mm)	1.3	0.7	1.2	0.8	1.9
Neutral extension (mm)	1.4	0.7	1.0	1.0	1.0

[a] Results are reported in millimeters. These results suggest that flexion or extension that is possible within the confines of the MR imaging environment does not affect the relative positions of vertebral and spinal cord segments.

Accounting for this variation will be paramount to accurate interpretation of the neuroanatomic origin of acquired MR signals in future imaging studies. This especially holds true for functional MR imaging studies that are challenging due to the low sensitivity for studying single subjects (notably due to a low signal-to-noise ratio and high physiologic noise), and by the intrinsic variability of spinal rootlet locations that hamper the use of grouped data. This argument is supported by a previous fMRI study on cats, which showed high interanimal variability on the rostrocaudal location of the blood oxygen level–dependent signal relative to the vertebral level, when stimulating the same peripheral nerve.[16]

After providing a neuroanatomic context to spinal imaging data, we then addressed 2 important concepts to account for interindividual variation in imaging studies conducted across a group of subjects: 1) the effect of using vertebral bodies as a surrogate for spinal segment location, and 2) the effect of patient positioning on localizing a spinal segment. Subdivision of the spinal cord into discrete segments begins as early as 4.5 gestational weeks in embryologic development during which time dorsal nerve rootlets engage the spinal cord from dorsal root ganglia and ventral nerve rootlets emerge from the spinal cord; this process is largely complete by the end of the first trimester, after which time the spinal cord white matter develops and is progressively myelinated.[17] Dorsal and ventral nerve rootlets aggregate in clusters, emerge from the spinal cord forming a spinal nerve, and traverse the closest caudal intervertebral foramen to innervate the corresponding segment of the body.[17] As such, cervical spinal cord segments are consistently located rostral to the corresponding numbered cervical vertebrae as illustrated in Fig 4. However, using vertebral bodies to localize a corresponding spinal cord segment is quite imprecise. The percentage volume overlap between, for example, the C6 vertebral bodies and C7 spinal cord segments is only 44%, by using all 20 subjects. We also investigated the effect of subject positioning (ie, neck flexion or extension) on the discrepancy between vertebral and spinal cord segments. Fortunately, this effect was relatively small as outlined in Table 2. This has important clinical implications because subject positioning can sometimes be imposed by the clinical condition.

CONCLUSIONS

Remarkable advances have been made during the past decade allowing improved imaging of the human spinal cord.[12,18] The development of methods to manage the hostile imaging environment and to account for cardiorespiratory-related motion has allowed improved applications to detect structural (such as diffusion and magnetization transfer imaging) and functional anomalies that occur in relation to traumatic injury of the spinal cord.[1,2,19,20] Other disorders, such as multiple sclerosis, have also benefited from spinal cord imaging.[21] Degenerative spinal disease, such as cervical spondylosis, is an increasing health burden due to the aging population.[22] Advanced imaging tools stand to play an important role in aiding with decision-making, such as the optimal time to offer decompressive surgery to maintain neurologic function before irreversible neurologic deficits are realized. Future work in the realm of spinal segmentation must focus on the neuroanatomic context of acquired images and use population-based probability data to develop improved methods that aim to identify segmental anatomy. Thus, the user may have to only ensure the accuracy of the segmentation rather than manually identify each spinal rootlet as we did here. Such advances will improve workflow and reduce postprocessing time. Ultimately,

this neuroanatomic knowledge may be used for the delivery of targeted therapeutics offering a regenerative strategy toward damaged cell populations.

Disclosures: David W. Cadotte—*RELATED*: *Grant*: Craig H. Neilsen Foundation (postdoctoral fellowship grant).* David Mikulis—*UNRELATED*: *Grants/Grants Pending*: Canadian Institutes of Health Research, Physicians Services Incorporated, Ontario Brain Institute. *Money paid to the institution.

REFERENCES

1. Cohen-Adad J, El Mendili MM, Lehericy S, et al. **Demyelination and degeneration in the injured human spinal cord detected with diffusion and magnetization transfer MRI.** *Neuroimage* 2011;55:1024–33
2. Cadotte DW, Bosma R, Mikulis D, et al. **Plasticity of the injured human spinal cord: insights revealed by spinal cord functional MRI.** *PLoS One* 2012;7:e45560
3. Okado N. **Onset of synapse formation in the human spinal cord.** *J Comp Neurol* 1981;201:211–19
4. Cabezas M, Oliver A, Lladó X, et al. **A review of atlas-based segmentation for magnetic resonance brain images.** *Comput Methods Programs Biomed* 2011;104:e158–77
5. Evans AC, Janke AL, Collins DL, et al. **Brain templates and atlases.** *Neuroimage* 2012;62:911–22
6. Fonov VS, Le Troter A, Taso M, et al. **MNI-Poly-AMU average anatomical template for automatic spinal cord measurements.** In: *Proceedings of the International Society of Magnetic Resonance in Medicine and the European Society for Magnetic Resonance in Medicine and Biology*, Milan, Italy. May 10–16, 2014:5358
7. Stracke CP, Pettersson LG, Schoth F, et al. **Interneuronal systems of the cervical spinal cord assessed with BOLD imaging at 1.5 T.** *Neuroradiology* 2005;47:127–33
8. Horsfield MA, Sala S, Neema M, et al. **Rapid semi-automatic segmentation of the spinal cord from magnetic resonance images: application in multiple sclerosis.** *Neuroimage* 2010;50:446–55
9. Bartlett RJ, Hill CA, Rigby AS, et al. **MRI of the cervical spine with neck extension: is it useful?** *Br J Radiol* 2012;85:1044–51
10. Bartlett RJ, Rigby AS, Joseph J, et al. **Extension MRI is clinically useful in cervical myelopathy.** *Neuroradiology* 2013;55:1081–88
11. Paxinos G, Mai JK, eds. *The Human Nervous System.* 2nd ed. London: Elsevier Academic Press; 2004
12. Wheeler-Kingshott CA, Stroman PW, Schwab JM, et al. **The current state-of-the-art of spinal cord imaging: applications.** *Neuroimage* 2014;84:1082–93
13. Fehlings MG, Tator CH. **The relationships among the severity of spinal cord injury, residual neurological function, axon counts, and counts of retrogradely labeled neurons after experimental spinal cord injury.** *Exp Neurol* 1995;132:220–28
14. Cadotte DW, Fehlings MG. **Spinal cord injury: visualizing plasticity and repair in the injured CNS.** *Nat Rev Neurol* 2013;9:546–47
15. Cadotte DW, Fehlings MG. **Will imaging biomarkers transform spinal cord injury trials?** *Lancet Neurol* 2013;12:843–44
16. Cohen-Adad J, Hoge RD, Leblond H, et al. **Investigations on spinal cord fMRI of cats under ketamine.** *Neuroimage* 2009;44:328–39
17. Altman J, Bayer SA. *Development of the Human Spinal Cord: An Interpretation based on Experimental Studies in Animals*. Oxford: Oxford University Press; 2001
18. Stroman PW, Wheeler-Kingshott C, Bacon M, et al. **The current state-of-the-art of spinal cord imaging: methods.** *Neuroimage* 2014;84:1070–81
19. Freund P, Weiskopf N, Ashburner J, et al. **MRI investigation of the sensorimotor cortex and the corticospinal tract after acute spinal cord injury: a prospective longitudinal study.** *Lancet Neurol* 2013;12:873–81
20. Freund P, Weiskopf N, Ward NS, et al. **Disability, atrophy and cortical reorganization following spinal cord injury.** *Brain* 2011;134:1610–22
21. Losseff NA, Webb SL, O'Riordan JI, et al. **Spinal cord atrophy and disability in multiple sclerosis: a new reproducible and sensitive MRI method with potential to monitor disease progression.** *Brain* 1996;119:701–08
22. Holly LT, Moftakhar P, Khoo LT, et al. **Surgical outcomes of elderly patients with cervical spondylotic myelopathy.** *Surg Neurol* 2008;69:233–40

Systematic Literature Review of Imaging Features of Spinal Degeneration in Asymptomatic Populations

W. Brinjikji, P.H. Luetmer, B. Comstock, B.W. Bresnahan, L.E. Chen, R.A. Deyo, S. Halabi, J.A. Turner, A.L. Avins, K. James, J.T. Wald, D.F. Kallmes, and J.G. Jarvik

ABSTRACT

BACKGROUND AND PURPOSE: Degenerative changes are commonly found in spine imaging but often occur in pain-free individuals as well as those with back pain. We sought to estimate the prevalence, by age, of common degenerative spine conditions by performing a systematic review studying the prevalence of spine degeneration on imaging in asymptomatic individuals.

MATERIALS AND METHODS: We performed a systematic review of articles reporting the prevalence of imaging findings (CT or MR imaging) in asymptomatic individuals from published English literature through April 2014. Two reviewers evaluated each manuscript. We selected age groupings by decade (20, 30, 40, 50, 60, 70, 80 years), determining age-specific prevalence estimates. For each imaging finding, we fit a generalized linear mixed-effects model for the age-specific prevalence estimate clustering in the study, adjusting for the midpoint of the reported age interval.

RESULTS: Thirty-three articles reporting imaging findings for 3110 asymptomatic individuals met our study inclusion criteria. The prevalence of disk degeneration in asymptomatic individuals increased from 37% of 20-year-old individuals to 96% of 80-year-old individuals. Disk bulge prevalence increased from 30% of those 20 years of age to 84% of those 80 years of age. Disk protrusion prevalence increased from 29% of those 20 years of age to 43% of those 80 years of age. The prevalence of annular fissure increased from 19% of those 20 years of age to 29% of those 80 years of age.

CONCLUSIONS: Imaging findings of spine degeneration are present in high proportions of asymptomatic individuals, increasing with age. Many imaging-based degenerative features are likely part of normal aging and unassociated with pain. These imaging findings must be interpreted in the context of the patient's clinical condition.

Low back pain has a high prevalence in industrialized countries, affecting up to two-thirds of adults at some point in their lifetime.[1] Back pain is associated with high health care costs and has substantial economic consequences due to loss of productivity from back pain–associated disability.[2] Advanced imaging (MR imaging and CT) is increasingly used in the evaluation of patients with low back pain.[3] Findings such as disk degeneration, facet hypertrophy, and disk protrusion are often interpreted as causes of back pain, triggering both medical and surgical interventions, which are sometimes unsuccessful in alleviating the patient's symptoms.[4] Prior studies have demonstrated that imaging findings of spinal degeneration associated with back pain are also present in a large proportion of asymptomatic individuals.[5-7]

Given the large number of adults who undergo advanced imaging to help determine the etiology of their back pain, it is important to know the prevalence of imaging findings of degenerative disease in asymptomatic populations. Such information will help both clinical providers and patients interpret the importance of degenerative findings noted in radiology reports. The aim of this study was to systematically review the literature to determine the age-specific prevalence of various imaging findings often associated with degenerative spine disease in asymptomatic individuals. We studied the age-specific prevalence of the following im-

Received August 5, 2014; accepted after revision October 3.

From the Department of Radiology (W.B., P.H.L., J.T.W., D.F.K.), Mayo Clinic, Rochester, Minnesota; Departments of Biostatistics (B.C.), Radiology (B.C., B.W.B., L.E.C., K.J., J.G.J.), Psychiatry and Behavioral Sciences (J.A.T.), and Neurological Surgery and Health Services (J.G.J.), Comparative Effectiveness Cost and Outcomes Research Center, University of Washington, Seattle, Washington; Departments of Family Medicine, Medicine, and Public Health and Preventive Medicine and the Oregon Institute of Occupational Health Sciences (R.A.D.), Oregon Health and Science University, Portland, Oregon; Department of Radiology (S.H.), Henry Ford Hospital, Detroit, Michigan; Department of Radiology (A.L.A.), University of California, San Francisco, San Francisco, California; and Division of Research (A.L.A.), Kaiser Permanente, Northern California, Oakland, California.

This work was supported by National Institutes of Health grant UH3 4UH3AR066795-02.

Please address correspondence to Patrick H. Luetmer, MD, Department of Radiology, W2, Mayo Clinic, 200 First St SW, Rochester, MN 55905; e-mail: luetmer.patrick@mayo.edu

Indicates open access to non-subscribers at www.ajnr.org

Indicates article with supplemental on-line tables.

http://dx.doi.org/10.3174/ajnr.A4173

aging findings in asymptomatic individuals: disk degeneration, disk signal loss, disk height loss, disk bulge, disk protrusion, annular fissures, facet degeneration, and spondylolisthesis.

MATERIALS AND METHODS

Data Sources and Searches

We performed a comprehensive search for articles describing relevant imaging findings by using MEDLINE and EMBASE. To identify studies on imaging of asymptomatic spinal disorders, we searched 3 databases through April 2014 (week 16): Ovid MEDLINE, Ovid EMBASE, and the Web of Science. Ovid MEDLINE and Ovid EMBASE use controlled vocabulary. EMBASE was searched from 1988 to week 16 of 2014, and MEDLINE was searched from 1946 to 2014. The Web of Science is text word–based but tends to be more current and multidisciplinary, so articles may be discovered that are not included in the other databases. The initial concept was spinal diseases or disorders affecting the spine: intervertebral disk degeneration or displacement, spondylolysis, low back pain, or specific vertebrae and joints (eg, lumbar vertebrae). This was combined with diagnostic imaging techniques (tomography, radiography, MR imaging) and the concept by text words of undetected, asymptomatic, and asymptomatic disease (subject heading available in EMBASE, but not MEDLINE). Details of the search strategy are provided in On-line Tables 1 and 2. Studies identified from the literature search were then further evaluated for inclusion in the meta-analysis. We also searched references from multiple articles to find any additional studies that reported lumbar spine CT or MR imaging findings in individuals without low back pain.

Study Selection and Data Extraction

To be included in our review, a study needed to be published in English and report the prevalence of degenerative findings in different age groups on spine MR imaging or CT in asymptomatic individuals. Asymptomatic individuals were defined as those with no history of back pain. Studies including patients with minor or low-grade back pain were excluded. Studies including patients with motor or sensory symptoms, tumors, or trauma were excluded. If studies did not explicitly state that patients were pain-free, they were excluded. Eleven reviewers (W.B., J.G.J., A.L.A., J.A.T., J.T.W., R.A.D., P.H.L., D.F.K., S.H., L.E.C., and B.W.B.) examined abstracts of studies identified from the literature search to determine whether the articles met the inclusion criteria. For each article that met the inclusion criteria, we used a standard form to abstract imaging technique, age-specific sample sizes, and prevalence rates for the following imaging findings: disk degeneration, disk signal loss (ie, desiccated disk), disk height loss, disk bulge, disk protrusion, annular fissures, facet degeneration, and spondylolisthesis. These entities are defined in detail by the combined task forces of the American Society of Neuroradiology, American Society of Spine Radiology, and North American Spine Society.[8] All articles were evaluated by 2 reviewers.

Findings from this systematic review are being used to help physicians with clinical decision-making for patients with low back pain in the Lumbar Imaging With Reporting of Epidemiology: A Pragmatic Cluster Randomized Trial, a multicenter randomized controlled trial aimed at determining whether inserting epidemiologic evidence into lumbar spine imaging reports reduces spine interventions, including further imaging, injections, and surgeries in subsequent years (clinicaltrials.gov identifier NCT02015455).

Data Synthesis and Analysis

For each age category and finding, the number of studies that contributed information and approximate patient-level sample size was tabulated. For some studies, only the mean (SD) age was provided, and we therefore used a normal approximation to estimate the number of patients in each age category. For each imaging finding, we fit a generalized linear mixed-effects model for the age-specific prevalence estimate (binomial outcome), clustering on study and adjusting for the midpoint of the reported age interval of each study. If a study reported prevalence estimates across multiple age ranges, we included each age-range-specific estimate as a separate record in the analysis. We examined whether the prevalence estimates varied across patient age by decade (20s, 30s, 40s, 50s, 60s, 70s, 80s). In each model, we therefore incorporated knots at ages 40 and 60 in an interaction with the age to allow the association between age and prevalence to differ among age groupings. We tested whether the association between prevalence and age differed by age grouping by using a likelihood ratio test, but we did not observe significant evidence for an interaction and therefore used age as a linear predictor in each model. For each finding, we generated generalized linear mixed-effects model–based prevalence predictions at ages 20, 30, 40, 50, 60, 70, and 80 years. All data analyses were performed by using the R statistics package (Version 3.0.1; http://www.r-project.org).

RESULTS

Literature Search

A summary of articles included in the literature review is provided in On-line Table 3. Our search yielded 379 unique articles. On the basis of the abstracts of these articles, we excluded 300 articles that did not meet our review inclusion criteria. Of the remaining 79 articles, we excluded 46 because they did not include asymptomatic individuals or the symptomatic status of patients was ambiguous, did not allow adequate separation of prevalences by age group, or included only patients younger than 18 years of age. Thirty-three studies reporting imaging findings for 3110 individuals met the inclusion criteria for this systematic review. Sample sizes ranged from 8 to 412 individuals. Thirty-two studies reported degenerative changes on MR imaging, and 1 study reported degenerative changes on CT. The search and selection process is summarized in Fig 1.

Age-Specific Prevalence Rates among Asymptomatic Individuals

The estimated number of individuals on which each estimate was made is presented in Table 1. We present age-specific prevalence estimates among asymptomatic individuals in Table 2. Disk degeneration prevalence ranged from 37% of asymptomatic individuals 20 years of age to 96% of those 80 years of age, with a large increase in the prevalence through 50 years. Disk signal loss ("black disk") was similarly present in more than half of individuals older than 40 years of age, and by 60 years, 86% of individuals

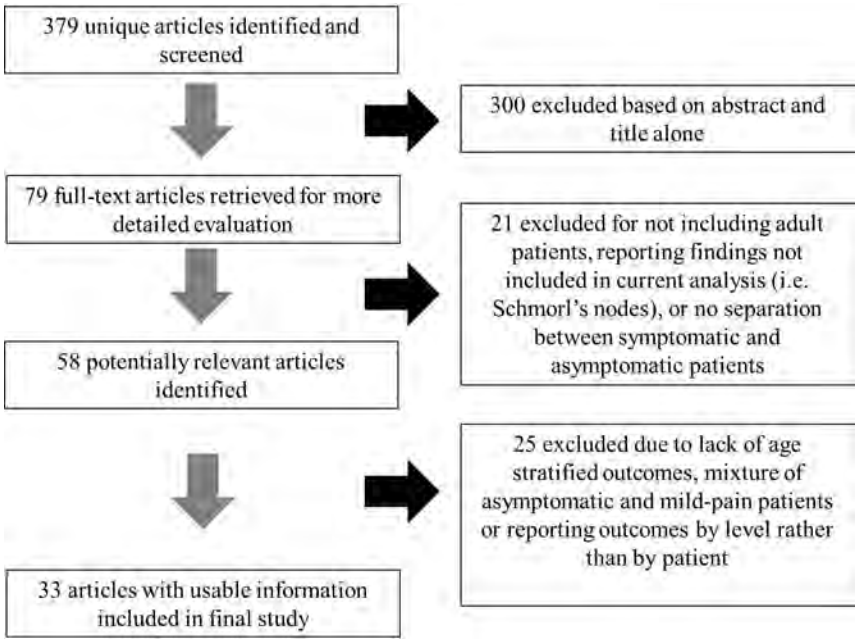

FIG 1. Results of literature search.

Table 1: Estimated number of patients by age used to inform prevalence of degenerative spine imaging findings in asymptomatic patients[a]

	Age (yr)						
Imaging Finding	20	30	40	50	60	70	80
Disk degeneration	273 (9)	604 (16)	415 (12)	311 (10)	80 (4)	20 (2)	19 (2)
Disk signal loss	46 (2)	142 (5)	352 (4)	73 (2)	35 (1)	15 (1)	14 (1)
Disk height loss	15 (1)	163 (5)	186 (5)	208 (5)	35 (1)	15 (1)	14 (1)
Disk bulge	55 (4)	101 (7)	151 (8)	123 (7)	66 (5)	24 (3)	22 (3)
Disk protrusion	87 (5)	468 (14)	490 (14)	363 (12)	86 (5)	19 (2)	17 (2)
Annular fissure	167 (5)	350 (5)	426 (7)	53 (3)	35 (3)	15 (1)	14 (1)
Facet degeneration	0 (0)	0 (0)	596 (3)	53 (3)	35 (3)	15 (1)	14 (1)
Spondylolisthesis	0 (0)	0 (0)	31 (1)	53 (1)	35 (1)	15 (1)	14 (1)

[a] The number of studies are in parentheses.

Table 2: Age-specific prevalence estimates of degenerative spine imaging findings in asymptomatic patients[a]

	Age (yr)						
Imaging Finding	20	30	40	50	60	70	80
Disk degeneration	37%	52%	68%	80%	88%	93%	96%
Disk signal loss	17%	33%	54%	73%	86%	94%	97%
Disk height loss	24%	34%	45%	56%	67%	76%	84%
Disk bulge	30%	40%	50%	60%	69%	77%	84%
Disk protrusion	29%	31%	33%	36%	38%	40%	43%
Annular fissure	19%	20%	22%	23%	25%	27%	29%
Facet degeneration	4%	9%	18%	32%	50%	69%	83%
Spondylolisthesis	3%	5%	8%	14%	23%	35%	50%

[a] Prevalence rates estimated with a generalized linear mixed-effects model for the age-specific prevalence estimate (binomial outcome) clustering on study and adjusting for the midpoint of each reported age interval of the study.

had disk signal loss. Disk height loss and disk bulge were moderately prevalent among younger individuals, and prevalence estimates for these findings increased steadily by approximately 1% per year. Disk protrusion and annular fissures were moderately prevalent across all age categories but did not substantially increase with age. Authors rarely reported facet degeneration in younger individuals (4%–9% in those 20 and 30 years of age), but the prevalence increased sharply with age. Spondylolisthesis was not commonly found in asymptomatic individuals until 60 years, when prevalence was 23%; prevalence increased substantially at 70 and 80 years of age.

DISCUSSION

This systematic review indicates that many imaging findings of degenerative spine disease have a high prevalence among asymptomatic individuals. All imaging findings examined in this review had an increasing prevalence with increasing age, and some findings (disk degeneration and signal loss) were present in nearly 90% of individuals 60 years of age or older. Our study suggests that imaging findings of degenerative changes such as disk degeneration, disk signal loss, disk height loss, disk protrusion, and facet arthropathy are generally part of the normal aging process rather than pathologic processes requiring intervention. The finding that >50% of asymptomatic individuals 30–39 years of age have disk degeneration, height loss, or bulging suggests that even in young adults, degenerative changes may be incidental and not causally related to presenting symptoms. The results from this systematic review strongly suggest that when degenerative spine findings are incidentally seen (ie, as part of imaging for an indication other than pain or an incidental disk herniation at a level other than where a patient's pain localizes), these findings should be considered as normal age-related changes rather than pathologic processes.

MR imaging is highly sensitive in detecting the degenerative changes examined in our study.[9] However, even among patients with back pain, prior studies have demonstrated that degenerative findings on MR imaging are not necessarily associated with the degree or the presence of low back pain. Berg et al[10] found that a composite MR imaging score taking into account Modic changes, posterior high intensity zones, disk signal changes, and disk height decrease was not correlated with disability or the intensity of low back pain in 170 disk prosthesis candidates. Takatalo et al[11] found that disk herniations were strongly associated with low back pain severity among 554 young adults. However, annular fissures, high-intensity zone lesions, Modic changes, and spondylotic defects were not associated with low back pain severity.[11] They also demonstrated that disk degeneration was found in one-third of asymptomatic 21-year-olds.[11] A systematic review of 12 studies found no consistent association between low back pain and MR imaging findings of Modic changes, disk degeneration, and disk herniation.[12] In a large case control study, vertebral endplate changes were not associated with chronic low back pain.[13] A number of studies of elite athletes have also demonstrated no association between degenerative changes on MR imaging and the presence or degree of low back pain.[14,15] Systematic reviews on the prognostic role of MR imaging findings for outcomes of conservative back pain therapies have failed to find an association between imaging findings and clinical outcomes.[16,17] Perhaps most important, the relationship between imaging findings and

surgical outcomes has not been well established.[18,19] This literature, combined with the results of our study, highlights the importance of caution and of knowledge of the prevalence of imaging findings in similarly aged asymptomatic individuals when interpreting the clinical significance of imaging findings in patients with low back pain.

A number of previously published studies have demonstrated the increasing prevalence of degenerative spine findings with increasing age in asymptomatic patients.[1,5,20] A cross-sectional study of 975 individuals (symptomatic and asymptomatic) found that the prevalence of an intervertebral disk space with disk degeneration increased from approximately 70% of individuals younger than 50 years of age to >90% of individuals older than 50 years of age.[21] These findings are largely consistent with the findings of our study. Some prior studies have failed to demonstrate an association between degenerative spine disease and low back pain.[22,23] With a prevalence of degenerative findings of >90% in asymptomatic individuals 60 years of age or older, our study supports the hypothesis that degenerative changes observed on CT and MR imaging are often seen with normal aging. The substantial variation in the prevalence of degenerative findings between age groups of asymptomatic individuals highlights the importance of establishing further diagnostic criteria to help distinguish age-related degenerative changes from pathologic, pain-generating degenerative changes.

Limitations

This study has several limitations. Many of the individuals included in the studies of this systematic review were recruited as volunteers. This recruitment could lead to selection bias because these volunteers are not necessarily representative of the general population. Another limitation is that many studies included in this analysis did not use multiple observers, and it is difficult to ascertain inter- and intraobserver agreement for the presence of these degenerative findings on MR imaging. Recently published studies have demonstrated that even with standardization of nomenclature, interobserver variability is moderate at best.[24,25] Furthermore, the studies included in this review span >25 years and did not always use standard nomenclature. Imaging findings were not stratified by the degree of severity. It is possible that asymptomatic individuals have less severe degenerative changes than those with symptoms. Our study does not imply or conclude that the above-mentioned degenerative findings are always age-related rather than pathologic. Our study applies more to cases in which such degenerative findings are incidentally seen in the evaluation of patients without low back pain or findings are found at a level that does not correlate with findings on physical examination. The data on which the systematic review is based may be affected by publication bias.[26] Despite the limitations of this study, this systematic review provides useful data to share with clinicians and patients when explaining the clinical significance of degenerative findings seen on advanced imaging.

CONCLUSIONS

Imaging evidence of degenerative spine disease is common in asymptomatic individuals and increases with age. These findings suggest that many imaging-based degenerative features may be part of normal aging and unassociated with low back pain, especially when incidentally seen. These imaging findings must be interpreted in the context of the patient's clinical condition.

Disclosures: Bryan Comstock—*RELATED*: *Grant*: National Institutes of Health.* Patrick H. Luetmer—*RELATED*: *Grant*: National Institutes of Health.* Brian W. Bresnahan—*RELATED*: *Grant*: National Institutes of Health,* *Comments*: Co-Investigator and institution received federally negotiated F&A compensation; *UNRELATED*: *Grants/Grants Pending*: University of Washington, *Comments*: education and research grants related to radiology, economics, health services research, and comparative effectiveness research as a career and profession, though no other specific grants related to inserting text in radiology reports; previous research grant with GE Healthcare related to risk and benefit assessment for CT imaging, with a focus on radiation-exposure mitigation strategies; *Other*: I pay United States taxes and Washington state taxes as an employed US citizen, resulting in known and unknown compensation, subsidies, and expenditures. Richard A. Deyo—*RELATED*: *Grant*: Agency for Healthcare Research and Quality*; *UNRELATED*: *Board Membership*: Informed Medical Decisions Foundation (nonprofit foundation in Boston); *Grants/Grants Pending*: National Institutes of Health,* Agency for Healthcare Research and Quality,* Patient-Centered Outcomes Research Institute,* *Comments*: multiple current and pending grants related to back pain research; *Royalties*: UpToDate, *Comments*: for authoring topics on low back pain for this on-line reference source. Judith A. Turner—*RELATED*: *Grant*: Agency for Healthcare Research and Quality.* Kathryn James—*RELATED*: *Grant*: National Institutes of Health*; *Support for Travel to Meetings for the Study or Other Purposes*: National Institutes of Health,* *Comments*: The grant supported travel for site visits. David F. Kallmes—*RELATED*: *Grant*: National Institutes of Health,* Micrus, *Comments*: research support for clinical trial; *UNRELATED*: *Grants/Grants Pending*: ev3,* NFocus,* Sequent,* MicroVention,* Cook,* ArthroCare,* CareFusion,* *Comments*: research support; *Payment for Development of Educational Presentations:* CareFusion,* eV3.* Jeffrey G. Jarvik—*RELATED*: *Grant*: National Institutes of Health*; *Support for Travel to Meetings for the Study or Other Purposes*: National Institutes of Health Health Care Systems Collaboratory meetings; *UNRELATED*: *Board Membership*: GE Healthcare CER Advisory Board, *Comments*: past activity, ended October 2012; *Consultancy*: HealthHelp (a radiology benefits management company); *Grants/Grants Pending*: National Institutes of Health,* Agency for Healthcare Research and Quality,* Patient-Centered Outcomes Research Institute*; *Patents (planned, pending or issued)*: PhysiSonics* (an ultrasound-based diagnostic company); *Royalties*: PhysiSonics*; *Stock/Stock Options*: PhysiSonics; *Travel/Accommodations/Meeting Expenses Unrelated to Activities Listed*: GE-Association of University Radiologists Radiology Research Academic Fellowship, *Comments*: I serve on the academic advisory board. *Money paid to the institution.

REFERENCES

1. Jarvik JG, Deyo RA. **Diagnostic evaluation of low back pain with emphasis on imaging.** *Ann Intern Med* 2002;137:586–97
2. Deyo RA, Cherkin D, Conrad D, et al. **Cost, controversy, crisis: low back pain and the health of the public.** *Annu Rev Public Health* 1991;12:141–56
3. Li AL, Yen D. **Effect of increased MRI and CT scan utilization on clinical decision-making in patients referred to a surgical clinic for back pain.** *Can J Surg* 2011;54:128–32
4. Carragee E, Alamin T, Cheng I, et al. **Are first-time episodes of serious LBP associated with new MRI findings?** *Spine J* 2006;6:624–35
5. Boden SD, Davis DO, Dina TS, et al. **Abnormal magnetic-resonance scans of the lumbar spine in asymptomatic subjects: a prospective investigation.** *J Bone Joint Surg Am* 1990;72:403–08
6. Kalichman L, Kim DH, Li L, et al. **Computed tomography-evaluated features of spinal degeneration: prevalence, intercorrelation, and association with self-reported low back pain.** *Spine J* 2010;10:200–08
7. Wiesel SW, Tsourmas N, Feffer HL, et al. **A study of computer-assisted tomography. I. The incidence of positive CAT scans in an asymptomatic group of patients.** *Spine (Phila Pa 1976)* 1984;9:549–51
8. Fardon DF, Milette PC. **Nomenclature and classification of lumbar disc pathology: recommendations of the combined task forces of the North American Spine Society, American Society of Spine Ra-**

diology, and American Society of Neuroradiology. *Spine (Phila Pa 1976)* 2001;26:E93–E113
9. Sasiadek MJ, Bladowska J. **Imaging of degenerative spine disease–the state of the art.** *Adv Clin Exp Med* 2012;21:133–42
10. Berg L, Hellum C, Gjertsen O, et al. **Do more MRI findings imply worse disability or more intense low back pain? A cross-sectional study of candidates for lumbar disc prosthesis.** *Skeletal Radiol* 2013;42:1593–602
11. Takatalo J, Karppinen J, Niinimäki J, et al. **Association of Modic changes, Schmorl's nodes, spondylolytic defects, high-intensity zone lesions, disc herniations, and radial tears with low back symptom severity among young Finnish adults.** *Spine (Phila Pa 1976)* 2012;37:1231–39
12. Steffens D, Hancock MJ, Maher CG, et al. **Does magnetic resonance imaging predict future low back pain? A systematic review.** *Eur J Pain* 2014;18:755–65
13. Kovacs FM, Arana E, Royuela A, et al. **Vertebral endplate changes are not associated with chronic low back pain among Southern European subjects: a case control study.** *AJNR Am J Neuroradiol* 2012;33:1519–24
14. Kaneoka K, Shimizu K, Hangai M, et al. **Lumbar intervertebral disk degeneration in elite competitive swimmers: a case control study.** *Am J Sports Med* 2007;35:1341–45
15. Kraft CN, Pennekamp PH, Becker U, et al. **Magnetic resonance imaging findings of the lumbar spine in elite horseback riders: correlations with back pain, body mass index, trunk/leg-length coefficient, and riding discipline.** *Am J Sports Med* 2009;37:2205–13
16. Modic MT, Obuchowski NA, Ross JS, et al. **Acute low back pain and radiculopathy: MR imaging findings and their prognostic role and effect on outcome.** *Radiology* 2005;237:597–604
17. Chou R, Fu R, Carrino JA, et al. **Imaging strategies for low-back pain: systematic review and meta-analysis.** *Lancet* 2009;373:463–72
18. Carlisle E, Luna M, Tsou PM, et al. **Percent spinal canal compromise on MRI utilized for predicting the need for surgical treatment in single-level lumbar intervertebral disc herniation.** *Spine J* 2005;5:608–14
19. Lurie JD, Moses RA, Tosteson AN, et al. **Magnetic resonance imaging predictors of surgical outcome in patients with lumbar intervertebral disc herniation.** *Spine (Phila Pa 1976)* 2013;38:1216–25
20. Greenberg JO, Schnell RG. **Magnetic resonance imaging of the lumbar spine in asymptomatic adults: cooperative study—American Society of Neuroimaging.** *J Neuroimaging* 1991;1:2–7
21. Teraguchi M, Yoshimura N, Hashizume H, et al. **Prevalence and distribution of intervertebral disc degeneration over the entire spine in a population-based cohort: the Wakayama Spine Study.** *Osteoarthritis Cartilage* 2014;22:104–10
22. Jarvik JJ, Hollingworth W, Heagerty P, et al. **The Longitudinal Assessment of Imaging and Disability of the Back (LAIDBack) study: baseline data.** *Spine (Phila Pa 1976)* 2001;26:1158–66
23. Jarvik JG, Hollingworth W, Heagerty PJ, et al. **Three-year incidence of low back pain in an initially asymptomatic cohort: clinical and imaging risk factors.** *Spine (Phila Pa 1976)* 2005;30:1541–48; discussion 1549
24. Arana E, Kovacs FM, Royuela A, et al. **Influence of nomenclature in the interpretation of lumbar disk contour on MR imaging: a comparison of the agreement using the combined task force and the Nordic nomenclatures.** *AJNR Am J Neuroradiol* 2011;32:1143–48
25. Arana E, Royuela A, Kovacs FM, et al. **Lumbar spine: agreement in the interpretation of 1.5-T MR images by using the Nordic Modic Consensus Group classification form.** *Radiology* 2010;254:809–17
26. Thornton A, Lee P. **Publication bias in meta-analysis: its causes and consequences.** *J Clin Epidemiol* 2000;53:207–16
27. Boden SD, Riew KD, Yamaguchi K, et al. **Orientation of the lumbar facet joints: association with degenerative disc disease.** *J Bone Joint Surg Am* 1996;78:403–11
28. Boos N, Rieder R, Schade V, et al. **1995 Volvo Award in clinical sciences: the diagnostic accuracy of magnetic resonance imaging, work perception, and psychosocial factors in identifying symptomatic disc herniations.** *Spine (Phila Pa 1976)* 1995;20:2613–25
29. Capel A, Medina FS, Medina D, et al. **Magnetic resonance study of lumbar disks in female dancers.** *Am J Sports Med* 2009;37:1208–13
30. Danielson B, Willen J. **Axially loaded magnetic resonance image of the lumbar spine in asymptomatic individuals.** *Spine (Phila Pa 1976)* 2001;26:2601–06
31. Dora C, Walchli B, Elfering A, et al. **The significance of spinal canal dimensions in discriminating symptomatic from asymptomatic disc herniations.** *Eur Spine J* 2002;11:575–81
32. Edmondston SJ, Song S, Bricknell RV, et al. **MRI evaluation of lumbar spine flexion and extension in asymptomatic individuals.** *Man Ther* 2000;5:158–64
33. Erkintalo MO, Salminen JJ, Alanen AM, et al. **Development of degenerative changes in the lumbar intervertebral disk: results of a prospective MR imaging study in adolescents with and without low-back pain.** *Radiology* 1995;196:529–33
34. Feng T, Zhao P, Liang G. **Clinical significance on protruded nucleus pulposus: a comparative study of 44 patients with lumbar intervertebral disc protrusion and 73 asymptomatic controls in tridimentional computed tomography** [in Chinese]. *Zhongguo Zhong Xi Yi Jie He Za Zhi* 2000;20:347–49
35. Gibson MJ, Szypryt EP, Buckley JH, et al. **Magnetic resonance imaging of adolescent disc herniation.** *J Bone Joint Surg Br* 1987;69:699–703
36. Hamanishi C, Kawabata T, Yosii T, et al. **Schmorl's nodes on magnetic resonance imaging. Their incidence and clinical relevance.** *Spine (Phila Pa 1976)* 1994;19:450–53
37. Healy JF, Healy BB, Wong WH, et al. **Cervical and lumbar MRI in asymptomatic older male lifelong athletes: frequency of degenerative findings.** *J Comput Assist Tomogr* 1996;20:107–12
38. Jensen MC, Brant-Zawadzki MN, Obuchowski N, et al. **Magnetic resonance imaging of the lumbar spine in people without back pain.** *N Engl J Med* 1994;331:69–73
39. Kanayama M, Togawa D, Takahashi C, et al. **Cross-sectional magnetic resonance imaging study of lumbar disc degeneration in 200 healthy individuals.** *J Neurosurg Spine* 2009;11:501–07
40. Karakida O, Ueda H, Ueda M, et al. **Diurnal T2 value changes in the lumbar intervertebral discs.** *Clin Radiol* 2003;58:389–92
41. Kjaer P, Leboeuf-Yde C, Korsholm L, et al. **Magnetic resonance imaging and low back pain in adults: a diagnostic imaging study of 40-year-old men and women.** *Spine (Phila Pa 1976)* 2005;30:1173–80
42. Kovacs FM, Arana E, Royuela A, et al. **Disc degeneration and chronic low back pain: an association which becomes nonsignificant when endplate changes and disc contour are taken into account.** *Neuroradiology* 2014;56:25–33
43. Matsumoto M, Okada E, Toyama Y, et al. **Tandem age-related lumbar and cervical intervertebral disc changes in asymptomatic subjects.** *Eur Spine J* 2013;22:708–13
44. Paajanen H, Erkintalo M, Parkkola R, et al. **Age-dependent correlation of low-back pain and lumbar disc degeneration.** *Arch Orthop Trauma Surg* 1997;116:106–07
45. Paajanen H, Erkintalo M, Kuusela T, et al. **Magnetic resonance study of disc degeneration in young low-back pain patients.** *Spine* 1989;14:982–85
46. Ranson CA, Kerslake RW, Burnett AF, et al. **Magnetic resonance imaging of the lumbar spine in asymptomatic professional fast bowlers in cricket.** *J Bone Joint Surg Br* 2005;87:1111–16
47. Savage RA, Whitehouse GH, Roberts N. **The relationship between the magnetic resonance imaging appearance of the lumbar spine and low back pain, age and occupation in males.** *Eur Spine J* 1997;6:106–14

48. Silcox DH 3rd, Horton WC, Silverstein AM. **MRI of lumbar intervertebral discs: diurnal variations in signal intensities.** *Spine (Phila Pa 1976)* 1995;20:807–11; discussion 811–12
49. Stadnik TW, Lee RR, Coen HL, et al. **Annular tears and disk herniation: prevalence and contrast enhancement on MR images in the absence of low back pain or sciatica.** *Radiology* 1998;206: 49–55
50. Szypryt EP, Twining P, Mulholland RC, et al. **The prevalence of disc degeneration associated with neural arch defects of the lumbar spine assessed by magnetic resonance imaging.** *Spine (Phila Pa 1976)* 1989;14:977–81
51. Weinreb JC, Wolbarsht LB, Cohen JM, et al. **Prevalence of lumbosacral intervertebral disk abnormalities on MR images in pregnant and asymptomatic nonpregnant women.** *Radiology* 1989;170: 125–28
52. Weishaupt D, Zanetti M, Hodler J, et al. **MR imaging of the lumbar spine: prevalence of intervertebral disk extrusion and sequestration, nerve root compression, end plate abnormalities, and osteoarthritis of the facet joints in asymptomatic volunteers.** *Radiology* 1998;209:661–66
53. Zobel BB, Vadalà G, Del Vescovo R, et al. **T1rho magnetic resonance imaging quantification of early lumbar intervertebral disc degeneration in healthy young adults.** *Spine (Phila Pa 1976)* 2012;37: 1224–30

Trevo® XP ProVue Retrievers

See package insert for complete indications, complications, warnings, and instructions for use.

INDICATIONS FOR USE

The Trevo Retriever is intended to restore blood flow in the neurovasculature by removing thrombus in patients experiencing ischemic stroke within 8 hours of symptom onset. Patients who are ineligible for intravenous tissue plasminogen activator (IV t-PA) or who fail IV t-PA therapy are candidates for treatment.

COMPLICATIONS

Procedures requiring percutaneous catheter introduction should not be attempted by physicians unfamiliar with possible complications which may occur during or after the procedure. Possible complications include, but are not limited to, the following: air embolism; hematoma or hemorrhage at puncture site; infection; distal embolization; pain/headache; vessel spasm, thrombosis, dissection, or perforation; emboli; acute occlusion; ischemia; intracranial hemorrhage; false aneurysm formation; neurological deficits including stroke; and death.

COMPATIBILITY

3x20 mm retrievers are compatible with Trevo® Pro 14 Microcatheters (REF 90231) and Trevo® Pro 18 Microcatheters (REF 90238).
4x20 mm retrievers are compatible with Trevo® Pro 18 Microcatheters (REF 90238). Compatibility of the Retriever with other microcatheters has not been established. Performance of the Retriever device may be impacted if a different microcatheter is used.
The Merci® Balloon Guide Catheters are recommended for use during thrombus removal procedures.
Retrievers are compatible with the Abbott Vascular DOC® Guide Wire Extension (REF 22260)

WARNINGS

- Contents supplied STERILE, using an ethylene oxide (EO) process.Nonpyrogenic.
- To reduce risk of vessel damage, adhere to the following recommendations:
  - Take care to appropriately size Retriever to vessel diameter at intended site of deployment.
  - Do not perform more than six (6) retrieval attempts in same vessel using Retriever devices.
  - Maintain Retriever position in vessel when removing or exchanging Microcatheter.
- To reduce risk of kinking/fracture, adhere to the following recommendations:
  - Immediately after unsheathing Retriever, position Microcatheter tip marker just proximal to shaped section. Maintain Microcatheter tip marker just proximal to shaped section of Retriever during manipulation and withdrawal.
  - Do not rotate or torque Retriever.
  - Use caution when passing Retriever through stented arteries.
- Do not resterilize and reuse. Structural integrity and/or function may be impaired by reuse or cleaning.
- The Retriever is a delicate instrument and should be handled carefully. Before use and when possible during procedure, inspect device carefully for damage. Do not use a device that shows signs of damage. Damage may prevent device from functioning and may cause complications.
- Do not advance or withdraw Retriever against resistance or significant vasospasm. Moving or torquing device against resistance or significant vasospasm may result in damage to vessel or device. Assess cause of resistance using fluoroscopy and if needed resheath the device to withdraw.
- If Retriever is difficult to withdraw from the vessel, do not torque Retriever. Advance Microcatheter distally, gently pull Retriever back into Microcatheter, and remove Retriever and Microcatheter as a unit. If undue resistance is met when withdrawing the Retriever into the Microcatheter, consider extending the Retriever using the Abbott Vascular DOC guidewire extension (REF 22260) so that the Microcatheter can be exchanged for a larger diameter catheter such as a DAC® catheter. Gently withdraw the Retriever into the larger diameter catheter.
- Administer anti-coagulation and anti-platelet medications per standard institutional guidelines.

PRECAUTIONS

- Prescription only – device restricted to use by or on order of a physician.
- Store in cool, dry, dark place.
- Do not use open or damaged packages.
- Use by "Use By" date.
- Exposure to temperatures above 54°C (130°F) may damage device and accessories. Do not autoclave.
- Do not expose Retriever to solvents.
- Use Retriever in conjunction with fluoroscopic visualization and proper anti-coagulation agents.
- To prevent thrombus formation and contrast media crystal formation, maintain a constant infusion of appropriate flush solution between guide catheter and Microcatheter and between Microcatheter and Retriever or guidewire.
- Do not attach a torque device to the shaped proximal end of DOC® Compatible Retriever. Damage may occur, preventing ability to attach DOC® Guide Wire Extension.

Concentric Medical
301 East Evelyn
Mountain View, CA 94041

EC REP

EMERGO Europe
Molenstraat 15
2513 BH, The Hague
The Netherlands

CE 0459

Stryker Neurovascular
47900 Bayside Parkway
Fremont, CA 94538

stryker.com/neurovascular
stryker.com/emea/neurovascular

Date of Release: JUN/2014

EX_EN_GL

PHYSICIANS BOOST THE ECONOMY.

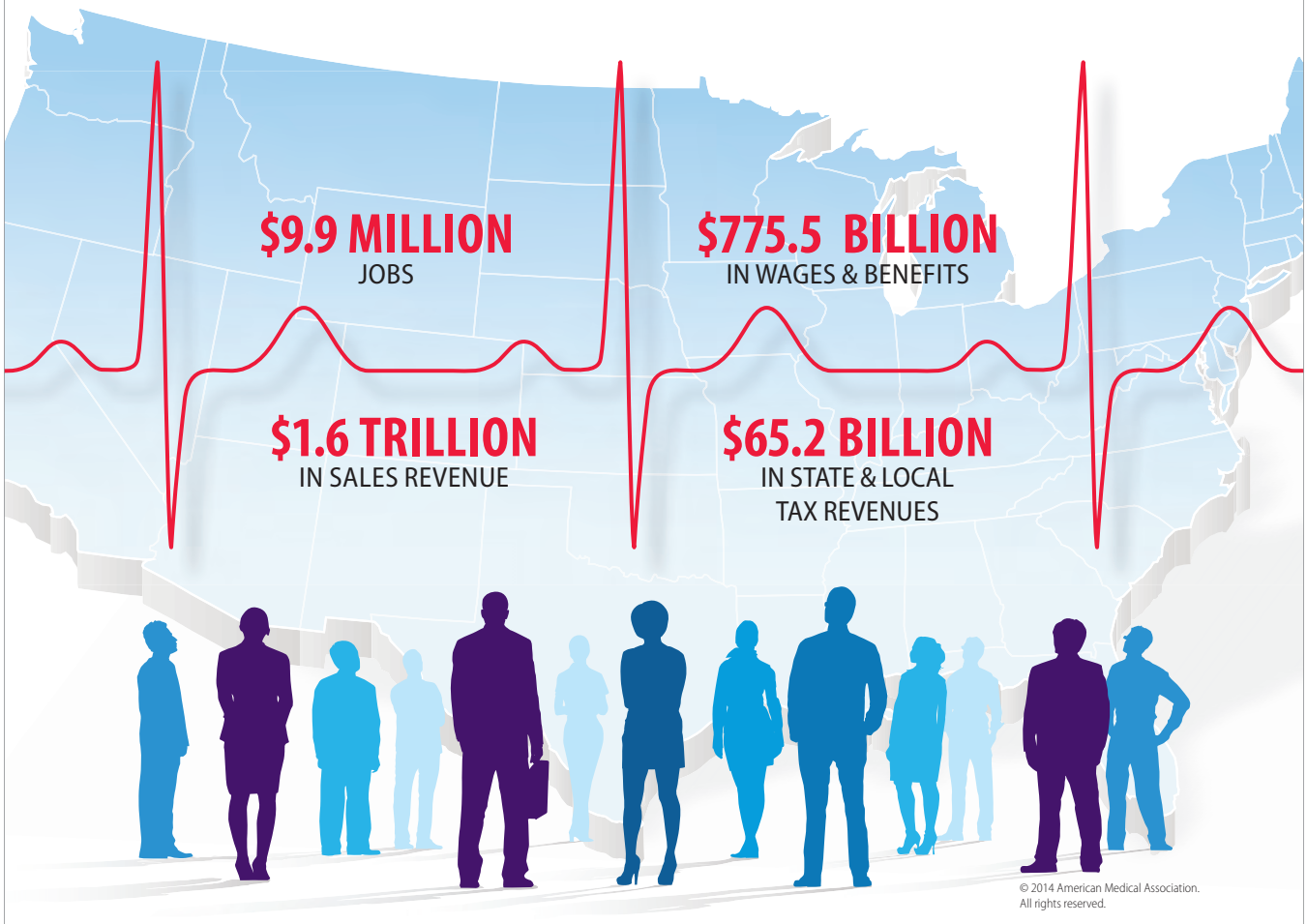

See the effects across the nation.

The American Medical Association 2014 Economic Impact Study shows how much physicians add to the economic health of our nation.

Check the effect physicians have on the U.S. economy by viewing the entire national report from the AMA Advocacy Resource Center at **ama-assn.org/go/eis**. Visit the AMA at the American Society of Neuroradiology 2015 Annual Meeting to learn more about this study and other AMA resources.

AMA
AMERICAN MEDICAL ASSOCIATION

Please activate your 2015 AMA membership by calling (800) 262-3211 or visit ama-assn.org/go/join.

American Society of Neuroradiology Future Annual Meetings

ASNR 2016 – 54th Annual Meeting & The Foundation of the ASNR Symposium 2016

May 21–26 • Washington Marriott Wardman Park • Washington, DC

ASNR 2017 – 55th Annual Meeting & The Foundation of the ASNR Symposium 2017

April 22-27 • Long Beach Convention & Entertainment Center • Long Beach, California

ASNR 2018 – 56th Annual Meeting & The Foundation of the ASNR Symposium 2018

June 2-7 • Vancouver Convention Centre • Vancouver, B.C., Canada

ASNR 2019 – 57th Annual Meeting & The Foundation of the ASNR Symposium 2019

May 18–23 • Hynes Convention Center • Boston, Massachusetts

Request Programming and Registration Materials for the ASNR 54th Annual Meeting, Contact:

ASNR 54th Annual Meeting
c/o American Society of Neuroradiology
800 Enterprise Drive, Suite 205
Oak Brook, Illinois 60523-4216

Phone: 630-574-0220
Fax: 630-574-0661
Email: meetings@asnr.org
Website: www.asnr.org/2016

Scan now to visit our website

A New Wave of Radiology

K-RAD

Open · Balanced · Sustainable

KCR 2015

The 71st Korean Congress of Radiology
And Annual Delegate Meeting of
The Korean Society of Radiology

The Korean Society of Radiology

About KCR 2015

Congress Title	The 71st Korean Congress of Radiology
Date	September 9 (Wed) – 12 (Sat), 2015
Venue	Coex, Seoul, Korea
Official Languages	English & Korean
Hosted by	The Korean Society of Radiology (KSR)
Website	www.kcr4u.org

KCR 2015 Highlights

- 3,000 participants from all around the world
- More than 180 world-renowned invited guests
- Instructive scientific programs in various fields of radiology
- Panel exhibition on KSR history in commemoration of the host society's 70th anniversary
- 150 technical exhibition booths
- Scholarships and awards
- Held in September, the best season to visit Korea

Call for Abstracts

The Scientific Committee of KCR 2015 invites all interested individuals to submit abstracts for the scientific sessions and exhibition at KCR 2015 from March to **May 18 (Mon), 2015**. Abstracts should be submitted through the e-submission system at the congress website.

Scientific Program

Opening Session
(President's Address, Congress Lecture)
Plenary Lecture I, II
Pre-congress
Joint Symposium with International Societies
Meet the Professor Sessions
Categorical Courses
Interactive Sessions
Refresher Courses
Special Focus Sessions
Scientific Sessions & Exhibition
Multisession Courses
Image Interpretation Session
Case of the Day
What's New Session
Visionary Education Session
Sunrise Sessions
Luncheon Symposia

Scholarships & Awards

Travel Awards (USD 500)

Awarded to foreign presenters of abstracts that are accepted for presentation at the scientific sessions or exhibition.

Best Scientific Exhibition Awards

Grand Prix	KRW 500,000 (1 winner)
Gold	KRW 300,000 each (2 winners or more)
Silver	KRW 200,000 each (5 winners or more)

KSR International Membership

Benefits

- No membership dues
- Discount of KCR registration fee
- Free subscription to KSR news
- Free on-line access to Korean Journal of Radiology (KJR)
- Free on-line access to KSR website and e-learning system
- Priority in the consideration for KSR fellowships

Please do not miss the chance to register for the KCR 2015 at a discounted fee by becoming a KSR International Member.

**Anyone who is interested in KSR International Membership should contact the KSR Office by e-mail (office@radiology.or.kr).*

KCR 2015 Secretariat InSession International Convention Services, Inc.
4Fl., 10, Yeoksam-ro 7-gil, Gangnam-gu, Seoul 135-936, Korea
Tel. +82-2-3452-7199, +82-2-3471-8555 Fax. +82-2-521-8683 E-mail. info@kcr4u.org

www.kcr4u.org

Simplify
the MOC Process

Manage
your CME Credits Online

CMEgateway.org

Available to Members of Participating Societies

- American Board of Radiology (ABR)
- American College of Radiology (ACR)
- American Roentgen Ray Society (ARRS)
- American Society of Neuroradiology (ASNR)
- Commission on Accreditation of Medical Physics Educational Programs, Inc. (CAMPEP)
- Radiological Society of North America (RSNA)
- Society of Interventional Radiology (SIR)
- SNM
- The Society for Pediatric Radiology (SPR)

It's Easy and Free!

Log on to CME Gateway to:

- View or print reports of your CME credits from multiple societies from a single access point.
- Print an aggregated report or certificate from each participating organization.
- Link to SAMs and other tools to help with maintenance of certification.

American Board of Radiology (ABR) participation!

By activating ABR in your organizational profile, your MOC–fulfilling CME and SAM credits can be transferred to your own personalized database on the ABR Web site.

Sign Up Today!

go to CMEgateway.org

AJNR

Go Green!

AJNR urges American Society of Neuroradiology members to reduce their environmental footprint by voluntarily suspending their print subscription.

The savings in paper, printing, transportation, and postage not only help members cut down on clutter, but go to fund new electronic enhancements and expanded content.

The digital edition of *AJNR* presents the print version in its entirety, along with extra features including:

- Publication Preview
- Case of the Week
- Podcasts
- Special Collections
- The *AJNR* Blog
- Weekly Poll

It also **reaches subscribers much faster than print**. An **electronic table of contents** will be sent directly to your mailbox to notify you as soon as it publishes.

Readers can **search, reference, and bookmark** current and archived content 24 hours a day on www.ajnr.org, rather than thumb through stacks of accumulated paper issues for articles and images they need.

http://www.ajnr.org/cgi/feedback

ASNR members who wish to opt out of print can do so by using the Feedback form on the *AJNR* Website (**http://www.ajnr.org/cgi/feedback**). Just type "Go Green" in the subject line to stop print and spare our ecosystem.

DOTAREM® (gadoterate meglumine) injection, for intravenous use
Initial U.S. Approval: 2013

BRIEF SUMMARY OF PRESCRIBING INFORMATION
CONSULT PACKAGE INSERT FOR FULL PRESCRIBING INFORMATION

WARNING: NEPHROGENIC SYSTEMIC FIBROSIS (NSF)

Gadolinium-based contrast agents (GBCAs) increase the risk for NSF among patients with impaired elimination of the drugs. Avoid use of GBCAs in these patients unless the diagnostic information is essential and not available with non-contrasted MRI or other modalities. NSF may result in fatal or debilitating fibrosis affecting the skin, muscle and internal organs.

- **The risk for NSF appears highest among patients with:**
  - **Chronic, severe kidney disease (GFR < 30 mL/min/1.73m^2), or**
  - **Acute kidney injury.**
- **Screen patients for acute kidney injury and other conditions that may reduce renal function. For patients at risk for chronically reduced renal function (e.g. age > 60 years, hypertension, diabetes), estimate the glomerular filtration rate (GFR) through laboratory testing (5.1).**
- **For patients at highest risk for NSF, do not exceed the recommended DOTAREM dose and allow a sufficient period of time for elimination of the drug from the body prior to any re-administration *[see Warnings and Precautions (5.1)]*.**

1 INDICATIONS AND USAGE

DOTAREM is a gadolinium-based contrast agent indicated for intravenous use with magnetic resonance imaging (MRI) in brain (intracranial), spine and associated tissues in adult and pediatric patients (2 years of age and older) to detect and visualize areas with disruption of the blood brain barrier (BBB) and/or abnormal vascularity. (1)

4 CONTRAINDICATIONS

History of clinically important hypersensitivity reactions to DOTAREM. (4)

5 WARNINGS AND PRECAUTIONS

5.1 Nephrogenic Systemic Fibrosis

Gadolinium-based contrast agents (GBCAs) increase the risk for nephrogenic systemic fibrosis (NSF) among patients with impaired elimination of the drugs. Avoid use of GBCAs among these patients unless the diagnostic information is essential and not available with non-contrast MRI or other modalities. The GBCA-associated NSF risk appears highest for patients with chronic, severe kidney disease (GFR < 30 mL/min/1.73m^2) as well as patients with acute kidney injury. The risk appears lower for patients with chronic, moderate kidney disease (GFR 30 - 59 mL/min/1.73m^2) and little, if any, for patients with chronic, mild kidney disease (GFR 60 - 89 mL/min/1.73m^2). NSF may result in fatal or debilitating fibrosis affecting the skin, muscle and internal organs. Report any diagnosis of NSF following DOTAREM administration to Guerbet LLC (1-877-729-6679) or FDA (1-800-FDA-1088 or www.fda.gov/medwatch).

Screen patients for acute kidney injury and other conditions that may reduce renal function. Features of acute kidney injury consist of rapid (over hours to days) and usually reversible decrease in kidney function, commonly in the setting of surgery, severe infection, injury or drug-induced kidney toxicity. Serum creatinine levels and estimated GFR may not reliably assess renal function in the setting of acute kidney injury. For patients at risk for chronically reduced renal function (e.g., age > 60 years, diabetes mellitus or chronic hypertension), estimate the GFR through laboratory testing.

Among the factors that may increase the risk for NSF are repeated or higher than recommended doses of a GBCA and the degree of renal impairment at the time of exposure. Record the specific GBCA and the dose administered to a patient. For patients at highest risk for NSF, do not exceed the recommended DOTAREM dose and allow a sufficient period of time for elimination of the drug prior to re-administration. For patients receiving hemodialysis, physicians may consider the prompt initiation of hemodialysis following the administration of a GBCA in order to enhance the contrast agent's elimination. The usefulness of hemodialysis in the prevention of NSF is unknown *[see Dosage and Administration (2) and Clinical Pharmacology (12)]*.

5.2 Hypersensitivity Reactions

Anaphylactic and anaphylactoid reactions have been reported with DOTAREM, involving cardiovascular, respiratory, and/or cutaneous manifestations. Some patients experienced circulatory collapse and died. In most cases, initial symptoms occurred within minutes of DOTAREM administration and resolved with prompt emergency treatment *[see Adverse Reactions (6)]*.

- Before DOTAREM administration, assess all patients for any history of a reaction to contrast media, bronchial asthma and/or allergic disorders. These patients may have an increased risk for a hypersensitivity reaction to DOTAREM.
- Administer DOTAREM only in situations where trained personnel and therapies are promptly available for the treatment of hypersensitivity reactions, including personnel trained in resuscitation.
- During and following DOTAREM administration, observe patients for signs and symptoms of hypersensitivity reactions.

5.3 Acute Kidney Injury

In patients with chronically reduced renal function, acute kidney injury requiring dialysis has occurred with the use of GBCAs. The risk of acute kidney injury may increase with increasing dose of the contrast agent; administer the lowest dose necessary for adequate imaging. Screen all patients for renal impairment by obtaining a history and/or laboratory tests. Consider follow-up renal function assessments for patients with a history of renal dysfunction.

5.4 Extravasation and Injection Site Reactions

Ensure catheter and venous patency before the injection of DOTAREM. Extravasation into tissues during DOTAREM administration may result in tissue irritation *[see Nonclinical Toxicology (13.2)]*.

6 ADVERSE REACTIONS

GBCAs have been associated with a risk for NSF *[see Warnings and Precautions (5.1)]*. NSF has not been reported in patients with a clear history of exposure to DOTAREM alone. For hypersensitivity reactions and acute kidney injury see Warnings and Precautions *(5.2) and (5.3)*.

6.1 Clinical Studies Experience

Because clinical trials are conducted under widely varying conditions, adverse reaction rates observed in the clinical trials of a drug cannot be directly compared to rates in the clinical trials of another drug and may not reflect the rates observed in clinical practice.

The data described below reflect DOTAREM exposure in 2813 patients, representing 2672 adults and 141 pediatric patients. Overall, 55% of the patients were men. In clinical trials where ethnicity was recorded the ethnic distribution was 74% Caucasian, 12% Asian, 4% Black, and 10% others. The average age was 53 years (range from 0.1 to 97 years).

Overall, 3.9% of patients reported at least one adverse reaction, primarily occurring immediately or several days following DOTAREM administration. Most adverse reactions were mild or moderate in severity and transient in nature.

Table 1 lists adverse reactions that occurred in ≥ 0.2% patients who received DOTAREM.

Table 1: Adverse Reactions in Clinical Trials

Reaction	Rate (%) n = 2813
Nausea	0.6%
Headache	0.5%
Injection Site Pain	0.4%
Injection Site Coldness	0.2%
Burning Sensation	0.2%

Adverse reactions that occurred with a frequency < 0.2% in patients who received DOTAREM include: feeling cold, rash, somnolence, fatigue, dizziness, vomiting, pruritus, paresthesia, dysgeusia, pain in extremity, anxiety, hypertension, palpitations, oropharyngeal discomfort, serum creatinine increased and injection site reactions, including site inflammation, extravasation, pruritus, and warmth.

Adverse Reactions in Pediatric Patients

During clinical trials, 141 pediatric patients (7 aged < 24 months, 33 aged 2 - 5 years, 58 aged 6 - 11 years and 43 aged 12 -17) received DOTAREM. Overall, 6 pediatric patients (4.3%) reported at least one adverse reaction following DOTAREM administration. The most frequently reported adverse reaction was headache (1.5%). Most adverse events were mild in severity and transient in nature, and all patients recovered without treatment.

6.2 Postmarketing Experience

The following additional adverse reactions have been identified during postmarketing use of DOTAREM. Because these reactions are reported voluntarily from a population of uncertain size, it is not always possible to reliably estimate their frequency or establish a causal relationship to drug exposure.

- bradycardia, tachycardia, arrhythmia
- hypersensitivity / anaphylactoid reactions including cardiac arrest, respiratory arrest, cyanosis, pharyngeal edema, laryngospasm, bronchospasm, angioedema, conjunctivitis, ocular hyperemia, eyelid edema, lacrimation increased, hyperhidrosis, urticaria
- coma, convulsion, syncope, presyncope, parosmia, tremor
- muscle contracture, muscle weakness
- diarrhea, salivary hypersecretion
- malaise, fever
- NSF, in patients whose reports were confounded by the receipt of other GBCAs or in situations where receipt of other GBCAs could not be ruled out. No unconfounded cases of NSF have been reported with DOTAREM.
- superficial phlebitis

7 DRUG INTERACTIONS

DOTAREM does not interfere with serum and plasma calcium measurements determined by colorimetric assays. Specific drug interaction studies with DOTAREM have not been conducted.

8 USE IN SPECIFIC POPULATIONS

8.1 Pregnancy

Pregnancy Category C

There are no adequate and well-controlled studies with DOTAREM conducted in pregnant women. Limited published human data on exposure to other GBCAs during pregnancy did not show adverse effects in exposed neonates. No effects on embryo fetal development were observed in rats or rabbits at doses up to 10 mmol/kg/day in rats or 3 mmol/kg/day in rabbits. The doses in rats and rabbits were respectively 16 and 10 times the recommended human dose based on body surface area. DOTAREM should be used during pregnancy only if the potential benefit justifies the potential risk to the fetus.

While it is unknown if DOTAREM crosses the human placenta, other GBCAs do cross the placenta in humans and result in fetal exposure.

Reproductive and developmental toxicity studies were conducted with gadoterate meglumine in rats and rabbits. Gadoterate meglumine was administered intravenously in doses of 0, 2, 4 and 10 mmol/kg/day (or 3.2, 6.5 and 16.2 times the recommended human dose based on body surface area) to female rats for 14 days before mating throughout the mating period and until gestation day (GD) 17. Pregnant rabbits were intravenously administered gadoterate meglumine at the dose levels of 0, 1, 3 and 7 mmol/kg/day (or 3.3, 10 and 23 times the human doses based on body surface area) from GD6 to GD19. No effects on embryo fetal development were observed in rats or rabbits at doses up to 10 mmol/kg/day in rats or 3 mmol/kg/day in rabbits. Maternal toxicity was observed in rats at 10 mmol/kg/day (or 16 times the human dose based on body surface area) and in rabbits at 7 mmol/kg/day (23 times the human dose based on body surface area).

8.3 Nursing Mothers

It is not known whether DOTAREM is excreted in human milk. Limited case reports on use of GBCAs in nursing mothers indicate that 0.01 to 0.04% of the maternal gadolinium dose is excreted in human breast milk. Because many drugs are excreted in human milk, exercise caution when DOTAREM is administered to a nursing woman. Nonclinical data show that gadoterate meglumine is excreted into breast milk in very small amounts (< 0.1% of the dose intravenously administered) and absorption via the gastrointestinal tract is poor.

8.4 Pediatric Use

The safety and efficacy of DOTAREM at a single dose of 0.1 mmol/kg have been established in pediatric patients from 2 to 17 years of age. No dosage adjustment according to age is necessary in this population *[See Dosage and Administration (2.1) and Clinical Studies (14)]*. The safety and efficacy of DOTAREM have not been established in pediatric patients below 2 years of age. GFR does not reach adult levels until 1 year of age *[see Warnings and Precautions (5.1)]*.

8.5 Geriatric Use

In clinical studies of DOTAREM, 900 patients were 65 years of age and over, and 312 patients were 75 years of age and over. No overall differences in safety or efficacy were observed between these subjects and younger subjects. In general, use of DOTAREM in elderly patients should be cautious, reflecting the greater frequency of impaired renal function and concomitant disease or other drug therapy. No age-related dosage adjustment is necessary.

8.6 Renal Impairment

No DOTAREM dosage adjustment is recommended for patients with renal impairment. Gadoterate meglumine can be removed from the body by hemodialysis *[see Warnings and Precautions (5.1) and Clinical Pharmacology (12.3)]*.

10 OVERDOSAGE

DOTAREM administered to healthy volunteers and to patients at cumulative doses up to 0.3 mmol/kg was tolerated in a manner similar to lower doses. Adverse reactions to overdosage with DOTAREM have not been reported. Gadoterate meglumine can be removed from the body by hemodialysis *[See Clinical Pharmacology (12.3)]*.

13 NONCLINICAL TOXICOLOGY

13.1 Carcinogenesis, Mutagenesis, Impairment of Fertility

Long-term animal studies have not been performed to evaluate the carcinogenic potential of gadoterate meglumine.

Gadoterate meglumine did not demonstrate mutagenic potential in *in vitro* bacterial reverse mutation assays (Ames test) using Salmonella typhimurium, in an *in vitro* chromosome aberration assay in Chinese hamster ovary cells, in an *in vitro* gene mutation assay in Chinese hamster lung cells, nor in an *in vivo* mouse micronucleus assay.

No impairment of male or female fertility and reproductive performance was observed in rats after intravenous administration of gadoterate meglumine at the maximum tested dose of 10 mmol/kg/day (16 times the maximum human dose based on surface area), given during more than 9 weeks in males and more than 4 weeks in females. Sperm counts and sperm motility were not adversely affected by treatment with the drug.

13.2 Animal Toxicology and/or Pharmacology

Local intolerance reactions, including moderate irritation associated with infiltration of inflammatory cells were observed after perivenous injection in rabbits suggesting the possibility of local irritation if the contrast medium leaks around the veins in a clinical setting *[see Warnings and Precautions (5.4)]*.

17 PATIENT COUNSELING INFORMATION

17.1 Nephrogenic Systemic Fibrosis

Instruct patients to inform their healthcare provider if they:

- have a history of kidney disease, or
- have recently received a GBCA.

GBCAs increase the risk for NSF among patients with impaired elimination of the drugs. To counsel patients at risk for NSF:

- Describe the clinical manifestations of NSF.
- Describe procedures to screen for the detection of renal impairment.

Instruct the patients to contact their physician if they develop signs or symptoms of NSF following DOTAREM administration, such as burning, itching, swelling, scaling, hardening and tightening of the skin; red or dark patches on the skin; stiffness in joints with trouble moving, bending or straightening the arms, hands, legs or feet; pain in the hip bones or ribs; or muscle weakness.

17.2 Common Adverse Reactions

Inform patients that they may experience:

- Reactions along the venous injection site, such as mild and transient burning or pain or feeling of warmth or coldness at the injection site.
- Side effects of headache, nausea, abnormal taste and feeling hot.

17.3 General Precautions

Instruct patients receiving DOTAREM to inform their physician if they:

- Are pregnant or breastfeeding.
- Have a history of allergic reaction to contrast media, bronchial asthma or allergy.
- Are taking any medications.

Rx Only

Guerbet LLC
120 W 7th Street. Suite 108
Bloomington, IN 47404

Pre-filled syringes manufactured by Catalent, Belgium for Guerbet
Vials manufactured by Recipharm, France for Guerbet

GU06131043
Revised 06/2013

DOTAREM®
(gadoterate meglumine) Injection

Macrocyclic and Ionic...

DOTAREM

...There is only One.

The first and only macrocyclic and ionic gadolinium agent in its class.[1]

Visit us at **ASNR 2015 Booth #401**

Global clinical experience with over **50 million doses** administered worldwide.[2]

INDICATION[1]

DOTAREM is a gadolinium-based contrast agent indicated for intravenous use with magnetic resonance imaging (MRI) in brain (intracranial), spine and associated tissues in adult and pediatric patients (2 years of age and older) to detect and visualize areas with disruption of the blood brain barrier (BBB) and/or abnormal vascularity.

IMPORTANT SAFETY INFORMATION[1]

WARNING: NEPHROGENIC SYSTEMIC FIBROSIS (NSF)

Gadolinium-based contrast agents (GBCAs) increase the risk for NSF among patients with impaired elimination of the drugs. Avoid use of GBCAs in these patients unless the diagnostic information is essential and not available with non-contrasted MRI or other modalities. NSF may result in fatal or debilitating fibrosis affecting the skin, muscle and internal organs.

- **The risk for NSF appears highest among patients with:**
  - **Chronic, severe kidney disease (GFR < 30 mL/min/1.73m²), or**
  - **Acute kidney injury.**
- **Screen patients for acute kidney injury and other conditions that may reduce renal function. For patients at risk for chronically reduced renal function (for example, age > 60 years, hypertension or diabetes), estimate the glomerular filtration rate (GFR) through laboratory testing [*see Warnings and Precautions*].**
- **For patients at highest risk for NSF, do not exceed the recommended DOTAREM dose and allow a sufficient period of time for elimination of the drug from the body prior to any re-administration [*see Warnings and Precautions*].**

Contraindicated in patients with a history of clinically important hypersensitivity reactions to DOTAREM.

The possibility of serious or life-threatening anaphylactoid/anaphylactic reactions with cardiovascular, respiratory or cutaneous manifestations, ranging from mild to severe, including death, should be considered. Monitor patients closely for need of emergency cardiorespiratory support.

In patients with chronically reduced renal function, acute kidney injury requiring dialysis has occurred with the use of GBCAs. The risk of acute kidney injury may increase with increasing dose of the contrast agent; administer the lowest dose necessary for adequate imaging. Screen all patients for renal impairment by obtaining a history and/or laboratory tests. Consider follow-up renal function assessments for patients with a history of renal dysfunction.

Ensure catheter and venous patency before the injection of DOTAREM. Extravasation into tissues during DOTAREM administration may result in tissue irritation.

The most common adverse reactions associated with DOTAREM in clinical studies were nausea, headache, injection site pain, injection site coldness, and burning sensation.

For more information about DOTAREM, including Boxed WARNING, please see the Full Prescribing Information.

Please see adjacent Brief Summary of Prescribing Information.

DOTAREM is a registered trademark of Guerbet and is available by prescription only.

GU02151008

References: 1. Dotarem [package insert]. Bloomington, IN: Guerbet LLC; 2014. **2.** Data on file, Guerbet LLC.

www.guerbet-us.com

Guerbet

Contrast for Life